

POLISH SOCIETY OF THEORETICAL AND APPLIED MECHANICS

**JOURNAL OF THEORETICAL
AND APPLIED MECHANICS**

No. 1 • Vol. 57

Quarterly

WARSAW, JANUARY 2019

JOURNAL OF THEORETICAL AND APPLIED MECHANICS

(until 1997 Mechanika Teoretyczna i Stosowana, ISSN 0079-3701)

Beginning with Vol. 45, No. 1, 2007, *Journal of Theoretical and Applied Mechanics* (JTAM) has been selected for coverage in Thomson Reuters products and custom information services. Now it is indexed and abstracted in the following:

- **Science Citation Index Expanded** (also known as SciSearch®)
- **Journal Citation Reports/Science Edition**

Advisory Board

MICHAŁ KLEIBER (Poland) – Chairman

- JORGE A.C. AMBROSIO (Portugal) * ANGEL BALTOV (Bulgaria) * ROMESH C. BATRA (USA)
* ALAIN COMBESCURE (France) * JÜRI ENGELBRECHT (Estonia) * WITOLD GUTKOWSKI (Poland)
* JÓZEF KUBIK (Poland) * ZENON MRÓZ (Poland) * RYSZARD PARKITNY (Poland)
* EKKEHARD RAMM (Germany) * EUGENIUSZ ŚWITOŃSKI (Poland) * HISAAKI TOBUSHI (Japan)
* ANDRZEJ TYLIKOWSKI (Poland) * DIETER WEICHERT (Germany) * JOSE E. WESFREID (France)
* JÓZEF WOJNAROWSKI (Poland) * JOSEPH ZARKA (France)
* VLADIMIR ZEMAN (Czech Republic)

Editorial Board

Editor-in-Chief – **WŁODZIMIERZ KURNIK**

Section Editors: IWONA ADAMIEC-WÓJCIK, PIOTR CUPIAŁ, KRZYSZTOF DEMS,
WITOLD ELSNER, ERIC FLORENTIN (France), ELŻBIETA JARZĘBOWSKA,
OLEKSANDR JEWTUSZENKO, PIOTR KOWALCZYK, ZBIGNIEW KOWALEWSKI, TOMASZ KRZYŻYŃSKI,
STANISŁAW KUKLA, TOMASZ ŁODYGOWSKI, EWA MAJCHRZAK, WIESŁAW NAGÓRKO,
JANUSZ NARKIEWICZ, PIOTR PRZYBYŁOWICZ, BŁAŻEJ SKOCZEŃ, ANDRZEJ STYCZEK,
JACEK SZUMBARSKI, UTZ VON WAGNER (Germany), JERZY WARMIŃSKI

Language Editor – PIOTR PRZYBYŁOWICZ

Technical Editor – EWA KOISAR

Secretary – ELŻBIETA WILANOWSKA



Articles in JTAM are published under Creative Commons Attribution – Non-commercial 3.0. Unported License <http://creativecommons.org/licenses/by-nc/3.0/legalcode>. By submitting an article for publication, the authors consent to the grant of the said license.



The journal content is indexed in Similarity Check, the Crossref initiative to prevent plagiarism.

* * * * *

Editorial Office

Al. Armii Ludowej 16, room 650

00-637 Warszawa, Poland

phone (+48 22) 825 7180, (+48) 664 099 345, e-mail: biuro@ptmts.org.pl

www.ptmts.org.pl/jtam.html

* * * * *



Ministerstwo Nauki
i Szkolnictwa Wyższego

Publication supported by Ministry of Science and Higher Education of Poland

(Journal of Theoretical and Applied Mechanics: 1) digitalizacja publikacji i monografi naukowych w celu zapewnienia i utrzymania otwartego dostępu do nich przez sieć Internet, 2) stworzenie anglojęzycznych wersji wydawanych publikacji, 3) wdrożenie procedur zabezpieczających oryginalność publikacji naukowych oraz zastosowane techniki zabezpieczeń – są finansowane w ramach umowy 699/P-DUN/2018 ze środków Ministra Nauki i Szkolnictwa Wyższego przeznaczonych na działalność upowszechniającą naukę)

NUMERICAL MODELING OF UNCERTAINTY IN ACOUSTIC PROPAGATION VIA GENERALIZED POLYNOMIAL CHAOS

KHALIL DAMMAK

*University of Sfax, National School of Engineers of Sfax, Mechanical Modeling and Manufacturing Laboratory (LA2MP),
Sfax, Tunisia, and*

*University of Rouen Normandie, LMN, National Institute of Applied Sciences (INSA Rouen), Rouen, France
e-mail: khalil.dammak@insa-rouen.fr*

SANA KOUBAA

*University of Sfax, National School of Engineers of Sfax, Mechanical Modeling and Manufacturing Laboratory (LA2MP),
Sfax, Tunisia*

ABDELKHALAK ELHAMI

University of Rouen Normandie, LMN, National Institute of Applied Sciences (INSA Rouen), Rouen, France

LASSAAD WALHA, MOHAMED HADDAR

*University of Sfax, National School of Engineers of Sfax, Mechanical Modeling and Manufacturing Laboratory (LA2MP),
Sfax, Tunisia*

This work aims at increasing the performance prediction for acoustic propagation systems that will operate in the presence of the inevitable parameters uncertainty. In the present contribution, the finite element method is applied to solve an acoustic problem described by the Helmholtz equation when the geometric and material properties present uncertainty. The influence of the uncertainty of physical parameters on the pressure field is discussed. The results using the polynomial chaos expansion method are compared with Monte Carlo simulations. It is shown that uncertainty levels in the input data could result in large variability in the calculated pressure field in the domain.

Keywords: finite element simulation, uncertainty quantification, acoustic propagation, generalized Polynomial Chaos

1. Introduction

The guided acoustic propagation is an important field of acoustics. This importance arises as a consequence of the need in reducing or increasing the sound intensity in some regions of wave-guides. The acoustic propagation in cylindrical wave-guides is a common field in structures like automotive and aircraft engines. The Helmholtz equation is normally used to model the propagation of acoustic waves (Cheung and Jin, 1991; Nark *et al.*, 2003, 2005; Taktak *et al.*, 2012). For a large set of problems, there is no analytical closed solution to this equation. Generally, a numerical procedure was applied to calculate the sound pressure field (Lins and Rochinha, 2009; Lan, 2005). The finite element (FE) simulation is a very powerful technique which can be applied to obtain an approximate solution to the Helmholtz equation. The deterministic simulation leads to an approximate and nominal solution of reality. In some cases, the behavior prediction of a system is especially difficult because of the variability induced by uncertainty. The challenge is to improve the performance of numerical simulations of guided acoustic propagation. Recently, the probabilistic modeling of mechanical problems has received attention of some researchers (Sepahvand and Marburg, 2014; Xia *et al.*, 2015). All of them are looking for

more robust models that take into account the random nature of some parameters: material properties, geometrical irregularities, boundary and initial conditions, operating conditions, loading. The numerical accuracy and error control have been employed in simulations for fluid structure interaction (Mansouri *et al.*, 2013) vibroacoustic problems (Dammak *et al.*, 20117b; Mansouri *et al.*, 2012a,b; Sepahvand and Marburg, 2014), CFD research (Xiu and Karniadakis, 2003) and dynamic responses of engineering structures (Yang and Kessissoglou, 2013). The application of the FE method to the Helmholtz equation has also been an object of certain studies concerning the error estimation and propagation (Ihlenburg and Babuska, 1995). In (Lins and Rochinha, 2009), the solution of acoustic problems was resolved numerically when the boundary conditions presented uncertainty. Nevertheless, according to (Lepage, 2006), there is a relative lack of information about how statistical distributions of some variables influence the distributional properties of the acoustic response. Based on literature reviews, one can distinguish two ways to include stochastic behavior in finite element simulations: the first is a statistical approach or a sampling method, like the Monte Carlo (MC) technique (Hurtado and Alvarez, 2012). In this method, a large number of samples of input variables are required for reasonable accuracy. The problem is then solved for each realization. This technique allows one to obtain the entire probability density function of any system variable. It is widely used since it is easier to implement and very robust. However, a huge number of realizations to be solved could lead to a prohibitive computational cost. The second probabilistic tool is a non-statistic approach or a non-sampling method, which results in analytical treatment of the stochastic process. It consists in the polynomial chaos (Fisher and Bhattacharya, 2008; Creamer, 2006; Ng and Eldred, 2012). It is a more efficient tool due to discretization of random parameters by a set of limited realizations. This theory was initiated by Ghanem and Spanos (1991) who used expansion in Wiener-Hermite polynomials to model stochastic processes with Gaussian random variables (Wiener, 1938). The convergence of such an expansion in the mean square sense has been shown (Cameron and Martin, 1947) and generalized to various continuous and discrete distributions using orthogonal polynomials following the so called Askey-scheme (Xiu and Karniadakis, 2002). This general extension is known as generalized polynomial chaos (gPC) (Wan and Karniadakis, 2006). Polynomial chaos gives a mathematical framework to separate the stochastic components of a system response from deterministic ones. According to (Xiu and Karniadakis, 2002, 2003), polynomial chaos did not receive much attention for a long time. In the numerical aspect, one can distinguish intrusive and non-intrusive methods. The first method is applied to systems in which the governing equations are known. In this case, the stochastic equations are used to generate a set of deterministic equations using the Galerkin method (Ghanem and Spanos, 1991), which are difficult to implement. Nonintrusive technique seems to be more efficient since it only requires simulations corresponding to particular samples of the random parameters, and no modifications are needed on the system model (Nechak *et al.*, 2013). It worth mentioning that works on numerical simulation of sound propagation in a three-dimensional duct coupled with uncertainty analysis remains infrequent. In (Taktak *et al.*, 2011), a numerical method of the modeling of sound propagation in circular and rectangular cross-section ducts in the presence of flow was developed and presented. The pressure acoustic field inside the duct was determined for several incident acoustic modes. In (Kesentini *et al.*, 2015), the wave finite element method was applied to study guided acoustical propagation. In those studies, uncertainties on the fluid-structure interaction were neglected.

In this paper, we aim at increasing the performance prediction for acoustic propagation systems that will operate in the presence of the inevitable parameters uncertainty associated with the geometric and material properties. The stochastic methods discussed above, MC and gPC, are implemented and integrated in finite element simulation for a circular cross-section duct. The simulation results are discussed, compared and validated with literature.

2. Governing equations of the physical problem

2.1. Acoustic propagation in a cylindrical duct

In this Section, the governing equations of sound propagation in circular cross-section ducts are presented in Fig. 1. The equation governing the acoustic behavior of a fluid is the Helmholtz

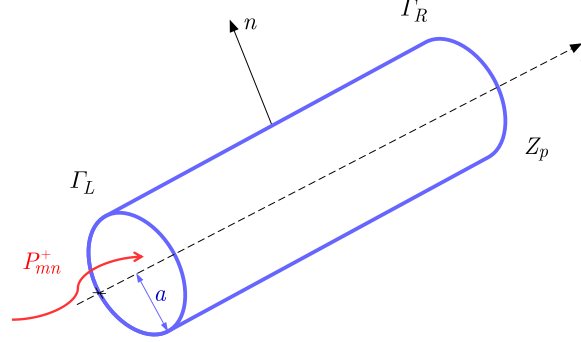


Fig. 1. Description of the cylindrical guide

equation (Taktak *et al.*, 2011; Kim and Nelson, 2004)

$$\Delta p_i + k^2 p_i = 0 \quad (2.1)$$

where Δ is the Laplacian operator, p_i is the acoustic pressure inside the studied duct and k is the total wave number. It is well noticed that the resolution of this equation depends on the duct geometry. In this work, a cylindrical cross-section duct is considered. For this kind of duct, the resolution Helmholtz equation in the cylindrical coordinates system is carried out by the variables separation method. The acoustic pressure is expressed as

$$P(r_i, \theta, z) = R(r_i)\Theta(\theta)Z(z) \quad (2.2)$$

where

$$Z(z) = Ae^{jk_z z} + Be^{-jk_z z} \quad \Theta(\theta) = \theta_1 e^{-jm\theta} + \theta_2 e^{jm\theta} \quad R(r_i) = C J_m(k_r r_i) \quad (2.3)$$

where A , B , $\theta_{1,2}$ and C are constants depending on boundaries conditions. The wave numbers are related by the dispersion relation (Taktak, 2008)

$$\Gamma_{mn}^2 + k_{mn}^2 - k^2 = 0 \quad (2.4)$$

In the case of a rigid wall, the radial wave number is defined by

$$\Gamma_{mn} = \frac{\chi_{mn}}{a} \quad (2.5)$$

where χ_{mn} is the n -th root of the derivative of J_m – the Bessel function of the first kind of the order m . Thus the modal analysis can be applied (Dammak *et al.*, 2017a; Blazejewski, 2013; Blazejewski *et al.*, 2014) and the acoustic pressure field inside the duct is obtained as

$$P(r_i, \theta, z, t) = \sum_{m=0}^{\infty} \sum_{n=0}^{\infty} P_{mn}(z) \Psi_{mn}(r_i, \theta) e^{-j\omega t} \quad (2.6)$$

where P_{mn} are the modal coefficients associated modes (m, n) defined by

$$P_{mn}(z) = A_{mn} e^{-jk_{mn} z} + B_{mn} e^{jk_{mn} z} \quad (2.7)$$

and Ψ_{mn} are the eigenfunctions of the enclosure (Blazejewski *et al.*, 2014; Meissner, 2008), which satisfy the Helmholtz equation and can be expressed as

$$\Psi_{mn}(r_i, \theta) = J_m\left(\chi_{mn} \frac{r_i}{a}\right) e^{jm\theta} \quad (2.8)$$

The Helmholtz equation will be solved numerically in Section 3.

2.2. Uncertainty modeling

In this Section, we introduce two classical techniques for representing random processes: the generalized Polynomial Chaos (gPC) and the Monte Carlo (MC) technique.

2.2.1. Polynomial chaos

The Polynomial Chaos was originally developed by Wiener (1938). It is a stochastic method based on spectral representation of the uncertainty. The PC decomposes a random function (or variable) into separable deterministic and stochastic components. Here, a brief mathematical review of this approach will be given. For instance, considering any random variable λ_i such as velocity, density, or pressure in a stochastic fluid dynamics problem, one can write (Nechak *et al.*, 2013)

$$\lambda_i(x, \xi) = \sum_{j=0}^{\infty} \bar{\lambda}_{i,j}(x) \phi_j(\xi) \quad (2.9)$$

where ξ is the random variable vector with a known joint density function $W(\xi)$, $\lambda_{i,j}$ is the deterministic component and $\phi_j(\xi)$ is the orthogonal polynomial function satisfying the orthogonality relation

$$\langle \phi_i, \phi_j \rangle = \int \phi_i \phi_j W(\xi) d\xi = \begin{cases} 0 & \text{if } i \neq j \\ \langle \phi_i, \phi_j \rangle & \text{if } i = j \end{cases} \quad (2.10)$$

where $\langle \cdot \rangle$ is the internal product operator. As a series expansion to infinity cannot be used in practice, the sum is truncated to a finite number of terms N_p , which is shown to be dependent on the gPC order p , and the stochastic dimension r denoting the number of uncertain parameters

$$\lambda_i(x, \xi) = \sum_{j=0}^{N_p} \bar{\lambda}_{i,j}(x) \phi_j(\xi) \quad (2.11)$$

with

$$N_p = \frac{(p+r)!}{p!r!} - 1 \quad (2.12)$$

For a random variable with certain distribution, the orthogonal function ϕ_j can be chosen in such a way that its weight function has the same form as the probability function $W(\xi)$. Then, computing λ_i is transformed into the problem of finding the coefficients $\bar{\lambda}_{i,j}$ of its truncated expansion (Smith *et al.*, 2007). To extend the application of the polynomial chaos theory to propagation of continuous non-normal input uncertainty distributions, Xiu and Karniadakis (2003) used a set of polynomials known as the Askey scheme to obtain the Wiener-Askey generalized Polynomial Chaos. Table 1 shows commonly used, Legendre, Hermite, and Laguerre polynomials and the associated probability density functions (PDF) included the Askey scheme. Legendre and Laguerre polynomials are optimal basis functions for uniform and exponential input uncertainty distributions respectively, whereas the Hermite polynomials are optimal for the normal distributions in terms of the convergence of the statistics.

The intrusive and non-intrusive approaches are generally defined to calculate these coefficients called stochastic modes. The non-intrusive approach seems to be more efficient since it only requires simulations corresponding to particular samples of random variables and it needs no modifications of the stochastic model, contrary to the intrusive approach. That is why only the non-intrusive approach is considered in this paper. This approach considers the deterministic model as a black-box and approximates the stochastic coefficients with formulas based

Table 1. Correspondence between the type of distribution and the type of base of chaos

Distribution	Density function	Polynomial	Weight function $W(\xi)$	Support range
Uniform	$\frac{1}{2}$	Legendre $L_e(\xi)$	1	$[-1, 1]$
Normal	$\frac{1}{\sqrt{2\pi}} \exp\left(-\frac{\xi^2}{2}\right)$	Hermite $H_n(\xi)$	$\exp\left(-\frac{\xi^2}{2}\right)$	$[-\infty, +\infty]$
Exponential	$\exp(-\xi)$	Lagrange $L_a(\xi)$	$\exp(-\xi)$	$[0, +\infty]$

on deterministic code assessment. The spectral projection (NISP) and regression are the main non-intrusive polynomial chaos methods used for uncertainty quantification. In the technique NISP (Ng and Eldred, 2012), once the solution is expressed in the base of polynomial chaos following general expression (2.11), it is projected, which determines stochastic coefficients as

$$\bar{\lambda}_{i,j}(x) = \frac{\langle \lambda_i(x, \xi), \phi_j(\xi) \rangle}{\langle \phi_j(\xi), \phi_j(\xi) \rangle} = \frac{1}{\langle \phi_j^2 \rangle} \int \lambda_i(x, \xi) \phi_j(\xi) W(\xi) d\xi \quad j = 0, \dots, N_p \quad (2.13)$$

The regression method (Blatman and Sudret, 2008) consists in calculating the stochastic coefficients so as to minimize the least squares sense, the gap ε between the solution of the stochastic model and its approximation in the base of generalized polynomial chaos

$$\varepsilon = \sum_{k=1}^Q \left[\lambda_i(x, \xi^{(k)}) - \sum_{j=0}^{N_p} \bar{\lambda}_{i,j}(x) \phi_j(\xi^{(k)}) \right] \quad (2.14)$$

The $\xi^{(k)}$ may be selected from the roots of a polynomial with the condition $Q > N_p + 1$, with Q being the number of Gauss points. By designating $\bar{\boldsymbol{\lambda}}_{i,j} = (\bar{\lambda}_{i,0}, \dots, \bar{\lambda}_{i,N_p})^T$, the vector of modal coefficients, \mathbf{Z} the matrix of elements $Z_{q,l} = \phi_l(\xi^{(q)})$ and $\boldsymbol{\lambda}_i = (\lambda_i(x, \xi^{(1)}), \dots, \lambda_i(x, \xi^{(q)}))$ the vector corresponding to the game simulations $\boldsymbol{\xi}^{(q)}$. and if the matrix $\mathbf{Z}^T \mathbf{Z}$ is non-singular then the optimal solution of the classical least squares problem is given by

$$\bar{\boldsymbol{\lambda}}_{i,j} = (\mathbf{Z}^T \mathbf{Z})^{-1} \mathbf{Z}^T \boldsymbol{\lambda}_i \quad (2.15)$$

The quality of the solution depends on the conditioning of the matrix $(\mathbf{Z}^T \mathbf{Z})$ called the Fischer matrix.

2.2.2. Monte Carlo theory

The MC method provides successive resolutions of a deterministic system incorporating uncertain parameters modeled by random variables. It generates, for all uncertain parameters and according to their probability distributions and their correlations, random simples. For each draw, a set of parameters is obtained and a deterministic calculation, following numerical (FES) or analytical models well defined, is made. The main advantage of this method is that it can be applied to any system, whatever is its size and complexity (linear, non-linear, etc.). A reasonable accuracy of the results requires a large number of draws which makes the MC method prohibitive in terms of computational cost. The standard MC approach considers functions of the following form

$$\mathbf{Y} = M(\mathbf{X}) \quad (2.16)$$

where M represents the model under consideration, $\mathbf{X} = [X_1, X_2, \dots, X_n]^T$ is a vector of uncertain input parameters and \mathbf{Y} represents the vector of estimated outputs that will be a random vector. The algorithm of this method can be summarized in 5 steps:

- Step 1:** probabilistic identification of uncertain parameters in the model;
- Step 2:** sampling and random generation of inputs following identified probabilistic distributions;
- Step 3:** spread of uncertainty i.e. of the data set resulting from step 2 into the model and determination of the corresponding outputs set;
- Step 4:** estimation of the outputs probabilistic distributions whose statistical characteristics are given by the mean value μ_γ and standard deviation σ_γ . These are calculated using a set of N simulations as follows

$$\mu_\gamma = \frac{1}{N} \sum_{i=1}^N M(X^{(j)}) \quad \sigma_\gamma^2 = \frac{1}{N-1} \sum_{i=1}^N [M(X^{(j)}) - \mu_\gamma]^2 \quad (2.17)$$

- Step 5:** convergence analysis of the distribution of the model output.

3. Numerical results

Finite element simulations are carried out to study the acoustic propagation in a cylindrical duct. The acoustic pressure P within a finite element can be written as

$$P = \sum_{i=1}^m N_i P_i \quad (3.1)$$

where N_i is a set of linear shape functions, P_i are acoustic nodal pressures at the node i , and m is the number of nodes forming the element. For the pressure formulated acoustic elements, the finite element equation for the fluid in matrix form is

$$\mathbf{M}_f \ddot{\mathbf{P}} + \mathbf{K}_f \mathbf{P} = \mathbf{F}_f, \quad (3.2)$$

where \mathbf{M}_f is the equivalent fluid mass matrix, \mathbf{K}_f is the equivalent fluid stiffness matrix, \mathbf{F}_f is the vector of applied fluid loads, \mathbf{P} is the vector of unknown nodal acoustic pressures, and $\ddot{\mathbf{P}}$ is the vector of the second derivative of acoustic pressure with respect to time.

Section 3.1 deals with numerical model validation without considering uncertainty. In Section 3.2, the stochastic methods discussed above, MC and gPC, are implemented and integrated in finite element simulation for the cylindrical duct. In this framework, geometrical (radius of the duct) and material properties (density) are presenting the probabilistic parameters.

3.1. Deterministic model

The chosen example consists in applying the modal pressure at the left boundary Γ_L of a cylindrical duct, as indicated in Fig. 1. The geometric characteristics of the studied duct are: radius $a = 0.02$ m and length $L = 0.25$ m. The magnitude of the imposed pressure is equal to 1 Pa. At the end of the duct Γ_R , a normalized acoustic impedance is applied ($Z_p = 2$) to reflect the acoustic wave plane. The duct has been modelled using 8000 *FLUID30* elements. This is an entirely acoustic analysis and there are no active displacement degrees of freedom. In the following, the acoustic pressure fields obtained by the present numerical simulation without probabilistic approach is discussed. Only the real parts of the pressure are studied. The ANSYS Finite Element model of the duct is given in Fig. 2.

Figure 3 presents the pressure field inside the duct at several frequencies. The wave propagation is clear and the localization of the maximum of the real part of the acoustic pressure is varying as a function of the frequency. Frequency evolution of the pressure magnitude in one point inside the cylindrical duct is depicted in Fig. 4. The results greatly agree those shown in (Kesentini *et al.*, 2015).

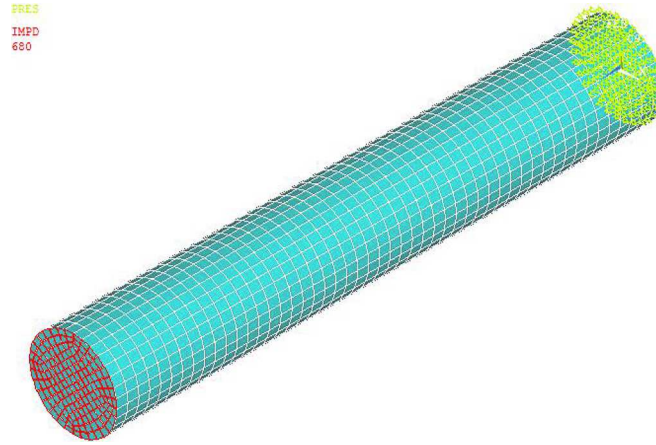


Fig. 2. ANSYS Finite Elements model of the cylindrical duct

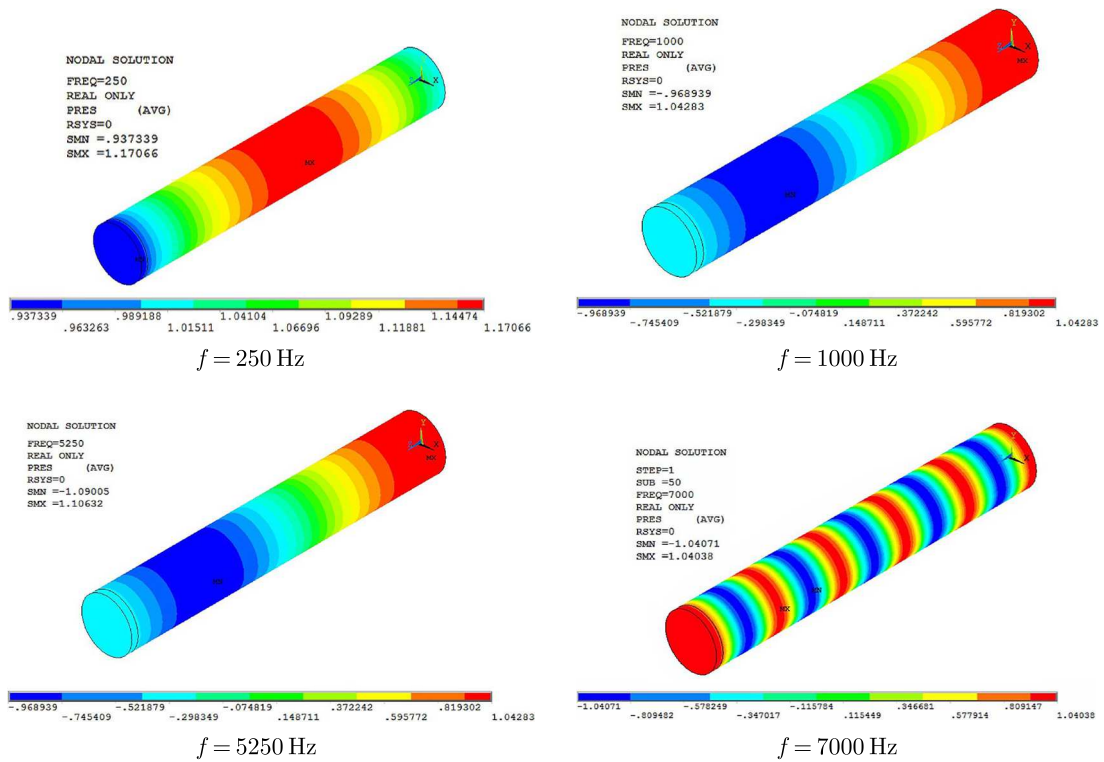


Fig. 3. Real part of the acoustic pressure inside of the studied cylindrical wall duct

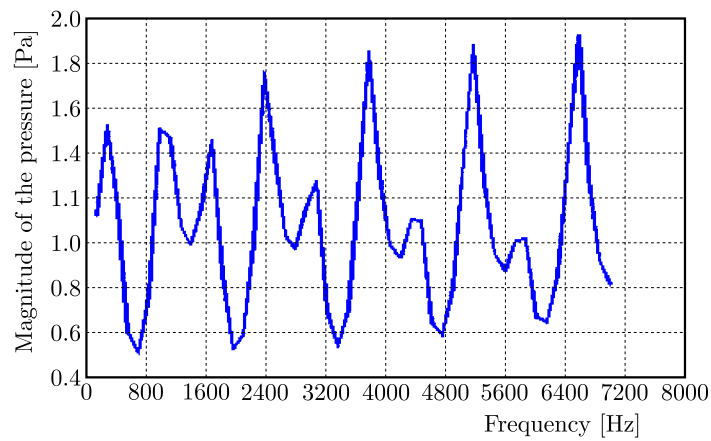


Fig. 4. Frequency evolution of the pressure magnitude in one point inside the cylindrical duct

3.2. Probabilistic analysis

In this Section, the stochastic methods discussed above, MC and gPC, are implemented and integrated in finite element simulation, see Section 3.1. The objective is to enhance the performance prediction for acoustic propagation systems that will operate in the presence of the inevitable parameters uncertainty associated simultaneously with the geometric and material properties. The geometric uncertain parameter considered here is a , radius of the cylindrical duct. The physical uncertain parameter is density ρ . These parameters are chosen to be uniform random following a progressive nomination around their nominal values $\pm 5\%$; $a = \bar{a}_0 + \xi \bar{a}_1$ and $\rho = \bar{\rho}_0 + \xi \bar{\rho}_1$, where \bar{a}_0 , $\bar{\rho}_0$ are the mean values, and \bar{a}_1 , $\bar{\rho}_1$ are convenient constants. Using the Monte Carlo method to analyze the pressure field consists in creating a grid of numerical values from the probabilistic uncertain parameters and calculating the quantity of interest of the linearized system for each value of the grid. The case of uniform distribution of the uncertain parameters is considered. The quantity of interest is analyzed for 500 drawings. Figure 5 shows the distribution of the input variables (a, ρ) in the case of uniform distribution of uncertainty.

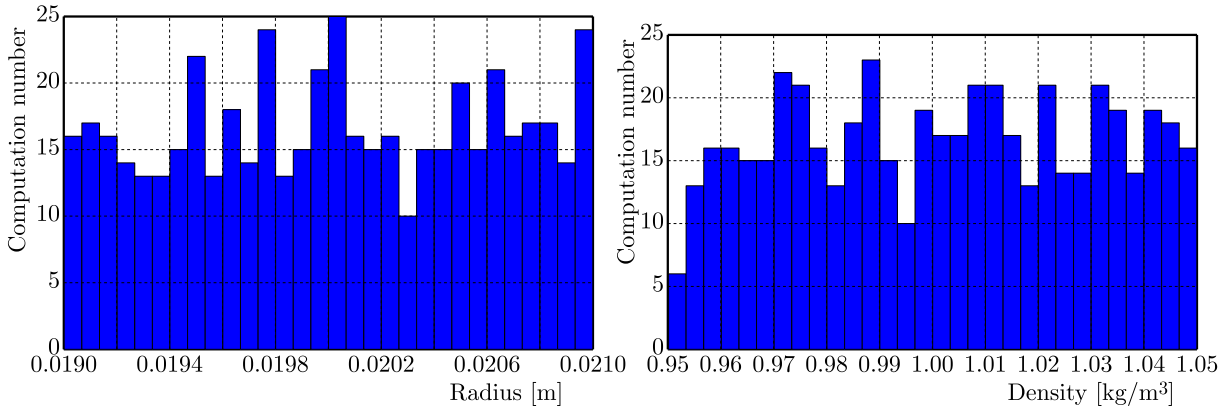


Fig. 5. Probability distribution of radius and density

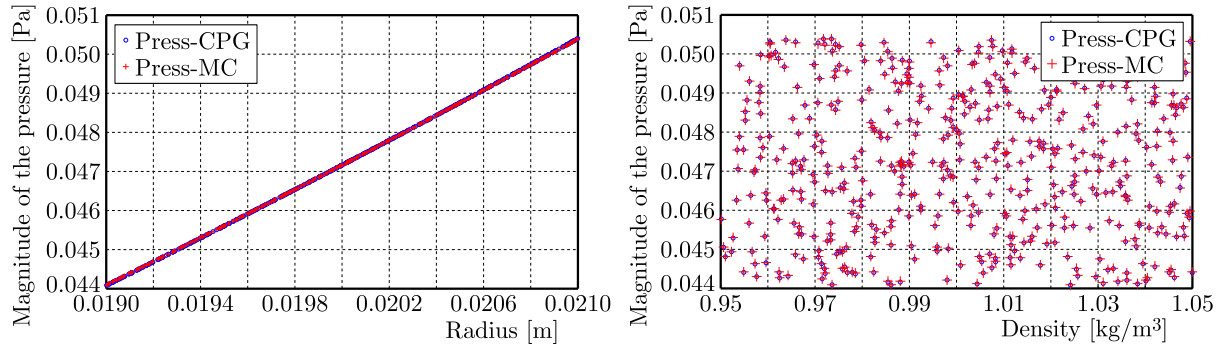


Fig. 6. Magnitude of the maximum pressure inside the duct as a function of geometric and material uncertain parameters

The results consist in the quantity of interest (the magnitude of pressure) plotted in Fig. 6 as a function of different duct radii and densities. The chaotic representation of the acoustic pressure is

$$P(r_i, \theta, z, \xi) = \sum_{j=0}^{N_p} \bar{P}_j(r_i, \theta, z) \phi_j(\xi) \quad (3.3)$$

The Monte Carlo representation for the acoustic pressure can be expressed as

$$P_{MC}(r_i, \theta, z, \xi) = M(\mathbf{X}) \quad (3.4)$$

where M is the finite element model and $\mathbf{X} = [a, \rho]^T$ is the vector of input uncertain parameters. The probability distribution and the relative errors are shown in Figs. 7 and 8. All results are compared with the direct method of MC. Models based on gPC are constructed using r uncertain parameters ($r = 1 \rightarrow 2$). It is well depicted from Fig. 6 that for $\pm 5\%$ of radius variation a , the maximum pressure magnitude is varying linearly, justifying the choice of the drawing number in MC. In the case of variability within density, one can remark that radius has a more effect on the pressure magnitude than density.

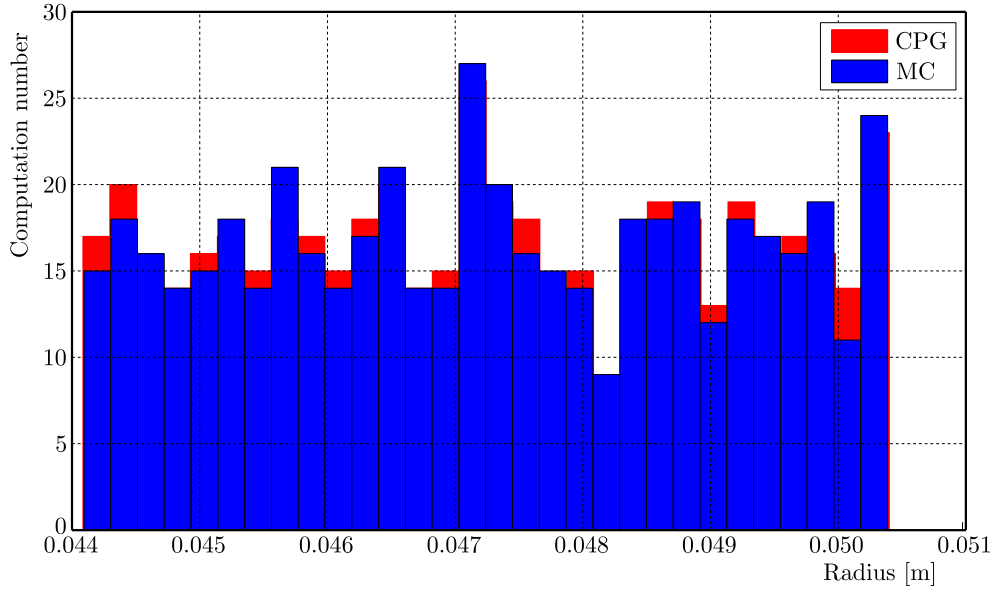


Fig. 7. Probability distribution of pressure

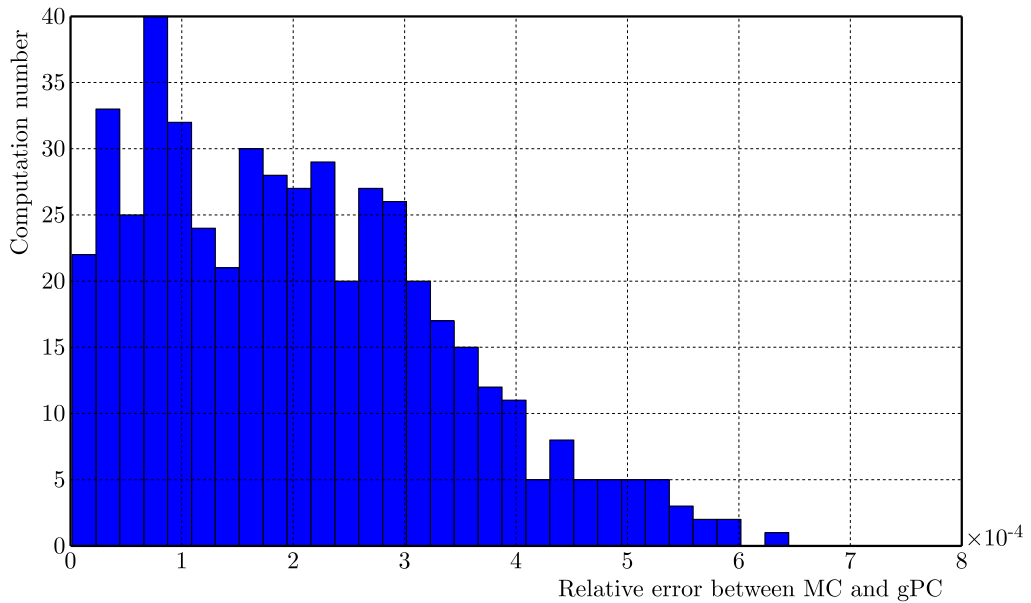


Fig. 8. Histogram of the relative error of pressure

We plot in Fig. 9 the mean value of the pressure as a function of the order p , for an uncertain parameter with variation of $\pm 5\%$. It is noted that there is a convergence of the average from $p = 4$. One can notice that the pressure distribution of the mean is very similar to that obtained when we use a deterministic model (Section 3.1). It is also proved that the results strongly depend on the frequency used.

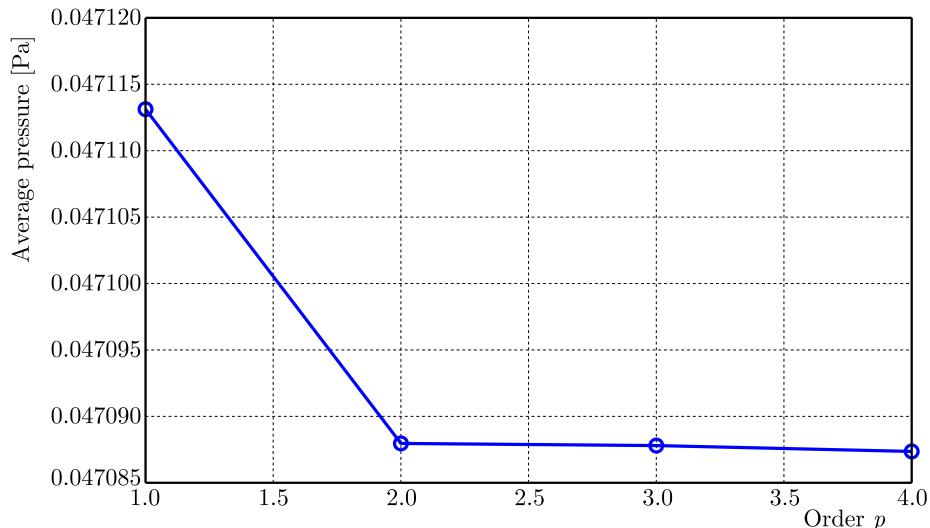


Fig. 9. Average of the pressure

Table 2 shows the main features of each technique. It is worth mentioning that the Monte Carlo technique is a very powerful method to solve complex systems with random parameters. In this work, 500 of samplings of two input variables are calculated and then the problem is solved for each sample of input variables. Nevertheless, according to results in Table 2, this technique has poor convergence for mean and standard deviation of the solution, requiring a large number of samples to achieve good precision in results, resulting in costly computation. This result is in a good agreement with (Nechak *et al.*, 2013).

Table 2. Comparison between MC and gPC

Frequency $f = 1000$ Hz	Monte Carlo	gPC($r = 2$)
Order p	–	4
Number of simulations	500	25
Maximum relative error between gPC and MC	–	$6.4e^{-4}$
Mean of the pressure (Pa)	0.047262	0.047262
Standard deviation	0.001821	0.001826
Time [s]	43438.96	0.5182

For high frequencies that are greater than 5000 Hz, Fig. 10 shows that the acoustic pressure is varying nonlinearly according to radius of the cylindrical duct. We plot in Figs. 11a and 11b, respectively, the mean value and the standard deviation of pressure as a function of the order p . It is clear that there is a convergence of these statistical results from $p = 7$.

4. Conclusions

In this work, the MC method and the gPC have been coupled to FE simulation discussed above in order to calculate statistical data from output pressure field. In this paper, a numerical solution of the Helmholtz equation is proposed based on finite element simulation. This solution is coupled to probabilistic approaches, when physical parameters present uncertainty. The case of a cylindrical duct has been considered. The influence of uncertain variables on the pressure field has been discussed. The results using the polynomial chaos expansion method have been compared with the Monte Carlo technique. Convergence has been verified with comparisons against exact solutions and solutions from Monte Carlo simulations. As regards efficiency, gPC

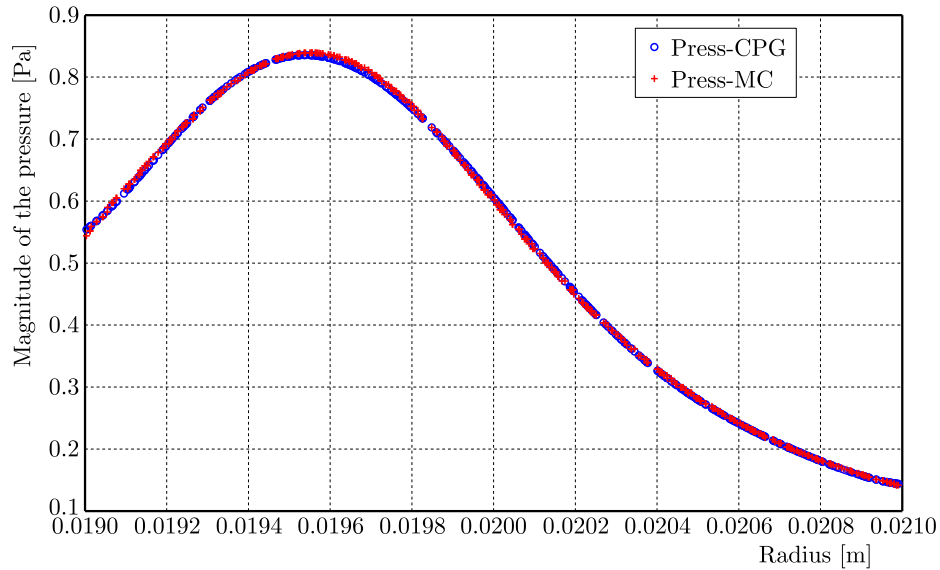


Fig. 10. Magnitude of the maximum pressure inside the duct as a function of radius at a high frequency

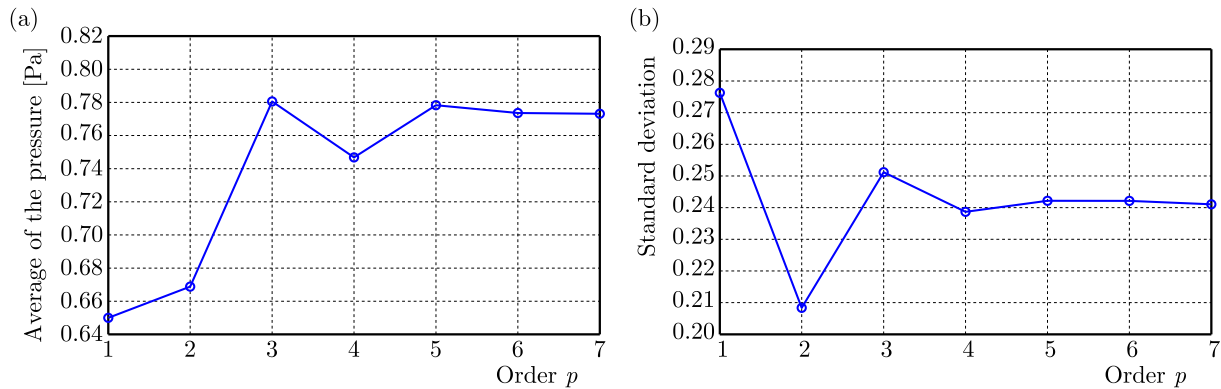


Fig. 11. (a) Average and (b) standard deviation of pressure

based simulation is computationally less expensive than the MC technique to generate the solution statistics. In the problems we have studied here, we can only make direct comparisons when using two random physical parameters, and no interaction is considered. The future track of work will consist in the study of uncertainty of the fluid-structure interaction when several uncertain input variables are included.

References

1. BLATMAN G., SUDRET B., 2008, Sparse polynomial chaos expansions and adaptive stochastic finite elements using a regression approach, *C.R. Mecanique*, **336**, 518-523
2. BLAZEJEWSKI A., 2013, Modal analysis application in passive sound level control inside bounded space in steady state, *12th Conference of Dynamical Systems Theory and Applications*, Dynamical Systems-Application, 409-420
3. BLAZEJEWSKI A., KOZIOL P., LUCZAK M., 2014, Acoustical analysis of enclosure as initial approach to vehicle induced noise analysis comparatively using STFT and wavelets, *Archives of Acoustics*, **39**, 385-394
4. CAMERON H., MARTIN W., 1947, The orthogonal development of non linear functionals in series of Fourier-Hermite functional, *Annals of Mathematics*, **48**, 385-392

5. CHEUNG Y.F., JIN W.G., 1991, Solution of Helmholtz equation by Trefftz method, *International Journal for Numerical Methods in Engineering*, **32**, 63-78
6. CREAMER D.B., 2006, On using polynomial chaos for modeling uncertainty in acoustic propagation, *Journal of the Acoustical Society of America*, **119**, 4, 1979-1994
7. DAMMAK K., ELHAMI A., KOUBAA S., WALHA L., HADDAR M., 2017a, Reliability based design optimization of coupled acoustic-structure system using generalized polynomial chaos, *International Journal of Mechanical Sciences*, **134**, 75-84
8. DAMMAK K., KOUBAA S., ELHAMI A., WALHA L., HADDAR M., 2017b, Numerical modelling of vibro-acoustic problem in presence of uncertainty: Application to a vehicle cabin, *Applied Acoustics*, DOI: 10.1016/j.apacoust.2017.06.001
9. FISHER J., BHATTACHARYA R., 2008, Stability analysis of stochastic systems using polynomial chaos, *American Control Conference*
10. GHANEM R.G., SPANOS P.D., 1991, *Stochastic Finite Elements: a Spectral Approach*, Dover Publication INC
11. HURTADO J.E., ALVAREZ D.A., 2012, The encounter of interval and probabilistic approaches to structural reliability at the design point, *Computer Methods in Applied Mechanics and Engineering*, **225-228**, 74-94
12. IHLENBURG F., BABUSKA I., 1995, Finite element solution of the Helmholtz equation with high wave number. Part I: The h-version of the FEM, *Computers and Mathematics with Applications*, **30**, 9-37
13. KESENTINI A., TAKTAK M., BEN SOUF M.A., BAREILLE O., ICHCHOU M.N., HADDAR M., 2015, Computation of the scattering matrix of guided acoustical propagation by the Wave Finite Element approach, *Applied Acoustics*
14. KIM Y., NELSON P.A., 2004, Estimation of acoustic source strength with in a cylindrical duct by inverse methods, *Journal of Sound and Vibration*, **275**, 391-413
15. LAN J.H., 2005, Validation of 3D acoustic propagation code with analytical and experimental results, *11th AIAA/CEAS Aeroacoustics Conference*
16. LEPAGE K.D., 2006, Estimation of acoustic propagation uncertainty through polynomial chaos expansions, *9th International Conference on Information Fusion*
17. LINS E.F., ROCHINHA F.A., 2009, Analysis of uncertainty propagation in acoustics through a sparse grid collocation scheme, *20th International Congress of Mechanical Engineering*
18. MANSOURI M., RADI B., EL-HAMI A., 2012a, Reliability-based design optimization for the analysis of vibro-acoustic problems, *Proceedings of the Eleventh International Conference on Computational Structures Technology*
19. MANSOURI M., RADI B., EL-HAMI A., 2013, Coupling modal synthesis and reliability for studying aero-acoustic problems, *21me Congrès Français de Mécanique*
20. MANSOURI M., RADI B., EL-HAMI A., BORZA D., 2012b, Reliability analysis of vibro-acoustic problems, *Proceedings of the 1st International Symposium on Uncertainty Quantification and Stochastic Modeling*
21. MEISSNER M., 2008, Influence of wall absorption on low-frequency dependence of reverberation time in room of irregular shape, *Applied Acoustics*, **69**, 583-590
22. NARK D.M., FARASSAT F., POPE D.S., VATSA V., 2003, *The Development of the Ducted Fan Noise Propagation and Radiation Code CDUCT-LARC*, American Institute of Aeronautics and Astronautics
23. NARK D.M., WATSON W.R., JONES M.G., 2005, *An Investigation of Two Acoustic Propagation Codes for Three-Dimensional Geometries*, American Institute of Aeronautics and Astronautics

24. NECHAK L., BERGER S., AUBRY E., 2013, Robust analysis of uncertain dynamic systems: combination of the centre manifold and polynomial chaos theories, *WSEAS Transactions on Systems*, **98**, 386-395
25. NG L.W.T., ELDRED M.S., 2012, Multifidelity uncertainty quantification using non-intrusive polynomial chaos and stochastic collocation, *Structural Dynamics and Materials Conference*
26. SEPAHVAND K., MARBURG S., 2014, On uncertainty quantification in vibroacoustic problems, *Proceedings of the 9th International Conference on Structural Dynamics, EUROLYN*
27. SMITH A.H.C., MONTI A., MEMBER S., PONCI F., 2007, Indirect measurements via a polynomial chaos observer, *IEEE Transactions on Instrumentation and Measurement*, **56**, 743-752
28. TAKTAK M., 2008, *Mesure de la matrice de diffusion d'un tronçon traité cylindrique e recouvert par un materiaux: application à la mesure de son efficacité et à la détermination de son impédance homogénéisée*, L'Université de Technologie de Compiègne
29. TAKTAK M., JRAD H., KARRA C., BENTAHAR M., HADDAR M., 2011, Numerical modeling of the acoustic propagation in a three-dimensional wave guide in the presence of flow, *ACTA Acoustica United with Acoustica*, **97**, 354-465
30. TAKTAK M., MAJDOUB M.A., BENTAHAR M., HADDAR M., 2012, Numerical modelling of the acoustic pressure inside an axisymmetric lined flow duct, *Archives of Acoustics*, **37**, 151-160
31. WAN X., KARNIADAKIS G.E., 2006, Multi-element generalized polynomial chaos for arbitrary probability measures, *Journal of Scientific Computing*, **28**, 901-928
32. WIENER N., 1938, The homogeneous chaos, *American Journal of Mathematics*, **60**, 897-936
33. XIA B., YIN S., YU D., 2015, A new random interval method for response analysis of structural acoustic system with interval random variables, *Applied Acoustics*, **99**, 31-42
34. XIU D., KARNIADAKIS G.E., 2002, The Wiener-Askey polynomial chaos for stochastic differential equations, *Journal of Scientific Computing*, **24**, 619-644
35. XIU D., KARNIADAKIS G.E., 2003, Modeling uncertainty in flow simulations via generalized polynomial chaos, *Journal of Computational Physics*, **187**, 137-167
36. YANG J., KESSISOLOU N., 2013, Modal analysis of structures with uncertainties using polynomial chaos expansion, *Proceedings of Acoustics*

Manuscript received August 24, 2017; accepted for print April 3, 2018

MATHEMATICAL MODELLING AND SIMULATION OF DELAMINATION CRACK GROWTH IN GLASS FIBER REINFORCED PLASTIC (GFRP) COMPOSITE LAMINATES

HASSAN IJAZ

University of Jeddah, Mechanical Engineering Department, Jeddah, Saudi Arabia
e-mail: hassan605@yahoo.com

Delamination crack growth is a major source of failure in composite laminates under static and fatigue loading conditions. In the present study, damage mechanics based failure models for both static and fatigue loadings are evaluated via UMAT subroutine to study the delamination crack growth phenomenon in Glass Fiber Reinforced Plastic (GFRP) composite laminates. A static local damage model proposed by Allix and Ladevèze is modified to a non-local damage model in order to simulate the crack growth behavior due to static loading. Next, the same classical damage model is modified to simulate fatigue delamination crack growth. The finite element analysis results obtained by the proposed models are successfully compared with the available experimental data on the delamination crack growth for GFRP composite laminates.

Keywords: finite element analysis, GFRP, damage mechanics, non-local, fatigue, delamination

1. Introduction

Composite laminates are frequently used in modern structural materials due to the high strength-to-weight ratio. Moreover, by adjusting the orientation of fibers one can also get desired mechanical properties in desired loading directions (Herakovich, 1997). Carbon and glass fibers are commonly used to manufacture composite laminates. Carbon fibers have better strength and less density than glass fibers, but they are not cost effective. Glass Fiber Reinforced Plastic (GFRP) composite laminates are used in avionic, automobile, ship and wind turbine industries. In the present study, delamination crack growth simulations for the GFRP composite laminates are performed under static and fatigue loadings. Delamination may be defined as a crack like an entity between the composite laminates. The cracks can grow within laminates under static and fatigue loadings and may result in failure of structural parts (Davies *et al.*, 1989; Allix and Ladevèze, 1992). Normally, damage or fracture mechanics based approaches are used to study the crack growth behavior in different structural elements. Fracture mechanics deals with the propagation of already existing crack (Meng and Wang, 2014) while, on the other hand, damage mechanics can not only simulate the propagation of cracks but also deals with initiation of the crack (Allix *et al.*, 1995, 1998; Allix and Ladevèze, 1996; Ijaz *et al.*, 2016).

Damage mechanics based formulations have been used to simulate the crack growth behavior in composite laminates mostly for CFRP (Corigliano, 1993; Corigliano and Allix, 2000; Chaboche *et al.*, 1997; Alfano and Crisfield, 2001). In the present study, delamination crack growth in the GFRP composite laminates is focused using the damage mechanics based formulation.

Classical static damage models proposed by earlier authors were mostly local in nature (Allix and Ladevèze, 1992; Corigliano, 1993; Chaboche *et al.*, 1997; Alfano and Crisfield, 2001). Localization means that damage tends to localize in a narrow zone in front of the crack tip rather than a uniform distribution over a certain region (Jirasek, 1998). Bažant and Pijaudier-Cabot

(1988, 1989) proposed an integral type non-local damage model for brittle concrete materials. Similarly, a rate dependent damage model is also proposed to avoid the localization issues in CFRP composite laminates by introducing a time delay in the damage evolution formulation (Allix *et al.*, 2000; Marguet *et al.*, 2007). To counter the localization problem, Peerlings introduced a gradient enhanced damage evolution model (Peerlings *et al.*, 2001). Borino gave the idea of using the integral type non-local damage model for the interface damage models for composite laminates (Borino *et al.*, 2007). Ijaz used the idea of an integral type non-local interface damage model for the study of delamination crack growth in CFRP composite laminates (Ijaz *et al.*, 2014). GFRP composite laminates also show a considerable amount of fiber bridging during crack growth (Davidson and Waas, 2012). In the present study, an integral type non-local damage is used to accommodate the spurious localization and fiber bridging issues during delamination crack growth in GFRP composite laminates under static loading conditions. The classical damage model proposed by Allix and Ladevèze (1992, 1996) is modified to a non-local one.

This article is organized as follows: in Section 2, basics of the classical interface damage model are recalled. The proposed non-local static interface damage model is discussed in Section 3. Finite element simulation results and their comparison with the experimental data are detailed in Section 4. Finally, some concluding remarks are given in Section 5.

2. Introduction to the classical local interface damage model

Simulation of delamination crack growth in composite laminates is performed by coupled interface damage modelling. The interface is a crack like entity that exists between two adjacent lamina layers. The relative displacement of the two adjacent layers with respect to each other can be described as

$$\mathbf{U} = \mathbf{U}^+ - \mathbf{U}^- = U_1\mathbf{N}_1 + U_2\mathbf{N}_2 + U_3\mathbf{N}_3 \quad (2.1)$$

where \mathbf{N}_1 , \mathbf{N}_2 and \mathbf{N}_3 are mutual perpendicular vectors in an orthotropic reference frame for the interface. The failure or deterioration of the interface is taken into account by the introduction of three damage variables, d_1 , d_2 and d_3 correspond to orthotropic direction vectors. Here, d_3 corresponds to the out-of-plane opening mode (Mode I), whereas d_1 and d_2 correspond to the in-plane shearing and tearing failure modes (Mode II and Mode III). The damage variable is divided into two parts, i.e. static damage variable d_{iS} and fatigue damage variable d_{iF} . Hence, the total damage d_i can be calculated by taking the sum of the two aforementioned damage variables $d_i = d_{iS} + d_{iF}$, $i = 1, 2, 3$.

If σ_{13} , σ_{23} and σ_{33} are interfacial stress components in N_1 , N_2 and N_3 directions, respectively, then the damage variables are related to the interfacial displacements as

$$\begin{bmatrix} \sigma_{13} \\ \sigma_{23} \\ \sigma_{33} \end{bmatrix} = \begin{bmatrix} k_1^0(1-d_1) & 0 & 0 \\ 0 & k_2^0(1-d_2) & 0 \\ 0 & 0 & k_3^0(1-d_3) \end{bmatrix} \begin{bmatrix} U_1 \\ U_2 \\ U_3 \end{bmatrix} \quad (2.2)$$

here k_1^0 , k_2^0 and k_3^0 are defined as interface rigidities corresponding to three failure modes. The damage model is built by considering thermodynamic forces combined with damage variables and are associated with three modes of delamination as follows (Allix *et al.*, 1995; Allix and Ladevèze, 1996)

$$Y_{d_3} = \frac{1}{2} \frac{\langle \sigma_{33} \rangle_+^2}{k_3^0(1-d_3)^2} \quad Y_{d_1} = \frac{1}{2} \frac{\sigma_{13}^2}{k_1^0(1-d_1)^2} \quad Y_{d_2} = \frac{1}{2} \frac{\sigma_{32}^2}{k_2^0(1-d_2)^2} \quad (2.3)$$

where $\langle \sigma_{33} \rangle_+$ represents the positive value of σ_{33} , i.e. damage will not grow during compression loading when a normal loading is applied. Now the three damage variables are assumed to be strongly coupled and are governed by a single equivalent damage energy release rate of the following form (Allix and Ladevèze, 1996)

$$\bar{Y}(t) = \max_{r \leq t} \left((Y_{d_3})^\alpha + (\gamma_1 \bar{Y}_{d_1})^\alpha + (\gamma_2 \bar{Y}_{d_2})^\alpha \right)^{\frac{1}{\alpha}} \quad (2.4)$$

where γ_1 and γ_2 are coupling parameters, and α is a material parameter which governs the damage evolution under mixed mode loading conditions. Now, the damage evolution law is defined as an isotropic material function of the following form

$$\begin{aligned} \text{if } [(d_{3S} < 1) \text{ and } (\bar{Y} < Y_R)] \quad \text{then } d_{1S} = d_{2S} = d_{3S} = \omega(\bar{Y}) \\ \text{else } d_{1S} = d_{2S} = d_{3S} = 1 \end{aligned} \quad (2.5)$$

where the damage evolution material function $\omega(\bar{Y})$ is defined as (Allix and Ladevèze, 1996)

$$\omega(\bar{Y}) = \left(\frac{n}{n+1} \frac{\langle \bar{Y} - Y_O \rangle_+}{Y_C - Y_O} \right)^n \quad (2.6)$$

where Y_O and Y_C are threshold and critical damage energy release rates. n is termed as a characteristic function of the material. Higher values of n correspond to a brittle interface. Y_R is defined as damage energy associated to rupture and can be calculated using following formula

$$Y_R = Y_O + \frac{n+1}{n} d_c^{\frac{1}{\alpha}} (Y_C - Y_O)$$

Now the identification of parameters Y_C , γ_1 and γ_2 can be done by comparing the energy dissipation yielded by the damage mechanics approach and LEFM (Linear Elastic Fracture Mechanics). For a pure mode case energy release rate G_{iC} ($i = I, II, III$) obtained from fracture mechanics, the experiments considering LEFM can be compared to the damage mechanics approach using the following relation (Allix *et al.*, 1995; Allix and Ladevèze, 1996)

$$G_{IC} = Y_C \quad G_{IIC} = \frac{Y_C}{\gamma_1} \quad G_{IIIC} = \frac{Y_C}{\gamma_2} \quad (2.7)$$

For a mixed-mode loading case, a standard LEFM model can be recovered as (Allix and Ladevèze, 1996)

$$\left(\frac{G_I}{G_{IC}} \right)^\alpha + \left(\frac{G_{II}}{G_{IIC}} \right)^\alpha + \left(\frac{G_{III}}{G_{IIIC}} \right)^\alpha = 1 \quad (2.8)$$

The equivalence between damage mechanics and LEFM also leads to the following relation during the complete debonding process (DP)

$$G_{IC} = \int_{DP} \sigma_{33} dU_3 \quad G_{IIC} = \int_{DP} \sigma_{13} dU_1 \quad G_{IIIC} = \int_{DP} \sigma_{23} dU_2 \quad (2.9)$$

Equation (2.9) states that for any pure mode debonding case, the area under the curve obtained from the damage mechanics approach is equal to the experimentally obtained critical energy release rate G_{iC} .

3. Non-local interface damage model for static loading

The classical interface damage model shows the strain softening phenomenon during the degradation process (Borino *et al.*, 2007; Ijaz *et al.*, 2014). Due to this softening behaviour, the stress tends to localize in a narrow region in front of the crack tip. This localization phenomenon is more obvious for 3D delamination simulations over 2D analysis. Moreover, fibre bridging also occurs during delamination crack growth in GFRP composite laminates (Yao, 2015; Davidson and Waas, 2012). The mathematical non-local interface damage model presented in this Section will also inherently accommodate the fibre bridging process.

In the proposed methodology, the damage variable is made non-local by taking spatial averaging over a certain domain using the Gaussian distribution methodology. The averaging domain is dictated by the characteristic length parameter l . A higher value of l means that more elements are used for the averaging. This domain dependent characteristic length l will also simulate the fibre bridging behaviour since bridging occurs over a certain domain during delamination crack growth in composite laminates.

Now one can write the average of damage variable d over the surrounding domain using the weight function $\alpha_0(r)$ (Ijaz *et al.*, 2014)

$$\bar{d}(x) = \frac{1}{V_r(x)} \int \alpha_0(\|x - \zeta\|) d(\zeta) d\zeta \quad (3.1)$$

where

$$V_r(x) = \int \alpha_0(\|x - \zeta\|) d\zeta \quad (3.2)$$

The damage variable calculated using Eq. (2.5) is made non-local using Eq. (2.10) over a prescribed selected domain. The isotropic weight function $\alpha_0(r)$ is calculated using the Gaussian distribution function of exponential form as follows

$$\alpha_0(r) = \exp\left(-\frac{r^2}{2l^2}\right) \quad (3.3)$$

From the above equation it is clear that the weight function $\alpha_0(r)$ depends on the distance between two points $r = \|x - \zeta\|$ and the characteristic length parameter l . A smaller value of l corresponds to a less number of elements available for averaging. Higher values mean that more elements will take part in the for averaging.

Equation (2.10) describes the damage variable d which is made non-local by taking spatial averaging. Similarly, like Eq. (2.10), two other variables like the equivalent damage energy release rate \bar{Y} and interfacial displacement U are also made non-local, and then the damage variable is calculated using these as

$$\begin{aligned} \bar{Y}(x) &= \frac{1}{V_r(x)} \int \alpha_0(\|x - \zeta\|) Y(\zeta) d\zeta \\ \bar{U}(x) &= \frac{1}{V_r(x)} \int \alpha_0(\|x - \zeta\|) U(\zeta) d\zeta \end{aligned} \quad (3.4)$$

Once the values of $\bar{Y}(x)$ and $\bar{U}(x)$ are known then the non-local damage variable can be calculated as a function of $\bar{Y}(x)$ and $\bar{U}(x)$, respectively. Once the value of the averaged non-local variable d is calculated either using Eqs. (2.10) and (2.13)₁ or (2.13)₂ then the updated value of d will be used in Eq. (2.2) to calculate the interfacial stresses.

4. Finite element analysis and results

In this Section, details and results of finite element simulations are presented and discussed separately for both static non-local and fatigue interface damage models for GFRP composite laminates. Double Cantilever Beam (DCB) specimen for Mode I is shown in Fig. 1. The specimen has total length L , initial crack length a_0 and total height $2h$, as shown in Fig. 1.

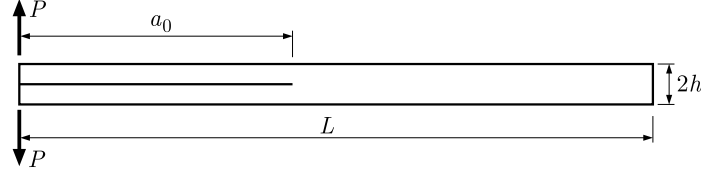


Fig. 1. DCB specimen for Mode I delamination crack growth

All simulations are performed in finite element software Cast3M (CEA) (Verpeaux *et al.*, 2000). The geometry of the beam is modelled with 2D plane strain quadrangles. The interface between the specimen arms is modelled with 2D interface element JOI2 to simulate the debonding process (Beer, 1985). Different parameters like Y_O , Y_C , γ_1 , n , k_1^0 and k_3^0 are needed to be identified for the finite element analysis of Mode I and Mode II delamination crack growth. The value of threshold damage energy Y_O is taken zero, i.e. $Y_O = 0$ for all the finite element simulations. The identification of Y_C and γ_1 can be done by using Eq. (2.7) provided that Mode I and Mode II critical energy release rates G_{IC} and G_{IIC} are already determined from LEFM experiments. The identification of value of n depends on the brittleness of the interface. The value of n varies between 0-1.0, and a good value can be identified by matching the experimental and numerical results. The values of interfacial rigidities can be calculated using the following relation (Ijaz *et al.*, 2011)

$$k_3^0 = \frac{(2n+1)^{\frac{2n+1}{n}}}{8n(n+1)Y_C} \sigma_{33}^2 \quad k_i^0 = \frac{\gamma_i(2n+1)^{\frac{2n+1}{n}}}{8n(n+1)Y_C} \sigma_{3i}^2 \quad i = 1, 2 \quad (4.1)$$

In Eq. (4.1), σ_{33} and σ_{3i} ($i = 1, 2$) are the maximum interfacial normal and in-plane shear stresses. The energy release rate calculated using fracture mechanics theory for pure Mode I is given as (Willams, 1988)

$$G_I = \frac{M^2}{bEI} \quad (4.2)$$

where M is the applied moment, b is width of the specimen, E is flexure modulus and I is the second moment of area of the beam arm.

5. FE analysis of delamination crack growth under static loading

In this Section, finite element analysis of Mode I delamination crack growth for GFRP composite laminates is performed using the non-local interface damage model. The experimental work of Davidson and Waas (2012) on Mode I delamination crack growth for GFRP composite laminates is used for finite element analysis. Nominal dimensions for DCB specimen are: $L = 130$, $h = 2.5$, $a_0 = 50$ and width is $b = 25.4$. All the dimensions mentioned above for DCB specimen are in mm. the Mode I critical energy release rate G_{IC} value is 1.45 KJ/m². The modulus E_{11} , in the fibre direction is 11.5 GPa and the major Poisson's ratio is 0.3 for GFRP (Davidson and Waas, 2012). In the interface damage model, different values are identified as discussed above. The interfacial rigidity k_3^0 is found to be 9000 MPa/mm for maximum normal stress value of 50 MPa. Figure 2

shows the evolution of normal stress with respect to the interfacial displacement for different identified damage parameters. From Fig. 2, one can also observe that the area under the curve is always equal to the critical energy release rate for the complete debonding process, Eq. (2.9).

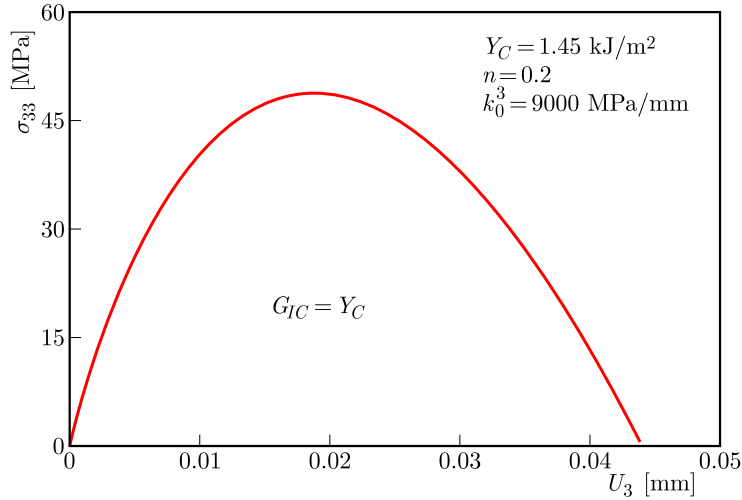


Fig. 2. Evolution of normal stress σ_{33} with interfacial displacement U_3

Three different formulations on averaging of the variables d , \bar{Y} and U are discussed earlier for the non-local interface damage model. These three different non-local interface damage formulations are implemented in finite element software Cast3M via procedure PERSO1 and user material subroutine UMAT.

Figure 3 shows the normalized value of evolution of the reaction force with crack opening displacement for Mode I delamination crack growth using d based non-local damage formulation. Reaction force values are normalized to 120 N for ease of presentation and comparison with the experimental results. Figure 3 presents the curves for the non-local model for three different characteristic lengths l with values of 0.2, 0.4 and 0.6.

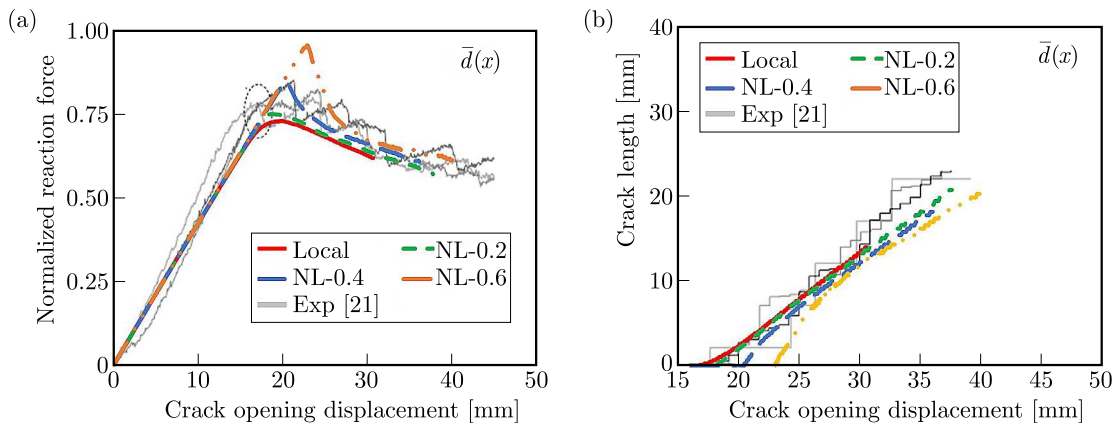


Fig. 3. (a) Normalized reaction force and (b) crack growth vs crack opening displacement for d based non-local formulation

From Fig. 3a, one can notice that as the characteristic length value reduces, the results coincide with the classical local damage model proposed by Allix and Ladevèze. The reason is that as the characteristic length value reduces, a fewer number of elements is available for the averaging and the results come close to those predicted by the local damage model. The finite element simulation results are also in good agreement with the experimental results of (Davidson and Waas, 2012). Peng and Xu (2013) proposed a damage model that accommodates

the bridging effect by dividing the damage variable into static d_S and bridging d_b parts. However, in the present work, the non-local model accommodates the bridging effect by controlling the characteristic length l . The model of Peng and Xu (2013) also demonstrated the similar behaviour of the increasing reaction force with an increase in the bridging force, whereas in the present case a larger value of the characteristic length causes an increase in the reaction force, see Fig. 3a. From Fig. 3a, one can also note that although the peak reaction force is different for various characteristic length values, but they all tend to converge close to each other once a stable crack growth is established.

Figure 3b presents the evolution of delamination crack growth as a function of the crack opening displacement. Figure shows the evolution of the crack for the non-local model using three different characteristic length values, i.e. 0.2, 0.4 and 0.6. In Fig. 3, the finite element analysis results are also compared with the experimental results. The start of crack growth corresponding to different l values is in accordance with the behaviour depicted in Fig. 3. The start of crack growth for the non-local damage model with a small value of l (0.2) and the classical local damage model is almost the same. Similarly, crack growth starts late for a larger l (0.6) value in comparison to smaller l (0.2, 0.4) values, and this behaviour is also in accordance with the one predicted in Fig. 3. The late start of crack growth is due to a relatively large value of l , which means that more elements are available for the averaging in the non-local zone and, thus, imparting extra resistance to crack growth resulting in an increase in the reaction force and, hence, the late start of crack growth. The actual fibre bridging behaviour during delamination crack growth in GFRP composite laminates is simulated by introducing the characteristic length l into the classical local damage model. The larger value of l indicates a wider fibre bridging zone, which means extra resistance to crack growth and a higher value of the reaction force. Moreover, there is a good agreement between numerical and experimental results for delamination crack growth with crack opening displacement, Fig. 3b.

Figure 4 shows the evolution of the reaction force and crack growth with crack opening displacement using the U based non-local damage model. Trend of the reaction force and crack growth for the U based non-local damage model is very similar to that predicted by d based formulation. In the case of d based non-local formulation, the reaction force and crack growth converge very close to each other while for U based formulation both almost converge to the same path for different values of l once the stable crack growth rate establishes. The results presented in Fig. 4 also show a similar trend as predicted by Peng and Xu (2013) for the reaction force in the GFRP composite laminate delamination crack growth for different bridging forces.

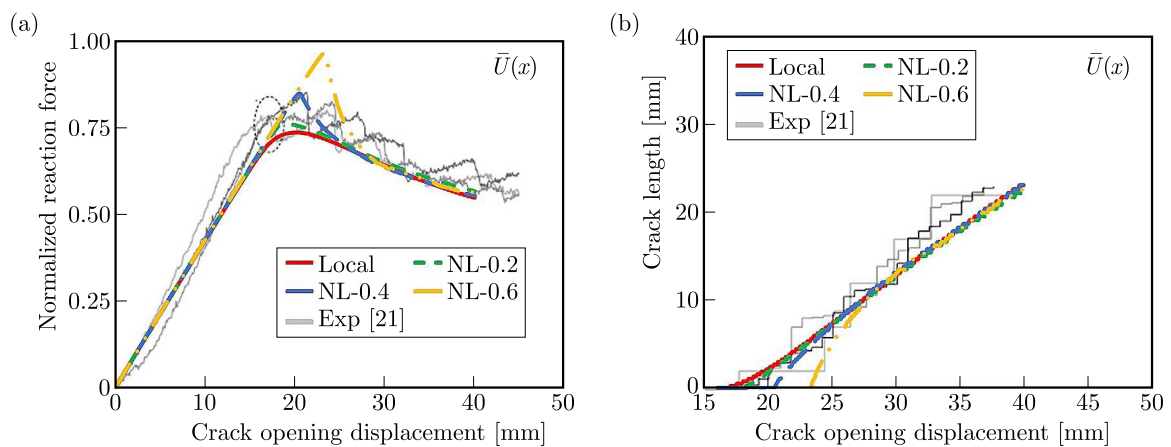


Fig. 4. (a) Normalized reaction force and (b) crack growth vs. crack opening displacement for U based non-local formulation

Similarly, Fig. 5 shows the evolution of the reaction force and crack growth with crack opening displacement using the \bar{Y} based non-local damage model. The results predicted by this non-local damage model show erratic behaviour. The results start to deviate from the experimental ones as the characteristic length l value increases for both the reaction force and crack growth, see Fig. 5.

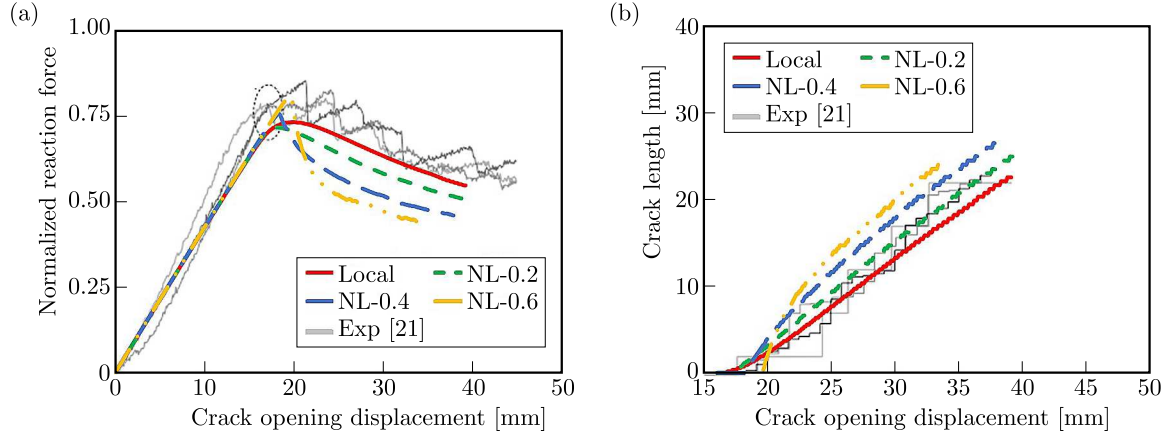


Fig. 5. (a) Normalized reaction force and (b) crack growth vs crack opening displacement for \bar{Y} based non-local formulation

From the above discussions, it can be inferred that d and U based non-local damage formulations give reasonable results for delamination crack growths in GFRP composite laminates. The proposed methodology will not only avoid the localization issue but will also compensate the fibre bridging effect.

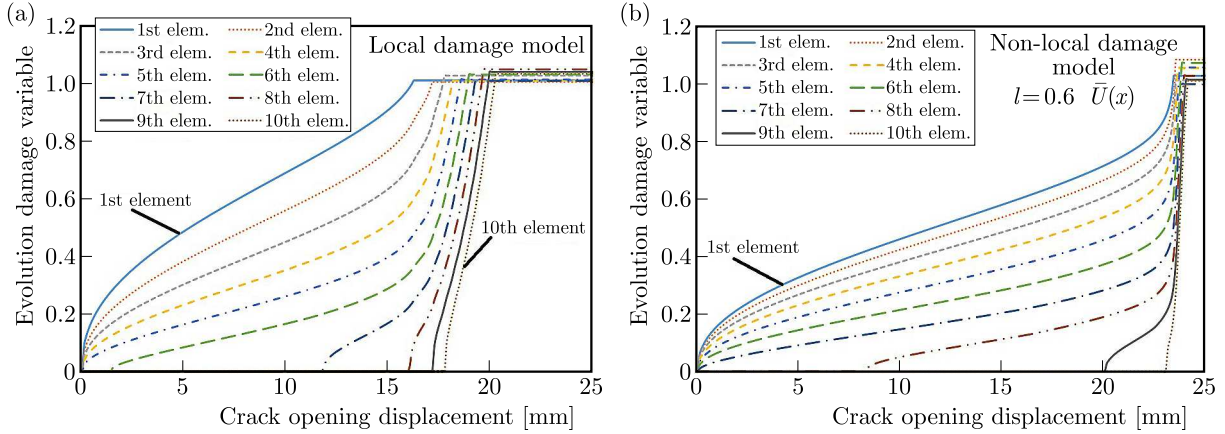


Fig. 6. Evolution of the damage variable with crack opening displacement: (a) local damage model, (b) non-local damage model, $l = 0.6$

Figure 6 shows the evolution of the damage variable with crack opening displacement for the first ten elements from the crack tip for local and U based non-local damage models. In the figure one can observe that for the first five elements, from the crack tip, the damage evolution starts as soon the load is applied in the local damage model, whereas in the non-local damage model, the damage evolution for the first seven elements starts as soon the load is applied. Similarly, for the eighth element, the damage evolution starts when the crack opening displacement is 17 mm in the local damage model, and it starts around 8 mm in the non-local damage model. The characteristic length l helps one to involve more elements in the averaging process and makes more elements be a part of damage initiation in the non-local model in comparison to the local damage model. Hence, one can say that for larger values of l , more elements will be available in

the averaging process and will take part in initial damage growth as soon as the load is applied. Since in the local damage model no averaging of damage variable is done over a certain area, therefore, fewer elements will take part in the initial damage growth in comparison with the non-local damage model, see Fig. 6.

6. Conclusion

Delamination crack growth in GFRP composite laminates under static loading is simulated in the present study. The original classical local damage proposed by Allix and Ladevèze is modified to a non-local static damage model and a fatigue damage model. The proposed models are implemented via UMAT subroutine and PERSO1 procedure in Cast3M FE software. The non-local damage model is not only capable of avoiding the accumulation of damage in front of the crack tip but also compensates the fibre bridging phenomenon at the interface by introducing characteristic length l . The reaction force and crack growth are plotted against the crack opening displacement for different values of l in pure Mode I static loading. Three different formulations based on averaging of variables d , \bar{Y} and U are proposed. FE simulation results show that d and U based non-local models predict good results. The results determined by finite element analysis for the static loading is successfully compared with the available experimental data of GFRP composite laminates.

References

1. ALFANO G., CRISFIELD M.A., 2001, Finite element interface models for the delamination analysis of laminated composites: mechanical and computational issue, *International Journal for Numerical Methods in Engineering*, **50**, 1701-1736
2. ALLIX O., LADEVÈZE P., 1992, Interlaminar interface modelling for the prediction of delamination, *Composite Structures*, **22**, 235-242
3. ALLIX O., LADEVÈZE P., 1996, Damage mechanics of interfacial media: basic aspects, identification and application to delamination, *Studies in Applied Mechanics*, **44**, 167-188
4. ALLIX O., LADEVÈZE P., CORIGLIANO A., 1995, Damage analysis of interlaminar fracture specimens, *Composite Structures*, **31**, 61-74
5. ALLIX O., LADEVÈZE P., DEU J.F., LÉVÊQUE D., 2000, A mesomodel for localization and damage computation in laminates, *Computer Methods in Applied Mechanics and Engineering*, **183**, 105-122
6. ALLIX O., LADEVÈZE P., GORNET L., PERRET L., 1998, A computational damage mechanics approach for laminates: identification and comparison with experimental result, *Studies in Applied Mechanics*, **46**, 481-500
7. BAŽANT Z.P., PIJAUDIER-CABOT G., 1988, Nonlocal continuum damage, localization instability and convergence, *Journal of Applied Mechanics*, **55**, 287-293
8. BAŽANT Z.P., PIJAUDIER-CABOT G., 1989, Measurement of characteristic length of nonlocal continuum, *Journal of Engineering Mechanics*, **115**, 755-767
9. BEER G., 1985, An isoparametric joint/interface element for finite element analysis, *International Journal for Numerical Methods in Engineering*, **21**, 585-600
10. BORINO G., FAILLA B. PARRINELLO F., 2007, Nonlocal elastic damage interface mechanical model, *International Journal for Multiscale Computational Engineering*, **5**, 153-165
11. CHABOCHE J.L., GIRARD R., LEVASSEUR P., 1997, On the interface debonding models, *International Journal of Damage Mechanics*, **6**, 220-257

12. CORIGLIANO A., 1993, Formulation, identification and use of interface models in the numerical analysis of composite delamination, *International Journal Solids and Structures*, **30**, 2779-2811
13. CORIGLIANO A., ALLIX O., 2000, Some aspects of interlaminar degradation in composites, *Computer Methods in Applied Mechanics and Engineering*, **185**, 203-224
14. DAVIDSON P., WAAS A.M., 2012, Non-smooth Mode I fracture of fibre-reinforced composites: an experimental, numerical and analytical study, *Philosophical Transactions of the Royal Society of London, Series A*, **370**, 1942-1965
15. DAVIES P., CANTWELL W., MOULIN C., KAUSCH, H.H., 1989, A study of delamination resistance of IM6/PEEK composites, *Composites Science and Technology*, **36**, 153-166
16. HERAKOVICH C.T., 1997, *Mechanics of Fibrous Composites*, 1st ed., John Wiley & Sons Ltd., New York, U.S.
17. IJAZ H., ASAD M., GORNET L., ALAM S.Y., 2014, Prediction of delamination crack growth in carbon/fiber epoxy composite laminates using non-local interface damage model, *Mechanics & Industry*, **15**, 293-300.
18. IJAZ H., KHAN M.A., SALEEM W., CHAUDRY S.R., 2011, Numerical modeling and simulation of delamination crack growth in cf/epoxy composite laminates under cyclic loading using cohesive zone model, *Advanced Materials Research*, **326**, 37-52
19. IJAZ H., ZAIN-UL-ABDEIN M., SALEEM W., ASAD M., MABROUKI T., 2016, A numerical approach on parametric sensitivity analysis for an aeronautic aluminium alloy turning process, *Mechanics*, **2**, 149-155
20. JIRASEK M., 1998, Nonlocal models for damage and fracture: comparison of approaches, *International Journal of Solids and Structures*, **35**, 4133-4145
21. MARGUET S., ROZYCKI P., GORNET L., 2007, A rate dependent constitutive model for carbon-fiber reinforced plastic woven fabric, *Mechanics of Advanced Materials and Structures*, **14**, 619-631
22. MENG Q., WANG Z., 2014, Extended finite element method for power-law creep crack growth, *Engineering Fracture Mechanics*, **127**, 148-160
23. PEERLINGS R.H.J., GEERS M.G.D., DE BORST R., BREKELMANS W.A.M., 2001, A critical comparison of nonlocal and gradient enhanced softening continua, *International Journal of Solids Structures*, **38**, 7723-7746
24. PENG L., XU J., 2013, Fatigue delamination growth of composite laminates with fiber bridging: Theory and simulation, [In:] *Proceeding of 13th International Conference on Fracture (ICF13)*, Yu S. and Feng X.-Q. (Edit.), Beijing, China, 16-21
25. VERPEAUX P., CHARRAS T., MILLARD A., 1998, *Castem 2000: Une Approche Moderne du Calcul des Structures*, Fouet J.M., Ladevèze P., Ohayon R. (Edit.), 227-261
26. WILLIAMS J.G., 1988, On the calculation of energy release rates for cracked laminates, *International Journal of Fracture*, **36**, 101-119
27. YAO L., 2015, Mode I fatigue delamination growth in composite laminates with fibre bridging, PhD Dissertation, Technische Universiteit Delft, Germany

A STEREOLOGICAL UBIQUITIFORMAL SOFTENING MODEL FOR CONCRETE

ZHUO-CHENG OU, GUAN-YING LI, ZHUO-PING DUAN, FENG-LEI HUANG

State Key Laboratory of Explosion Science and Technology, Beijing Institute of Technology, Beijing, China

e-mail address: zcou@bit.edu.cn

A stereological ubiquitiformal softening model for describing the softening behavior of concrete under quasi-static uniaxial tensile loadings is presented in this paper. In the model, both the damage evaluation process of fracture cross-sections and their distribution along the specimens axis are taken into account. The numerical results of a certain kind of full grade concrete made of crushed coarse aggregate are found to be in good agreement with the experimental data. Moreover, an experiential relation between the lower bound to the scale invariance of concrete and its tensile strength is also obtained by data fitting of the experimental data, which provides an effective approach to determine the lower bound to scale invariance of concrete.

Keywords: ubiquitiform, fractal, concrete, softening curve

1. Introduction

Fractals have been widely used as a nonlinear mathematical tool to describe mechanical behavior of heterogeneous materials such as concrete since the pioneer work of Mandelbrot (1982), Mandelbrot *et al.* (1984). It has been found that the internal structure of concrete appears quite a well approximate self-similarity in many aspects over certain ranges of scale. For example, it has been verified experimentally that the fracture surface of concrete can be described by fractals (Saouma and Barton, 1994; Charkaluk *et al.*, 1998). Stroeven has shown that for almost all the aggregate grading in concrete, the distribution of the aggregate particles in various diameters appears the self-similarity feature (Stroeven, 1973, 2000). Moreover, fractals have also been widely used to describe the fracture behavior of concrete (Borodich, 1997; Carpinteri *et al.*, 2002; Khezzzadeh and Mofid, 2006). However, there are still many intrinsic difficulties in fractal applications, especially in the case when the measure of a real geometrical or physical object must be taken into account because kinds of density of fractal parameters defined on the unit fractal measure are not only lacking unambiguous physical meanings but also very difficult to be determined in practice. Recently, Ou *et al.* (2014) demonstrated that such a difficulty was caused by contradiction between the integral dimensional immeasurability of a fractal and the integral dimensional characteristic of a real physical or geometrical object in nature, and proposed a new concept of ubiquitiform. According to Ou *et al.* (2014), a ubiquitiform is defined as a finite order self-similar (or self-affine) physical configuration constructed usually by a finite iterative procedure. It has been shown that a ubiquitiform has a finite integral dimensional measure and must be of integral dimension in Euclidean space, whereas the Hausdorff dimension of a fractal is usually not integral. The Hausdorff dimension of the initial element of a fractal changes abruptly at the point of infinite iteration, which results in divergence of the integral dimensional measure of the fractal and makes the fractal approximation of a real geometrical or physical object to a ubiquitiform unreasonable.

One important phenomenon in tensile failure of concrete is softening, and the most widely used theory is the so-called cohesive crack model (Barenblatt, 1959, 1962). Over the past decades,

several softening curves have been proposed, such as the linear curve (Hillerborg *et al.*, 1976), the bilinear curve (Pettersson, 1981), the nonlinear curve (Reinhardt *et al.*, 1986) and the power-law curve (Gopalaratnam and Shah, 1985; Karihaloo, 1995). Recently, Khezzadeh and Mofid (2006) proposed a quasi-fractal softening curve based on fractal concepts, in which, however, only the damage evaluation process of the fractured cross-section was considered. On the other hand, as demonstrated by Ou *et al.* (2014), a ubiquitous, rather than a fractal, should be used in describing a real geometrical or physical object in the case of the integral dimensional measure of the object.

Therefore, in this study, based on the concept of the ubiquitous, a stereological ubiquitous softening model for concrete, in which both the damage evaluation process of fractured cross-sections and their distribution along the specimens axis are taken into account, and the calculated results of softening curves of concrete are compared with previous experimental data. Moreover, it is interesting to find that there exists a good correspondence between the lower bound to scale invariance and the tensile strength of concrete, and then an exponential formula for the corresponding relationship is obtained.

2. Stereological ubiquitous softening model

To describe the damage evaluation process of a concrete specimen, a stereological damage region is assumed in this paper, based on the fracture band theory (Bažant and Oh, 1983). Namely, fracture of a heterogeneous aggregate material such as concrete can be assumed to occur in the form of a blunt smeared crack band. Such a stereological damage region consists of a series of fracture surfaces distributed along the axis of the specimen as a generalized ubiquitous Cantor set, and each of the fracture surface will be described by a generalized ubiquitous Sierpinski carpet having different complexity. The generalized ubiquitous Sierpinski carpet is generated by a series of recursive procedures, i.e. an iteration process from the initial square of unit side length. In each step of the iteration, each remaining square is divided into p^2 identical smaller squares, and the generalized ubiquitous Sierpinski carpet is then obtained by repeatedly removing q ($q/p^2 < 1$) small squares from the remaining squares. According to Khezzadeh and Mofid (2006), the removing area represents the cracked area of the fractured cross-sections. As has been defined by Ou *et al.* (2014), the complexity D of such a generalized ubiquitous Sierpinski carpet is

$$D = \frac{\ln(p^2 - q)}{\ln p} \quad (2.1)$$

Therefore, taking different values of p and q , the generalized ubiquitous Sierpinski carpet can be used to describe a surface with any complexity. The removed area in the n -th iteration is

$$\Delta a_n = A_p \frac{q}{p^2} \left(\frac{p^2 - q}{p^2} \right)^{n-1} \quad (2.2)$$

where A_p is the nominal area of the generalized ubiquitous Sierpinski carpet. The total area of the increased crack surface, when the specimen is failed, is

$$A_1 = \sum_{n=1}^{n_c} \Delta a_n = A_p \left[1 - \left(\frac{p^2 - q}{p^2} \right)^{n_c} \right] = A_p \left[1 - \left(\frac{1}{p^{n_c}} \right)^{2-D} \right] \quad (2.3)$$

where n_c represents the critical iteration number of the generalized ubiquitous Sierpinski carpet when the specimen is failed.

According to the fracture band theory (Bažant and Oh, 1983), in this study, a multiple crack surface hypothesis is proposed in the ubiquitous softening model. That is to say, to

describe the damage evolution of the concrete material, besides the main crack surface, there are still several secondary crack surfaces, each of which is described as the above-mentioned generalized ubiquitousformal Sierpinski carpet with different iteration orders. These crack surfaces are assumed to be distributed along the axis of the specimen as a generalized ubiquitousformal Cantor set (Fig. 1). Hereinafter, we denote these crack surfaces as the i -th order crack surfaces ($i = 1, 2, 3, \dots, m$), and the first order ($i = 1$) one is the main crack surface. According to the structure of the generalized ubiquitousformal Cantor set, the number of the i -th order crack surface is $k_i = 2^{i-1}$. It is also assumed that the iteration number of the i -th order crack surface is one less than that of the $(i - 1)$ -th order crack surface. Thus, the increase of the i -th order crack surface in the n -th iteration can be calculated by the equation

$$\Delta a_n^i = A_p \frac{q}{p^2} \left(\frac{p^2 - q}{p^2} \right)^{n-i} \quad (2.4)$$

The total increase of the crack surface in the n -th iteration is

$$\Delta a_n = \sum_{i=1}^m k_i \Delta a_n^i = \sum_{i=1}^m 2^{i-1} A_p \frac{q}{p^2} \left(\frac{p^2 - q}{p^2} \right)^{n-i} = A_p \frac{2^m q p^{2m} (p^2 - q)^{n-m} - q (p^2 - q)^n}{p^{2n} (p^2 + q)} \quad (2.5)$$

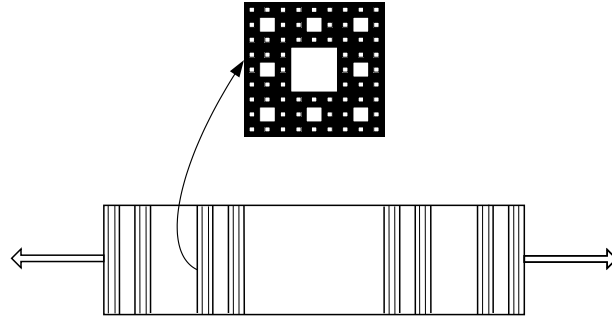


Fig. 1. Stereological ubiquitousformal softening model

According to the iteration law of the generalized ubiquitousformal Sierpinski carpet, the ratio of the area of the $(i + 1)$ -th crack surface to that of the i -th crack surface is

$$A_{i+1} = \frac{p^2 - q}{p^2} A_i \quad (2.6)$$

where $i = 1, 2, 3, \dots, m$, and, from Eq. (2.6), we have

$$A_i = \left(\frac{p^2 - q}{p^2} \right)^{i-1} A_1 \quad (2.7)$$

Then, the total crack surface increased in the fracture process is

$$A = \sum_{i=1}^m k_i A_i = A_1 \sum_{i=1}^m 2^{i-1} \left(\frac{p^2 - q}{p^2} \right)^{i-1} = A_1 \frac{p^{2m} - 2^m (p^2 - q)^m}{(2q - p^2) p^{2m-2}} \quad (2.8)$$

For convenience, here, the homogeneous deformation along the axis of the specimen is assumed, and then the elongations generated in each iteration Δw are the same, which can be written as

$$\Delta w = \frac{w_c}{n_c} \quad (2.9)$$

where w_c is the critical elongation of the specimen.

In general, on the one hand, the energy consumed in each iteration is proportional to the increase of the area of the crack surface, that is

$$\Delta U_n = G_f \Delta a_n \quad (2.10)$$

where G_f is the fracture energy. On the other hand, the required energy to generate new cracks equal to the area under the softening curve in a interval of length Δw implies that

$$\Delta W_n = A \sigma_n \Delta w \quad (2.11)$$

Thus, from Eqs.(2.10) and (2.11), there is

$$G_f \frac{\Delta a_n}{A} = \sigma_n \Delta w \quad (2.12)$$

The relationship between the stress and the elongation in each iteration can be obtained from Eqs. (2.5), (2.8), (2.9) and (2.12), as

$$\begin{aligned} \sigma_n &= \frac{G_f \Delta a_n}{A \Delta w} = \frac{G_f A_p n_c p^{2m-2} (2q - p^2) 2^m q p^{2m} (p^2 - q)^{n-m}}{A_1 w_c p^{2n} (p^2 + q) [p^{2m} - 2^m (p^2 - q)^m]} \\ &\quad - \frac{G_f A_p n_c p^{2m-2} (2q - p^2) q (p^2 - q)^n}{A_1 w_c p^{2n} (p^2 + q) [p^{2m} - 2^m (p^2 - q)^m]} \quad 1 \leq n \leq n_c \end{aligned} \quad (2.13)$$

It should be noticed that the values of both the stress and the elongation in Eq. (2.13) are discrete, starting from $n = 1$. In order to obtain a continuous stress-elongation curve in the interval of $[0, w_c]$, the Khezzadeh and Mofid modification (Khezzadeh and Mofid, 2006) is used, which is described briefly below. Firstly, it is assumed that the value of the softening function in $w = 0$ is equal to the tensile strength of the specimen, i.e., $\sigma(0) = f_t$, and that the stress-elongation curve is linear in the interval of $[0, \Delta w]$. Next, an energy modification factor μ is then introduced to make sure that the area under the softening curve is equal to G_f , namely,

$$(1 - \mu)G_f = \left[f_t + \sigma \left(\frac{\Delta w}{2} \right) \right] \frac{\Delta w}{2} \quad (2.14)$$

Thus one has

$$\begin{aligned} \sigma &= \frac{\mu A_p G_f n_c p^{2m-2} (2q - p^2) 2^m q p^{2m} (p^2 - q)^{\frac{n_c}{w_c} w - m}}{A_1 w_c p^{2 \frac{n_c}{w_c} w} (p^2 + q) [p^{2m} - 2^m (p^2 - q)^m]} \\ &\quad - \frac{\mu A_p G_f n_c p^{2m-2} (2q - p^2) q (p^2 - q)^{\frac{n_c}{w_c} w}}{A_1 w_c p^{2 \frac{n_c}{w_c} w} (p^2 + q) [p^{2m} - 2^m (p^2 - q)^m]} \quad \frac{w_c}{n_c} \leq w \leq w_c \end{aligned} \quad (2.15)$$

For convenience, we assume that $q = 1$ in the ubiquitous softening model, then Eq. (2.15) can be rewritten as

$$\begin{aligned} \sigma &= \frac{\mu A_p G_f n_c p^{2m-2} (2 - p^2) 2^m p^{2m} (p^2 - 1)^{\frac{n_c}{w_c} w - m}}{A_1 w_c p^{2 \frac{n_c}{w_c} w} (p^2 + 1) [p^{2m} - 2^m (p^2 - 1)^m]} \\ &\quad - \frac{\mu A_p G_f n_c p^{2m-2} (2 - p^2) (p^2 - 1)^{\frac{n_c}{w_c} w}}{A_1 w_c p^{2 \frac{n_c}{w_c} w} (p^2 + 1) [p^{2m} - 2^m (p^2 - 1)^m]} \quad \frac{w_c}{n_c} \leq w \leq w_c \end{aligned} \quad (2.16)$$

For $w = \Delta w$, we have

$$\begin{aligned} \sigma(\Delta w) &= \frac{\mu A_p G_f n_c p^{2m-4} (2 - p^2) 2^m p^{2m} (p^2 - 1)^{1-m}}{A_1 w_c (p^2 + 1) [p^{2m} - 2^m (p^2 - 1)^m]} \\ &\quad - \frac{\mu A_p G_f n_c p^{2m-4} (2 - p^2) (p^2 - 1)}{A_1 w_c (p^2 + 1) [p^{2m} - 2^m (p^2 - 1)^m]} \end{aligned} \quad (2.17)$$

We can obtain the slope of the softening curve in the interval $[0, \Delta w]$

$$C = \frac{\sigma(\Delta w) - f_t}{\Delta w} = \frac{\mu A_p G_f n_c^2 p^{2m-4} (2-p^2) 2^m p^{2m} (p^2-1)^{1-m}}{A_1 w_c^2 (p^2+1) [p^{2m} - 2^m (p^2-1)^m]} - \frac{\mu A_p G_f n_c^2 p^{2m-4} (2-p^2) (p^2-1)}{A_1 w_c^2 (p^2+1) [p^{2m} - 2^m (p^2-1)^m]} - \frac{n_c}{w_c} f_t \quad (2.18)$$

Then we have

$$\sigma = \frac{\mu A_p G_f n_c^2 p^{2m-4} (2-p^2) 2^m p^{2m} (p^2-1)^{1-m}}{A_1 w_c^2 (p^2+1) [p^{2m} - 2^m (p^2-1)^m]} w - \frac{\mu A_p G_f n_c^2 p^{2m-4} (2-p^2) (p^2-1)}{A_1 w_c^2 (p^2+1) [p^{2m} - 2^m (p^2-1)^m]} w - \frac{n_c}{w_c} f_t w + f_t \quad 0 \leq w \leq \frac{w_c}{n_c} \quad (2.19)$$

From Eq. (2.14) and Eq. (2.19) one can obtain the energy modification factor μ as

$$\mu = 1 - \frac{A_p p^{2m-4} (2-p^2) [2^m p^{2m} (p^2-1)^{1-m} - (p^2-1)]}{4A_1 (p^2+1) [p^{2m} - 2^m (p^2-1)^m]} - \frac{3f_t w_c}{4G_f n_c} = \frac{4G_f n_c - 3f_t w_c}{4G_f n_c} \cdot \frac{4A_1 (p^2+1) [p^{2m} - 2^m (p^2-1)^m]}{A_p p^{2m-4} (2-p^2) [2^m p^{2m} (p^2-1)^{1-m} - (p^2-1)] + 4A_1 (p^2+1) [p^{2m} - 2^m (p^2-1)^m]} \quad (2.20)$$

The ubiquitous formal softening curve of concrete is then

$$\sigma = \begin{cases} \frac{\mu A_p G_f n_c p^{2m-2} (2-p^2) [2^m p^{2m} (p^2-1)^{-m} - 1]}{A_1 w_c (p^2+1) [p^{2m} - 2^m (p^2-1)^m]} \left(1 - \frac{1}{p^2}\right) \frac{n_c}{w_c} w & \frac{w_c}{n_c} \leq w \leq w_c \\ \left(\frac{\mu A_p G_f n_c^2 p^{2m-4} (2-p^2) [2^m p^{2m} (p^2-1)^{1-m} - (p^2-1)]}{A_1 w_c^2 (p^2+1) [p^{2m} - 2^m (p^2-1)^m]} - \frac{n_c}{w_c} f \right) w + f_t & 0 \leq w \leq \frac{w_c}{n_c} \end{cases} \quad (2.21)$$

In the ubiquitous formal softening model, the iteration number is calculated by the relation

$$\left(\frac{1}{p}\right)^N = \frac{\delta_{min}}{l} \quad (2.22)$$

where δ_{min} and l are the minimum and maximum scales of the concrete respectively, which are related to the micro and macro structure of the concrete. However, the iteration number calculated from Eq. (2.22) is always not an integer, whereas the iteration number of the generalized ubiquitous formal Cantor set should be an integer. Thus we assume that $n = [N]$ in this paper, where the square brackets represents the maximum integer no larger than the argument.

3. Numerical results of full grade concrete

To confirm the availability of the ubiquitous formal softening model, the model is used to calculate the softening curve of a full grade concrete specimen made of crushed coarse aggregate, and the numerical results are compared with the experimental result (Deng *et al.*, 2005). In the experiment, the uniaxial tension-compression behavior of the full grade concrete specimens made of crushed coarse aggregate was studied on an INSTRON8506 material testing machine under constant-displacement loading, with the maximum load of 3000 kN. Four displacement extensometers were set around the test specimen, and the data collection and the loading control were completed by using a computer. The composition of the concrete and the experimental data are listed in Tables 1 and 2, respectively.

Table 1. Concrete mix of the concrete [kg/m³]

Water	Cement	Ash	Artificial sand	Artificial stone [mm]				Superplasticizerits	
				5-20	20-40	40-80	80-150	JGB	DH9
87	131	44	585	328	328	492	492	10.5	1.23

Table 2. Experimental data of the concrete specimen

Curing period [day]	Tensile strength f_t [MPa]	Elastic modulus E_t [GPa]	Critical elongation w_c [mm]	Fracture energy G_f [N/m]
110	1.908	40.0	1.390	497.220
55	1.508	37.0	1.355	448.401
46	1.310	35.0	1.199	422.878
16	1.180	31.1	1.680	445.738
15	1.044	28.9	1.289	369.463
11	0.804	22.0	1.193	273.233

In the ubiquitousformal softening model, the parameter is: $p = 2.07$, which is the same as in Khezzadeh and Mofid (2006), and the adaptive result for m is $m = 2$.

For a certain concrete, the parameters p , m , A_p and n_c in the softening model are determined, and the material parameters G_f , w_c and f_t are also known. Thus the parameter A_1 and μ can be regarded as constants. Therefore, for convenience, we rewrite Eq. (2.21) as

$$\sigma = \begin{cases} C_1 C_2^w & \frac{w_c}{n_c} \leq w \leq w_c \\ f_t - C_3 w & 0 \leq w \leq \frac{w_c}{n_c} \end{cases} \quad (3.1)$$

where C_1 , C_2 and C_3 are constant. The values of these parameters for concrete specimens with different curing periods as well as the experimental data are all listed in Table 3.

Table 3. Parameters of the ubiquitousformal softening model for concrete specimen

Curing period [day]	Tensile strength f_t [MPa]	Crit. elongation w_c [mm]	Iteration number n_c	δ_{min} [μm]	C_1	C_2	C_3
110	1.908	1.390	12	24	1.145	0.1008	8.894
55	1.508	1.355	11	50	1.0047	0.1156	5.9895
46	1.310	1.199	10	104	1.0188	0.1090	4.4188
16	1.180	1.680	10	104	0.7080	0.2055	3.7931
15	1.044	1.289	9	215	0.7194	0.1563	3.4388
11	0.804	1.193	8	445	0.4916	0.1682	2.8644

The comparison between the softening curves calculated by using the ubiquitousformal model and the experimental results are shown in Fig. 2. It can be seen that the ubiquitousformal softening model is in good agreement with the experimental data. It should be pointed out that the difference of the stress between the softening curve in the interval $[0, \Delta w]$ increases with the tensile strength of the specimen, except for the specimen with a curing period of 16 days. However, it can also be seen that the experimental data for this specimen, especially the critical elongation, is abnormal. The difference of the softening curve of this specimen is caused mainly by abnormality of the experimental data.

As has been mentioned by Ou *et al.* (2014), the lower bound to the scale invariance δ_{min} , namely, the minimum scale of concrete, is a crucial parameter for a ubiquitousformal, and it can be

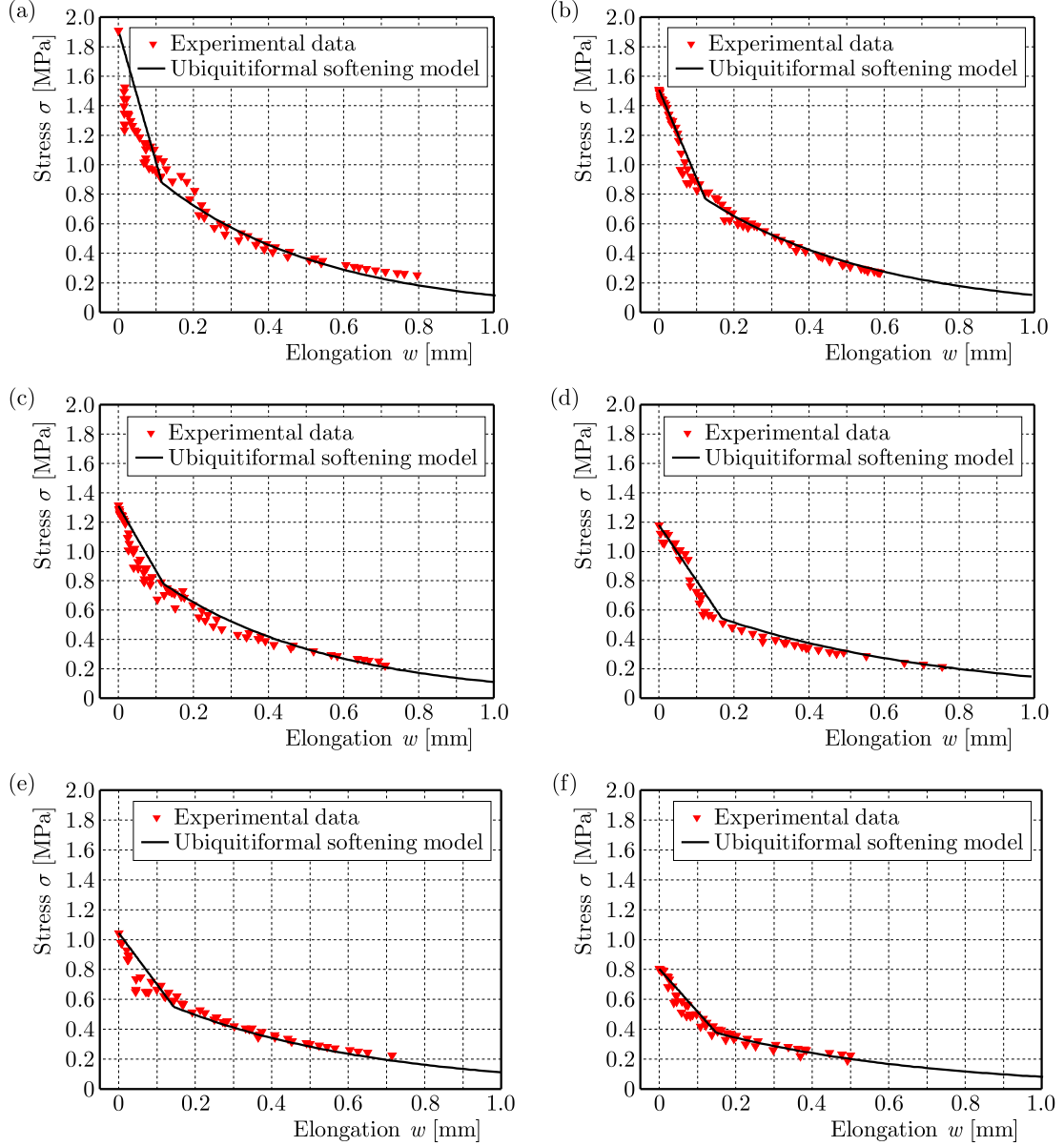


Fig. 2. The ubiquitous softening curve: (a) specimen of 1.908 MPa, (b) specimen of 1.508 MPa, (c) specimen of 1.310 MPa, (d) specimen of 1.180 MPa, (e) specimen of 1.044 MPa, (f) specimen of 0.804 MPa

seen that this crucial parameter is related with the tensile strength of the concrete specimen with different curing periods. The lower bound to the scale invariance δ_{min} for the specimen with different tensile strength is shown in Fig. 3. By fitting the data with a power function, the relation between the lower bound to the scale invariance δ_{min} and the tensile strength can be obtained as

$$\delta_{min} = 221.28 \cdot f_t^{-3.24} \quad (3.2)$$

where the units of δ_{min} and f_t are μm and MPa, respectively. This relationship provides a reasonable approach to determine the lower bound to the scale invariance of concrete. Furthermore, by analysing the influencing factors of the concrete tensile strength, the approach to determine the lower bound to the scale invariance of concrete by other physical parameters may be obtained.

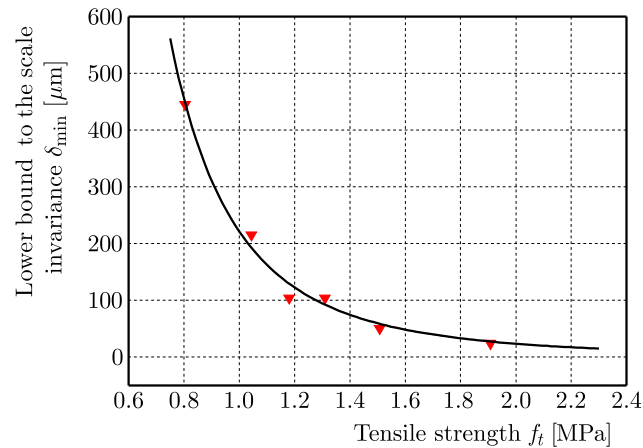


Fig. 3. The relation between the lower bound to the scale invariance δ_{min} and tensile strength of concrete

It should be mentioned that, although such an ubiquitous softening model for concrete seems to be similar to the fractal one (Khezzadeh and Mofid, 2006), it has more definite physical meanings. The relation between the lower bound to the scale invariance and tensile strength of concrete is obtained numerically, which may provide a reasonable approach to determine the lower bound to the scale invariance of concrete.

4. Conclusion

A stereological type of ubiquitous softening model that can well describe the softening behavior of concrete under quasi-static tensile loadings is proposed in this paper. Both the damage evaluation process of fracture cross-sections and their distribution along the specimens axis are considered. Moreover, by fitting the experimental data, a relation between the lower bound to the scale invariance and the tensile strength of concrete is obtained, which provides a reasonable approach to determine the lower bound to the scale invariance of concrete.

Acknowledgements

This work were supported by The National Natural Science Foundation of China under Grant 11772056 and also The National Science Foundation of China under Grant 11521062.

References

1. BARENBLATT G.I., 1959, The formation of equilibrium cracks during brittle fracture: General ideas and hypotheses, axially symmetric cracks, *Journal of Applied Mathematics and Mechanics*, **23**, 622-636
2. BARENBLATT G.I., 1962, The mathematical theory of equilibrium cracks in brittle fracture, *Advances in Applied Mechanics*, **7**, 55-129
3. BAŽANT Z.P., OH B.H., 1983, Crack band theory for fracture of concrete, *Matériaux et Construction*, **16**, 155-177
4. BORODICH F.M., 1997, Some fractal models of fracture, *Journal of the Mechanics and Physics of Solids*, **45**, 239-259
5. CARPINTERI A., CHIAIA B., CORNETTI P., 2002, A scale-invariant cohesive crack model for quasi-brittle materials, *Engineering Fracture Mechanics*, **69**, 207-217

6. CHARKALUK E., BIGERELLE M., IOST A., 1998, Fractals and fracture, *Engineering Fracture Mechanics*, **61**, 119-139
7. DENG Z.C., LI Q.B., FU H., 2005, Mechanical properties of tension and compression about artificial full-graded aggregate concrete dam (in Chinese), *Journal of Hydraulic Engineering*, **36**, 214-218
8. GOPALARATNAM V.S., SHAH S.P., 1985, Softening response of plain concrete in direct tension, *Journal Proceedings (American Concrete Institute)*, **82**, 310-323
9. HILLERBORG A., MODEER M., PETERSSON P.E., 1976, Analysis of crack formation and crack growth in concrete by means of fracture mechanics and finite elements, *Cement and Concrete Research*, **6**, 773-782
10. KARIHALOO B.L., 1995, *Fracture Mechanics and Structural Concrete*, Longman Scientific & Technical, Harlow
11. KHEZRZADEH H., MOFID M., 2006, Tensile fracture behavior of heterogeneous materials based on fractal geometry, *Theoretical and Applied Fracture Mechanics*, **46**, 46-56
12. MANDELBROT B.B., 1982, *The Fractal Geometry of Nature*, Freeman, New York
13. MANDELBROT B.B., PASSOJA D.E., PAULLAY A.J., 1984, Fractal character of fracture surfaces of metals, *Nature*, **308**, 721-722
14. OU Z.C., LI G.Y., DUAN Z.P., HUANG F.L., 2014, Ubiquitiform in applied mechanics, *Journal of Theoretical and Applied Mechanics*, **52**, 37-46
15. PETERSSON P.E., 1981, Crack growth and development of fracture zone in plain concrete and similar materials, Division of Building Materials, Lund Institute of Technology
16. REINHARDT H.W., CORNELISSEN H.A.W., HORDIJK D.A., 1986, Tensile tests and failure analysis of concrete, *Journal of Structural Engineering*, **112**, 2462-2477
17. SAOUMA V.E., BARTON C.C., 1994, Fractals, fractures, and size effects in concrete, *Journal of Engineering Mechanics*, **120**, 835-854
18. STROEVEN P., 1973, Some aspects of the micro-mechanics of concrete, Ph.D. Thesis, Delft University of Technology, Delft
19. STROEVEN P., 2000, A stereological approach to roughness of fracture surfaces and tortuosity of transport paths in concrete, *Cement and Concrete Composites*, **22**, 331-341

Manuscript received August 1, 2017; accepted for print June 12, 2018

TIME INTEGRATION OF STOCHASTIC GENERALIZED EQUATIONS OF MOTION USING SSFEM

MARIUSZ POŃSKI

*Czestochowa University of Technology, Department of Civil Engineering, Częstochowa, Poland
e-mail: mponski@bud.pcz.czyst.pl*

The paper develops an integration approach to stochastic nonlinear partial differential equations (SPDE's) with parameters to be random fields. The methodology is based upon assumption that random fields are from a special class of functions, and can be described as a product of two functions with dependent and independent random variables. Such an approach allows one to use Karhunen-Loève expansion directly, and the modified stochastic spectral finite element method (SSFEM). It is assumed that a random field is stationary and Gaussian while the autocovariance function is known. A numerical example of one-dimensional heat waves analysis is shown.

Keywords: spectral stochastic finite element method, time integration, heat waves

1. Introduction

In the literature, one can find works describing SPDE's solutions using SSFEM for stationary problems (Le Maitre and Knio, 2010; Matthies and Keese, 2005). There are also methods handling transient problems such as the Monte Carlo method (MC), perturbation method (Kamiński, 2013; Służalec, 2003), stochastic collocation method (SCM) (Acharjee and Zabaras, 2006; Babuška *et al.*, 2007; Xiu and Hesthaven, 2005). These methods are widely used for many problems, e.g. continuum mechanics, fluid dynamics, heat flow and have their advantages and disadvantages (Stefanou, 2009; Xiu, 2010). As the leading in the literature, the SCM method is listed due to the possibility of analyzing complex nonlinear problems. It reduces analysis time by using multithreading and can be simply implemented (deterministic solver is treated as so-called "black box"). Competitive to SCM is the method of Stochastic Spectral Finite Element Method proposed by Ghanem and Spanos (2003). This method is one of the so-called intrusive methods, which is very effective in solving linear problems, but requires building the source code from scratch. An important disadvantage that is mentioned in many works is the coupling of equations that prevent the use of parallel solvers. This problem was solved by applying the domain decomposition method (Subber and Sarkar, 2014). Another important disadvantage mentioned in the works on numerical solution with SSFEM is the considerable difficulty of solving nonlinear problems. Mathematical formulation of nonlinear stationary equations can be found in works (Arregui-Mena *et al.*, 2016; Ghosh *et al.*, 2008; Hu *et al.*, 2015; Matthies and Keese, 2005; Nouy, 2008; Nouy and Le Maitre, 2009; Stefanou *et al.*, 2017; Xiu and Karniadakis, 2003; Zakian and Khaji, 2016) rather than description of a general numerical approach. There is also no comprehensive solution to transient problems. This paper presents a methodology based upon a special class of functions occurring in constitutive equations which can be described as a product of two functions, respectively with dependent and independent variables. This approach allows one to extend the applicability of SSFEM to solve wide range of nonstationary nonlinear stochastic PDE's.

2. Stochastic description

In this work, a modified SSFEM is used. This method is based upon notion of a random field. The random field $\alpha(x, \omega)$ (Acharjee and Zabaras, 2007; Xiu, 2010) ($x \in \mathbb{D} \subset \mathbb{R}$, $\omega \in \Omega$) is a real valued measurable function which assigns a random variable $\alpha(\omega)$ to each point x on a fixed probability space $(\Omega, \mathbb{Z}, \mathbb{P})$. Here Ω is the set of elementary events, \mathbb{Z} is the σ -algebra and $\mathbb{P} : \mathbb{Z} \rightarrow [0, 1]$ is a probability measure. To obtain a computationally useful representation of the process $\alpha(x, \omega)$, it will be presented in the canonical form. Among various forms of such a representation, a spectral representation - Karhunen-Loève expansion will be adopted in further considerations (Ghanem and Spanos, 2003). This expansion may be presented in the following form

$$\alpha(x, \omega) = \xi_0 \overline{\alpha(x)} + \sum_{i=1}^{\infty} \xi_i(\omega) \sqrt{\lambda_i} f_i(x) \quad x \in \mathbb{D}, \quad \omega \in \Omega \quad (2.1)$$

Such a Karhunen-Loève expansion is truncated to M terms

$$\alpha(x, \omega) \approx \xi_0 \overline{\alpha(x)} + \sum_{i=1}^M \xi_i(\omega) \sqrt{\lambda_i} f_i(x) \quad x \in \mathbb{D}, \quad \omega \in \Omega \quad (2.2)$$

In equation (2.1), $\{\xi_i(\omega)\}_{i=1}^{\infty}$ is a set of orthonormal independent Gaussian random variables with mean $\xi_0 = 1$ and standard deviations equal to one, $\overline{(\cdot)}$ is the expected value operator. Constants $\{\lambda_i\}_{i=1}^{\infty}$ and deterministic functions $\{f_i(x)\}_{i=1}^{\infty}$ are the eigenvalues and eigenfunctions of the covariance kernel

$$\int_{\mathbb{D}} C_{kernel}(x_1, x_2) f_i(x_2) dx_2 = \lambda_i f_i(x_1) \quad i \in \mathbb{N} = \{1, 2, \dots\} \quad (2.3)$$

The polynomial chaos (Ghanem and Spanos, 2003; Le Maitre and Knio, 2010) representation of the random variable $U(\omega)$, truncated to P terms, can be written as

$$U(\omega) \approx U(\boldsymbol{\xi}) = \sum_{i=0}^P u_i \Phi_i(\boldsymbol{\xi}) \quad (2.4)$$

where $\{\Phi_i(\boldsymbol{\xi})\}_{i=0}^P$ denotes polynomial chaoses (Ghanem and Spanos, 2003), and $\{u_i\}_{i=0}^P$ are coefficients of the expansion. The coefficient P described by the expression (Ghanem and Spanos, 2003)

$$P = 1 + \sum_{s=1}^p \frac{2}{s!} \prod_{r=0}^{s-1} (M + r) \quad (2.5)$$

is the total number of polynomial chaoses used in the expansion, excluding the zero-th order term, with p denoting the order of polynomial chaoses (detailed description of polynomial chaoses can be found in Ghanem and Spanos (2003), Le Maitre and Knio (2010)).

3. Governing equations formulation of SSFEM – an approach for a special class of equations

3.1. Method of solution of the stochastic problem (SSFEM)

First step in solving SPDE's, after finite element discretisation, is the stochastic random field discretisation. Let K denotes the number of nodes of the discretized domain. The equation of

motion with given initial and boundary conditions, which is analyzed, can be written in a well known matrix form (Bathe, 1996)

$$\mathbf{M}(\mathbf{x}, \omega, \mathbf{q}(t, \omega))\ddot{\mathbf{q}}(t, \omega) + \mathbf{C}(\mathbf{x}, \omega, \mathbf{q}(t, \omega))\dot{\mathbf{q}}(t, \omega) + \mathbf{K}(\mathbf{x}, \omega, \mathbf{q}(t, \omega))\mathbf{q}(t, \omega) = \mathbf{F}(\mathbf{x}, \omega, \mathbf{q}(t, \omega)) \quad (3.1)$$

where $t \in \mathbb{T}$ denotes time, $\mathbf{x} \in \mathbb{D} \times \mathbb{D} \times \mathbb{D} \stackrel{def}{=} \mathbb{D}^3 \subset \mathbb{R}^3$ denotes space variables, $\mathbf{q}(t, \omega)$ is a generalized $K \times 1$ displacement vector and $\dot{\mathbf{q}}(t, \omega), \ddot{\mathbf{q}}(t, \omega)$ is the first and second derivative in time. Suppose that for the $K \times K$ matrices $\mathbf{M}, \mathbf{C}, \mathbf{K}$ and $K \times 1$ vector \mathbf{F} separation of dependent and independent variables can be made, which allows one to use Karhunen-Loève expansion directly, e.g.

$$\mathbf{K}(\mathbf{x}, \omega, \mathbf{q}(t, \omega)) = \mathbf{K}(\mathbf{x}, \omega) f_K(\mathbf{q}(t, \omega)) \quad (3.2)$$

where $f_K(\mathbf{q}(t, \omega))$ is a real valued Riemann integrable function on a suitable space and $\mathbf{K}(\mathbf{x}, \omega)$ is a $K \times K$ matrix. Such an approach limits applicability of this method to problems in which constitutive equations or nonlinear boundary conditions can be written as a product of functions of independent and dependent variables, e.g. $k(\mathbf{x}, q(\mathbf{x}, t)) = k_a(\mathbf{x})k_b(q(\mathbf{x}, t))$. Many physical relations can be written in this way or can be reduced to either $k(\mathbf{x}, q(\mathbf{x}, t)) = k_b(q(\mathbf{x}, t))$ or $k(\mathbf{x}, q(\mathbf{x}, t)) = k_a(\mathbf{x})$.

Assume that the discretized function of generalized displacement at each node has representations in polynomial chaos

$$q_k(t, \omega) \approx \sum_{i=0}^P (q_{spect}(t))_{k,i} \Phi_i(\boldsymbol{\xi}(\omega)) \quad k = 1, 2, \dots, K \quad (3.3)$$

(index k denotes node number) and let it be derived its first and second order derivative with respect to the time

$$\begin{aligned} \dot{q}_k(t, \omega) &\approx \sum_{i=0}^P (\dot{q}_{spect}(t))_{k,i} \Phi_i(\boldsymbol{\xi}(\omega)) & k = 1, 2, \dots, K \\ \ddot{q}_k(t, \omega) &\approx \sum_{i=0}^P (\ddot{q}_{spect}(t))_{k,i} \Phi_i(\boldsymbol{\xi}(\omega)) & k = 1, 2, \dots, K \end{aligned} \quad (3.4)$$

The vector of nodal generalized displacement can be written as

$$\mathbf{q}(t, \omega) \approx \mathbf{q}(t, \boldsymbol{\xi}) = \mathbf{q}_{spect}^{matrix}(t) \boldsymbol{\Phi}_{node}(\boldsymbol{\xi}) \quad (3.5)$$

where $\mathbf{q}_{spect}^{matrix}(t)$ is a $K \times (P + 1)$ matrix built from spectral coefficients and

$$\boldsymbol{\Phi}_{node}(\boldsymbol{\xi}) = [\Phi_0(\boldsymbol{\xi}) \quad \Phi_1(\boldsymbol{\xi}) \quad \dots \quad \Phi_P(\boldsymbol{\xi})]^T \quad (3.6)$$

is a vector built from the polynomial chaoses.

Substituting appropriate derivatives of equation (3.5) to equation (3.1) and using (3.2), (3.5)-(3.6), the following equation

$$\begin{aligned} &\mathbf{M}(\mathbf{x}, \omega) f_M(\mathbf{q}_{spect}^{matrix}(t) \boldsymbol{\Phi}_{node}(\boldsymbol{\xi})) \ddot{\mathbf{q}}_{spect}^{matrix}(t) \boldsymbol{\Phi}_{node}(\boldsymbol{\xi}) \\ &+ \mathbf{C}(\mathbf{x}, \omega) f_C(\mathbf{q}_{spect}^{matrix}(t) \boldsymbol{\Phi}_{node}(\boldsymbol{\xi})) \dot{\mathbf{q}}_{spect}^{matrix}(t) \boldsymbol{\Phi}_{node}(\boldsymbol{\xi}) \\ &+ \mathbf{K}(\mathbf{x}, \omega) f_K(\mathbf{q}_{spect}^{matrix}(t) \boldsymbol{\Phi}_{node}(\boldsymbol{\xi})) \mathbf{q}_{spect}^{matrix}(t) \boldsymbol{\Phi}_{node}(\boldsymbol{\xi}) = \mathbf{F}(\mathbf{x}, \omega) f_F(\mathbf{q}_{spect}^{matrix}(t)) \end{aligned} \quad (3.7)$$

can be obtained.

Let us represent the matrices $\mathbf{M}(\mathbf{x}, \omega)$, $\mathbf{C}(\mathbf{x}, \omega)$, $\mathbf{K}(\mathbf{x}, \omega)$, $\mathbf{F}(\mathbf{x}, \omega)$ using the Karhunen-Loève expansion, e.g.

$$\mathbf{K}(\mathbf{x}, \omega) \approx \mathbf{K}(\mathbf{x}, \boldsymbol{\xi}) = (\mathbf{K}(\mathbf{x}))_0 \xi_0 + \sum_{i=1}^M \xi_i(\omega) (\mathbf{K}^0(\mathbf{x}))_i \quad (3.8)$$

where $(\cdot)_0$ denotes a matrix computed for the mean value of the process and $(\cdot)^0$ denotes a matrix built of the shape functions and Karhunen-Loève expansion terms (e.g. $(\mathbf{K}^0(\mathbf{x}))_i = \int_{\mathbb{D}} \nabla \mathbf{N}(\sqrt{\lambda_i} f_i(x)) \nabla \mathbf{N}^T d\mathbf{x}$, where \mathbf{N} is a vector built of test functions from the Sobolev space $H^1(0, l_{elem})$ where l_{elem} is a finite element length).

In order to formulate a suitable system of equations, let us represent the matrix of stochastic eigenmodes of the solution as a vector $\mathbf{q}_{spect}^{matrix} \rightarrow \mathbf{q}_{spect}^{vector}$ where

$$\mathbf{q}_{spect}^{vector}(t) = \left[\left[q_{00}(t) \quad q_{01}(t) \quad \cdots \quad q_{0P}(t) \right] \left[\cdots \quad q_{K0}(t) \quad \cdots \quad q_{KP}(t) \right] \right]^T \quad (3.9)$$

where P , as before, is the total number of polynomial chaoses used in the expansion and K is the total number of nodes in the FEM solution. The global vector of polynomial chaoses takes the form

$$\boldsymbol{\Phi}(\boldsymbol{\xi}) = \left[(\boldsymbol{\Phi}_{node}(\boldsymbol{\xi}))_0 \quad (\boldsymbol{\Phi}_{node}(\boldsymbol{\xi}))_1 \quad \cdots \quad (\boldsymbol{\Phi}_{node}(\boldsymbol{\xi}))_K \right]^T \quad (3.10)$$

where the vectors of polynomial chaoses are the same for each node

$$(\boldsymbol{\Phi}_{node}(\boldsymbol{\xi}))_0 = (\boldsymbol{\Phi}_{node}(\boldsymbol{\xi}))_1 = \cdots = (\boldsymbol{\Phi}_{node}(\boldsymbol{\xi}))_K \quad (3.11)$$

After substitution of appropriate expansions (3.8) of the matrices $\mathbf{M}(\mathbf{x}, \omega)$, $\mathbf{C}(\mathbf{x}, \omega)$, $\mathbf{K}(\mathbf{x}, \omega)$, $\mathbf{F}(\mathbf{x}, \omega)$, equation (3.9) and (3.10) into (3.7), then multiplying by $\boldsymbol{\Phi}(\boldsymbol{\xi})$ and averaging with respect to the random space

$$\begin{aligned} & \left\langle \boldsymbol{\Phi}(\boldsymbol{\xi}) \left((\mathbf{M}(\mathbf{x}))_0 \xi_0 + \sum_{i_M=1}^{M_M} \xi_{i_M} (\mathbf{M}^0(\mathbf{x}))_{i_M} \right) f_{M_T} \left((\mathbf{q}_{spect}^{vector}(t))^T \boldsymbol{\Phi}(\boldsymbol{\xi}) \right) \left(\ddot{\mathbf{q}}_{spect}^{vector}(t) \right)^T \boldsymbol{\Phi}(\boldsymbol{\xi}) \right\rangle \\ & + \left\langle \boldsymbol{\Phi}(\boldsymbol{\xi}) \left((\mathbf{C}(\mathbf{x}))_0 \xi_0 + \sum_{i_C=1}^{M_C} \xi_{i_C} (\mathbf{C}^0(\mathbf{x}))_{i_C} \right) f_{C_T} \left((\mathbf{q}_{spect}^{vector}(t))^T \boldsymbol{\Phi}(\boldsymbol{\xi}) \right) \left(\dot{\mathbf{q}}_{spect}^{vector}(t) \right)^T \boldsymbol{\Phi}(\boldsymbol{\xi}) \right\rangle \\ & + \left\langle \boldsymbol{\Phi}(\boldsymbol{\xi}) \left((\mathbf{K}(\mathbf{x}))_0 \xi_0 + \sum_{i_K=1}^{M_K} \xi_{i_K} (\mathbf{K}^0(\mathbf{x}))_{i_K} \right) f_{K_T} \left((\mathbf{q}_{spect}^{vector}(t))^T \boldsymbol{\Phi}(\boldsymbol{\xi}) \right) \left(\mathbf{q}_{spect}^{vector}(t) \right)^T \boldsymbol{\Phi}(\boldsymbol{\xi}) \right\rangle \\ & = \left\langle \boldsymbol{\Phi}(\boldsymbol{\xi}) \left((\mathbf{F}(\mathbf{x}))_0 \xi_0 + \sum_{i_F=1}^{M_F} \xi_{i_F} (\mathbf{F}^0(\mathbf{x}))_{i_F} \right) f_F \left((\mathbf{q}_{spect}^{vector}(t))^T \boldsymbol{\Phi}(\boldsymbol{\xi}) \right) \right\rangle \end{aligned} \quad (3.12)$$

can be obtained, where

$$\langle \cdot \rangle = \int_{\Omega} (\cdot) d\mathbb{P}(\omega) \quad (3.13)$$

and M_M , M_C , M_K , M_F denote the numbers of terms in the Karhunen-Loève expansion.

Finally, the set of $(P+1)K$ nonlinear deterministic equations of the SSFEM method is obtained

$$\begin{aligned} & \mathbf{M}^{expand}(\mathbf{x}, \mathbf{q}_{spect}^{vector}(t)) \ddot{\mathbf{q}}_{spect}^{vector}(t) + \mathbf{C}^{expand}(\mathbf{x}, \mathbf{q}_{spect}^{vector}(t)) \dot{\mathbf{q}}_{spect}^{vector}(t) \\ & + \mathbf{K}^{expand}(\mathbf{x}, \mathbf{q}_{spect}^{vector}(t)) \mathbf{q}_{spect}^{vector}(t) = \mathbf{F}^{expand}(\mathbf{x}, \mathbf{q}_{spect}^{vector}(t)) \end{aligned} \quad (3.14)$$

where, for example, the generalized stiffness matrix (matrices \mathbf{M}^{expand} and \mathbf{C}^{expand} can be written in the same way)

$$\begin{aligned} & \mathbf{K}^{expand}(\mathbf{x}, \mathbf{q}_{spect}^{vector}(t)) \\ &= \left\langle \Phi(\xi) \left((\mathbf{K}(\mathbf{x}))_0 \xi_0 + \sum_{i_K=1}^{M_K} \xi_i (\mathbf{K}^0(\mathbf{x}))_{i_K} \right) f_K \left((\mathbf{q}_{spect}^{vector}(t))^T \Phi(\xi) \right) (\Phi(\xi))^T \right\rangle \end{aligned} \quad (3.15)$$

and the generalized force vector

$$\mathbf{F}^{expand}(\mathbf{x}, \mathbf{q}_{spect}^{vector}(t)) = \left\langle \Phi(\xi) \left((\mathbf{F}(\mathbf{x}))_0 \xi_0 + \sum_{i_F=1}^{M_F} \xi_i (\mathbf{F}^0(\mathbf{x}))_{i_F} \right) f_F \left((\mathbf{q}_{spect}^{vector}(t))^T \Phi(\xi) \right) \right\rangle \quad (3.16)$$

For $f_r(\mathbf{q}^T \Phi(\xi)) = 1$, $r = M, C, K, F$ equation (3.14) is linear. Moreover, the terms $\langle \xi_i \Phi(\xi) (\Phi(\xi))^T \rangle$ and $\langle \xi_i \Phi(\xi) \rangle$ of the above stated matrices obtained from integration over the random space have a lot of zero entries (Ghanem and Spanos, 2003). In addition, this terms may be determined in advance and only once.

In the proposed solution of nonlinear equation (3.14), the matrices in this equation have to be numerically integrated both in the iteration step and time step, over a random and geometric space. This is due to nonlinear functions f_r (where $r = M, C, K, F$) of the dependent variable q appearing in the parts $\langle \xi_i \Phi(\xi) f_g(\mathbf{q}^T \Phi(\xi)) (\Phi(\xi))^T \rangle$ (where $g = M, C, K$) and $\langle \xi_i \Phi(\xi) f_F(\mathbf{q}^T \Phi(\xi)) \rangle$ of these matrices. Methods of evaluating the above mentioned inner product for different types of nonlinearities of the functions f_r can be found in work of Le Maitre and Knio (2010).

For a complete presentation of the stochastic process $q(\mathbf{x}, t, \omega)$, the covariance matrix is determined (Ghanem and Spanos, 2003)

$$\mathbf{Cov}_{qq}(t) = \sum_{j=0}^P \langle \Phi_j(\xi) \Phi_j(\xi) \rangle (\mathbf{q}_{spect}^{vector}(t))_j [(\mathbf{q}_{spect}^{vector}(t))_j]^T \quad (3.17)$$

where $\mathbf{Cov}_{qq} = \{ \{ Cov_{qq} \}_{i,j} \}_{i,j=1}^P$, the j -th eigenmode of the vector $\mathbf{q}_{spect}^{vector}(t)$ has been written as $(\mathbf{q}_{spect}^{vector}(t))_j$. Therefore, the expected value may be calculated

$$E(\mathbf{q}_{spect}^{vector}(t)) = (\mathbf{q}_{spect}^{vector}(t))_0 \quad (3.18)$$

and the variance

$$Var_q(t)_i = Cov_{qq}(t)_{i,i} \quad i = 1, 2, \dots, P \quad (3.19)$$

Matrix equation (3.14) is a deterministic system of nonlinear equations, therefore, in order to solve it, one of methods of direct integration, for example Newmark method, can be used (Bathe, 1996).

3.2. Application of SSFEM to non-classical stochastic heat conduction constitutive model – heat waves analysis

The most widely used model for many engineering problems is the classic equation of Fourier (Fourier, 1822), which can be represented as a function of a random field. The expression for the heat flux can be written

$$\mathbf{q}_F(\mathbf{x}, t, \omega) = -k_F(\mathbf{x}, \omega, T) \nabla T(\mathbf{x}, t, \omega) \quad \mathbf{x} \in \mathbb{D}^3 \subset \mathbb{R}^3, \quad \omega \in \Omega, \quad t \in \mathbb{T} \quad (3.20)$$

where $k_F(\mathbf{x}, \omega, T)$ is Fourier thermal conductivity.

Because of the anomalies associated with the Fourier model (Vernotte, 1958) and the presence of finite speed propagation of heat, a Cattaneo model that takes into account heat flux relaxation has been introduced (Cattaneo, 1948; Słuzalec, 2003)

$$\tau \partial_t \mathbf{q}_C(\mathbf{x}, t, \omega) + \mathbf{q}_C(\mathbf{x}, t, \omega) = -k_C(\mathbf{x}, \omega, T) \nabla T(\mathbf{x}, t, \omega) \quad \mathbf{x} \in \mathbb{D}^3 \subset \mathbb{R}^3, \quad \omega \in \Omega, \quad t \in \mathbb{T} \quad (3.21)$$

where τ represents the relaxation time and $k_C(\mathbf{x}, \omega, T)$ is the Cattaneo thermal conductivity.

The Jeffreys type model is another heat conduction constitutive model of which the Cattaneo model and a Fourier-like diffusive model are subcases that can be obtained from this model (Joseph and Preziosi, 1989; Straughan, 2011; Tamma and Zhou, 1998; Ván and Fülöp, 2012)

$$\tau \partial_t \mathbf{q}(\mathbf{x}, t, \omega) + \mathbf{q}(\mathbf{x}, t, \omega) = -k(\mathbf{x}, \omega, T) [\nabla T(\mathbf{x}, t, \omega) - K(\mathbf{x}, \omega, T) \partial_t (\nabla T(\mathbf{x}, t, \omega))] \quad (3.22)$$

where $\mathbf{x} \in \mathbb{D}^3 \subset \mathbb{R}^3$, $\omega \in \Omega$, $t \in \mathbb{T}$, and

$$k(\mathbf{x}, \omega, T) = k_F(\mathbf{x}, \omega, T) + k_C(\mathbf{x}, \omega, T) \quad (3.23)$$

and

$$K(\mathbf{x}, \omega, T) = \frac{\tau k_F(\mathbf{x}, \omega, T)}{k(\mathbf{x}, \omega, T)}$$

is the so-called retardation time.

When the retardation time, $K = 0$, the Jeffreys model is reduced to the Cattaneo model. When selecting, $K = \tau$, the Jeffreys model only degenerates to a Fourier-like diffusive model with relaxation (Tamma and Zhou, 1998).

Zhou and co-workers (Tamma and Zhou, 1998) introduced C-process and F-process models which are a linear combination of the Fourier and Cattaneo models. The basic assumption is the simultaneous occurrence of a fast process based on equation (3.21) and a slow process related to equation (3.22). This model is a generalization of the above stated relations. The equations describing connection between heat flux and temperature have the following form (Tamma and Zhou, 1998)

$$\mathbf{q}_{CF}(\mathbf{x}, t, \omega) = \mathbf{q}_F(\mathbf{x}, t, \omega) + \mathbf{q}_C(\mathbf{x}, t, \omega) \quad \mathbf{x} \in \mathbb{D}^3 \subset \mathbb{R}^3, \quad \omega \in \Omega, \quad t \in \mathbb{T} \quad (3.24)$$

where

$$\begin{aligned} \mathbf{q}_C(\mathbf{x}, t, \omega) + \tau \partial_t \mathbf{q}_C(\mathbf{x}, t, \omega) &= -(1 - F_T(\mathbf{x}, \omega, T)) k(\mathbf{x}, \omega, T) \nabla T(\mathbf{x}, t, \omega) \\ \mathbf{q}_F(\mathbf{x}, t, \omega) &= -F_T(\mathbf{x}, \omega, T) k(\mathbf{x}, \omega, T) \nabla T(\mathbf{x}, \omega) \\ F_T(\mathbf{x}, \omega, T) &= \frac{k_F(\mathbf{x}, \omega, T)}{k_F(\mathbf{x}, \omega, T) + k_C(\mathbf{x}, \omega, T)} \\ k(\mathbf{x}, \omega, T) &= k_F(\mathbf{x}, \omega, T) + k_C(\mathbf{x}, \omega, T) \end{aligned} \quad (3.25)$$

After substitution of equation (3.25)_{1,2} into (3.24), it can be obtained

$$\begin{aligned} \mathbf{q}_{CF}(\mathbf{x}, t, \omega) + \tau \partial_t \mathbf{q}_{CF}(\mathbf{x}, t, \omega) \\ = -[k(\mathbf{x}, \omega, T) \nabla T(\mathbf{x}, t, \omega) + \tau \partial_t (k(\mathbf{x}, \omega, T) F_T(\mathbf{x}, \omega, T) \nabla T(\mathbf{x}, t, \omega))] \end{aligned} \quad (3.26)$$

Indexes F and C in the conductivity coefficient and in the heat flux vector respectively refer to the Fourier model with infinite propagation speed of wave and to the Cattaneo model, occurring simultaneously. Also the model number $F_T \in [0, 1]$ has been introduced. It can be seen that for $F_T \in [0, 1]$ the Jeffrey model is obtained, for $F_T = 1$ the Fourier one, and for $F_T = 0$ the equation is reduced to the Cattaneo model.

4. Stochastic nonlinear 1D transport equation

To obtain equations describing the flow of heat in a rigid conductor, the following energy balance equation (for clarity the shorthand notation is adopted $T \equiv T(x, t, \omega)$)

$$C(x, \omega, T)\partial_t T + \nabla \cdot \mathbf{q}_{CF} = 0 \quad x \in \mathbb{D}, \quad \omega \in \Omega, \quad t \in \mathbb{T} \quad (4.1)$$

where $C(x, \omega, T) = \rho c(x, \omega, T)$ is combined with one of the model constitutive equation, initial condition $T(x, t = 0, \omega) = T_0$ and a suitable boundary condition on $\partial\mathbb{D}$. The equation associated with C- and F-process models (which can be reduced to the above mentioned models) is stated below

$$\begin{aligned} \tau \partial_t (C(x, \omega, T)\partial_t T) + C(x, \omega, T)\partial_t T - \partial_x (k_F(x, \omega, T)\partial_x T) - \tau \partial_t (\partial_x (k_F(x, \omega, T)\partial_x T)) \\ - \partial_x ((1 - F_T(x, \omega, T))k(x, \omega, T)\partial_x T) = 0 \end{aligned} \quad (4.2)$$

5. Governing equations formulation of the Galerkin Finite Element Method (GFEM) – C- and F-processes model

The first step to solve the stochastic problem is discretisation of a deterministic space by the use of the finite element method in the Galerkin approach (Bathe, 1996). To this end, the response in terms of the temperature field is approximated by the expression

$$T(\mathbf{x}, t, \omega) = (\mathbf{T}(t, \omega))^T \mathbf{N}(\mathbf{x}) \quad (5.1)$$

where $\mathbf{N}(\mathbf{x})$ is a vector built of the test functions (as defined in Section 3.1), $\mathbf{T}(t, \omega)$ is a vector representing the discretized temperature field and the upper index T denotes transposition. The final equations after appropriate transformations read

$$\mathbf{M}(\mathbf{T})\ddot{\mathbf{T}} + \mathbf{C}(\mathbf{T})\dot{\mathbf{T}} + \mathbf{K}(\mathbf{T})\mathbf{T} = \mathbf{F}(\mathbf{T}) \quad (5.2)$$

where $\dot{\mathbf{T}}$ and $\ddot{\mathbf{T}}$ denote the first and second order temperature derivative with respect to time. The individual matrices in equation (5.2) can be obtained through a standard FE method (Bathe, 1996).

6. Numerical example

Distributions of temperature statistical moments as functions of time of the considered model for a thin steel sheet (similar to the work (Al-Nimr, 1997)) (Fig. 1) heated by a sudden heat impulse (Ván and Fülöp, 2012) will be analyzed. For this purpose and for further analysis, the following data will be adopted (Joseph and Preziosi, 1989; Ván and Fülöp, 2012).

Pulsed heating can be modeled as an internal heat source (Bargmann and Favata, 2014) with various time characteristics or as external boundary conditions. Let the heating function for the mixed boundary condition (convection-radiation) takes the form

$$T_{pulse}(t) = T_0 + a \sin(bt) \exp(-ct) \quad (6.1)$$

with parameters $T_0 = 293.15$ K, $a = 15 \cdot 10^4$ K, $b = \pi/10$, $c = 50$.

One dimensional region of the sample (modeled as a bar) is divided into 20 elements. The adopted heating time is equal to $t_{max} = 0.6 \cdot 10^{-10}$ s with 60 time steps (time increment $\Delta t = 0.01 \cdot 10^{-10}$). Cattaneo thermal conductivity has been considered as a random function independent

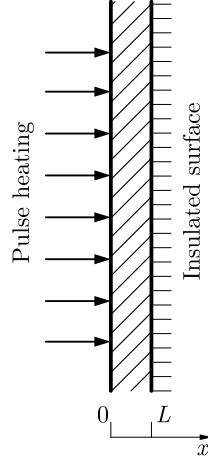


Fig. 1. Schematic of a thin steel plate heated by a pulse

of temperature (stationary and Gaussian process), $k_C(x, \omega, T) = k_C(x, \omega)$ with the covariance kernel

$$C_{kernel}(x_1, x_2) = \sigma_{k_C}^2 \exp\left(\frac{-|x_1 - x_2|}{b}\right) \quad (6.2)$$

where the coefficient of variation $\sigma_{k_C}^2$ and correlation length b are stated in Table 1.

Table 1. Parameters used in analysis

Parameter	Value
Heat capacity per unit volume (deterministic)	$c = 434.0 \text{ J}/(\text{kgK})$
Density (deterministic)	$\rho = 7850.0 \text{ kg}/\text{m}^3$
Fourier thermal conductivity (deterministic)	$k_F = 54 \text{ W}/(\text{mK})$
Cattaneo thermal conductivity (random – mean)	$\langle k_C(x, \omega) \rangle = 1210.0 \cdot 10^{10} \text{ W}/(\text{mKs})$
Cattaneo thermal conductivity (random – coefficient of variance)	$\sigma_{k_C}^2 = 2500.0 \cdot 10^{10} \text{ W}/(\text{mKs})$
Relaxation time	$\tau = 20.0 \cdot 10^{-12} \text{ s}$
Heat convection coefficient (deterministic)	$\alpha_c = 9.0 \text{ W}/(\text{m}^2\text{K})$
Emissivity (deterministic)	$\varepsilon_r = 0.625$
Stefan-Boltzmann constant	$\sigma_B = 5.67 \cdot 10^{-8} \text{ W}/(\text{m}^2\text{K}^4)$
Thickness	$L = 0.005 \text{ m}$
Correlation length	$b = 0.001 \text{ m}$

Using the Karhunen-Loève expansion, the Cattaneo thermal conductivity can be written in the form

$$k_C(x, \omega) \approx \langle k_C(x, \omega) \rangle + \sum_{i=1}^M \xi_i(\omega) \sqrt{\lambda_i} f_i(x) \quad (6.3)$$

Therefore, the random matrix present in equation (3.14) can be expressed as

$$\begin{aligned} \mathbf{F}_{x=0}^{expand}(x=0, \mathbf{T}_{spect}^{vector}(t)) \\ = \left\langle \Phi(\xi) \left((\mathbf{F}_{x=0}(x=0))_0 \xi_0 + \sum_{i_F=1}^{M_F} \xi_i (\mathbf{F}^0(x=0))_{i_F} \right) f_F \left((\mathbf{T}_{spect}^{vector}(t))^T \Phi(\xi) \right) \right\rangle \end{aligned} \quad (6.4)$$

This matrix takes non-zero values for the boundary node ($x=0$). The matrices $(\mathbf{F}(x))_0 = \mathbf{0}$, $(\mathbf{F}^0(x))_{i_F} = \mathbf{0}$ are generally equal to zero, only for $x=0$ $(\mathbf{F}_{x=0}(x=0))_0 = \mathbf{I}$. For the mixed boundary condition (convection-radiation) it can be assumed that (parameters in Table 1)

$$\begin{aligned} f_F \left((\mathbf{T}_{spect}^{vector}(t))^T \Phi(\xi) \right) = \alpha_c \left(T_{pulse}(t) - \left((\mathbf{T}_{spect}^{vector}(t))^T \Phi(\xi) \right) \right) \\ + \varepsilon_r \sigma_B \left[T_{pulse}(t)^4 - \left((\mathbf{T}_{spect}^{vector}(t))^T \Phi(\xi) \right)^4 \right] \end{aligned} \quad (6.5)$$

Because the Cattaneo thermal conductivity is independent of the temperature function f_K included in the matrix

$$\begin{aligned} \mathbf{K}^{expand}(x, \mathbf{T}_{spect}^{vector}(t)) \\ = \left\langle \Phi(\xi) \left((\mathbf{K}(x))_0 \xi_0 + \sum_{i_K=1}^{M_K} \xi_{i_K} (\mathbf{K}^0(x))_{i_K} \right) f_K \left((\mathbf{T}_{spect}^{vector}(t))^T \Phi(\xi) \right) (\Phi(\xi))^T \right\rangle \end{aligned} \quad (6.6)$$

(6.6) can be written as $f_K(\cdot) = 1$, and the matrices $(\mathbf{K}(x))_0$, $(\mathbf{K}^0(x))_{i_K}$ can be determined from

$$\begin{aligned} (\mathbf{K}(x))_0 &= \int_{\mathbb{D}} \nabla \mathbf{N} k_F \nabla \mathbf{N}^T dx + \int_{\mathbb{D}} \nabla \mathbf{N} \langle k_C(x, \omega) \rangle \nabla \mathbf{N}^T dx \\ (\mathbf{K}^0(x))_{i_K} &= \int_{\mathbb{D}} \nabla \mathbf{N} (\sqrt{\lambda_{i_K}} f_{i_K}(x)) \nabla \mathbf{N}^T dx \end{aligned} \quad (6.7)$$

the proposed modified SSFEM has been compared to the Monte Carlo method using the C- and F-process models. As the relevant set of points, the heated surface has been chosen. As shown in Fig. 2, there is a good correlation between the methods. SSFEM is giving smaller values for the

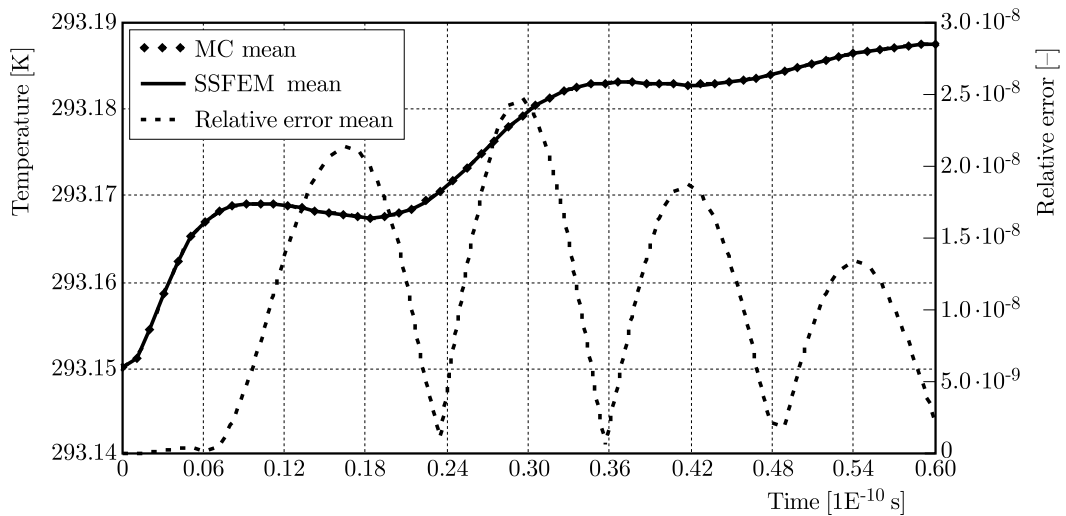


Fig. 2. Temperature mean value and relative error between SSFEM (3rd order polynomial chaos, 2nd order Karhunen-Loève expansion) and Monte Carlo (5000 samples) solution in function of time at the heated surface

standard deviation than MC (Fig. 3), which is typical for this method (Ghanem and Spanos, 2003). It can be seen that the biggest relative error for the standard deviation occurs in time nodes with smallest values. The relative error of temperature (Fig. 2) between the mean value obtained from the SSFEM and Monte Carlo solution is small with the extremum not exceeding $2.5 \cdot 10^{-8}$. Computations have been performed for $P = 3$ order of polynomial chaos and $M = 2$ order of Karhunen-Loève expansion.

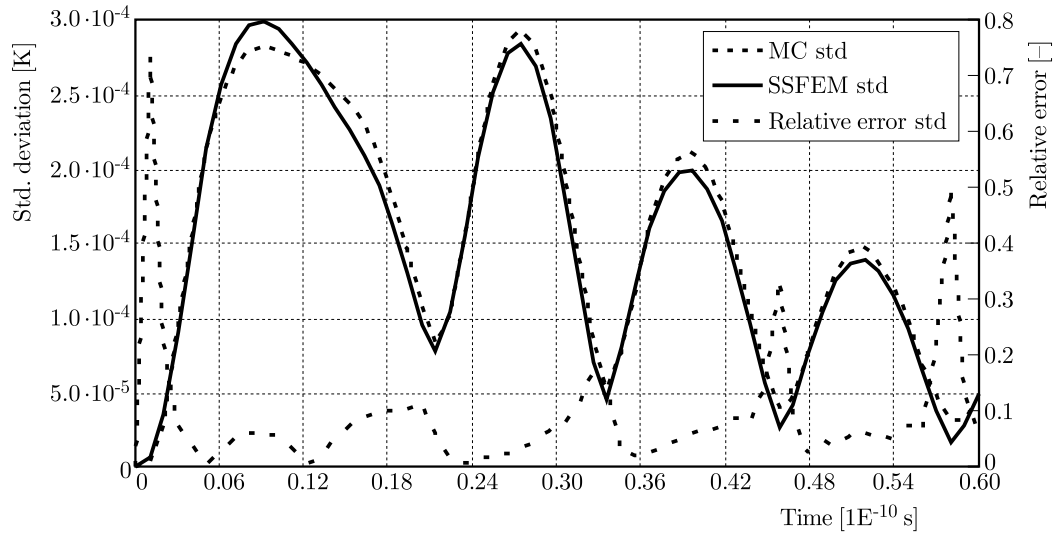


Fig. 3. Temperature standard deviation and relative error between SSFEM (3rd order polynomial chaos, 2nd order Karhunen-Loève expansion) and Monte Carlo (5000 samples) solution in function of time at the heated surface

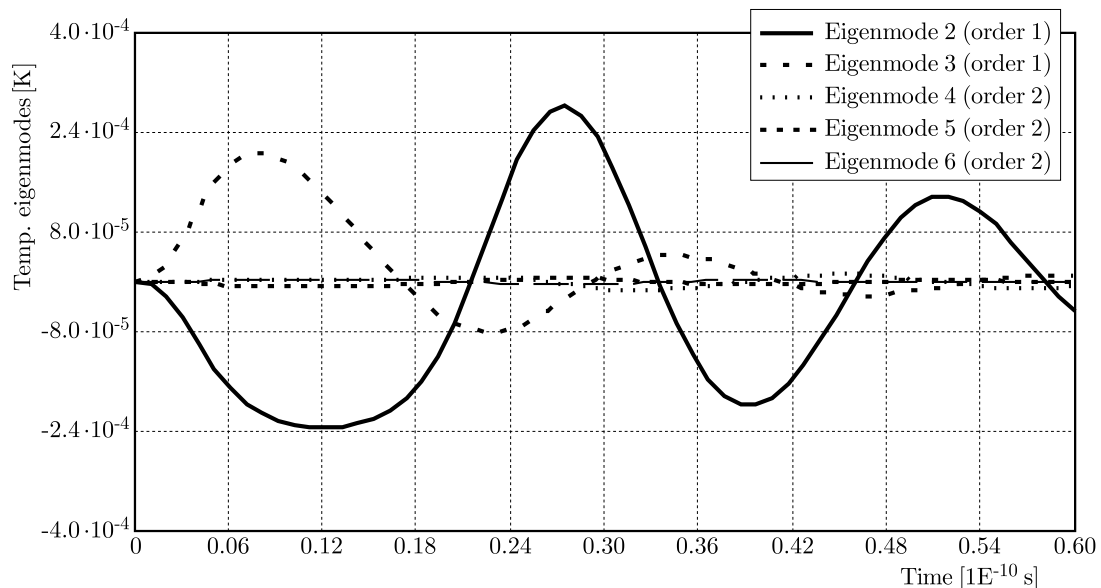


Fig. 4. Temperature eigenmodes obtained from SSFEM solution in function of time at the heated surface – 1st and 2nd order of polynomial chaos, 2nd order Karhunen-Loève expansion

Figure 4 illustrates solutions for successive orders of polynomial chaos. As can be seen, the biggest influence is the first order of the expansion on the basis of which it can be concluded that the improvement of the convergence of statistical moments by increasing the order of expansion in polynomial chaos will be small.

7. Concluding remarks

The paper develops an approach to analysis stochastic nonlinear partial differential equations (SPDE's). As an example of stochastic analysis, the heat waves equation has been shown. The C-F-processes constitutive model has been chosen for the analysis. It can be reduced to the Fourier, Cattaneo and Jeffery types of models. A modified SSFEM, which consists in the separation of dependent and independent variables in the main matrices, has been proposed to solve nonlinear governing equations. The modified SSFEM has been compared to the Monte Carlo method. The comparison has shown that the proposed method works with nonlinear problems well and for equation (4.1) the solutions generated by the SSFEM method are convergent to solutions generated by the Monte Carlo method due to the first and second statistical moment. The analysis has revealed that the largest difference in the results obtained from the SSFEM and MC method is generated in time nodes with the smallest standard deviation (local minima). Comparison of the results from the methods has aimed at demonstrating compliance rather than efficiency or time consumption of the SSFEM. In order to check time consumption of the method in relation to MC or SCM, one should use the domain decomposition method (Subber and Sarkar, 2014) and methods of reducing the integration time of the main matrices (e.g. Smolyak sparse grid method (Smolyak, 1963)) which would allow one to use parallel processing.

References

1. ACHARJEE S., ZABARAS N., 2006, Uncertainty propagation in finite deformations – a spectral stochastic Lagrangian approach, *Computer Methods in Applied Mechanics and Engineering*, **195**, 19, 2289-2312
2. ACHARJEE S., ZABARAS N., 2007, A non-intrusive stochastic Galerkin approach for modeling uncertainty propagation in deformation processes, *Computational Stochastic Mechanics*, **85**, 5, 244-254
3. AL-NIMR, M., 1997, Heat transfer mechanisms during short-duration laser heating of thin metal films, *International Journal of Thermophysics*, **18**, 5, 1257-1268
4. ARREGUI-MENA J.D., MARGETTS L., MUMMERY P.M., 2016, Practical application of the stochastic finite element method, *Archives of Computational Methods in Engineering*, **23**, 1, 171-190
5. BABUŠKA I., NOBILE F., TEMPONE R., 2007, A stochastic collocation method for elliptic partial differential equations with random input data, *SIAM Journal on Numerical Analysis*, **45**, 3, 1005-1034
6. BARGMANN S., FAVATA A., 2014, Continuum mechanical modeling of laser-pulsed heating in polycrystals: a multi-physics problem of coupling diffusion, mechanics, and thermal waves, *ZAMM – Journal of Applied Mathematics and Mechanics/Zeitschrift für Angewandte Mathematik und Mechanik*, **94**, 6, 487-498
7. BATHE K.J., 1996, *Finite Element Procedures*, Prentice Hall, New Jersey
8. CATTANEO M., 1948, Sulla Conduzione de Calor, *Mathematics and Physics Seminar*, **3**, 3, 83-101
9. FOURIER J., 1822, *Theorie Analytique de la Chaleur*, Chez Firmin Didot, Paris
10. GHANEM R.G., SPANOS P.D., 2003, *Stochastic Finite Elements: A Spectral Approach*, Dover Publications, Mineola, USA
11. GHOSH D., AVERY P., FARHAT C., 2008, A method to solve spectral stochastic finite element problems for large-scale systems, *International Journal for Numerical Methods in Engineering*, **00**, 1-6
12. HU J., JIN S., XIU,, D., 2015, A stochastic Galerkin method for Hamilton-Jacobi equations with uncertainty, *SIAM Journal on Scientific Computing*, **37**, 5, A2246-A2269

13. JOSEPH D.D., PREZIOSI L., 1989, Heat waves, *Reviews of Modern Physics*, **61**, 1, 41-73
14. KAMIŃSKI M., 2013, *The Stochastic Perturbation Method for Computational Mechanics*, John Wiley & Sons, Chichester
15. LE MAITRE O.P., KNIO O.M., 2010, *Spectral Methods for Uncertainty Quantification: with Applications to Computational Fluid Dynamics*, Springer Science & Business Media, Dordrecht
16. MATTHIES H.G., KEESE A., 2005, Galerkin methods for linear and nonlinear elliptic stochastic partial differential equations, *Computer Methods in Applied Mechanics and Engineering*, **194**, 2, 1295-1331
17. NOUY A., 2008, Generalized spectral decomposition method for solving stochastic finite element equations: invariant subspace problem and dedicated algorithms, *Computer Methods in Applied Mechanics and Engineering*, **197**, 51, 4718-4736
18. NOUY A., LE MAITRE O.P., 2009, Generalized spectral decomposition for stochastic nonlinear problems, *Journal of Computational Physics*, **228**, 1, 202-235
19. SŁUŻALEC A., 2003, Thermal waves propagation in porous material undergoing thermal loading, *International Journal of Heat and Mass Transfer*, **46**, 9, 1607-161
20. SMOLYAK S.A., 1963, Quadrature and interpolation formulas for tensor products of certain classes of functions, *Doklady Akademii Nauk SSSR*, **4**, 240-243
21. STEFANOUC G., 2009, The stochastic finite element method: past, present and future, *Computer Methods in Applied Mechanics and Engineering*, **198**, 9, 1031-1051
22. STEFANOUC G., SAVVAS D., PAPADRAKAKIS M., 2017, Stochastic finite element analysis of composite structures based on mesoscale random fields of material properties, *Computer Methods in Applied Mechanics and Engineering*, **326**, 319-337
23. STRAUGHAN B., 2011, *Heat Waves*, Springer, New York
24. SUBBER W., SARKAR A., 2014, A domain decomposition method of stochastic PDEs: An iterative solution techniques using a two-level scalable preconditioner, *Journal of Computational Physics*, **257**, 298-317
25. TAMMA K.K., ZHOU X., 1998, Macroscale and microscale thermal transport and thermo-mechanical interactions: some noteworthy perspectives, *Journal of Thermal Stresses*, **21**, 3-4, 405-449
26. VÁN P., FÜLÖP T., 2012, Universality in heat conduction theory: weakly nonlocal thermodynamics, *Annalen der Physik*, **524**, 8, 470-478
27. VERNOTTE P., 1958, Les paradoxes de la theorie continue de l'equation de la chaleur, *Comptes Rendus*, **246**, 3154-3155
28. XIU D., 2010, *Numerical Methods for Stochastic Computations: A Spectral Method Approach*, Princeton University Press, Princeton
29. XIU D., HESTHAVEN J.S., 2005, High-order collocation methods for differential equations with random inputs, *SIAM Journal on Scientific Computing*, **27**, 3, 1118-1139
30. XIU D., KARNIADAKIS G.E., 2003, A new stochastic approach to transient heat conduction modeling with uncertainty, *International Journal of Heat and Mass Transfer*, **46**, 24, 4681-4693
31. ZAKIAN P., KHAJI N., 2016, A novel stochastic-spectral finite element method for analysis of elastodynamic problems in the time domain, *Meccanica*, **51**, 4, 893-920

INVESTIGATION OF FLEXIBILITY CONSTANTS FOR A MULTI-SPRING MODEL: A SOLUTION FOR BUCKLING OF CRACKED MICRO/NANOBEAMS

MAJID AKBARZADEH KHORSHIDI, MAHMOUD SHARIATI

Ferdowsi University of Mashhad, Department of Mechanical Engineering, Mashhad, Iran

e-mail: mshariati44@um.ac.ir

In this paper, a multi-spring model is used for modelling of the crack in a micro/nanobeam under axial compressive load based on a modified couple stress theory. This model includes an equivalent rotational spring to transmit the bending moment and an equivalent longitudinal spring to transmit the axial force through the cracked section, which leads to promotion of the modelling of discontinuities due to the presence of the crack. Moreover, this study considers coupled effects between the bending moment and axial force on the discontinuities at the cracked section. Therefore, four flexibility constants appear in the continuity conditions. In this paper, these four constants are obtained as a function of crack depth, separately. This modelling is employed to solve the buckling problem of cracked micro/nanobeams using a close-form method, Euler-Bernoulli theory and simply supported boundary conditions. Finally, the effects of flexibility constants, crack depth and crack location on the critical buckling load are studied.

Keywords: flexibility constants, multi-spring model, MCST, buckling, crack

1. Introduction

It is clear that presence of cracks or any other defects into any structure leads to a decrease of its capabilities. The issue of cracking in the structures is interested in both macro and small scale dimensions. Thus, presentation of an accurate and appropriate model to capture crack conditions is very important. In many studies, cracks have been modeled by means of different types of springs. The type of the spring model depends on problem type, such as the type of loading and geometry. In fact, kinds of displacements at the cracked section determine what modelling should be selected. For example, a longitudinal spring model is used when the axial displacement is dominant (Hsu *et al.*, 2011), a rotational spring model is applicable for a wide range of problems in which the angle changes between the crack surfaces are important (Akbarzadeh Khorshidi *et al.*, 2017; Akbarzadeh Khorshidi and Shariati, 2017b; Hasheminejad *et al.*, 2011; Ke *et al.*, 2009; Loya *et al.*, 2006; Shaat *et al.*, 2016; Torabi and Nafar Dastegerdi, 2012; Wang and Wang, 2013; Yang and Cheng, 2008). Structures under torsion incorporate a torsional spring to describe discontinuity at the cracked section (Loya *et al.*, 2014). Rice and Levy (1972) stated that the presence of a crack leads to a local reduction in bending and extensional stiffness along the crack line. Therefore, it is more accurate to use a model which considers these two local reductions. Akbarzadeh Khorshidi and Shariati (2017a) presented buckling analysis of cracked nanobeams based on a modified couple stress theory and using a two-spring model at the cracked section. The authors used the mentioned model according to the historical background expressed by Rice and Levy (1972) and the discontinuity relations presented by Loya *et al.* (2009).

In majority of recent studies on static and dynamic behavior of micro/nanobeams in the presence of a micro or nano-scale crack, the flexibility constant which introduces the crack

severity is considered as a hypothetical input. However, there are studies which formulate the severity of the crack as a function of the crack depth, the material length scale parameter and other mechanical characteristics of the beam (Shaht *et al.*, 2016; Akbarzadeh Khorshidi *et al.*, 2017). These papers use energy stored in the spring and compare it with the strain energy release rate at the crack surfaces.

In the present study, the two-spring model is employed to describe discontinuities at the cracked section and, consequently, four flexibility constants appear, which gives the severity of the crack. Each flexibility constant is presented as a function of crack depth (as an unknown parameter) and other parameters (given values). Therefore, the continuity relations are formulated against the crack depth. The macroscopic fracture mechanics is used for micro/nano-scale beams based on atomistic simulation models and continuum models (Joshi *et al.*, 2010; Tsai *et al.*, 2016; Hu *et al.*, 2017). Then, a modified couple stress based solution is proposed for buckling analysis of the cracked beams.

2. Modelling

Consider an Euler-Bernoulli beam with length L , width b , thickness h and a crack with depth a is located at distance L_c from the left side of the beam (Fig. 1a). In the present modelling, the cracked beam is modelled as two separate segments connected by two massless elastic longitudinal and rotational springs (Fig. 1b). Therefore, the total strain energy of the cracked beam is equal to the strain energy of these two segments plus the strain energy stored in the springs. With this explanation, the released potential energy due to the presence of the crack is equal to the strain energy stored by the springs. The continuity conditions governed between the two beam segments are defined as follows (Akbarzadeh Khorshidi and Shariati, 2017a; Loya *et al.*, 2009)

$$\begin{aligned} w_1 = w_2 & \quad N_1 = N_2 & \quad M_1 = M_2 & \quad x = L_c \\ \Delta\theta = \overline{K}_{MM}M + \overline{K}_{MN}N & & \quad \Delta u = \overline{K}_{NN}N + \overline{K}_{NM}M & \end{aligned} \quad (2.1)$$

where $\Delta\theta$ is the difference in the rotation angles between two crack surfaces (or the angle rotated by the rotational spring) and Δu is the longitudinal displacement occurred at the cracked section (or amount of longitudinal spring compression). N and M are, respectively, the axial force and the bending moment. Also, \overline{K}_{MM} , \overline{K}_{MN} , \overline{K}_{NN} and \overline{K}_{NM} are four coefficients to represent the coupled effects between the axial force and bending moment in discontinuity relations.

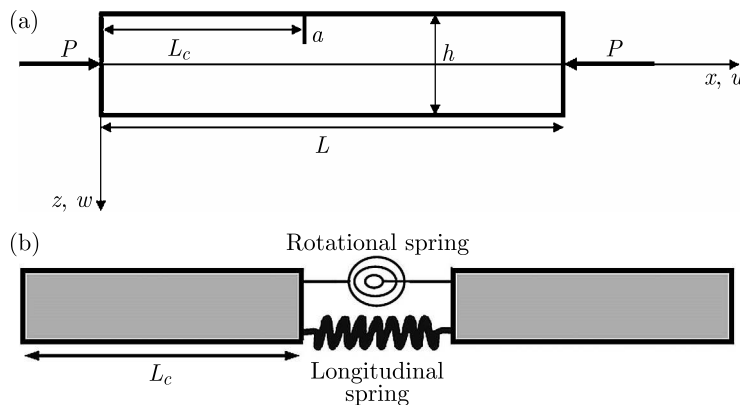


Fig. 1. (a) A schematic of the cracked beam and (b) the springs model for a cracked section

Therefore, the strain energy of springs $U_{springs}$ is stated as

$$U_{springs} = \frac{1}{2}M\Delta\theta + \frac{1}{2}N\Delta u = \frac{1}{2}M(\overline{K}_{MM}M + \overline{K}_{MN}N) + \frac{1}{2}N(\overline{K}_{NM}M + \overline{K}_{NN}N) \quad (2.2)$$

Based on generalized Irwin's (Irwin, 1960) relation, the potential energy-release rate G is introduced as (Rice and Levy, 1972)

$$G = \frac{(1 - \nu^2)a}{E} (\pi\sigma_b^2 Y_b^2 + 2\sqrt{\pi}\sigma_t\sigma_b Y_t Y_b + \sigma_t^2 Y_t^2) \quad (2.3)$$

where E is Young's modulus, ν is Poisson's ratio, σ and Y , respectively, reflect the stress and a dimensionless function of the crack depth to thickness ratio $\bar{a} = a/h$. Indices t and b represent the status of the parameters in tension and bending, respectively.

When a cracked beam is subjected to compression, it senses a local compliance at the cracked section, and the zones around the crack tend to open the crack lips. Based on the stress concentration at the crack tip, a uniform stress field distributes along the beam thickness (see Akbarzadeh Khorshidi and Shariati, 2017b). Therefore, the crack lips suffer stretching and bending (Fig. 2). The bending stress and tensile stress (thickness average stress) defined in Eq. (2.3) are shown as

$$\sigma_b = \frac{Mh}{2I} = \frac{6M}{bh^2} \quad \sigma_t = \frac{N}{A} = \frac{N}{bh} \quad (2.4)$$

where I in Eq. (2.4)₁ represents the moment of inertia and, for a rectangular cross section, is equal to $bh^3/12$. Also, A in Eq. (2.4)₂ denotes the cross section area and, for the mentioned cross section, is equal to bh .

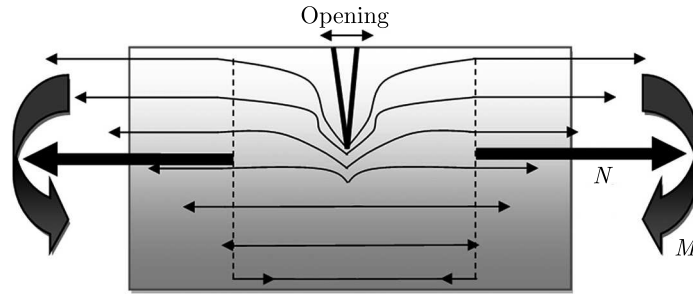


Fig. 2. The stress field due to the applied load and moment along the thickness

The strain energy due to the presence of the crack is obtained as

$$U_c = \int_0^a G dA_c = b \int_0^a G da \quad (2.5)$$

Substituting Eqs. (2.3) and (2.4) into Eq. (2.5), we have

$$U_c = \frac{(1 - \nu^2)}{Eb} \left(\frac{36\pi M^2}{h^2} \int_0^{\bar{a}} \bar{a} Y_b^2 d\bar{a} + \frac{12\sqrt{\pi}MN}{h} \int_0^{\bar{a}} \bar{a} Y_t Y_b d\bar{a} + N^2 \int_0^{\bar{a}} \bar{a} Y_t^2 d\bar{a} \right) \quad (2.6)$$

where $\bar{a} = a/h$ introduces the crack depth to thickness ratio. The dimensionless function Y_t is defined as (Gross and Srawley, 1965)

$$Y_t = 1.99 - 0.41\bar{a} + 18.70\bar{a}^2 - 38.48\bar{a}^3 + 53.85\bar{a}^4 \quad (2.7)$$

Also, the dimensionless function Y_b is defined as (Ke *et al.*, 2009)

$$Y_b = 1.15 - 1.662\bar{a} + 21.667\bar{a}^2 - 192.451\bar{a}^3 + 909.375\bar{a}^4 - 2124.310\bar{a}^5 + 2395.830\bar{a}^6 - 1031.750\bar{a}^7 \quad (2.8)$$

We consider that U_{spring} represented in Eq. (2.2) is equal to U_c obtained in Eq. (2.6), so, the flexibility constants \bar{K}_{MM} , \bar{K}_{MN} , \bar{K}_{NN} and \bar{K}_{NM} are separately achieved as follows

$$\begin{aligned}\bar{K}_{MM} &= \frac{72\pi(1-\nu^2)}{Ebh^2} \int_0^{\bar{a}} \bar{a}Y_b^2 d\bar{a} & \bar{K}_{MN} = \bar{K}_{NM} &= \frac{12\sqrt{\pi}(1-\nu^2)}{Ebh} \int_0^{\bar{a}} \bar{a}Y_bY_t d\bar{a} \\ \bar{K}_{NN} &= \frac{2(1-\nu^2)}{Eb} \int_0^{\bar{a}} \bar{a}Y_t^2 d\bar{a}\end{aligned}\quad (2.9)$$

As we know, the stress resultants introduced in Eqs. (2.1) and (2.2) (the bending moment M and the axial force N) are defined as

$$N = \int_A \sigma_{xx} dA \quad M = M_1 + M_2 = \int_A z\sigma_{xx} A + \int_A m_{xy} dA \quad (2.10)$$

where M_1 is the conventional bending moment and M_2 is the couple moment that comes from the modified couple stress theory proposed by Yang *et al.* (2002). The displacement field for the Euler-Bernoulli beam is

$$u_1 = u(x) - z\frac{dw}{dx} \quad u_2 = 0 \quad u_3 = w(x) \quad (2.11)$$

where u and w are the axial and lateral displacements of the midplane, respectively. Therefore, the nonzero strains and stresses are shown as

$$\varepsilon_{xx} = \frac{du_1}{dx} = \frac{du}{dx} - z\frac{d^2w}{dx^2} \quad \sigma_{xx} = E\varepsilon_{xx} = E\left(\frac{du}{dx} - z\frac{d^2w}{dx^2}\right) \quad (2.12)$$

Also, the nonzero terms of the symmetric curvature tensor χ and the deviatoric part of the couple stress tensor \mathbf{m} are defined as (Akbarzadeh Khorshidi and Shariati, 2017a; Yang *et al.*, 2002)

$$\chi_{xy} = -\frac{1}{2}\frac{d^2w}{dx^2} \quad m_{xy} = -\ell^2\mu\frac{d^2w}{dx^2} \quad (2.13)$$

These tensors consider the couple stress effects in the modified couple stress theory, and ℓ is a material length scale parameter to capture the size effect (Yang *et al.*, 2002). $\mu = E/(2 + 2\nu)$ is the shear modulus.

Now, substituting Eqs. (2.12) into Eq. (2.10), we have

$$N = EA\frac{du}{dx} \quad M = -(EI + \ell^2GA)\frac{dw^2}{dx^2} \quad (2.14)$$

where $D_{eff} = EI + \ell^2GA$ is the effective beam stiffness obtained based on the modified couple stress theory. According to Eq. (2.14), we can rewrite Eq. (2.1) as

$$\begin{aligned}w_1 = w_2 & \quad \frac{du_1}{dx} = \frac{du_2}{dx} & \quad \frac{d^2w_1}{dx^2} = \frac{d^2w_2}{dx^2} & \quad x = L_c \\ \frac{dw_2}{dx} - \frac{dw_1}{dx} &= K_{MM}\frac{d^2w}{dx^2} + K_{MN}\frac{du}{dx} & \quad u_2 - u_1 &= K_{NN}\frac{du}{dx} + K_{NM}\frac{d^2w}{dx^2}\end{aligned}\quad (2.15)$$

where

$$\begin{aligned}K_{MM} &= D_{eff}\bar{K}_{MM} & K_{MN} &= EA\bar{K}_{MN} \\ K_{NM} &= D_{eff}\bar{K}_{NM} & K_{NN} &= EA\bar{K}_{NN}\end{aligned}$$

Thus, we have

$$\begin{aligned}
K_{MM} &= 36\pi(1 - \nu)h \left[\frac{1 + \nu}{6} + \left(\frac{\ell}{h} \right)^2 \right] \int_0^{\bar{a}} \bar{a} Y_b^2 d\bar{a} \\
K_{MN} &= 12\sqrt{\pi}(1 - \nu^2) \int_0^{\bar{a}} \bar{a} Y_b Y_t d\bar{a} \\
K_{NM} &= 6\sqrt{\pi}(1 - \nu)h^2 \left[\frac{1 + \nu}{6} + \left(\frac{\ell}{h} \right)^2 \right] \int_0^{\bar{a}} \bar{a} Y_b Y_t d\bar{a} \\
K_{NN} &= 2(1 - \nu^2)h \int_0^{\bar{a}} \bar{a} Y_t^2 d\bar{a}
\end{aligned} \tag{2.16}$$

Using Eqs. (2.7) and (2.8), and integrating from Eqs. (2.16), the flexibility constants are obtained as functions of the crack depth to thickness ratio, and they are represented as follows

$$\begin{aligned}
K_{MM} &= 36\pi(1 - \nu)h \left[\frac{1 + \nu}{6} + \left(\frac{\ell}{h} \right)^2 \right] \bar{a}^2 (0.6612 - 1.2742\bar{a} + 13.1490\bar{a}^2 - 102.9316\bar{a}^3 \\
&\quad + 533.4547\bar{a}^4 - 2321.1924\bar{a}^5 + 11126.9823\bar{a}^6 - 50267.9855\bar{a}^7 + 175186.4492\bar{a}^8 \\
&\quad - 4399132.5842\bar{a}^9 + 772269.2856\bar{a}^{10} - 927343.5821\bar{a}^{11} + 723108.2196\bar{a}^{12} \\
&\quad - 329586.3470\bar{a}^{13} + 66531.7539\bar{a}^{14}) \\
K_{MN} &= 12\sqrt{\pi}(1 - \nu^2)\bar{a}^2 (1.1442 - 1.2596\bar{a} + 16.3259\bar{a}^2 - 93.4384\bar{a}^3 + 403.2692\bar{a}^4 \\
&\quad - 1303.1856\bar{a}^5 + 3902.0329\bar{a}^6 - 9790.7006\bar{a}^7 + 17593.8331\bar{a}^8 - 20534.4869\bar{a}^9 \\
&\quad + 14059.7654\bar{a}^{10} - 4273.8259\bar{a}^{11}) \\
K_{NM} &= 6\sqrt{\pi}(1 - \nu)h^2 \left[\frac{1 + \nu}{6} + \left(\frac{\ell}{h} \right)^2 \right] \bar{a}^2 (1.1442 - 1.2596\bar{a} + 16.3259\bar{a}^2 \\
&\quad - 93.4384\bar{a}^3 + 403.2692\bar{a}^4 - 1303.1856\bar{a}^5 + 3902.0329\bar{a}^6 - 9790.7006\bar{a}^7 \\
&\quad + 17593.8331\bar{a}^8 - 20534.4869\bar{a}^9 + 14059.7654\bar{a}^{10} - 4273.8259\bar{a}^{11}) \\
K_{NN} &= 2(1 - \nu^2)h\bar{a}^2 (1.9800 - 0.5439\bar{a} + 18.6485\bar{a}^2 - 33.6968\bar{a}^3 + 99.2611\bar{a}^4 \\
&\quad - 211.9012\bar{a}^5 + 436.8375\bar{a}^6 - 460.4773\bar{a}^7 + 289.9822\bar{a}^8)
\end{aligned} \tag{2.17}$$

3. Solutions

According to the Euler-Bernoulli beam theory, the governing equations for buckling of a cracked micro/nanobeam are derived as (Akbarzadeh Khorshidi and Shariati, 2017b)

$$\begin{aligned}
(EI + \ell^2 GA) \frac{d^4 w_i}{dx_i^4} + P \frac{d^2 w_i}{dx_i^2} &= 0 & \begin{cases} i = 1 & 0 \leq x \leq L_c \\ i = 2 & L_c \leq x \leq L \end{cases} \\
\frac{d^2 w_i}{dx_i^2} &= 0 & \begin{cases} i = 1 & 0 \leq x \leq L_c \\ i = 2 & L_c \leq x \leq L \end{cases}
\end{aligned} \tag{3.1}$$

Here the subscript $i = 1, 2$ refers to the left and right segments of the cracked beam. The boundary conditions of a simply supported beam are expressed as

$$\begin{aligned}
u_1(0) = w_1(0) = 0 & \quad u_2(L) = w_2(L) = 0 \\
\left. \frac{d^2 w_1}{dx^2} \right|_{x=0} = 0 & \quad \left. \frac{d^2 w_2}{dx^2} \right|_{x=L} = 0
\end{aligned} \tag{3.2}$$

The general solution to Eqs. (3.1) can be obtained as

$$\begin{aligned} w_i(x) &= A_i \sin(\alpha x) + B_i \cos(\alpha x) + C_i x + D_i & i = 1, 2 \\ u_i(x) &= F_i x + H_i & i = 1, 2 \end{aligned} \quad (3.3)$$

where $\alpha = \sqrt{P/D_{eff}}$, A_i , B_i , C_i , D_i , F_i and H_i are unknown constants to be determined from the boundary and continuity conditions.

Applying continuity conditions (2.15) and boundary conditions (3.2) into Eqs. (3.3), the unknown constants are derived as

$$\begin{aligned} A_1 &= \left(1 - \frac{\tan(\alpha L)}{\tan(\alpha L_c)}\right) A_2 & B_1 &= D_1 = 0 & C_1 &= 2\alpha \frac{\tan(\alpha L)}{\sin(\alpha L_c)} \frac{L - L_c}{L} A_2 \\ B_2 &= -\tan(\alpha L) A_2 & C_2 &= -2\alpha \frac{\tan(\alpha L)}{\sin(\alpha L_c)} \frac{L_c}{L} A_2 & D_2 &= 2\alpha L_c \frac{\tan(\alpha L)}{\sin(\alpha L_c)} A_2 \\ F_1 &= F_2 & H_1 &= 0 & H_2 &= -L F_2 \\ F_2 &= \frac{A_2 \alpha}{K_{MN}} \left(K_{MM} \alpha [\sin(\alpha L_c) - \tan(\alpha L) \cos(\alpha L_c)] - \frac{\tan(\alpha L)}{\sin(\alpha L_c)} \right) \end{aligned} \quad (3.4)$$

also

$$\alpha = \frac{L + K_{NN}}{K_{MN} K_{NM}} \frac{K_{MM} \alpha \left(\sin^2(\alpha L_c) - \frac{1}{2} \tan(\alpha L) \sin(2\alpha L_c) \right) - \tan(\alpha L)}{\sin^2(\alpha L_c) - \frac{1}{2} \tan(\alpha L) \sin(2\alpha L_c)} \quad (3.5)$$

The critical buckling load can be obtained by solving Eq. (3.5). For example, when we have an intact beam ($a = 0 \rightarrow K_{MM} = K_{MN} = K_{NN} = K_{NM} = 0$), according to Eq. (3.5) we have

$$\tan(\alpha L) = 0 \rightarrow \alpha = \frac{n\pi}{L} \xrightarrow{n=1} P_{cr} = D_{eff} \left(\frac{\pi}{L} \right)^2 \quad (3.6)$$

This is quite similar to the results obtained by Mohammad-Abadi and Daneshmehr (2014) for modified couple stress based intact microbeams.

Using Eq. (3.5), the critical buckling load corresponding to each crack depth and crack location can be determined. Also, the present model (four flexibility constants) can be compared with the common model (only one constant) by removing the other constants. Moreover, the coupled effects between the bending moment and axial force can be evaluated by neglecting the crossover flexibility constants (K_{MN} and K_{NM}).

Thus, the following equation can be used when only one flexibility constant K_{MM} is employed

$$K_{MM} L \alpha \left(\sin^2(\alpha L_c) - \frac{1}{2} \tan(\alpha L) \sin(2\alpha L_c) \right) - \tan(\alpha L) = 0 \quad (3.7)$$

Also, the following equation can be used when the crossover flexibility constants are removed

$$(L + K_{NN}) K_{MM} \alpha \left(\sin^2(\alpha L_c) - \frac{1}{2} \tan(\alpha L) \sin(2\alpha L_c) \right) - \tan(\alpha L) = 0 \quad (3.8)$$

4. Results

To illustrate the flexibility constants effects on the buckling behavior of cracked micro/nanobeams, some numerical examples of the obtained solution are presented in this Section. Also, the effects of the crack depth and crack location on the critical buckling load are investigated. First, the obtained results are validated with (Ke *et al.*, 2009; Wang and Quek,

2005) for macro-scale cracked beams ($\ell = 0$). This comparison can be observed in Table 1, so that $\bar{P} = P_{cr}/P_{cr0}$ is the nondimensional critical buckling load (where P_{cr0} denotes the critical buckling load of an intact beam). In (Ke *et al.*, 2009; Wang and Quek, 2005), only one flexibility constant K_{MM} (one equivalent rotational spring model) was employed, so, the present results have two separate columns for the one-spring model where we have only K_{MM} and the two-spring model where all flexibility constants appear. In Table 1, each crack depth corresponds to the crack severity, for example, $a/h = 0.1$ corresponds to $K_{MM} = 0.01$ (this parameter is introduced with symbol Θ in (Ke *et al.*, 2009)).

Table 1. Nondimensional critical buckling load \bar{P} of a cracked beam ($L_c = 0.5L$, $\nu = 0.33$, $E = 70$ GPa and $L = 10$ h)

a/h	Present		Ke <i>et al.</i> (2009)	Wang & Quek (2005)
	Two springs	One spring		
0.1000	0.9802	0.9801	0.9809	0.9830
0.1425	0.9614	0.9611	0.9622	0.9630
0.1757	0.9432	0.9426	0.9442	0.9450
0.2038	0.9257	0.9245	0.9266	0.9250
0.2280	0.9092	0.9071	0.9096	0.9070

Now, Table 2 and Figs. 3-6 present the critical buckling load for cracked micro/nanobeams based on the modified couple stress theory and the two-spring model. All results are obtained as a parametric study where $\nu = 0.33$, $L/h = 10$ and $\ell/h = 0.5$. The present study is applicable for both micro and nano-scale problems (this issue is dependent on the scale of the material length scale parameter).

Table 2 presents nondimensional critical buckling loads for different crack depths. In this table, three types of nondimensional critical buckling loads are shown, where each load denotes a special case of the flexibility field. \bar{P}_1 is the nondimensional critical buckling load for the one-spring model where we have only K_{MM} (conventional model), \bar{P}_2 is for the two-spring model, but the crossover flexibility constants are vanished (the coupled effects between the axial force and bending moment are neglected) and \bar{P}_3 is for the two-spring model where all four flexibility constants are considered. The results of Table 2 indicate that there are some differences between \bar{P}_3 and \bar{P}_1 , and this discrepancy increases when the crack depth is increased. Also, comparison between \bar{P}_2 and \bar{P}_1 reveals that the use of two springs without consideration of the crossover constants has no considerable impact on the obtained results. Figure 3 approves Table 2, graphically. It is found that the two-spring model presents a greater buckling capacity of cracked beams than the conventional model. Therefore, it is found that the local flexibility at the cracked section (crack severity) caused by a particular crack depth is different for the one-spring model \bar{P}_1 and the two-spring model \bar{P}_3 .

Table 2. Nondimensional critical buckling load \bar{P} of cracked micro/nanobeams ($L_c = 0.5L$)

a/h	\bar{P}_1	\bar{P}_2	\bar{P}_3
0	1	1	1
0.1	0.9584	0.9584	0.9586
0.2	0.8545	0.8545	0.8567
0.3	0.7130	0.7130	0.7232
0.4	0.5489	0.5489	0.5772
0.5	0.3901	0.3901	0.4504

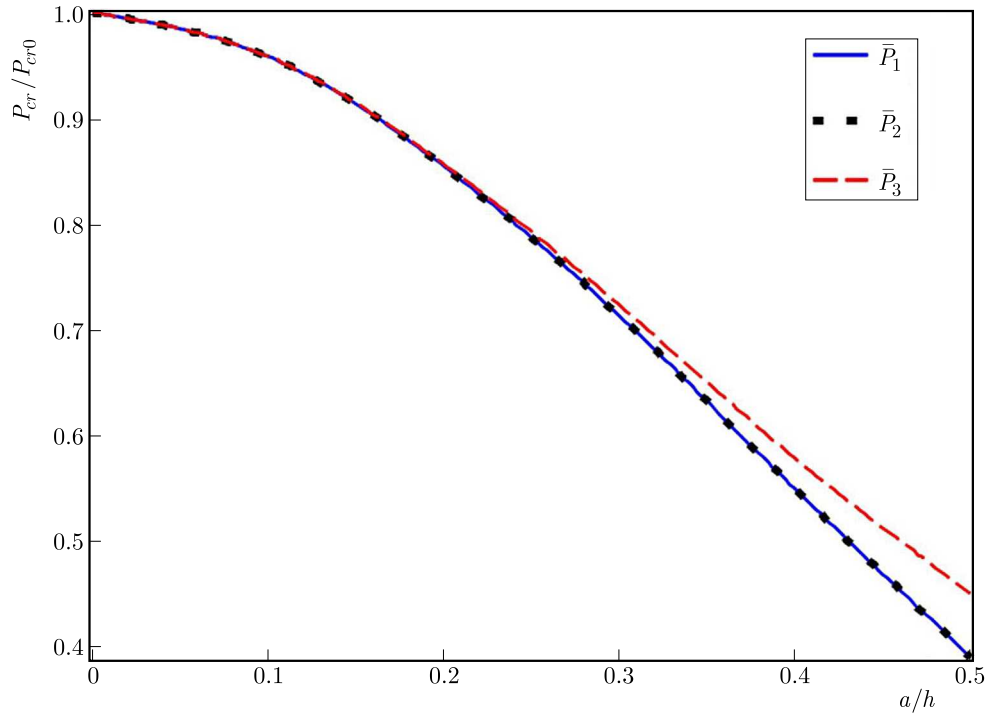


Fig. 3. Comparison of the two-spring model and the conventional model in terms of crack depth

The effect of crack location is shown in Fig. 4 for different crack depths. This figure indicates that the crack has the greatest sensitivity when it is located in middle of the beam ($L_c = 0.5L$). When the crack approaches the two ends, its effect is continuously decreased. This fact is directly related to deformation of various points of the beam and, finally, the opening of the crack tip.

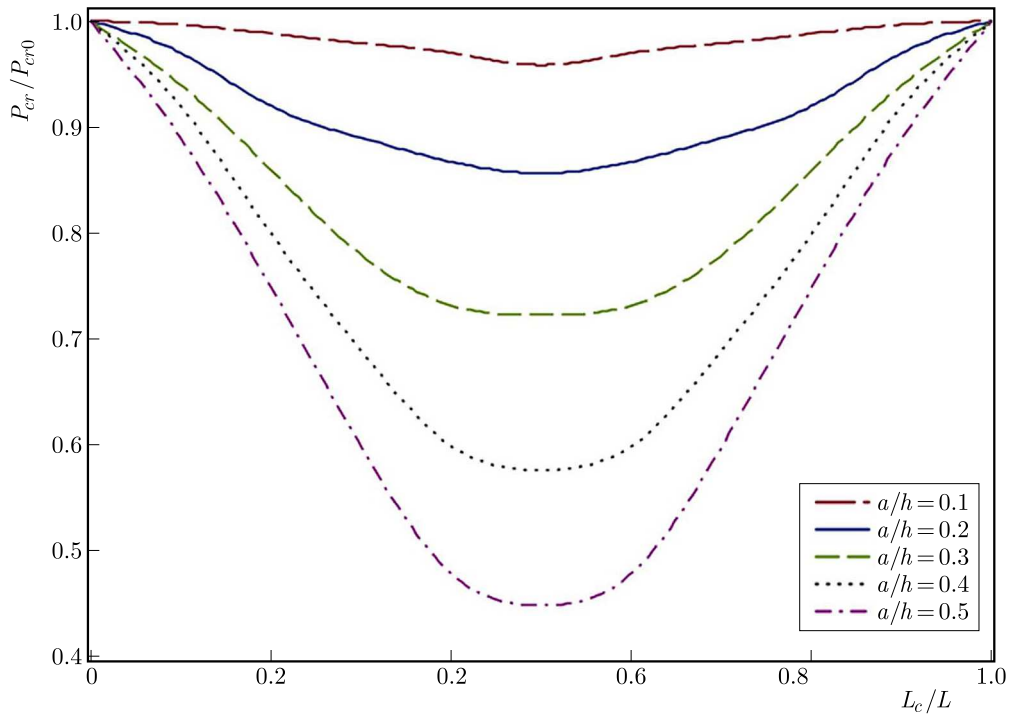


Fig. 4. The effect of crack location on the nondimensional critical buckling load with different crack depths

Also, variations of the nondimensional critical buckling load versus crack depth are demonstrated in Fig. 5 in different crack locations. It is observed that not only the increasing of the crack depth leads to a decrease in the buckling resistance of the beam, but also makes the effect of crack location more considerable.

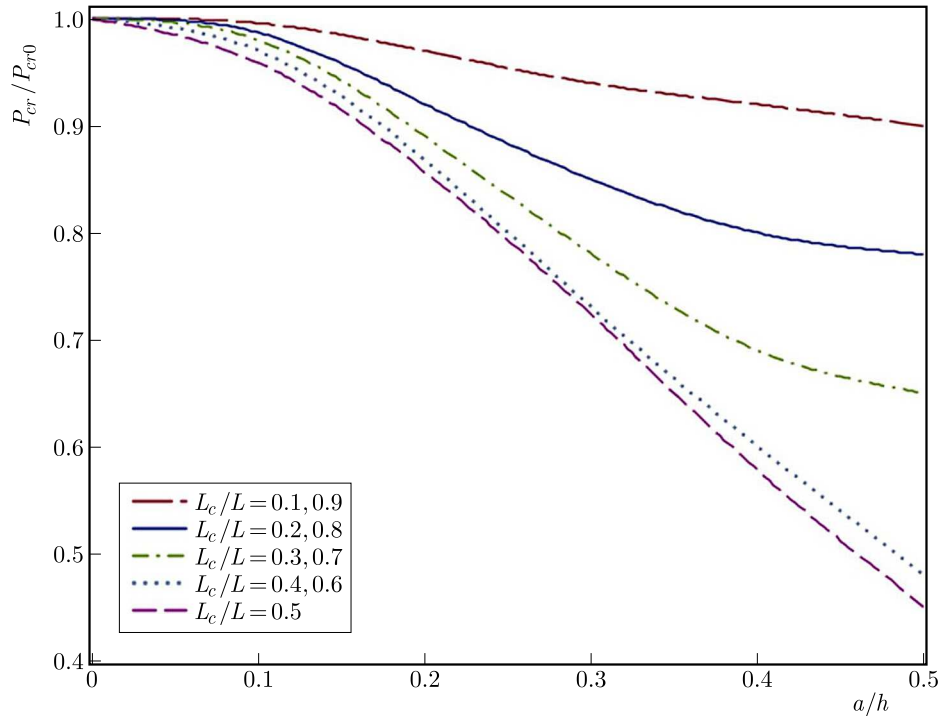


Fig. 5. The effect of crack depth on the nondimensional critical buckling load with different crack locations

5. Conclusion

The flexibility constants of the cracked section are investigated using a multi-spring model (rotational and longitudinal spring) to describe local flexibilities and discontinuities at the cracked section of micro/nanobeams. This model not only promotes the discontinuities but also considers the coupled effects between the bending moment and axial force on the discontinuities due to the presence of the crack. Then, the buckling problem is solved for cracked micro/nanobeams and the influence of crack depth and crack location is studied. Also, different configurations of the flexibility constants are compared together. The results show that the flexibility constant related with the bending moment (KMM) has the greatest impact on the local flexibility due to the crack (crack severity). But, this crack severity changes by adding more flexibility constants. It is found that the coupled effects between the bending moment and axial force (crossover constants) are considerable, and the making use of the multi-spring model without consideration of the crossover constants will not be useful. Therefore, the use of four constants (multi-spring model) instead of only one (conventional model) estimates the buckling capacity better, and this difference increases with an increase in the crack depth.

References

1. AKBARZADEH KHORSHIDI M., SHAAT M., ABDELKEFI A., SHARIATI M., 2017, Nonlocal modeling and buckling features of cracked nanobeams with von Karman nonlinearity, *Applied Physics A: Material Science and Processing*, **123**, 62

2. AKBARZADEH KHORSHIDI M., SHARIATI M., 2017a, A multi-spring model for buckling analysis of cracked Timoshenko nanobeams based on modified couple stress theory, *Journal of Theoretical and Applied Mechanics*, **55**, 4, 1127-1139
3. AKBARZADEH KHORSHIDI M., SHARIATI M., 2017b, Buckling and postbuckling of size-dependent cracked microbeams based on a modified couple stress theory, *Journal of Applied Mechanics and Technical Physics*, **58**, 4, 717-724
4. GROSS B., SRAWLEY J.E., 1965, Stress-intensity factors for single edge notch specimens in bending or combined bending and tension by boundary collocation of a stress function, *NASA Technical Note*, **D-2603**
5. HASHEMINEJAD M., GHESHLAGHI B., MIRZAEI Y., ABBASION S., 2011, Free transverse vibrations of cracked nanobeams with surface effects, *Thin Solid Films*, **519**, 2477-2482
6. HSU J.CH., LEE H.L., CHANG W.J., 2011, Longitudinal vibration of cracked nanobeams using nonlocal elasticity theory, *Current Applied Physics*, **11**, 1384-1388
7. HU K.M., ZHANG W.M., PENG Z.K., MENG G., 2016, Transverse vibrations of mixed-mode cracked nanobeams with surface effect, *Journal of Vibration and Acoustics*, **138**, 1, 011020
8. IRWIN G.R., 1960, Fracture mechanics, [In:] *Structural Mechanics*, J.N. Goodier, and N.J. Hoff (Edit.), Pergamon Press, p. 557
9. JOSHI A.Y., SHARMA S.C., HARSHA S., 2010, Analysis of crack propagation in fixed-free single-walled carbon nanotube under tensile loading using XFEM, *ASME Journal of Nanotechnology in Engineering and Medicine*, **1**, 4, 041008
10. KE L.L., YANG J., KITIPORNCHAI S., 2009, Postbuckling analysis of edge cracked functionally graded Timoshenko beams under end shortening, *Composite Structures*, **90**, 152-160
11. LOYA J.A., ARANDA-RUIZ J., FERNANDEZ-SAEZ J., 2014, Torsion of cracked nanorods using a nonlocal elasticity model, *Journal of Physics D: Applied Physics*, **47**, 115304 (12pp)
12. LOYA J.A., RUBIO L., FERNANDEZ-SAEZ J., 2006, Natural frequencies for bending vibrations of Timoshenko cracked beams, *Journal of Sound and Vibration*, **290**, 640-653
13. LOYA J., LOPEZ-PUENTE J., ZAERA R., FERNANDEZ-SAEZ J., 2009, Free transverse vibrations of cracked nanobeams using a nonlocal elasticity model, *Journal of Applied Physics*, **105**, 044309
14. MOHAMMAD-ABADI M., DANESHMEHR A.R., 2014, Size dependent buckling analysis of microbeams based on modified couple stress theory with high order theories and general boundary conditions, *International Journal of Engineering Science*, **74**, 1-14
15. RICE J.R., LEVY N., 1972, The part-through surface crack in an elastic plate, *Journal of Applied Mechanics: Transaction of the ASME*, March, 185-194
16. SHAAT M., AKBARZADEH KHORSHIDI M., ABDELKEFI A., SHARIATI M., 2016, Modeling and vibration characteristics of cracked nano-beams made of nanocrystalline materials, *International Journal of Mechanical Sciences*, **115-116**, 574-585
17. TORABI K., NAFAR DASTGERDI J., 2012, An analytical method for free vibration analysis of Timoshenko beam theory applied to cracked nanobeams using a nonlocal elasticity model, *Thin Solid Films*, **520**, 6595-6602
18. TSAI J.L., TZENG S.H., TZOU Y.J., 2010, Characterizing the fracture parameters of a graphene sheet using atomistic simulation and continuum mechanics, *International Journal of Solids and Structures*, **47**, 3, 503-509
19. WANG Q., QUEK S.T., 2005, Repair of cracked column under axially compressive load via piezoelectric patch, *Computers and Structures*, **83**, 1355-1363
20. WANG K., WANG B., 2013, Timoshenko beam model for the vibration analysis of a cracked nanobeam with surface energy, *Journal of Vibration and Control*, **21**, 12, 2452-2464
21. YANG J., CHENG Y., 2008, Free vibration and buckling analyses of functionally graded beams with edge cracks, *Composite Structures*, **83**, 48-60
22. YANG F., CHONG A.C.M., LAM D.C.C., TONG P., 2002, Couple stress based strain gradient theory for elasticity, *International Journal of Solids and Structures*, **39**, 2731-2743

AN EXTENDED CONTACT MODEL OF THE ANGULAR BEARING

JAN KOSMOL

Silesian University of Technology, Gliwice, Poland

e-mail: jkosmol@polsl.pl

The article presents a new contact model of an angular bearing, called the extended model. The model takes account of the effects of centrifugal load caused by the rotating ring of the bearing and the issue of elasticity. Present models, encountered in literature and referred to in the article as classical, consider the centrifugal force caused by the rotating ball only. Results of analytical research on the extended model and of FEM simulation show explicitly that the contact angles of bearings, and thus contact loads, differ very much from those values obtained in the classical model. These differences are disadvantageous for designing bearing assemblies, since contact loads are greater than those obtained in the classical model. This means, among others, that the present structures with angular contact bearings are in reality subject to greater loads than the constructor has envisaged. The motto of the article is to design analytical calculation models in such a form which would enable the constructor to estimate contact loads, just using a standard scientific calculator or MS Excel type applications; so that there would be no need for solving complex models using numerical methods.

Keywords: contact model, angular bearing, FEM

1. Introduction

One of the major constructional issues of HSC machine tools is the heat generated in rolling-contact bearings, e.g. in bearing seatings of high-speed spindles. The designer of the bearing seating should have a possibility of estimating the amount of heat generated in the bearing, so that he would be able to foresee, if needed, the necessity of applying a cooling system. In order to estimate the amount of heat generated in the bearing, there is the need for, among others, information on motion resistance existing in the bearing. Motion resistance in the bearing, measured on the driving shaft, is determined according to the so-called formula (Palmgren, 1951), i.e.

$$M_f = M_1 + M_v \quad (1.1)$$

where M_f is the total bearing friction torque, M_1 – friction torque due to external load, M_v – friction torque due to lubrication.

Motion resistance due to the lubricant or oil M_v can be determined using common mathematical formulae (Harris and Kotzalas, 2013). At the same time, motion resistance due to rolling friction in the bearing M_1 , according to Palmgren (1951) formula, is represented as follows

$$M_1 = z \left(\frac{F_s}{C_s} \right)^y (0.9F_a \cot \alpha - 0.1F_r) d_m \quad (1.2)$$

where: F_a , F_r are axial and radial loads, F_s – bearing static equivalent load, C_s – bearing basic static load rating, α – contact angle, z , y – coefficients dependent on the bearing structure and the lubrication method.

It presents results approximating reality for relatively low rotational speeds. As rotational speeds increase, the difference between the friction torque calculated according to formula (1.1), and the real motion friction torque, increases. Hence, the amount of heat generated in the bearing, calculated according to formula (1.1), is lower than in the real system.

Technical literature draws attention to numerous models which take account the influence of rotational speed, applied bearing load and preload on contact angles in angular bearings and on contact loads Q taking place between the ball or shaft and the raceways of bearing rings (Alfares and Elsharkawy, 2003; Antoine *et al.*, 2005; Chen and Hwang, 2006; Jiang and Mao, 2010). Friction torque M_1 as per Musiał and Styp-Rekowski (1999), Styp-Rekowski (1999) is a function of contact loads Q and rolling friction coefficient f between the rolling element and bearing raceways. Hence, familiarity of contact loads Q and the assumption of rolling friction coefficient f enabled determination of the friction torque M_1 .

Harris and Kotzalas (2013) presented a model which takes into account the influence of preload on the bearings contact angle α and on the contact load Q . This model assumes that contact of the bearing ball with raceway falls under Hertz theory, whereas the mathematical formula connecting the contact load with contact deformation has been assumed under the form of Jones model (Haris and Kotzalas, 2013)

$$Q = K\delta^n \quad (1.3)$$

here: K is the contact stiffness, δ – contact deformation, n – constant value (for ball bearings $n = 1, 5$). Contact stiffness coefficient K is a function of ball curvature and bearing raceways.

Several authors, among others, Alfares and Elsharkawy (2013), Altintas and Cao (2005), Chen and Hwang (2006), Cao and Altintas (2007), Jiang and Mao (2010), Jędrzejewski and Kwaśny (2010), Abele *et al.* (2010), and Noel *et al.* (2013) have taken account the effects in contact zones, which generates centrifugal load from rotating raceways, balls or shafts. One of these is the difference in the bearings contact angles on inner and outer raceways and their dependence on rotational speed. These models take into account simultaneous application of the preload force of the angular bearing and the centrifugal load. A notable progress in the development of modelling contact effects in bearings was the work of Antoine *et al.* (2005). Considering the case of the bearings preload with the use of a spring, they presented an analytical relationship between the bearings contact angles, present on both raceways, the inner and outer one. This dependence has a substantially facilitated analytical solution in calculating contact angles.

Few are publications on calculation of the total friction torque. The exceptions are some articles (Musiał and Styp-Rekowski, 1999; Styp-Rekowski, 1999). Analytical formula has been presented, which enables calculation of the friction torque on the driving shaft, basing on the familiarity of contact loads and on the rolling friction coefficients. A common characteristic of all encountered in literature contact models of angular bearings is the assumption of non-deformity of all elements of the bearings except for the ball or shaft. Only contact deformations of the ball or shaft are considered in calculation of the contact angles or contact loads (Fig. 1a)

A second common characteristic relates to the loads. The loads resulting from rotating rolling elements are considered in analysis of contact effects only. At the same time, there have been completely disregarded the loads resulting from the rotating inner ring of the bearing and resulting from deformation of the ring due to the centrifugal force.

2. Classical contact model of the angular bearing

In order to compare the used till now contact models of angular rolling bearings with the recommended, new extended model, there shall be presented both models on the example of an angular bearing subject to the preload F_a and centrifugal load F_c , arising from rotating balls.

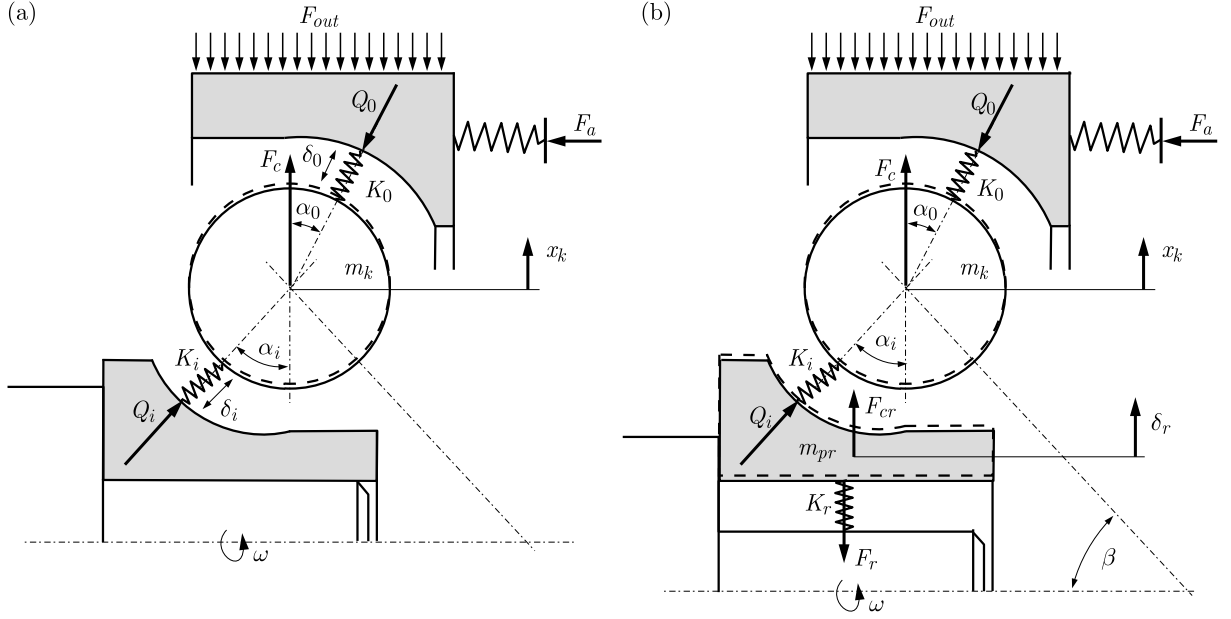


Fig. 1. Contact models of angular bearings: (a) classical, (b) extended

The procedure of solving the contact problem in angular bearings boils down to determination of the contact angles. Their familiarity enables determination of the other parameters, e.g. contact loads. The procedure can be split down into at least three steps:

- identification of the position of centres of curvatures of the bearing inner and outer raceways and of the ball centre with the bearing being subject to load and not being subject to loads,
- generation of conditions of equilibrium of loads acting on the bearings elements,
- generation of the geometrical condition, which shall enable determination of one of the contact angles.

Figure 2 presents the state of the angular bearing subject only to the preload F_a (Fig. 2a) as well as preload F_a and the centrifugal load F_c from the rotating ball (Fig. 2b).

For configuration depicted in Fig. 2a, the position of centres of raceway curvatures and of the centre of the ball in a state not subject to the load is indicated as i , o and O . Geometric constructional characteristic of such a state is the distance between points i and o , marked as A . It is a constructional characteristic of each bearing. Equally important constructional characteristics of bearing are the radii of curvature of the bearing raceways r_i and r_o , as well as the contact angle α .

After the bearing is subject to the preload F_a^* (in this example applied to the inner ring) displacement of the inner ring takes place. As a result the centre of curvature of the inner raceway is displaced into the position i^* . This means that the distance between the points i^* and o changes and assumes the value A_p and the contact angle assumes the value α_p .

In the load configuration depicted in Fig. 2b (preload and centrifugal load of the rotating ball), the centres of curvatures of both raceways i^* and o are not subject to change, however the ball centre gets displaced to point O_1 . At this stage of resolving the contact problem, there is also determined the distance between the centres of curvatures, in this case it is A_p .

The second step of the procedure resolving the contact problem defines the conditions of equilibrium of the loads acting on the bearing elements. For instance, for configuration depicted

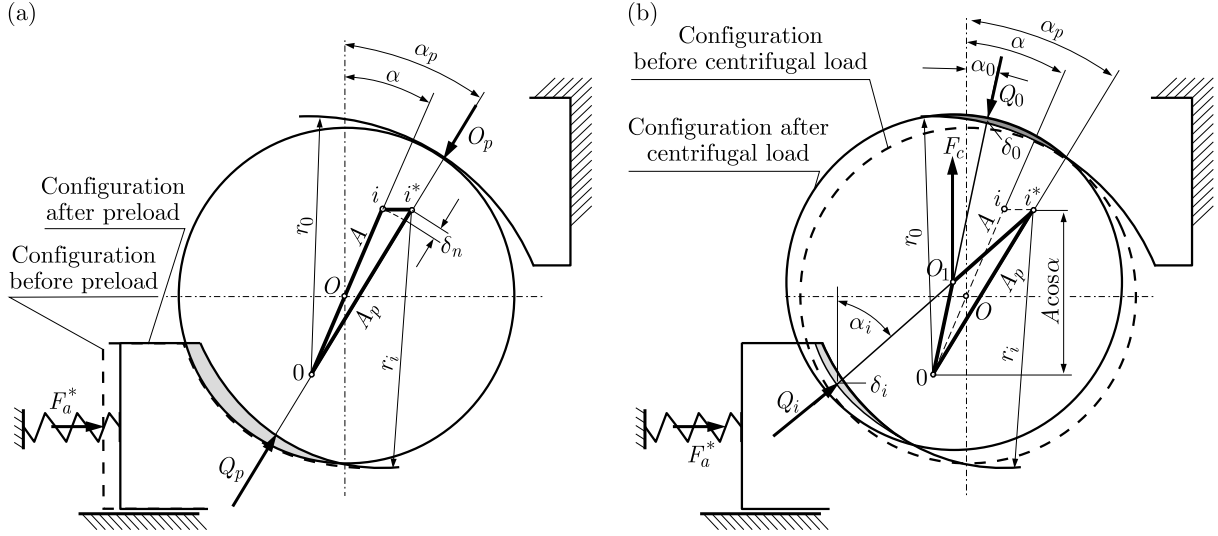


Fig. 2. Configurations of the angular bearing subject to: (a) preload F_a^* and (b) preload F_a^* and centrifugal load F_c from rotating bearing balls: δ_i, δ_o – contact deformations, Q_i, Q_o, Q_p – contact loads, $\alpha, \alpha_i, \alpha_o, \alpha_p$ – contact angles, r_i, r_o – raceway curvature radii, i – index relating to the inner raceway, o – index relating to the outer raceway, p – index relating to the state of preload F_a^*

in Fig. 2b (simultaneous preload and centrifugal load from the rotating ball), from the equations of equilibrium of loads acting on the ball, it follows that

$$Q_i \sin \alpha_i = Q_o \sin \alpha_o \quad F_c = Q_i \cos \alpha_i - Q_o \cos \alpha_o \quad (2.1)$$

From the conditions of equilibrium of loads acting on the inner and outer ring, it can be seen that

$$F_a^* = Q_i \sin \alpha_i \quad F_a^* = Q_o \sin \alpha_o \quad (2.2)$$

If relationships (2.2) are inserted into the second equation of (2.1), we obtain a very interesting relationship, coupling together both contact angles as

$$\frac{1}{\tan \alpha_o} - \frac{1}{\tan \alpha_i} = \frac{F_c}{F_a^*} \quad (2.3)$$

Relationship (2.3), published by Antoine *et al.* (2005), is very significant for resolving the contact problem of angular bearings as it reduces the number of unknowns by 1.

The third step of the procedure resolving the contact problem, defines the geometrical condition, which shall enable determination of the single contact angle. The geometrical condition includes, among others, contact deformations δ_i and δ_o as well as the distance connecting the centres of curvatures i or i^* and o , i.e. A or A_p .

Formulation of the geometrical condition, for example, for configuration depicted in Fig. 2b is somewhat more complicated. For the triangle oi^*O_1 , it can be stated as follows

$$i^*O_1 \cos \alpha_i + O_1o \cos \alpha_o = A \cos \alpha \quad (2.4)$$

Since i^*O_1 and O_1o can be expressed as

$$i^*O_1 = r_i + \delta_i - \frac{1}{2}D \quad O_1o = r_o + \delta_o - \frac{1}{2}D \quad (2.5)$$

then, by inserting (2.5) into (2.4) we obtain the sought geometrical condition

$$\left(r_i + \delta_i - \frac{1}{2}D\right) \cos \alpha_i + \left(r_o + \delta_o - \frac{1}{2}D\right) \cos \alpha_o = A \cos \alpha \quad (2.6)$$

If relationship (2.6) considers equations (1.3), then it should assume the following form (Kosmol, 2016)

$$\left(r_i + \sqrt[n]{\frac{F_a^*}{\sin \alpha_i K_i} - \frac{1}{2}D}\right) \cos \alpha_i + \left(r_o + \sqrt[n]{\frac{F_a^*}{\sin \alpha_o K_o} - \frac{1}{2}D}\right) \cos \alpha_o = A \cos \alpha \quad (2.7)$$

Equations (2.7) and (2.3) form a system of equations, the solution to which determines the contact angles α_i and α_o in function of the centrifugal load F_c and preload F_a^* .

Knowing the contact angles, we can calculate contact loads by using formulae (2.1).

Figure 3 features the influence of rotational speed on the contact loads Q_i and Q_o for selected values of the preload determined by the presented methodology.

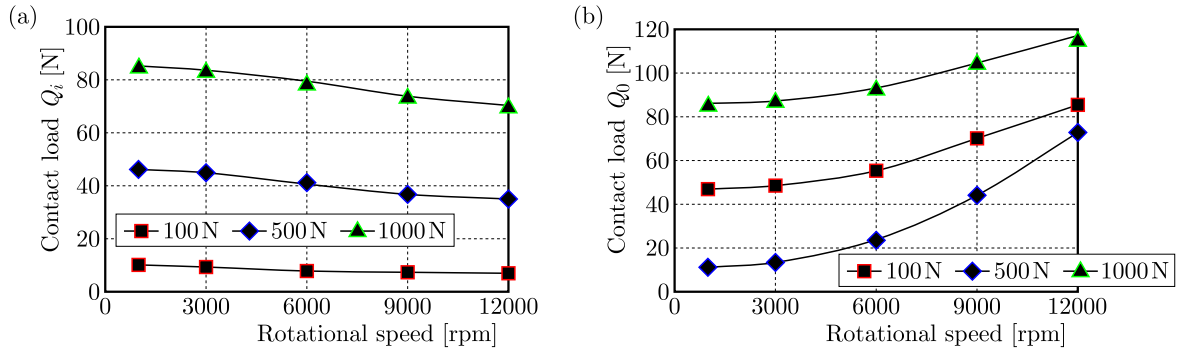


Fig. 3. Influence of rotational speed of the bearing on contact loads: (a) on the inner raceway Q_i , (b) on the outer raceway Q_o , for selected values of the preload F_a

The simulation results in Fig. 3 confirm the known regularities that the contact load Q_i on the inner raceway slightly decreases with an increased rotational speed, whereas on the outer raceway Q_o , it increases substantially with the increased speed.

3. Extended contact model of angular bearings

As already mentioned, the present contact models of angular bearings take into account just contact deformations of balls. Section 1 shows in form of an example what centrifugal load is generated by the rotating inner bearing ring and what are its radial deformations. These values are big enough to presume that they can change considerably the conditions of contact of the ball with the raceways. Hence, a concept has been conceived of a contact model of the bearing, also known as the extended model. It is depicted in Fig. 1b.

Figure 4 portrays the extended contact model of the bearing in convention of the classical model (Fig. 2b).

The procedure of solving such a contact problem is the same as presented in Section 2. First of all identified are the positions of centres of curvatures of both raceways of the bearing. The starting point is the configuration corresponding to the force of preload, i.e. similar to that presented in Fig. 2a. The centres of curvatures are in points i^* and o , and the section connecting both points has length A_p . The bearing contact angle is α_p . The emergence of the centrifugal load F_{cr} of the rotating bearing ring shall cause expansion of that ring and, in effect, the displacement in the radial direction δ_r . In consequence, the centre of curvature of the inner raceway is displaced, which assumes position i^{**} (Fig. 4). The displacement of centre of curvature of the inner raceway from point i^* to point i^{**} is equal to the displacement δ_r . The section connecting the points i^{**} and i^* has length A_{cr} , and the inclination angle of that section is α_{cr} .

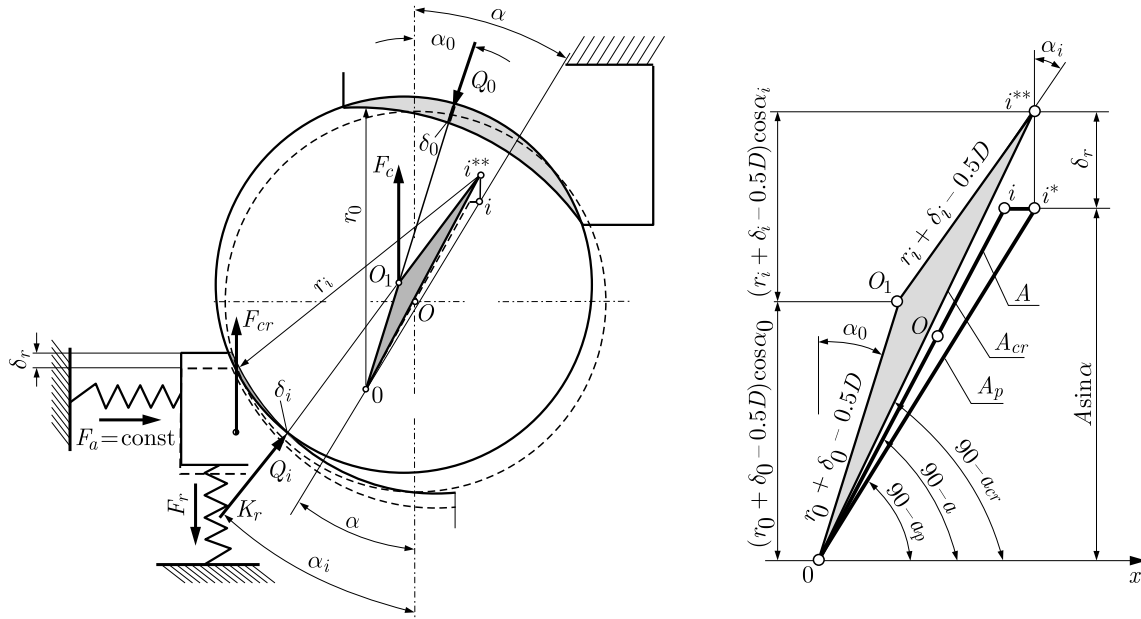


Fig. 4. Extended contact model of the bearing

In effect of action of the centrifugal load F_c from the rotating ball, the ball centre is displaced to point O_1 . As a result, there can be formed a triangle $i^{**}i^*O_1$, which enables one to formulate the geometrical condition.

In the second step, we define conditions of equilibrium of loads acting on the bearing elements. These are the same equations as (2.1) and (2.2), and resulting relationship (2.3). A new equation, with respect to the bearings configuration, as presented in Fig. 3b, is the equation of equilibrium of loads acting on the inner ring of the bearing (Fig. 4), namely

$$F_{cr} - F_r - Q_i \cos \alpha_i = 0 \quad (3.1)$$

where: F_{cr} is the centrifugal load from the rotating bearing ring acting on a single bearing ball, F_r – elastic force from elastically deformed bearing ring.

By assuming a linear model of a deformable ring in the form

$$F_r = K_r \delta_r \quad (3.2)$$

where: K_r is the stiffness coefficient of the bearing ring, δ_r – elastic displacement of the bearing ring, and inserting relationship (3.2) into (3.1), and finally, by considering Jones model (1.3), we obtain the equation of equilibrium of loads acting on the inner ring

$$F_{cr} - K_r \delta_r - \frac{F_a^*}{\tan \alpha_i} = 0 \quad (3.3)$$

from which we determine the radial displacement δ_r , namely

$$\delta_r = \frac{1}{K_r} \left(F_{cr} - \frac{F_a^*}{\tan \alpha_i} \right) \quad (3.4)$$

Relationship (3.4) together with (2.3) shall be the basis for determination of the contact angles. Relationship (3.4) shows that as long as the following condition is met

$$F_{cr} < \frac{F_a^*}{\tan \alpha_i} \quad \delta_r = 0 \quad (3.5)$$

then δ_r cannot assume negative values.

This means that as long as condition (3.5) is met, the solution of the contact problem is the same as for the classical model (see identity (2.7)). However, when this condition is not met, both solutions, i.e. for the classical model and for the extended one, shall differ.

Since the centrifugal load F_{cr} from the rotating ring is a function of rotational speed of the bearing (speed of inner ring), then the threshold speed ω_{gr} can be determined, below which condition (3.5) is met, namely

$$\omega_{gr} < \sqrt{\frac{2F_a}{m_{pw}d_{sr} \tan \alpha_i}} \quad (3.6)$$

where: m_{pw} is mass of the inner ring, d_{sr} – average diameter of the inner ring, ω_{gr} – threshold angular speed of the inner ring.

In step three of solution of the contact problem, the geometrical condition should be defined, since there are two unknowns: contact angles α_i and α_o , and just single equation (2.3). The geometrical condition, which can be formulated, is very similar to condition (2.6), as it assumes the following form

$$\left(r_i + \delta_i - \frac{1}{2}D\right) \cos \alpha_i + \left(r_o + \delta_o - \frac{1}{2}D\right) \cos \alpha_o = A_{cr} \cos \alpha_{cr} \quad (3.7)$$

From Fig. 4, it may be inferred that there exists the following relationship between A_{cr} and A

$$A_{cr} \cos \alpha_{cr} = A \cos \alpha + \delta_r \quad (3.8)$$

By inserting (3.8) into (3.7) and by applying relationships (2.2), Jones model (1.3) and relationship (3.4), we get the first equation for determining the contact angles α_i and α_o

$$\left(r_i + \sqrt[n]{\frac{F_a^*}{\sin \alpha_i K_i} - \frac{1}{2}D}\right) \cos \alpha_i + \left(r_o + \sqrt[n]{\frac{F_a^*}{\sin \alpha_o K_o} - \frac{1}{2}D}\right) \cos \alpha_o - \frac{1}{K_r} \left(F_{cr} - \frac{F_a^*}{\tan \alpha_i}\right) = A \cos \alpha \quad (3.9)$$

Equation (3.9) together with (2.3) form a system the solution of which are the contact angles α_i and α_o . When solving it, one should keep in mind condition (3.5).

Solving the system of equations (3.9) and (2.3) requires application of recurrence methods.

Further on, there shall be presented results of simulation tests of the angular bearing FAG 7013B. The tests consisted in the evaluation of the influence of rotational speed of the bearing (of inner ring) on contact angles α_i and α_o , and on contact loads Q_i and Q_o for selected values of the preload F_a . The tests have been performed for the extended contact model of the bearing.

Figure 5a presents the influence of rotational speed on contact angles of the bearing. There are presented the results of tests for the extended model and the classical one (dashed line).

By comparing the results of tests of the influence of rotational speed on contact angles for both contact models, it should be said that the consideration of centrifugal load from the rotating bearing ring F_{cr} and its elasticity, significantly affects the contact angle α_i on inner raceway. The contact angle on the inner raceway decreases with an increased speed (in the classical model this angle increases), and the model differs from the other by up to over 75%.

Such differences are not observed for the contact angle α_o on the outer raceway. The runs for both models are similar, i.e. the contact angle decreases with an increased speed, and the differences do not exceed 20%.

Figure 5b represents the influence of speed on contact loads Q_i and Q_o for selected value of the preload F_a . The diagrams put together the test results for the extended and the classical model (dashed line).

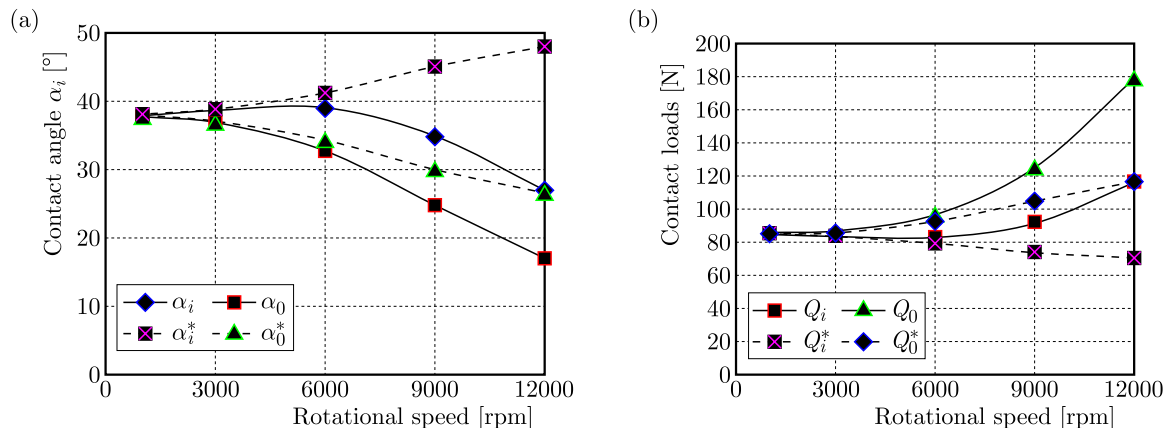


Fig. 5. Influence of rotational speed of the bearing on: (a) contact angles, (b) contact loads, for preload 1000 N; solid line relates to the extended model, dashed line relates to the classical model

The conclusions drawn from the presented test results can have substantial practical meaning, since by generalizing, it can be said that according to the extended model, the contact loads are greater than those according to the classical model.

Qualitatively, the runs of contact loads are similar, i.e. they increase with an increased speed, however, they differ quantitatively. This refers to both, the load on the inner and outer raceways. The loads determined by both models differ by 20% to 30% to the disadvantage of the bearing, i.e. the loads determined according to the extended model are greater. This means, among others, a greater resistance to bearing motion (greater amount of heat in the bearing) and smaller durability of the latter.

On diagrams in Fig. 5, one can also observe the speed range with respect to which both models present the same results. Depending on a given preload, this relates to the speed range of 2000-2500 rotations/min, which results from inequality (3.6).

To get a full picture of the influence of centrifugal load from the rotating ring and its elasticity on contact effects in the bearing, Fig. 6a demonstrates the influence of rotational speed on radial displacements δ_r for the ring itself (dashed line) and for the complete bearing with three preload values.

Depending on the preload of the bearing and on its rotational speed, the difference between deformation of the inner ring alone and the displacement δ_r of the ring mounted in the bearing is 30%.

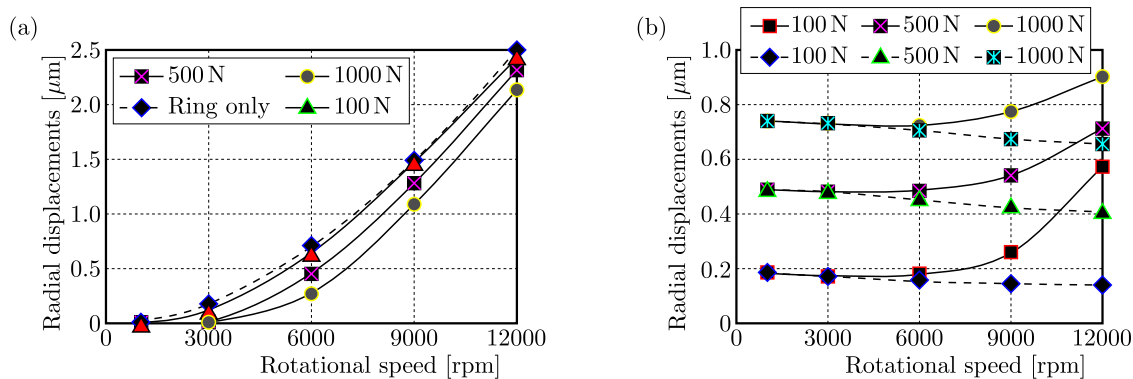


Fig. 6. Influence of rotational speed on: (a) radial displacements δ_r for the ring itself (dashed line) and for the complete bearing, (b) contact displacements of the inner raceway (dashed line relates to the classical model)

However, Fig. 6b shows the influence of rotational speed on contact deformations in the zone of the inner raceway, for both contact models (dashed line relates to the classical model). Contact deformations determined for both models differ qualitatively and quantitatively, whereas these differences can reach 40% and more.

4. Verification of the extended contact model

Verification of the contact model of an angular rolling bearing shall be performed using two methods:

- numerical method, with the use of the finite elements method (Kosmol and Gatys, 2016),
- experimental method.

The first method can be qualified as a direct method, since it enables direct comparison of contact angles of the bearing or the effects in contact zones of the balls action with the bearings raceways (contact loads).

The second method is qualified as an indirect method, since it only facilitates comparison of the total friction torque in the bearing, which depends, among others, on contact loads.

4.1. Numerical analysis of contact effects in bearings using the finite elements method

The object of model tests has been the angular rolling bearing FAG B7013.

Due to the existence of numerous axes of symmetry, only a single rolling element has been modelled as well as a section of inner and outer rings.

System Ansys offers 6 ways of modelling consolidations and 5 ways of modelling contacts. Bearing rings have been deprived of the degrees of freedom corresponding to models *Compression only* and *Friction less*.

It has been decided to model contact effects with the use of the standard frictional model, which enables consideration of friction between adjacent bodies.

It is important for precision of calculations to define a calculation algorithm which predominantly determines the manner of contact detection. The *Augmented Lagrange* algorithm has been selected on the basis of software producer recommendations.

The preload of the bearing has been modelled in the form of thrust on the front surface of the outer ring, whereas the dynamical effects in the form of centrifugal loads acting on movable elements have been modelled using the standard Ansys mechanism.

The results of simulation are: relationships of the contact angles α_i and α_o and contact loads Q_i and Q_o in function of rotational speed of the bearing (of the inner ring) for a selected value of preload. Figure 7 portrays examples of the results for a preload of 1000 N with consideration to both the centrifugal load from the rotating ball (dashed lines) and the thrust from the bearing ring.

The contact angles determined according to the extended model are smaller than those calculated according to the conventional model. The differences measured up even to 40%. But on the outer raceway, there was not so much difference observed between the angles.

A similar thing can be said about the contact loads. For the extended model, the contact loads are clearly bigger for the load on the inner and outer raceways.

By comparing the results of FEM simulations featured by Fig. 7, with the results of analytical tests, presented by Fig. 5, we observe their high qualitative similarity. Hence the results of simulation tests confirm these which have resulted from the analytical research.

Quantitative comparative evaluation of analytical and FEM methods is shown in Fig. 8.

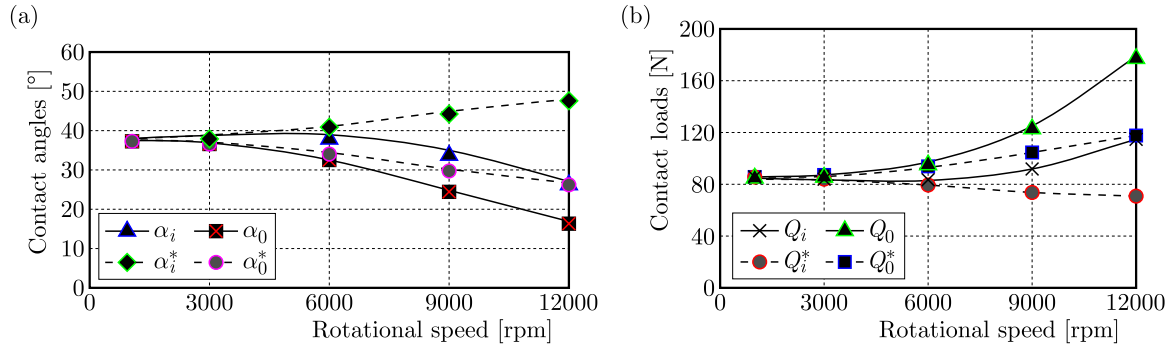


Fig. 7. Influence of rotational speed on: (a) contact angles α_i and α_o , (b) contact loads Q_i and Q_o , for preload 1000 N; the solid line relates to a combined thrust of the rotating ball and the ring, the dashed line relates to the thrust of the rotating ball solely

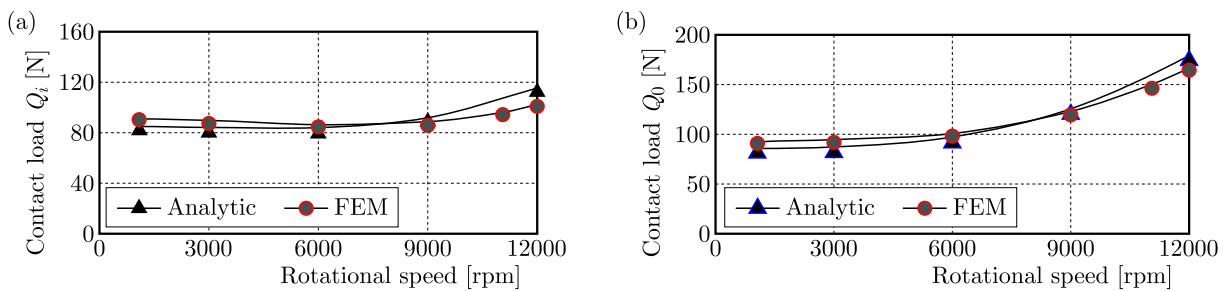


Fig. 8. Comparative evaluation of analytical and FEM methods for the assesment of the influence of rotational speed (centrifugal load from the ball and ring combined) on the contact loads: (a) Q_i , (b) Q_o , for the preload 1000 N

A high degree of consistence is demonstrated by both calculation methods, i.e. analytical method and FEM for the contact load on the outer raceway (Fig. 8b). For the inner raceway (Fig. 8a), there are observed greater differences between both methods.

Thus, an opinion can be formulated, stating that FEM tests confirm the results of analytical tests, which constitutes a certain verification of the extended analytical model.

4.2. Experimental verification of the extended model

As has already been mentioned, experimental verification of the developed model can be performed through indirect methods. There are no technical possibilities for direct measurement of neither contact angles in the bearing nor contact loads. However, there exists a possibility of direct measurement of torque on the driving shaft, which is the friction torque in the bearing. Since the friction torque in the bearing is a direct function of contact loads (Musiał and Styp-Rekowski, 1999; Styp-Rekowski, 1999), then, its measurement represents indirect information on the magnitude of these loads. The friction torque is also a function of coefficients of friction which should be assumed arbitrarily, guided by information provided in technical literature.

At the Department of Machine Technology of the Silesian University of Technology in Gliwice, there has been developed a research site which facilitates measurement of the torque on the driving shaft, the preload of angular bearings and the rotational speed.

A system of a spindle box, in which the spindle and two angular bearings are located, is mounted on the torque sensor made by Kistler, type 7292. The spindle drive comes from a special motor with a steplessly adjustable speed up to 18.000 rotations/min. The preload of bearings can be adjusted steplessly and measured by a sensor of the axial load manufactured by Kistler, type 9102A.

At that site, there have been performed several tests consisting in measurement of the friction torque for certain selected values of rotational speeds and for certain values of bearing preloads (Muszyński, 2017).

As we were interested exclusively in the motion resistance of bearings depending on rolling friction of balls on bearing raceways, the bearings alone have been bereft of lubricant.

Figure 9 shows examples of the obtained results of tests of the motion resistance of two angular bearings. Figure 9a presents the influence of preload and Fig. 9b, the influence of rotational speed on the friction torque of bearings with no lubricant.

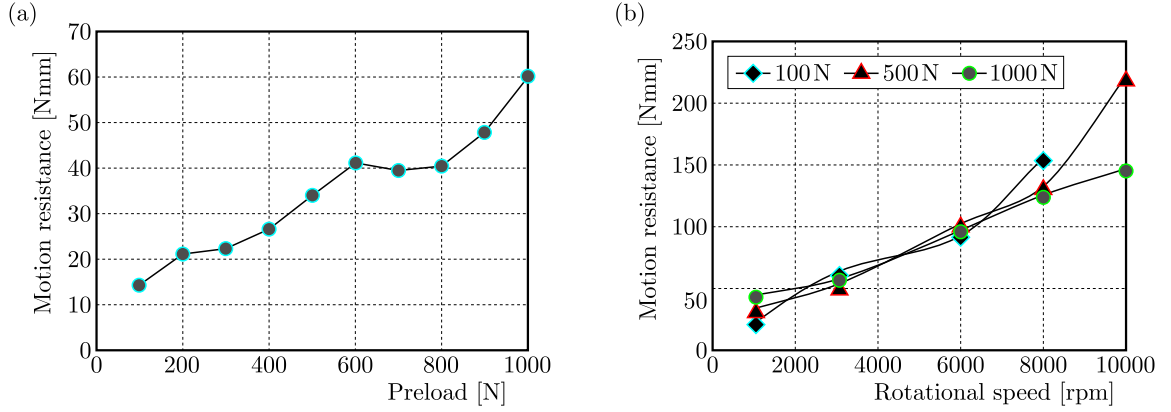


Fig. 9. Examples of measurements of motion resistance at the research site: (a) influence of preload, (b) influence of rotational speed

Thus we are speaking of the resistance resulting from rolling friction of balls which are rolling on the raceways of the bearings.

Musiał and Styp-Rekowski (1999) and Styp-Rekowski (1999) showed an analytical model of bearings motion resistance in function of contact loads, in the following form

$$M_{1(T)} = \left(\frac{d_m}{D} + \frac{1}{2} \right) \sum_{j=0}^{j=Z-1} Q_j f_{kj} \quad (4.1)$$

where: $M_{1(T)}$ is the friction torque of the bearing, Q_j – j -th equivalent load at the contact site of the ball and raceway, Z – number of balls in the bearing, d_m – pitch diameter of the bearing, D – diameter of the ball, f_{kj} – j -th rolling friction coefficient of the ball on the raceway.

For verification, a developed extended contact model has been assumed (Kosmol, 2016), in which

$$Q_j = Q_i + Q_o \quad (4.2)$$

where: Q_i , Q_o are contact loads on the internal i and external o raceway. In the model, the rolling friction coefficients are the same for every ball in the bearing. The value of this coefficient has been assumed arbitrarily.

For such assumptions, the total friction torque of the bearing can be presented as follows

$$M_{1(T)} = Z \left(\frac{d_m}{D} + \frac{1}{2} \right) (Q_i + Q_o) f_k \quad (4.3)$$

By converting relationship (4.3) and assuming $M_{1(T)} = M_{op}$, we can write down

$$Q_i + Q_o = \frac{M_{op}}{2Z \left(\frac{d_m}{D} + \frac{1}{2} \right) f_k} \quad (4.4)$$

where M_{op} is the friction torque measured at the research site.

In relationship (4.4), the fact has been considered that at the research site there are two angular bearings.

For the tested angular bearings FAG 7013B, relationship (4.4) assumes the following form

$$Q_i + Q_o = \frac{M_{op}}{309.7 f_k} \text{ [N]} \quad (4.5)$$

where M_{op} is in Nmm and f_k in mm.

Relationship (4.5) allows indirect verification of the developed extended contact model through comparing the sum of contact loads calculated analytically and determined experimentally for arbitrarily assumed rolling friction coefficients.

Figure 10 portrays a comparison of the sum of contact loads $Q_i + Q_o$ determined on the basis of experimental research as per relationship (4.5), with recourse to the extended model and with recourse to the classical model and the given FEM simulation results.

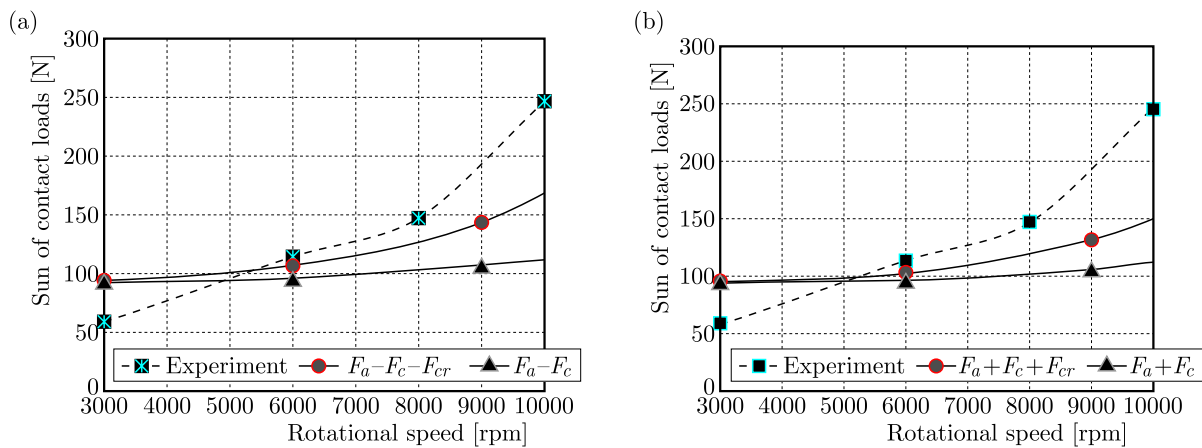


Fig. 10. Comparison of sums of contact loads $Q_i + Q_o$ obtained from experimental research and (a) analytical tests, (b) FEM simulation: $F_a + F_c + F_{cr}$ – extended model, $F_a + F_c$ – classical model, $f_k = 0.0029$ – friction coefficient, $F_a = 500$ N – preload of the bearing

The comparison of the sums of contact loads obtained from the experimental research (relationship (4.5)) with the analytical tests and FEM obtained from the extended model (Fig. 10) demonstrates their reasonable consistence, but qualitatively only. Over 6000 rpm, an increase in the experimental sum of contact loads is much more similar to the results obtained for the extended model than for the classical model. This can be interpreted as an indirect confirmation of the correctness of the extended model. But below 6000 rpm, the experimental and theoretical results differ. It means that the motion resistance depends not only on the friction torque due to load (4.1) but on other resistances, for example on the spinning effect or cage resistance, too (Kosmol, 2016).

Figure 10 presents also the results in the form of the sum of contact loads for the classical model. They show that the sums of contact loads are explicitly smaller (by approx. 20% and more) from the results obtained from the extended model and from the experiment.

The results shown in Fig. 10 have been obtained by fine-tuning of the friction coefficient f_k (see the relationship (4.5)) for the best match with the analytical results and FEM. The value of the friction coefficient fine-tuned in that way amounts to approx. 0.0029, i.e. it is in the range which has been presented in publications on angular rolling bearings, i.e. 0.002-0.005.

5. Summary

The article presents a new contact model of an angular bearing, called the extended model. The model takes into account the effects of the centrifugal load caused by the rotating ring of the bearing and the issue of elasticity. Present models, encountered in literature and referred to in the article as classical, consider the centrifugal force caused by the rotating ball only. Results of analytical research on the extended model and FEM simulations show explicitly that the contact angles of bearings, and thus the contact loads, differ very much from those values obtained in the classical model. These differences are disadvantageous while designing bearing assemblies, since the contact loads are greater than those obtained in the classical model. This means, among others, that the present structures with angular contact bearings are in reality subject to greater loads than the constructor has envisaged.

The motto of the article is to design analytical calculation models in such a form which would enable the constructor to estimate the contact loads using just a standard scientific calculator or MS Excel type applications, so that there would be no need for solving complex models using numerical methods.

The article also features the results of verification of the developed extended model. The verification encompassed both, FEM numerical analysis and experimental investigation. The results of the verification (experimental research and FEM simulation) have confirmed relative consistence with the results of the analytical examination developed on the basis of the extended model. They have shown that the present classical model leads to an erroneous evaluation of contact loads in the bearing.

Hence, the article formulates a viewpoint that for engineering purposes, the suggested extended contact model enables calculation of contact loads in angular bearings with a sufficient practical accuracy.

References

1. ABELE E., ALTINTAS Y., BRECHER C., 2010, Machine tool spindle units, *CIRP Annals – Manufacturing Technology*, **59**, 781-802
2. ALFARES M.A., ELSHARKAWY A., 2003, Effects of axial preloading of angular contact ball bearings on the dynamics of a grinding machine spindle system, *Journal of Materials Processing Technology*, **136**, 48-59
3. ALTINTAS Y., CAO Y., 2005, Virtual design and optimization on machine tool spindles, *Annals of the CIRP*, **54**, 1, 379-382
4. ANTOINE F., ABBA G., MOLINARI A., 2005, A new proposal for explicit angle calculation in angular contact ball bearing, *Journal of Mechanical Design*, **128**, 2, 468-478
5. CAO Y., ALTINTAS Y., 2007, Modelling of spindle-bearing and machine tool systems for virtual simulation of milling operations, *International Journal of Machine Tools and Manufacture*, **47**, 1342-1350
6. CHEN J.-S., HWANG Y.-W., 2006, Centrifugal force induced dynamics of motorized high-speed spindle, *International Journal of Machine Tools and Manufacture*, **30**, 10-19
7. CHOJNACKI M., 2016, Experimental research of motion resistance in angular bearings (in Polish), M.Sc. Thesis, Silesian University of Technology, Gliwice
8. HARRIS T., KOTZALAS M., 2013, *Essential Concepts of Bearing Technology. Rolling Bearing Analysis*, 5th Ed., Taylor & Francis Group, London
9. JĘDRZEJEWSKI J., KWAŚNY W., 2010, Modelling of angular contact ball bearings and axial displacements for high-speed spindles, *CIRP Annals-Manufacturing Technology*, **59**, 377-383

10. JIANG S., MAO H., 2010, Investigation of variable optimum preload for machine tool spindle, *International Journal of Machine Tools and Manufacture*, **50**, 19-28
11. KOSMOL J., 2016, *Determination of Motion Resistances in High-Speed Spindle Angular Bearings*, Monograph, Silesian University of Technology Publisher, Gliwice
12. KOSMOL J., GATYS R., 2016, Simulation research of the influence of rotational speed on contact loads in angular bearings (in Polish), *Inżynieria Maszyn*, **21**, 1, 32-45
13. MUSIAŁ J., STYP-REKOWSKI M., 1999, Analytical and experimental method of determination of the coefficient of motion resistance in rolling friction (in Polish), *Proceedings of Conference "Problems of Unconventional Bearing Configuration"*, Łódź, 59-65
14. MUSZYŃSKI M., 2017, Experimental research of motion resistance in angular bearings (in Polish), M.Sc. Thesis, Silesian University of Technology, Gliwice
15. NOEL D., RITHOU M., FURET B., LELOCH S., 2013, Complete analytical expression of the stiffness matrix of angular contact ball bearing, *Journal of Tribology*, **135**, 4
16. PALMGREN A., 1951, *Rolling Bearings* (in Polish), PWT, Warszawa, 235
17. STYP-REKOWSKI M., 1999, *Problems of the Internal Resistance of Motion in an Angle Bearing* (in Polish), University Press of Technology and Agriculture Academy in Bydgoszcz, Thesis, 99, Bydgoszcz

Manuscript received May 16, 2017; accepted for print June 30, 2018

NUMERICAL ANALYSIS OF CONTACT PLASTIC BODIES MADE BY ALUMINIUM ALLOY WITH TAKING ACCOUNT OF MICRO-ROUGHNESS SURFACES

PAWEŁ SIDUN

Białystok University of Technology, Faculty of Mechanical Engineering, Białystok, Poland
e-mail: pawel.sidun.pb@gmail.com

JAN PIWNIK

COBRABID Warszawa, Research Center, Poland and
Road and Bridge Research Institute, Warsaw, Poland

The following article describes selected aspects of numerical modeling of the process of bonding metal alloys with consideration for micro-roughness. Plastic contact between two deformable bodies is studied within a DEFROM FEM environment. The paper presents selected numerical analysis results for an aluminum alloy. The mathematical model of surface roughness has been created on the basis of the surface real profile. The dependence between the tool lathe angle and the feed has been used to build a numerical model of roughness after completion of the turning process. The article investigates the impact of wave roughness in respect to the size effect and the possibility of cold welding as well as the simplification process of real surface roughness.

Keywords: bonding process, FEM analysis, cold welding, wave roughness

1. Introduction

Methods of forming metals are widely used in industry increasing production rates. They are characterized by high accuracy, repeatability of dimensions and shapes as well as excellent surface quality. It is possible to apply them on the micro scale, however, it results in specific new technological problems, the so called “size effect”, caused by the objects small dimensions, especially when the method employs specimens with dimensions smaller than 1 mm. In micro-scale, the entire volume of the material is treated as its surface without distinctions into layers. This is the reason why methods used in carrying out experiments as well as those used in physical, analytical and numerical analyses should always account for scale. Piwnik and Mogielnicki (2010) investigated the influence of the scale effect during the process of micro-extrusion. The results of their numerical simulations showed that extrusion forces increase significantly with very coarse surfaces.

Literature contains numerous studies related to elastic-plastic contact between surfaces. Sun and his team (Sun *et al.*, 2013) investigated the process of flattening sinusoidal surfaces from the perspective of the effect of plastic deformation on wear parameters. Manoylovet *et al.* (2013) studied elastic-plastic contact of dry surfaces to establish their wear parameters while Wang *et al.* (2007) examined elastic-plastic contact in the extrusion process in relation to microvillic roughness. Matsumoto *et al.* (2014) studied elastic-plastic contact in the extrusion process utilizing the retreat and advance pulse ram motion on a servo press. The effects of scale were also studied by Zhang *et al.* (2003) in respect to micro-mechanical friction during metal forming. Furthermore, literature shows an analytical approach to solving the issue of full plastic contact using statistical tools (Ma *et al.*, 2010). Abdo and Farhgang (2005) investigated elasto-plastic

contact of rough surfaces and compared forming methods and models with the results of their own experiments while Cai and Bhushan (2005) developed a numerical approach to modeling elastic-plastic contact of uneven surfaces investigating multi-layered elastic/plastic surfaces. Poulos and Klit (2013) also studied this kind of problem. The way they approached the issue was both innovative and very interesting since before them, situations in which both contact surfaces were elastic-plastic had not been considered.

The final item which must be included in the above-mentioned review of literature is the semi-analytical model of elastic-plastic contact. Zhang *et al.* (2014) presented the impact of surface roughness on the effectiveness of the elastic-plastic area of contact. Additionally, similar works dealing with modeling of elasto-plastic surface contact with boundary roughness (Brzoza and Pauk, 2007) and (Buczowski and Kleiber, 1992) contact problems connected with a nonlinear interface compliance can also be found in literature. The article presents a new approach to modeling entirely plastic rough contact areas of two aluminum alloy deformable bodies which take into consideration the parameters of wavy roughness on the obtained values of stress, strain, and strain rate fields in micro-scale. These fields are also used to determine strain forces as well as to investigate the influence of wavy roughness on the possibility of cold welding during the bonding process.

2. Modeling of roughness

In the process of modeling metal forming processes, it is possible to distinguish many models of friction. The appropriate selection of a friction model mainly depends on friction conditions. An excellent comparison of friction models occurring during metal forming processes was presented by Tan (2002). On the basis of this list and the commonly accepted laws describing friction models, it is possible to distinguish two laws describing problems connected with elastic-plastic issues. The FEM environments implement these two laws as necessary dependencies describing the impact of stress and deformation caused by friction:

— Coulomb's law – describes friction in the elastic range

$$\mu = \frac{F_f}{N} = \frac{\tau_f A}{\sigma_n A} = \frac{\tau_f}{\sigma_n} \Rightarrow \tau_f = \mu \sigma_n \quad (2.1)$$

— constant shear stress law – for plastic friction

$$\tau_f = f \bar{\sigma} = m \frac{\bar{\sigma}}{\sqrt{3}} = mk \quad (2.2)$$

where: τ_f is the frictional stress [MPa], N – normal force [N], F_f – frictional force [N], A – contact area [mm²], μ – friction coefficient, m – frictional shear factor $0 \leq m \leq 1$, k – shear yield strength [MPa], $\bar{\sigma}$ – effective stress [MPa], f – friction factor.

The simplest way to describe a micro-roughness model is through the use of Fourier series (2.3) which is also practical for the analysis of periodic signals. When it comes to numerical analyses, this method of describing roughness is the easiest and makes it possible to investigate the influence of both wavelengths and wave amplitudes, which is very useful in the analysis of the process of cold welding:

— for integer $N \geq 1$, the Fourier series is expressed as

$$S_N = \frac{A_0}{2} + \sum_{i=1}^N A_i \sin\left(\frac{2\pi i x}{T} + \varphi_i\right) \quad (2.3)$$

— for $i = 1$, $A_0 = 0$, $\varphi_1 = 0$, $T = 2\pi$, equation (2.3) takes the form

$$S_N = A_1 \sin x \quad (2.4)$$

Equation (2.4) is used for describing the geometry of surfaces after the turning process. Figure 1 presents the dependency between surface micro-roughness after turning with the simplest form of the Fourier series equation.

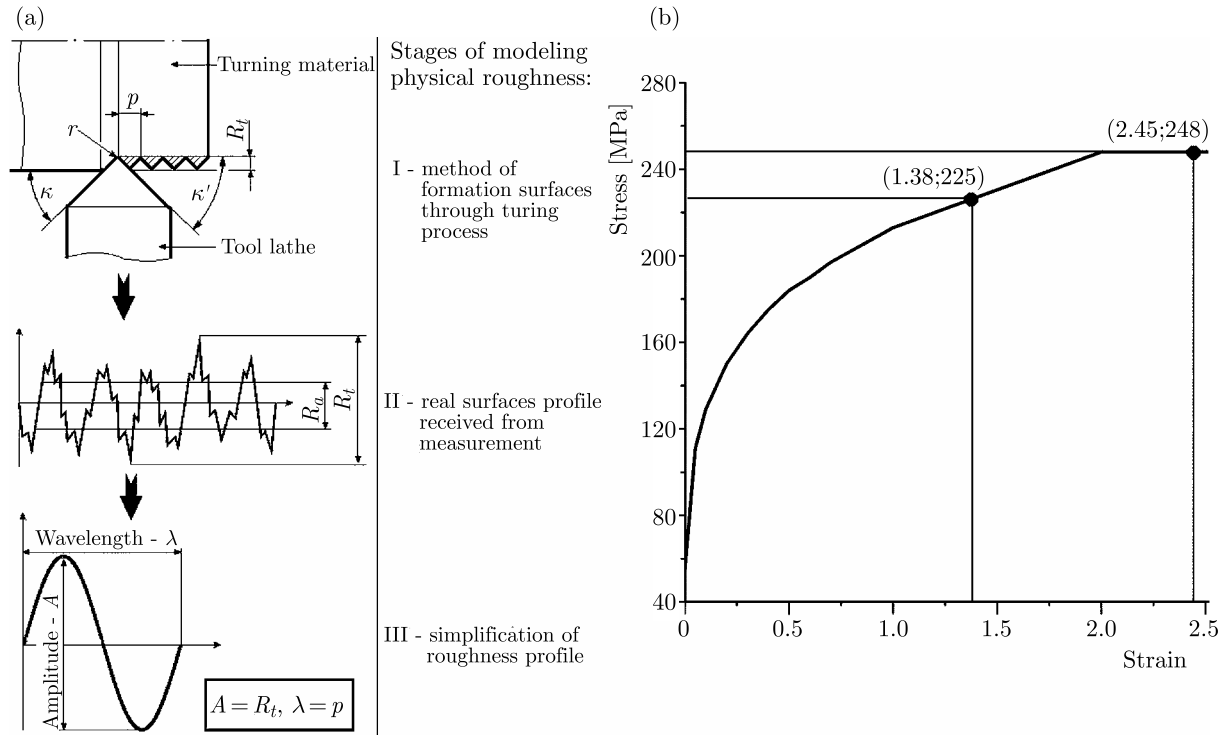


Fig. 1. (a) Stages of modeling physical roughness. (b) The stress-strain curve of aluminum alloy 6061-T0, the strain values in the deformation environment are multiplied ten times

Equation (2.5)₁ describes the dependency between the lathe feed during the turning process and the maximum height of the roughness profile, whereas equation (2.5)₂ is a well-known fundamental law describing the dependence between the feed rate, the radius of the corner and the arithmetic average values of the roughness profile

$$R_t = p \frac{\tan \kappa \tan \kappa'}{\tan \kappa + \tan \kappa'} \quad R_a = \frac{p^2}{32r} \quad (2.5)$$

where: R_t is the theoretical maximum roughness [mm], R_a – arithmetic average values of the roughness profile, p – feed [mm/rev], κ – primary and secondary lead angle of the lathe [°], r – radius of the corner.

Selecting turning parameters in the machining process, such as the feed, primary and secondary lathe angle as well as the value of radius of the corner, results in surface roughness having a sinusoidal character, which is a good method for representing work results (D'Addona and Raykarb, 2016). As was shown by Griffin *et al.* (2017), the real-time adjustment of other turning parameters such as rotation speed, tool pressure and tool wear (new tools in machining) or the use of acoustic emission signals allows a decrease in the distribution of height roughness. The use of acoustic emission signals in real-time control of parameters during the turning process produces surfaces without any defects such as waviness and height of roughness less than the parameter R_t . Griffin's work (Griffin *et al.*, 2017) shows that proper steering of cutting parameters during the machining process results in R_t parameter values nearly equal to R_a . Hence in our considerations of this issue, the roughness parameter R_t is used instead of the parameter R_a . During the bonding process, small vertices of roughness disappear much faster than high ver-

tices, and the calculation of two extreme positions of roughness (Fig. 2b) allows calculation of mean values of the height profile which will be the closest to that of the real roughness profile.

3. Finite element analysis of the bonding process

This paper presents a numerical study of the bonding process (Fig. 1a). Using the Finite Element Method (FEM), the authors have performed a numerical analysis of a model only within the plastic aspect of material deformation within the DEFORM environment. The numerical experiment was conducted on samples having dimensions of $\emptyset 1 \times 0.75$ mm made of 6061-T0 aluminum alloy on the assumption of specimen symmetry. The material stress-strain curve is presented in (Fig. 1b). The total displacement of the upper die used in the experiment was 1.37 mm with the direction of movement also being marked. The speed of the upper die during the bonding process was equal to 0.02 mm/s while the starting temperature was 20°C.

The plastic model is based on the HMM criterion as well as the isotropic material hardening model developed by Ottosen and Ritismannm (2005). The contact between the elements in FEM analysis is defined in the following manner: the dies are rigid (III and IV), samples show only plastic behavior (I and II) and the contact in pairs is assumed without the coefficient of friction. The discrete model of specimens has been made using 4500 quad elements for each sample.

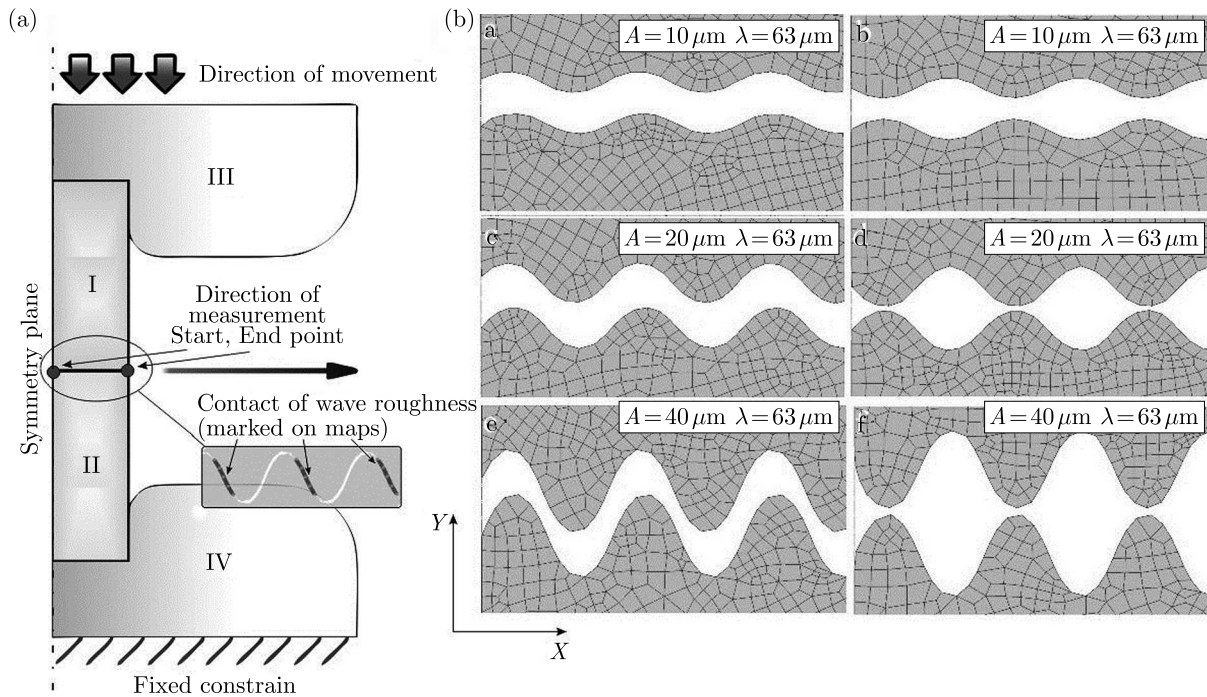


Fig. 2. (a) A diagram of the analysis of the bonding process. (b) Wave roughness profile: a, c, e wave in contact throughout the entire geometry (“wg” for short); b, d, f wave only in contact at its peak (“tow” for short)

The first wave (a, b) has an amplitude equal to $10 \mu\text{m}$ and a length of $63 \mu\text{m}$ (Fig. 2b), the second (c, d) has an amplitude of $20 \mu\text{m}$ and a length of $63 \mu\text{m}$ and the third wave (e, f) has an amplitude equal to $40 \mu\text{m}$ and a length of $63 \mu\text{m}$. Two variants of the same wave are also considered to examine the impact of wavy roughness on the assumption that $f = 0$. In the case of (b, d, f) only, the contact on the wave peak is considered while in (a, c, e), the contact is evaluated throughout the entire wave geometry. These two variants of wave positions allow a certain lack of perfect congruency of specimens relative to one other. Having the two extreme wave positions

makes it possible to investigate the discrepancies in the results of any wave positions relative to one another and to calculate an average value. We should add that the roughness, microstructure as well as surface phenomena (adsorption etc.) play a significant role in welding technologies (including cold welding) which was confirmed in the work of Danwood *et al.* (2015). At the end of this Section we must stipulate however, that omission of the influence of the shear factor and creation of a friction model based only on micro-cutting does not adequately describe the entire frictional process. Such an approach to the modeling allows a quantitative description of the entire problem or differentiation between phenomena occurring during micro-cutting and the impact of the surface force in the frictional process. Further quantitative analysis of the friction process will allow a better understanding of the phenomena occurring in both friction and wear processes.

4. Effective stress-strain distribution

In attempting the analysis of effective plastic strain maps, it is necessary to identify fields of effective stress because their distributions are the same. After analyzing the charts of effective plastic strain (Fig. 3) it is clear that the material has a more homogeneous strain distribution for the “wg” contact than for the “tow” contact. Additionally, the “tow” contact displays a substantial strengthening of the material at vertices of wave roughness.

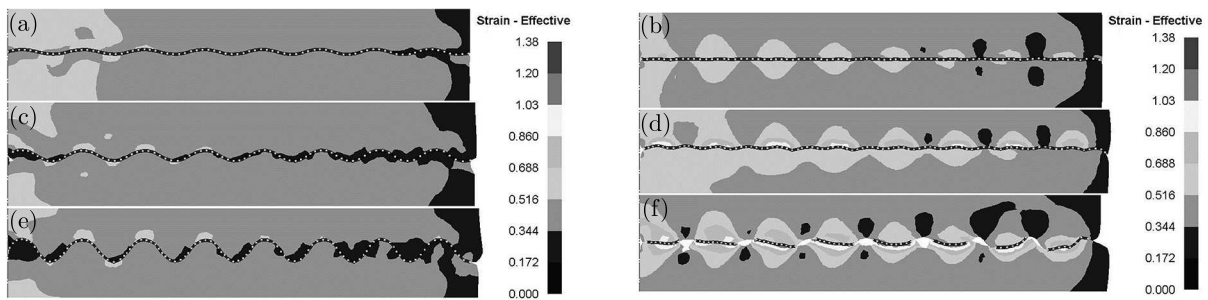


Fig. 3. Maps of the effective plastic strain for the upper die displacement equal to 0.5 mm

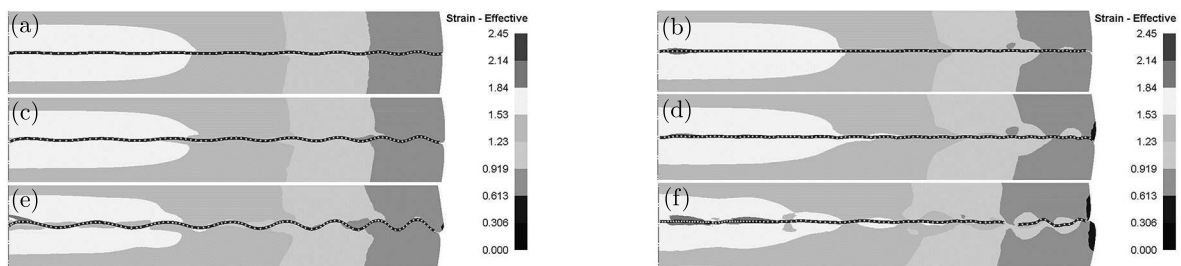


Fig. 4. Maps of the effective plastic strain for the upper die displacement equal to 1 mm

During further movement of the upper die equal to 1 mm, the effective plastic strain for each wave (Fig. 4) is homogeneously distributed. What is essential is that the whole process can be considered to be “cold” since the speed of the upper die, equal to 0.02 mm/s, caused a temperature increase by only about 5°C. This small increase in temperature allows making an assumption that no phase transitions occur within the material. Based on the obtained stress and strain results, it is necessary to draw attention to the fact that the wave roughness has become flattened but has not been sheared off. This proves that the elements can not become bonded during the process because the oxidation of the surfaces is not eliminated through friction. Adjustment of bonding process parameters such as making the strain rate greater or

the pressure higher does not create a plastic weld because contact surfaces are oxidized. The only proven way to make cold welding possible, described by Tang *et al.* (2009), is to previously purify the surfaces from contaminants and oxides and to conduct the entire process in a vacuum. In their experiment, they flattened copper-water micro heat pipe ends to achieve cold welds where plastic welds in a vacuum were obtained after the deformation of a copper tube at approximately one and a half of its yield strength. During their work, Tang *et al.* (2009) did not determine the criterion of cold welding but only determined an approximate starting point of the process of plastic welding on the compression force curve.

5. Impact of micro-roughness

Before we begin our discussion on the results obtained for contact surfaces, it is necessary to take another look at the diagram in Fig. 2a to ensure that the results of the analysis are being read correctly. In the zone of the plastic contact, it is possible to see the impact of the parameters of wave roughness. An increase in the amplitude of the wave causes a significant increase in the plastic strain in the area of contact (Fig. 5). A higher rise in strain is particularly observable in respect to the “tow” contact (Fig. 3). The growth of the strain during the bonding process is maintained despite the high deformation of the material. The upper die displacement equal to 1 mm (Fig. 5) causes a reduction in the obtained strain values between different waves. On the basis of this measurement, we can conclude that further deformation of the material does not cause plastic welding of contacting elements because most of the roughness vertices have already been flattened.

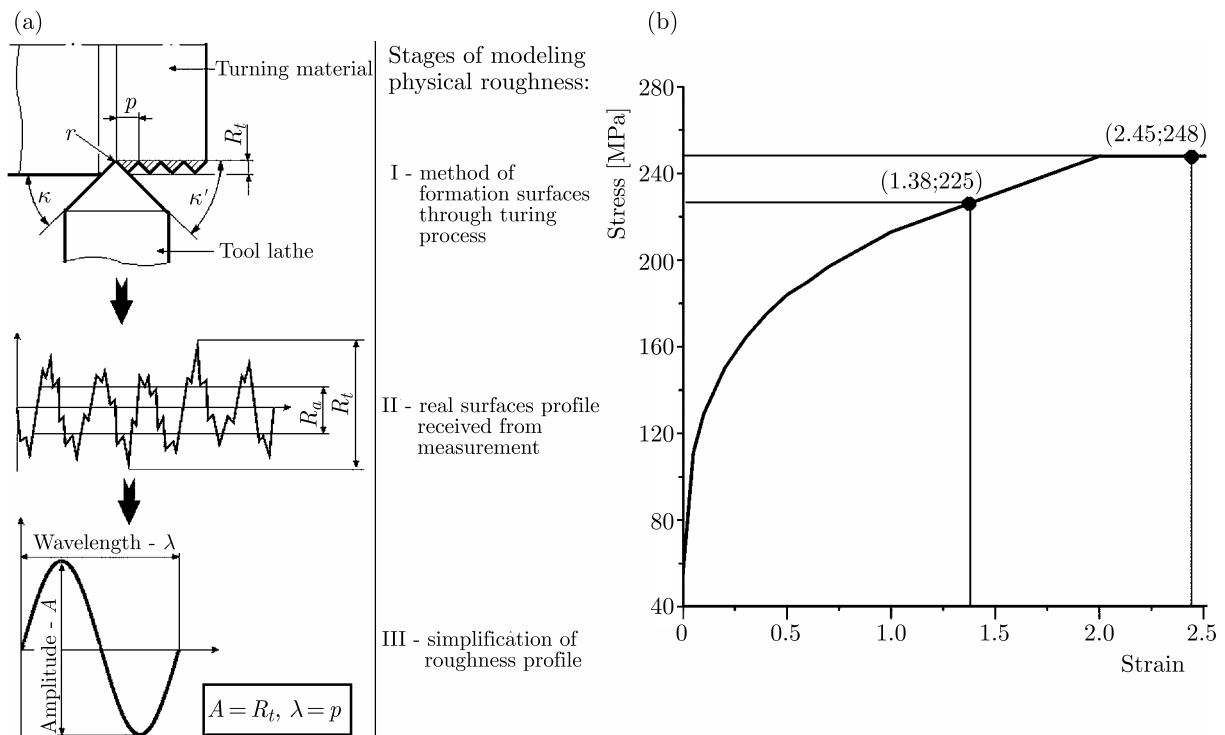


Fig. 5. Strain distribution for the upper die displacement equal to 0.5 mm

When it comes to the micro-scale effect, Fig. 5 shows that a four-fold increase in the wave amplitude causes a 2-fold increase in the plastic strain for the “tow” contact. This effect varies (Fig. 6) and, at larger deformations, disappears much later for the “wg” contact than for the

“tow” contact. Since this does not occur on the macro scale, it must be accredited to the micro-forming processes.

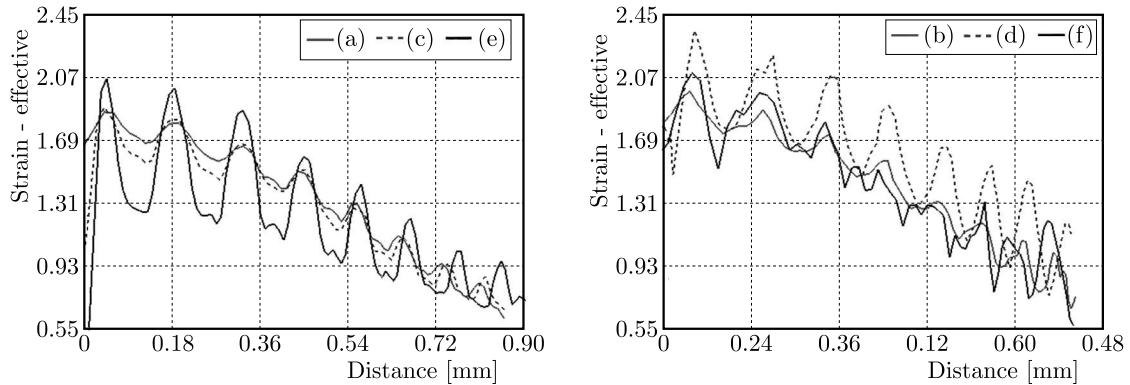


Fig. 6. Strain distribution for the upper die displacement equal to mm

Table 1. Maximum, minimum and average strain values

Die displ. [mm]	Average strain values						Max	Min
	a	c	e	b	d	f		
0.5	0.4	0.49	0.39	0.37	0.56	0.69	1.21	0.2
1	1.36	1.32	1.21	1.43	1.59	1.45	2.34	0.55

During the analysis of the contact zone, it is also important to determine the average strain values since, on their basis, a specific relationship between the increase of plastic strain and the wave height can be established. Looking at Table 1, it is necessary to pay attention to the fact that a rise in wave height only causes an increase in the average strain value at the beginning of the bonding process (die displacement equal to 0.5 mm). For “tow” contact surfaces an increase between wave b and wave d was equal to 0.19 (33%) while between wave b and wave f it reached 0.32 (46%), but no such a dependency was observed for the “wg” contact. Further deformation (die displacement equal to 1 mm) for “wg” contact resulted in a decrease of the average strain value between wave a and wave c equal to 0.04 (2.9%) and between wave a and wave e equal to 0.15 (11%) while no such dependency was observed for the “tow” contact.

An analysis of the maximum shear stress on contact surfaces shows that vertices of micro-roughness are compressed rather than sheared, a fact which is confirmed by data in graphs of the effective plastic strain and shear stress. The authors emphasize this fact because it is essential to the performed analysis. A greater share of shear stress, no less than 57%, than that of the normal stress in the effective stress is a prerequisite for obtaining plastic welds.

Looking at Fig. 7, it is possible to observe that the impact of micro-roughness on the distribution of shear stress is much less than that on of the effective plastic strain. The differences between different waves and positions of fields are small. Displacement of the upper die equal to 1 mm (Fig. 8) shows that the distribution of shear stress is much more uneven than that of the effective plastic strain. Disturbances occurring only at the ends of measurement fields have no significant impact on the bonding process.

The dependence between wave height and high deformation of specimens in the bonding process cannot be seen by studying the received average values of shear stress presented in Table 2. An analysis of the obtained average shear stress values shows a diminishing difference between any wave and its positions as the sample deformation increases. Additionally, a study of the average shear stress values proves that their share in the effective stress is less than 52%, making creation of a plastic weld impossible.

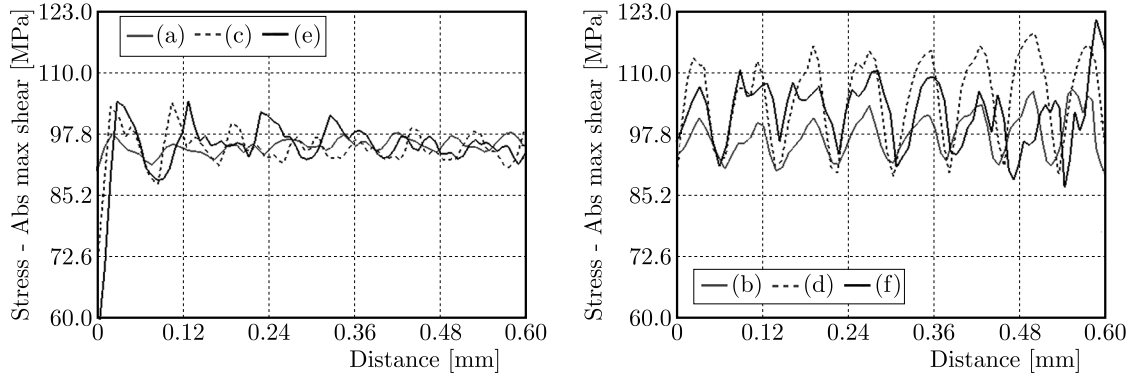


Fig. 7. Shear stress distribution for the upper die displacement equal to 0.5 mm

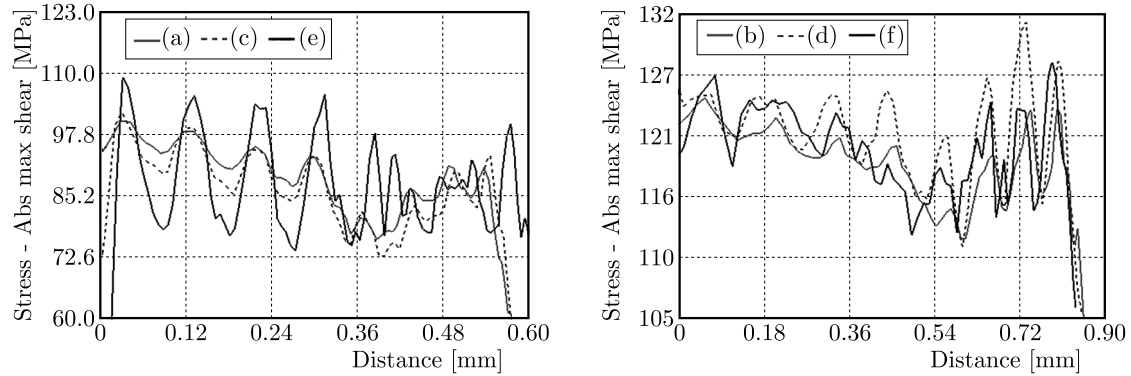


Fig. 8. Shear stress distribution for the upper die displacement equal to 1 mm

Table 2. Maximum, minimum and average stress values

Die displ. [mm]	Average strain values						Max	Min
	a	c	e	b	d	f		
0.5	93	94	84	97	105	102	121	60
1	117	116	116	119	121	120	131	105

The results of strain rate distribution in the initial stage of specimen deformation (upper die displacement equal to 0.5 mm) along with the data presented in Fig. 9 show a substantial influence of the wave amplitude. The impact of the parameters of wave roughness decreases with an increase in sample deformation. Figure 10 shows that the importance of wave parameters remained significant only for wave e. Further deformation causes the influence of wave roughness on the strain rate distribution to disappear all together. The last two graphs of the strain rate distribution indicate a significant growth in the deformation speed and a homogeneous distribution of these values on both contacting surfaces. This fact suggests that the point where there is an increase in the rate of high strain determines weld formation, something that has been proven in the work of Piwnik *et al.* (2011, 2014). In this case, the anastomosis of both contact surfaces does not occur because flattened vertices of roughness are too highly oxidized.

An analysis of Table 3 shows that the values of average strain rate decrease as sample deformation increases for any contact (“wg” and “tow”). The first step of deformation (upper die displacement equal to 0.5 mm) shows a decrease in the average strain rate between waves a and c equal to 0.001 (4.3%), between a and e equal to 0.003 (13%), between b and d equal to 0.002 (8.3%), and between b and f equal to 0.004 (16%). Further deformation (upper die displacement equal to 1 mm) results in a decrease of the average strain rate between waves a

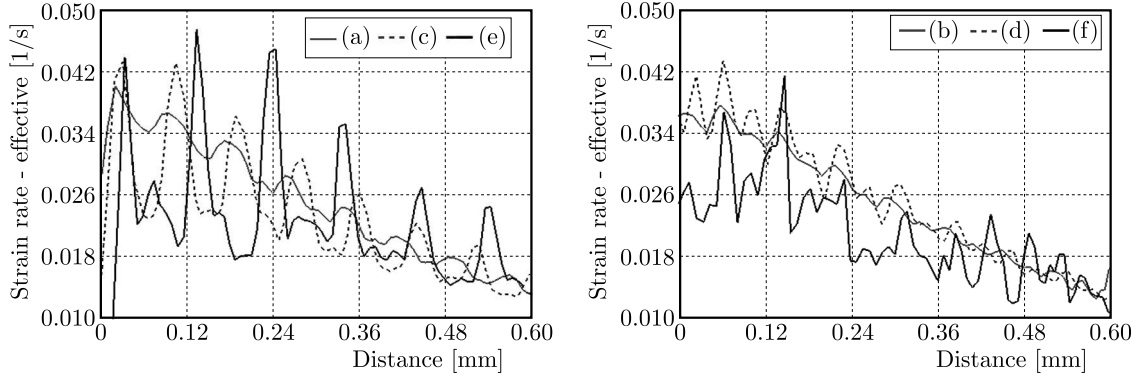


Fig. 9. Strain rate distribution for the upper die displacement equal to 0.5 mm

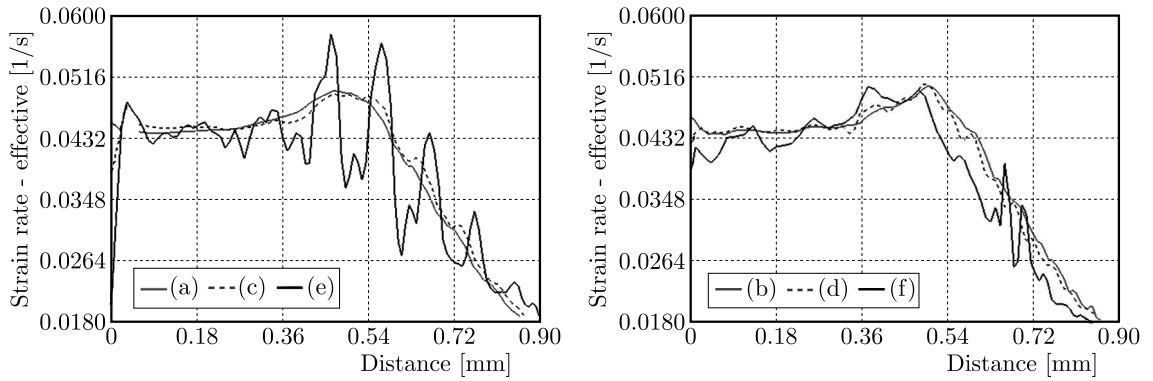


Fig. 10. Strain rate distribution for the upper die displacement equal to 1 mm

Table 3. Maximum, minimum and average stress values

Die displ. [mm]	Average strain values						Max	Min
	a	c	e	b	d	f		
0.5	0.023	0.022	0.02	0.024	0.022	0.02	0.046	0.01
1	0.041	0.041	0.038	0.041	0.04	0.039	0.055	0.018

and c of less than 1%, between a and e equal to 0.003 (7.3%), between b and d equal to 0.001 (2.4%), and between b and f equal to 0.002 (4.8%).

6. Strain work of “grains”

When analyzing the presented issue, we should also consider the aspects of grain micro-mechanics. Based on the work of Ortiz *et al.* (2007), the average grain size of aluminum alloy 6061 is approximately $30 \mu\text{m}$ long and about $13 \mu\text{m}$ wide. These values are an average, and their approximation is intended to indicate the number of grains in one vertex of roughness. Based on these estimates, we can establish that one grain accrues for wave a, b, two grains accrue for wave c, d, and three grains accrue for wave e, f. The surface roughness resulting from the turning process changes the properties of these grains and, grains near the surface will display varying values of yield strength. Insignificant differences between the yield strength of single grains of the contact surfaces can affect the cold welding process because the fast local growth of the coefficient of friction on the two different, newly created surfaces of a medium, can cause formation of local welds. A different strain rate of both surfaces causes an increase in

the coefficient of friction. A prerequisite for this increase is a more significant share of the shear stress in the effective plastic stress. Tiny pieces of this material, $1\ \mu\text{m} \times 1\ \mu\text{m}$ in size, have been isolated and the strain calculated (6.1) along the trajectory of plastic flow (Fig. 11.)

$$W = \iint_A \sigma \dot{\epsilon} dA \quad W_\tau = \iint_A \sigma_\tau \dot{\epsilon} dA \quad (6.1)$$

where: W is the strain work [J], W_τ – strain work of shear [J], $\dot{\epsilon}$ – effective strain rate [1/s], A – grain surface area [μm^2], σ – effective plastic stress [MPa], σ_τ – abs. max shear [MPa].

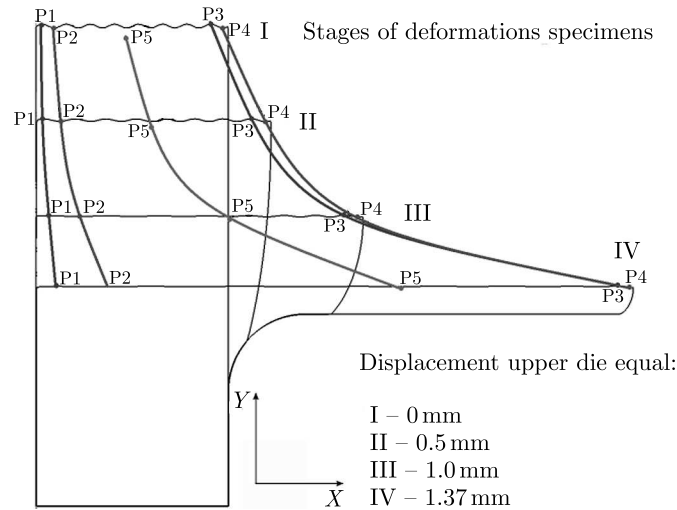


Fig. 11. Trajectory of the material plastic flow

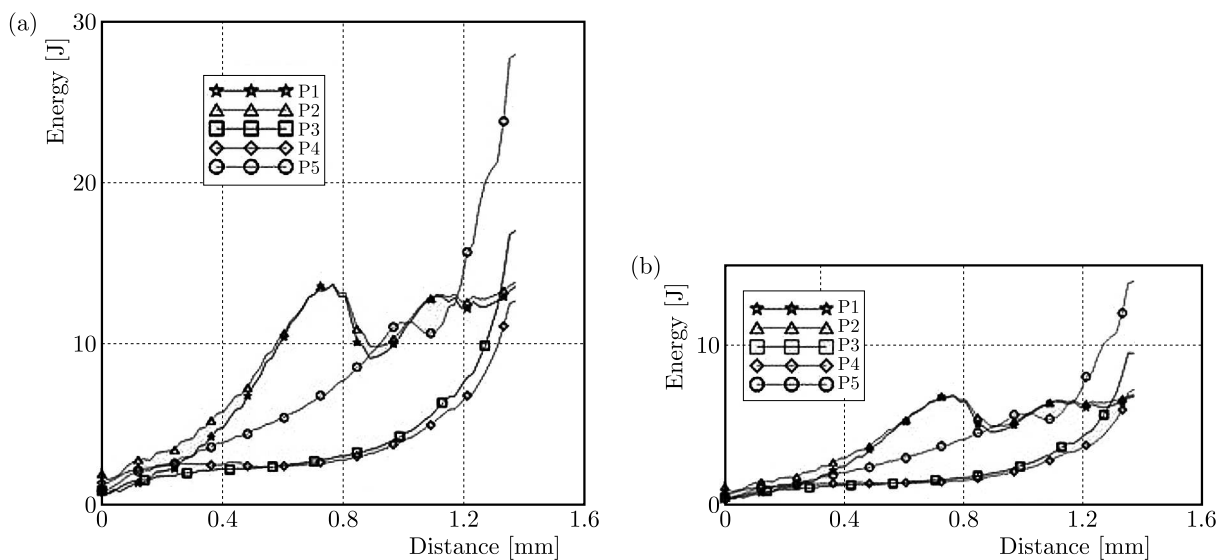


Fig. 12. (a) Effective strain rate. (b) Strain rate of shearing

The results of deformation studies show that the effective strain under stress (Fig. 12a) is much higher than shear stress (Fig. 12b). These results also suggest that further deformation of specimens will not result in a plastic weld because the share of shear stress in the effective plastic stress is too small, and the oxidation of the surfaces cannot be removed through friction. In analysis of the obtained graphs presenting the deforming forces, it is also possible to see that the increase of the plastic flow intensity results in considerable energy demand for carrying out

the bonding process. At points $P1$ and $P2$, a significant energy demand occurs much earlier than at other points and increases for the upper die displacement equal to 0.76 mm (13.6 J, 6.8 J) then slowly decreases and increases gradually for the upper die displacement of 0.9 mm (9.5 J, 4.7 J). A slow exponential growth for the energy demand can be seen in points $P3$ and $P4$. Point $P5$ seems to be the most interesting because at the beginning of the bonding process it shows an almost linear increase of the energy demand at 0.92 mm (10 J, 5.1 J) with a sinusoidal energy demand at 1.1 mm (10.8 J, 5.5 J) and then a rapid exponential growth at 1.37 mm (29 J, 14.5 J). At any set of points the share of shear strain is less than 57% in relation to the effective strain which makes it impossible to obtain a plastic weld. If the test surfaces are free of contaminants and are not oxidized then the first plastic welds would occur at point $P5$. The choice of points at which energy is measured is random, and the real starting point of weld formation must be determined in an experimental study. Although this would not allow creation of a plastic weld it would at least confirm the presented hypothesis that cold welding of materials is possible under large plastic deformation during the bonding process as proven in the previously mentioned works (Tang *et al.*, 2009) where plastic welds were achieved with flattened copper-water micro heat pipe ends in vacuum after deformation of approximately one and a half of the yield strength.

7. Conclusions

Analysis of the bonding process between two perfectly plastic bodies revealed the influence of roughness at the micro-scale and enabled formulation of a hypothesis that metal alloys can be cold welded. The following have been observed in micro-scale: tremendous impact of the wave amplitude on the obtained values of plastic strain in the initial stages of deformation, growth equal to 33% for 2-fold wave amplitude and 46% for 4-fold wave amplitude. The wave amplitude as well as its relative position to other waves impact its rate of decay and, with increasing deformation of specimens, on the obtained values of strain, strain rate and stress. A decrease in strain rate values has also been observed with the increasing wave amplitude within the range from 2.4% to 16%. Based on the map of the strain and stress distribution as the specimen deformation increases, it can be concluded that an increase in the wavelength has a lesser impact on the obtained values and on the rate of decay of wave roughness. Analysis of the bonding process from the perspective of cold welding revealed that an insufficient share of shear stress, less than 57%, relative to effective plastic stress makes it impossible to remove the oxidized layer of the material, which prevents the surfaces from bonding. An increase in the wave roughness and grain size effect promotes the effectiveness of the cold welding process. The strain along the trajectory of the material plastic flow is probably the site of plastic weld formation.

References

1. ABDO J., FARHGANG K., 2005, Elastic-plastic contact model for rough surfaces based on plastic asperity concept, *International Journal of Non-Linear Mechanics*, **40**, 4, 495-506
2. BRZOZA A., PAUK V., 2007, Axially symmetric contact involving friction and boundary roughness, *Journal of Theoretical and Applied Mechanics*, **45**, 2, 277-288
3. BUCZKOWSKI R., KLEIBER M., 1992, Finite element analysis of elastic-plastic plane contact problem with nonlinear interface compliance, *Journal of Theoretical and Applied Mechanics*, **4**, 30.
4. CAI S., BHUSMAN B., 2005, A numerical three-dimensional contact model for rough, multilayered elastic/plastic solid surfaces, *Wear*, **259**, 7-12, 1408-1423
5. D'ADDONA D.M., RAYKARB S.J., 2016, Analysis of surface roughness in hard turning using wiper insert geometry, *Procedia CIRP*, **41**, 841-846

6. DANWOOD H.I., MOHAMMED K.S., RAHMAT A., UDAY M.B., 2015, The influence of the surface roughness on the microstructures and mechanical properties of 6061 aluminum alloy using friction stirwelding, *Surface and Coatings Technology*, **270**, 272-283
7. GRIFFIN J.M., DIAZ F., GEERLING E., CLASING M., PONCE V., TAYLOR C., TUNER S., MICHAEL E.A., MENA F.P., BRONFMAN L., 2017, Control of deviations and prediction of surface roughness from micro machining of THz waveguides using acoustic emission signals, *Mechanical Systems and Signal Processing*, **85**, 1020-1034
8. MA X., ROOIJ M., SCHIPPER D., 2010, A load dependent friction model for fully plastic contact conditions, *Wear*, **269**, 11-12, 28, 790-796
9. MANOYLOV A.V., BRYANT M.J., EVANS H.P., 2013, Dry elasto-plastic contact of nominally flat surfaces, *Tribology International*, **65**, 248-258
10. MATSUMOTO R., HAYASHI K., UTSUNOMIYA H., 2014, Experimental and numerical analysis of friction in high aspect ratio combined forward-backward extrusion with retreat and advance pulse ram motion on a servo press, *Journal of Materials Processing Technology*, **214**, 936-944
11. ORTIZ D., ABDELSHEID M., DALTON R., SOLTERO J., CLARK R., 2007, Effect of cold work on the tensile properties of 6061, 2024, and 7075 Al alloys, *Journal of Materials Engineering and Performance*, **16**, 5, 515-520
12. OTTOSEN N.S., RITISMANM., 2005, *The Mechanics of Constitutive Modeling*, Lund University, Sweden
13. PIWNIK J., MOGIELNICKI K., 2010, The friction influence on stress in micro extrusion, *Archives of Foundry Engineering*, **10**, Special Issue 1/2010, 451-454
14. PIWNIK J., KUPRIANOWICZ J., MOGIELNICKI K., 2011, Numerical modeling of the welding phenomenon in forward aluminum extrusion process, *Archives of Foundry Engineering*, **11**, Special Issue 2/2011, 191-194
15. PIWNIK J., MOGIELNICKI K., KUPRIANOWICZ J., 2014, Numerical analysis of friction influence on the transverse welding phenomenon in the forward extrusion process, *Journal of Theoretical and Applied Mechanics*, **52**, 2, 547-555
16. POULIOS S., KLIT P., 2013, Implementation and applications of a finite-element model for the contact between rough surfaces, *Wear*, **303**, 1-2, 15, 1-8
17. SUN F., GIESSEN E.V., NICOLA L., 2012, Plastic flattening of a sinusoidal metal surface: A discrete dislocation plasticity study, *Wear*, **296**, 672-680
18. TAN X., 2002, Comparison of friction models in bulk metal forming, *Tribology International*, **35**, 385-393
19. TANG Y., LU L., DENG D., YUAN D., 2009, Cold welding sealing of copper-water micro heat pipe ends, *Transactions of Nonferrous Metals Society of China*, **19**, 568-574
20. WANG L.G., SUN X.P., HUANG Y., 2007, Friction analysis of microcosmic elastic-plastic contact for extrusion forming, *Journal of Materials Processing Technology*, **187-188**, 631-634
21. ZHANG S., HODGSON P.D., CARDEW-HALL M.J., KALYANASUNDARAM S., 2003, A finite simulation of micro-mechanical frictional behavior in metal forming, *Journal of Materials Processing Technology*, **134**, 81-91
22. ZHANG S., WANG W., ZHAO Z., 2014, The effect of surface roughness characteristic on the elastic-plastic contact performance, *Tribology International*, **79**, 59-73

NUMERICAL AND EXPERIMENTAL ANALYSIS OF A SEGMENTED WIND TURBINE BLADE UNDER ASSEMBLING LOAD EFFECTS

MAJDI YANGUI, SLIM BOUAZIZ, MOHAMED TAKTAK

Mechanics, Modelling and Production Laboratory (LA2MP), National School of Engineers of Sfax, University of Sfax, Tunisia; e-mail: yanguimajdi@gmail.com; slim.bouaziz1@gmail.com; mohamed.taktak@fss.rnu.tn

VINCENT DEBUT, JOSE ANTUNES

*Centro de Ciências e Tecnologias Nucleares, Instituto Superior Técnico, Universidade de Lisboa, Portugal
e-mail: vincentdebut@ctn.tecnico.ulisboa.pt; jantunes@ctn.tecnico.ulisboa.pt*

MOHAMED HADDAR

Mechanics, Modelling and Production Laboratory (LA2MP), National School of Engineers of Sfax, University of Sfax, Tunisia; e-mail: mohamed.haddar@enis.rnu.tn

In this paper, numerical and experimental modal analysis of a segmented wind turbine blade assembled with a steel threaded shaft and a nut are presented. The blade segments are built by a 3D printer using ABS material. The experimental modal parameters identification has been achieved using the Eigen system Realization Algorithm (ERA) method for different values of the blade segments assembly force caused by the nut tightening torque. Furthermore, a three dimensional finite element model has been built using DTK18 three node triangular shell elements in order to model the blade and the threaded shaft structure, taking into account the additional stiffness caused by the nut tightening torque. This study covers the blade segments assembly force effects on the rotating blade vibration characteristics. The numerical model is adjusted and validated by the identified experimental results. This work highlights the significant variation of the natural frequencies of the segmented wind turbine blade by the assembling load of the segments versus blade rotating speed.

Keywords: segmented wind turbine blade, experimental modal analysis, shell element modeling, assembling load

1. Introduction

In recent years, due to the dramatic increase of energy demands, the concerns about environmental pollution resulting from energy extraction have made development of renewable energy more and more important for a sustainable future. Wind energy is considered as one of the most profitable renewable energy sources. To extract more energy from wind, manufacturers aim at increasing the wind turbine blade size, which led many researchers to investigate emerging problems like vibration, in order to reduce wind turbine component failures and extend their life cycle. Modal or resonance frequencies must be investigated during the blade design process where the blade natural frequencies must be well above the wind turbine working frequencies, see McKittrick *et al.* (2001). Maalawi and Negm (2002) employed the Euler Bernoulli beam theory and presented an optimization model for the design of a typical wind turbine blade structure in order to make an exact placement of natural frequencies of the blade to avoid resonance. Therefore, wind turbine blade modal analysis was established by experimental and theoretical studies. For instance, an experimental modal analysis of a wind turbine using accelerometers was performed by Molenaar (2003). The identified natural frequencies were used to validate the presented wind turbine modeling approach. To improve the calibration process of the blade

structural model parameters, Griffith *et al.* (2009) developed a hybrid calibration approach using experiments.

The FEM is the most widely used in the wind turbine blade development for investigating their dynamic behavior. The Beam Element Method, in which the blade is idealized as a cantilever beam have been used in many researches by dint of its several merits such as simplicity of formulation. Park *et al.* (2010) proposed an analytical procedure based on the Beam Element Method to examine blade natural frequencies in relation with its operating speed. Sheibani and Akbari (2015) developed a blade beam finite element model with an arbitrary cross section, ignoring the effects of rotational speed and pitch angle on the natural frequencies and the mode shapes. Several researchers tried to verify the finite element model experimentally to ensure the model validity. Actually, a scaled-down wind turbine blade model has been built to validate the numerical model by testing the built model and comparing the obtained experimental results with those determined by the numerical study. Tartibu *et al.* (2012) represented the wind turbine blade by some simplified shapes of a stepped beam to establish experimental and numerical modal analyses. Some discrepancies were observed for highest frequencies between the measured and the computed natural frequencies. Sami *et al.* (2014) extracted the fundamental flapwise and edgewise modal frequencies of a composite wind turbine blade using the Finite Element Method. The extracted frequencies were validated experimentally from modal testing using an electrodynamic shaker. Dhar (2006) developed a wind turbine model using Finite Element Method and proposed a methodology to design a small-scale test set-up of the full-scale wind turbine to reach structural invariants which were used to design structural components of a wind turbine. The most common method to measure vibration is to attach accelerometers to the blade and tap it with a hammer or excite it with a mechanical shaker. Experimental modal analysis of a 19.1 meter wind turbine blade was established by Larsen *et al.* (2002) to determine the blade natural frequencies, damping and mode shapes. It was also stated that there was a good agreement between the obtained results from the experimental work and those obtained by the FEM analysis. Abdulaziz *et al.* (2015) applied the Buckingham π -Theorem to develop an approach in which measurements and analysis of a scaled-down model can be used to predict the performance of full-scale wind turbine blades. The obtained results were used to predict and validate numerical solutions using ANSYS software of the full-scale blade. White dealing with an object with small mass, mass of the accelerometer changes resonant frequencies of the tested scaled-down blade in which this method would be inappropriate. Therefore, modal tests were performed by Kim *et al.* (2011) using the embedded fiber Bragg grating (FBG) sensors and the laser Doppler Vibrometer to investigate dynamic characteristics of a wind turbine blade. The tested blade was 1/23 scale of 750 kW blade. Natural frequencies obtained from FBG sensors were found to be consistent with those from the laser Doppler Vibrometer. Ha *et al.* (2015) used the optical deformation measurement technique called Digital Image Correlation (DIC) to measure the natural frequencies, damping ratios and mode shapes of a blade excited by a shaker. Due to geometrical complexity of the wind turbine blade, a precise numerical model of the blade requires the use of shell elements rather than beam elements. Bayoumy *et al.* (2013) applied the absolute nodal thin plate element to model the complex shape of the wind turbine blade structure, to show the transient response of the blade due to gravitational and aerodynamic forces. Kang *et al.* (2014) developed a geometrically exact shell element for a rotorcraft based on assumptions of arbitrarily large displacements and rotations and small strain. The shell finite elements were compared with the beam element for the modeling of three typical blade structures. Modal analysis was established by Branner *et al.* (2007) using the FEM software Nastran. The wind turbine blade FEM model comprised 8-node shell elements. The FEM model was updated and validated against measurement results for the non rotating blade, identified by means of experimental modal analysis. To reduce the blade manufacturing and transport costs, a new approach was proposed to decompose the blade into several parts. Many segmentation

techniques were proposed by Saldanha *et al.* (2013) and Broehl (2014). Nevertheless, the development of segmented blades remains an engineering problem and a tough challenge. Most of the work related to segmentation of wind turbine blades, by Bhat *et al.* (2015a,b) and Saldanha *et al.* (2013), shows that the natural frequency and static displacement versus the blade length can be considered as the primary parameters to design a segmented wind turbine. Yangui *et al.* (2016) studied the dynamic behavior of a segmented wind turbine blade using the three node triangular shell element DKT18. To validate the accuracy and reliability of the developed model, the obtained numerical results were compared to benchmark problems and modal analysis using ANSYS software. Several researchers tried to develop a numerical model to study the dynamic behavior of a wind turbine blade taking into account several external effects such as aerodynamic load, gyroscopic and rotation speed effects, see Hamdi *et al.* (2014). However, they ignored the assembly effort of the segments which must be studied in priority during design of the segmented blade.

In the present work, an attempt has been made to address this requirement by investigating natural frequencies and mode shapes of a segmented horizontal axis wind turbine blade subjected to the assembling load. Experimental modal analysis of a scaled-down segmented blade, assembled by a thread shaft and a nut has been performed using the laser Doppler Vibrometer. The ERA method is used to identify the blade modal parameters, i.e. natural frequencies and damping. The three node triangular shell element DKT18 is adopted in this paper to model the segmented blade and the thread shaft structure. The assembling load effects are assumed to concentrate in the thread shaft, seeing that its section is very small compared to the blade segments section. Displacements between segments are also neglected in the blade modeling. The developed FEM model parameters have been adjusted by the obtained experimental results to highlight the significant influence of the assembling load produced by the tightening torque versus the rotating speed on the natural frequencies of the wind turbine blade.

This paper is structured as follows. In Section 2, the assembled blade numerical model is presented. Section 3 is dedicated to the measuring system and the modal identification procedure. The experimental results are discussed in Section 4 to adjust and validate the developed numerical model. In the conclusions Section, some final reflections are raised.

2. Blade numerical model

In this Section, the three node triangular shell element DTK18 is used to develop the wind turbine blade model. It consists of five segments assembled together with a steel threaded shaft, as demonstrated in Fig. 1.

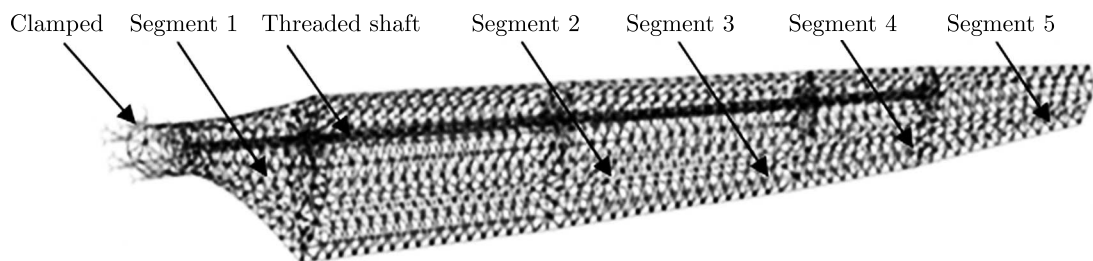


Fig. 1. Segmented wind turbine blade model

For rotating blades modeled by three nodes triangular shell elements, it has been demonstrated in previous works (Yangui *et al.*, 2016) that the blade equation of motion can be written as

$$\mathbf{M}\ddot{\mathbf{q}} + \mathbf{C}\dot{\mathbf{q}} + (\mathbf{K}_e + \mathbf{K}_R)\mathbf{q} = \mathbf{F} \quad (2.1)$$

where \mathbf{M} , \mathbf{C} , \mathbf{K}_e , \mathbf{K}_R , and \mathbf{F} are the global mass matrix, damping matrix, elastic stiffness matrix, centrifugal stiffness matrix and the global force vector, respectively.

Considering the presence of the tightening torque applied by the nut to assemble the blade segments, an additional strain energy increases the blade structure rigidity. Logically, the same solicitation, i.e. traction, will be applied by blade rotation and the tightening torque on the threaded shaft. Thus, this additional stiffness matrix may be assumed to have the same form of the centrifugal stiffness matrix, proportional to the nut tightening torque and depending on threaded shaft geometry.

The global tightening torque stiffness matrix \mathbf{K}_S can be formulated as

$$\mathbf{K}_S(i, j) = \frac{C_s}{R_s L_s} T_p \frac{\mathbf{K}_R(i, j)}{|\mathbf{K}_R(i, j)|} \quad (2.2)$$

where C_s , R_s , and T_p are, respectively, the tightening torque, threaded shaft radius and a proportional coefficient that will be empirically determined.

The resulting equations of motion are obtained as

$$\mathbf{M}\ddot{\mathbf{q}} + \mathbf{C}\dot{\mathbf{q}} + (\mathbf{K}_e + \mathbf{K}_R + \mathbf{K}_S)\mathbf{q} = \mathbf{F} \quad (2.3)$$

3. Experimental analysis

3.1. Experimental procedure

The 3D printing technology has been used to manufacture the blade segments. Teeth connected with holes in the segments interfaces were designed to prevent relative displacements between the segments. Thus, friction effects between the segments are neglected. The measuring system is shown in Fig. 2, which consists of an impact hammer to excite the blade structure, laser Vibrometer, charge amplifier, and a data acquisition system with a computer to process and display signals.

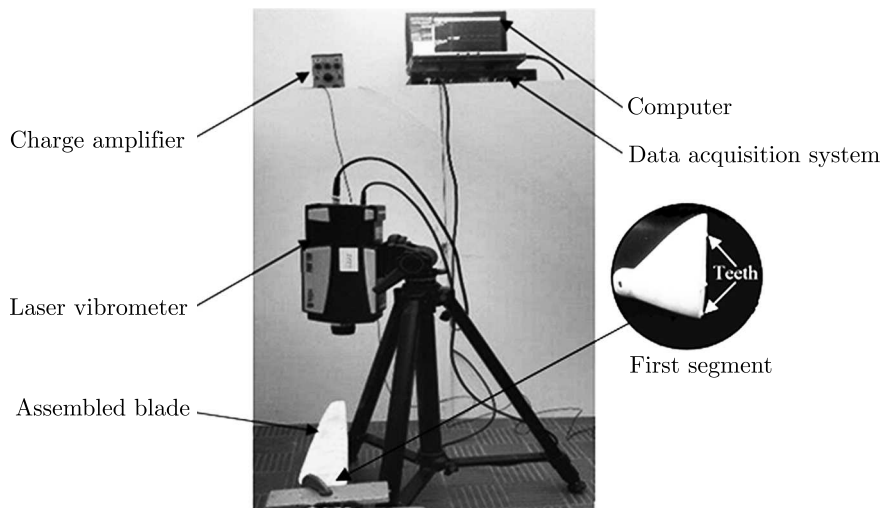


Fig. 2. Test stand for the assembled blade

To localize the measuring and excitation points, the blade has been discretized into 32 measuring points. In the third point, the blade is excited along the vertical direction (flap direction) and the horizontal direction (edge direction), as shown in Fig. 3. The vertical motion at all localized points is measured using the laser Vibrometer.

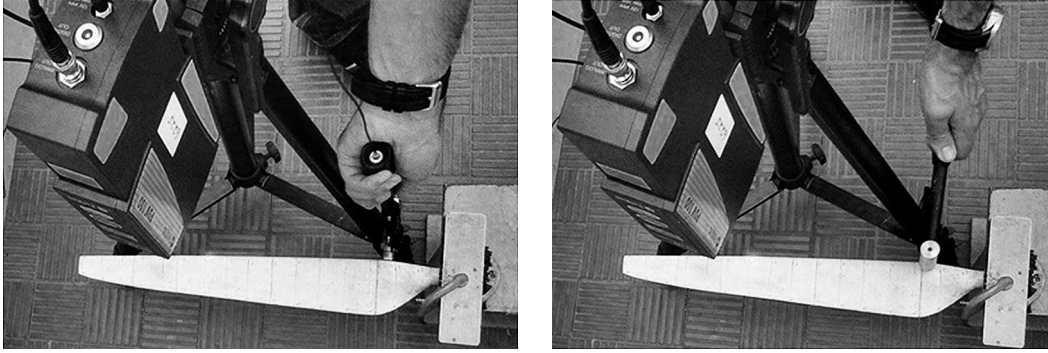


Fig. 3. Horizontal and vertical blade excitation

3.2. Analysis procedure

A schematic representation of the computation and validation process is shown in Fig. 4. The process starts from the time data of the excitation force $F(t)$ and the velocity response $V(t)$ to which the FFT is applied in order to determine the measured Frequency Response Functions (FRF) $H_{me}(f)$. The Eigen system Realization Algorithm (ERA) identification method is used to find the system poles and residues to identify natural frequencies ω_i , damping ratios ξ_i and vibration mode shapes Φ_i .

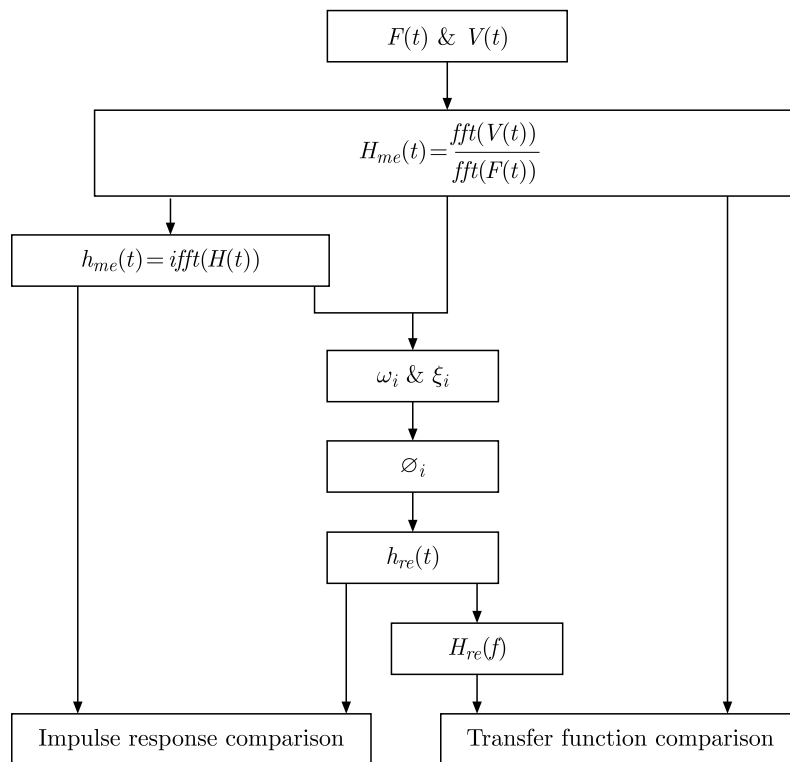


Fig. 4. Computational and validation process scheme

The reconstructed impulsion response h_{re} is determined according to the number of mode N by the equation

$$h_{re}(t) = \sum_{i=1}^N \Phi_i e^{\lambda_i t} \quad (3.1)$$

where the eigenvalues λ_i are written as

$$\lambda_i = -\omega_i \xi_i \pm j\omega_i \sqrt{1 - \xi_i^2} \quad (3.2)$$

The identified modal parameter validation is based on the comparison between the measured and the reconstructed impulse responses as well as transfer functions.

4. Results and discussion

4.1. Experimental modal parameter identification

The presented analysis procedure has been applied to the 32 measured signals as regard to the vertical excitation. Figure 5 shows the measured excitation force and velocity response of the seventh node.

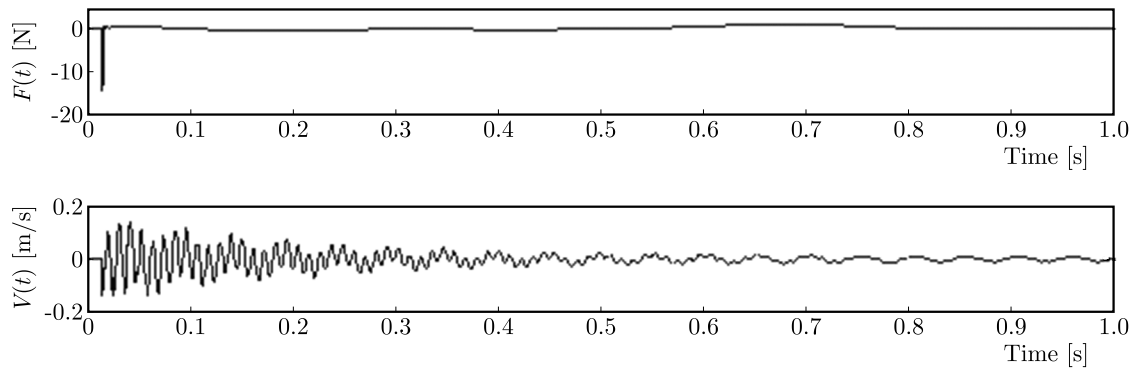


Fig. 5. Excitation force and the seventh node velocity response

Using the measured signals, the transfer function in addition to the impulse response has been determined, Fig. 6.

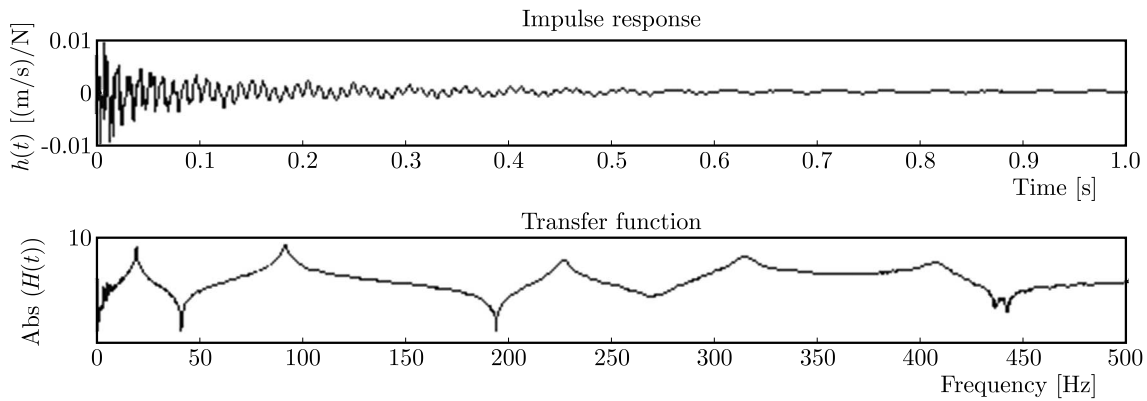


Fig. 6. Seventh node transfer function and impulse response

Table 1 presents the first five natural frequencies and damping ratios identified using the ERA method.

For each of the 32 nodes, the reconstructed impulse response and transfer function is determined and re-plotted with those obtained from measurement to validate the identified modal parameter. Figure 7 shows some of the measured and reconstructed fitted curves.

An acceptable agreement is obtained between the measured and the reconstructed impulse responses as well as the transfer functions. So, the identified modal parameters have been validated.

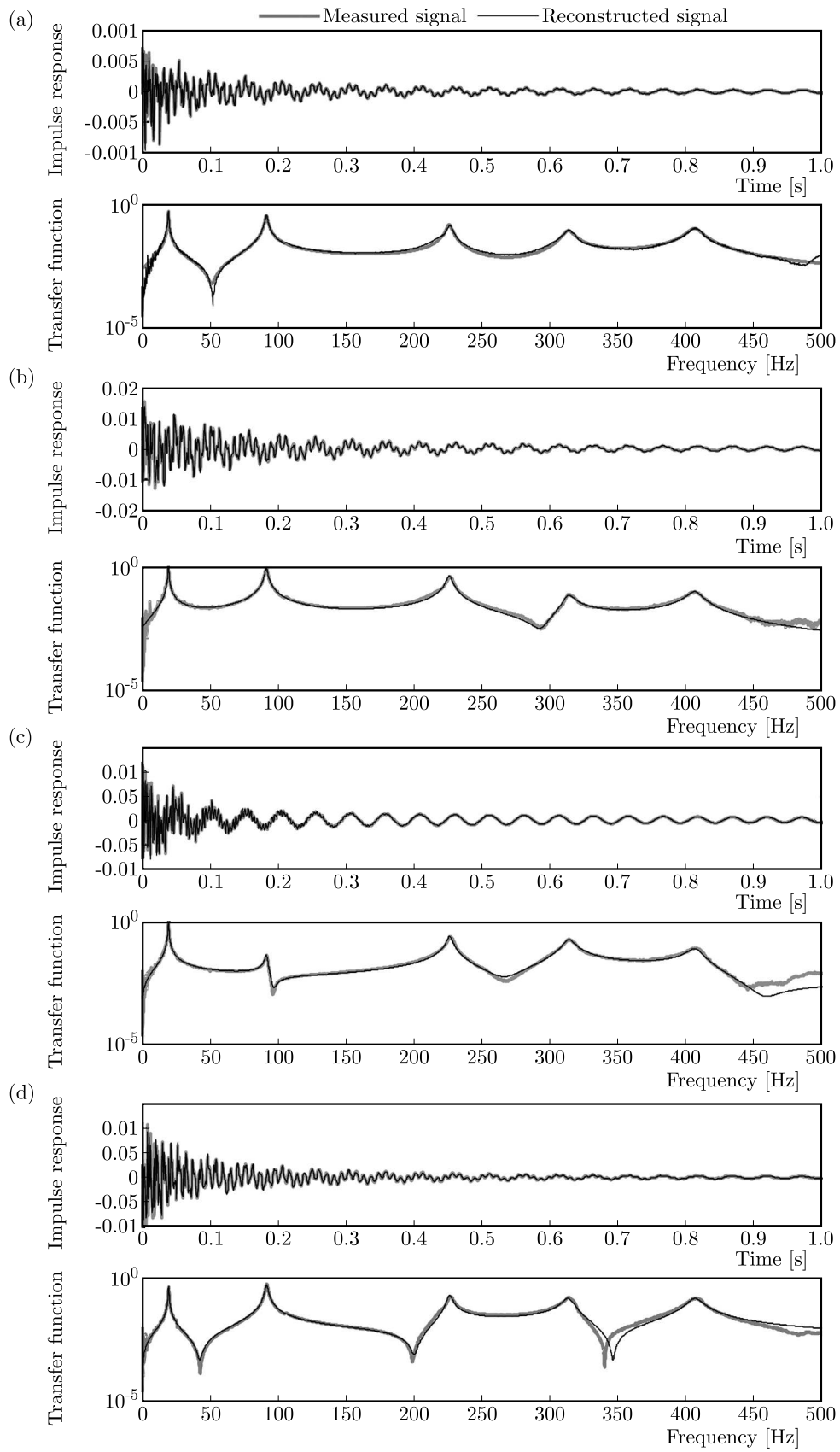


Fig. 7. Measured and reconstructed impulse responses and transfer functions: (a) Node 9, (b) Node 15, (c) Node 21, (d) Node 26

Table 1. The identified natural frequencies and damping ratios

	Mode 1	Mode 2	Mode 3	Mode 4	Mode 5
ω [Hz]	19.5	95.7	226.5	314.3	407.6
ξ [%]	1.08	0.93	0.75	1.14	1.19

4.2. Experimental mode shape identification

To estimate the blade mode shape for each identified natural frequency, the previous process is repeated regarding the horizontal excitation direction. Figure 8 shows the transfer functions of the measured signals in the seventh node with respect to the excitation direction.

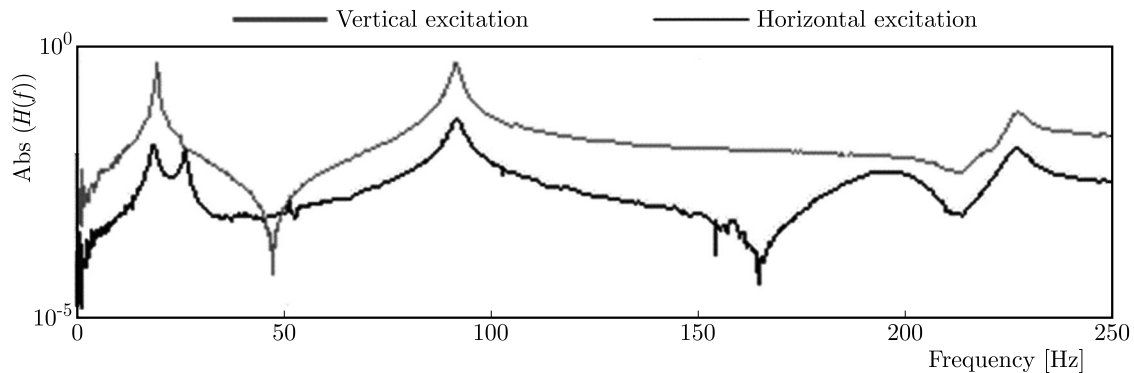


Fig. 8. Vertical and horizontal excitation transfer functions

Lower than 250 Hz, two natural frequencies are more clearly observed from the transfer function of the horizontal excitation than from the vertical excitation. Table 2 presents the identified natural frequencies of the measured signals in the seventh node with respect to the horizontal excitation direction, using the ERA method.

Table 2. The identified natural frequencies with respect to the horizontal excitation

Mode order	Mode 1	Mode 2	Mode 3	Mode 4	Mode 5
F [Hz]	19.4	27.2	95.8	194.8	226.4

Therefore, the natural frequencies determined by the vertical excitation present the blade flapwise or torsional mode. The other two mode shapes present the blade edgewise or torsional mode. The identified eigenvectors have been normalized in order to plot the blade mode shape as shown in Fig. 9.

4.3. Mechanical characteristics adjustment

To adjust the mechanical characteristics of the numerical model corresponding to the printed 3D model, an initial frequency analysis has been carried out in which the contacts between the blade segments are assured by teeth insertion in holes and conserved by the nut without applying the assembling preload to avoid tightening torque effects. The blade has length $L = 500$ mm and thickness $h = 3$ mm. The material blade segment properties are $E = 2.4$ GPa, $\nu = 0.38$ and $\rho = 1140$ kg/m³. The threaded shaft material properties are $E = 210$ GPa, $\nu = 0.3$ and $\rho = 7850$ kg/m³. E , ν and ρ are, respectively, the elastic modulus, Poisson's ratio and density. Table 3 shows a comparison between the obtained natural frequencies by the developed FEM model and those identified through the experimental setup.

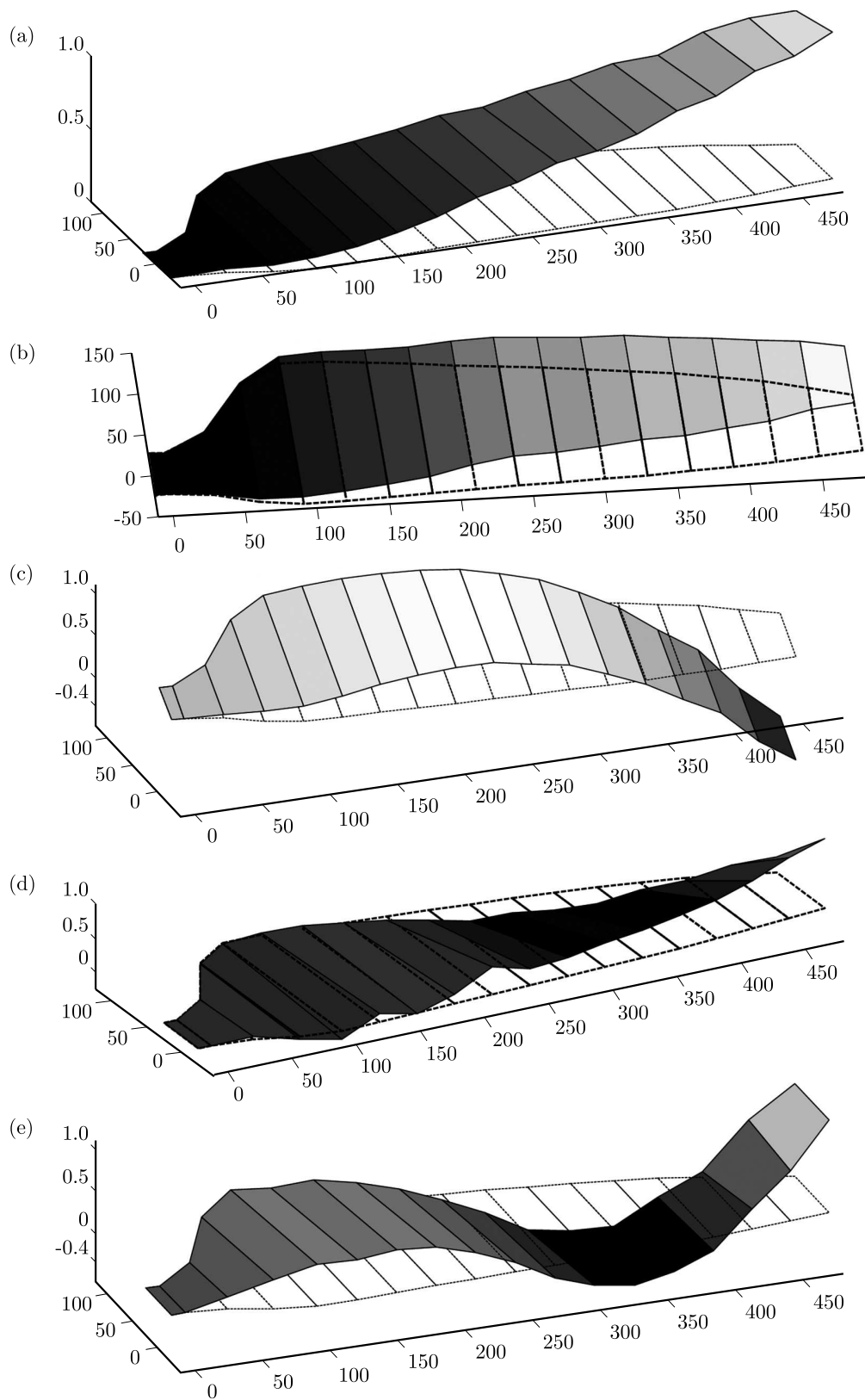


Fig. 9. The segmented blade mode shapes: (a) 1st mode (1st flapwise mode), (b) 2nd mode (1st edgewise mode), (c) 3rd mode (2nd flapwise mode), (d) 4th mode (1st torsional mode), (e) 5th mode (3rd flapwise mode)

Table 3. The blade without preload of the threaded shaft: Natural frequencies before adjustment of the elastic modulus

Mode order	FEM	Experimental	Diff [%]
1	18.37	17.4	5.28
2	25.21	24.8	1.62
3	90.19	85.7	4.97
4	187.91	180.2	4.10
5	214.07	219.2	2.34

To match the elastic modulus of the numerical model with the built model, an iterative process has been done to adjust the first natural frequency obtained by FEM with that obtained from experimental analysis. Thus, the adjusted elastic modulus is $E_r = 2.25$ GPa.

Table 4. The blade without preload of the threaded shaft: Natural frequencies after adjustment of the elastic modulus

Mode order	FEM	Experimental	Diff [%]
1	17.4	17.4	0
2	24.19	24.8	2.45
3	84.25	85.7	1.69
4	178.79	180.2	0.78
5	213.71	219.2	2.5

As long as the maximum difference is about 2.5%, the presented numerical model is validated, at least without the threaded shaft preload effects, and the adjusted elastic modulus puts the numerical model much closer to reality.

4.4. Threaded shaft preload effects

To determine the proportional tightening torque coefficient T_p , a tightening torque $C_s = 0.6$ Nm is applied by the nut. The proportional tightening torque coefficient is determined by adjusting the first natural frequency obtained from the numerical model to that identified through experimental study. Thus, the determined tightening torque coefficient is $T_p = 1.62$. Table 5 shows the first five natural frequencies determined by the FEM and the experimental study.

Table 5. Natural frequencies of the blade with the threaded shaft preload: $C_s = 0.6$ Nm

Mode order	The threaded shaft preload $C_s = 0.6$ Nm		
	FEM	Exp	Diff [%]
1	19.5	19.5	0
2	27.2	26.7	1.83
3	95.8	93.5	2.4
4	194.8	197.2	1.21
5	226.8	234.4	3.24

To validate the chosen torque proportional coefficient, the second torque $C_s = 1$ Nm is applied.

Table 4 shows that the maximum difference is about 3.62% between the FEM modeling and the experimental results. So, the assumed stiffness matrix form for the threaded shaft preload is adequate. Furthermore, from Tables 5 and 6, it is observed that the blade natural frequencies are proportional to the tightening torque.

Table 6. Natural frequencies of the blade with the threaded shaft preload: $C_s = 1 \text{ Nm}$

Mode order	The threaded shaft preload $C_s = 1 \text{ Nm}$		
	FEM	Exp	Diff [%]
1	23.8	24.1	1.24
2	31.81	30.9	2.86
3	113.43	110.6	2.49
4	214.48	207.8	3.11
5	243.35	252.5	3.62

4.5. Rotating blade frequencies analysis

Several researchers have investigated the effects of the rotating speed on the blade natural frequencies. However, those researches limited their examinations to simple blade shapes, or they ignored the effects of the segments assembling load. In this study, based on the adjusted numerical model of the segmented shell type wind turbine blade, the natural frequencies are investigated taking into account both the rotation speed and the effects of the segments assembling load.

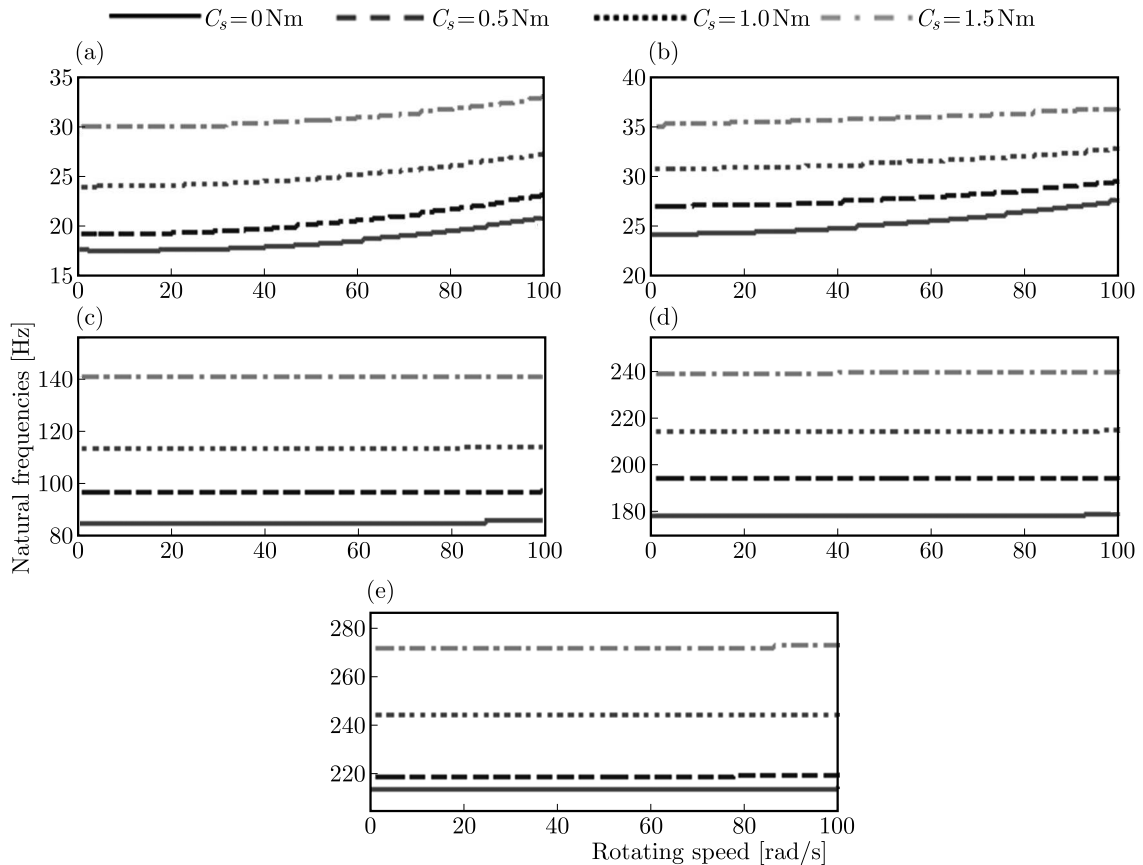


Fig. 10. Natural frequency variation versus rotating speeds for various tightening torque: (a) 1st natural frequency, (b) 2nd natural frequency, (c) 3rd natural frequency, (d) 4th natural frequency, (e) 5th natural frequency

The segments assembling load influences the rotating blade natural frequencies as illustrated in Fig. 10. Natural frequencies variations maintain the same curve shape for different tightening torque, as regards to the rotating speed increase. Furthermore, an increase in the natural frequencies is clearly affected by the applied tightening torque. Interestingly, the tightening effect on

modal frequencies is clearly more dramatic than the effects stemming from the blade rotation. From the first two natural frequencies variation curves, it is observed that the additional stiffness generated by the tightening torque attenuates the rotating speed effects on variation of the natural frequencies.

5. Conclusions

In this study, natural frequencies and mode shapes of a segmented wind turbine blade have been established by experimental and numerical studies. The segmented blade shape assembled with a threaded shaft and a nut has been modeled using linear triangular shell elements. The proposed numerical model has been adjusted through experimental study to better approach the real system. The identified modal parameters using the ERA method were validated by reconstructing the measured impulse responses and transfer functions. The tightening torque effects on the natural frequencies of a non rotating segmented blade were investigated by experimental means and incorporated into the numerical model to study their influence on the dynamic behavior of the rotating blade. The obtained numerical results present a good correlation with those identified by the experimental study. The results show the increase of the blade natural frequencies of all modes due to increasing tightening torque applied by the nut to assemble the blade segments, in addition to an increase in the rotational speed.

The adjusted numerical method presented in this study can be used to evaluate vibration characteristics of the segmented wind turbine blade with a complex shape, taking into consideration the segments assembly load. This study is limited to the rotation speed and tightening torque effects, and can be extended by taking into account the aerodynamic effect. Interestingly, friction effects between the blade segments will be considered in the future adjustment of the numerical model.

References

1. ABDULAZIZ A.H., ELSABBAGH A.M., AKL W.N., 2015, Dynamic and static characterization of horizontal axis wind turbine blades using dimensionless analysis of scaled-down models, *International Journal of Renewable Energy Research (IJRER)*, **5**, 2, 404-418
2. BAYOUMY A.H., NADA A.A., MEGAHEH S.M., 2013, A continuum based three-dimensional modeling of wind turbine blades, *Journal of Computational and Nonlinear Dynamics*, **8**, 3, 031004
3. BHAT C., NORONHA D.J., SALDANHA F.A., 2015a, Structural performance evaluation of modularized wind turbine blade through finite element simulation, *International Journal of Mechanical, Aerospace, Industrial, Mechatronic and Manufacturing Engineering*, **9**, 6, 930-942
4. BHAT C., NORONHA D.J., SALDANHA F.A., 2015b, Structural performance evaluation of segmented wind turbine blade through finite element simulation, *International Journal of Mechanical, Aerospace, Industrial, Mechatronic and Manufacturing Engineering*, **9**, 6, 996-1005
5. BRANNER K., BERRING P., BERGGREEN C., KNUDSEN H.W., 2007, Torsional performance of wind turbine blades – Part II: Numerical validation, *International Conference on Composite Materials (ICCM-16)*
6. BROEHL J., 2014, *Wind Energy Innovations: Segmented Blades*, <http://www.navigantresearch.com/blog/>
7. DHAR S., 2006, Development and validation of small-scale model to predict large wind turbine behavior, Doctoral dissertation, Indian Institute of Technology, Bombay
8. GRIFFITH D.T., 2009, Structural dynamics analysis and model validation of wind turbine structures, *50th AIAA/ASME/ASCE/AHS/ASC Structures, Structural Dynamics, and Materials Conference 17th AIAA/ASME/AHS Adaptive Structures Conference 11th AIAA*, p. 2408

9. HA N.S., VANG H.M., GOO N.S., 2015, Modal analysis using digital image correlation technique: An application to artificial wing mimicking beetles hind wing, *Experimental Mechanics*, **55**, 5, 989-998
10. HAMDI H., MRAD C., HAMDI A., NASRI R., 2014, Dynamic response of a horizontal axis wind turbine blade under aerodynamic, gravity and gyroscopic effects, *Applied Acoustics*, **86**, 154-164
11. KANG H., CHANG C., SABERI H., ORMISTON R.A., 2014, Assessment of beam and shell elements for modeling rotorcraft blades, *Journal of Aircraft*, **51**, 2, 520-531
12. KIM S.W., KIM E.H., RIM M.S., SHRESTHA P., LEE I., KWON I.B., 2011, Structural performance tests of down scaled composite wind turbine blade using embedded fiber Bragg grating sensors, *International Journal Aeronautical and Space Sciences*, **12**, 4, 346-353
13. LARSEN G.C., HANSEN M.H., BAUMGART A., CARLÉN I., 2002, *Modal Analysis of Wind Turbine Blades*, Riso National Laboratory, Denmark
14. MAALAWI K.Y., NEGM H.M., 2002, Optimal frequency design of wind turbine blades, *Journal of Wind Engineering and Industrial Aerodynamics*, **90**, 8, 961-986
15. MCKITTRICK L.R., CAIRNS D.S., MANDELL J., COMBS D.C., RABERN D.A., VAN LUCHENE R.D., 2001, Analysis of a composite blade design for the AOC 15/50 wind turbine using a finite element model, *Sandia National Laboratories Report*
16. MOLENAAR D.P., 2003, Experimental modal analysis of a 750 kW wind turbine for structural model validation. *ASME 2003 Wind Energy Symposium*, American Society of Mechanical Engineers, 322-339
17. PARK J.H., PARK H.Y., JEONG S.Y., LEE S.I., SHIN Y.H., PARK J.P., 2010, Linear vibration analysis of rotating wind-turbine blade, *Current Applied Physics*, **10**, 2, S332-S334
18. SALDANHA F.A., RAO V.V., CHRISTOPHER J., ADHIKARI R., 2013, Investigations on concepts for modularizing a horizontal axis wind turbine blade, *ASME 2013 International Design Engineering Technical Conferences and Computers and Information in Engineering Conference*, pp. V008T12A003-V008T12A003, American Society of Mechanical Engineers
19. SAMI S., ZAI B.A., KHAN M.A., 2014, Dynamic analysis of a 5KW wind turbine blade with experimental validation, *Journal of Space Technology*, **4**, 1, 82-87
20. SHEIBANI M., AKBARI A.A., 2015, Finite element modeling of a wind turbine blade, *Journal of Vibroengineering*, **17**, 7
21. TARTIBU L.K., KILFOIL M., VAN DER MERWE A.J., 2012, Vibration analysis of a variable length blade wind turbine, *International Journal of Advances in Engineering and Technology*, **4**, 1, 630-639
22. YANGUI M., BOUAZIZ S., TAKTAK M., HADDAR M., EL-SABBAGH A., 2016, Nonlinear analysis of twisted wind turbine blade, *Journal of Mechanics*, doi:10.1017/jmech.2016.120, 1-10

AN INVERSE KINEMATIC MODEL OF THE HUMAN TRAINING CENTRIFUGE MOTION SIMULATOR

RAFAŁ LEWKOWICZ

Military Institute of Aviation Medicine, Warsaw, Poland
e-mail: rlewkowicz@wiml.waw.pl

GRZEGORZ KOWALECZKO

Air Force Institute of Technology, Warsaw, Poland
e-mail: grzegorz.kowaleczko@itwl.pl

The paper presents an inverse kinematic model for a centrifuge motion simulator used to verify newly defined absolute acceleration profiles. The modelling is concerned with a human training centrifuge with three degrees of freedom. The values of kinematic parameters have been obtained for this three-jointed manipulator. Validation of the developed model has been performed by comparing the results obtained from the centrifuge motion simulator with the results of numerical simulations. The simulation revealed that the inverse kinematic model enabled calculation of the angular displacement, velocity and acceleration of the links that are needed for the given linear acceleration of the simulator cabin.

Keywords: inverse kinematic, simulator, centrifuge, motion system

1. Introduction

High-performance aircraft pilots as well as civilian aerobatic pilots are exposed to high linear accelerations during flight (Newman, 2015). In order to properly prepare for work in this environment, pilots are evaluated and trained to increase their acceleration tolerance level (Wojtkowiak, 1991). This training is carried out in a specially designed centrifuge motion simulator or, so-called, human training centrifuge (HTC) (Dančuo *et al.*, 2012b; Truszczyński and Kowalczyk, 2012). From the standpoint of classical mechanics, the task of the HTC is to achieve accelerations through rotations around three axes that simulate the load the pilot is exposed to in a real flight. This type of simulator makes it possible to create high and prolonged linear accelerations. Moreover, the centrifuge provides a safe ground-based platform to train pilots, especially in the field of increasing pilot's awareness about unwanted effects of accelerations, such as G-induced loss of consciousness or spatial disorientation. In addition, the HTC is an important tool for researchers to understand the changes taking place in human physiology during accelerative stress.

In this paper, a dynamic flight simulator has been considered, namely the HTC shown in Fig. 1, manufactured by the AMST-Systemtechnik GmbH (Austria), located at the Military Institute of Aviation Medicine (Warsaw, Poland).

The gondola/cabin of the centrifuge is assembled on an eight-meter-long arm and allowed longitudinal accelerations (in the direction from pilot's head to foot) to be achieved in the range from $-3g$ to $+16g$ (g is the Earth's gravitational acceleration) with the maximal onset rate of acceleration (G-onset rate) at $n = 14.5g/s$. Additionally, the gyroscopic suspension of the cabin allowed it to achieve transversal and lateral accelerations in the range of $\pm 10g$ and $\pm 6g$, respectively.

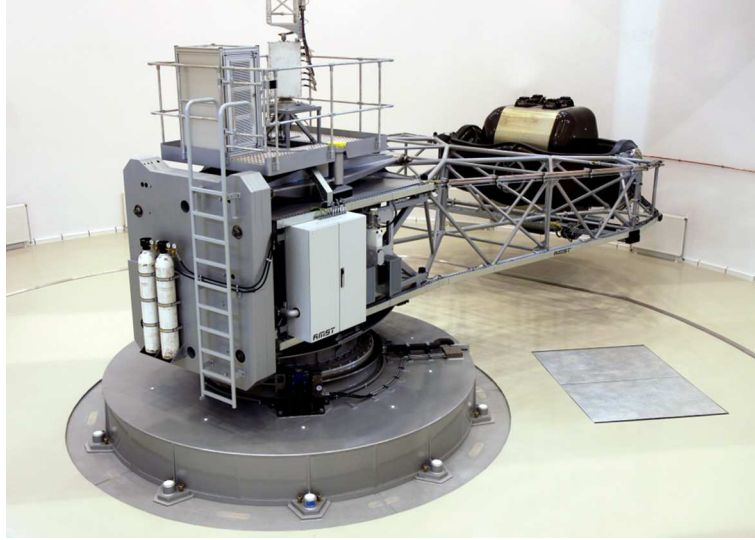


Fig. 1. Dynamic flight simulator – human training centrifuge HTC-07

2. Problem formulation

Within the centrifuge simulator, there is a pre-programmed standard open loop mode that contains predefined nonlinear profiles of the absolute acceleration in the centre of the cabin. In these profiles, which are independent for each of the three axes of the pilot's head-fixed coordinate system, a positive or negative acceleration that is constant for given periods of time is determined. When this acceleration profile is created, the angular accelerations in the individual links of the simulator motion system may be exceeded (Table 1). There is also a problem concerning hypogravity ($< 1g$), which cannot be obtained in this simulator. In that case, the simulator software reports an error, which is then eliminated using a trial and error method. This problem makes it difficult to define more complex acceleration profiles that should not be tested on a real device. The solution to this problem should be sought in the inverse kinematics of the HTC's motion system. The inverse kinematics of the centrifuge motion simulator will be based on calculating the angular position, velocity and acceleration of each motion system link. This approach will make it possible to indicate maximum values of angular acceleration that are necessary to achieve a given linear acceleration of the simulator cabin. In this way, how the position of individual links of the motion system should change over time in order to achieve the desired movement of the cabin will be determined.

3. Physical model of the HTC simulator

A centrifuge motion simulator is modelled as a three-joint manipulator (Fig. 2) with rotational axes, where the pilot's head is considered to be the end-effector (Crosbie, 1988). The model consists of three links: arm, ring and cabin (Fig. 2).

The arm rotation around the vertical axis is the main motion that achieves the desired acceleration force. The arm carries a gimbaled cabin system with two rotational axes providing pitch and roll capabilities. The task of the roll and pitch axes is to direct the acceleration force into the desired direction. The pilot's head is placed in the intersection of the cabin roll and pitch axes. The arm rotation angle is denoted by ψ_A , the roll ring rotation angle by φ_R and the pitch cabin rotation angle by θ_C . The centrifuge has the following parameters: arm length $d_A = 8$ m, roll and pitch axis rotation range of $\pm 360^\circ$. Other parameters of the simulator motion system kinematics are shown in Table 1.

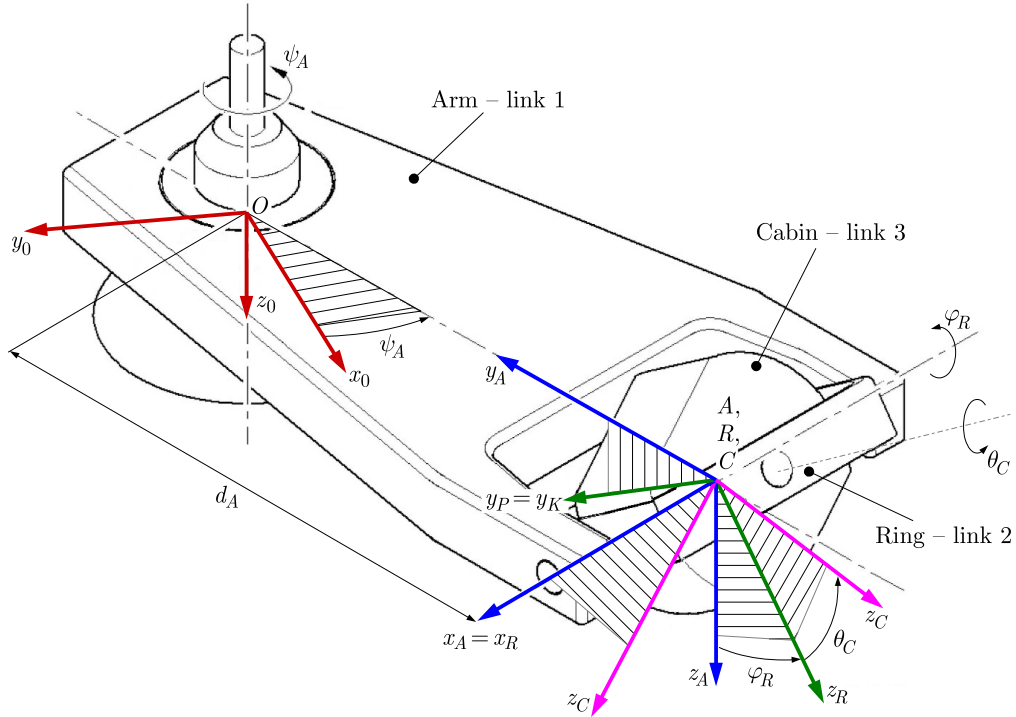


Fig. 2. A physical model of the centrifuge motion simulator HTC-07

Table 1. Motion capabilities of the HTC-07 simulator (AMST-Systemtechnik GmbH, 2011)

Parameter	z_c -axis	y_c -axis	x_c -axis
Maximum acceleration rate [g/s]	14.5	6	10
Maximum angular acceleration [rad/s ²]	2.82	8	5

4. Kinematics of the centrifuge motion simulator

The forward kinematics that is related to the simulator motion system geometry is used to calculate the linear acceleration components of the end-effector (the pilot's head), where $\mathbf{G}_H = [G_{x_H}, G_{y_H}, G_{z_H}]^T$ with respect to the centrifuge variables ψ_A , ϕ_R and θ_C (these angles are determined in the next Section). Thus, for a given joint coordinate vector $\mathbf{q} = [\psi_A, \dot{\psi}_A, \theta_C, \dot{\theta}_C, \phi_R, \dot{\phi}_R]^T$, the forward kinematics equation must be solved as follows

$$\mathbf{G}_H = f(\mathbf{q}) \quad (4.1)$$

where f is a nonlinear, continuous and differentiable function. The simulator kinematic model can be derived by different methods, such as the Lagrange equation (Siciliano *et al.*, 2009; Wu *et al.*, 2010), the Newton-Euler method (Grotjahn *et al.*, 2004; Tsai, 1999) and the virtual work principle (Wu *et al.*, 2009, 2013; Zhao and Gao, 2009). The method based on the Lagrange formulation is conceptually simple and systematic. The method based on the Newton-Euler formulation yields a model in a recursive form. It is composed of forward computation of velocities and accelerations of each link, followed by backward computation of forces and moments in each joint (Wu *et al.*, 2010). This algorithm is computationally more efficient because it exploits the typically open structure of the manipulator kinematic chain (Djuric *et al.*, 2012; Siciliano *et al.*, 2009). On the other hand, the Newton-Euler procedure is very difficult to use in an advanced control application because of the closed structure, as the expense of calculation is considerably high (Gherman *et al.*, 2012). Despite this, the Newton-Euler equations of motion

are used to model the kinematics of centrifuge motion simulator due to the fact that these equations incorporate all accelerations that act on the individual links of the motion system (Chen and Repperger, 1996; Dančuo *et al.*, 2012a; Kvrđić *et al.*, 2014; Vidaković *et al.*, 2012). During kinematic modelling of the centrifuge, the small elastic deformation of the centrifuge links is neglected.

4.1. Coordinate frames and matrices determining relations for centrifuge links

This Section defines coordinate frames for the centrifuge links (Fig. 2) and matrices that determine their relations. The centrifuge links and their coordinate frames are denoted by using the Euler angle convention. The centrifuge base coordinates are denoted by $Ox_0y_0z_0$ (the Earth-fixed system), the arm coordinates by $Ax_Ay_Az_A$ (link 1), the roll ring coordinates by $Rx_Ry_Rz_R$ (link 2), the cabin coordinates by $Cx_Cy_Cz_C$ (link 3) and the pilot head-fixed coordinates system by $Hx_Hy_Hz_H$. The pilot's head is placed in the intersection of the cabin roll and pitch axes, therefore $x_C = x_H$, $y_C = y_H$, and $z_C = z_H$. To determine the mutual position of the defined coordinate systems, the following angles are used (Fig. 2):

- ψ_A – the yaw angle between the x_0 -axis and the y_A -axis. This angle, enlarged by 90° , provides coverage of the y_0 -axis with the y_A -axis, in this way defining the position of the Earth-fixed coordinate system $Ox_0y_0z_0$ relative to the arm-fixed coordinate system $Ax_Ay_Az_A$ (link 1),
- ϕ_R – the roll angle between the z_A -axis and the z_P -axis. This angle determines the position of the arm-fixed coordinate system $Ax_Ay_Az_A$ (link 1) relative to the ring-fixed coordinate system $Rx_Ry_Rz_R$ (link 2),
- θ_C – the pitch angle between the z_P -axis and the z_C -axis. This angle determines the position of the ring-fixed coordinate system $Rx_Ry_Rz_R$ (link 2) relative to the cabin-fixed coordinate system $Cx_Cy_Cz_C$ (link 3).

To derive the kinematic equations for the motion simulator, the matrices for the relation between the centrifuge link coordinate frames are defined. These transformation matrices are obtained for the $Z \rightarrow Y \rightarrow X$ rotation convention of the coordinate systems in the following way:

— $\mathbf{L}_{0/A}$ – matrix for transformation from the Earth-fixed coordinate system $Ox_0y_0z_0$ to the arm-fixed coordinate system $Ax_Ay_Az_A$

$$\mathbf{L}_{0/A} = \mathbf{L}_{z_r}(90^\circ)\mathbf{L}_{z_0}(-\psi_A) \quad (4.2)$$

where

$$\mathbf{L}_{z_0}(-\psi_A) = \begin{bmatrix} \cos \psi_A & -\sin \psi_A & 0 \\ \sin \psi_A & \cos \psi_A & 0 \\ 0 & 0 & 1 \end{bmatrix} \quad \mathbf{L}_{z_r}(90^\circ) = \begin{bmatrix} 0 & -1 & 0 \\ 1 & 0 & 0 \\ 0 & 0 & 1 \end{bmatrix} \quad (4.3)$$

— $\mathbf{L}_{x_r}(\phi_R)$ – matrix for transformation from the arm-fixed coordinate system $Ax_Ay_Az_A$ to the ring-fixed coordinate system $Rx_Ry_Rz_R$

$$\mathbf{L}_{x_r}(\phi_R) = \begin{bmatrix} 1 & 0 & 0 \\ 0 & \cos \phi_R & \sin \phi_R \\ 0 & -\sin \phi_R & \cos \phi_R \end{bmatrix} \quad (4.4)$$

— $\mathbf{L}_{y_p}(\theta_C)$ – matrix for transformation from the ring-fixed coordinate system $Rx_Ry_Rz_R$ to the cabin-fixed coordinate system $Cx_Cy_Cz_C$

$$\mathbf{L}_{y_p}(\theta_C) = \begin{bmatrix} \cos \theta_C & 0 & -\sin \theta_C \\ 0 & 1 & 0 \\ \sin \theta_C & 0 & \cos \theta_C \end{bmatrix} \quad (4.5)$$

The matrix $\mathbf{L}_{0/C}$ for transformation from the cabin-fixed coordinate system, $Cx_Cy_Cz_C$, to the Earth-fixed coordinate system, $Ox_0y_0z_0$, is determined by multiplying transformation matrices (4.2)-(4.5), in the following way

$$\mathbf{L}_{0/C} = \mathbf{L}_{y_p}(\theta_C)\mathbf{L}_{x_r}(\phi_R)\mathbf{L}_{0/A} \quad (4.6)$$

By using the convenient shorthand notation $c = \cos$ and $s = \sin$, the components of the transformation matrix (4.6) $L_{0/A} = \mathbf{L}_{z_r}(90^\circ)\mathbf{L}_{z_0}(-\psi_A)$ (4.2) become the following

$$\mathbf{L}_{0/C} = \begin{bmatrix} s\psi_{AC}\theta_C + c\psi_{AS}\phi_Rs\theta_C & c\psi_{AC}\phi_R & -s\psi_{AS}\theta_C + c\psi_{AS}\phi_Rc\theta_C \\ -c\psi_{AC}\theta_C + s\psi_{AS}\phi_Rs\theta_C & s\psi_{AC}\phi_R & c\psi_{AS}\theta_C + s\psi_{AS}\phi_Rc\theta_C \\ c\phi_Rs\theta_C & -s\phi_R & c\phi_Rc\theta_C \end{bmatrix} \quad (4.7)$$

Assuming that $\psi_A = 0$, for further calculations matrix (4.7) is reduced to the form

$$\mathbf{L}_{0/C}(\psi_A=0) = \begin{bmatrix} \sin \phi_R \sin \theta_C & \cos \phi_R & \sin \phi_R \cos \theta_C \\ -\cos \theta_C & 0 & \sin \theta_C \\ \cos \phi_R \sin \theta_C & -\sin \phi_R & \cos \phi_R \cos \theta_C \end{bmatrix} \quad (4.8)$$

On the basis of these transformational matrices, the equations of forward kinematics that relate to the velocities and accelerations of the links and the end-effector-pilot's head are developed in the next Section.

5. Linear acceleration acting on the pilot's head

The linear acceleration components at the intersection point of the roll (link 2) and pitch (link 3) axes are: the normal (radial) a_n , tangential a_t and gravitational g accelerations (Fig. 3). From these accelerations, the orthogonal components G_{x0} , G_{y0} , and G_{z0} for the normal, tangential and vertical accelerations, respectively, are calculated as follows

$$\begin{bmatrix} G_{x0} \\ G_{y0} \\ G_{z0} \end{bmatrix} = \frac{1}{g} \begin{bmatrix} -a_n \\ -a_t \\ g \end{bmatrix} = \begin{bmatrix} d_A\dot{\psi}_A^2/g \\ -d_A\ddot{\psi}_A/g \\ 1 \end{bmatrix} \quad (5.1)$$

where d_A is the simulator arm length, $\dot{\psi}_A$ and $\ddot{\psi}_A$ are angular velocity and acceleration of the arm (link 1), respectively.

The link angles ϕ_R and θ_C , angular velocity $\dot{\psi}_A$ and acceleration $\ddot{\psi}_A$ of the arm define the orthogonal components G_{x_C} , G_{y_C} and G_{z_C} of the resultant vector \mathbf{G}_C that are experienced by the pilot. Based on equations (4.8) and (5.1), the resultant vector \mathbf{G}_C experienced by the pilot can be found from

$$[G_{x_C}, G_{y_C}, G_{z_C}]^T = \mathbf{L}_{0/C}^{-1}(\psi_A=0)[G_{x0}, G_{y0}, G_{z0}]^T \quad (5.2)$$

The transverse G_{x_C} , lateral G_{y_C} and longitudinal G_{z_C} components of the acceleration \mathbf{G}_C that act on the pilot's head are

$$\begin{aligned} G_{x_C} &= \sin \theta_C (G_{x0} \sin \phi_R + G_{z0} \cos \phi_R) - G_{y0} \cos \theta_C \\ G_{y_C} &= G_{x0} \cos \phi_R - G_{z0} \sin \phi_R \\ G_{z_C} &= \cos \theta_C (G_{x0} \sin \phi_R + G_{z0} \cos \phi_R) + G_{y0} \sin \theta_C \end{aligned} \quad (5.3)$$

Equations (5.3) develop the inverse kinematics algorithm which determines the link angles that are required to generate a desired trajectory of the cabin-centrifuge and accelerations in the centrifuge axes.

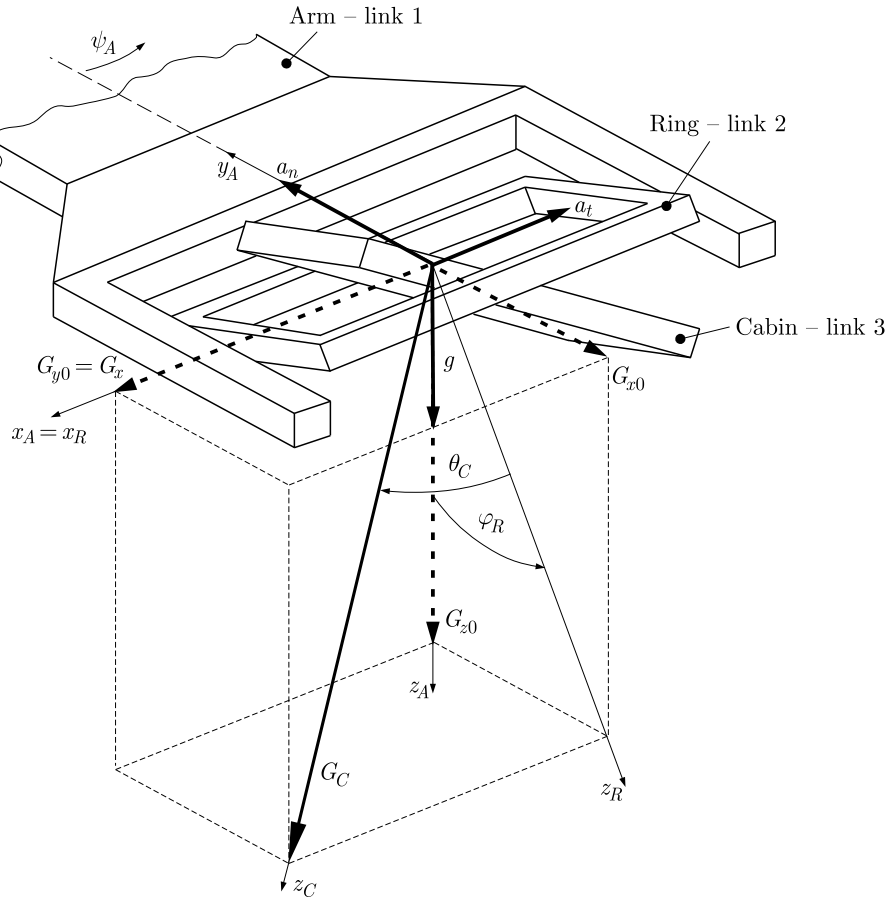


Fig. 3. The acceleration components at the intersection point of the roll and pitch axes

6. An inverse kinematics of the cabin simulator

The inverse kinematics is defined as the problem of determining a set of appropriate joint configurations for which the end effector (the pilot's head) moves to desired positions as smoothly, rapidly and as accurately as possible. The inverse kinematics of the centrifuge motion system is first based on calculating the angular displacement, velocity and acceleration of the links that are needed for the given linear acceleration of the simulator cabin. Then, taking into account the limitations of the motion system (Table 1), it is checked whether this system can achieve such accelerations. If it cannot, the maximum successive link angular accelerations that the motion system can achieve are calculated. The inverse kinematics for the centrifuge motion simulator can be described by the relationship

$$[\ddot{\psi}_A, \dot{\psi}_A, \theta_C, \ddot{\theta}_C, \phi_R, \ddot{\phi}_R]^T = f^{-1}[G_{x_H}, G_{y_H}, G_{z_H}]^T \quad (6.1)$$

where f^{-1} is a nonlinear, continuous and differentiable function that performs the inverse transformation to the function f , (4.1). There are two distinct methods for solving Eq. (6.1) of inverse kinematics, namely iterative and analytical. The iterative method gives the solution by solving an approximation of the system, and by updating the system with the output from the solver for each iteration until it converges. The analytical method solves the whole system at once; however, the complexity of it arises when large chains of joints attempt to be solved. The most prominent among iterative methods are based on the Jacobian matrix, which describes the nonlinear and configuration dependent transformation between velocities in the joint configuration coordinates and the task spaces. There are several versions of Jacobian-based methods, such as

the Jacobian Transpose (Wolovich and Elliott, 1984), damped least squares (Wampler, 1986), damped least squares with singular value decomposition (Wampler, 1986), selectively damped least squares (Buss and Kim, 2005) and several extensions (Baillieul, 1985; Nakamura and Hanafusa, 1986). An iterative method can be also viewed as an optimization task solved with general-purpose methods (neural networks (Tejomurtula and Kak, 1999) and genetic algorithms (Nearchou, 1998)), but those approaches are usually computationally ineffective.

Due to small chains of joints (a centrifuge simulator is a three-joint manipulator), direct and analytical computations of inverse kinematics are chosen. Based on the acceleration vector \mathbf{G}_C components, Eqs. (5.3), the link angles in each joint in the system are derived. To determine the angular accelerations and velocities of the arm (link 1), ring (link 2) and cabin (link 3), the following calculation algorithm for the inverse kinematics is used (Kvrgic *et al.*, 2014).

Step 1: Determination of the arm angular acceleration $\dot{\psi}_A$. The angular acceleration $\dot{\psi}_A$ is derived from Eq. (5.1) that describes linear acceleration components at the intersection point of the roll and pitch axes (Fig. 3). The resultant acceleration of this point is a sum of the normal a_n , tangential a_t , and gravitational g acceleration. This acceleration is as follows

$$a_A^2 = d_A^2 \dot{\psi}_A^4 + d_A^2 \ddot{\psi}_A^2 + g^2 \quad (6.2)$$

For a positive angular acceleration $\ddot{\psi}_A$, the angular velocity $\dot{\psi}_A$ in the i -th moment of time is equal to

$$\dot{\psi}_A(i) = \dot{\psi}_A(i-1) + \ddot{\psi}_A(i)dt \quad (6.3)$$

By substituting (6.3) to equation (6.2), the resultant acceleration takes the form

$$a_A^2(i) = d_A^2 [\dot{\psi}_A(i-1) + \ddot{\psi}_A(i)dt]^4 + d_A^2 \ddot{\psi}_A^2(i) + g^2 \quad (6.4)$$

After calculations have been performed, this equation becomes

$$a_A^2(i) = d_A^2 [\dot{\psi}_A^4(i-1) + 4\dot{\psi}_A^3(i-1)\ddot{\psi}_A(i)dt + 6\dot{\psi}_A^2(i-1)\ddot{\psi}_A^2(i)dt^2] + d_A^2 \ddot{\psi}_A^2(i) + g^2 \quad (6.5)$$

and then

$$\frac{a_A^2(i) - g^2}{d_A^2} = \dot{\psi}_A^4(i-1) + 4\dot{\psi}_A^3(i-1)\ddot{\psi}_A(i)dt + 6\dot{\psi}_A^2(i-1)\ddot{\psi}_A^2(i)dt^2 + \ddot{\psi}_A^2(i) \quad (6.6)$$

By reducing equation (6.6) to the form of a quadratic equation

$$[1 + 6\dot{\psi}_A^2(i-1)dt^2]\ddot{\psi}_A^2(i) + 4\dot{\psi}_A^3(i-1)\ddot{\psi}_A(i)dt + \dot{\psi}_A^4(i-1) - \frac{a_A^2(i) - g^2}{d_A^2} = 0 \quad (6.7)$$

it is possible to obtain its solution in the form of two roots

$$\ddot{\psi}_A(i) = \frac{-2\dot{\psi}_A^3(i-1)dt \pm \sqrt{-2\dot{\psi}_A^6(i-1)dt^2 - \dot{\psi}_A^4(i-1) + [1 + 6\dot{\psi}_A^2(i-1)dt^2]k(i)}}{1 + 6\dot{\psi}_A^2(i-1)dt^2} \quad (6.8)$$

where

$$k(i) = \frac{a_A^2(i) - g^2}{d_A^2} \quad (6.9)$$

Kvrgic *et al.* (2014) noted that equation (6.8) is valid for the movement that has a positive acceleration onset. For a negative acceleration onset, the discriminant $-2\dot{\psi}_A^6(i-1)dt^2 - \dot{\psi}_A^4(i-1) + [1 + 6\dot{\psi}_A^2(i-1)dt^2]k(i)$ is mostly negative, which means that this equation cannot be used

directly. Vidaković *et al.* (2012, 2013) proposed a solution in the form of a Jacobi elliptic function, which describes the arm angular velocity as

$$\dot{\psi}_A(t) = \sqrt[4]{k} sn(\sqrt[4]{k}t + \sqrt[4]{k}C_1, -1) \quad (6.10)$$

where k is constant for every interpolation period of time and is given by Eq. (6.9), sn is a Jacobian elliptic function and C_1 is the constant obtained from the value of angular velocity from the previous interpolation period.

After equation (6.10) has been developed in Taylor series expansions of the Jacobi elliptic function (Wrigge, 1981), it becomes

$$\dot{\psi}_A(i) = \sqrt[4]{k(i)} \left(t_1(i) - \frac{t_1^5(i)}{10} + \frac{t_1^9(i)}{120} - \frac{11t_1^{13}(i)}{15600} + \frac{211t_1^{17}(i)}{3536000} \right) \quad (6.11)$$

where $t_1(i) = \sqrt[4]{k(i)}(dt + C_1)$.

Equation (6.11) describes the arm angular velocity, $\dot{\psi}_A(i)$, for each i -th interpolation period of time. The angular acceleration, $\ddot{\psi}_A(i)$, of the arm for every interpolation period of time is calculated as

$$\ddot{\psi}_A(i) = \frac{\dot{\psi}_A(i+1) - \dot{\psi}_A(i)}{dt} \quad (6.12)$$

Another approach to solve the problem of calculation of the negative acceleration was proposed by Liwen *et al.* (2015). The researchers generated both a trapezoidal G-load curve and three-axis G-load commands using a real-time motion planning algorithm with two G-dimensional interpolation. Dančuo *et al.* (2018) and Vidaković *et al.* (2012) indicated that equation (6.8) could be also solved numerically for a small time increment $dt \rightarrow 0$.

Step 2: Determination of the angular velocity $\dot{\psi}_A$ of the arm (6.3) and accelerations components (5.1) at the intersection point of the roll and pitch axes (Fig. 3).

Step 3: Determination of the roll ring angle ϕ_R based on equation (5.3)₂, which describes the lateral acceleration G_{yC} . Expressing $\sin \phi_R$ and $\cos \phi_R$ by using the tangent function

$$\cos \phi_R = \frac{1}{\sqrt{1 + \tan^2 \phi_R}} \quad \sin \phi_R = \frac{\tan \phi_R}{\sqrt{1 + \tan^2 \phi_R}} \quad (6.13)$$

and by substituting these functions to equation (5.3)₂, multiplying both sides by $\sqrt{1 + \tan^2 \phi_R}$, and then raising to the power, the following expression is obtained

$$G_{x0}^2 - 2G_{x0}G_{z0} \tan \phi_R + G_{z0}^2 \tan^2 \phi_R = G_{yC}^2 (1 + \tan^2 \phi_R) \quad (6.14)$$

After the next transformation, Eq. (6.14) is reduced to the form

$$(G_{z0}^2 - G_{yC}^2) \tan^2 \phi_R - 2G_{x0}G_{z0} \tan \phi_R + G_{x0}^2 - G_{yC}^2 = 0 \quad (6.15)$$

for which the roots are the following

$$\tan \phi_R = \frac{2G_{x0} \pm \sqrt{4G_{x0}^2 - 4(G_{z0}^2 - G_{yC}^2)(G_{x0}^2 - G_{yC}^2)}}{2(G_{z0}^2 - G_{yC}^2)} \quad (6.16)$$

By substituting $G_{z0} = 1$ to Eq. (6.16), and then performing manipulations, the following result is obtained

$$\tan \phi_R = \frac{G_{x0} \pm G_{yC} \sqrt{1 + G_{x0}^2 - G_{yC}^2}}{1 - G_{yC}^2} \quad (6.17)$$

For $G_{x_0}^2 + 1 \geq G_{y_C}^2$, the roll ring angle is equal to

$$\phi_R = \arctan \frac{G_{x_0} + G_{y_C} \sqrt{1 - G_{y_C}^2 + G_{x_0}^2}}{1 - G_{y_C}^2} \quad (6.18)$$

otherwise

$$\phi_R = \arctan \frac{G_{x_0}}{1 - G_{y_C}^2} \quad (6.19)$$

If $G_{y_C} < 0$, and $G_{y_C}^2 > 1$, the roll ring angle is equal to $\phi_R = \phi_R + \pi$. The angular velocity $\dot{\phi}_R$ and acceleration $\ddot{\phi}_R$ of the ring (link 2) are determined as follows

$$\dot{\phi}_R(i) = \frac{\phi_R(i) - \phi_R(i-1)}{dt} \quad \ddot{\phi}_R(i) = \frac{\dot{\phi}_R(i) - \dot{\phi}_R(i-1)}{dt} \quad (6.20)$$

Step 4: Completion of the pitch cabin angle θ_C calculation. This angle can be derived from equation (5.3)₁ that describes the lateral acceleration G_{x_C} or based on Eq. (5.3)₃ which defines the longitudinal acceleration G_{z_C} . Equations (5.3)₁ and (5.3)₃ indicate that it is not possible to obtain simultaneously the desired values of G_{x_C} and G_{z_C} acceleration, even if they do not exceed the limit ranges (Table 1). Therefore, to determine the pitch cabin angle, Eq. (5.3)₁ is used. For the known lateral acceleration G_{x_C} , using similar substitution (6.13) for the pitch cabin angle θ_C , equation (5.3)₁ takes the form

$$G_{x_C} = \frac{\tan \theta_C}{\sqrt{1 + \tan^2 \theta_C}} (G_{x_0} \sin \phi_R + G_{z_0} \cos \phi_R) - G_{y_0} \frac{1}{\sqrt{1 + \tan^2 \theta_C}} \quad (6.21)$$

Performing analogous transformations (6.14) and (6.15) as for the angle of tilting the ring, the above equation takes the form

$$G_{x_C}^2 (1 + \tan^2 \theta_C) = \tan^2 \theta_C (G_{x_0} \sin \phi_R + G_{z_0} \cos \phi_R)^2 - 2G_{y_0} \tan \theta_C (G_{x_0} \sin \phi_R + G_{z_0} \cos \phi_R) + G_{y_0}^2 \quad (6.22)$$

By substituting $G_{x_0} \sin \phi_R + G_{z_0} \cos \phi_R = d$, and then performing some manipulations, a quadratic equation is obtained

$$(d^2 - G_{x_C}^2) \tan^2 \theta_C - 2G_{y_0} d \tan \theta_C + G_{y_0}^2 + G_{x_C}^2 = 0 \quad (6.23)$$

for which the roots are the following

$$\tan \theta_C = \frac{G_{y_0} d \pm G_{x_C} \sqrt{d^2 - G_{y_0}^2 - G_{x_C}^2}}{d^2 - G_{x_C}^2} \quad (6.24)$$

For $(d^2 + G_{y_0}^2) \geq G_{x_C}^2$, the pitch cabin angle θ_C is equal to

$$\theta_C = \arctan \frac{G_{y_0} d + G_{x_C} \sqrt{d^2 + G_{y_0}^2 - G_{x_C}^2}}{d^2 - G_{x_C}^2} \quad (6.25)$$

otherwise, if $(d^2 + G_{y_0}^2) < G_{x_C}^2$, it is not possible to obtain the desired transverse acceleration G_{x_C} . Then equation (6.21) takes the form

$$\theta_C = \arctan \frac{G_{y_0}}{d - G_{x_C}^2/d} \quad (6.26)$$

The angular velocity $\dot{\theta}_C$ and acceleration of the cabin $\ddot{\theta}_C$ (link 3) are determined as follows

$$\dot{\theta}_C(i) = \frac{\theta_C(i) - \theta_C(i-1)}{dt} \quad \ddot{\theta}_C(i) = \frac{\dot{\theta}_C(i) - \dot{\theta}_C(i-1)}{dt} \quad (6.27)$$

A centrifuge is capable of simulating all three load components, but simulating a pure G_{zC} profile becomes a problem due to motor limitation. A pure G_{zC} training profile is a profile without the transverse G_{xC} and lateral G_{yC} loads. The transverse load G_{xC} in the centrifuge is a result of the tangential acceleration a_t (Fig. 3) and has a large value at the beginning and at the end of planetary arm motion. The greater the tangential acceleration is, the greater is the G_{xC} acceleration. The emergence of the large tangential acceleration a_t decreases the angular velocity of the arm motion and has negative effects on the overall centrifuge performance (Dančuo *et al.*, 2013). These effects are minimized by adjusting the pitch cabin angle by $\theta_C = \arctan(a_t/\sqrt{a_n^2 + 1})$.

Equations (6.3), (6.8), (6.18), (6.20), (6.25) and (6.27) compose a system of 8 ordinary differential equations that describe an inverse kinematics model of the HTC motion simulator. Based on these equations, the centrifuge kinematic parameters: ψ_A , $\dot{\psi}_A$, $\ddot{\psi}_A$, ϕ_R , $\dot{\phi}_R$, $\ddot{\phi}_R$, θ_C , $\dot{\theta}_C$, and $\ddot{\theta}_C$ are calculated in three phases, according to the algorithm described by Kvrđić *et al.* (2014).

7. Verification of the inverse kinematics model

The presented inverse kinematics model of the HTC motion simulator has been tested using numerical calculations. The simulation was performed for the G_{xC} , G_{yC} and G_{zC} acceleration forces profile (Fig. 5, solid line), which was generated by the software of the HTC control system. This acceleration forces profile changes as follows:

- starting from 1g with G-onset rate $n = 0.2g/s$ up to the baseline level (1.41g),
- constant baseline level at 1.41g,
- increase of the acceleration with G-onset rate $n = 3g/s$ up to 6g,
- constant acceleration at 6g,
- decrease of the acceleration with G-onset rate $n = -3g/s$ up to the baseline level (1.41g).

Additionally, for calculations the following data, namely $d_A = 8$ m, $g = 9.81$ m/s², time step $dt = 0.005$ s and Matlab/Simulink MathWorks software, have been used. Figures 4-7 present the results of numerical simulations (dotted line) plotted together with the corresponding parameters which were recorded during operation of the HTC simulator (solid line). The figures show:

- angular velocity $\dot{\psi}_A$ and acceleration $\ddot{\psi}_A$ of the arm (link 1) (Fig. 4),
- G_{xC} , G_{yC} , and G_{zC} acceleration forces profile (Fig. 5),
- angle ϕ_R , angular velocity $\dot{\phi}_R$ and acceleration $\ddot{\phi}_R$ of the roll ring (link 2) (Fig. 6),
- angle θ_C , angular velocity $\dot{\theta}_C$ and acceleration $\ddot{\theta}_C$ of the pitch cabin (link 3) (Fig. 7).

The calculated angular velocity of the arm $\dot{\psi}_A$ (dotted line on the upper plot in the Fig. 4), which is responsible for generating the centripetal acceleration a_n , largely covers the envelope of the angular velocity obtained from the HTC control system (solid line). The difference between the two curves of $\dot{\psi}_A$ (Fig. 4, model vs. HTC) is noticeable only during a decrease in the acceleration from 6g to 1.41g with G-onset rate $n = -3g/s$ (Fig. 5). The maximum of this difference is approximately 0.2 rad/s. A similar difference was found in the study by Vidaković *et al.* (2012).

In Fig. 5, the G_{xH} , G_{yH} , and G_{zH} components of the absolute acceleration force obtained by equations (5.3) are given. The curves are very close to each other, except for the phase of

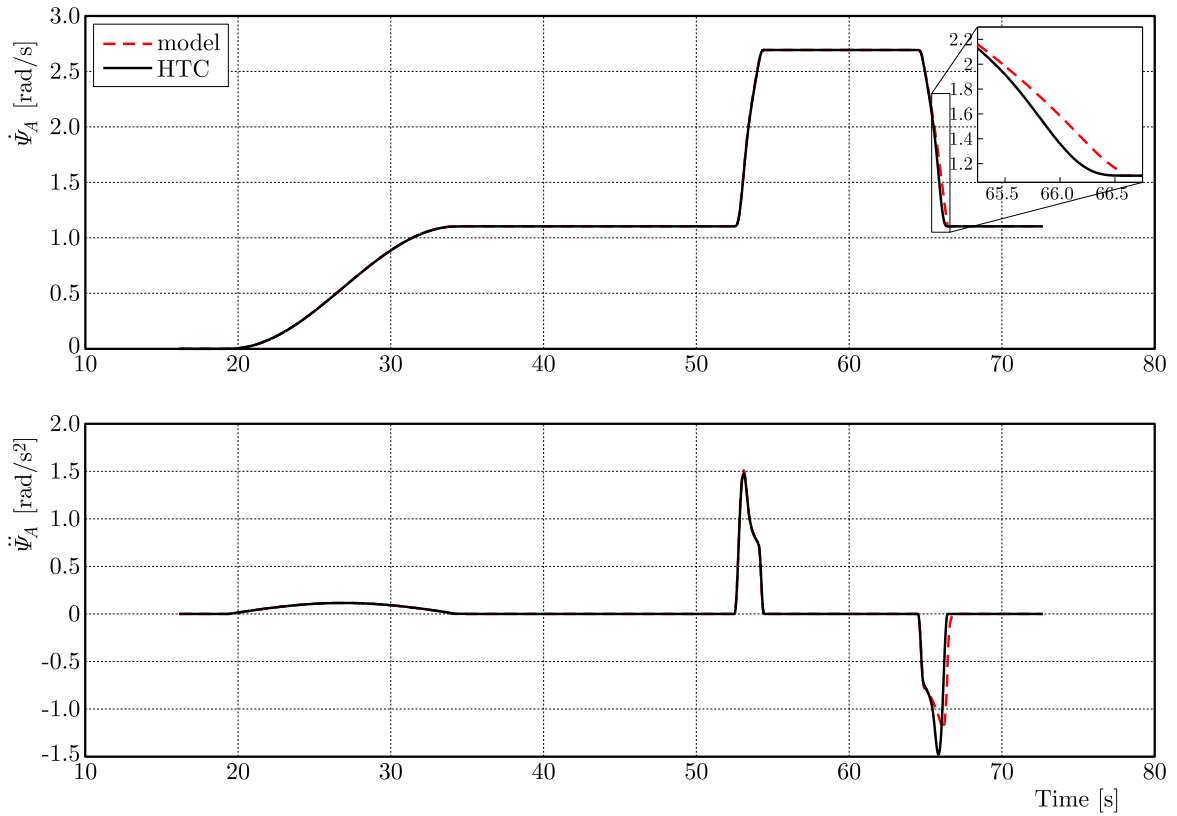


Fig. 4. Angular velocity and acceleration of the centrifuge arm

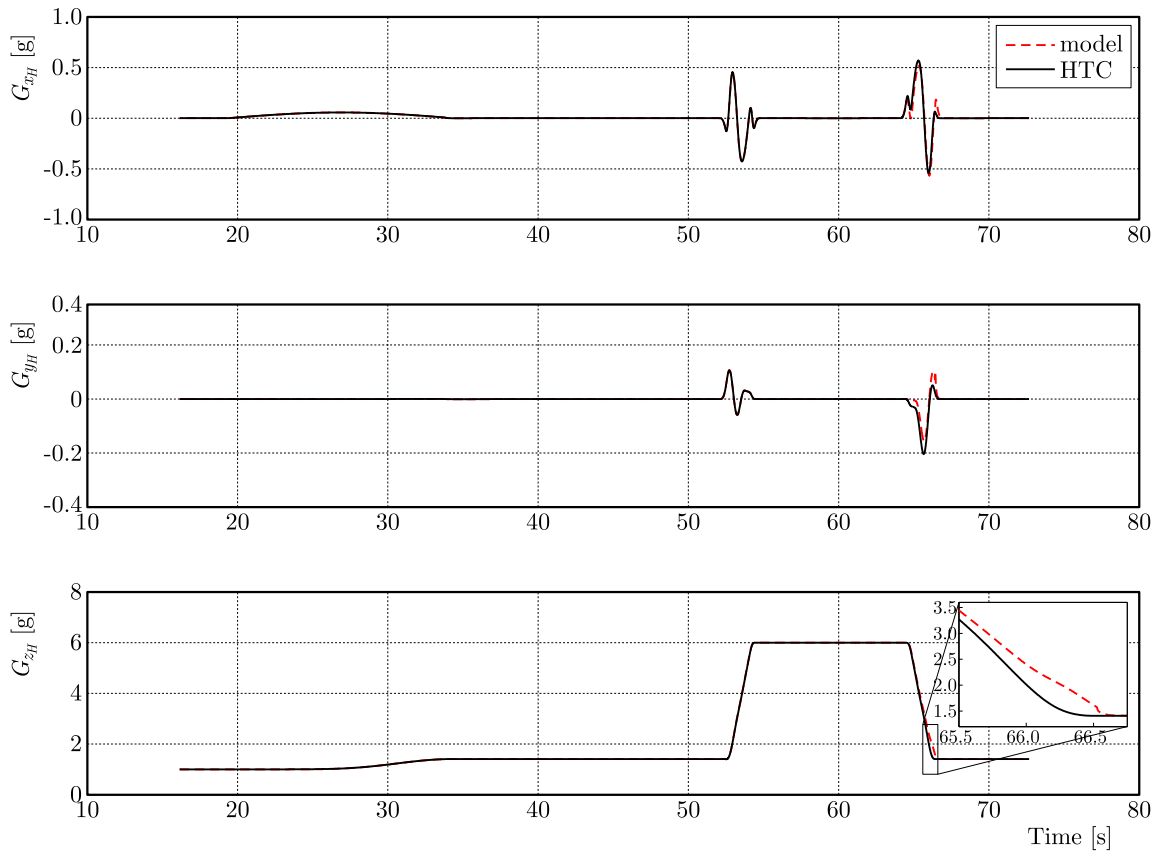


Fig. 5. Components of the absolute acceleration

deceleration (negative angular acceleration $\ddot{\psi}_A$ shown in Fig. 4), when a small difference has appeared. The maximum error of the absolute acceleration does not exceed the value of $0.2g$ (G_{zH}).

From Fig. 6, it is clear that the presented angle ϕ_R , angular velocity $\dot{\phi}_R$ and acceleration $\ddot{\phi}_R$ of the roll ring (link 2) provide good results. A difference between the desired (HTC) and calculated (model) angle ϕ_R is minimal. The angle ϕ_R is derived from equation (6.17) and depends on G_{x0} acceleration (5.1). Thus, the observed difference in the calculated angle ϕ_R comes from angular velocity of the arm $\dot{\psi}_A$ (Fig. 4) which affects G_{x0} acceleration. Moreover, according to equation (6.20), the angular velocity $\dot{\phi}_R$, and acceleration $\ddot{\phi}_R$ of the roll ring are calculated on the basis of the angle ϕ_R . Therefore, these parameters curves (model vs. HTC) are also different.

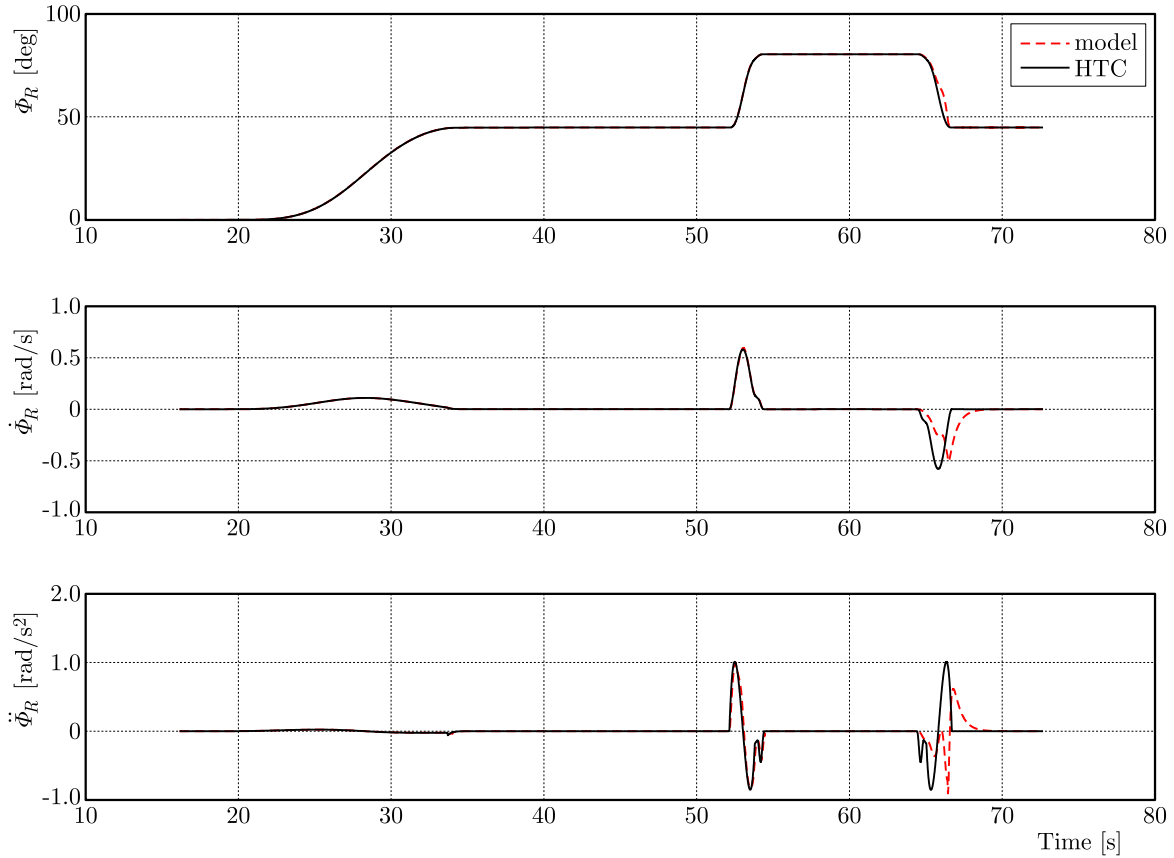


Fig. 6. Kinematic parameters of the roll ring: angle, angular velocity and acceleration

Figure 7 shows the angle θ_C , angular velocity $\dot{\theta}_C$ and acceleration $\ddot{\theta}_C$ of the pitch cabin (link 3) obtained by equations (6.25), and (6.27), respectively. A difference between the desired (solid line) and calculated (dotted line) angle θ_C appears only for the phase of deceleration (negative angular acceleration $\ddot{\psi}_A$, shown in Fig. 4) of the arm. Similar to the kinematic parameters calculated for the ring (link 2), the observed difference in the calculated angle θ_C (6.25) depends on the centrifuge arm movement (angular acceleration of the arm $\ddot{\psi}_A$, which affects G_{y0} acceleration (5.1)). The angular velocity $\dot{\theta}_C$ and acceleration $\ddot{\theta}_C$ of the roll ring (Fig. 7) are calculated based on equation (6.27). Therefore, the differences between two curves (model vs. HTC) of these parameters are easily observed.

The obtained kinematic model is not completely accurate, but the calculated link accelerations, velocities and angles do not differ much from their actual values. It is a concern, especially for maximum and minimum values indicating whether the limit ranges (Table 1) have not been exceeded to achieve the desired values of the acceleration vector \mathbf{G}_C components. In order to eliminate the differences between the desired (HTC) and calculated (model) parameters for the

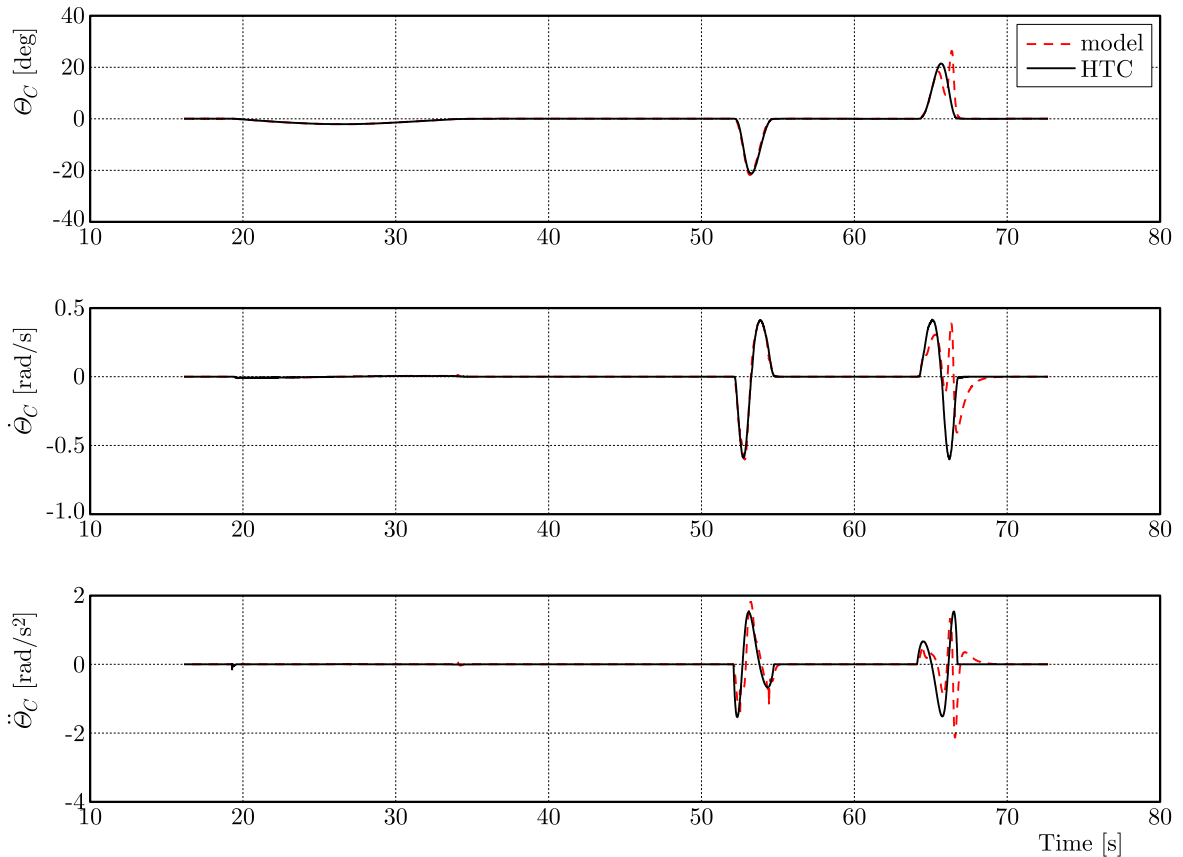


Fig. 7. Kinematic parameters of the pitch cabin: angle, angular velocity and acceleration

movement having a negative acceleration onset, Kvrjic *et al.* (2014) proposed a simple solution in which the values of the positive G-onset rate n of the same magnitude are reversed.

8. Conclusions

The purpose of the work is to present a way to solve the problem of correctly defining complex acceleration profiles that are recreated by a centrifuge motion simulator. The proposed solution, in the form of an inverse kinematic model of the centrifuge, indicates not only the exceeded limit values of the parameters, but also their changes over time. The simulation has revealed that the developed inverse kinematic model makes it possible to calculate the angular displacement, velocity and acceleration of the links, which is needed for the given linear acceleration of the simulator cabin. Simulation performed in Simulink proved the correctness of the presented expressions for angular displacement, velocity and acceleration of the centrifuge links. The presented algorithm achieved the predefined profile of absolute acceleration in the centrifuge cabin where the onset rate of the absolute acceleration is constant. The developed model of the inverse kinematics can be used for computer simulation of motion of the centrifuge simulator system. Through an overview of the behaviour of the model under various operating conditions, it is possible to predict how a real system will behave.

References

1. AMST-Systemtechnik GmbH, 2011, User manual Human Training Centrifuge HTC-07
2. BAILLIEUL J., 1985, Kinematic programming alternatives for redundant manipulators, *Proceedings of 1985 IEEE International Conference on Robotics and Automation*, St. Louis, MO, USA, 722-728

3. BUSS S.R., KIM J.S., 2005, Selectively damped least squares for inverse kinematics, *Journal of Graphics Tools*, **10**, 37-49
4. CHEN Y.C., REPPERGER D.W., 1996, A study of the kinematics, dynamics and control algorithms for a centrifuge motion simulator, *Mechatronics*, **6**, 829-852
5. CROSBIE R.J., 1988, *Dynamic Flight Simulator Control System*, United States Patent, Number 4,751,662
6. DANČUO Z., RASUO B., BENGİN A., ZELJKOVIĆ V., 2018, Flight to Mars: Envelope simulation in a ground based high-performance human centrifuge, *FME Transactions*, **46**, 1-9
7. DANČUO Z., RASUO B., VIDA KOVIĆ J., KVRGIĆ V., BUĆAN M., 2013, On mechanics of a high-G human centrifuge, *Proceedings in Applied Mathematics and Mechanics*, 39-40
8. DANČUO Z., VIDA KOVIĆ J., KVRGIĆ V., FERENC G., LUTOVAC M., 2012a, Modeling a human centrifuge as three-DoF robot manipulator, *2012 Mediterranean Conference on Embedded Computing, MECO, IEEE*, 149-152 ISBN 9940943601
9. DANČUO Z., ZELJKOVIĆ V., RAŠUO B., DAPIĆ M., 2012b, High-G training profiles in a high performance human centrifuge, *Scientific and Technical Review*, **62**, 64-69
10. DJURIC A., AL SAIDI R., ELMARAGHY W., 2012, Dynamics solution of n-DOF global machinery model, *Robotics and Computer-Integrated Manufacturing*, **28**, 621-630
11. GHERMAN B., PISLA D., VAIDA C., PLITEA N., 2012, Development of inverse dynamic model for a surgical hybrid parallel robot with equivalent lumped masses, *Robotics and Computer-Integrated Manufacturing*, **28**, 402-415
12. GROTJAHN M., HEIMANN B., KUEHN J., GREDEL H., 2004, Dynamics of robots with parallel kinematic structure, *The 11th World Congress in Mechanism and Machine Science*, 1689-1693
13. KVRGIĆ V.M., VIDA KOVIĆ J., LUTOVAC M.M., FERENC G.Z., CVIJANOVIC V.B., 2014, A control algorithm for a centrifuge motion simulator, *Robotics and Computer-Integrated Manufacturing*, **30**, 399-412
14. LIWEN G., HUI L.I.U., MENG F.U., 2015, Real-time motion planning algorithm for dynamic flight simulators (in Chinese), *Tsinghua Science and Technology*, **55**, 709-715
15. NAKAMURA Y., HANAFUSA H., 1986, Inverse kinematic solutions with singularity robustness for robot manipulator control, *Journal of Dynamic Systems Measurement and Control*, **108**, 163-171
16. NEARCHOU A.C., 1998, Solving the inverse kinematics problem of redundant robots operating in complex environments via a modified genetic algorithm, *Mechanism and Machine Theory*, **33**, 273-292
17. NEWMAN D.G., 2015, *High G Flight: Physiological Effects and Countermeasures*, 1st ed., Ashgate Publishing Ltd., Monash University, Australia, ISBN 9781472414571
18. SICILIANO B., SCIAVICCO L., VILLANI L., ORIOLO G., 2009, *Robotics: Modelling, Planning and Control, Soft Computing*, Springer, ISBN 9781846286414
19. TEJOMURTULA S., KAK S., 1999, Inverse kinematics in robotics using neural networks, *Information Sciences (Ny)*, **116**, 147-164
20. TRUSZCZYŃSKI O., KOWALCZUK K., 2012, The Polish centrifuge as a dynamic flight simulator. New application and ideas, *Polish Journal of Aviation Medicine and Psychology*, **18**, 71-80
21. TSAI L., 1999, *Robot Analysis: the Mechanics of Serial and Parallel Manipulators*, 1st ed., John Wiley & Sons, Inc., New York, NY, USA, ISBN 978-0-471-32593-2
22. VIDA KOVIĆ J., FERENC G., LUTOVAC M., KVRGIĆ V., 2012, Development and implementation of an algorithm for calculating angular velocity of main arm of human centrifuge, *15th International Power Electronics and Motion Control Conference (EPE/PEMC)*, Novi Sad, Serbia, DS2a.17-1-DS2a.17-6

23. VIDAKOVIĆ J., LAZAREVIC M., KVRGIC V.M., DANČUO Z., LUTOVAC M.M., 2013, Comparison of numerical simulation models for open loop flight simulations in the human centrifuge, *Proceedings in Applied Mathematics and Mechanics*, 485-486
24. WAMPLER C.W., 1986, Manipulator inverse kinematic solutions based on vector formulations and damped least-squares methods, *IEEE Transactions on Systems, Man, and Cybernetics*, **16**, 93-101
25. WOJTKOWIAK M., 1991, Human centrifuge training of men with lowered +Gz acceleration tolerance, *Physiologist*, **34**, 80-82
26. WOLOVICH W.A., ELLIOTT H., 1984, A computational technique for inverse kinematics, *The 23rd IEEE Conference on Decision and Control*, Las Vegas, Nevada, USA, 1359-1363
27. WRIGGE S., 1981, Calculation of the Taylor series expansion coefficients of the Jacobian elliptic function $sn(x, k)$, *Mathematics of Computation*, **36**, 555-564
28. WU J., CHEN X., LI T., WANG L., 2013, Optimal design of a 2-DOF parallel manipulator with actuation redundancy considering kinematics and natural frequency, *Robotics and Computer-Integrated Manufacturing*, **29**, 80-85
29. WU J., WANG J., WANG L., LI T., 2009, Dynamics and control of a planar 3-DOF parallel manipulator with actuation redundancy, *Mechanism and Machine Theory*, **44**, 835-849
30. WU J., WANG J., YOU Z., 2010, An overview of dynamic parameter identification of robots, *Robotics and Computer-Integrated Manufacturing*, **26**, 414-419
31. ZHAO Y., GAO F., 2009, Inverse dynamics of the 6-DOF out-parallel manipulator by means of the principle of virtual work, *Robotica*, **27**, 259-268

Manuscript received January 14, 2018; accepted for print July 26, 2018

DESIGN WITH SADSF METHOD AND ANALYSES OF ELASTIC PROPERTIES OF TORSION-LOADED STRUCTURES BASED ON DOUBLE-TEE SECTIONS

IRENEUSZ MARKIEWICZ

Kielce University of Technology, Faculty of Mechatronics and Mechanical Engineering, Kielce, Poland
e-mail: ireneusz.markiewicz@tu.kielce.pl

The paper presents results of the preliminary strength design using the method of statically admissible discontinuous stress fields (SADSF) of two new and interesting thin-walled structures based on double-tee sections. Although these constructions are intended to carry torsion moment loads, all their surfaces are accessible from outside. The paper is completed with the selected results of linearly-elastic FEM analyses of the presented solutions. They show surprisingly good strength properties and significantly higher load-carrying capacity comparing to structures designed in an intuitive way. The objectives of the paper, among other things, are as follows: popularization of the SADSF method, presentation of its new solutions and confirmation of practical usefulness in the design of thin-walled structures.

Keywords: thin-walled structures, design, limit analysis, shape and topology optimization, SADSF method

1. Introduction

Due to their properties, thin-walled structures are commonly applied, and the methods concerning strength design are intensively developed and represent the centre of interests of scientists.

The main difficulty encountered in designing these systems is that even apparently minor changes in their constructional details or changes in boundary conditions may cause large and non-local changes in stress and deformation fields (e.g. Bodaszewski, 2013). For this reason, the design methods based on intuitive or iterative improvements, including contemporary, quickly developed methods of topology optimization (Bendsoe and Sigmund, 2003; Huang and Xie, 2010; Mróz and Bojczuk, 2003), must be applied with great caution.

The paper presents a method which does not make use of iterative procedures and uses statically admissible, discontinuous stress fields, and is justified by the lower-bound theorem of limit analysis and is called SADSF (Szczepiński, 1968; Dietrich *et al.*, 1970; Frąckiewicz *et al.*, 1986; Szczepiński and Szlagowski, 1990; Szlagowski, 1990; Zowczak, 2004; Bodaszewski and Szczepiński, 2005; Bodaszewski, 2013).

A manner of formulating the design problem typical for this method is presented in Fig. 1a (Bodaszewski, 2013). The only data is: limit load at the boundary S_p reduced to two pairs of forces Ph , geometry of this part of the boundary (dimensions: L , h , e), and the yield point of the structure material σ_Y .

One should notice that analogical formulations which use only the data on boundary conditions, appear during designing each new structure.

In order to solve the presented problem using the SADSF method, it is necessary to construct a statically admissible, discontinuous stress field, which would satisfy the given boundary conditions and specify the structure configuration, i.e. number, spatial positioning and system of mutual connections of component elements as well as determine the shape and dimensions of these elements. Therefore, this field will completely define the sought for structure.

Statically admissible stress fields satisfy only the equilibrium equations and static boundary conditions and do not infringe the assumed yield condition. The SADSf method assumes making use of discontinuous fields wherein lines of discontinuity are sections of straight lines which cause that stress states are homogenous within any area. During construction of the fields, one strives for a situation where the yield condition is achieved within all or at least as many areas as possible. Moreover, it is assumed that the constructed spatial fields consist of plane fields fragments.

Basic difficulty during construction of such fields is that for arbitrarily selected networks of lines of stress discontinuities (division to homogenous areas), there is usually no solution. At the beginning, even the arrangement of conditions that need to be set is unknown, and one must notice that these are non-linear equations and inequalities which include singularities, and usually large number of variables (Bodaszewski, 2004, 2005). This causes that direct approaches in the SADSf method cannot be applied.

These difficulties are bypassed within the scope of the application version of the SADSf method, created especially for engineers. An engineer does not have to solve any new statically admissible stress fields. He or she uses a set of ready-made library fields (Fig. 1b) of a low level of complexity, which are delivered together with the software. The fields are assembled into more complex ones in such a way that the assumed boundary conditions and equilibrium conditions are satisfied.

At the moment, the most advanced package of the application version is SADSfAM (Bodaszewski, 2013). It is based on the concept of a multi-level idea of constructing complex fields and allows simple design of even the most complex thin-walled structures consisting of flat elements.

In this idea, the library fields of the package, presented in Fig. 1b, represent the fields of level I and are oriented at designing thin-walled structures. Flat and spatial solutions of average complexity made of them are the fields of level II. Fields such as these are constructed and catalogued by a designer in order to use them as fragments – usually repeating ones – of even more complex fields, which represent solutions of the considered problems (e.g. Fig. 1c and 1d) and are classified as fields of level III or higher. A fragment of the existing library of fields of level II is presented in Fig. 1e (Bodaszewski, 2013).

The satisfaction of the criterion of yield condition utilized in the SADSf method, within as many areas as possible, does not lead to unequivocal solutions. This plurality of possible solutions is useful from the standpoint of the designer because it allows satisfying additional conditions, for example resulting from preliminary design assumptions or related to the simplicity of execution, strength, etc. The number of solutions that may be constructed is limited to these which can be assembled based on the fields available in the library.

Two new and original solutions of the problem, Fig. 1a, developed within the scope of the paper are presented in Figs. 1c and 1d. They may be used, for example, as cross-beams of load-carrying frames of vehicles. All their surfaces are accessible from outside and, despite this, the structures exhibit high rigidity to torsion.

The constructed statically admissible fields require application of systems of additional elements in the central part of the structures. In the solution from Fig. 1c, these elements have the shape of letter X (solution denoted as *Z2x93*) while in the solution from Fig. 1d (the solution denoted as *Z2x94*) they look like a rectangular pipe.

In each library field, one assumes realization of a plane state of stress, the result of which is that the membrane state should be able to transfer the assumed load. Therefore, structures may successfully utilize the load-carrying properties of materials used to build them. If any of their elements is removed or not connected with welds at the edges, where the fields show non-zero interactions, the load-carrying capacity would be reduced by one order. This is a cardinal error.

The designed structures are free of cardinal errors, therefore, one may expect their high quality level.

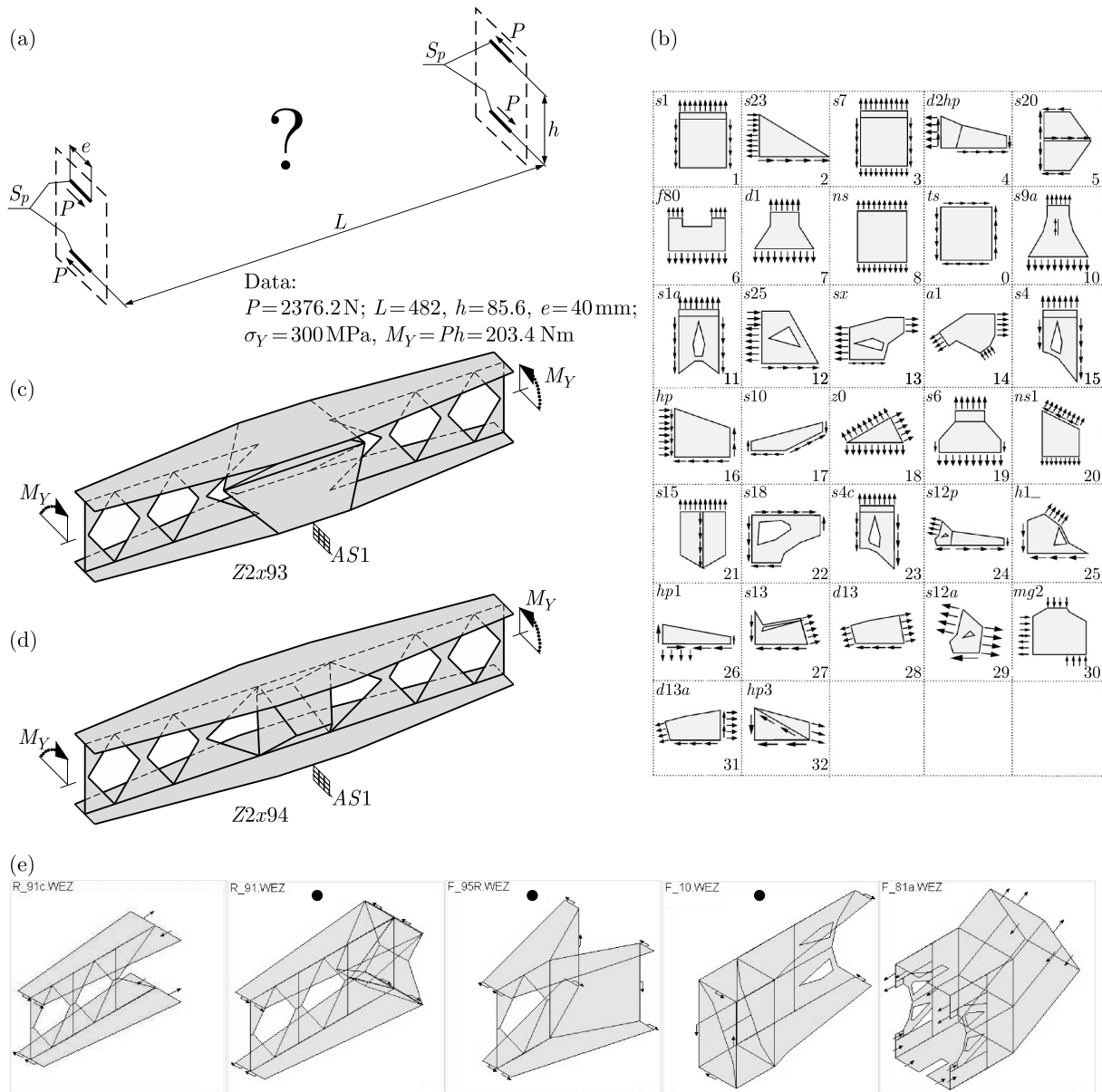


Fig. 1. Formulation and solutions of the complex field construction problem: (a) graphical illustration of the design problem formulation; (b) library of ready-made particular solutions from SADSfAM software package, without stress discontinuity lines; (c), (d) solutions: contours of statically admissible stress fields which specify the sought for structures; (e) fragment of an existing library of a designer, without stress discontinuity lines

These properties are proven by e.g. elastic FEM analyses of one of the developed solutions included in the paper. They also show possible benefits emerging from utilization of the SADSf method during designing the thin-walled structures. These properties are expected also based on the conclusions presented, among other things, in the papers by Markiewicz (2007, 2013).

2. Basic information concerning SADSfAM package (Bodaszewski, 2013)

Examples of four types of library fields of SADSfAM package, which have been used to design the solutions presented in the paper, are shown in Figs. 2a-d. As one can see, each of them

satisfies different but relatively simple boundary conditions and is described within own local coordinate system $\{a\}$ and has individual designation (here: Hp , Ts , $Ns1$, $s1$).

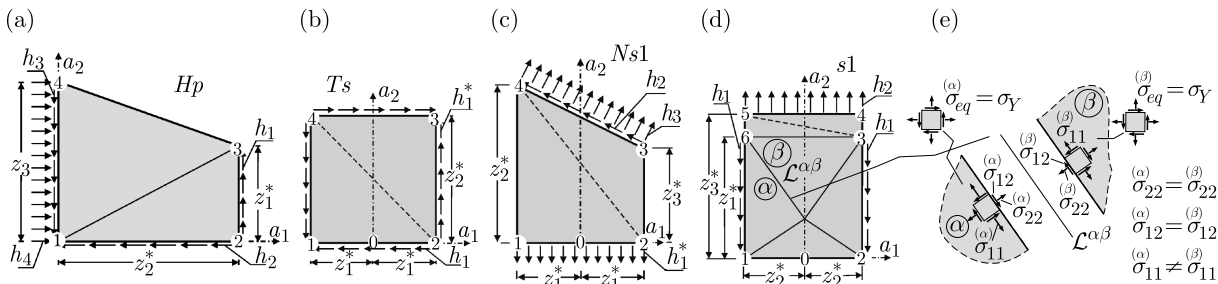


Fig. 2. The library fields of the SADSFaM package, which are used in the solutions presented in the paper and the interactions along the line of stress discontinuity $\mathcal{L}^{\alpha\beta}$ in the system related to this line

The field loads are described by external stress parameters h_i , which are coordinates of stress vectors applied at the edges. Location of loaded edges is described by external geometrical parameters z_i , which have the form of linear dimensions.

In the case of each of such fields, equilibrium equations for each stress discontinuity line must be met. An example of such a line $\mathcal{L}^{\alpha\beta}$ separating two different homogenous stress areas α and β , together with equilibrium conditions, is presented in Fig. 2e. As it can be seen, the coordinates $\sigma_{22}^{(\alpha)}$, $\sigma_{22}^{(\beta)}$ and $\sigma_{12}^{(\alpha)}$, $\sigma_{12}^{(\beta)}$ must be equal. Only the coordinates $\sigma_{11}^{(\alpha)}$ and $\sigma_{11}^{(\beta)}$ can differ (if these were equal, the states of stress in both regions would be identical as well).

Satisfaction of these conditions on each of the field discontinuity line results in that its global equilibrium equations must be identically satisfied. Therefore, not all parameters h_i and z_i can be assumed as independent. Figures 2a-d show parameters, identified with asterisks, that are assumed as independent, and their values may be given in the package.

As mentioned before, while assembling the library fields, the conditions of equilibrium at the connecting edges must be satisfied. These conditions are called joining conditions and include:

- geometrical conditions, i.e. overlapping conditions of common border segments;
- static conditions, i.e. conditions concerning satisfaction of equality of mutual interactions on these segments.

Each of the library fields in the complex solution is given its unique index s (inscribed in quadrilateral rims), and thickness of its element is denoted as $\delta^{(s)}$.

The package SADSFaM makes use of Treska's yield criterion, so the stress coordinates given on the boundaries of fields are calculated with reference to: $k = \sigma_Y/2 = 150$ MPa.

3. Construction of statically admissible stress fields

While designing the presented solutions, it is assumed that they will show symmetry of shape and antisymmetry of internal forces with reference to three antisymmetry planes of the applied load, which are denoted as $AS1$, $AS2$ and $AS3$ (Figs. 3 and 4).

The method of constructing a statically admissible field in the half of the solution $Z2x93$ (Fig. 1c), which is denoted as R_93 , is presented in Fig. 3.

Two fields of level II of complexity, which are presented in Figs. 3a and 3b, are used. Thin arrows in the figures show the resultants of interactions between the component fields and thick arrows show the resultants of external reactions. Component numbers of the library fields are also given together with the fields names in the tables next to these numbers.

The first field, denoted as $Ad93-94$ adjoins the boundaries S_p , satisfies boundary conditions given therein and determines the shape and dimensions of flanges and web (Fig. 3a). This is a

By combining the fields Ad_{93-94} and Ad_{93} , one gets the statically admissible field R_{93} , in the half of the solution $Z2x_{93}$, which is presented in Fig. 3c. This field is also qualified as the field of level II of complexity.

The discussed Figs. 3a-c are mostly a sheet of screen copies provided by the SADSFaM package, complemented by selected dimensions and additional denotations. These figures, however, do not include most of the numerical data. That is why, with the use of a graphic software, one carries out additional Fig. 3d which presents the positioning of component fields in the antisymmetric half of the fields from Fig. 3c (in spaced form). Dimensions and interaction values given in this figure may be easily assigned to external parameters of the applied library fields from Fig. 2. Transformation matrices, which specify the position of library fields in space, are not discussed in this paper.

As one may see, normal interactions from the fields Hp ($s = 13, 14$) are taken over by the fields $s1$ ($s = 1, 3$), and tangent interactions by the fields Ts ($s = 2, 4$), which perform pure shear. The fields Hp and Ts are located one above another and represent together an extension of flanges within the area where additional skew elements are introduced.

Balancing the tangent interactions at the external edges of the fields Ts ($s = 2, 4$) and $s1$ ($s = 1, 3$) necessitate introduction of additional, skew positioned, fields Hp ($s = 5, 6$). These fields have different values of external parameters comparing to the fields Hp in the flanges.

Independent geometrical parameters of the component fields result from the given dimensions: L , h , e and the adopted dimension t (Fig. 3) as well as geometrical conditions of joining.

One must notice that the tangent stress τ applied at the edges of the fields Hp ($s = 13, 14$) adjacent to S_p is not given while entering data of these fields (it is only specified after introduction of independent external parameters). After its determination, it is possible to determine the thickness of elements of the fields Hp using the formula

$$M_Y = \tau \delta e h$$

Thicknesses of elements of the remaining fields are determined using the static joining conditions. For example, at the common edge of the fields Hp ($s = 14$), $s1$ ($s = 1$) and Ts ($s = 2$) such conditions have the following form

$$1.980k\delta^{(14)} = 1.992k\delta^{(1)} \quad 0.198k\delta^{(14)} = 1.0k\delta^{(2)}$$

In the SADSFaM package, these conditions are arranged and solved automatically. The obtained thicknesses are given in Fig. 3d.

The total thickness of the flange in the area with additional skew elements equals the sum of thicknesses of elements of the fields Ts and $s1$: $\delta_p = \delta^{(3)} + \delta^{(4)}$ – layer superimposition of these fields has not been performed (Szlagowski, 1990; Bodaszewski, 2004, 2005; Bodaszewski and Szczepiński, 2005).

Only the thickness of elements of the not loaded web may be assumed arbitrarily. It is assumed that it is the same as the thickness of flanges and equals δ .

The second of the complex fields, which is constructed for the half of the solution $Z2x_{94}$ and denoted as R_{94} , is presented in Fig. 4c. The presentation method is similar to the previous example.

This solution is derived by combining the already discussed field Ad_{93-94} (Fig. 4a) with the field Ad_{94} , which is presented in Fig. 4b.

As one may see, the fields $s1$ ($s = 1, 5$) play the same role here as in the previous solution (Fig. 4d). One adopted reverse directions of interactions in the fields Ts ($s = 2, 6$), therefore, it is possible to zero the total interactions on the free edges of the external flanges.

Tangent interactions from the fields Hp ($s = 17, 18$) and Ts ($s = 2, 6$) in this case sum up and are balanced by tangent interactions from additionally introduced fields $s1$ ($s = 3, 7$).

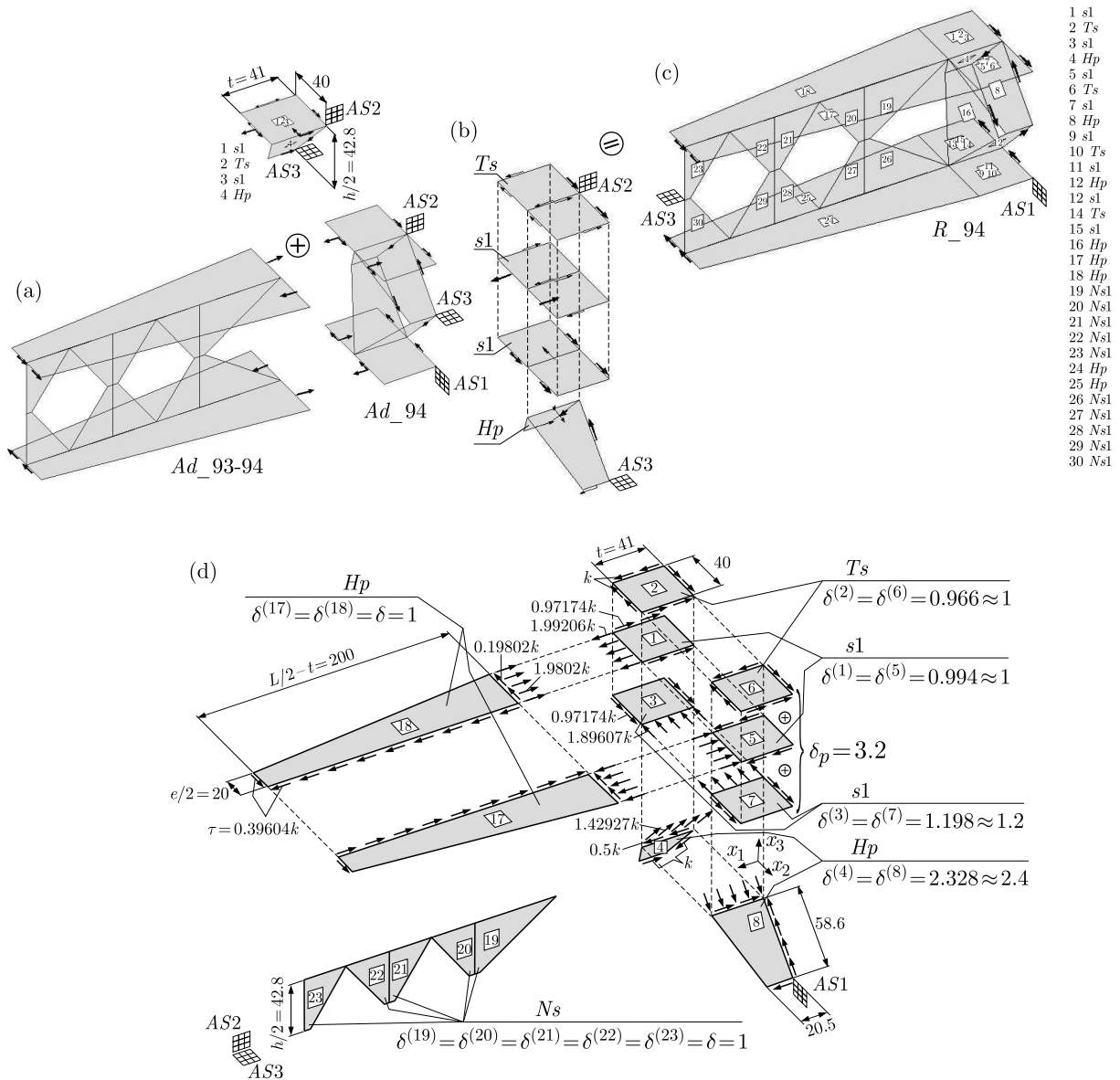


Fig. 4. Construction of the field in the antisymmetric half of the solution $Z2x94$ from Fig. 1d: (a) field Ad_{93-4} ; (b) field Ad_{94} , which determines the shape and dimensions of additional skew elements and flanges in the area adjacent to $AS1$; (c) field R_{94} , which represents a half of the solution to the problem $Z2x94$; (d) position of the library fields components, interactions between them and thickness of their elements in the top half of the field R_{94}

Normal interactions from these additional fields, which act in the web plane, are balanced by normal interactions from the skew located fields Hp ($s = 4, 8$).

Complete solutions of the problem from Fig. 1a are derived by combining two fields R_{93} and two fields R_{94} , as shown in Figs. 5a and 5b. As one may see, the joining conditions, due to symmetry of fields geometry and antisymmetry of internal forces, are satisfied identically.

The solutions R_{93} and R_{94} expand the designer library. Exemplary fields of such a library, which includes hundreds solutions derived by Bodaszewski (2013), are presented in Fig. 1e. The dots denote these fields which can be used to solve the problem from Fig. 1a.

The derived solutions $Z2x93$ and $Z2x94$ are, however, not too complicated fields. Based on the fields in the designer library, solutions of the complete load-carrying frames of vehicles are designed by connecting and copying them (Bodaszewski, 2013). The solutions presented in the paper may be used as cross-beams in these frames.

Interactions at the edges of the component fields show that the presented structures consist of elements bent in their planes. They will, therefore, form bending axes, and stresses will increment together with an increase in the distance from these axes. Obtaining a balanced elastic equivalent stress in these elements is thus not possible. It is worth to remember when analysing FEM results.

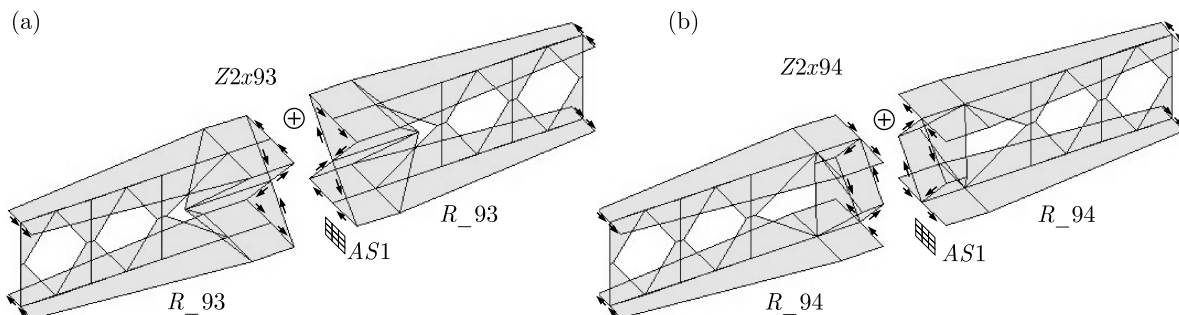


Fig. 5. Composing the derived complex fields R_{93} and R_{94} into complete solutions of the problem from Fig. 1a

One must also notice that in the planes denoted in Fig. 5a and 5b as $AS1$, there are no reactions towards perpendicular direction, which would generate a bimoment. In both cases, the bimoment increases together with receding from the extreme sections, however, only to the point of occurrence of additional skew elements. Then it decreases, and in the $AS1$ section it equals zero. One must mention that near the sections with the greatest bimoment, there are the greatest stress concentrations within the elastic range.

4. Properties of structures designed using the SADSf method

The thin-walled structures derived using the SADSf method have structure configurations adapted to the applied load and are free of cardinal errors. However, the method itself is an approximate one and assumes that, among other things, using the rigid-ideally plastic model of material only considers the limit state of the structure corresponding to the beginning of its collapse and assumes maintenance of the membrane state until it is reached. That is why, studies of actual properties of the designed systems at stages and under working conditions, which the SADSf method does not include (elastic, elastic-plastic or time-variable loads), have been carried out since the beginning of its existence (e.g., Szczepiński, 1968; Dietrich *et al.*, 1970; Kapkowski and Stupnicki, 1973; Frąckiewicz *et al.*, 1986; Szczepiński and Szlagowski, 1990; Szlagowski, 1990; Bodaszewski, 1994; Zowczak, 2004; Markiewicz, 2007).

Good or very good properties at these stages proved under these research, require conformation and examination of many case studies so that their results would be representative for a considered class of thin-walled structures. Therefore, within the recent years, a wide range research program has been initiated, which covered (Markiewicz, 2013):

- within the range of elastic-plastic deformations – examinations of yield zones development using thermovision and actual mechanisms of collapse and paths of equilibrium within the whole range of the applied loads;
- within the elastic range – analysis of distribution of the equivalent stress fields using FEM;
- at time-variable loads – estimated fatigue strength using the local strain-life method.

Research within the elastic-plastic range showed, among other things, the same limit load capacities of their components, yielding of significant segments of volumes at the moment of collapse and maintenance of membrane state domination for loads slightly less than the actual

limit load. The collapse itself was however always caused by great deformation changes of the geometry, and in each case the actual limit load was greater than the one assumed during design.

A few dozen thin-walled structures designed using the SADSF method were subjected to FEM analyses within the elastic range, which was usually the operational one. Small deformations and domination of membrane states, almost accurate equalization of equivalent stress along free borders and relatively low stress concentrations were the rule in that case. It was also found that the designed systems had strength properties far more better comparing to structures designed using intuitive methods.

Results of the linearly-elastic FEM analyses of the structure *Z2x94* present hereinafter complement the results given in the aforementioned monograph and confirm the mentioned rules within full extent.

Very good properties have been revealed while estimating fatigue strength. It turns out that thin-walled structures designed using the SADSF method have a fatigue life longer by few orders comparing to structures designed using traditional methods, and fatigue cracks can initiate almost simultaneously at various locations.

Based on the performed studies, one may expect good load-carrying properties of the structures. Moreover, the case with poor strength conditions has not been reported so far.

Structures like these can be accepted straight away and in very rare cases further improved. Improvements should apply to geometrical parameters (shape and dimensions of elements) the change of which does not significantly affect the considered class of structures.

5. FEM analysis results

To show the quality of the designed structures within the linearly-elastic range, one presents distribution of equivalent stresses derived by means of FEM for the structure model denoted as *Z2x94*. These distributions were compared to distributions specified for a model of “regular” double-tee section which is not designed using SADSF method and the structure of which is not adapted to the torsion moment load. This model includes thus a cardinal error.

During the analyses, the shell model is used, which is approximated and does not allow analysing local three-dimensional states formed within areas of component elements connections. However, it still shows the scale of possible changes in load-carrying properties.

Structural diagrams of both models and the boundary conditions adopted during calculations are presented in Figs. 6a and 7a.

The shape and dimensions of the model from Fig. 6a accurately corresponds to the solution derived from SADSF. The value of the force F is selected so that the value of torsion moment load equals to the half of the moment assumed in the design M_Y . Taking the accepted yield point value: $\sigma_Y = 300$ MPa and assuming that, in the elastic state of stress, there exists an ideally equalized state of stress, one should obtain the equivalent stress value at each point of the analysed structure equal to: $\sigma_{eq} = 150$ MPa.

The parameters of regular double-tee section model are adopted so that its weight approximately corresponds to the weight of the model designed in SADSF. Thickness of all elements is 1.2 mm, and width of flanges is fixed and equal to the greatest width derived from statically admissible fields. This change forced minor widening of the membranes $p1$ and $p2$.

The boundary conditions adopted for this model are the same as in the model *Z2x94*. Only the value of load is assumed to be 16.5-times less so that the level of the greatest equivalent stresses in both models is approximately the same.

The derived distributions of equivalent stresses for the model *Z2x94* are presented in Fig. 6. Figure 6b shows the distribution of total equivalent stress (membrane and bending), however, Fig. 6c shows a distribution from the component membrane state to the bending state in Fig. 6d.

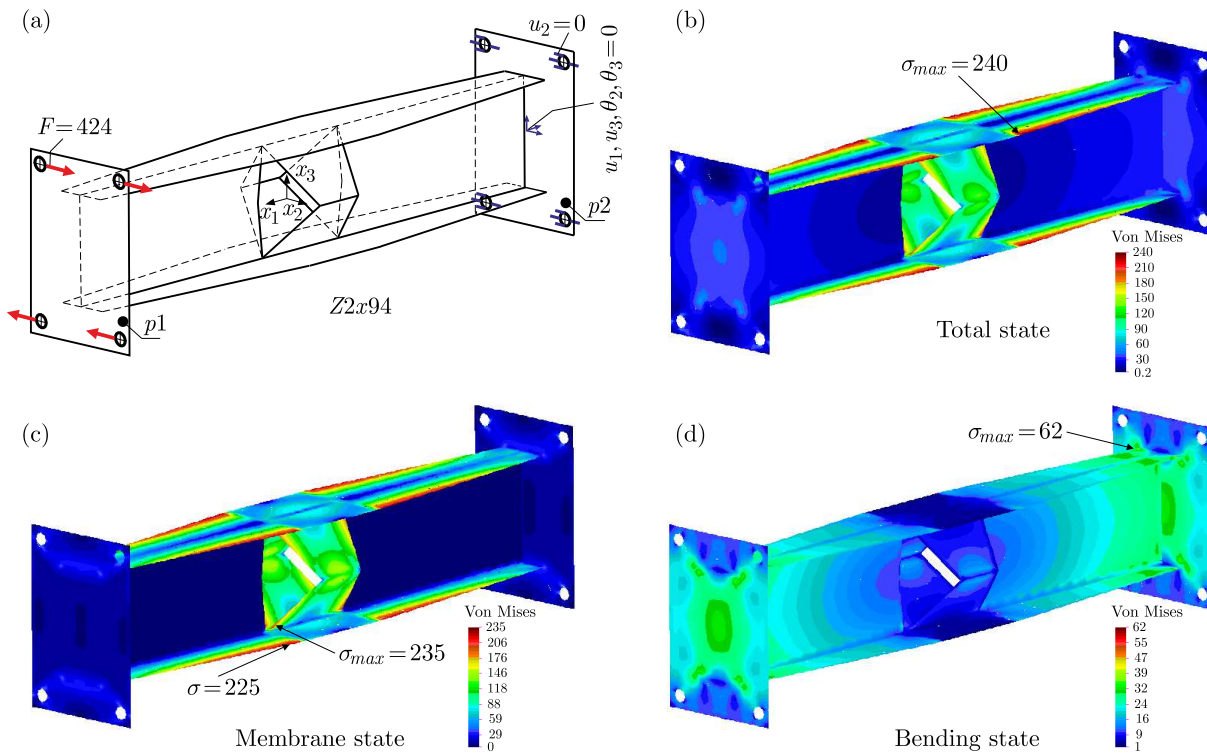


Fig. 6. The adopted boundary conditions and distribution of equivalent stresses calculated according to Huber-Mises-Hencky criterion for the model *Z2x94*

Based on the results, one may determine that:

- domination of the membrane state: the derived value of the greatest equivalent stress from the bending state reaches ca. 26% of the greatest value derived for the membrane state ($62/235 \approx 0.26$), and the distribution of total stress corresponds approximately to the distribution of the membrane state (Figs. 6b and 6c);
- presence of minor local stress concentrations at various structure locations (e.g. indicated by arrows, where: $\sigma_{eq} = 235$ MPa, $\sigma_{eq} = 225$ MPa), however, values in these locations are similar;
- relatively good equalization of the equivalent stresses from the membrane state along the free edges of flanges;
- occurrence of the greatest total equivalent stresses and from the membrane state on the flange edges near the sections with the greatest bimoment;
- lack of load transfer in the membrane state through the web, wherein zero stress condition is adopted in the design (Fig. 4);
- occurrence of the greatest stresses from the bending state near the extreme membranes, which confirms that a small bimoment is introduced into these elements.

Rigidity of this model is: $\kappa = M/\phi \approx 318$ Nm/deg; where: M is the applied torsional moment value, ϕ – angle of rotation of the upper border of the membrane $p1$ (Fig. 6a) calculated based on displacements of its extreme nodes.

In the case of the regular model of double-tee section (Fig. 7), it is found that:

- it is necessary to reduce the applied forces by 16.5-times in order to derive the level of the greatest equivalent stress as in the case of the structure designed using the SADF method;
- load is transferred mostly through the bending state: value of the greatest equivalent stress from the bending state is ca. 2.4-times greater than the greatest value derived for

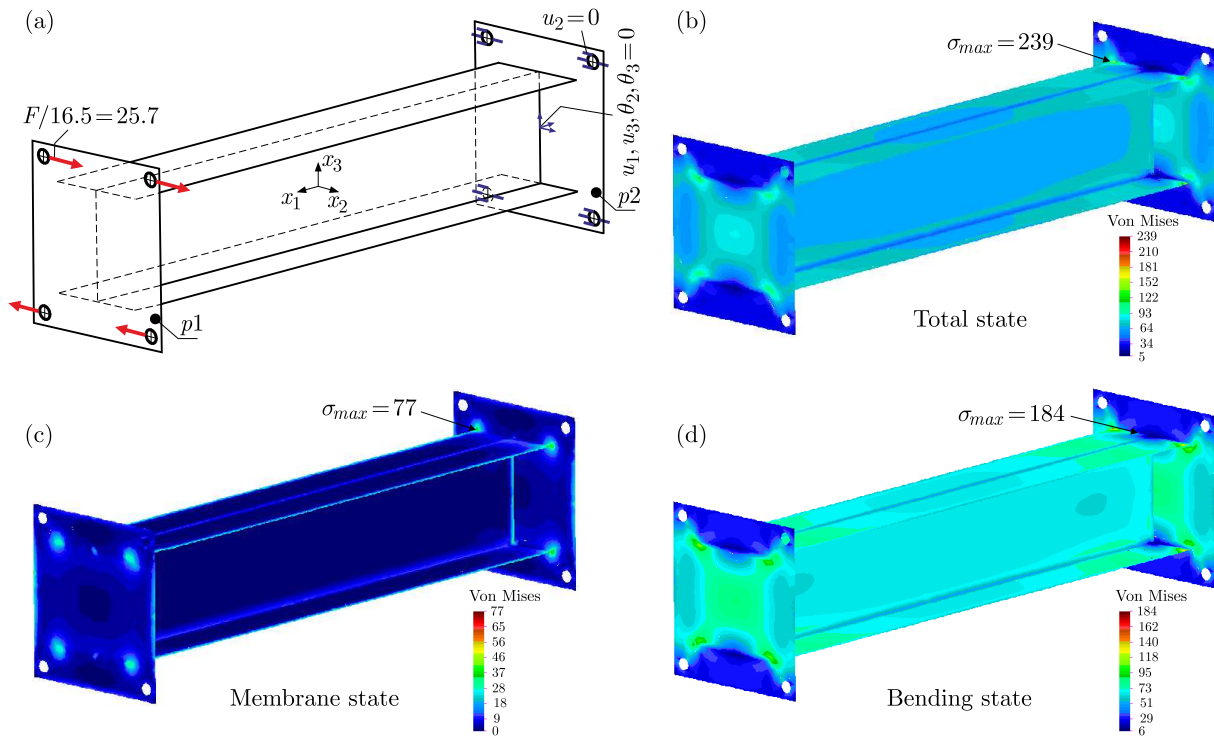


Fig. 7. The adopted boundary conditions and distribution of equivalent stresses calculated according to Huber-Mises-Hencky criterion for the model of regular double-tee section

the membrane state ($184/77 \approx 2.4$), and the distribution of the total stress corresponds approximately to the distribution of the membrane state (Figs. 7b and 7d);

Rigidity of this model is: $\kappa \approx 6.2 \text{ Nm/deg}$ and is as much as 51-times ($318/6.2 \approx 51$) less comparing to rigidity of the model *Z2x94*.

The above presentation of the equivalent stresses distribution shows how radically one may improve load-carrying properties and benefit from SADSf method application.

6. Conclusions

The application of the SADSf method, which does not make use of iterative procedures, can be successfully utilized while designing thin-walled structures wherein even a minor change of structural parameters may cause radical changes to load-carrying properties.

It may be applied already at the initial stage of designing, where only boundary conditions are known. At this stage, major load-carrying properties of thin-walled systems are determined.

The package of the application version of SADSfAM is not limited by complexity of a designed structure, it is easy to use and can be used by any engineer who knows the basics of statics. This means that it can be widely used in many practical applications.

As presented in the paper, having the given boundary conditions, sometimes one may construct a few solutions. This ambiguity can be used to search for such solutions which satisfy additional criteria, covering e.g. technological or strength limitations.

The designed structures do not include cardinal errors. Their structure configurations are adopted to transfer the assumed load, and one may expect in advance good load-carrying properties, radically better comparing to these systems designed using intuitive method.

Current capabilities of the software in the application version of SADSf method as well as good strength properties of the designed structures show that this method is more and more popular among engineers.

References

1. BENDSOE M.P., SIGMUND O., 2003, *Topology Optimization: Theory, Methods, and Applications*, Springer
2. BODASZEWSKI W., 1994, The investigation of the models of structural joint shells shaped from the condition of equalized effort in limit state (in Polish), *XVI Sympozjum Mechaniki Eksperymentalnej Ciężkiego*
3. BODASZEWSKI W., 2004, 2005, Algorithms of the method of statically admissible discontinuous stress fields (SADSf), *Engineering Transactions*, **52**, 3, 175-193, 2004, **52**, 4, 281-302, 2004, **53**, 1, 15-30, 2005, **53**, 2, 119-131, 2005
4. BODASZEWSKI W., 2013, *Static Analyses and Shaping of Complex Thin-Walled Structures* (in Polish), BEL Studio, Warszawa
5. BODASZEWSKI W., SZCZEPIŃSKI W., 2005, *Shaping Structure Elements by the Method of Discontinuous Stress Fields* (in Polish), BEL Studio, PWN, Warszawa
6. DIETRICH L., MIASTKOWSKI J., SZCZEPIŃSKI W., 1970, *Load-Carrying Capacity of Structural Elements* (in Polish), PWN, Warszawa
7. FRĄCKIEWICZ H., SZCZEPIŃSKI W., TERESZKOWSKI Z., SZLAGOWSKI J., BODASZEWSKI W., TRELA S., BARCHAN A., 1985, *Joints and Structural Connections* (in Polish), WNT, Warszawa
8. HUANG X., XIE Y.M., 2010, *Evolutionary Topology Optimization of Continuum Structures, Methods and Applications*, Wiley
9. KAPKOWSKI J., STUPNICKI J., 1973, Experimental investigations of machine elements designed by the method of load carrying capacity (in Polish), *Rozprawy Inżynierskie*, **21**, 161-173
10. MARKIEWICZ I., 2007, Analysis of elastic effort fields in truck frame designed by the SADSf method, *Eksplatacja i Niezawodność – Maintenance and Reliability*, **2**, 34, 22-27
11. MARKIEWICZ I., 2013, *Investigating the Behaviour of Structures Designed with the SADSf Method* (in Polish), Monografie, Studia, Rozprawy M47, Wydawnictwo Politechniki Świętokrzyskiej, Kielce
12. MRÓZ Z., BOJCZUK D., 2003, Finite topology variations in optimal design of structures, *Structural and Multidisciplinary Optimization*, **25**, 3, 153-173
13. SZCZEPIŃSKI W., 1968, *Plastic Design of Machine Parts* (in Polish), PWN, Warszawa
14. SZCZEPIŃSKI W., SZLAGOWSKI J., 1990, *Plastic Design of Complex Shape Structures*, Ellis Horwood & PWN, Warszawa-Chichester
15. SZLAGOWSKI J., 1990, Methodology of strength design of structural elements according to the limit load carrying capacity criterion (in Polish), *IFTR Reports*, **25**
16. ZOWCZAK W., 2004, *Strength Design by Means of Slip-Line Method* (in Polish), Monografie, Studia, Rozprawy M-41, Wydawnictwo Politechniki Świętokrzyskiej, Kielce

INFLUENCES OF THE DIAMETER AND POSITION OF THE INNER HOLE ON THE STRENGTH AND FAILURE OF DISC SPECIMENS OF SANDSTONE DETERMINED USING THE BRAZILIAN SPLIT TEST

TANTAN ZHU

State Key Laboratory of Coal Mine Disaster Dynamics and Control, Chongqing University, Chongqing, China

DA HUANG

School of Civil and Transportation Engineering, Hebei University of Technology, Tianjin, China

e-mail: dahuang@hebut.edu.cn

The Brazilian split test on a centrally holed disc (referred to as a ring-disc specimen) is an important indirect method for determining the tensile strength of rock. This paper studies the effect of the diameter d of the center hole and its position, defined by the eccentricity b and the inclination angle of the eccentric hole, on the peak load, failure pattern and horizontal stress of the disc specimen via laboratory experiments and numerical modeling using the finite element method (FEM). Static Brazilian split tests are conducted on an intact disc and three types of holed discs: C-specimens containing a central hole with different diameters, EH-specimens with a horizontally eccentric hole and ER-specimens with a rotationally eccentric hole.

Keywords: Brazilian test, rock, eccentric hole, strength, failure pattern

1. Introduction

Crack initiation, propagation and coalescence in rocks is often caused by tensile stress (Song *et al.*, 2001; Shang *et al.*, 2008; Zhang *et al.*, 2014; Huang and Zhu, 2018). Thus, it is very important to determine the tensile strength of rocks. The Brazilian test is widely adopted as an indirect method that benefits from the compressive strength of rocks being much higher than their tensile strength. This test method has been widely used for more than 50 years (Mellor and Hawkes, 1971) and was recommended by the International Society of Rock Mechanics as one method to measure the tensile strength of rocks (ISRM, 1978) due to its simplicity of operation. Using the Brazilian split test method, the indirect tensile strength σ_t is given by the following analytic elastic solution (ISRM, 1978)

$$\sigma_t = \frac{2P_t}{\pi Dt} \quad (1.1)$$

where P_t is the peak vertical load and D and t are the diameter and the thickness of the disc, respectively.

The conventional Brazilian split test methods include flat loading platens, flat platens with cushion, flat loading platens with small diameter rods as well as curved loading jaws and others (Perras and Diederichs, 2014). Because the vertical load is applied in a narrow range of the disc using the above methods, crack initiation may occur at the position of the loading points, which may produce inaccurate results (Fairhurst, 1964; Mellor and Hawkes, 1971). To determine the tensile strength of brittle materials more precisely, discs with different shapes (Fowell, 1995; Lambert and Ross, 2000; Tong *et al.*, 2007; Dai *et al.*, 2010; Keles and Tutluoglu, 2011; Cai, 2013; Surendra, 2013; Hua *et al.*, 2015; Riazi *et al.*, 2015; Lin *et al.*, 2015, 2016) have been

proposed, including ring specimens that are placed under a pair of radial loads (Hobbs, 1964; Hudson, 1969). Significant stress and steep stress gradients appear in the specimens, which causes initiation and propagation of the resulting cracks (Wang *et al.*, 2014). Fischer *et al.* (1995) and Hossain *et al.* (2006) studied the features of both stress development and failure of discs with a central hole. Steen *et al.* (2005) investigated how the fracture patterns of discs are controlled by the size of the hole based on their horizontal diameters. A calculation of the tensile strength for discs with a hole located in their vertical or horizontal diameters was given by Hobbs (1965).

In this study, laboratory Brazilian split tests and numerical modeling using the finite element method (FEM) are conducted on three types of holed discs: discs with a central hole (C-specimen), discs containing a horizontally eccentric hole (EH-specimen) and discs with a rotationally eccentric hole (ER-specimen), which have rarely been studied in previous research. Based on the laboratory tests, the peak load and failure pattern of the discs are investigated. Moreover, the horizontal stress field in addition to the position and value of the maximum horizontal tensile stress are analyzed using the FEM. The simulated results further demonstrate the influence of the diameters and positions of the holes on the peak load and failure pattern of holed Brazilian disc specimens.

2. Test program

2.1. Specimen preparation

The tested sandstone specimens are light gray in color with some dark spots and lack visible cracks, holes and other defects. The average bulk density is 2.36 g/cm^3 . The dimensions of the disc specimens obtained from a sandstone block are 30 mm in thickness T and 50 mm in diameter D after coring and grinding. In addition, an inner round hole with a smooth wall was drilled in the disc using high-strength ceramic bits. Three types of holed specimens – C-specimens, EH-specimens and ER-specimens – were manufactured, as illustrated in Fig. 1. In the figure, d is the diameter of the hole, b is the eccentricity (the distance between the two centers of the hole and disc), and α is the angle between the horizontal line and the line segment connecting the centers of the disc and the hole. To recognize the two centers, two referenced lines are marked on the disc specimens. As shown in Fig. 1, VL is the vertical diameter line and the loading direction, and IL is a horizontal radial line for the C-specimens and an inclined radial line passing through the centers of the hole and the disc for the ER-specimens.

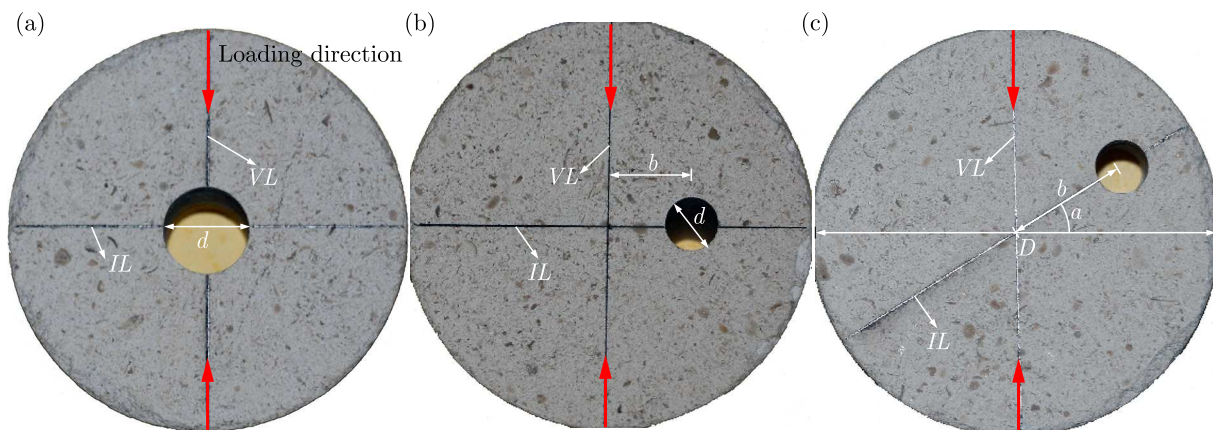


Fig. 1. Disc specimens containing a round hole: (a) C-specimen ($\alpha = 0^\circ$, $b = 0$ and d is variable); (b) EH-specimen ($\alpha = 0^\circ$, $d = 6 \text{ mm}$ and b is variable); (c) ER-specimen ($b = 15 \text{ mm}$, $d = 6 \text{ mm}$ and α is variable)

2.2. Experimental scheme

Radial loading tests were conducted to investigate the strength and failure pattern of the discs with a hole of different diameters, eccentricities and inclination angles. The tests were performed using a DNS100 servo-controlled machine with the maximum loading capacity of 100 kN. The displacement-control mode with a constant loading rate of 3.33×10^{-4} mm/s was adopted. During the tests, a vertical load and a vertical displacement were recorded automatically by the test system. The geometry and location of the hole in the disc specimens are listed in Table 1, where two repeated tests for each specimen were conducted. As indicated in the table, the hole diameter d of the C-specimen (numbered Z1-1 to Z5-2) ranged from 4 mm to 12 mm with an interval of 2 mm; the eccentricity b ranged from 0 mm to 20 mm with an interval of 5 mm in the EH-specimens (numbered P1-1 to P4-2); and the ER-specimen (numbered Q1-1 to Q6-2) had an inclination angle α of 0° to 90° with a 15° interval. The three intact specimens (referred to as without a hole) were numbered W1 to W3, separately. Based on the study by Mellor and Hawkes (1971), the calculated strength from the tests on the ring specimens was much higher than that by a direct tensile test when the hole diameter was very small. Thus, the same hole diameter of 6 mm for the EH-specimens and ER-specimens was considered moderate. The eccentricity was fixed at 15 mm in the ER-specimens.

Table 1. Geometry and location of the hole in the disc specimens

Specimen*	d [mm]	b [mm]	α [$^\circ$]	Specimen*	d [mm]	b [mm]	α [$^\circ$]	Specimen*	d [mm]	b [mm]	α [$^\circ$]
Z1-1	4	0	–	P1-2	6	5	0	Q3-1	6	15	45
Z1-2	4	0	–	P2-1	6	10	0	Q3-2	6	15	45
Z2-1	6	0	–	P2-2	6	10	0	Q4-1	6	15	60
Z2-2	6	0	–	P3-1	6	15	0	Q4-2	6	15	60
Z3-1	8	0	–	P3-2	6	15	0	Q5-1	6	15	75
Z3-2	8	0	–	P4-1	6	20	0	Q5-2	6	15	75
Z4-1	10	0	–	P4-2	6	20	0	Q6-1	6	15	90
Z4-2	10	0	–	Q1-1	6	15	15	Q6-2	6	15	90
Z5-1	12	0	–	Q1-2	6	15	15	W1	Intact specimens		
Z5-2	12	0	–	Q2-1	6	15	30	W2			
P1-1	6	5	0	Q2-2	6	15	30	W3			

* Z represents the specimen with a central hole;

P represents the specimen with a hole of varying eccentricities;

Q represents the specimen with a hole of varying inclination angle;

W represents intact specimens

3. Experimental results

3.1. Deformation and failure of the intact sample

Figure 2 gives the vertical load-displacement curves of the three intact specimens. Overall, the three load-displacement curves of the intact discs are similar in strength and deformation. The shape of the curves is slightly concave-up at the beginning stage due to gradual densification of the sample with micro defects. With an increase in the vertical load, the load-displacement curves gradually develop into the linear elasticity segments. The curves are characterized by a sudden force drop to zero, suggesting brittle failure immediately after the peak load.

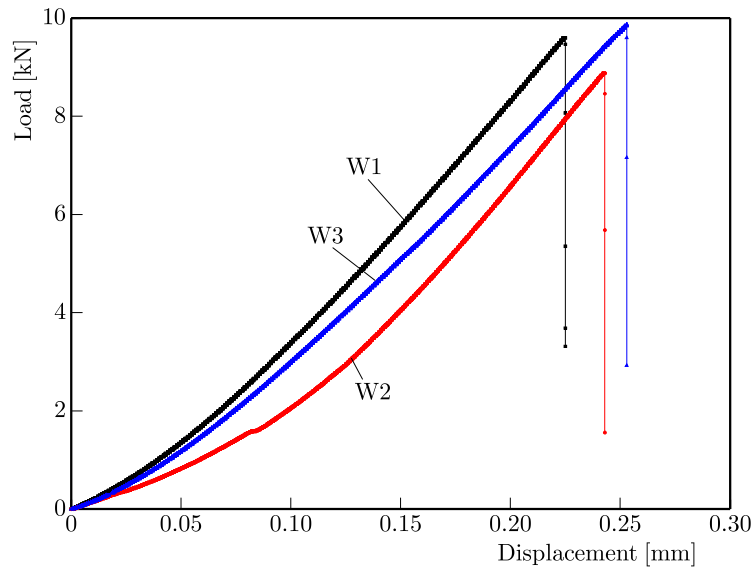


Fig. 2. Load-displacement curves of intact disc specimens

The peak loads of the three intact specimens are 9.60 kN, 8.88 kN and 9.87 kN. The corresponding tensile strengths calculated by Eq. (1.1) are 4.89 MPa, 4.52 MPa and 5.02 MPa, respectively. The dispersion coefficient (ratio of standard deviation to the mean) of the tensile strengths is only 4.4%, implying that the tested sandstone samples exhibited good homogeneity. The fractures of the intact specimens occurred only in the vertical direction through the approximate centers of the discs, as shown in Fig. 3. Additionally, distinctly opening fractures at the top or bottom of the specimens such as in W2 and W3 are observed. Hence, the center initiation, which is the basic hypothesis in the Brazilian split test, may be doubtful for the intact disc owing to the end effect observed in this study.

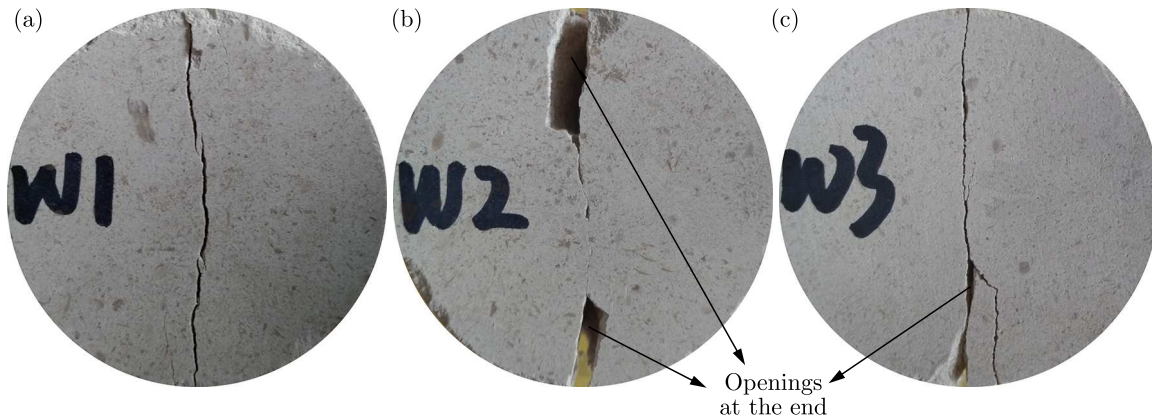


Fig. 3. Failure of intact specimens: (a) specimen W1; (b) specimen W2; (c) specimen W3

3.2. Strength of the holed disc

The relationship between the peak load and the ratio of the diameter of the center hole to that of the disc d/D for C-specimens is presented in Fig. 4a. The results indicate that with the increasing diameter d of the center hole, the peak load of the discs decreases gradually, especially when the ratio d/D is less than 0.12. When the ratio d/D is greater than 0.2, the peak load decreases rapidly. However, for the ratio d/D in the range of 0.12 to 0.2, the peak load has only a small reduction from 4.32 kN to 4.08 kN (the average values of two of the same specimens, the

same below) with a decrease of approximately 5.55%. With an increase in the diameter ratio d/D ranging from 0.08 to 0.12 and 0.2 to 0.24, the peak load decreases by 18.48% and 33.09%, respectively.

The relationship of the peak load versus the eccentricity for EH-specimens is presented in Fig. 4b. The curve demonstrates that the peak load of EH-specimens generally increases with the increasing eccentricity when $2b/D$ is less than 0.4. However, the peak load reaches a plateau after the ratio $2b/D$ exceeds 0.4. As a result, for the discs with a horizontally eccentric hole, when the eccentricity is larger than 0.4 times the radius (50 mm) of discs, the hole has little or even no effect on the peak load.

With an increased inclination angle α for the ER-specimen, the peak load exhibits first a slight increase and then gradually decreases, with a maximum of 9.02 kN and a minimum of 4.67 kN observed at $\alpha = 15^\circ$ and 90° separately, as shown in Fig. 4c. The average peak load of the ER-specimens with an inclination angle of 15° is 9.02 kN, which is close to 9.45 kN of the intact specimens. Thus, the tensile stress around the hole has the maximum value when the hole is located on the vertical diameter of the disc while the hole with an inclination angle less than 45° has little effect on the peak load of the discs.

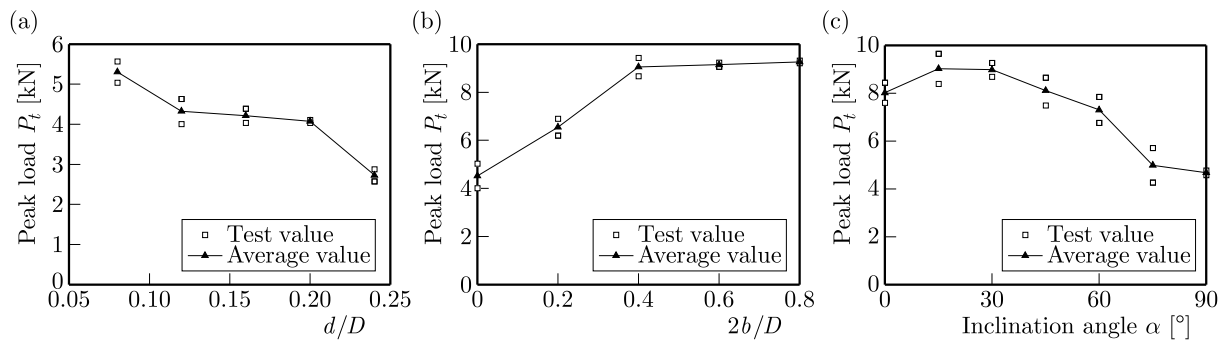


Fig. 4. Peak load of the disc containing a hole versus (a) the ratio of d/D ($\alpha = 0^\circ$ and $b = 0$ mm); (b) the ratio of $2b/D$ ($\alpha = 0^\circ$ and $d = 6$ mm) and (c) the inclination angle α ($b = 15$ mm and $d = 6$ mm)

3.3. Failure of the holed disc

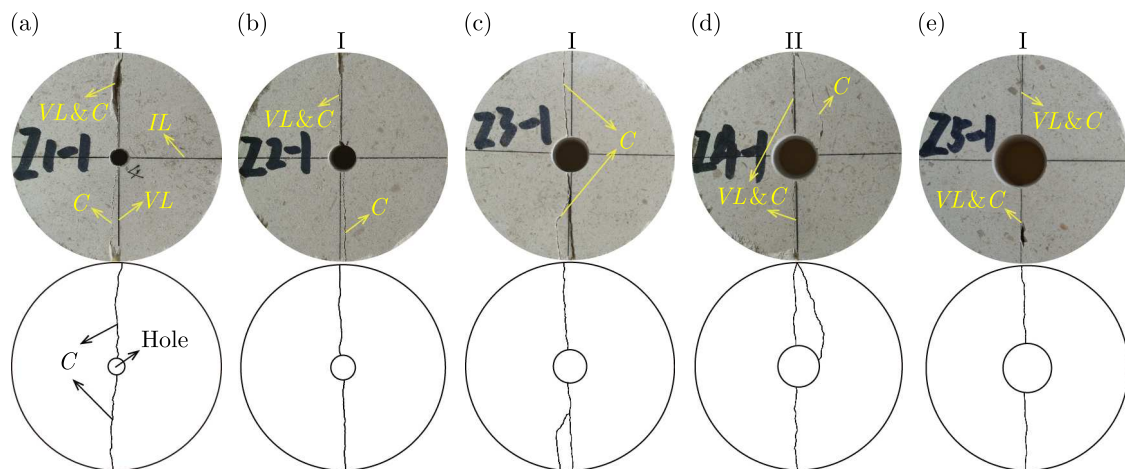


Fig. 5. Failure patterns of C-specimens ($\alpha = 0^\circ$ and $b = 0$): (a) $d/D = 0.08$; (b) $d/D = 0.12$; (c) $d/D = 0.16$; (d) $d/D = 0.20$; (e) $d/D = 0.24$. Note: above is the failure pattern and below is the sketch; VL and IL represent marked/referenced lines; C denotes a crack; I and II denote failure pattern I and failure pattern II, respectively

Figures 5 and 6 show the failure patterns of the holed specimens, which can be classified into five types, illustrated in Table 2.

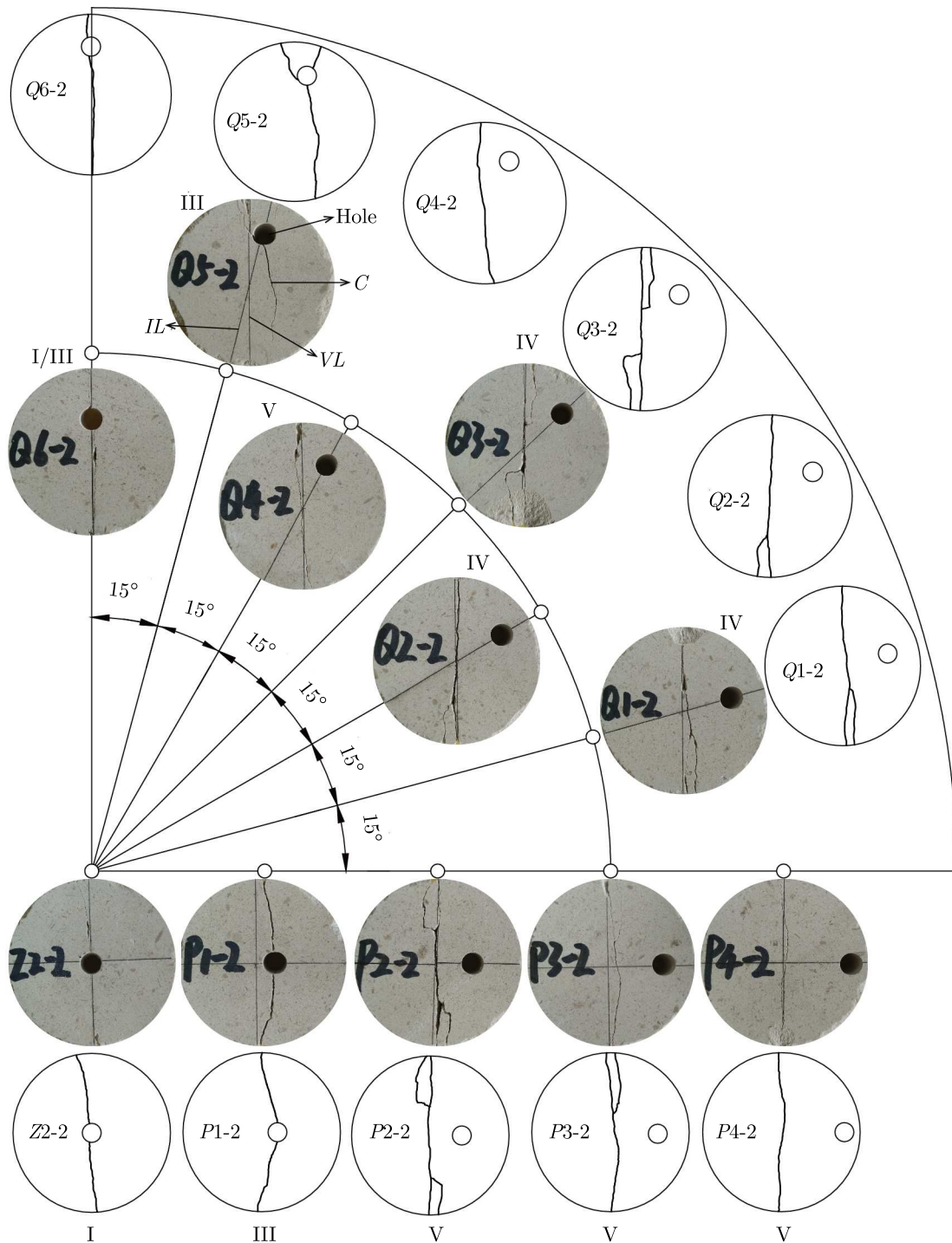
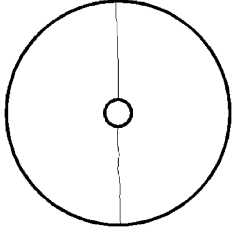
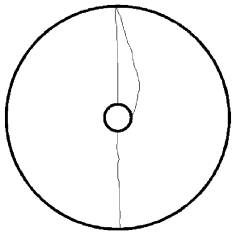
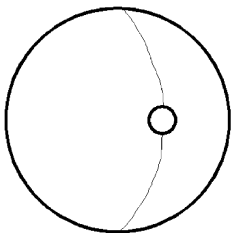
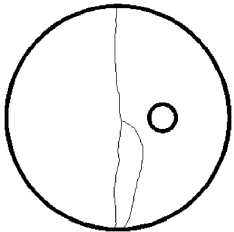
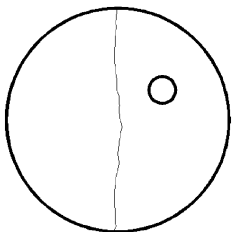


Fig. 6. Failure patterns of EH-specimens ($\alpha = 0^\circ$ and $d = 6$ mm) and ER-specimens ($b = 15$ mm and $d = 6$ mm). Note: I, III, IV and V represent failure patterns I, III, IV and V, respectively

The characteristics of each failure pattern are described as follows.

Failure pattern I: Two cracks propagate in a straight manner in the load direction. The straight cracks connect the points at the top and bottom of the hole with the upper and lower loading points. This failure pattern is found only when the hole is located at the vertical diameter of the discs, e.g., the C-specimens except for the specimen of Z4-1 and the

Table 2. Failure patterns of the holed discs

Failure pattern	Specimens	Characteristics
I	 <p>Z1-1, Z1-2 (C-specimen, $d = 4$ mm) Z2-1, Z2-2 (C-specimen, $d = 6$ mm) Z3-1, Z3-2 (C-specimen, $d = 8$ mm) Z5-1, Z5-2 (C-specimen, $d = 12$ mm) Q6-1, Q6-2 (ER-specimen, $\alpha = 90^\circ$)</p>	<ul style="list-style-type: none"> • Two straight cracks • Cracking along the load line • Initiated from and propagated through the top and the bottom of the hole
II	 <p>Z4-1, Z4-2 (C-specimen, $d = 10$ mm)</p>	<ul style="list-style-type: none"> • Two straight cracks and an arc crack • The straight cracks are similar to the two in pattern I • The arc crack passes through a loading point at the left or right side of the hole
III	 <p>P1-1, P1-2 (EH-specimen, $b = 5$ mm) Q4-1 (ER-specimen, $\alpha = 60^\circ$) Q5-1, Q5-2 (ER-specimen, $\alpha = 75^\circ$) Q6-1, Q6-2 (ER-specimen, $\alpha = 90^\circ$)</p>	<ul style="list-style-type: none"> • An arc ipsilateral crack pair • The endpoints of the arc cracks are the top or bottom of the hole and the position close to/at one of the load points • Two arc cracks have an approximately top-bottom symmetric distribution with the axis of the horizontal diameter
IV	 <p>P2-1, P2-2 (EH-specimen, $b = 10$ mm) P3-1, P3-2 (EH-specimen, $b = 15$ mm) Q1-1, Q1-2 (ER-specimen, $\alpha = 15^\circ$) Q2-1, Q2-2 (ER-specimen, $\alpha = 30^\circ$) Q3-1, Q3-2 (ER-specimen, $\alpha = 45^\circ$)</p>	<ul style="list-style-type: none"> • An approximately straight crack and an arc crack • The approximately straight crack propagates in the loading direction • The arc crack passes through the loading point and points to the hole, then turns to the line of loading and coalesces at a point that lies on the straight crack
V	 <p>P4-1, P4-2 (EH-specimen, $b = 20$ mm) Q4-2 (ER-specimen, $\alpha = 60^\circ$)</p>	<ul style="list-style-type: none"> • An approximately straight crack

ER-specimens with an inclination angle of 90° (namely Q6-1 and Q6-2). Notably, there is no conspicuous opening failure at the specimen boundary adjacent to loading points, which might suggest that the straight cracks initiated at the wall of the hole and propagated towards the loading points along the vertical diameter direction.

Failure pattern II: Three cracks including two straight cracks and one arc crack developed. This failure pattern appears only in the C-specimens with a hole diameter of 10 mm, whereas pattern I occurred in all other C-specimens. The two straight cracks are similar to the features of pattern I in formation, and the arc crack connected one of the load points and the left/right side of the hole.

Failure pattern III: An arc ipsilateral crack pair developed at the upper and lower halves of the specimen separately. The two arc cracks exhibited an approximately up-down symmetric distribution with the axis of the horizontal diameter. The endpoints of the arc cracks were the top or bottom of the hole boundary and the position close to/at one of the load points. This failure pattern occurred in the EH-specimens of $2b/D = 0.2$ and the ER-specimens of $\alpha \geq 60^\circ$. In addition, one of the ER-specimens with an α of 60° was also fractured with that pattern, but the failure of the other ER-specimens exhibited failure pattern IV (described in the next section). Because of the special position of the hole in specimens Q6-1 and Q6-2 (ER-specimens with α of 90°), their failure patterns are classified into failure pattern III and pattern I.

Failure pattern IV: This failure pattern is similar to the failure features of the intact specimens. The main crack (approximately straight) grew in the vertical diameter of the disc, and a secondary arc crack developed at the position adjacent to the loading point. The arc crack intersected with the approximately straight crack, and one of the endpoints of the arc crack was one of the loading points. That failure pattern primarily occurred in the EH-specimens with $2b/D = 0.4$ and 0.6 and the ER-specimens of $\alpha \leq 45^\circ$.

Failure pattern V: For the EH-specimen with the eccentricity b of 20 mm (where the ratio of $2b/D = 0.8$), only an approximately straight crack was produced along the vertical diameter direction, which was similar to the intact specimen W1. In addition, the specimen numbered Q4-2 with α of 60° also broke with that failure pattern.

Based on the above observations, the following can be concluded:

- The failure of all the C-specimens occurred under failure pattern I except for the specimens with a hole diameter of 10 mm, which followed pattern II.
- Three failure patterns appeared in the EH-specimens with different eccentricity b : when the disc had an eccentricity of 0 (i.e., C-specimen), pattern I occurred. With an increased eccentricity, the failure pattern developed into pattern III ($b = 5$ mm) and pattern IV ($b = 10$ mm and 15 mm). When the eccentricity b was 20 mm, failure pattern V occurred.
- The ER-specimens had four failure patterns changing from pattern IV ($\alpha = 10^\circ, 30^\circ$ and 45°) to pattern V ($\alpha = 60^\circ$), pattern III ($\alpha = 60^\circ, 75^\circ$ and 90°) and pattern I ($\alpha = 90^\circ$) with the increasing inclination angle α .

4. Numerical modeling to determine the location of crack initiation

According to the test results, the peak loads and the failure patterns of the holed discs are affected by the parameters of the hole diameter d , the eccentricity b , and the inclination angle α . The characteristics of the crack initiation in Brazilian discs are the basis for studies of fracture mechanical properties. Based on the basic theory of fracture mechanics, the potential location

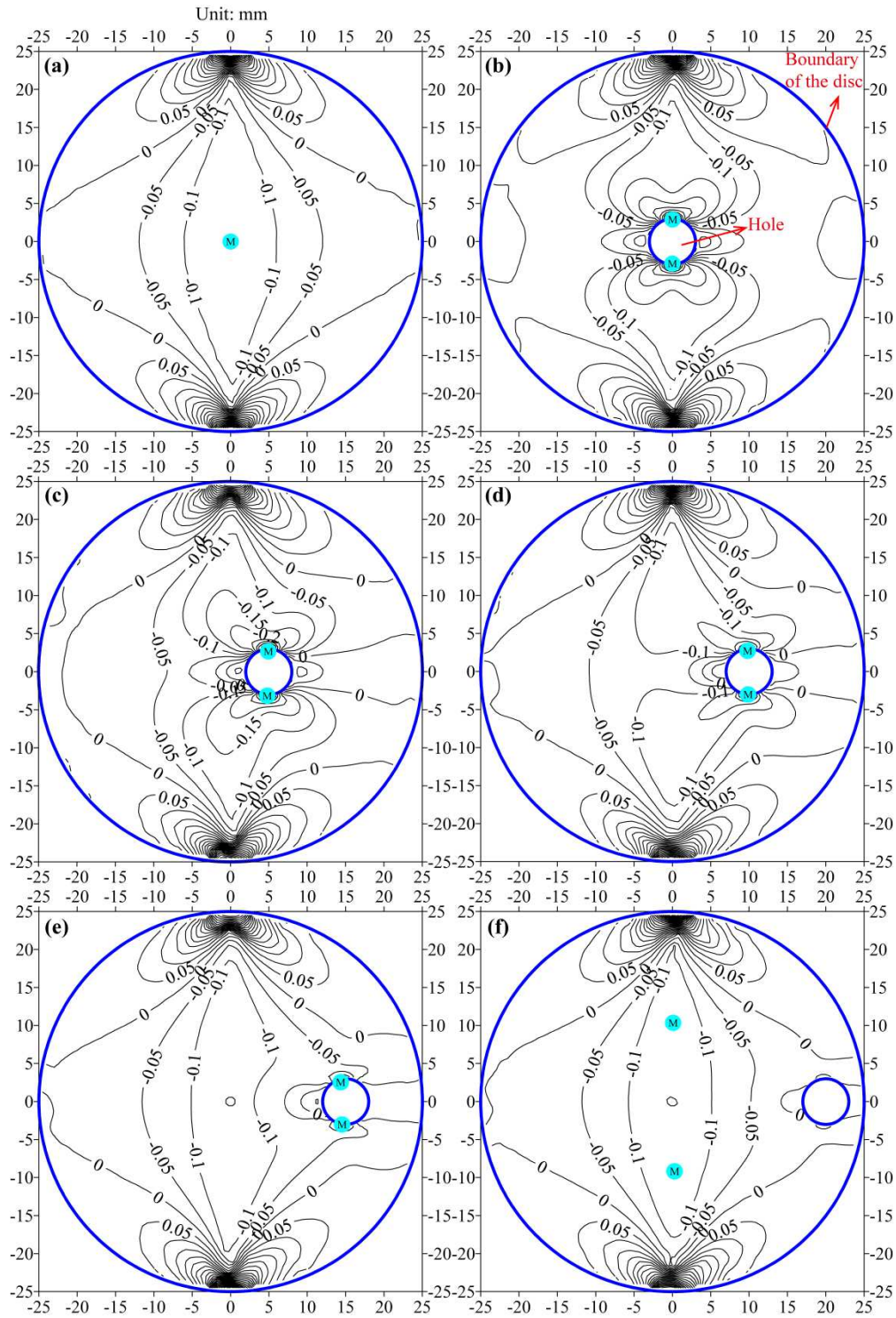


Fig. 7. Contour plots of the horizontal stress (compressive stress is positive, and tensile stress is negative) of the (a) intact disc and EH-specimen with an eccentricity of (b) $b = 0$, (c) $2b/D = 0.2$, (d) $2b/D = 0.4$, (e) $2b/D = 0.6$, (f) $2b/D = 0.8$. Note: EH-specimens have the same hole diameter of 6 mm; (M) is the position of maximum tensile stress

of crack initiation in a disc specimen is where the tensile stress is maximal. Therefore, the finite element method (FEM) is used to analyze the distribution of the horizontal stress, particularly tensile stress in the holed disc specimens. The geometry of discs built in ANSYS was the same as for the experimental specimens, i.e., the hole diameter d of the C-specimen ranged from 4

to 12 mm with an interval of 2 mm, the eccentricity b ranged from 0 to 20 mm with an interval of 5 mm in the EH-specimens (hole diameter $d = 6$ mm) and the inclination angle α ranged from 0° to 90° with an interval of 15° for the ER-specimens. The 2D linear elastic constitutive model was adopted in ANSYS to reveal the distribution of stress in the holed discs. In accordance with the Brazilian split test method, a pair of balanced point loads of 10 kN was applied in the vertical diameter direction, which was approximately the peak load of the tested intact specimens. The linear-elastic model constructed for simulation had Poisson's ratio and Young's modulus of 0.25 and 5.12 GPa, respectively. Poisson's ratio and Young's modulus used here were the same as those of the rock samples measured by uniaxial compression test.

The contour plots of horizontal stress of the numerical simulations are illustrated in Figs. 7 and 8, where compressive stress is positive and tensile stress is negative, and the position of the maximum tensile stress is marked by a circled letter M. The variations in the maximum tensile stress with the diameter d of the center hole, the eccentricity b and the inclination angle α are presented in Fig. 9. Within the intact disc, the horizontal stress exhibits a symmetrical distribution with the vertical and horizontal diameter line of the disc as the axis of symmetry (Fig. 7a). At the positions adjacent to the load points, the horizontal stress shows compression. The tensile stress appears in other areas, especially at the center of the disc where a maximum value of 0.13 MPa is observed.

Within the C-specimen, except for the locations near the load points, most of other regions exhibit tensile stress, as shown in Fig. 7b. The contour of tensile stress exhibits an "8" shape, and the center of the "8" is located at the hole around which the maximum tensile stress is attained due to concentration of stress. The horizontal stress distributions are similar and only differ in values within the C-specimens. Thus, the horizontal stress of the C-specimen with a diameter of 6 mm is illustrated in Fig. 7b. As shown in Fig. 9a, as the ratio d/D is increased from 0.08 to 0.24, the maximum tensile stress exhibits a distinct increase from 0.69 to 0.95 MPa, an increase of approximately 37.68%. This explains the decrease in the peak load of the C-specimen with an increased diameter of the central hole (See Fig. 4a).

The horizontal stress and the position of the maximum tensile stress in the EH-specimens change gradually with the eccentricity, as shown in Figs. 7 and 9b, respectively. However, the maximum tensile stress always appears at the boundary of the hole, except for the EH-specimen with the ratio $2b/D$ of 0.8 ($b = 20$ mm), for which the maximum is at a point located at the vertical load line and off the center of the disc (Fig. 7f). That explains why the failure pattern of the EH-specimen evolves from a straight crack to an arc crack then back to a straight crack again with an increased eccentricity b . The maximum tensile stress of the EH-specimen decreases with the eccentricity, and when the ratio $2b/D$ is 0.8, the maximum is 0.13 MPa, which is equal to that of the intact disc. This finding agrees with the variation in the peak load presented in Fig. 4b, which exhibits a gradual increase tending toward the peak load of the intact disc. For the ER-specimens, the maximum tensile stresses are all observed at the boundary of the hole (Fig. 8). Only a negligible decrease of 0.41% is found when the inclination angle α increases from 0° to 15° , which explains why the peak load of the ER-specimens exhibits only a slight increase between the angle intervals presented in Fig. 4c.

An interesting characteristic of the horizontal stress in the holed discs from the FEM simulation is that almost all the locations of the maximum tensile stress are at the boundary of the hole except the EH-specimen with an eccentricity of 20 mm. In addition, the angle β defined in Fig. 10a is the deflection angle of the segment between the center of the hole and the point of crack initiation (namely maximum tensile stress, when there are two maximums the point refers to above that point) off the vertical radius line of the disc. The changes of the β with the eccentricity b and the inclination angle α are shown in Figs. 10b and 10c. When the ratio $2b/D$ is 0 or 0.2, the β is 0° , which means that the position of the maximum tensile stress is located at the boundary point of the vertical diameter of the hole. As the ratio $2b/D$ is increased from 0.4

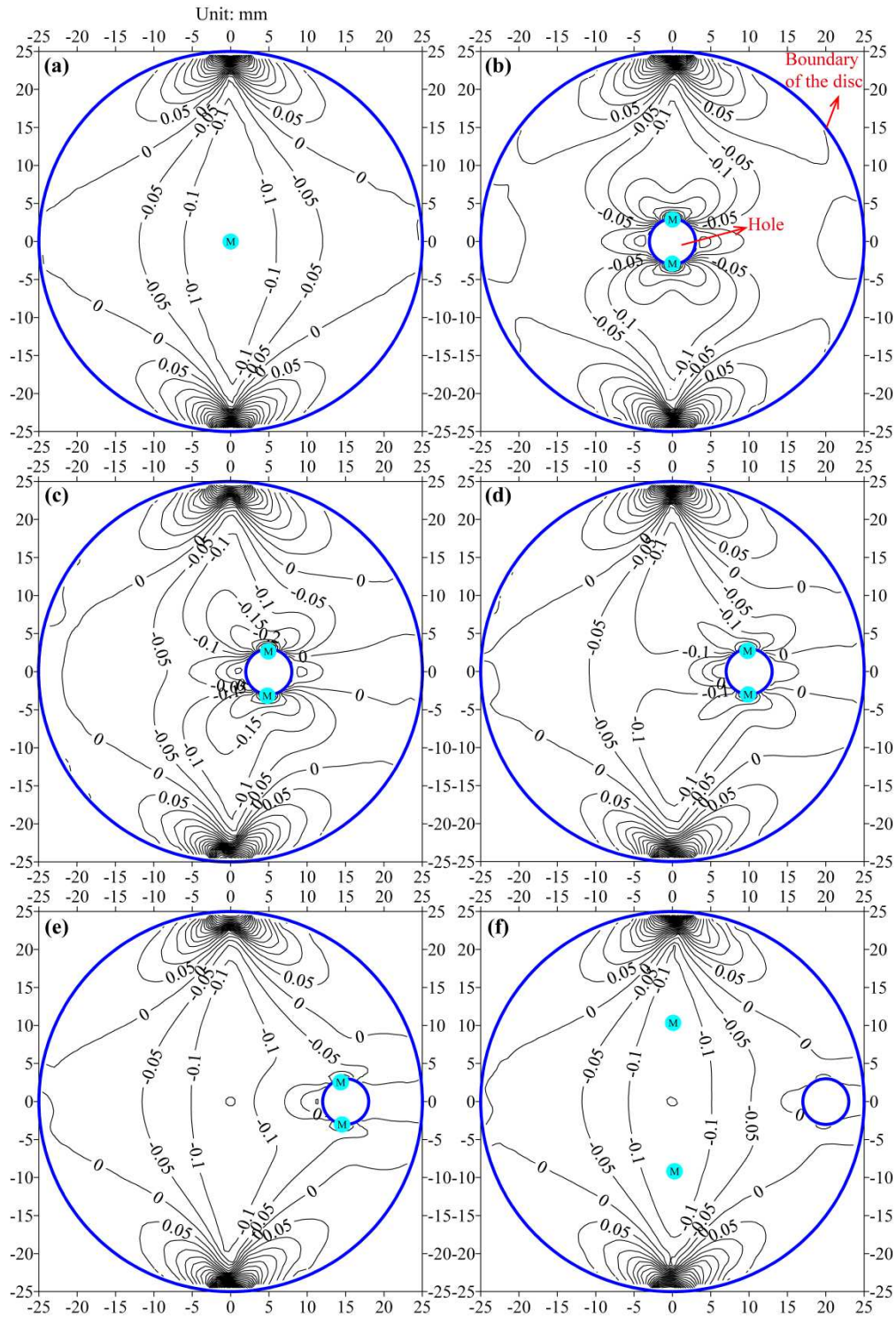


Fig. 8. Contour plots of the horizontal stress of the ER-specimens with inclination angles of (a) $\alpha = 15^\circ$, (b) $\alpha = 30^\circ$, (c) $\alpha = 45^\circ$, (d) $\alpha = 60^\circ$, (e) $\alpha = 75^\circ$, and (f) $\alpha = 90^\circ$; \textcircled{M} is the position of maximum tensile stress

to 0.6, the deflection angle β increases from 6.51° to 13.05° . When the ratio is 0.8, the position of the maximum tensile stress lies on the vertical load line, and the angle β increases to 63.89° .

For the ER-specimens (Fig. 10c), the angle β increases after first decreasing and then decreases again with an increased inclination angle α . The maximum β is approximately 25° - 26° in the cases of α ranging from 45° to 60° . The angle β achieves a minimum of 0° when $\alpha = 90^\circ$.

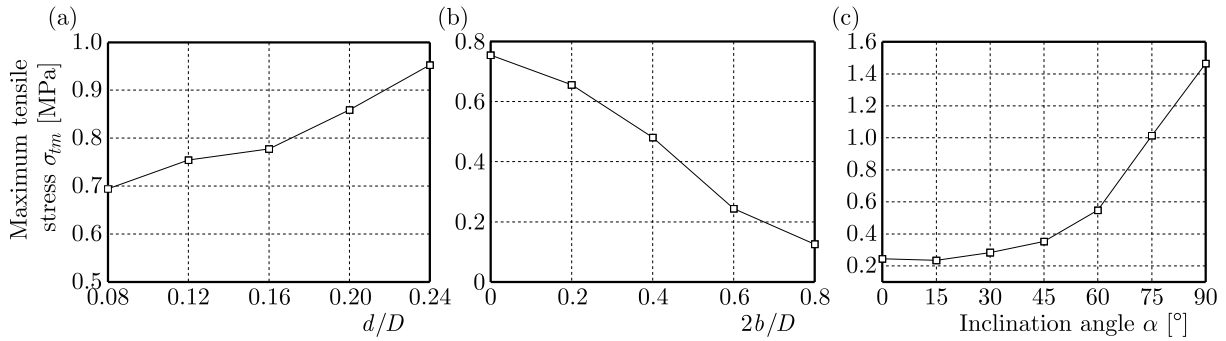


Fig. 9. Variation in the maximum tensile stress (absolute value) of (a) C-specimen, (b) EH-specimen, (c) ER-specimen

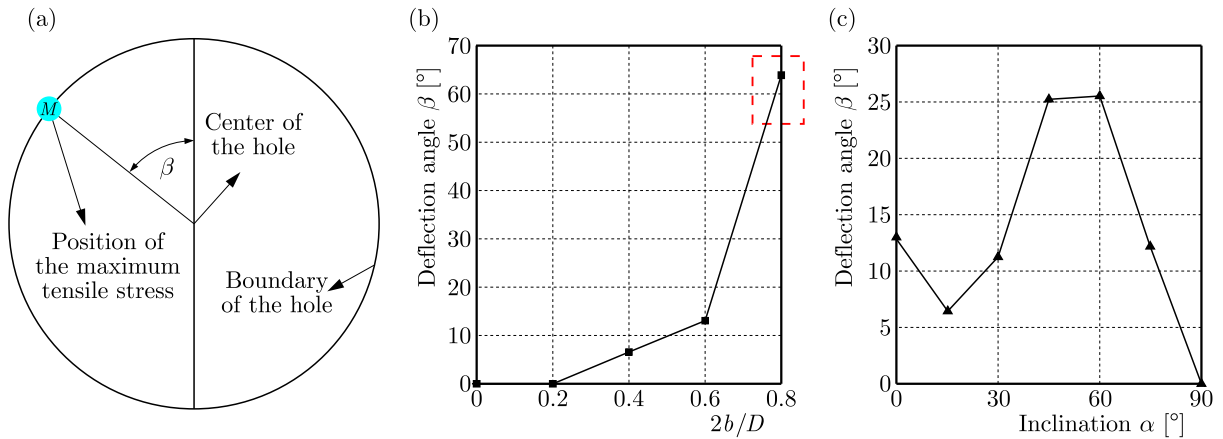


Fig. 10. (a) Sketch of the position of the maximum tensile stress at the boundary of the hole.

Note: β is the deflection angle of the segment between the center of the hole and the point of the maximum tensile stress off the upper vertical radius. Curves of the deflection angle β versus the ratio of (b) $2b/D$ and (c) the inclination angle α

5. Conclusions

- The three parameters of the holes – diameter d , eccentricity b and the inclination angle α – have significant influences on the peak load and the failure pattern of the holed discs. The peak load decreases with the increasing diameter of the central hole. The peak load of the EH-specimens gradually increases to that of intact specimens with the increasing eccentricity b . For the ER-specimen, the peak load exhibits first a slight increase and then a distinct decrease with the increasing inclination angle α (the maximum is observed at $\alpha = 15^\circ$ and 30° , and the minimum is found at $\alpha = 90^\circ$).
- When the holes are located along the vertical diameter of the discs, i.e., the C-specimens and the ER-specimens with an inclination angle α of 90° , the failure pattern generally exhibits two straight cracks between the top and bottom sides of the hole and load points. For the EH-specimens, with the increasing eccentricity b , the failure is characterized by the pattern changing from two straight cracks to an arc crack and then a straight crack again. The failure of the ER-specimens is similar to that of the EH-specimens, but the ends of the discs do not evolve into a straight crack.
- The position and value of the maximum tensile stress changes with the eccentricity b and the inclination angle α . All the positions are located on the boundaries of the holes. There is a deflection angle β between the upper vertical radius of the holes and the connecting line of the position of the maximum tensile stress and the center of the holes. The angle β increases as the ratio $2b/d$ increases. With the increasing inclination angle α , the angle β

first decreases and then increases again after an obvious increase when the angle α ranges from 15° to 60° . When the hole lies at the center of the disc, the angle β has a constant value of 0° . Variations in the stress field and the position of the maximum horizontal tensile stress result in different failure patterns.

Acknowledgments

This work has been supported by the Fundamental Research Funds for the Central Universities (No. 106112017CDJXSYY002), the Graduate Research and Innovation Foundation of Chongqing, China (No. CYB17043), the National Natural Science Foundation of China (No. 41472245, 41672300), the Scientific Research Foundation of State Key Lab. of Coal Mine Disaster Dynamics and Control (No. 2011DA105287-MS201502).

References

1. CAI M., 2013: Fracture initiation and propagation in a Brazilian disc with a plane interface: a numerical study, *Rock Mechanics and Rock Engineering*, **46**, 289-302
2. DAI F., CHEN R., IQBAL M.J., XIA K., 2010: Dynamic cracked chevron notched Brazilian disc method for measuring rock fracture parameters, *International Journal of Rock Mechanics and Mining Sciences*, **47**, 606-613
3. FAIRHURST C., 1964: On the validity of the 'Brazilian' test for brittle materials, *International Journal of Rock Mechanics and Mining Science and Geomechanics Abstracts*, **1**, 535-546
4. FISCHER M.P., ALLEY R.B., ENGELDER T., 1995, Fracture toughness of ice and firn determined from the modified ring test, *Journal of Glaciology*, **41**, 383-394
5. FOWELL R.J., 1995, Suggested method for determining mode I fracture toughness using Cracked Chevron Notched Brazilian Disc (CCNBD) specimens, *International Journal of Rock Mechanics and Mining Sciences and Geomechanics Abstracts*, **32**, 57-64
6. HOBBS D.W., 1964, The tensile strength of rocks, *International Journal of Rock Mechanics and Mining Science and Geomechanics Abstracts*, **1**, 385-396
7. HOBBS D.W., 1965, An assessment of a technique for determining the tensile strength of rock, *British Journal of Applied Physics*, **16**, 259-268
8. HOSSAIN A.B., WEISS J., 2006, The role of specimen geometry and boundary conditions on stress development and cracking in the restrained ring test, *Cement and Concrete Research*, **36**, 189-199
9. HUA W., LI Y., DONG S., LI N., WANG Q., 2015, T-stress for a centrally cracked Brazilian disk under confining pressure, *Engineering Fracture Mechanics*, **149**, 37-44
10. HUANG D., ZHU T.T., 2018, Experimental and numerical study on the strength and hybrid fracture of sandstone under tension-shear stress, *Engineering Fracture Mechanics*, **200**, 387-400
11. HUDSON J.A., 1969, Tensile strength and the ring test, *International Journal of Rock Mechanics and Mining Science and Geomechanics Abstracts*, **6**, 91-97
12. ISRM, 1978, Suggested methods for determining tensile strength of rock materials, *International Journal of Rock Mechanics and Mining Science and Geomechanics Abstracts*, **15**, 99-103
13. KELES C., TUTLUOGLU L., 2011, Investigation of proper specimen geometry for mode I fracture toughness testing with flattened Brazilian disc method, *International Journal of Fracture*, **169**, 61-75
14. LAMBERT D.E., ROSS C.A., 2000, Strain rate effects on dynamic fracture and strength, *International Journal of Impact Engineering*, **24**, 985-998
15. LIN H., XIONG W., XIONG Z., GONG F., 2015, Three-dimensional effects in a flattened Brazilian disk test, *International Journal of Rock Mechanics and Mining Sciences*, **74**, 10-14

16. LIN H., XIONG W., YAN Q., 2016, Modified formula for the tensile strength as obtained by the flattened Brazilian disk test, *Rock Mechanics and Rock Engineering*, **49**, 1-8
17. MELLOR M., HAWKES I., 1971, Measurement of tensile strength by diametral compression of discs and annuli, *Engineering Geology*, **5**, 173-225
18. PERRAS M.A., DIEDERICHS M.S., 2014, A review of the tensile strength of rock, concepts and testing, *Geotechnical and Geological Engineering*, **32**, 525-546
19. RIAZI R., TORABI A.R., AMININEJAD S., SABOUR M.H., 2015, Combined tension-shear fracture analysis of V-notches with end holes, *Acta Mechanica*, **226**, 3717-3736
20. SHANG Y., PARK H.D., YUAN G., SUN Y., GAO Q., 2008, From in situ stress and discontinuities to the strength of granites, comparison and case study, *Geosciences Journal*, **12**, 361-372
21. SONG I., SUH M., WON K.S., HAIMSON B., 2001, A laboratory study of hydraulic fracturing breakdown pressure in tablerock sandstone, *Geosciences Journal*, **5**, 263-271
22. STEEN B.D., VERVOORT A., NAPIER J.L., 2005, Observed and simulated fracture pattern in diametrically loaded discs of rock material, *International Journal of Fracture*, **131**, 35-52
23. SURENDRA K.N., SIMHA K.Y., 2013, Design and analysis of novel compression fracture specimen with constant form factor, Edge Cracked Semicircular Disk, ECSD, *Engineering Fracture Mechanics*, **102**, 235-248
24. TONG J., WONG K.Y., LUPTON C., 2007, Determination of interfacial fracture toughness of bone-cement interface using sandwich Brazilian disks, *Engineering Fracture Mechanics*, **74**, 1904-1916
25. WANG S.Y., SLOAN S.W., TANG C.A., 2014, Three-dimensional numerical investigations of the failure mechanism of a rock disc with a central or eccentric hole, *Rock Mechanics and Rock Engineering*, **47**, 2117-2137
26. ZHANG W., GAO L., JIAO X., YU J., SU X., DU S., 2014, Occurrence assessment of earth fissure based on genetic algorithms and artificial neural networks in Su-Xi-Chang land subsidence area, China, *Geosciences Journal*, **18**, 485-493

Manuscript received November 4, 2017; accepted for print August 1, 2018

FREE VIBRATIONS SPECTRUM OF PERIODICALLY INHOMOGENEOUS RAYLEIGH BEAMS USING THE TOLERANCE AVERAGING TECHNIQUE

MARCIN ŚWIĄTEK, ŁUKASZ DOMAGALSKI, JAROSŁAW JĘDRYSIAK

Lodz University of Technology, Department of Structural Mechanics, Łódź, Poland

e-mail: marcin.swiatek@dokt.p.lodz.pl; lukasz.domagalski@p.lodz.pl; jarek@p.lodz.pl

In this paper, linear-elastic Rayleigh beams with a periodic structure are considered. Dynamics of such beams is described by partial differential equations with non-continuous highly oscillating coefficients. The analysis of dynamic problems using the aforementioned equations is very often problematic to perform. Thus, other simplified models of Rayleigh beams are proposed. Some of these models are based on the concept of the effective stiffness. Among them, one can distinguish the theory of asymptotic homogenization. However, in these models, the size of the mesostructure parameter (the size of a periodicity cell) is often neglected. Therefore, a non-asymptotic averaged model of the periodic beam is introduced, called the tolerance model, which is derived by applying the tolerance averaging technique (TA). The obtained tolerance model equations have constant coefficients, and in contrast to other averaged models, some of them depend on the size of the periodicity cell.

Keywords: periodicity cell, Rayleigh beam, tolerance averaging technique

1. Preface

Beams are the simplest representations of periodic structures. Numerous examples of engineering applications, for instance in acoustic isolations, are the main reason for interest in such objects. In such beams, one can distinguish a small repetitive element called the periodicity cell. Periodic objects can represent approximate models of some complex systems.

Propagation of the elastic wave and linear vibrations in periodic beams are considered in many papers. Vibration band gaps were investigated by Xiang and Shi (2009) by the differential quadrature method. A comprehensive research on inhomogeneous beams vibrations was presented by Hajianmaleki and Qatu (2013). The transfer matrix method, adapted in analysis of flexural wave propagation in a beam on an elastic foundation and in investigating natural frequencies of non-uniform beams, can be found in Yu *et al.* (2012) and Xu *et al.* (2016), respectively. Wave propagation in beams with periodically varying stiffness is considered in Chen (2013) by the use of the multireflection method. In this paper, linear-elastic Rayleigh beams with a periodic structure are considered. Dynamics of such beams is described by partial differential equations with non-continuous highly oscillating coefficients. The analysis of dynamic problems using the aforementioned equations is very often problematic to perform. Thus, other simplified models of Rayleigh beams are proposed. Some of these models are based on the concept of the effective stiffness. Among them, one can distinguish the theory of asymptotic homogenization introduced in works by Kohn and Vogelius (1984), Papanicolau *et al.* (1978), Bakhvalov and Panasenko (1989), Sánchez-Palencia (1980) and Zhikov *et al.* (1994). The microperiodic beam equilibrium equations in frames of the homogenization theory were studied by Kolpakov (1991, 1998, 1999). However, in governing equations of these models, the size of the mesostructure parameter (the size of the periodicity cell) is often neglected. Therefore, a non-asymptotic averaged model of the periodic beam is introduced. This model is called the tolerance model and is

derived by applying the tolerance modelling technique, c.f. Woźniak *et al.* (2008), Awrejcewicz (2010), Woźniak and Wierzbicki (2000). The obtained tolerance model equations have constant coefficients and, in contrast to other averaged models, some of them depend on the size of the periodicity cell. The proposed method can be adopted to any differential equations with highly oscillating coefficients. The suggested approach, in contrast to the asymptotic homogenization, enables analysis of the mesostructure size. The method found numerous applications in structural mechanics. Macro-dynamics of microperiodic elastic beams was analysed by Mazur-Śniady (1993). Geometrically nonlinear vibrations of slender mesoperiodic beams were investigated in the paper by Domagalski and Jędrzyński (2016). The method was widely applied in the analysis of microstructured plates: thin plates with an elastic periodic foundation, Jędrzyński (2003), honeycomb lattice-type plates, Cielecka and Jędrzyński (2006), geometrically nonlinear thin plates, Domagalski and Jędrzyński (2015) and thin functionally graded plates, Jędrzyński (2013, 2014) and Kaźmierczak and Jędrzyński (2011). The TA technique was also applied in plates stability problems, cf. Jędrzyński (2000) and Jędrzyński and Michalak (2011). The tolerance averaging technique was also applied in the analysis of wavy type plates Michalak (2001) and many other engineering problems.

In this paper, a new tolerance model of a Rayleigh beam with weakly slowly-varying functions is proposed Tomczyk (2013), Jędrzyński (2017). Natural boundary conditions are also obtained and presented for a newly derived tolerance model. The presented tolerance model equations are used to determine natural vibration frequencies and natural forms of vibrations. Solutions obtained from the proposed model are compared with those corresponding to the finite element model. The paper is arranged as follows: basic assumptions of the inhomogeneous Rayleigh beams are presented in Section 2. The elemental and essential basis of the tolerance averaging technique are quoted in Section 3. The main model equations for examples considered in this paper are derived in Section 4. The numerical methods of solution, validation of the model, final results and comparison with the finite element method are presented in Section 5. Finally, the discussion and conclusions are given in Section 6.

2. Formulation of the problem

A beam made of a linear-elastic material, associated with a three-dimensional Cartesian coordinate system $Oxyz$ is considered. The beam axis is collinear with the x -axis of the local coordinate system. The problem can be treated as one-dimensional, so that there is defined a region $\Omega \equiv [0, L]$ occupied by the beam, where L is the beam length. The considered beam consists of many repetitive elements, called periodicity cells. The basic cell is defined as $\Delta \equiv [-l/2, l/2]$,

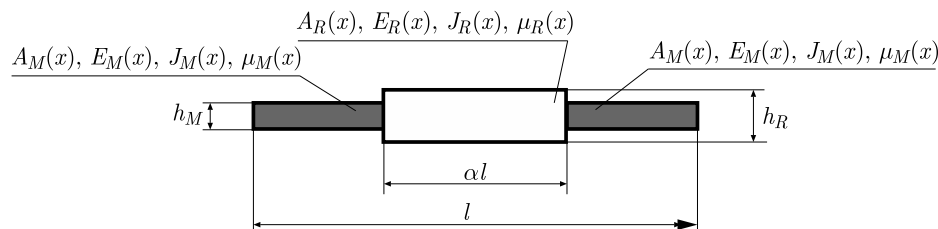


Fig. 1. A periodicity cell

where $l \ll L$ is length of the cell and is named the mesostructure parameter. The following denotations are introduced: lateral deflection $w = w(x, t)$, lateral stiffness $EJ = E(x)J(x)$, mass per unit length $\mu = \mu(x)$, rotational moment of inertia per unit length $\vartheta = \vartheta(x)$ and transverse load $q = q(x, t)$. Furthermore, let $\partial^k = \partial^k / \partial x^k$ be the k -th derivative of a function taken with respect to the x coordinate, and the overdot stands for the derivative taken with respect to time.

Thus, the strain and kinetic energy of the beam can be described in the following form

$$\mathcal{W} = \frac{1}{2}EJ\partial^2 w \partial^2 w \quad \mathcal{K} = \frac{1}{2}\mu\dot{w}\dot{w} + \frac{1}{2}\vartheta\partial\dot{w}\partial\dot{w} \quad (2.1)$$

The Lagrangian function $\mathcal{L} = \mathcal{L}(x, t, w, \dot{w}, \partial\dot{w}, \partial^2 w)$ is defined as

$$\mathcal{L} = \mathcal{W} - \mathcal{K} - qw \quad (2.2)$$

The equations of motion are given by Hamilton's principle

$$\delta\mathcal{A} = \delta \int_{t_0}^{t_1} \int_0^L \mathcal{L} dx dt = \int_{t_0}^{t_1} \int_0^L \delta\mathcal{L} dx dt = 0 \quad (2.3)$$

After some common variation calculus operations, the equation of motion of the Rayleigh beam with highly oscillating non-continuous coefficients is obtained

$$\partial^2(EJ\partial^2 w) + \mu\ddot{w} - \partial(\vartheta\partial\ddot{w}) = q \quad (2.4)$$

3. Tolerance modelling

3.1. Preliminary notions

The main objective of this paper is to propose a new averaged model of the Rayleigh beam. This new approach is based on the concept of *weakly slowly-varying functions*. The averaged equations of the periodic beam are derived using the tolerance modelling technique. The fundamental concepts of the tolerance modelling approach – tolerance relations, slowly-varying functions (*SV*), tolerance periodic functions (*TP*), fluctuation shape functions (*FSFs*) and averaging operation, are outlined in the monographs by Woźniak and Wierzbicki (2000), Woźniak *et al.* (2008), Awrejcewicz (2010). There are introduced the following denotations: $\Delta(x) \equiv x + \Delta$, $\Omega_\Delta \equiv \{x \in \Omega : \Delta(x) \in \Omega\}$, $x \in R^m$. Subsequently, a subset Δ of R^m is called the periodicity cell with l as a cell dimension. Every cell $\Delta(x)$, $x \in \Omega_\Delta$, refers to the cell in Ω with the center at x . The averaging operator for an arbitrary integrable function f is defined by

$$\langle f \rangle(x) = \frac{1}{l} \int_{\Delta(x)} f(y) dy \quad x \in \Omega_\Delta \quad y \in \Delta(x) \quad (3.1)$$

The micro-macro decomposition is a fundamental operation of the tolerance averaging technique. It states that the transverse deflection of the beam $w(x, t)$ (unknown of the partial differential equations describing behavior of the microheterogeneous structure) can be decomposed into: the unknown averaged displacement $W(x, t)$ (a weakly slowly-varying function in the periodicity direction) and the highly oscillating fluctuation of the displacement, represented by the known highly oscillating Δ -periodic fluctuation shape function $h^A(x)$ multiplied by the unknown fluctuation amplitude $V^A(x, t)$ – weakly slowly-varying (*WSV*) in the periodicity direction. In this case, the micro-macro decomposition becomes

$$w(x, t) = W(x, t) + h^A(x)V^A(x, t) \quad A = 1, \dots, N \quad W(\cdot), V^A(\cdot) \in WSV_d^2(\Omega, \Delta) \quad (3.2)$$

From now, $W(x, t)$ is a new basic kinematic unknown and $V^A(x, t)$ is an additional kinematic unknown. The uppercase integer states that the unknown functions are assumed to be weakly slowly-varying up to the second derivative order. The function $F(\cdot)$ will be referred to as the

weakly slowly-varying with respect to the cell Δ and the tolerance given by $\delta \equiv (\alpha, \delta_0, \delta_1, \dots, \delta_R)$, if and only if the following condition is satisfied

$$\exists(x, y) \in \Omega^2 \quad \left[(x \overset{\alpha}{\approx} y) \Rightarrow F(x) \overset{\delta_0}{\approx} F(y) \wedge \partial^k F(x) \overset{\delta_k}{\approx} \partial^k F(y), k = 1, 2, \dots, R \right] \quad (3.3)$$

where $\partial^0 F(\cdot) \equiv F(\cdot)$.

Under the above conditions, it can be written $F \in WSV_\delta^R(\Omega, \Delta)$. In the applications of the tolerance modelling, the tolerance parameter $\alpha = l$ is known *a priori* as a certain mesostructure length, whereas values of the tolerance parameters $\delta_0, \delta_1, \dots, \delta_R$ can be determined only *a posteriori*, i.e. after obtaining a solution to the considered initial-boundary value problem. The highly oscillating fluctuation shape functions h^A are postulated *a priori* in every problem under consideration and describe the unknown fields oscillations caused by the structure inhomogeneity. Apart from the restriction of l -periodicity, the *FSFs* have to satisfy the following conditions

$$\begin{aligned} \langle \mu h^A \rangle &= 0 & \langle \mu h^A h^B \rangle &= 0 \quad \text{for } A \neq B \\ \partial^m h^A &\in O(l^{2-m}) & A, B &= 1, \dots, N \end{aligned} \quad (3.4)$$

Another assumption is the tolerance averaging approximation. For the purposes of this article, the following denotations are introduced. Let $e, f \in L_{loc}^2(R)$ be the known l -periodic functions and let $F \in WSV_d^1(0, L)$, $d \equiv (l, \delta_0, \delta_1)$. By the tolerance averaging of $eF + f\partial_1 F$ is meant $\langle eF + f\partial_1 F \rangle_T(x) \equiv \langle e \rangle F(x) + \langle f \rangle \partial_1 F(x)$ for every $x \in (l/2, L - l/2)$. The tolerance averaging approximation is an approximation of $\langle eF + f\partial_1 F \rangle(x)$ by $\langle eF + f\partial_1 F \rangle_T(x)$ for every $x \in (l/2, L - l/2)$. Thus, the tolerance averaging approximation has the form

$$\langle eF + f\partial_1 F \rangle(x) = \langle eF + f\partial_1 F \rangle_T(x) + O(l) \quad d \equiv (l, \delta_0, \delta_1) \quad (3.5)$$

where $e(\cdot), f(\cdot)$ are the known functions and $F(\cdot)$ is unknown in the initial-boundary value problem under consideration.

3.2. The averaged model equations

The averaging operation is performed, after substituting micro-macro decomposition (3.2) into Lagrangian (2.2). Thus, the variation of the averaged action functional can be written as

$$\delta \mathcal{A} = \delta \int_{t_0}^{t_1} \int_0^L \langle \mathcal{L}_h \rangle dx dt = \int_{t_0}^{t_1} \int_0^L \delta \langle \mathcal{L}_h \rangle dx dt = 0 \quad (3.6)$$

Knowing that

$$\begin{aligned} -\kappa &= \partial^2 w = \partial^2 W + \partial^2 (h^A V^A) = \partial^2 W + \partial(\partial h^A V^A + h^A \partial V^A) \\ &= \partial^2 W + \partial^2 h^A V^A + 2\partial h^A \partial V^A + h^A \partial^2 V^A \\ -\delta \kappa &= \partial^2 \delta W + \partial^2 h^A \delta V^A + 2\partial h^A \delta \partial V^A + h^A \partial^2 \delta V^A \\ -M &= EJ \partial^2 w = EJ(\partial^2 W + \partial^2 h^B V^B + 2\partial h^B \partial V^B + h^B \partial^2 V^B) \end{aligned} \quad (3.7)$$

the Lagrangian variation is

$$\delta \mathcal{L} = \delta \mathcal{W} - \delta \mathcal{K} - q \delta w = M \delta \kappa - \mu \dot{w} \delta \dot{w} - \vartheta \partial \dot{w} \delta \dot{w} - q \delta w \quad (3.8)$$

Finally

$$\int_{t_0}^{t_1} \int_0^L \delta \mathcal{K} dx dt = \int_{t_0}^{t_1} \int_0^L (\mu \ddot{w} \delta w + \vartheta \partial \ddot{w} \delta w) dx dt \quad (3.9)$$

and

$$\delta\mathcal{L} = M\delta\kappa + (\mu\ddot{w} - q)\delta w + \vartheta\partial\ddot{w}\partial\delta w \quad (3.10)$$

Let micro-macro decomposition (3.2) be substituted into the components of the Lagrangian and averaged over a periodicity cell. It should be noted that

$$\delta w = \delta W + h^A\delta V^A \quad (3.11)$$

The variation of the averaged bending energy gives

$$\langle\delta\mathcal{L}\rangle = \langle M\delta\kappa\rangle = \langle M\rangle\partial^2\delta W + \langle M\partial^2 h^A\rangle\delta V^A + 2\langle M\partial h^A\rangle\partial\delta V^A + \langle Mh^A\rangle\partial^2\delta V^A \quad (3.12)$$

where

$$\begin{aligned} \langle M\rangle &= \langle EJ\rangle\partial^2 W + \langle EJ\partial^2 h^B\rangle V^B + 2\langle EJ\partial h^B\rangle\partial V^B + \langle EJh^B\rangle\partial^2 V^B \\ \langle M\partial^2 h^A\rangle &= \langle EJ\partial^2 h^A\rangle\partial^2 W + \langle EJ\partial^2 h^A\partial^2 h^B\rangle V^B + 2\langle EJ\partial^2 h^A\partial h^B\rangle\partial V^B \\ &\quad + \langle EJ\partial^2 h^A h^B\rangle\partial^2 V^B \\ \langle M\partial h^A\rangle &= \langle EJ\partial h^A\rangle\partial^2 W + \langle EJ\partial h^A\partial^2 h^B\rangle V^B + 2\langle EJ\partial h^A\partial h^B\rangle\partial V^B + \langle EJ\partial h^A h^B\rangle\partial^2 V^B \\ \langle Mh^A\rangle &= \langle EJh^A\rangle\partial^2 W + \langle EJh^A\partial^2 h^B\rangle V^B + 2\langle EJh^A\partial h^B\rangle\partial V^B + \langle EJh^A h^B\rangle\partial^2 V^B \end{aligned} \quad (3.13)$$

The total variation of the Lagrangian is

$$\begin{aligned} \delta\mathcal{L} &= \langle M\rangle\partial^2\delta W + \left(\langle\vartheta\rangle\partial\ddot{W} + \langle\vartheta\partial h^A\rangle\ddot{V}^A\right)\partial\delta W + \left(\langle\mu\rangle\ddot{W} + \langle\mu h^A\rangle\ddot{V}^A - \langle q\rangle\right)\delta W \\ &\quad + \left(\langle M\partial^2 h^A\rangle + \langle\mu h^A\rangle\ddot{W} + \langle\mu h^A h^B\rangle\ddot{V}^B + \langle\vartheta\partial h^A\rangle\partial\ddot{W}\right. \\ &\quad \left.+ \langle\vartheta\partial h^A\partial h^B\rangle\ddot{V}^B - \langle qh^A\rangle\right)\delta V^A + 2\langle M\partial h^A\rangle\partial\delta V^A + \langle Mh^A\rangle\partial^2\delta V^A \end{aligned} \quad (3.14)$$

After some transformations

$$\begin{aligned} \delta\mathcal{L} &= \left[\partial^2\langle M\rangle - \partial\left(\langle\vartheta\rangle\partial\ddot{W} + \langle\vartheta\partial h^A\rangle\ddot{V}^A\right) + \langle\mu\rangle\ddot{W} + \langle\mu h^A\rangle\ddot{V}^A - \langle q\rangle\right]\delta W \\ &\quad + \left(\langle M\partial^2 h^A\rangle - 2\partial\langle M\partial h^A\rangle + \langle\mu h^A\rangle\ddot{W} + \langle\mu h^A h^B\rangle\ddot{V}^B + \langle\vartheta\partial h^A\rangle\partial\ddot{W}\right. \\ &\quad \left.+ \langle\vartheta\partial h^A\partial h^B\rangle\ddot{V}^B + \partial^2\langle Mh^A\rangle - \langle qh^A\rangle\right)\delta V^A + \partial\left(\langle M\rangle\partial\delta W\right) \\ &\quad + \partial\left[\left(\langle\vartheta\rangle\partial\ddot{W} + \langle\vartheta\partial h^A\rangle\ddot{V}^A - \partial\langle M\rangle\right)\delta W\right] \\ &\quad + \partial\left(\langle Mh^A\rangle\partial\delta V^A\right) - \partial\left[\left(\partial\langle Mh^A\rangle - 2\langle M\partial h^A\rangle\right)\delta V^A\right] \end{aligned} \quad (3.15)$$

This leads to a system of differential equations

$$\begin{aligned} \delta W : \quad &\partial^2\langle M\rangle - \partial\left(\langle\vartheta\rangle\partial\ddot{W} + \langle\vartheta\partial h^A\rangle\ddot{V}^A\right) + \langle\mu\rangle\ddot{W} + \langle\mu h^A\rangle\ddot{V}^A - \langle q\rangle = 0 \\ \delta V^A : \quad &\langle M\partial^2 h^A\rangle - 2\partial\langle M\partial h^A\rangle + \langle\mu h^A\rangle\ddot{W} + \langle\mu h^A h^B\rangle\ddot{V}^B \\ &\quad + \langle\vartheta\partial h^A\rangle\partial\ddot{W} + \langle\vartheta\partial h^A\partial h^B\rangle\ddot{V}^B + \partial^2\langle Mh^A\rangle - \langle qh^A\rangle = 0 \end{aligned} \quad (3.16)$$

and natural boundary conditions

$$\begin{aligned} &\left(\langle\vartheta\rangle\partial\ddot{W} + \langle\vartheta\partial h^A\rangle\ddot{V}^A - \partial\langle M\rangle\right)\delta W\Big|_0^L + \langle M\rangle\partial\delta W\Big|_0^L + \langle Mh^A\rangle\partial\delta V^A\Big|_0^L \\ &\quad + \left(\partial\langle Mh^A\rangle - 2\langle M\partial h^A\rangle\right)\delta V^A\Big|_0^L = 0 \end{aligned} \quad (3.17)$$

The $N + 1$ differential equations for the macro-deflection and its fluctuation amplitudes are

$$\begin{aligned} \partial^2 \langle M \rangle - \langle \vartheta \rangle \partial^2 \ddot{W} - \langle \vartheta \partial h^A \rangle \partial \ddot{V}^A + \langle \mu \rangle \ddot{W} + \langle \mu h^A \rangle \ddot{V}^A - \langle q \rangle &= 0 \\ \langle M \partial^2 h^A \rangle - 2 \partial \langle M \partial h^A \rangle + \langle \mu h^A \rangle \ddot{W} + \langle \mu h^A h^B \rangle \ddot{V}^B + \langle \vartheta \partial h^A \rangle \partial \ddot{W} & \\ + \langle \vartheta \partial h^A \partial h^B \rangle \ddot{V}^B + \partial^2 \langle M h^A \rangle - \langle q h^A \rangle &= 0 \end{aligned} \quad (3.18)$$

The weight-averaged bending moments have the following form

$$\begin{pmatrix} \langle M \rangle \\ \langle M \partial^2 h^A \rangle \\ \langle M \partial h^A \rangle \\ \langle M h^A \rangle \end{pmatrix} = \begin{bmatrix} \langle EJ \rangle & \langle EJ \partial^2 h^B \rangle & \langle EJ \partial h^B \rangle & \langle EJ h^B \rangle \\ \langle EJ \partial^2 h^A \rangle & \langle EJ \partial^2 h^A \partial^2 h^B \rangle & \langle EJ \partial^2 h^A \partial h^B \rangle & \langle EJ \partial^2 h^A h^B \rangle \\ \langle EJ \partial h^A \rangle & \langle EJ \partial h^A \partial h^B \rangle & \langle EJ \partial h^A \partial h^B \rangle & \langle EJ \partial h^A h^B \rangle \\ \langle EJ h^A \rangle & \langle EJ h^A \partial^2 h^B \rangle & \langle EJ h^A \partial h^B \rangle & \langle EJ h^A h^B \rangle \end{bmatrix} \begin{pmatrix} \partial^2 W \\ V^B \\ 2 \partial V^B \\ \partial^2 V^B \end{pmatrix} \quad (3.19)$$

where $W(x, t)$, $V^A(x, t)$ and their derivatives are the new kinematic unknowns. Together with the averaged equation of motion, the following natural boundary conditions (for $x = 0, L$) with averaged coefficients are obtained

$$\begin{aligned} \langle \vartheta \rangle \partial \ddot{W} + \langle \vartheta \partial h^A \rangle \ddot{V}^A - \partial \langle M \rangle &= 0 \quad \text{or} \quad \delta W = 0 \\ \langle M \rangle &= 0 \quad \text{or} \quad \partial \delta W = 0 \\ \partial \langle M h^A \rangle - 2 \langle M \partial h^A \rangle &= 0 \quad \text{or} \quad \delta V^A = 0 \\ \langle M h^A \rangle &= 0 \quad \text{or} \quad \partial \delta V^A = 0 \end{aligned} \quad (3.20)$$

It is worth mentioning that expressions (3.20) reduce to classic natural boundary conditions for a homogeneous beam (Fung, 1965). Moreover, the underlined coefficients are dependent on the mesostructure size l . The external load is assumed to be zero in the analysis of natural vibrations of the beam.

4. Examples of applications

In this Section, the derived averaged model is adapted in a study of some special problems. The object under consideration is a simply supported beam with length L . The beam has a rectangular cross section and is made of some small repetitive elements. The periodicity cell, presented in Fig. 1, has a symmetrical shape and is divided into three segments. The segment material and geometrical properties may vary depending on each case.

One of the most significant components of the tolerance modelling is determination of the fluctuation shape functions. The fluctuation shape functions can be assumed as forms of eigen vibrations one the periodicity cell. In this model, *FSFs* are obtained from finite element analysis of the periodicity cell, although the common practice is to use approximate solutions such as l -periodic trigonometric functions.

In order to obtain a system of algebraic equations of motion, the Galerkin method is applied. The trial solutions are assumed in the form of truncated trigonometric series

$$W(x, t) = \sum_{m=1}^{M_w} X_m(x) W_m(t) \quad V^A(x, t) = \sum_{n=1}^{M_V^A} Y_m^A(x) V_m^A(t) \quad A = 1, \dots, N \quad (4.1)$$

where the weight functions X_m and Y_m^A are chosen to satisfy the boundary conditions of a simply supported beam

$$X_m(x) = \sin \frac{m\pi x}{L} \quad Y_m^A = \begin{cases} \sin \frac{n\pi x}{L} & \text{for } A \in \text{ESF} \\ \cos \frac{(n-1)\pi x}{L} & \text{for } A \in \text{OSF} \end{cases} \quad (4.2)$$

The functions X_m and Y_m^A satisfy the assumed boundary conditions at $x = 0, L$, where *ESF* and *OSF* stands for an even and odd fluctuation shape function respectively. The known relation is solved with respect to the unknown trial function coefficients (Zienkiewicz *et al.*, 2013). The number of terms in the expansion results from the condition of convergence of the solution. In order to obtain the natural frequencies of the beam, the eigenproblem of the dynamic stiffness matrix is solved. In the numerical solutions, the size of the matrix is limited to the finite value

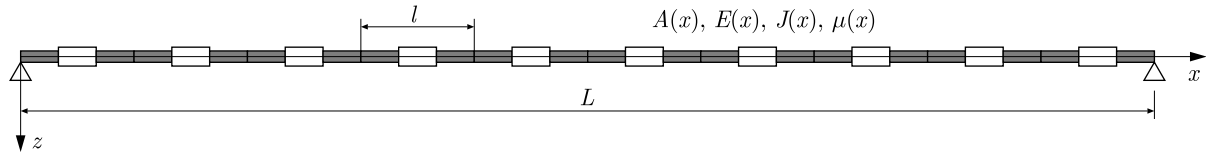


Fig. 2. The considered beam

5. Results and discussion

This Section is dedicated to the analysis of free vibrations of a Rayleigh beam. The beam has length $L = 1.0$ m and is composed of 10 periodicity cells with length $l = 0.1$ m and cross section width $b = 0.01$ m. Three different beams with variable cross section height h_M , Young's modulus E_M and mass density ρ_M are analyzed. For each beam, there are considered three individual cases. The properties of the central periodicity cell segment – height $h_R = 0.008$ m, Young's modulus $E_R = 205$ GPa and density $\rho_R = 7850$ kg/m³ are constant in all analyzed cases.

As an example, 3 cases: A, B and C are analyzed. For each case, one of the material or geometrical parameter of the periodicity cell has an individual value. The values of h_M , E_M and ρ_M parameters for all cases are presented in Table 1.

Table 1. Analyzed-cases

Case	h_M [m]	E_M [GPa]	ρ_M [kg/m ³]		
A1	0.004	205.000	7850.00		
A2	0.005				
A3	0.006				
B1	0.008		102.500	3925.00	
B2				1962.50	
B3				981.25	
C1			51.250	7850.00	
C2					25.625
C3					25.625

In order to validate the tolerance model, a finite element method procedure is applied in *Maple* software. The finite element model is assembled with 30 Rayleigh beam elements with Hermitian polynomials and the consistent mass matrix. As a result, the model has 31 nodes with 62 degrees of freedom.

The natural frequencies, which are obtained using the tolerance averaging technique (TA) and the finite element method (FE), are compared in Table 2. The validation of first 22 natural frequencies for cases A2, B2 and C2 for the mesostructure $\alpha = 0.5$ is performed. The TA model results are presented as gray dots, and the FE model as black rings. The received values of frequencies are given in [Hz]. The first five natural frequencies for cases A2, B2, C2 are listed in Table 2. 80.878 Hz, 147.330 Hz, and 73.581 Hz are the least derived values of natural frequencies in cases A2, B2, and C2, respectively. The relative error does not exceed 2% for the first five

frequencies. It is noticeable that the presented bandwidth is not entirely continuous and uniform. Among all obtained frequencies in Fig. 3, separated bands of frequencies can be observed – the chains preceded and followed by some intervals. These interruptions in the bandwidth, highlighted with gray backgrounds, are called *band gaps*. In case A, the first band interval reveals between the 9th and 10th natural frequency. The difference between these frequencies arrives at 3133 Hz. Another gap appears between the 20th and 21st natural frequency. In this case, the difference rises to 8454 Hz. In case B, the gaps occur between the 10th, 11th and 20th, 21st free vibration frequencies, and the intervals in the bandwidth reach 7657 and 14164 Hz, respectively. In case C, the band gaps reveal at the same frequencies as in case A, and the magnitudes of the interludes are 3663 Hz and 7171 Hz, respectively.

Table 2. Natural frequencies for case A2, B2 and C2

ω_i	A2			B2			C2		
	TA	FE	$\frac{ \Delta\omega }{ \omega^{FE} }$	TA	FE	$\frac{ \Delta\omega }{ \omega^{FE} }$	TA	FE	$\frac{ \Delta\omega }{ \omega^{FE} }$
n	[Hz]	[Hz]	[%]	[Hz]	[Hz]	[%]	[Hz]	[Hz]	[%]
1	80.878	80.971	0.115	147.330	147.314	0.011	73.581	73.659	0.105
2	322.607	324.108	0.463	589.309	589.054	0.043	293.269	294.534	0.430
3	722.358	730.114	1.062	1325.846	1324.555	0.097	655.683	662.294	0.998
4	1274.964	1300.213	1.942	2356.475	2352.406	0.173	1154.338	1176.231	1.861
5	2043.391	2036.098	0.358	3679.510	3669.598	0.270	1843.340	1834.854	0.462

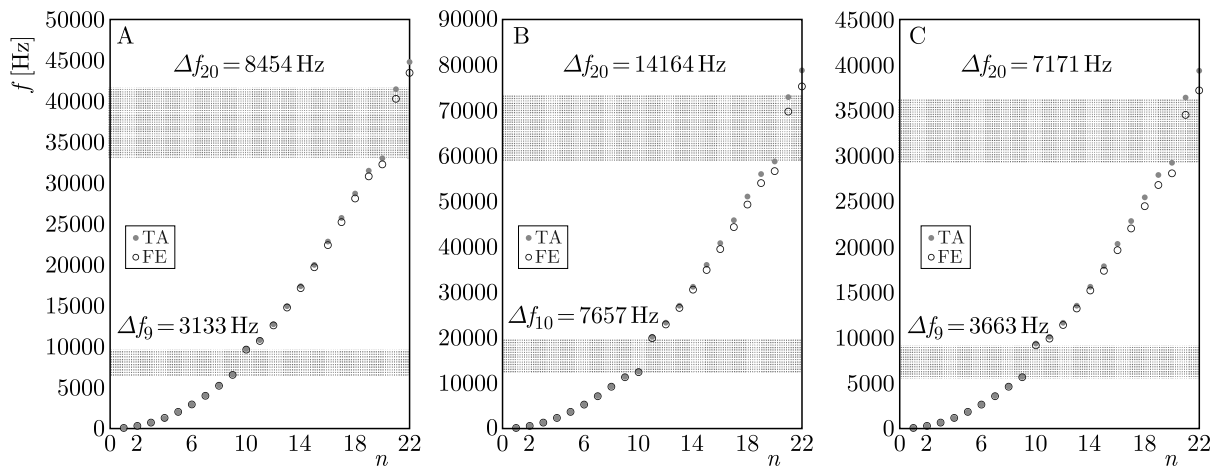


Fig. 3. Comparison of natural frequencies bandwidth of the considered beam for $\alpha = 1/2$, case A2, B2, C2

In Figs. 4-6, the band gaps neighborhood is shown. The tolerance solutions are represented by solid lines, and the finite element solutions are represented by dashed lines. In this case, the presented frequencies are functions of the saturation parameter α . All frequencies are presented in relation to the constant value – the natural frequency obtained from the finite element method. As a result, the solutions are presented in the dimensionless form. The first two gaps in the observed bandwidth range are analyzed. In cases A and C, the analyzed frequencies are increasing with the argument of a function. In case B, a decreasing relationship can be observed. In the enclosed figures, two types of band gaps can be noticed. The first type of the gap is between the same frequencies in the entire domain of the mesostructure parameter. The second type of the gap changes its character along with the α parameter. The following relationship can be observed: the compared models have the best convergence for low natural frequencies and low values of the α parameter.

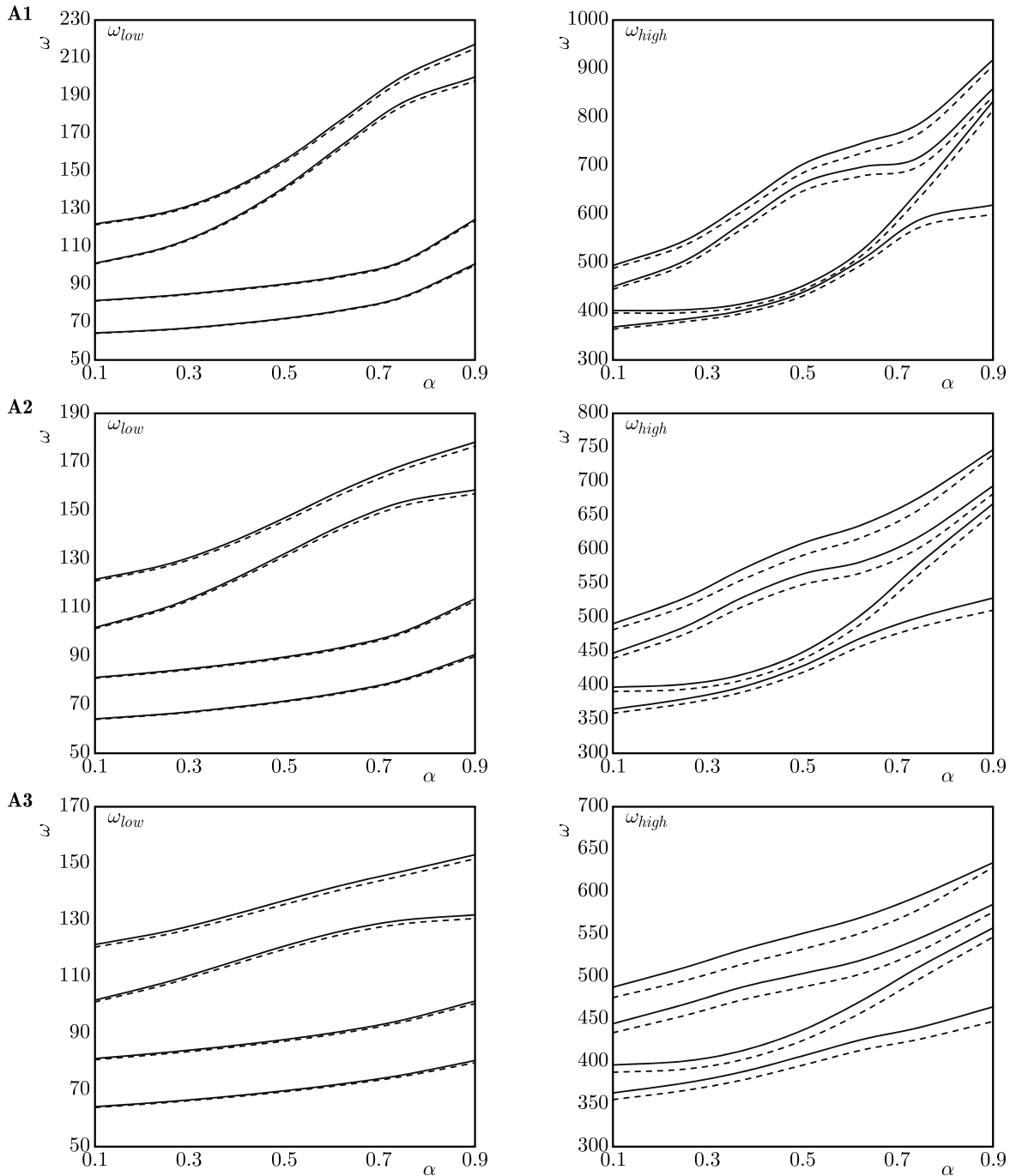


Fig. 4. Band-gap neighboring eigenfrequencies as a function of the α parameter, case A

In Table 3, the eigenmodes of the considered beam model for $\alpha = 1/2$ are compared. It can be noticed that in B2 case the band gaps occur in different places in comparison with A2, B2 and C2 cases (Fig. 3). What is more, there is a difference in the order of symmetrical and antisymmetrical eigenmodes (cf. Table 3).

6. Final remarks

In this paper, the authors present a new averaged model of a linear-elastic periodic Rayleigh beam. Dynamics of the beam is described by partial differential equations with non-continuous

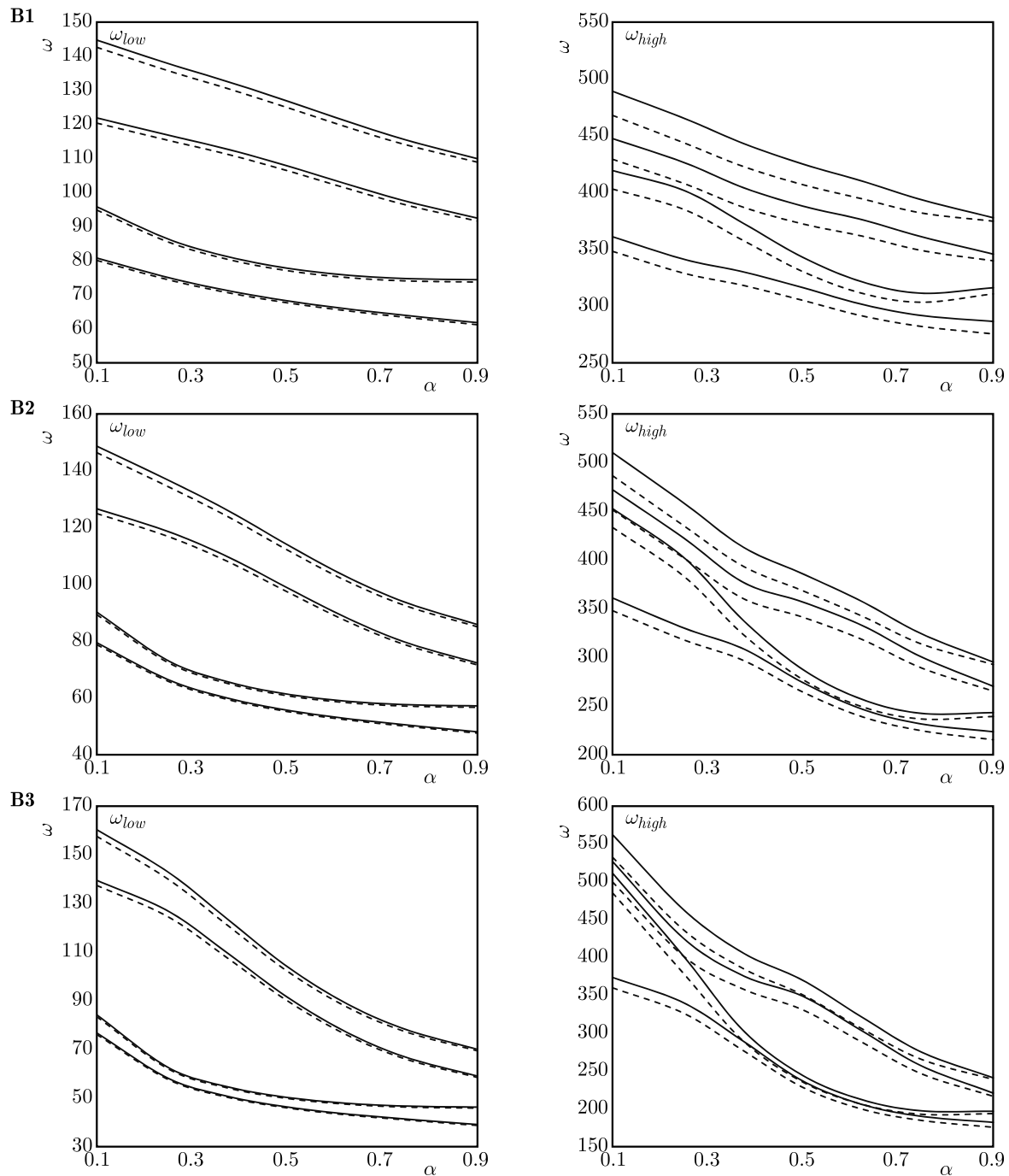


Fig. 5. Band-gap neighboring eigenfrequencies as a function of the α parameter, case B

highly oscillating coefficients. The exact model equations are transformed into a form that can be solved numerically.

The new model implements the notion of weakly slowly-varying functions. The proposed equations are derived using the tolerance averaging approach. In contradiction to other homogenized models, the tolerance averaging technique allows one to observe some averaged effective properties of a structure. Despite the inhomogeneity of the structure, this new model introduces some new unknowns – averaged deflection. It also allows one to observe some dynamic properties of the beam, depending on the size of the periodicity cell.

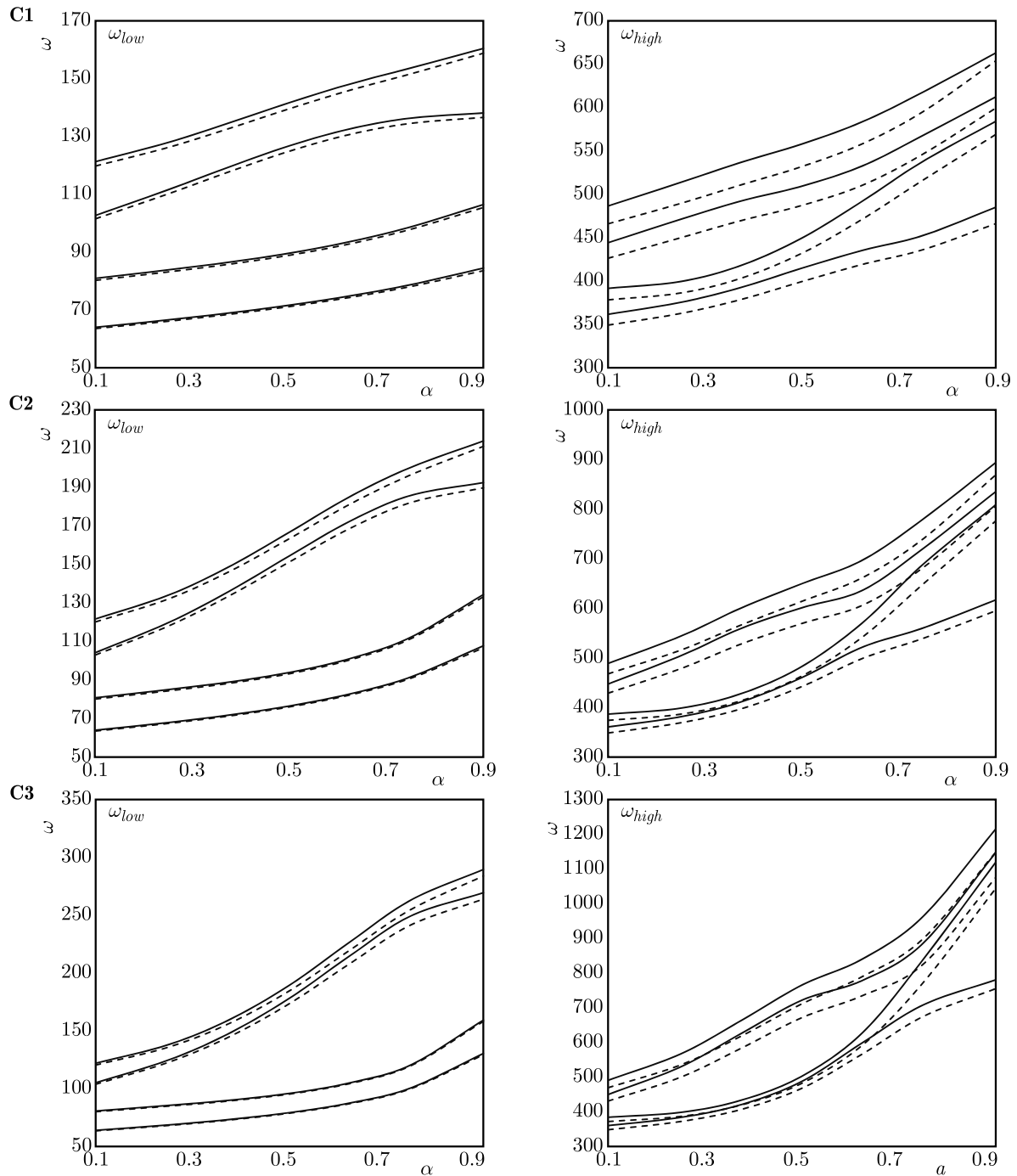


Fig. 6. Band-gap neighboring eigenfrequencies as a function of the α parameter, case C

The solutions derived from tolerance averaging have been compared with the finite element model solutions. The finite element model has 31 nodes with 62 degrees of freedom.

In this paper, 3 cases have been compared: A, B and C. A good agreement has been obtained between the two methods in all analyzed cases. What is more, there is an evident dependency between the occurrence of band gaps and the shape of eigenmodes. Therefore, the proposed solution enables one to formulate model equations which can be solved with known numerical methods (e.g. Galerkin method). That is why the suggested technique can be used in the parametric analysis of the structures under consideration. The problems that can be considered in

Table 3. Comparison of natural frequency bandwidths of the considered beam for $\alpha = 1/2$

Case		ω_9	ω_{10}	ω_{11}	ω_{20}	ω_{21}
A2	TA					
	FE					
B2	TA					
	FE					
C2	TA					
	FE					

future works are: forced vibrations of inhomogeneous Rayleigh beams, greater diversity of boundary conditions, analysis of structural and material heterogeneity of the beam and a viscoelastic subsoil.

Acknowledgements

This contribution was supported by the National Science Centre of Poland under grant No. 2014/15/B/ST8/03155

References

1. AWREJCWICZ J., 2010, *Mathematical Modelling and Analysis in Continuum Mechanics of Microstructured Media: Professor Margaret Woźniak Pro Memoria: Sapiens Mortem Non Timet*, Silesian University of Technology Publisher
2. CHEN T., 2013, Investigations on flexural wave propagation of a periodic beam using multi-reflection method, *Archive of Applied Mechanics*, **83**, 2, 315-329
3. CIELECKA I., JĘDRYSIAK J., 2006, A non-asymptotic model of dynamics of honeycomb lattice-type plates, *Journal of Sound and Vibration*, **296**, 1, 130-149
4. DOMAGALSKI L., JĘDRYSIAK J., 2015, On the tolerance modelling of geometrically nonlinear thin periodic plates, *Thin-Walled Structures*, **87** (Supplement C), 183-190
5. DOMAGALSKI L., JĘDRYSIAK J., 2016, Geometrically nonlinear vibrations of slender meso-periodic beams. The tolerance modeling approach, *Composite Structures*, **136**, 270-277

6. FUNG Y., 1965, *Foundations of Solid Mechanics*, Prentice-Hall International Series in Dynamics, Prentice-Hall
7. HAJIANMALEKI M., QATU M.S., 2013, Vibrations of straight and curved composite beams: A review, *Composite Structures*, **100** (Supplement C), 218-232
8. JĘDRYSIAK J., 2000, On the stability of thin periodic plates, *European Journal of Mechanics – A/Solids*, **19**, 3, 487-502
9. JĘDRYSIAK J., 2003, Free vibrations of thin periodic plates interacting with an elastic periodic foundation, *International Journal of Mechanical Sciences*, **45**, 8, 1411-1428
10. JĘDRYSIAK J., 2013, Modelling of dynamic behaviour of microstructured thin functionally graded plates, *Thin-Walled Structures*, **71** (Supplement C), 102-107
11. JĘDRYSIAK J., 2014, Free vibrations of thin functionally graded plates with microstructure, *Engineering Structures*, **75** (Supplement C), 99-112
12. JĘDRYSIAK J., 2017, General and standard tolerance models of thin two-directional periodic plates, [In:] *Shell Structures: Theory and Applications*, Vol. 4, W. Pietraszkiewicz, W. Witkowski (Edit.), 101-104
13. JĘDRYSIAK J., MICHALAK B., 2011, On the modelling of stability problems for thin plates with functionally graded structure, *Thin-Walled Structures*, **49**, 5, 627-635
14. KAŻMIERCZAK M., JĘDRYSIAK J., 2011, Tolerance modelling of vibrations of thin functionally graded plates, *Thin-Walled Structures*, **49**, 10, 1295-1303
15. KOHN R.V., VOGELIUS M., 1984, A new model for thin plates with rapidly varying thickness, *International Journal of Solids and Structures*, **20**, 4, 333-350
16. KOLPAKOV A., 1991, Calculation of the characteristics of thin elastic rods with a periodic structure, *Journal of Applied Mathematics and Mechanics*, **55**, 3, 358-365
17. KOLPAKOV A., 1998, Application of homogenization method to justification of 1-D model for beam of periodic structure having initial stresses, *International Journal of Solids and Structures*, **35**, 22, 2847-2859
18. KOLPAKOV A., 1999, The governing equations of a thin elastic stressed beam with a periodic structure, *Journal of Applied Mathematics and Mechanics*, **63**, 3, 495-504
19. MAZUR-ŚNIADY K., 1993, Macro-dynamic of micro-periodic elastic beams, *Journal of Theoretical and Applied Mechanics*, **31**, 4, 781-793
20. MICHALAK B., 2001, The meso-shape functions for the meso-structural models of wavy-plates, *ZAMM – Journal of Applied Mathematics and Mechanics / Zeitschrift für Angewandte Mathematik und Mechanik*, **81**, 9, 639-641
21. PAPANICOLAOU G., BENSOUSSAN A., LIONS J., 1978, *Asymptotic Analysis for Periodic Structures*, Studies in Mathematics and its Applications, Elsevier Science
22. SÁNCHEZ-PALENCIA E., 1980, *Non-Homogeneous Media and Vibration Theory*, Lecture Notes in Physics, Springer-Verlag
23. TOMCZYK B., 2013, Length-scale effect in dynamics and stability of thin periodic cylindrical shells, *Research Bulletin*, **466**, 1-163
24. WOŹNIAK C., MICHALAK B., JĘDRYSIAK J., 2008, *Thermomechanics of Microheterogeneous Solids and Structures: Tolerance Averaging Approach*, Monografie – Lodz University of Technology, Lodz University of Technology Publisher
25. WOŹNIAK C., WIERZBICKI E., 2000, *Averaging Techniques in Thermomechanics of Composite Solids: Tolerance Averaging Versus Homogenization*, Czestochowa University of Technology Publisher
26. XIANG H.-J., SHI Z.-F., 2009, Analysis of flexural vibration band gaps in periodic beams using differential quadrature method, *Computers and Structures*, **87**, 23, 1559-1566

27. XU Y., ZHOU X., WANG W., WANG L., PENG F., LI B., 2016, On natural frequencies of non-uniform beams modulated by finite periodic cells, *Physics Letters A*, **380**, 40, 3278-3283
28. YU D., WEN J., SHEN H., XIAO Y., WEN X., 2012, Propagation of flexural wave in periodic beam on elastic foundations, *Physics Letters A*, **376**, 4, 626-630
29. ZHIKOV V., KOZLOV S., OLEĀNIK O., 1994, *Homogenization of Differential Operators and Integral Functionals*, Springer-Verlag
30. ZIENKIEWICZ O., TAYLOR R., ZHU J., 2013, *The Finite Element Method: Its Basis and Fundamentals. The Finite Element Method*, Elsevier Science

Manuscript received March 24, 2018; accepted for print August 8, 2018

FORCED VIBRATIONS OF A THERMOELASTIC DOUBLE POROUS MICROBEAM SUBJECTED TO A MOVING LOAD

RAJNEESH KUMAR

Kurukshetra University, Department of Mathematics, Kurukshetra, Haryana, India

RICHA VOHRA

H.P. University, Department of Mathematics and Statistics, Shimla, HP, India

e-mail: richavhr88@gmail.com

The present paper deals with forced vibrations of a homogeneous, isotropic thermoelastic double porous microbeam subjected to moving load, in context of Lord-Shulman theory of thermoelasticity with one relaxation time. The Laplace transform has been applied to obtain expressions for the axial displacement, lateral deflection, volume fraction field and temperature distribution. A numerical inversion technique has been used to recover the resulting quantities in the physical domain. Effects of velocity and time parameters are shown graphically by plotting axial displacement, lateral deflection, volume fraction field and temperature distribution against distance. Some particular cases are also deduced.

Keywords: double porosity, thermoelasticity, Lord-Shulman theory, microbeam, moving load

1. Introduction

Recently, dynamical analysis of engineering structures subjected to moving loads has gained great importance. Vehicle-bridge interactions are a vast area of interest in the moving load problem. Advances in transport technology and automobile engineering have resulted in high speeds and heaviness of vehicles and other moving bodies. As a result, corresponding structures have been subjected to vibration and dynamic stress much higher than ever before. The engineering structures with moving loads often come out in buildings, bridges, railways and cranes. Beam type structures are widely used in many fields like civil, mechanical and aerospace engineering. Many researchers have investigated dynamical behavior of beams on elastic foundations subjected to moving loads, especially in railway engineering. The modern trend towards higher speeds in the railways has further intensified the research in order to accurately predict the vibration behavior of railway tracks.

Pores or fractures can be observed in engineering structures due to reasons like erosion, corrosion, fatigue or accidents which affect the dynamic behavior of the entire structure to a considerable extent. This leads to the development of the double porosity model which has its applications in geophysics, rock mechanics and many branches of engineering like civil engineering, chemical engineering and the petroleum industry. Biot (1941) proposed a model for porous media with single porosity. Later on Barenblatt *et al.* (1960) introduced a model for porous media with a double porosity structure. The double porosity model consists of two coexisting degrees of porosity in which one corresponds to the porous matrix and the other to the fissure matrix.

Nunziato and Cowin (1979) developed a nonlinear theory of an elastic material with voids. Later, Cowin and Nunziato (1983) developed a theory of linear elastic materials with voids for mathematical study of the mechanical behavior of porous solids. In this theory, the skeletal materials are elastic, and interstices are void of material, hence an additional degree of freedom,

the volume fraction of the void, is added. Iesan and Quintanilla (2014) derived a theory of thermoelastic solids with a double porosity structure by using the theory developed by Nunziato and Cowin (1979). Darcy's law was not used in developing that theory. So far, not much work has been done on the theory of thermoelasticity with the double porosity based on the model proposed by Iesan and Quintanilla (2014). Recent investigations have been started in the theory of thermoelasticity with double porosity which has a significant application in continuum mechanics. Kumar *et al.* (2015) applied the state space approach to a boundary value problem for thermoelastic materials with double porosity.

The dynamic behavior of different isotropic structures subjected to moving loads has been investigated by many researchers. Olsson (1991) studied the dynamic problem of a simply supported beam subjected to a constant force moving at a constant speed. The linear dynamic response of a simply supported uniform beam under a moving load of constant magnitude and velocity was investigated by Michaltsos *et al.* (1996). Rao (2000) studied the dynamic response of a multi-span Euler-Bernoulli beam due to moving loads. Mehri *et al.* (2009) presented the linear dynamic response of uniform beams with different boundary conditions under a moving load based on the Euler-Bernoulli beam theory. Sharma and Grover (2011) analysed a thermoelastic vibrations in micro-/nano-scale beam resonators with the presence of voids. Kargarnovin *et al.* (2012) studied the dynamic response of a delaminated composite beam under the action of a moving oscillatory mass. Esen (2015) investigated the transverse and longitudinal vibrations of a thin plate which carried a load moving along an arbitrary trajectory with variable velocity. Kumar (2016) studied the response of a thermoelastic beam due to the thermal source in the modified couple stress theory. Kaghazian *et al.* (2017) investigated free vibrations of a piezoelectric nanobeam using nonlocal elasticity theory. Zenkour (2017) studied the thermoelastic response of a microbeam embedded in visco-Pasternak's medium based on GN-III model.

In the present work, forced vibrations of a homogeneous, isotropic thermoelastic double porous microbeam, subjected to a moving load in the context of Lord-Shulman theory of thermoelasticity has been investigated. The Laplace transform has been applied to find expressions for axial displacement, lateral deflection, volume fraction fields and temperature distribution. The resulting quantities are obtained in the physical domain by using a numerical inversion technique. Variations of the axial displacement, lateral deflection, volume fraction field and temperature distribution against the axial distance are depicted graphically to show the effect of the velocity parameter. Some particular cases have also been deduced.

2. Basic equations

Following Iesan and Quintanilla (2014) as well as Lord and Shulman (1967); the field equations and the constitutive relation for a homogeneous isotropic thermoelastic material with a double porosity structure in the absence of body forces, extrinsic equilibrated body forces and heat sources can be written as

$$\begin{aligned} \mu \nabla^2 u_i + (\lambda + \mu) u_{j,j} + b \varphi_{,i} + d \psi_{,i} - \beta T_{,i} &= \rho \ddot{u}_i \\ \alpha \nabla^2 \varphi + b_1 \nabla^2 \psi - b u_{r,r} - \alpha_1 \varphi - \alpha_3 \psi + \gamma_1 T &= \kappa_1 \ddot{\varphi} \\ b_1 \nabla^2 \varphi + \gamma \nabla^2 \psi - d u_{r,r} - \alpha_3 \varphi - \alpha_2 \psi + \gamma_2 T &= \kappa_2 \ddot{\psi} \end{aligned} \quad (2.1)$$

and

$$\left(1 + \tau_0 \frac{\partial}{\partial t}\right) (\beta T_0 \dot{u}_{j,j} + \gamma_1 T_0 \dot{\varphi} + \gamma_2 T_0 \dot{\psi} + \rho C^* \dot{T}) = K^* \nabla^2 T \quad (2.2)$$

$$t_{ij} = \lambda e_{rr} \delta_{ij} + 2\mu e_{ij} + b \varphi \delta_{ij} + d \psi \delta_{ij} - \beta T \delta_{ij} \quad (2.3)$$

where λ and μ are Lamé's constants, ρ is mass density, $\beta = (3\lambda + 2\mu)\alpha_t$, α_t is linear thermal expansion, C^* is specific heat at a constant strain, u_i are displacement components, t_{ij} is the stress tensor, κ_1 and κ_2 are coefficients of equilibrated inertia, φ is the volume fraction field corresponding to pores, and ψ is the volume fraction field corresponding to fissures, K^* is the coefficient of thermal conductivity, τ_0 is the thermal relaxation time, κ_1 and κ_2 are coefficients of equilibrated inertia, and $b, d, b_1, \gamma, \gamma_1, \gamma_2$ are constitutive coefficients, δ_{ij} is Kronecker's delta, T is the temperature change measured from the absolute temperature T_0 ($T_0 \neq 0$), a superposed dot represents differentiation with respect to time variable t .

3. Formulation of the problem

We consider a homogeneous, isotropic thermoelastic double porous microbeam having dimensions: length L ($0 \leq x \leq L$), width a ($-a/2 \leq y \leq a/2$) and thickness h ($-h/2 \leq z \leq h/2$) in a Cartesian coordinate system $Oxyz$ as shown in Fig. 1. The microbeam undergoes bending vibrations of a small amplitude about the x -axis such that the deflection is consistent with the linear Euler-Bernoulli theory. Therefore, the displacements can be written as

$$u_1 = u = -z \frac{\partial w}{\partial x} \quad u_2 = 0 \quad u_3 = w(x, t) \quad (3.1)$$

where w is the lateral deflection and u is the axial displacement.

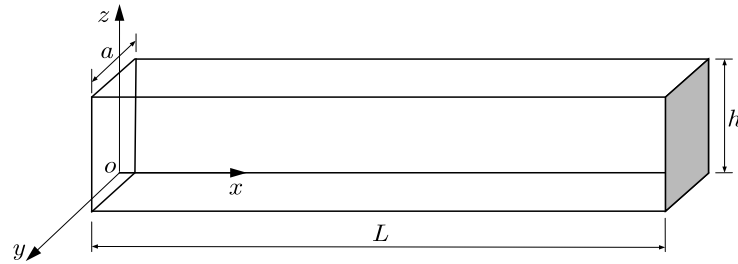


Fig. 1. Geometry of the beam

The equation of motion for forced vibrations of the beam can be written as

$$\frac{\partial^2 M}{\partial x^2} + \rho A \frac{\partial^2 w}{\partial t^2} = F(x, t) \quad (3.2)$$

where $A = ah$ is the cross-section area, M is the flexural moment of cross section of the microbeam and $F(x, t)$ is the applied moving load. By substituting Eqs. (2.3) and (3.1) into Eq.(3.2), we obtain the equation of motion for forced vibrations of an Euler-Bernoulli thermoelastic double porous microbeam subjected to moving load as

$$(\lambda + 2\mu)I \frac{\partial^4 w}{\partial x^4} + \rho A \frac{\partial^2 w}{\partial t^2} - \frac{\partial^2 M_\varphi}{\partial x^2} - \frac{\partial^2 M_\psi}{\partial x^2} + \frac{\partial^2 M_T}{\partial x^2} = F(x, t) \quad (3.3)$$

where $F = F_0 \delta(x - vt)$ is the applied moving load, v is its velocity, δ is the Dirac delta function, t is time in seconds, $I = ah^3/12$ is the moment of inertia of the cross-section and M_φ , M_ψ are the volume fraction field moments, and M_T is the thermal moment of the beam given by

$$M_\varphi = b \int_{-h/2}^{h/2} a\varphi z \, dz \quad M_\psi = d \int_{-h/2}^{h/2} a\psi z \, dz \quad M_T = \beta \int_{-h/2}^{h/2} aTz \, dz \quad (3.4)$$

Equations (2.1)_{2,3} and (2.2) with the help of Eq. (3.1) can be written as

$$\begin{aligned} \alpha \left(\frac{\partial^2 \varphi}{\partial x^2} + \frac{\partial^2 \varphi}{\partial z^2} \right) + b_1 \left(\frac{\partial^2 \psi}{\partial x^2} + \frac{\partial^2 \psi}{\partial z^2} \right) + bz \frac{\partial^2 w}{\partial x^2} - \alpha_1 \varphi - \alpha_3 \psi + \gamma_1 T &= \kappa_1 \frac{\partial^2 \varphi}{\partial t^2} \\ b_1 \left(\frac{\partial^2 \varphi}{\partial x^2} + \frac{\partial^2 \varphi}{\partial z^2} \right) + \gamma \left(\frac{\partial^2 \psi}{\partial x^2} + \frac{\partial^2 \psi}{\partial z^2} \right) + dz \frac{\partial^2 w}{\partial x^2} - \alpha_3 \varphi - \alpha_2 \psi + \gamma_2 T &= \kappa_2 \frac{\partial^2 \psi}{\partial t^2} \\ K^* \left(\frac{\partial^2 T}{\partial x^2} + \frac{\partial^2 T}{\partial z^2} \right) &= \left(1 + \tau_0 \frac{\partial}{\partial t} \right) \left[-\beta T_0 z \frac{\partial}{\partial t} \left(\frac{\partial^2 w}{\partial x^2} \right) + \gamma_1 T_0 \dot{\varphi} + \gamma_2 T_0 \dot{\psi} + \rho C^* \dot{T} \right] \end{aligned} \quad (3.5)$$

4. Solution of the problem

For the present microbeam, we assume that there is no flow of heat and the volume fraction fields across the surfaces ($z = \pm h/2$) so that $\partial T/\partial z = \partial \varphi/\partial z = \partial \psi/\partial z = 0$ at $z = \pm h/2$. For a very thin beam, assuming that the volume fraction fields and temperature increment in terms of $\sin(\pi z/h)$ function along the thickness direction one obtains

$$\varphi(x, z, t) = \Phi(x, t) \sin \frac{\pi z}{h} \quad \psi(x, z, t) = \Psi(x, t) \sin \frac{\pi z}{h} \quad T(x, z, t) = \Theta(x, t) \sin \frac{\pi z}{h} \quad (4.1)$$

Introducing non-dimensional variables as

$$\begin{aligned} x' &= \frac{1}{L}x & u' &= \frac{1}{L}u & t'_x &= \frac{t_x}{E} \\ \Phi' &= \frac{L}{\alpha}\Phi & \Psi' &= \frac{L}{\alpha}\Psi & \Theta' &= \frac{\beta}{E}\Theta \\ t' &= \frac{c_1}{L}t & \tau'_0 &= \frac{c_1}{L}\tau_0 & F'_0 &= \frac{L^2}{ah^2(\lambda + 2\mu)}F_0 \end{aligned} \quad (4.2)$$

where $c_1^2 = (\lambda + 2\mu)/\rho$ and $E = \mu(3\lambda + 2\mu)/(\lambda + \mu)$ is Young's modulus.

Making use of Eqs. (4.1) in Eq. (3.3) and with the aid of Eqs. (4.2), yields (after suppressing primes)

$$\frac{\partial^4 w}{\partial x^4} + a_1 \frac{\partial^2 w}{\partial t^2} - a_2 \frac{\partial^2 \Phi}{\partial x^2} - a_3 \frac{\partial^2 \Psi}{\partial x^2} + a_4 \frac{\partial^2 \Theta}{\partial x^2} = F_0 \delta(x - vt) \quad (4.3)$$

On multiplying Eqs. (3.5) by z and integrating them with respect to z from $-h/2$ to $h/2$ and after using Eq.(4.2), we obtain (suppressing primes for convenience)

$$\begin{aligned} a_5 \frac{\partial^2 \Phi}{\partial x^2} - a_6 \Phi + a_7 \frac{\partial^2 \Psi}{\partial x^2} - a_8 \Psi + a_9 \frac{\partial^2 w}{\partial x^2} - a_{10} \Phi - a_{11} \Psi + a_{12} \Theta &= \frac{\partial^2 \Phi}{\partial t^2} \\ a_{13} \frac{\partial^2 \Phi}{\partial x^2} - a_{14} \Phi + a_{15} \frac{\partial^2 \Psi}{\partial x^2} - a_{16} \Psi + a_{17} \frac{\partial^2 w}{\partial x^2} - a_{18} \Phi - a_{19} \Psi + a_{20} \Theta &= \frac{\partial^2 \Psi}{\partial t^2} \end{aligned} \quad (4.4)$$

and

$$\frac{\partial^2 \Theta}{\partial x^2} - a_{21} \Theta = \left(1 + \tau_0 \frac{\partial}{\partial t} \right) \left[a_{22} \frac{\partial}{\partial t} \left(\frac{\partial^2 w}{\partial x^2} \right) + a_{23} \frac{\partial \Phi}{\partial t} + a_{24} \frac{\partial \Psi}{\partial t} + a_{25} \frac{\partial \Theta}{\partial t} \right] \quad (4.5)$$

where

$$\begin{aligned}
a_1 &= \frac{\rho c_1^2 L}{I(\lambda + 2\mu)} & a_2 &= \frac{2b\alpha}{I\pi^2(\lambda + 2\mu)L} & a_3 &= \frac{2d\alpha}{I\pi^2(\lambda + 2\mu)L} \\
a_4 &= \frac{2E}{I\pi^2(\lambda + 2\mu)} & a_5 &= \frac{\alpha}{\kappa_1 c_1^2} & a_6 &= \frac{\alpha\pi^2 L^2}{\kappa_1 c_1^2 h^2} & a_7 &= \frac{b_1}{\kappa_1 c_1^2} \\
a_8 &= \frac{b_1 \pi^2 L^2}{\kappa_1 c_1^2 h^2} & a_9 &= \frac{bh\pi^2 L^2}{24\alpha\kappa_1 c_1^2} & a_{10} &= \frac{\alpha_1 L^2}{\kappa_1 c_1^2} & a_{11} &= \frac{\alpha_3 L^2}{\kappa_1 c_1^2} \\
a_{12} &= \frac{\gamma_1 E L^3}{\alpha\beta\kappa_1 c_1^2} & a_{13} &= \frac{b_1}{\kappa_2 c_1^2} & a_{14} &= \frac{b_1 \pi^2 L^2}{\kappa_2 c_1^2 h^2} & a_{15} &= \frac{\gamma}{\kappa_2 c_1^2} \\
a_{16} &= \frac{\gamma\pi^2 L^2}{\kappa_2 c_1^2 h^2} & a_{17} &= \frac{dh\pi^2 L^2}{24\alpha\kappa_2 c_1^2} & a_{18} &= \frac{\alpha_3 L^2}{\kappa_2 c_1^2} & a_{19} &= \frac{\alpha_2 L^2}{\kappa_2 c_1^2} \\
a_{20} &= \frac{\gamma_2 E L^3}{\alpha\beta\kappa_2 c_1^2} & a_{21} &= \frac{\pi^2 L^2}{h^2} & a_{22} &= -\frac{\beta^2 T_0 h c_1 \pi^2}{24EK^*} \\
a_{23} &= \frac{\alpha\beta T_0 \gamma_1 c_1}{EK^*} & a_{24} &= \frac{\alpha\beta T_0 \gamma_2 c_1}{EK^*} & a_{25} &= \frac{\rho C^* c_1 L}{K^*}
\end{aligned}$$

The initial conditions of the problem are assumed to be homogeneous and are taken as

$$\begin{aligned}
w(x, t)\Big|_{t=0} &= \frac{\partial w(x, t)}{\partial t}\Big|_{t=0} = \Phi(x, t)\Big|_{t=0} = \frac{\partial \Phi(x, t)}{\partial t}\Big|_{t=0} = \Psi(x, t)\Big|_{t=0} = \frac{\partial \Psi(x, t)}{\partial t}\Big|_{t=0} = 0 \\
\Theta(x, t)\Big|_{t=0} &= \frac{\partial \Theta(x, t)}{\partial t}\Big|_{t=0} = 0
\end{aligned} \tag{4.6}$$

These initial conditions are supplemented by considering that the two ends of the microbeam are clamped and remain at zero increment of the volume fraction fields and temperature. Mathematically, it can be written as

$$\begin{aligned}
w(x, t)\Big|_{x=0, L} &= \frac{\partial w(x, t)}{\partial x}\Big|_{x=0, L} = 0 & \Phi(x, t)\Big|_{x=0, L} &= 0 \\
\Psi(x, t)\Big|_{x=0, L} &= 0 & \Theta(x, t)\Big|_{x=0, L} &= 0
\end{aligned} \tag{4.7}$$

5. Solution in the Laplace transform domain

Applying the Laplace transform defined by

$$\bar{f}(s) = L[f(t)] = \int_0^{\infty} f(t)e^{-st} dt \tag{5.1}$$

to Eqs. (4.3)-(4.5) under initial conditions (4.6), and after some simplifications, we obtain

$$\left(\frac{d^{10}}{dx^{10}} + B_1 \frac{d^8}{dx^8} + B_2 \frac{d^6}{dx^6} + B_3 \frac{d^4}{dx^4} + B_4 \frac{d^2}{dx^2} + B_5 \right) (\bar{w}, \bar{\Phi}, \bar{\Psi}, \bar{\Theta}) = (f_1, f_2, f_3, f_4) e^{-\frac{s}{v}x} \tag{5.2}$$

where $B_1, B_2, B_3, B_4, B_5, f_1, f_2, f_3, f_4$, are given in Appendix I.

The solution to system of Eqs. (5.2), in the Laplace transform domain, can be written as

$$\begin{aligned}
\bar{w} &= H_1 e^{-\frac{s}{v}x} + \sum_{i=1}^5 (D_i e^{-m_i x} + D_{i+5} e^{m_i x}) \\
\bar{\Phi} &= H_2 e^{-\frac{s}{v}x} + \sum_{i=1}^5 g_{1i} (D_i e^{-m_i x} + D_{i+5} e^{m_i x}) \\
\bar{\Psi} &= H_3 e^{-\frac{s}{v}x} + \sum_{i=1}^5 g_{2i} (D_i e^{-m_i x} + D_{i+5} e^{m_i x}) \\
\bar{\Theta} &= H_4 e^{-\frac{s}{v}x} + \sum_{i=1}^5 g_{3i} (D_i e^{-m_i x} + D_{i+5} e^{m_i x})
\end{aligned} \tag{5.3}$$

where

$$H_i = \frac{f_i \nu^{10}}{s^{10} + B_1 s^8 \nu^2 + B_2 s^6 \nu^4 + B_3 s^4 \nu^6 + B_4 s^2 \nu^8 + B_5 \nu^{10}} \quad i = 1, 2, 3, 4$$

and g_{1i}, g_{2i}, g_{3i} ; ($i = 1, 2, 3, 4, 5$) are given in Appendix II.

Here $\pm m_i$, $i = 1, 2, \dots, 5$ are the roots of the characteristic equation

$$m^{10} + B_1 m^8 + B_2 m^6 + B_3 m^4 + B_4 m^2 + B_5 = 0$$

Therefore, the corresponding expressions for the axial displacement in the Laplace transform domain can be written as

$$\bar{u} = -z \frac{d\bar{w}}{dx} = -z \left[\sum_{i=1}^5 (-m_i D_i e^{-m_i x} + m_i D_{i+5} e^{m_i x}) - \frac{s}{v} H_1 e^{-\frac{s}{v}x} \right] \tag{5.4}$$

Boundary conditions (4.7) in the Laplace transform domain take the form as

$$\begin{aligned}
\bar{w}(x, s) \Big|_{x=0, L} = \frac{d\bar{w}(x, s)}{\partial x} \Big|_{x=0, L} &= 0 & \bar{\Phi}(x, s) \Big|_{x=0, L} &= 0 \\
\bar{\Psi}(x, s) \Big|_{x=0, L} &= 0 & \bar{\Theta}(x, s) \Big|_{x=0, L} &= 0
\end{aligned} \tag{5.5}$$

By substituting Eqs. (5.3) into boundary conditions (5.5), we obtain a system of ten linear equations in the matrix form as

$$\mathbf{AD} = \mathbf{E} \tag{5.6}$$

where

$$\mathbf{A} = \begin{bmatrix}
1 & 1 & 1 & 1 & 1 & 1 & 1 & 1 & 1 & 1 \\
b_1 & b_2 & b_3 & b_4 & b_5 & a_1 & a_2 & a_3 & a_4 & a_5 \\
-m_1 & -m_2 & -m_3 & -m_4 & -m_5 & m_1 & m_2 & m_3 & m_4 & m_5 \\
-m_1 b_1 & -m_2 b_2 & -m_3 b_3 & -m_4 b_4 & -m_5 b_5 & m_1 a_1 & m_2 a_2 & m_3 a_3 & m_4 a_4 & m_5 a_5 \\
g_{11} & g_{12} & g_{13} & g_{14} & g_{15} & g_{11} & g_{12} & g_{13} & g_{14} & g_{15} \\
g_{11} b_1 & g_{12} b_2 & g_{13} b_3 & g_{14} b_4 & g_{15} b_5 & g_{11} a_1 & g_{12} a_2 & g_{13} a_3 & g_{14} a_4 & g_{15} a_5 \\
g_{21} & g_{22} & g_{23} & g_{24} & g_{25} & g_{21} & g_{22} & g_{23} & g_{24} & g_{25} \\
g_{21} b_1 & g_{22} b_2 & g_{23} b_3 & g_{24} b_4 & g_{25} b_5 & g_{21} a_1 & g_{22} a_2 & g_{23} a_3 & g_{24} a_4 & g_{25} a_5 \\
g_{31} & g_{32} & g_{33} & g_{34} & g_{35} & g_{31} & g_{32} & g_{33} & g_{34} & g_{35} \\
g_{31} b_1 & g_{32} b_2 & g_{33} b_3 & g_{34} b_4 & g_{35} b_5 & g_{31} a_1 & g_{32} a_2 & g_{33} a_3 & g_{34} a_4 & g_{35} a_5
\end{bmatrix}$$

$$a_i = e^{m_i L} \quad b_i = e^{-m_i L} \quad i = 1, 2, 3, 4, 5$$

$$\mathbf{D} = [D_1 \ D_2 \ D_3 \ D_4 \ D_5 \ D_6 \ D_7 \ D_8 \ D_9 \ D_{10}]^T$$

$$\mathbf{E} = [E_1 \ E_2 \ E_3 \ E_4 \ E_5 \ E_6 \ E_7 \ E_8 \ E_9 \ E_{10}]^T$$

and

$$\begin{aligned} E_1 &= -H_1 & E_2 &= -H_1 e^{-\frac{s}{v}L} & E_3 &= \frac{s}{v}H_1 & E_4 &= \frac{s}{v}H_1 e^{-\frac{s}{v}L} \\ E_5 &= -H_2 & E_6 &= -H_2 e^{-\frac{s}{v}L} & E_7 &= -H_3 & E_8 &= -H_3 e^{-\frac{s}{v}L} \\ E_9 &= -H_4 & E_{10} &= -H_4 e^{-\frac{s}{v}L} \end{aligned}$$

By solving the above system of equations (5.6), we obtain the values of unknown parameters D_i , $i = 1, 2, \dots, 10$.

This completes the solution of the problem in the Laplace transform domain.

In order to determine the axial displacement, lateral deflection, volume fraction field and temperature distribution in the physical domain, we will adopt a numerical inversion method given by Honig and Hirdes (1984).

In this method, the Laplace domain $\bar{f}(s)$ can be inverted to the time domain $f(t)$ as

$$f(t) = \frac{1}{t_1} \exp(\Omega t) \left[\frac{1}{2} \bar{f}(\Omega) + \operatorname{Re} \sum_{k=1}^N \bar{f} \left(\Omega + \frac{ik\pi}{t_1} \right) \exp \left(\frac{ik\pi t}{t_1} \right) \right] \quad 0 < t_1 < 2t$$

where Re is the real part and i is the imaginary unit. The value of N is chosen sufficiently large and it represents the number in terms of the truncated Fourier series such that

$$f(t) = \exp(\Omega t) \operatorname{Re} \left[\bar{f} \left(\Omega + \frac{iN\pi}{t_1} \right) \exp \left(\frac{iN\pi t}{t_1} \right) \right] \leq \varepsilon_1$$

where ε_1 is a prescribed small positive number. Also, the value of Ω should satisfy the relation $\Omega t \simeq 4.7$ for faster convergence, Tzou (1996).

Particular cases

- i) If $\tau_0 = 0$ in equations (5.6), it yields corresponding expressions for the thermoelastic double porous microbeam in context of the coupled theory (CT) of thermoelasticity.
- ii) If $b_1 = \alpha_3 = \gamma = \alpha_2 = \gamma_2 = d \rightarrow 0$ in equations (5.6), we obtain the corresponding expressions for the thermoelastic single porous microbeam (thermoelastic microbeam with voids).

6. Numerical results and discussion

Numerical computations have been done for a copper like material microbeam. The material parameters are taken as in Kumar *et al.* (2015): $\lambda = 7.76 \cdot 10^{10} \text{ Nm}^{-2}$, $C^* = 3.831 \cdot 10^3 \text{ m}^2 \text{ s}^{-2} \text{ K}^{-1}$, $\mu = 3.86 \cdot 10^{10} \text{ Nm}^{-2}$, $K^* = 3.86 \cdot 10^3 \text{ N s}^{-1} \text{ K}^{-1}$, $T_0 = 298 \text{ K}$, $\rho = 8.954 \cdot 10^3 \text{ Kgm}^{-3}$, $\alpha_t = 1.78 \cdot 10^{-5} \text{ K}^{-1}$, $\alpha_2 = 2.4 \cdot 10^{10} \text{ Nm}^{-2}$, $\alpha_3 = 2.5 \cdot 10^{10} \text{ Nm}^{-2}$, $\gamma = 1.1 \cdot 10^{-5} \text{ N}$, $\alpha = 1.3 \cdot 10^{-5} \text{ N}$, $\gamma_2 = 0.219 \cdot 10^5 \text{ Nm}^{-2}$, $\kappa_1 = 0.1456 \cdot 10^{-12} \text{ Nm}^{-2} \text{ s}^2$, $b = 0.9 \cdot 10^{10} \text{ Nm}^{-2}$, $\alpha_1 = 2.3 \cdot 10^{10} \text{ Nm}^{-2}$, $\kappa_2 = 0.1546 \cdot 10^{-12} \text{ Nm}^{-2} \text{ s}^2$, $\tau_0 = 0.01 \text{ s}$.

The aspect ratio of the beam is fixed as $L/h = 10$, $a/h = 0.5$, $z = h/6$. When h is varied, L and a change accordingly with h . For the microscale beam, we take the range of the beam length $L = (1 - 10) \cdot 10^{-6} \text{ m}$. The plots are prepared by using the dimensionless variables for a wide range of the beam length when, unless otherwise stated, $L = 4.0$, $a = h/2$ and $z = h/6$.

The software MATLAB has been used to find the values of axial displacement, lateral deflection, volume fraction field and temperature distribution. Variations of these quantities with respect to the axial distance have been shown in Figs. 2-5 to indicate the effects of velocity and time parameters. In Figs. 2 and 3, solid line, small and big dashes lines correspond to the values of velocity $v = 1.0, 2.0$ and 3.0 , respectively with the fixed value of time $t = 0.15$, whereas in

Figs. 4 and 5, solid line, small and big dashes lines correspond to the values of time $t = 0.15$, 0.175 and 0.2, respectively with the fixed value of velocity $v = 1.0$.

Effect of the velocity parameter

In Fig. 2a, it is noticed that the value of axial displacement u initially decreases in $0 < x < 1$, then increases in $1 \leq x < 2.8$ and again decreases slowly and steadily in the remaining region. It is also found that the magnitude of u decreases with an increase in the value of velocity v near the source application point while the trend gets reversed as moving away from the source. Figure 2b depicts that the lateral deflection w decreases in $0 < x < 1$, increases in $1 \leq x \leq 2.2$ and then becomes stationary as $x \geq 2.2$. The amplitude of variation is higher near the point of application of the source while as moving away from the source, the values become almost stationary for all the values of velocity v . Figure 3a shows that the volume fraction field φ initially decreases sharply in $0 < x < 1$, then increases abruptly in $1 \leq x < 3.5$ and then decreases slowly and steadily in the remaining region. Also, the magnitude of φ decreases as v increases near the source application point while the trend gets reversed away from the source. From Fig. 3b, it is clear that the value of temperature distribution T initially increases in the region $0 < x < 1$ and decreases monotonically as $x \geq 1$. It is also evident that the magnitude of T increases with an increase in velocity v .

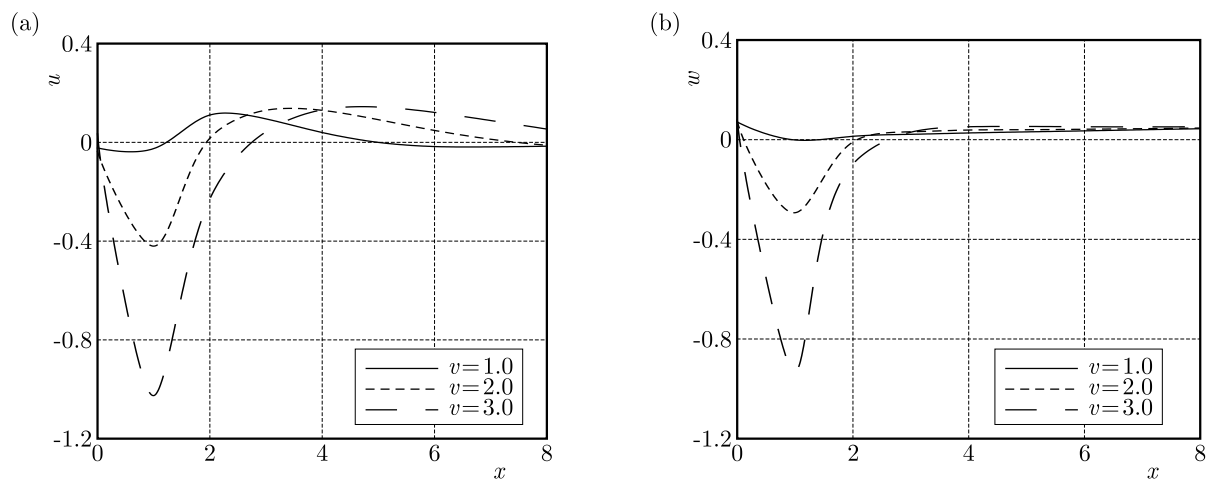


Fig. 2. (a) Axial displacement u and (b) lateral deflection w versus axial distance x

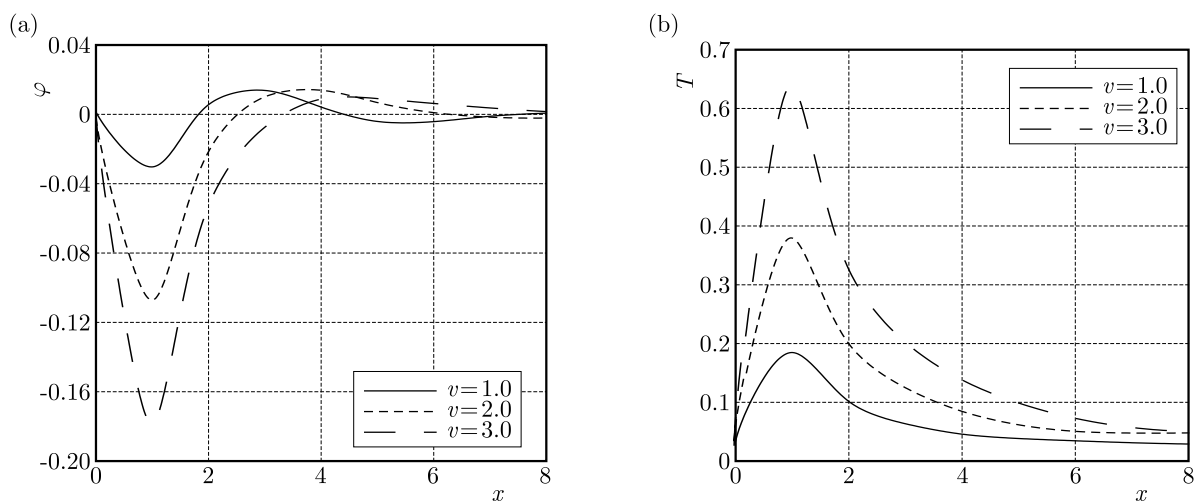


Fig. 3. (a) Volume fraction field φ and (a) temperature distribution T versus axial distance x

Effect of the time parameter

In Fig. 4a, it is noticed that the value of axial displacement u initially decreases in $0 < x < 1$, then increases in $1 \leq x < 2.8$ and again decreases in the remaining region. Also, the magnitude of u increases with an increase in the value of time t . Figure 4b depicts that the lateral deflection w decreases in $0 < x < 1$ and then increases afterwards as $x \geq 1$. It is found that as time t increases, the magnitude of w decreases. Figure 5a shows that the volume fraction field φ is oscillatory in nature. The value of φ initially decreases in the range $0 < x < 1$, then increases in $1 \leq x < 3.5$ and then decreases in $3.5 \leq x < 5.3$ and again starts increasing slowly as $x \geq 5.3$. The magnitude value of φ also increases with an increase in the value of time t . From Fig. 5b, it is clear that the value of temperature distribution T initially increases in the region $0 < x < 1$ and decreases monotonically as $x \geq 1$. It is also found that the magnitude of T decreases with an increase in the value of time t .

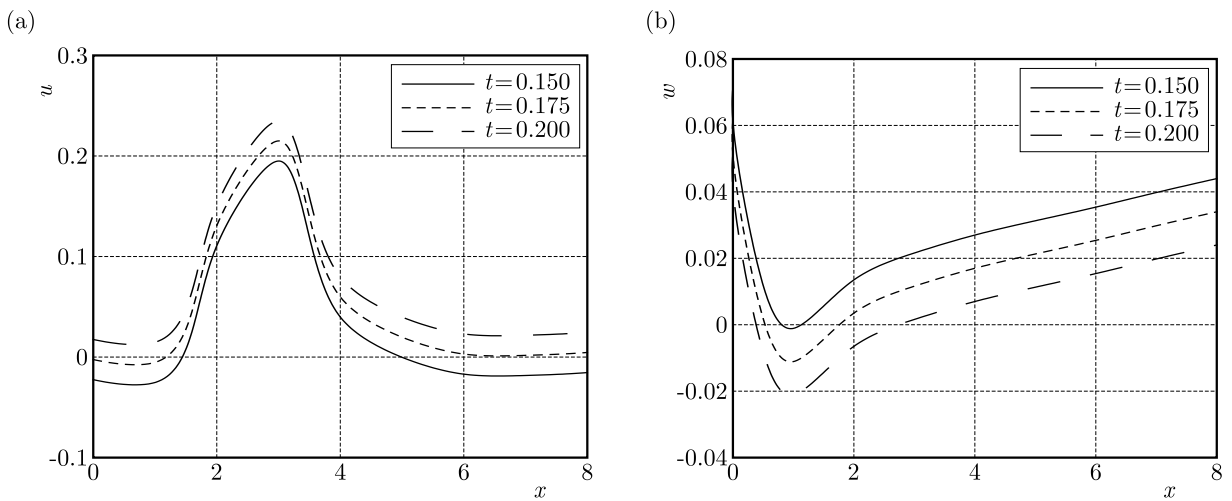


Fig. 4. (a) Axial displacement u and (b) lateral deflection w versus axial distance x

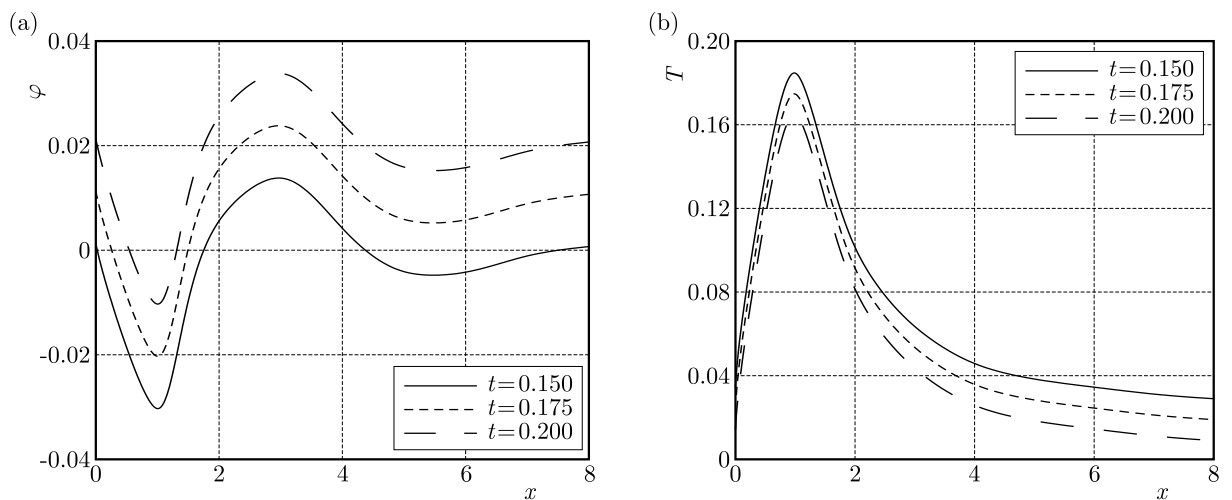


Fig. 5. (a) Volume fraction field φ and (b) temperature distribution T versus axial distance x

7. Conclusions

In the present work, forced vibrations of an Euler-Bernoulli thermoelastic double porous microbeam, in context of Lord-Shulman theory of thermoelasticity, subjected to moving load has been investigated. Effects of velocity and time parameters are shown graphically on axial displacement, lateral deflection, volume fraction field and temperature distribution. All field quantities are observed to be very sensitive towards the velocity as well as time parameters.

- It is observed that the amplitude of variation is higher near the application point of the source while the values become almost stationary as moving away from the source due to the effect of velocity. The values of axial displacement u and volume fraction field φ decrease with an increase in the velocity v near the application point of the source, whereas an opposite trend of variation is noticed away from the source. The values of lateral deflection w also decrease as the velocity parameter increases near the point of application of the source and becomes stationary as moving away from the source. The magnitude of temperature distribution T gets greater with an increase in the velocity parameter.
- Due to the effect of time parameter, the values of axial displacement u and volume fraction field φ increase with an increase in the value of time t , whereas an opposite trend and behavior of variation is observed in the case of lateral deflection w and temperature distribution T , i.e. the values of w and T decrease as there is an increase in the value of time t .

This type of study is useful due to its physical application in many fields of engineering like civil, mechanical, aerospace and industrial sectors. The results obtained in this investigation should prove to be beneficial for researchers working on the theory of thermoelasticity with the double porosity structure. The introduction of the double porous parameter to the thermoelastic medium represents a more realistic model for further studies.

Appendix I

$$\begin{aligned}
 a_{26} &= s(1 + \tau_0 s) & a_{27} &= -s(1 + \tau_0 s)a_{22} & a_{28} &= -s(1 + \tau_0 s)a_{23} \\
 a_{29} &= -s(1 + \tau_0 s)a_{24} & a_{30} &= -[a_{21} + s(1 + \tau_0 s)a_{25}] \\
 n_1 &= -(a_6 + a_{10} + s^2) & n_2 &= -(a_8 + a_{11}) \\
 n_3 &= -(a_{18} + a_{14}) & n_4 &= -(a_{16} + a_{19} + s^2) \\
 r_1 &= a_5 a_{15} - a_7 a_{13} & r_2 &= a_5(a_{15} a_{30} + n_4) - a_{13} n_2 + n_1 a_{15} - a_7(a_{13} a_{30} + n_3) \\
 r_3 &= n_1(a_{15} a_{30} + n_4) + a_5(n_4 a_{30} - a_{20} a_{29}) - a_7(n_3 a_{30} - a_{20} a_{28}) - n_2(a_{13} a_{30} + n_3) \\
 &\quad + a_{12}(a_{13} a_{29} - a_{15} a_{28}) \\
 r_4 &= n_1(n_4 a_{30} - a_{20} a_{29}) + a_{12}(n_3 a_{29} - n_4 a_{28}) + n_2(a_{20} a_{28} - n_3 a_{30}) \\
 r_5 &= a_9 a_{15} - a_7 a_{17} & r_6 &= a_9(a_{15} a_{30} + n_4) - a_7(a_{17} a_{30} - a_{20} a_{27}) - n_2 a_{17} - a_{12} a_{15} a_{27} \\
 r_7 &= a_9(n_4 a_{30} - a_{20} a_{29}) + a_{12}(a_{17} a_{29} - n_4 a_{27}) - n_2(a_{17} a_{30} - a_{20} a_{27}) \\
 r_8 &= a_9 a_{13} - a_5 a_{17} & r_9 &= a_9(a_{13} a_{30} + n_3) - n_1 a_{17} - a_5(a_{17} a_{30} - a_{20} a_{27}) - a_{12} a_{10} a_{27} \\
 r_{10} &= a_9(n_3 a_{30} - a_{20} a_{28}) - n_1(a_{30} a_{17} - a_{27} a_{20}) + a_{12}(a_{17} a_{28} - n_3 a_{27}) \\
 r_{11} &= a_{27}(a_5 a_{12} + a_7 a_{13}) \\
 r_{12} &= a_9(a_{13} a_{29} - a_{15} a_{28}) + a_5(n_4 a_{27} - a_{17} a_{29}) + a_{27}(n_1 a_{15} + a_3 a_{13}) - a_7(a_{17} a_{28} - n_3 a_{27}) \\
 r_{13} &= a_9(n_3 a_{29} - n_4 a_{28}) - n_1(a_{17} a_{29} - n_4 a_{27}) - n_2(a_{17} a_{28} - n_3 a_{27})
 \end{aligned}$$

$$\begin{aligned}
B_1 &= \frac{r_2 + a_2 r_5 - a_3 r_8 - a_4 r_{11}}{r_1} & B_2 &= \frac{a_1 r_1 s^2 + a_2 r_6 - a_3 r_9 - a_4 r_{12} + r_3}{r_1} \\
B_3 &= \frac{a_1 r_3 s^2 + a_2 r_7 - a_3 r_{10} - a_4 r_{13} + r_4}{r_1} & B_4 &= \frac{a_1 r_3 s^2}{r_1} & B_5 &= \frac{a_1 r_4 s^2}{r_1} \\
f_1 &= \frac{1}{v^7} F_0 (r_1 s^6 + r_2 s^4 v^2 + r_3 s^2 v^4 + r_4 v^6) & f_2 &= -\frac{1}{v^7} F_0 (r_5 s^6 + r_6 s^4 v^2 + r_7 v^4 s^2) \\
f_3 &= \frac{1}{v^7} F_0 (r_8 s^6 + r_9 s^4 v^2 + r_{10} v^4 s^2) & f_4 &= -\frac{1}{v^7} F_0 (r_{11} s^6 + r_{12} s^4 v^2 + r_{13} v^4 s^2)
\end{aligned}$$

Appendix II

$$\begin{aligned}
g_{1i} &= -\frac{r_5 m_i^6 + r_6 m_i^4 + r_7 m_i^2}{r_1 m_i^6 + r_2 m_i^4 + r_3 m_i^2 + r_4} & g_{2i} &= \frac{r_8 m_i^6 + r_9 m_i^4 + r_{10} m_i^2}{r_1 m_i^6 + r_2 m_i^4 + r_3 m_i^2 + r_4} \\
g_{3i} &= -\frac{r_{11} m_i^6 + r_{12} m_i^4 + r_{13} m_i^2}{r_1 m_i^6 + r_2 m_i^4 + r_3 m_i^2 + r_4} & i &= 1, 2, \dots, 5
\end{aligned}$$

References

1. BARENBLATT G.I., ZHELTOV I.P., KOCHINA I.N., 1960, Basic concept in the theory of seepage of homogeneous liquids in fissured rocks (strata), *Journal of Applied Mathematics and Mechanics*, **24**, 1286-1303
2. BIOT M.A., 1941, General theory of three-dimensional consolidation, *Journal of Applied Physics*, **12**, 155-164
3. CHANG T.P., LIU Y.N., 1996, Dynamic finite element analysis of a nonlinear beam subjected to a moving load, *International Journal of Solids and Structures*, **33**, 12, 1673-1688
4. COWIN S.C., NUNZIATO J.W., 1983, Linear elastic materials with voids, *Journal of Elasticity*, **13**, 125-147
5. ESEN I., 2015, A new FEM procedure for transverse and longitudinal vibration analysis of thin rectangular plates subjected to a variable velocity moving load along an arbitrary trajectory, *Latin American Journal of Solids and Structures*, **12**, 808-830
6. HONIG G., HIRDES U., 1984, A method for the numerical inversion of the Laplace transforms, *Journal of Computational and Applied Mathematics*, **10**, 113-132
7. IESAN D., QUINTANILLA R., 2014, On a theory of thermoelastic materials with a double porosity structure, *Journal of Thermal Stresses*, **37**, 1017-1036
8. KAGHAZIAN A., HAJNAYEB A., FORUZANDE H., 2017, Free vibration analysis of a piezoelectric nanobeam using nonlocal elasticity theory, *Structural Engineering and Mechanics*, **61**, 5, 617-624
9. KARGARNOVIN M.H., AHMADIAN M.T., TALOOKOLAEI R.A.J., 2012, Dynamics of a delaminated Timoshenko beam subjected to a moving oscillatory mass, *Mechanics Based Design of Structures and Machines*, **40**, 2, 218-240
10. KHALILI N., 2003, Coupling effects in double porosity media with deformable matrix, *Geophysical Research Letters*, **30**, 22, 2153, DOI: 10.1029/2003GL018544
11. KUMAR R., 2016, Response of thermoelastic beam due to thermal source in modified couple stress theory, *Computational Methods in Science and Technology*, **22**, 2, 95-101
12. KUMAR R., VOHRA R., GORLA M.G., 2015, State space approach to boundary value problem for thermoelastic material with double porosity, *Applied Mathematics and Computation*, **271**, 1038-1052

13. LORD H., SHULMAN Y., 1967, A generalized dynamical theory of thermoelasticity, *Journal of Mechanics and Physics of Solids*, **15**, 299-309
14. MEHRI B., DAVAR A., RAHMANI O., 2009, Dynamic Green function solution of beams under a moving load with different boundary conditions, *Scientia Iranica*, **16**, 3, 273-279
15. MICHALTSOS G., SOPIANOPOULOU D., KOUNADIS A.N., 1996, The effect of moving mass and other parameters on the dynamic response of a simply supported beam, *Journal of Sound and Vibration*, **191**, 357-362
16. NUNZIATO J.W., COWIN S.C., 1979, A nonlinear theory of elastic materials with voids, *Archive of Rational Mechanics and Analysis*, **72**, 175-201
17. OLSSON M., 1991, On the fundamental moving load problem, *Journal of Sound and Vibration*, **145**, 2, 299-307
18. RAO G.W., 2000, Linear dynamics of an elastic beam under moving loads, *Journal of Vibration and Acoustics*, **122**, 3, 281-289
19. SHARMA J.N., GROVER D., 2011, Thermoelastic Vibrations in micro-/nano-scale beam resonators with voids, *Journal of Sound and Vibration*, **330**, 2964-2977
20. SHERIEF H., SALEH H., 2005, A half space problem in the theory of generalized thermoelastic diffusion, *International Journal of Solids and Structures*, **42**, 4484-4493
21. SUN Y., FANG D, SAKA M , SOH A.K., 2008, Laser-induced vibrations of micro-beams under different boundary conditions, *International Journal of Solids and Structures*, **45**, 1993-2013
22. TZOU D., 1996, *Macro-to-Micro Heat transfer*, Taylor & Francis, Washington DC
23. ZENKOUR A.M., 2017, Thermoelastic response of a microbeam embedded in visco-Pasternak's medium based on GN-III model, *Journal of Thermal Stresses*, **40**, 2, 198-210

Manuscript received May 9, 2017; accepted for print August 23, 2018

APPLICATION OF LINEAR SIX-PARAMETER SHELL THEORY TO THE ANALYSIS OF ORTHOTROPIC TENSEGRITY PLATE-LIKE STRUCTURES

PAULINA OBARA

Kielce University of Technology, Faculty of Civil Engineering and Architecture, Kielce, Poland

e-mail: paula@tu.kielce.pl

Application of the linear six-parameter shell theory to the analysis of orthotropic tensegrity plate-like structures is proposed in the paper. A continuum model of a tensegrity plate with the self-stress state included is used. The tensegrity module, which is based on 4-strut expanded octahedron modules with additional connecting cables is proposed as an example. Different planes of support of the structures are taken into account and thus different reference surfaces of the plate model are considered. The self-stress state and some geometrical parameters are introduced for parametric analysis.

Keywords: linear six-parameter shell theory, tensegrity plate-like structures, self-stress state

1. Introduction

The concept of tensegrity structures covers trusses consisting of isolated compressed elements (struts) inside a continuous net of tensioned members (cables) (Motto, 2003; Skelton and Oliveira, 2009). The specificity of these structures lies in infinitesimal mechanisms balanced with self-stress states. Tensegrity as a structural system offers many advantages over conventional structural systems. Proper actuation can keep it stiff during deployment without requiring external members, which is the main benefit of the system. The tensegrity concept has found applications in civil engineering structures such as towers (Schlaich, 2004; Gilewski *et al.*, 2015), bridges (Gilewski and Kasprzak, 2011) and domes (Gómez-Jáuregui, 2010). Tensegrity based on spatial reticulated systems are double-layer tensegrity grids (Gómez-Jáuregui *et al.*, 2012) with two parallel horizontal networks of members in tension forming the top and bottom layers. The grid nodes are linked by vertical and inclined bracing members in compression and tension. These systems can be treated as tensegrity plate-like structures. Examples are Kono's structure (Kono *et al.*, 1999) and Blur building (Crawfordt, 2016; Gilewski *et al.*, 2016). Tensegrity plate-like structures can also be built with tensegrity modules, such as a simplex or an expanded octahedron. Even very simple tensegrity structures have complex geometry and unique features. Their structural behaviour can be explained using a continuum model of a three-dimensional tensegrity plate-like structure (Al Sabouni-Zawadzka *et al.*, 2016).

In the paper, a continuum model of the plate is used. The model includes the effect of self-stress initially applied to the tensegrity structure. In the analysis, a linear six-parameter shell theory (Chróścielewski *et al.*, 2004; Pietraszkiewicz, 2016) is proposed. In considerations, the shell theory is simplified by assuming that the plates have no curvature. As a result, the two-dimensional plate model for moderately thick plates is obtained for both membrane and bending deformations. Additionally, different planes of support of tensegrity plate-like structures are taken into account, thus different reference planes of the plate model – the lower surface, the middle surface and the upper surface are considered. The proposed approach allows one to analyse the influence of self-stress states and some geometrical parameters on average displacements, strains and internal forces in the structures.

The model used in the paper is valid for all structures composed of tensegrity modules with orthotropic properties.

2. Material and methods

2.1. Linear six-parameter shell theory for the orthotropic model

Developments of the theory of elastic shells have been widely discussed in papers and monographs. In the paper, the six-parameter (six-field) shell theory is used (Burzyński *et al.*, 2016; Chróścielewski *et al.*, 2004, 2011, 2016; Pietraszkiewicz, 2016; Witkowski, 2011). This kinematic model is formally equivalent to the Cosserat continuum with six independent degrees of freedom: three translations and three rotations (with the drilling degree of freedom). It is assumed that translations and rotations are small, i.e., the linear six-parameter shell theory can be used. As one of the first, the linear constitutive equation for Cosserat continuum was derived by Nowacki (1971). In this approach, the linear six-parameter shell theory is applied to the analysis of tensegrity plate-like structures.

The rectangular plate of a constant thickness h in the Cartesian coordinate system (x_1, x_2, z) is considered (Fig. 1). According to the Hencky-Boole kinematic hypothesis, a displacement field in the 3D space is described as

$$\tilde{\mathbf{u}}(x_\alpha, z) = \mathbf{u}(x_\alpha) + z\boldsymbol{\beta}(x_\alpha) \quad \text{for} \quad \alpha = 1, 2 \quad (2.1)$$

where \mathbf{u} is the translation vector and $\boldsymbol{\beta}$ is the rotation vector of the reference surface (2D)

$$\mathbf{u}(x_\alpha) = [u_\alpha, w]^T \quad \boldsymbol{\beta}(x_\alpha) = [\phi_\alpha, \psi]^T \quad (2.2)$$

The proposed approach, compared to the classical five-parameter theory, includes additionally third independent non-vanishing rotation – the drilling degree of freedom ψ (rotation about the normal to the surface).

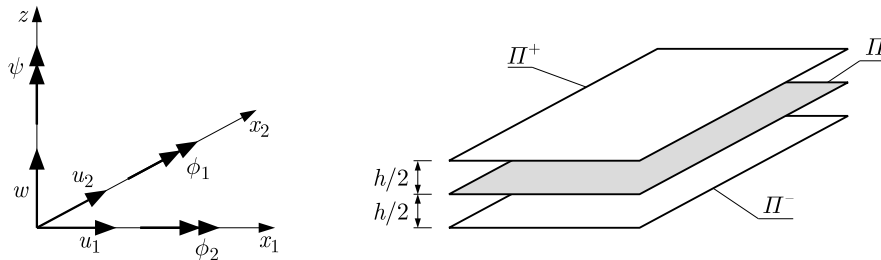


Fig. 1. Geometry of a 3D plate-like body

In a plate, there is no curvature, which means that the curvature of tensors is equal to zero, consequently, a model analysed in the paper is simpler than that shown by Chróścielewski *et al.* (2004) and by Pietraszkiewicz (2016). Consequently, the linear six-parameter shell theory is simplified. Below the reduced relations and equations are showed:

— the kinematic relations

$$\gamma_{\alpha\beta} = u_{\alpha,\beta} - \epsilon_{\alpha\beta}\psi \quad \gamma_{\alpha 3} = \phi_\alpha + w_{,\alpha} \quad \kappa_{\alpha\beta} = \phi_{\alpha,\beta} \quad \kappa_{\alpha 3} = \psi_{,\alpha} \quad (2.3)$$

where $\gamma_{\alpha\beta}$, $\gamma_{\alpha 3}$, $\kappa_{\alpha\beta}$, $\kappa_{\alpha 3}$ are the strain components and $\epsilon_{\alpha\beta}$ is the Ricci symbol,

— the internal forces

$$\begin{aligned} N_{\alpha\beta} &= \int_{z_1}^{z_2} S_{\alpha\beta} dz & N_{\alpha 3} &= \int_{z_1}^{z_2} S_{\alpha 3} dz \\ M_{\alpha\beta} &= \int_{z_1}^{z_2} S_{\alpha\beta} z dz & M_{\alpha 3} &= \int_{z_1}^{z_2} S_{\alpha 3} z dz \end{aligned} \quad (2.4)$$

where $S_{\alpha\beta}$ and $S_{\alpha 3}$ are the stress components,
— the equilibrium equations

$$\begin{aligned} N_{\alpha\beta,\alpha} + f_\beta &= 0 & N_{\alpha 3,\alpha} + f_3 &= 0 \\ M_{\alpha\beta,\alpha} + N_{\beta 3} + m_\beta &= 0 & M_{\alpha 3,\alpha} + \epsilon_{\alpha\beta} N_{\alpha\beta} + m_3 &= 0 \end{aligned} \quad (2.5)$$

where f_β , f_3 , m_β , m_3 are the external loads.

Internal forces (2.4) depend on the reference surface. In the paper, three different reference surfaces of the plate model are considered: the lower Ω^L , the middle Ω^M and the upper Ω^U . In the mentioned approaches, the domains of the plate are defined as follows (Fig. 1)

$$\begin{aligned} \Omega^L &= \{x_K : x_\alpha \in \Pi^-, z \in \langle z_1, z_2 \rangle; z_1 = 0, z_2 = h\} \\ \Omega^M &= \{x_K : x_\alpha \in \Pi, z \in \langle z_1, z_2 \rangle; z_1 = -h/2, z_2 = h/2\} \\ \Omega^U &= \{x_K : x_\alpha \in \Pi^+, z \in \langle z_1, z_2 \rangle; z_1 = -h, z_2 = 0\} \end{aligned} \quad (2.6)$$

Consequently, limitation of integrations (2.4) for each surface follows from the domains definitions.

A complete six-parameter linear shell theory containing the drilling rotation ψ , two work-conjugate drilling bending measures $\kappa_{\alpha 3}$ and two drilling couples $M_{\alpha 3}$ is presented in the paper. The constitutive equation for the linear theory of elasticity is expressed as

$$S_{ij} = D_{ijkl} E_{kl} \quad i, j, k, l = 1, 2, 3 \quad (2.7)$$

where S_{ij} is the component of the stress tensor, E_{kl} is the component of the strain tensor and D_{ijkl} is the component of the fourth-rank tensor of elasticity. In general, a tensor of elasticity contains 36 independent components, but taking into account the symmetry of strain energy 21 distinct components can be set out. The number of independent components is further reduced if the material has symmetry planes. There are exactly eight different sets of symmetry planes (Chadwick *et al.*, 2001). One of them is orthogonal symmetry (orthotropic material). This material requires 9 elastic constants in a two-dimensional case.

In the paper, the orthotropic tensegrity plate-like structures based on the Reissner-Mindlin theory are discussed. For this model, the tensor of elasticity can be written as a matrix $\{D_{ijkl}\} \equiv \mathbf{d}$ which contains 6 nonzero independent components

$$\begin{aligned} B_{1111}^0 &= d_{11} & B_{2222}^0 &= d_{22} & 2B_{2323}^0 &= d_{44} \\ 2B_{1313}^0 &= d_{55} & 2B_{1212}^0 &= d_{66} & B_{1122}^0 &= d_{12} \end{aligned} \quad (2.8)$$

The stress tensor and the strain tensor are written as

$$S_{ij} = \left\{ S_{11} \quad S_{22} \quad S_{23} \quad S_{13} \quad S_{12} \right\}^T \quad E_{kl} = \left\{ E_{11} \quad E_{22} \quad 2E_{23} \quad 2E_{13} \quad 2E_{12} \right\}^T \quad (2.9)$$

where

$$\begin{aligned} E_{11} &= \gamma_{11} + z\kappa_{11} & E_{22} &= \gamma_{22} + z\kappa_{22} & E_{23} &= \frac{1}{2}(\gamma_{23} + z\kappa_{23}) \\ E_{13} &= \frac{1}{2}(\gamma_{13} + z\kappa_{13}) & E_{12} &= \frac{1}{2}(\gamma_{12} + \gamma_{21} + z\kappa_{12} + z\kappa_{21}) \end{aligned} \quad (2.10)$$

Stress components (2.9)₁ are received from constitutive equations (2.7). Next, taking into account the lower, middle and upper reference surfaces, the internal forces (2.4) are calculated

$$\begin{aligned} N_{11} &= h_0 d_{11} \gamma_{11} + h_0 d_{12} \gamma_{22} + h_1 d_{11} \kappa_{11} + h_1 d_{12} \kappa_{22} \\ N_{22} &= h_0 d_{12} \gamma_{11} + h_0 d_{22} \gamma_{22} + h_1 d_{12} \kappa_{11} + h_1 d_{22} \kappa_{22} \\ N_{12} &= h_0 d_{66} (\gamma_{12} + \gamma_{21}) + h_1 d_{66} (\kappa_{12} + \kappa_{21}) \\ N_{13} &= \alpha_0 h_0 d_{55} \gamma_{13} + \alpha_1 h_1 d_{55} \kappa_{13} & N_{23} &= \alpha_0 h_0 d_{44} \gamma_{23} + \alpha_1 h_1 d_{44} \kappa_{23} \end{aligned} \quad (2.11)$$

and

$$\begin{aligned}
M_{11} &= h_1 d_{11} \gamma_{11} + h_1 d_{12} \gamma_{22} + h_2 d_{11} \kappa_{11} + h_2 d_{12} \kappa_{22} \\
M_{22} &= h_1 d_{12} \gamma_{11} + h_1 d_{22} \gamma_{22} + h_2 d_{12} \kappa_{11} + h_2 d_{22} \kappa_{22} \\
M_{12} &= h_1 d_{66} (\gamma_{12} + \gamma_{21}) + h_2 d_{66} (\kappa_{12} + \kappa_{21}) \\
M_{13} &= \alpha_1 h_1 d_{55} \gamma_{13} + \alpha_2 h_2 d_{55} \kappa_{13} & M_{23} &= \alpha_1 h_1 d_{44} \gamma_{23} + \alpha_2 h_2 d_{44} \kappa_{23}
\end{aligned} \tag{2.12}$$

where h_i ($i = 0, 1, 2$) are parameters depending on the reference surfaces (values are shown in Table 1) and α_i ($i = 0, 1, 2$) are shear correction factors.

The problem of determining the shear factor was created in the Timoshenko beam theory, which takes into account the transverse shear deformation and the rotatory inertia (Khorshidi and Shariati, 2017; Obara and Gilewski, 2016; Timoshenko and Gere, 1961). Within the general six-parameter shell model used here, the shear correction factors α_0 and α_2 are introduced into the constitutive equations for the respective transverse shear stress resultants and stress couples (Chróścielewski *et al.*, 1997). The values of two correction factors $\alpha_0 = 5/6$ and $\alpha_2 = 7/10$, with detailed derivation of these values, were arrived by Pietraszkiewicz (1979). The more information about the shear factors and the influence of different values of these factors on the results of static and dynamic behaviour of shell structures can be found in Chróścielewski *et al.* (2000). In the paper, additionally a correction factor α_1 is introduced. This factor is significant if the lower surface or the upper surface is used as the reference plane.

The closed form of the equilibrium equations for a plate ($x_1 \in \langle 0, a \rangle$ and $x_2 \in \langle 0, b \rangle$) and a plate strip ($x_1 \in \langle 0, a \rangle$ and $x_2 \in (-\infty, +\infty)$) can be obtained by inserting Eqs. (2.11) and (2.12) into Eq. (2.5).

2.1.1. Plate

The behaviour at any point of the considered plate is defined by generalized displacements \mathbf{q} and the corresponding to them internal forces \mathbf{Q}

$$\begin{aligned}
\mathbf{q} &= \mathbf{q}(x_1, x_2) = [u_1, u_2, \psi, \phi_1, \phi_2, w]^T \\
\mathbf{Q} &= \mathbf{Q}(x_1, x_2) = -[f_1, f_2, m_3, m_1, m_2, f_3]^T
\end{aligned} \tag{2.13}$$

The first three displacements in (2.13)₁ describe the membrane state and the last three – the bending state. In general, these states are coupled. Equilibrium equations (2.5) for the plate can be written as

$$\mathbf{Lq} = \mathbf{Q} \tag{2.14}$$

where

$$\mathbf{L} = \begin{bmatrix} h_0 L_1 & h_0 L_4 & 0 & h_1 L_1 & h_1 L_4 & 0 \\ h_0 L_4 & h_0 L_2 & 0 & h_1 L_4 & h_1 L_2 & 0 \\ 0 & 0 & \alpha_2 h_2 L_3 & \alpha_1 h_1 L_5 & \alpha_1 h_1 L_6 & \alpha_1 h_1 L_3 \\ h_1 L_1 & h_1 L_4 & -\alpha_1 h_1 L_5 & h_2 L_1 - \alpha_0 h_0 d_{55} & h_2 L_4 & -\alpha_0 h_0 L_5 \\ h_1 L_4 & h_1 L_2 & -\alpha_1 h_1 L_6 & h_2 L_4 & h_2 L_2 - \alpha_0 h_0 d_{44} & -\alpha_0 h_0 L_6 \\ 0 & 0 & \alpha_1 h_1 L_3 & \alpha_0 h_0 L_5 & \alpha_0 h_0 L_6 & \alpha_0 h_0 L_3 \end{bmatrix} \tag{2.15}$$

where

$$\begin{aligned}
L_1 &= d_{11} \frac{\partial^2}{\partial x_1^2} + d_{66} \frac{\partial^2}{\partial x_2^2} & L_2 &= d_{66} \frac{\partial^2}{\partial x_1^2} + d_{22} \frac{\partial^2}{\partial x_2^2} & L_3 &= d_{55} \frac{\partial^2}{\partial x_1^2} + d_{44} \frac{\partial^2}{\partial x_2^2} \\
L_4 &= (d_{12} + d_{66}) \frac{\partial^2}{\partial x_1 \partial x_2} & L_5 &= d_{55} \frac{\partial}{\partial x_1} & L_6 &= d_{44} \frac{\partial}{\partial x_2}
\end{aligned} \tag{2.16}$$

2.1.2. Plate strip

The behaviour of the considered plate strip, with width a , is defined by generalized displacements $\tilde{\mathbf{q}}$ and the corresponding to them internal forces $\tilde{\mathbf{Q}}$

$$\tilde{\mathbf{q}} = \tilde{\mathbf{q}}(x_1) = [u_1, \psi, \phi_1, w]^T \quad \tilde{\mathbf{Q}} = \tilde{\mathbf{Q}}(x_1) = -a^2[f_1, m_3, m_1, f_3]^T \quad (2.17)$$

Equilibrium equations (2.5) for the plate strip can be written as

$$\tilde{\mathbf{L}}\tilde{\mathbf{q}} = \tilde{\mathbf{Q}} \quad (2.18)$$

where

$$\tilde{\mathbf{L}} = \begin{bmatrix} A_0\tilde{L}_1 & 0 & A_1\tilde{L}_1 & 0 \\ 0 & B_2\tilde{L}_1 & aB_1\tilde{L}_2 & B_2\tilde{L}_1 \\ A_1\tilde{L}_1 & -aB_1\tilde{L}_2 & -a^2B_0 + A_2\tilde{L}_1 & -aB_0\tilde{L}_2 \\ 0 & B_1\tilde{L}_1 & aB_0\tilde{L}_2 & B_0\tilde{L}_1 \end{bmatrix} \quad (2.19)$$

where

$$\begin{aligned} \tilde{L}_1 &= \frac{d^2}{d\xi^2} & \tilde{L}_2 &= \frac{d}{d\xi} & \xi &= \frac{x_1}{a} \\ A_i &= h_i d_{11} & B_i &= \alpha_i h_i d_{55} & \text{for } i &= 0, 1, 2 \end{aligned} \quad (2.20)$$

The parameters A_i and B_i depend on the reference surfaces. The formulas of these parameters are shown in Table 1. For the plate strip, as in the case of the plate, the membrane state and the bending state are coupled.

Table 1. Formulas of the parameters h_i , A_i and B_i for the reference surfaces

Parameters	Lower surface	Middle surface	Upper surface
h_0	h	h	h
h_1	$h^2/2$	0	$-h^2/2$
h_2	$h^3/3$	$h^3/12$	$h^3/3$
A_0	hd_{11}	hd_{11}	hd_{11}
A_1	$h^2d_{11}/2$	0	$-h^2d_{11}/2$
A_2	$h^3d_{11}/3$	$h^3d_{11}/12$	$h^3d_{11}/3$
B_0	α_0hd_{55}	α_0hd_{55}	α_0hd_{55}
B_1	$\alpha_1h^2d_{55}/2$	0	$-\alpha_1h^2d_{55}/2$
B_2	$\alpha_2h^3d_{55}/3$	$\alpha_2h^3d_{55}/12$	$\alpha_2h^3d_{55}/3$

Solving the set of differential equations (2.18) it is possible to obtain explicit formulas of the displacement and internal force. The mentioned formulas are described as follows

$$\begin{aligned} u_1(\xi) &= C_5 + C_6\xi + \frac{3A_1}{aA_0}C_4\xi^2 - \frac{a^2}{2A_0}f_1\xi^2 + \frac{a^3E_1}{6}f_3\xi^3 \\ \psi(\xi) &= C_7 + C_8\xi + \frac{a^2}{2}(D_1f_3 - D_0m_3)\xi^2 \\ \phi_1(\xi) &= -\frac{1}{a}\left(C_2 + 2C_3\xi + 3C_4\xi^2 + \frac{6}{a^2B_0E_0}C_4 + \frac{B_1}{B_0}C_8\right) - \frac{a}{B_0}(1 + B_1D_1)f_3\xi \\ &\quad - \frac{a^3E_0}{6}f_3\xi^3 + aD_1m_3\xi + \frac{1}{B_0}m_1 - \frac{A_1}{A_0B_0}f_1 \\ w(\xi) &= C_1 + C_2\xi + C_3\xi^2 + C_4\xi^3 + \frac{a^4E_0}{24}f_3\xi^4 \end{aligned} \quad (2.21)$$

and

$$\begin{aligned}
N_{11}(\xi) &= -\frac{2A_1}{a^2}C_3 + \frac{A_0}{a}C_6 - af_1\xi - \frac{A_1}{B_0}(1 + B_1D_1)f_3 + A_1D_1m_3 \\
N_{13}(\xi) &= -\frac{6}{a^3E_0}C_4 - af_3\xi - \frac{A_1}{A_0}f_1 + m_1 \\
M_{11}(\xi) &= -\frac{2A_2}{a^2}C_3 - \frac{6}{a^2E_0}C_4\xi + \frac{A_1}{a}C_6 - \frac{aA_1}{A_0}f_1\xi + \frac{a^2}{2}(A_1E_1 - A_2E_0)f_3\xi^2 \\
&\quad - \frac{A_2}{B_0}(1 + B_1D_1)f_3 + A_2D_1m_3 \\
M_{13}(\xi) &= -\frac{6B_1}{a^3B_0E_0}C_4 + \frac{1}{aD_0}C_8 + a(B_1D_1 - B_2D_2)m_3\xi - \frac{A_1B_1}{A_0B_0}f_1 + \frac{B_1m_1}{B_0}
\end{aligned} \tag{2.22}$$

where

$$D_i = \frac{B_i}{B_0B_2 - B_1^2} \quad E_i = \frac{A_i}{A_0A_2 - A_1^2} \quad \text{for } i = 0, 1, 2 \tag{2.23}$$

The results for the plate and plate strip can be used in analysis of different types of orthotropic systems, such as beams, plate strips, plates or more complicated multi-module plate-like structures. The displacement and internal force functions of these systems depend on the components of elastic matrix (2.8).

To illustrate the proposed approach, a continuum orthotropic model of the tensegrity plate-like structure is used. The internal and external plane of support of the structure is taken into account. For tensegrity systems, the components of the elastic matrix depend on stiffness of cables and struts and on the level of self-stress.

2.2. Orthotropic tensegrity plate-like structure

The orthotropic model of a tensegrity plate-like structure is based on the energetic equivalence between the discrete tensegrity repeatable element and the continuum model of the orthotropic material element shown in Fig. 2 (Al Sabouni-Zawadzka and Gilewski, 2016; Kebiche *et al.*, 2008). This approach can be used to a chosen structure of repeatable tensegrity elements creating plate-like structures.

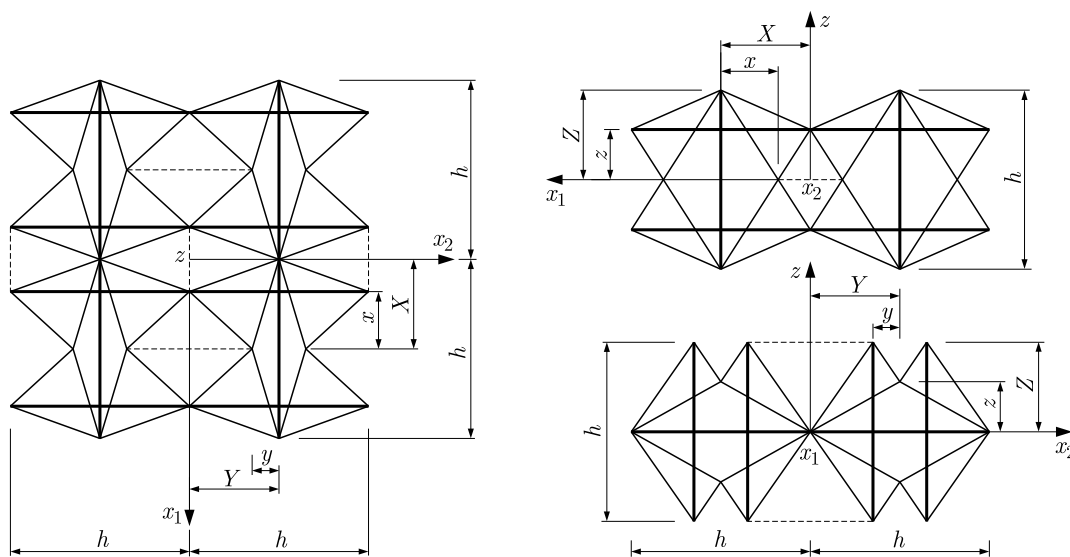


Fig. 2. Views of expanded four-strut octahedron modules with additional cables (dotted line)

A system of fully connected, repeating expanded four-strut octahedron modules with additional cables (Al Sabouni-Zawadzka *et al.*, 2016) is used as an example. The system is orthotropic for the following geometric parameters $x/X = 0.65$, $y/Y = 0.3$ and $z/Z = 0.56$. This system consists of struts, regular cables and connecting cables, which are described by the following coefficients

$$n = \frac{(EA)_{cable}}{(EA)_{struct}} \quad m = \frac{(EA)_{conection}}{(EA)_{struct}} \quad \sigma = \frac{S}{(EA)_{struct}} \quad (2.24)$$

where E is the Young modulus, A is cross section area and S is the axial force. The coefficients n and m describe the proportions of member properties, and σ describes the level of self-stress in tensegrity structures.

The self-stress state is the most important feature of tensegrity structures. This state makes the structure as strong as the self-supporting structure and stabilizes the infinitesimal mechanisms occurred in tensegrity structures. The impact of the self-stress state in the structure is taken into account by using the geometric stiffness matrix.

The coefficients of elastic matrix (2.8) of the tensegrity plate-like structure are as follows:

$$\begin{aligned} d_{11} &= \frac{2EA}{h^2} \delta_{11} & d_{22} &= \frac{2EA}{h^2} \delta_{22} & d_{12} &= \frac{EA}{h^2} \delta_{12} \\ d_{44} &= \frac{EA}{h^2} \delta_{23} & d_{55} &= \frac{EA}{h^2} \delta_{13} & d_{66} &= \frac{EA}{h^2} \delta_{12} \end{aligned} \quad (2.25)$$

where

$$\begin{aligned} EA &= (EA)_{struct} & \delta_{12} &= 0.845615n - 0.105243\sigma \\ \delta_{11} &= 1 + 1.52325n + 0.13125m + 0.129225\sigma & \delta_{13} &= 1.26604n - 0.153207\sigma \\ \delta_{22} &= 1 + 1.35912n + 0.35m + 0.137028\sigma & \delta_{23} &= 1.51283n - 0.168813\sigma \end{aligned} \quad (2.26)$$

3. Results and discussion

Displacements and the internal forces for tensegrity plate-like structures, as a function of parameters (2.26), and, in consequence, coefficients (2.24) are determined. The jointly supported rectangular plate and plate strips with different kinds of boundary conditions are discussed. The different planes of support in tensegrity plate-like structures are analysed. The results of the analysis are described using L for the lower surface, M for the middle surface and U for the upper surface.

The displacements and internal forces are presented in the closed form. Displacements as a function of coefficients n and σ are presented in the form of graphs. Constants C_i ($i = P, F, M$) are not taken into account in the graphs.

3.1. Jointly supported rectangular plate

The first example is the jointly supported plate with a sinusoidal load (Fig. 3)

$$f_3(x_1, x_2) = -q_0 \sin \frac{\pi x_1}{a} \cos \frac{\pi x_2}{b} \quad (3.1)$$

Solving equation (2.14) by applying the Fourier sine and cosine series that satisfy the boundary conditions, leads to determining the displacements for the lower, the middle and the upper surface. The closed form of solutions for the maximum deflection $w_{max} = w(0.5a, 0.5b)$ for a square plate ($b = a$) are as follows

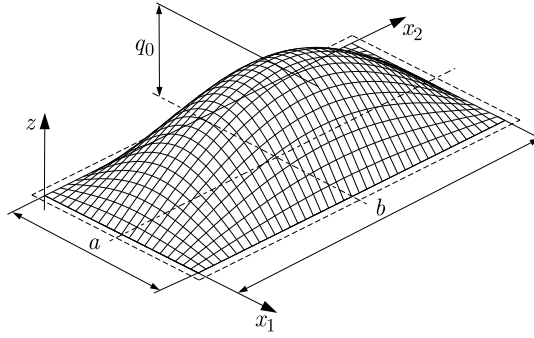


Fig. 3. Rectangular plate jointly supported

$$\begin{aligned}
 w_{max}^M &= C_P \left(\frac{144\alpha_0^2 a^4 \beta_0 + h^2 \pi^2 \beta_2 + 12\alpha_0 a^2 h^2 \pi^2 \beta_3}{\alpha_0 (\beta_1 \beta_2 + \beta_4)} \right) \\
 w_{max}^L &= w_{max}^U = C_P \left(\frac{4(36\alpha_0 \alpha_3 a^4 \beta_0 + \alpha_2 h^2 \pi^2 \beta_2) \beta_1 + 12a^2 h^2 \pi^2 (4\alpha_0 \alpha_2 \beta_1 \beta_3 - \beta_5)}{\alpha_3 (\beta_1 \beta_2 + \beta_4) \beta_1} \right)
 \end{aligned} \tag{3.2}$$

where

$$\begin{aligned}
 C_P &= \frac{a^2 q_0}{EA h \pi^4} & \beta_0 &= \delta_{13} \delta_{23} & \beta_1 &= \delta_{13} + \delta_{23} \\
 \beta_2 &= h^2 \pi^2 [\delta_{12} (2\delta_{22} - 3\delta_{12}) + 2\delta_{11} (\delta_{12} + 2\delta_{22})] \\
 \beta_3 &= \delta_{13} (\delta_{12} + 2\delta_{22}) + \delta_{23} (\delta_{12} + 2\delta_{11}) & \beta_4 &= 24\alpha_0 a^2 \delta_{13} \delta_{23} (\delta_{11} + \delta_{22} + 3\delta_{12}) \\
 \beta_5 &= 3\alpha_1^2 [\delta_{13}^2 (\delta_{12} + 2\delta_{22}) + \delta_{23}^2 (\delta_{12} + 2\delta_{11}) - 4\delta_{12} \delta_{13} \delta_{23}]
 \end{aligned} \tag{3.3}$$

For any rectangular plate, the decoupling of bending and membrane behaviour occurs only for the middle reference surface. It means that for this surface the displacements describing the membrane state are equal to zero: $u_1^M(\xi) = u_2^M(\xi) = \psi^M(\xi) = 0$. For the lower and the upper surface, the vertical displacements are the same (3.2)₂, and the membrane displacements are as follows: $u_1^L(\xi) = -u_1^U(\xi)$, $u_2^L(\xi) = -u_2^U(\xi)$ and $\psi^L(\xi) = -\psi^U(\xi)$. The rotations $\phi_\alpha(\xi)$ do not depend on the reference surface: $\phi_1^L(\xi) = \phi_1^M(\xi) = \phi_1^U(\xi)$ and $\phi_2^L(\xi) = \phi_2^M(\xi) = \phi_2^U(\xi)$. For the analysed plate, the displacements depend on three shear correction factors α_i ($i = 0, 1, 2$) and on the parameter

$$\alpha_3 = 4\alpha_0 \alpha_2 - 3\alpha_1^2 \tag{3.4}$$

However, if the middle reference surface is considered only one shear factor α_0 occurs.

The paper refers to the application of the linear six-parameter shell theory to the analysis of orthotropic tensegrity plate-like structures. These systems are double-layer tensegrity grids. To establish values of the shear correction factors for such a plate, it is necessary to build and next to verify the proper model which should be based on the knowledge of the modelled material and the phenomenon. The aim of future research will establish values of the three shear correction factors within the six-parameter linear theory of elastic tensegrity plate-like structures and test their influence on numerical results of static behavior of such structures.

Now, to illustrate the influence of the reference plane on the behaviour of tensegrity structures, it is that the assumed values of the shear factors are: $\alpha_0 = 5/6$, $\alpha_2 = 7/10$ (Chróscielewski *et al.*, 1997, 2000; Pietraszkiewicz, 1979; Witkowski, 2011; Woźniak, 2001) and $\alpha_1 = 8/10$. The last correction factor has been assumed so that parameter (3.4) is positive definite.

On the basis of Eq. (3.2), the influence of the self-stress and stiffness of cables and struts on the displacement in tensegrity plate-like structures can be estimated in a simple way. The parametric analysis can be carried for any moderately thick plates. As an example, results for the thickness to length ratio $h/a = 0.25$, on the assumption $m = n$, are shown in Fig. 4. Formulas (3.2) are valid only for $n > 0.2\sigma$.

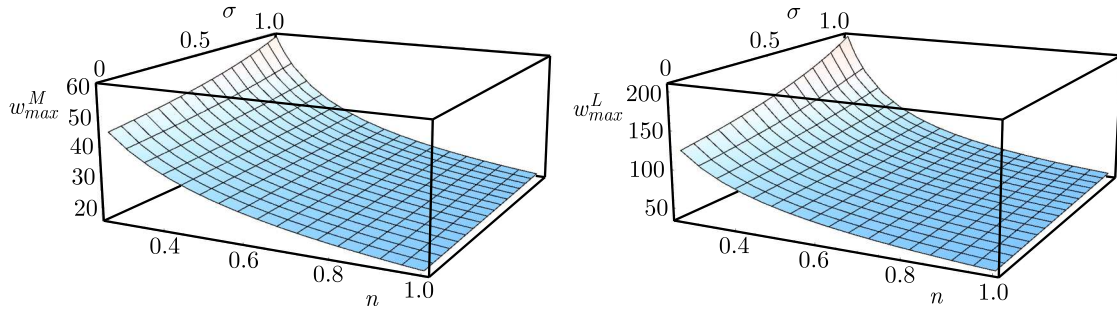


Fig. 4. Maximum deflection of the plate

3.2. Plate strips

The displacements and the internal forces for plate strips are determined based on Eqs. (2.21) and (2.22). These formulas depend on boundary conditions. Plate strips with the force mass $f_3(x_1) = -q_0$ taken into account are studied. Three kinds of support, i.e., cantilever (Fig. 5a), simply supported (Fig. 5b) and clamped-clamped (Fig. 5c) are considered. The formulas of the maximum deflection are derived:

— the cantilever plate strip

$$w_{max}^M = C_M \left[6 \frac{1}{\delta_{11}} + \frac{4}{\alpha_0} \left(\frac{h}{a} \right)^2 \frac{1}{\delta_{13}} \right] \quad w_{max}^L = w_{max}^U = C_M \left[6 \frac{1}{\delta_{11}} + 16 \frac{\alpha_2}{\alpha_3} \left(\frac{h}{a} \right)^2 \frac{1}{\delta_{13}} \right] \quad (3.5)$$

— the simply supported plate strip

$$w_{max}^M = C_M \left[\frac{5}{8} \frac{1}{\delta_{11}} + \frac{1}{\alpha_0} \left(\frac{h}{a} \right)^2 \frac{1}{\delta_{13}} \right] \quad w_{max}^L = w_{max}^U = C_M \left[\frac{1}{4} \frac{1}{\delta_{11}} + 4 \frac{\alpha_2}{\alpha_3} \left(\frac{h}{a} \right)^2 \frac{1}{\delta_{13}} \right] \quad (3.6)$$

— the clamped-clamped plate strip

$$w_{max}^M = C_M \left[\frac{1}{8} \frac{1}{\delta_{11}} + \frac{1}{\alpha_0} \left(\frac{h}{a} \right)^2 \frac{1}{\delta_{13}} \right] \quad w_{max}^L = w_{max}^U = C_M \left[\frac{1}{8} \frac{1}{\delta_{11}} + 4 \frac{\alpha_2}{\alpha_3} \left(\frac{h}{a} \right)^2 \frac{1}{\delta_{13}} \right] \quad (3.7)$$

where $C_M = -a^4 q_0 / (8EAh)$. In these cases, the deflection functions depend on the correction factors α_i ($i = 0, 1, 2, 3$) but for the middle reference surface only on the factor α_0 .

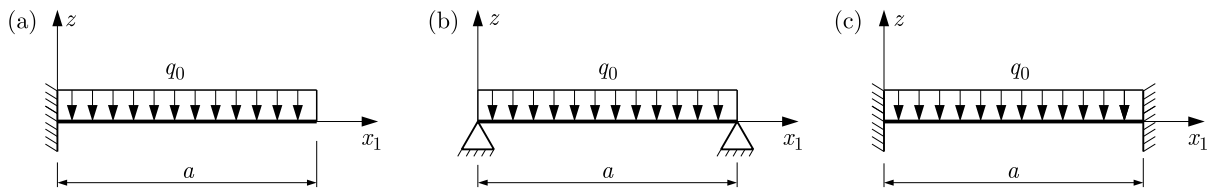


Fig. 5. Plate strips: (a) cantilever, (b) simply supported, (c) clamped-clamped

For all analysed plate strips, displacements describing the membrane state are equal to zero only for the middle reference surface: $u_1^M(\xi) = \psi^M(\xi) = 0$. For the lower and the upper surfaces, the axial displacement is a polynomial function of the degree three, and for each surface there is an equality: $u_1^L(\xi) = -u_1^U(\xi)$. The drilling rotation is a polynomial function of the degree two and $\psi^L(\xi) = -\psi^U(\xi)$. The rotations $\phi_\alpha(\xi)$ do not depend on the reference surface, and for each surface: $\phi_1^L(\xi) = \phi_1^M(\xi) = \phi_1^U(\xi)$ and $\phi_2^L(\xi) = \phi_2^M(\xi) = \phi_2^U(\xi)$.

For the cantilever and the clamped-clamped plate strip, the internal forces do not depend on the reference surface. The membrane force and the drilling couple are equal to zero: $N_{11}(\xi) = 0$, $M_{13}(\xi) = 0$, and the transverse force and the bending couple are as follows:

— the cantilever plate strip

$$N_{13}(\xi) = -aq_0(1 - \xi) \quad M_{11}(\xi) = -\frac{a^2q_0}{2}(1 + 2\xi - \xi^2) \quad (3.8)$$

— the clamped-clamped plate strip

$$N_{13}(\xi) = -\frac{aq_0}{2}(1 - 2\xi) \quad M_{11}(\xi) = \frac{a^2q_0}{12}(1 - 6\xi + 6\xi^2) \quad (3.9)$$

For the simply supported plate strip, the transverse force and the bending couple do not depend on the reference surface, as for previous cases

$$N_{13}(\xi) = -\frac{aq_0}{2}(1 - 2\xi) \quad M_{11}(\xi) = -\frac{a^2q_0}{2}(\xi - \xi^2) \quad (3.10)$$

the drilling couple is equal to zero $M_{13}(\xi) = 0$, but for the lower and the upper surface, the constant axial force occurs additionally

$$N_{11}^L(\xi) = -N_{11}^U(\xi) = -\frac{a^2q_0}{8h} \quad N_{11}^M(\xi) = 0 \quad (3.11)$$

Internal forces (3.8)-(3.11) do not depend on geometric and physical properties of tensegrity plate-like structures. Based on Eqs. (3.5)-(3.7), the influence of the self-stress and the stiffness of cables and struts on the displacement in tensegrity plate-like structures can be estimated. As an example, the parametric results, for $h/a = 0.25$, on the assumption $m = n$, are represented graphically in Figs. 6-8. Values of the correction factors are assumed like for the analysed jointly supported plate. Formulas (3.5)-(3.7) are specified only for $n > 0.121\sigma$.

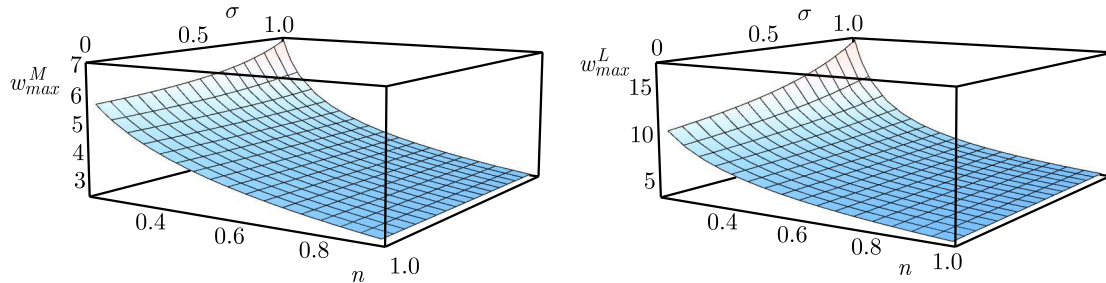


Fig. 6. Maximum deflection of the cantilever plate strip

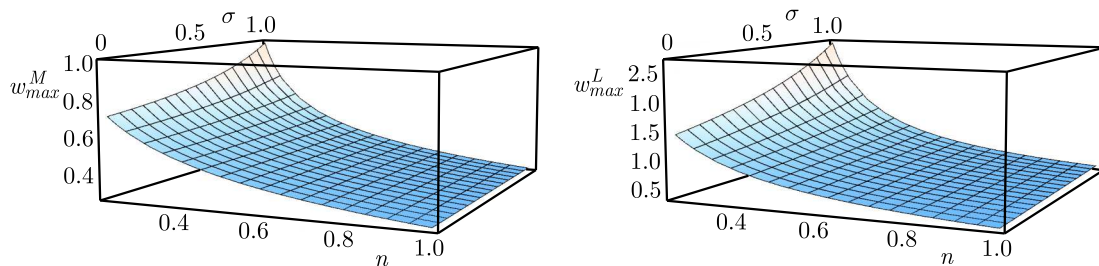


Fig. 7. Maximum deflection of the simple-supported plate strip

4. Conclusions

The paper proposes the application of the linear six-parameter shell theory to the analysis of orthotropic tensegrity plate-like structures. The continuum model of the plate is used. The

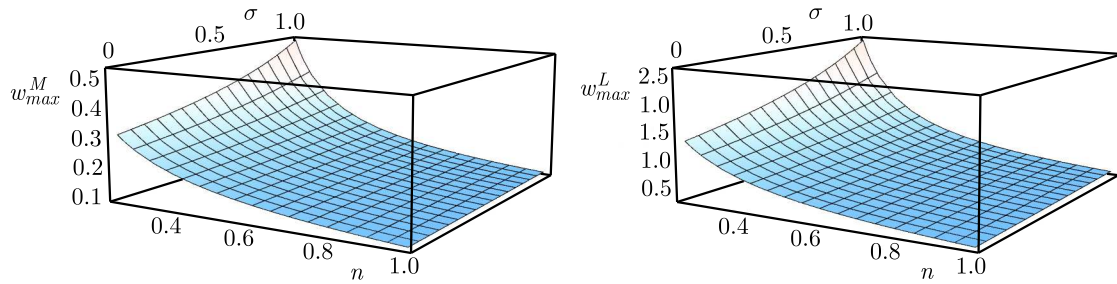


Fig. 8. Maximum deflection of the clamped-clamped plate strip

parametric analysis including the self-stress and selected geometrical parameters of tensegrity are considered. In the analysis, different planes of support of tensegrity plate-like structures are taken into account. The proposed approach helps one to understand unique properties and structural behaviour of tensegrities.

Comparing the obtained results, it can be noticed that displacements depend on the reference surface. Additionally, the influence of the self-stress level on the displacements also depends on the reference surface – is bigger when the lower (or upper) surface is considered. It means that the plane of support of tensegrity structures significantly affect the displacements. Furthermore, the results of parametric analysis shown that the influence of the self-stress level on the displacements decreases with an increase in the stiffness of cables (the parameter n increases).

The closed form of the displacements and the internal forces obtained in the paper simplifies calculations. It is not necessary to describe the whole complex tensegrity structures with the use of computational methods. The closed formulas can be useful in the design process and construction of different types of tensegrity systems, such as beams, plates or more complex structures. Additionally, the obtained in the paper functions of the displacements and the internal forces can be used for analysis of orthotropic plate strips with any external loads and any boundary conditions.

References

1. AL SABOUNI-ZAWADZKA A., GILEWSKI W., 2016, On orthotropic properties of tensegrity structures, *Procedia Engineering*, **153**, 887-894
2. AL SABOUNI-ZAWADZKA A., GILEWSKI W., KŁOSOWSKA J., OBARA P., 2016, Continuum model of orthotropic tensegrity plate-like structures with self-stress included, *Engineering Transactions*, **64**, 4, 501-508
3. BURZYŃSKI S., CHRÓŚCIELEWSKI J., DASZKIEWICZ K., WITKOWSKI W., 2016, Geometrically nonlinear FEM analysis of FGM shells based on neutral physical surface approach in 6-parameter shell theory, *Composites Part B*, **107**, 203-213
4. CHADWICK P., VIANELLO M., COWIN S.C., 2001, A new proof that the number of linear elastic symmetries is eight, *Journal of the Mechanics and Physics of Solids*, **49**, 2471-2492
5. CHRÓŚCIELEWSKI J., KREJA I., SABIK A., WITKOWSKI W., 2011, Modeling of composite shells in 6-parameter nonlinear theory with drilling degree of freedom, *Mechanics of Advanced Materials and Structures*, **18**, 403-419
6. CHRÓŚCIELEWSKI J., MAKOWSKI J., PIETRASZKIEWICZ W., 2004, *Statics and Dynamics of Multifold Shell: Nonlinear Theory and Finite Element Method* (in Polish), IPPT PAN, Warszawa
7. CHRÓŚCIELEWSKI J., MAKOWSKI J., STUMPF H., 1997, Finite element analysis of smooth, folded and multi-shell structures, *Computer Methods in Applied Mechanics and Engineering*, **41**, 1-46

8. CHRÓŚCIELEWSKI J., PIETRASZKIEWICZ W., WITKOWSKI W., 2000, On shear correction factors in the non-linear theory of elastic shells, *International Journal of Solids and Structures*, **47**, 3537-3545
9. CHRÓŚCIELEWSKI J., PIETRASZKIEWICZ W., WITKOWSKI W., 2016, Geometrical nonlinear FEM analysis of 6-parameter resultant shell theory based on 2-D Cosserat constitutive model, *ZAMM*, **96**, 2, 191-204
10. CRAWFORDT, 2016, *Transgender Architectonics: The Shape of Change in Modernist Space*, Routledge, New York
11. GILEWSKI W., KASPRZAK A., 2011, Tensegrities in bridge structures (in Polish), *Acta Scientiarum Polonorum: Architectura*, **10**, 3, 35-43
12. GILEWSKI W., KŁOSOWSKA J., OBARA P., 2015, Applications of tensegrity structures in civil engineering, *Procedia Engineering*, **111**, 242-248
13. GILEWSKI W., KŁOSOWSKA J., OBARA P., 2016, Verification of tensegrity properties of Kono structure and Blur Building, *Procedia Engineering*, **153**, 173-179
14. GÓMEZ-JÁUREGUI V., 2010, *Tensegrity Structures and their Application to Architecture*, Servicio de Publicaciones de la Universidad de Cantabria
15. GÓMEZ-JÁUREGUI V., ARIAS R., OTERO C., MANCHADO C., 2012, Novel technique for obtaining double-layer tensegrity grids, *International Journal of Space Structures*, **27**, 2-3, 155-166
16. KEBICHE K., KAZI M., AOUAL N., MOTRO R., 2008, Continuum model for systems in a self-stress state, *International Journal of Space Structures*, **23**, 103-115
17. KHORSHIDI M.A., SHARIATI M., 2017, A multi-spring model for buckling analysis of cracked Timoshenko nanobeams based on modified couple stress theory, *Journal of Theoretical and Applied Mechanics*, **55**, 4, 1127-1139
18. KONO Y., CHOONG K.K., SHIMADA T., KUNIEDA H., 1999, Experimental investigation of a type of double-layer tensegrity grids, *Journal of the IASS*, **40**, 130, 103-111
19. MOTRO R., 2003, *Tensegrity: Structural Systems for the Future*, Kogan Page Science, London
20. NOWACKI W., 1971, *Theory of Asymmetrical Elasticity* (in Polish), IPPT PAN, Warszawa
21. OBARA P., GILEWSKI W., 2016, Dynamic stability of moderately thick beams and frames with the use of harmonic balance and perturbation methods, *Bulletin of the Polish Academy of Sciences: Technical Sciences*, **64**, 4, 739-750
22. PIETRASZKIEWICZ W., 1979, *Finite Rotations and Lagrangean Description in The Non-linear Theory of Shells*, Polish Scientific Publishers, Warszawa-Poznań
23. PIETRASZKIEWICZ W., 2016, The resultant linear six-field theory of elastic shells: What it brings to the classical linear shell models?, *ZAMM*, **96**, 8, 899-915
24. SCHLAICH M., 2004, The messeturm in Rostock – a tensegrity tower (in German), *Journal of the IASS*, **45**, 145, 93-98
25. SKELTON R.E., DE OLIVEIRA M.C., 2009, *Tensegrity Systems*, Springer, London
26. TIMOSHENKO S.P., GERE J.M., 1961, *Theory of Elastic Stability*, McGraw-Hill, New York
27. WITKOWSKI W., 2011, *Synthesis of Formulation of Nonlinear Mechanics of Shells Undergoing Finite Rotations in the Context of FEM* (in Polish), Wydawnictwo Politechniki Gdańskiej, Gdańsk
28. WOŹNIAK C., 2001, *Mechanics of Elastic Shells and Plates* (in Polish), Polish Scientific Publishing House, Warszawa

MAGNETO-ELASTIC INTERNAL RESONANCE OF AN AXIALLY MOVING CONDUCTIVE BEAM IN THE MAGNETIC FIELD

JIE WANG

*Key Laboratory of Mechanical Reliability for Heavy Equipments and Large Structures of Hebei Province,
Yanshan University, Qinhuangdao, P.R. China and*

Department of Mechanics, School of Aerospace Engineering, Beijing Institute of Technology, Beijing, P.R. China

YUDA HU

*Key Laboratory of Mechanical Reliability for Heavy Equipments and Large Structures of Hebei Province,
Yanshan University, Qinhuangdao, P.R. China; e-mail: huyuda03@163.com*

YU SU

Department of Mechanics, School of Aerospace Engineering, Beijing Institute of Technology, Beijing, P.R. China

LIANGFEI GONG

State Key Laboratory of Explosion Science and Technology, Beijing Institute of Technology, Beijing, P.R. China

QINGNAN ZHANG

Department of Mechanics, School of Aerospace Engineering, Beijing Institute of Technology, Beijing, P.R. China

The Hamiltonian principle is applied to the nonlinear vibration equation of an axially moving conductive beam in the magnetic field with consideration of the axial velocity, axial tension, electromagnetic coupling effect and complex boundary conditions. Nonlinear vibration characteristics of the free vibrating beam under 1:3 internal resonances are studied based on our approach. For beams with one end fixed and the other simply supported, the nonlinear vibration equation is dispersed by the Galerkin method, and the vibration equations are solved by the multiple-scales method. As a result, the coupled relations between the first-order and second-order vibration modes are obtained in the internal resonance system. Firstly, the influence of initial conditions, axial velocity and the external magnetic field strength on the vibration modes is analysed in detail. Secondly, direct numerical calculation on the vibration equations is carried out in order to evaluate the accuracy of the perturbation approach. It is found that through numerical calculations, in the undamped system, the vibration modes are more sensitive to the initial value of vibration amplitude. The amplitude changes of the first-order and second-order modes resulting from the increase of the initial amplitude value of the vibration modes respectively are very special, and present a “reversal behaviour”. Lastly, in the damped system, the vibration modes exhibit a trend of coupling attenuation with time. Its decay rate increases when the applied magnetic field strength becomes stronger.

Keywords: magneto-elastic, conductive beam, internal resonance, axially moving, multiple scales

1. Introduction

Axial motion structures and devices are widely used in the the engineering in form of magnetically levitated trains, electromotors, and telfers. When such components work in an environment with an electromagnetic field there appears a number of multi-physics coupling effects such as force, electricity and magnetism, which affect safety and reliability of the system. A great number of in-depth theoretical studies have been carried out on such traditional problems of axially moving beams, plates and strings. For an axial motion system, Chen *et al.* (2010) and Ding and

Chen (2010) studied nonlinear forced vibration of an axially moving viscoelastic beam. As a result, the influence from the axial velocity and boundary conditions on the structure vibration frequency and dynamic stability was analyzed. Hu *et al.* (2015) established a coupled nonlinear magneto-elastic vibration equation of the axial motion of a conducting plate, and investigated nonlinear vibration and chaotic motion of the plate. Pellicano (2005) obtained the complex dynamic response of an axial motion system under the external excitation load from a needle. Based on the generalized integral transform technique (GITT), Yan *et al.* (2015) investigated nonlinear dynamic behavior in the transverse vibration of an axially accelerating viscoelastic Timoshenko beam with an external harmonic excitation. Sahoo *et al.* (2015, 2016) analyzed the nonlinear transverse vibration of an axially moving beam subject to two-frequency excitation. Analytical and numerical approach was applied to find the steady-state and dynamic behavior of an axially accelerating viscoelastic beam subject to two-frequency parametric excitation in the presence of internal resonance. Pratiher and Dwivedy (2009) and Pratiher (2011) studied non-linear dynamics of a soft magneto-elastic Cartesian manipulator with a large transverse deflection. In addition, the non-linear response of a magneto-elastic translating beam having a prismatic joint for higher resonance conditions was studied by them. Wu (2007) investigated dynamic instability of a pinned beam subjected to an alternating magnetic field and thermal load with nonlinear strain, and made of a physically nonlinear thermoplastic material. Applying Hamilton's principle, the equation of motion with a damping factor, the induced current and thermal load was derived. Wang *et al.* (2011) proposed an H method for vibration control of an iron cantilever beam with axial velocity by applying a non-contact force through permanent magnets. For the internal resonance, Li *et al.* (2017) investigated magneto-elastic internal resonances of a rectangular conductive thin plate with different size ratios. They obtained amplitude-frequency response equations of 1:3 internal resonances by Galerkin and multi-scale methods. Mao *et al.* (2016a,b) firstly studied the forced vibration response of a pipe conveying fluid and super-harmonic resonances of a super-critical axially moving beam, with 3:1 internal resonance. Parametric and 3:1 internal resonance of axially moving viscoelastic beams on elastic foundation was analytically and numerically investigated by Tang *et al.* (2016).

In this paper, the internal resonance of an axially moving conductive beam in the magnetic field is investigated. The magnetic elastic vibration equation is to be obtained for the axially moving beam in a magnetic field, and 1:3 internal resonances are to be analyzed as well.

2. The vibration equation

The mechanical model of an axially moving conductive beam in a constant magnetic field is shown in Fig. 1. The magnetic field intensity is described by $\mathbf{B}_0(0, B_{0y}, 0)$; where l , h and b denote length, height and width of the beam, respectively; the axial speed is c .

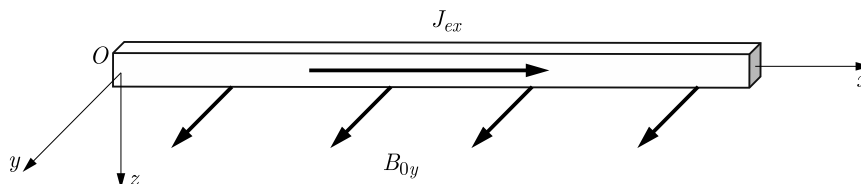


Fig. 1. An axially moving conducting elastic beam in a magnetic field. The letters x , y and z represent cartesian coordinates, and J_{ex} denotes the x -axis component of the induced current density caused by the moving beam in an external magnetic field

The magneto-elastic vibration equation of the axially moving current carrying beam in the transverse magnetic field, shown as Eq. (2.1), is derived from the Hamilton variational principle.

Interested readers are referred to the work of Hu and Wang (2017) for the derivation and origin of this vibration equation

$$\begin{aligned} \rho A \frac{\partial^2 w}{\partial t^2} + 2\rho A c \frac{\partial^2 w}{\partial x \partial t} + \left[\rho A c^2 - F_{0x} - \frac{3}{2} E A \left(\frac{\partial w}{\partial x} \right)^2 \right] \frac{\partial^2 w}{\partial x^2} + \sigma_0 A B_{0y}^2 \frac{\partial w}{\partial t} \\ + E I \frac{\partial^4 w}{\partial x^4} + \sigma_0 c A B_{0y}^2 \frac{\partial w}{\partial x} = 0 \end{aligned} \quad (2.1)$$

where $w(x, t)$ is the transverse displacement of the beam. E , ρ , σ_0 denote Young's modulus, material density and conductivity, respectively. F_{0x} is the axial tension, and I is the area moment of inertia. The rectangular cross section is $A = b \times h$. t is the time variable.

3. Magneto-elastic internal resonance

For the one end fixed and the other simply supported boundary condition, the expression is

$$w|_{x=0} = 0 \quad \left. \frac{\partial w}{\partial x} \right|_{x=0} = 0 \quad \text{and} \quad w|_{x=l} = 0 \quad \left. \frac{\partial^2 w}{\partial x^2} \right|_{x=l} = 0 \quad (3.1)$$

The assumed displacement solution satisfying the particular boundary condition is described in the following form

$$w = \sum_{n=1}^2 Q_n(t) X_n(x) \quad (3.2)$$

where $Q(t)$ denotes the amplitude of the mode, and the function $X_n(x)$ is determined by

$$\begin{aligned} X_n(x) &= \cosh p_n x - \cos p_n x - \zeta_n (\sinh p_n x - \sin p_n x) \\ \zeta_n &= \frac{\cosh p_n l + \cos p_n l}{\sinh p_n l + \sin p_n l} \quad p_n = \frac{(4n+1)\pi}{4l} \end{aligned}$$

When Eq. (3.2) is substituted into Eq. (2.1), the vibration differential equations of the axially moving beam in the magnetic field are derived by the Galerkin method

$$\begin{aligned} \rho A \sum_{n=1}^2 A_{ni} \ddot{Q}_n(t) + \sum_{n=1}^2 (c A \sigma_0 B_{0y}^2 B_{ni} + \rho A c^2 C_{ni} - F_{0x} C_{ni} + E I D_{ni}) Q_n(t) \\ + \sum_{n=1}^2 (2\rho A c B_{ni} + \sigma_0 A B_{0y}^2 A_{ni}) \dot{Q}_n(t) - \frac{3}{2} E A (S_{1i} Q_1^3 + S_{2i} Q_2^3 + S_{3i} Q_1 Q_2^2 + S_{4i} Q_1^2 Q_2) = 0 \end{aligned} \quad (3.3)$$

where $i = 1, 2$ and the coefficients are provided in Appendix I.

After the coefficients of Eq. (3.3) are simplified, the differential equations of transverse vibration of the beam can be obtained by the dimensionless method

$$\begin{aligned} \ddot{q}_1(\tau) + g_1^2 q_1(\tau) &= -\varepsilon \mu_{11} \dot{q}_1(\tau) - \varepsilon \mu_{12} \dot{q}_2(\tau) + \varepsilon (s_{11} q_1^3 + s_{21} q_2^3 + s_{31} q_1 q_2^2 + s_{41} q_1^2 q_2) \\ \ddot{q}_2(\tau) + g_2^2 q_2(\tau) &= -\varepsilon \mu_{21} \dot{q}_1(\tau) - \varepsilon \mu_{22} \dot{q}_2(\tau) + \varepsilon (s_{12} q_1^3 + s_{22} q_2^3 + s_{32} q_1 q_2^2 + s_{42} q_1^2 q_2) \end{aligned} \quad (3.4)$$

where ε denotes a small parameter. The main coefficients are shown below, and the others are provided in Appendix I

$$\begin{aligned} q_n(\tau) &= \frac{Q_n(t)}{l} & \tau &= \omega_n t & \dot{q}_1(\tau) &= \frac{\dot{Q}_n(t) l}{\omega_n} \\ \ddot{q}_1(\tau) &= \frac{\ddot{Q}_n(t) l}{\omega_n^2} & \omega_n &= p_1^2 \sqrt{\frac{E I}{\rho A}} \end{aligned}$$

3.1. Perturbation approach

The displacement $w(x, t)$ is spread out into a combination of time and space variables. Adopting the assumed mode form of the first two order truncation in space, Eq. (3.2), so the nonlinear vibration equation, has been dispersed by the Galerkin method and rearranged by dimensionless processing from Eqs. (3.2)-(3.4). Finally, it can be solved by the multiple-scales method. The derivations of Eq. (3.5) are referred to the solution by the multiple-scales method (Li *et al.*, 2017; Hu and Wang, 2017). It is worth noting that the multi-scale method, a widely used but complex solving process, is a mature and an effective nonlinear solution theory (Nayfeh and Mook, 1979)

$$\begin{aligned}
a_1'(T_1)g_1 + \frac{1}{2}\mu_{11}a_1(T_1)g_1 &= \frac{1}{8}s_{41}a_1^2(T_1)a_2(T_1)\sin\gamma \\
a_2'(T_1)g_2 + \frac{1}{2}\mu_{22}g_2a_2(T_1) &= -\frac{1}{8}s_{12}a_1^3(T_1)\sin\gamma \\
\gamma'(T_1) &= \sigma + \left(\frac{9s_{11}}{8g_1} - \frac{s_{42}}{4g_2}\right)a_1^2(T_1) + \left(\frac{3s_{31}}{4g_1} - \frac{3s_{22}}{8g_2}\right)a_2^2(T_1) \\
&\quad + \left(\frac{3s_{41}a_1(T_1)a_2(T_1)}{8g_1} - \frac{s_{12}a_1^3(T_1)}{8g_2a_2(T_1)}\right)\cos\gamma(T_1)
\end{aligned} \tag{3.5}$$

where $a_1(T_1)$ and $a_2(T_1)$ denote the amplitudes of the first-order and second-order modes of the system, and $\gamma(T_1)$ denotes the phase angle. g_1 and g_2 denote the natural frequency of the first-order and second-order modes of the system, and $\sigma = (g_2 - 3g_1)/\varepsilon$ is the tuning parameter of g_1 and g_2 . s_{ij} denote the coefficients of nonlinear terms (other definitions in the multiple-scales method are provided in Appendix I).

3.2. System stability analysis

After having done the work above, the next step is to find the solution to Eqs. (3.5). For the electromagnetically damped system, multiplying Eq. (3.5)₁ by $g_1^{-1}a_1$ and Eq. (3.5)₂ by $g_2^{-1}\nu a_2$, where $\nu = s_{41}g_2/(s_{12}g_1)$, and adding the results together, we obtain

$$a_1'a_1 + \nu a_2'a_2 = -\frac{1}{2}\mu_{11}a_1^2 - \frac{1}{2}\nu\mu_{22}a_2^2 \tag{3.6}$$

Equation (3.6) can be integrated for a no electromagnetically damped system is

$$a_1^2 + \nu a_2^2 = E \tag{3.7}$$

where E is a constant of integration, which is related to the initial energy of the system.

Changing the independent variable from T_1 to a_2 in Eq. (3.5)₃, and using Eq. (3.5)₂, we obtain

$$-a_1^3 a_2 \sin\gamma \frac{d\gamma}{da_2} = \frac{8g_2\sigma}{s_{12}}a_2 + \lambda_1 a_2^3 + \lambda_2 a_1^2 a_2 + (3\nu a_1 a_2^2 - a_1^3) \cos\gamma \tag{3.8}$$

where

$$\lambda_1 = \frac{6g_2s_{31}}{g_1s_{12}} - \frac{3s_{22}}{s_{12}} \quad \lambda_2 = \frac{9g_2s_{11}}{g_1s_{12}} - \frac{2s_{42}}{s_{12}}$$

Using Eq. (3.7) and the result of integration of Eq. (3.8), we are able to acquire

$$a_1^3 a_2 \cos\gamma - \left(\frac{4g_2\sigma}{s_{12}} + \frac{1}{2}\lambda_2 E\right)a_2^2 - \frac{1}{4}(\lambda_2\nu - \lambda_1)a_2^4 = M \tag{3.9}$$

where M is a constant of integration.

Setting $a_1^2 = E\xi$, $a_2^2 = E\nu^{-1}(1-\xi)$ and eliminating γ from Eq. (3.5)₁ and Eq. (3.9), we obtain the following formula. At the same time, in order to simplify the expression, we introduce two new functions $F(\xi)$ and $G(\xi)$ (Nayfeh and Mook, 1979)

$$\frac{16\nu g_1^2}{E^2 s_{41}^2} (\xi')^2 = \xi^2(1-\xi) - \frac{G^2\nu}{E^4} = F^2(\xi) - G^2(\xi) \quad (3.10)$$

where

$$\begin{aligned} F(\xi) &= \pm\sqrt{\xi^2(1-\xi)} \\ G(\xi) &= \frac{\sqrt{\nu}}{E^2} \left[L + \frac{E}{\nu} \left(\frac{4g_2\sigma}{s_{12}} + \frac{1}{2}\lambda_2 E \right) (1-\xi) + \frac{E^2}{4\nu^2} (\lambda_2\nu - \lambda_1)(1-\xi)^2 \right] \end{aligned} \quad (3.11)$$

To find the steady-state solutions of a_1 and a_2 , we set $a_1' = a_2' = \gamma' = 0$ in Eqs. (3.5). Then, the steady-state solution without damping is given by

$$\begin{aligned} \sin \gamma &= 0 \\ a_2\sigma + \left(\frac{9s_{11}}{8g_1} - \frac{s_{42}}{4g_2} \right) a_1^2 a_2 + \left(\frac{3s_{31}}{4g_1} - \frac{3s_{22}}{8g_2} \right) a_2^3 + \left(\frac{3s_{41}a_1a_2^2}{8g_1} - \frac{s_{12}a_1^3}{8g_2} \right) \cos n\pi &= 0 \end{aligned} \quad (3.12)$$

4. Numerical simulations

The model of the simulation is supposed to be a conductive axially moving beam of a copper material. The main parameters are presented as follows: length of the beam is $l = 0.3$ m, width of the beam is $b = 0.02$ m, height of the beam is $h = 0.01$ m, axial tension is $F_{0x} = 30000$ N, elastic modulus is $E = 108$ GPa, mass density is $\rho = 8920$ kg/m³.

4.1. System without electromagnetic damped

4.1.1. Vibration mode

Based on the numerical solution to Eqs. (3.5) without electromagnetic damping, graphs of relevant vibration modes can be made as follows. Figures 2-5 describe vibration modes versus time for different initial conditions and system parameters. They all show the same phenomenon that the coupled first-order and second-order vibration modes change with time, which means the system energy constantly exchanges between different vibration modes because of internal resonance. One may find correlative descriptions about the internal resonance in the book by Nayfeh and Mook (1979).

Figures 2a-2d show vibration modes versus time for different axial velocity and the initial conditions $a_{10} = a_{20} = 0.05$, $\gamma_0 = 0$. They show that both the variation amplitudes and the intersections of vibration modes continuously grow up while the axial velocity c increases from 5 m/s to 95 m/s.

Figures 3-5 describe vibration modes versus time for different initial conditions when and the axial velocity $c = 5$ m/s. And the primary distinction between them is the emphasis on effects of different parameters taken into account, in which the first picture focuses on the influence of the initial value γ_0 , and the other two care about a_0 .

As the initial value of the phase angle γ_0 moves on, the first-order and the second-order modes have different manifestations, the former is overall upward and the latter goes down integrally, see Fig. 3. In addition, the curves of vibration modes are intertwined when $0 < \gamma_0 < 9.4$, but they will separate when γ_0 goes beyond that range.

Then, we investigate the influence of the initial value a_0 on vibration modes when taking $\gamma_0 = 0$ and $\gamma_0 = 9.4$, respectively. As shown in Figs. 4 and 5, the amplitude changes of the

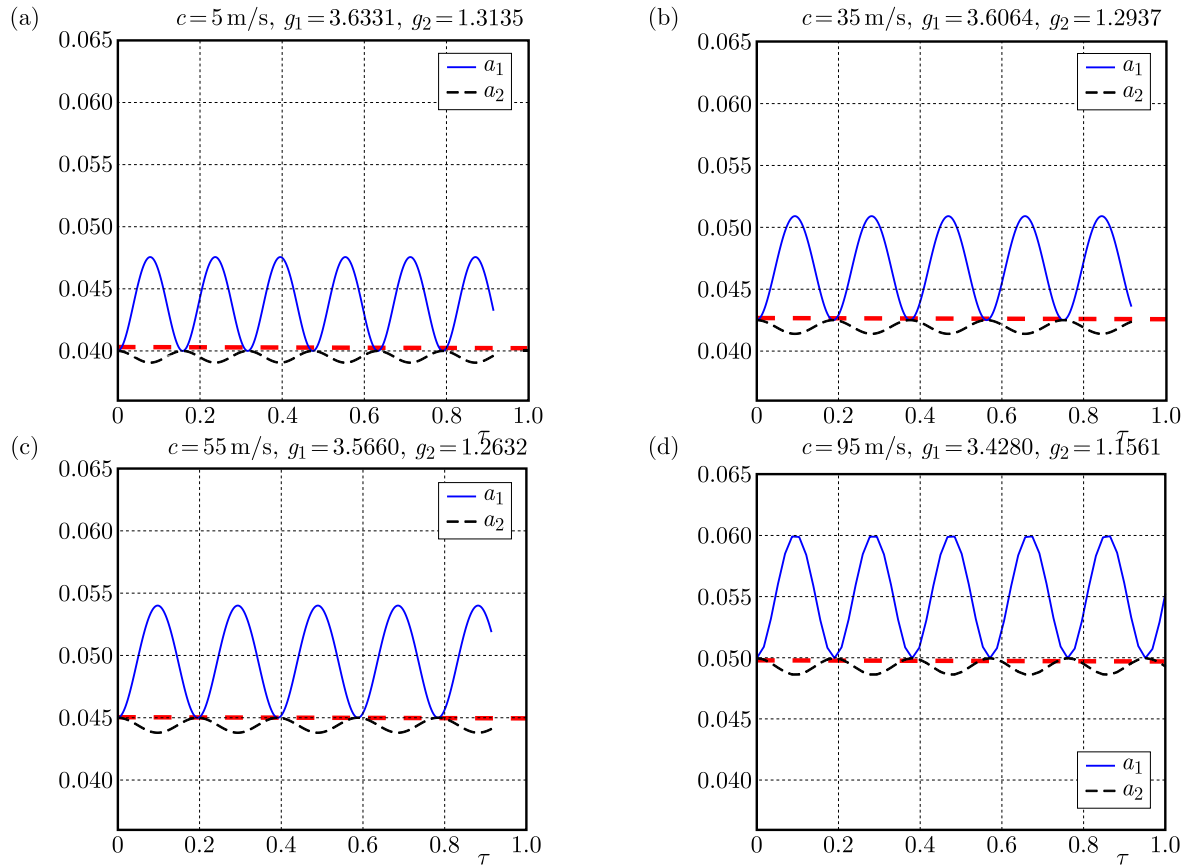


Fig. 2. Variation modes for the axial velocity c ($a_{10} = a_{20} = 0.05, \gamma_0 = 0$). The letters g_1 and g_2 represent natural frequencies of the first-order and second-order vibration modes

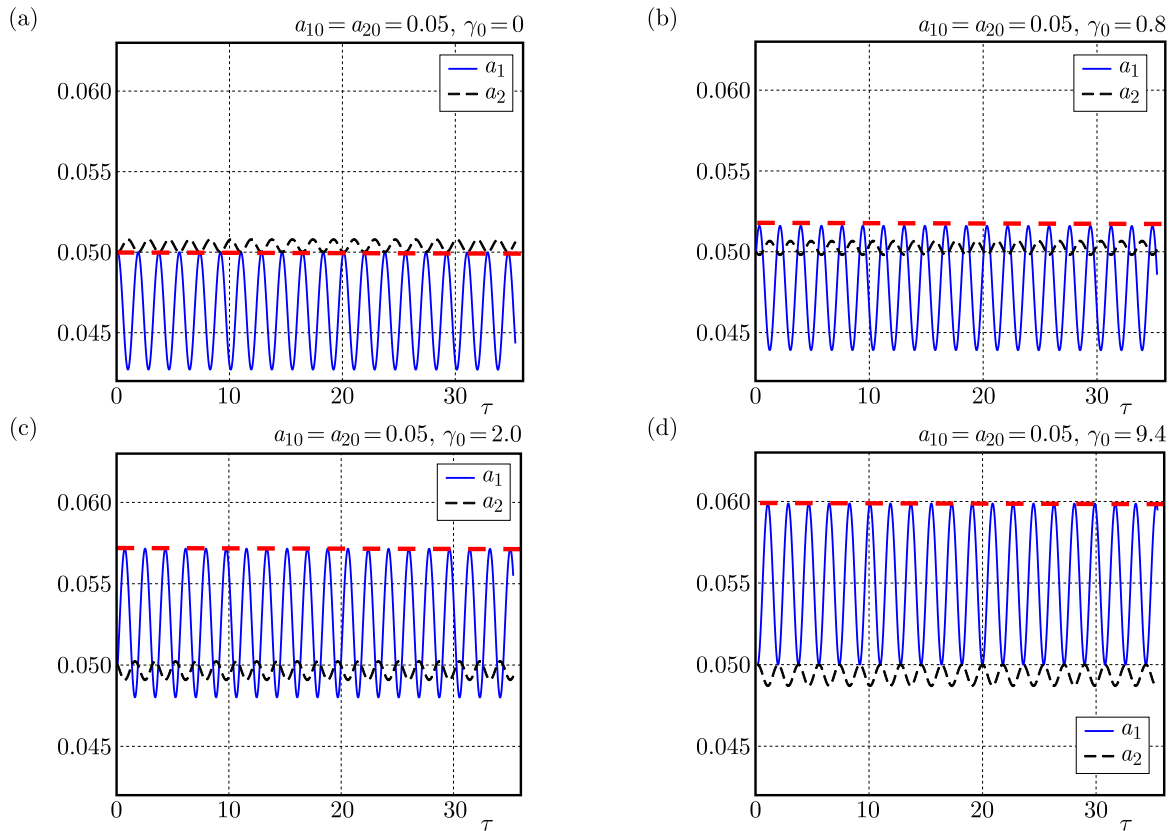


Fig. 3. Variation modes for different initial conditions γ_0 ($a_0 = 0.05, c = 55 \text{ m/s}$)

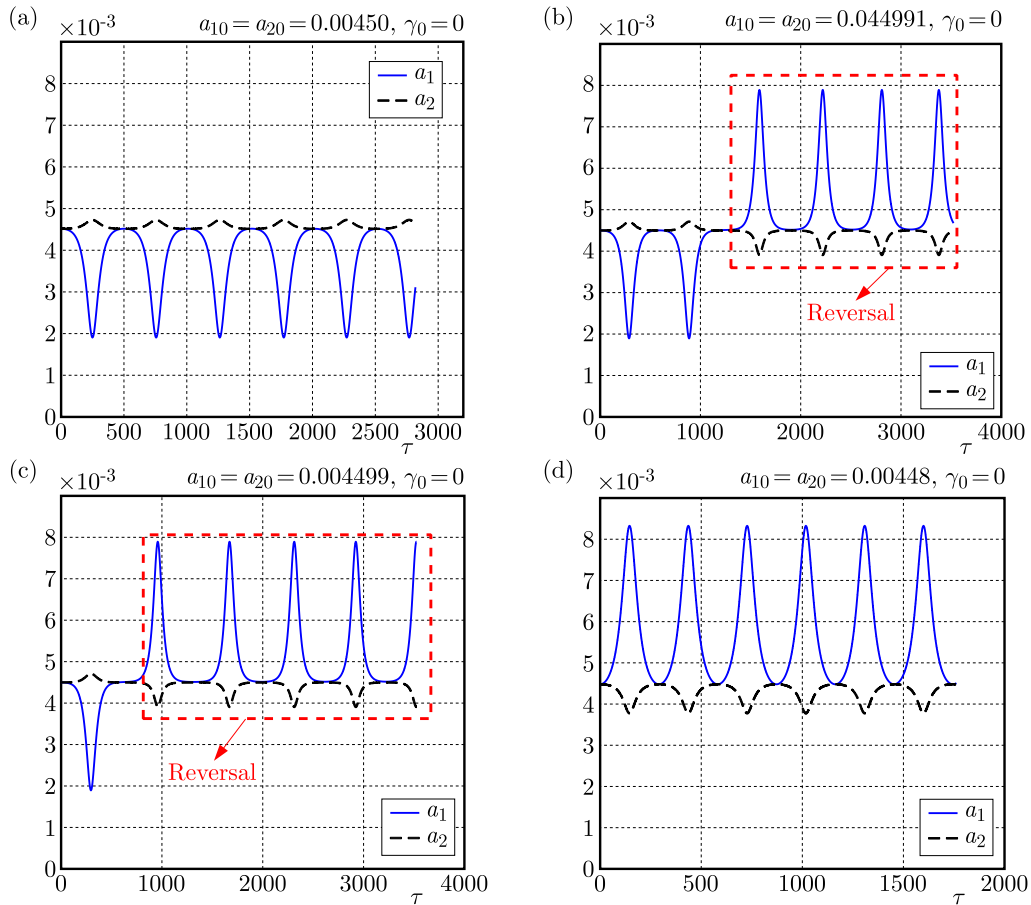


Fig. 4. Variation modes for different initial conditions a ($\gamma_0 = 0, c = 55$ m/s)

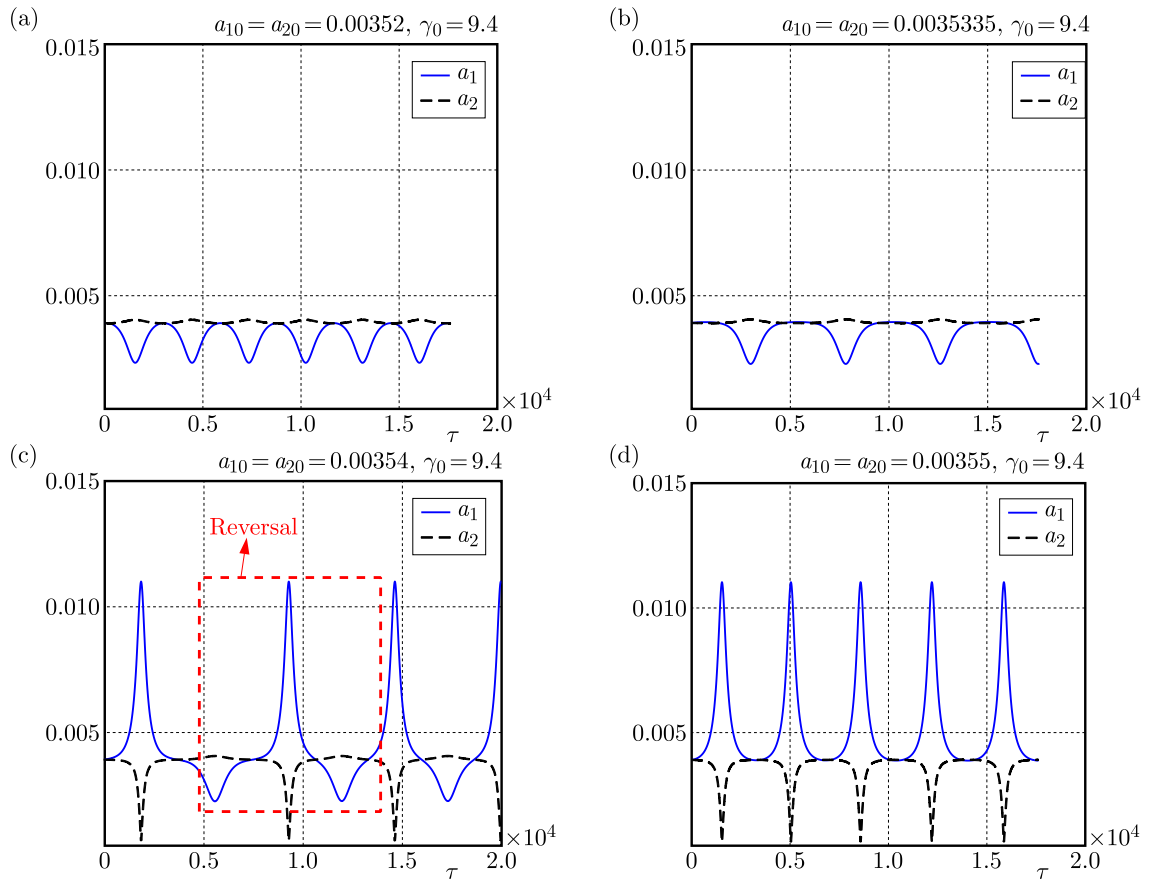


Fig. 5. Variation modes for different initial conditions a ($\gamma_0 = 9.4, c = 55$ m/s)

first-order and second-order mode are very special, similar to “reversal behavior” in Figs. 4b,c and Figs. 5b,c rather than the whole moving up and down in Fig. 3. From the contrast between Figs. 3, 4 and 5, we can conclude that the vibration modes are more sensitive to the initial amplitude of the vibration mode a_0 than the phase angle γ_0 .

Subsequently, we have carried out direct simulations of equations Eq. (3.3) in order to evaluate the accuracy of the perturbation approach. When using different values of the initial conditions, we obtained time-history graphs, phase-plane diagrams and Poincaré maps of the vibration amplitudes q_1 and q_2 .

Figures 6, 7 and 8 demonstrate the responses of the system for different initial conditions $a_{10} = a_{20} = q_{10} = q_{20} = 0.00055$, $a_{10} = a_{20} = q_{10} = q_{20} = 0.005$ and $a_{10} = a_{20} = q_{10} = q_{20} = 0.012$. Compared to the amplitudes a_1 and a_2 from the perturbation approach depicted in (a) of Figs. 6-8, the numerical amplitudes q_1 and q_2 displayed in (b) of Figs. 6-8 present good consistency. Besides, Figs. (c), (d) and (e), (f) describe the corresponding phase diagram and Poincaré map of q_1 and q_2 . It can be clearly seen that the responses of the system firstly change from the periodic motion to period-2 motion and, finally, develop into chaotic motion when the initial conditions q_{10} and q_{20} increase.

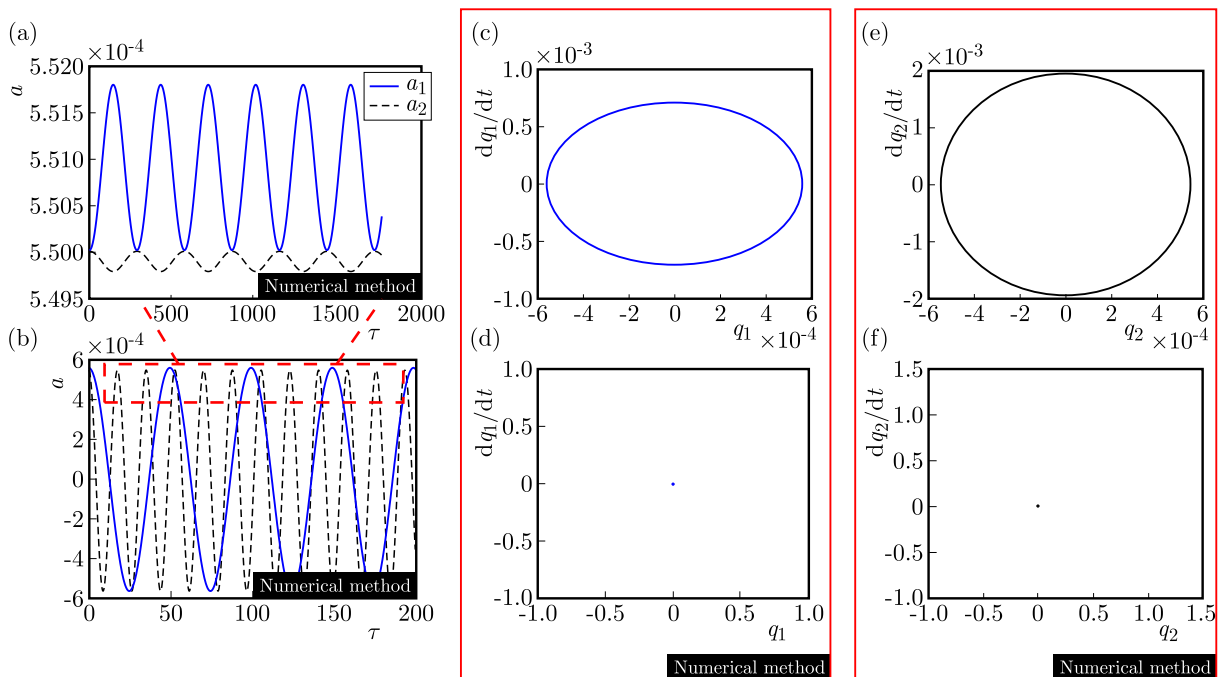


Fig. 6. Periodic motion of the system for the initial condition equal to 0.00055 ($\gamma_0 = 0$, $c = 55$ m/s); (c) and (e) are phase diagrams of q_1 and q_2 , (d) and (f) are Poincaré maps of q_1 and q_2

When we calculate and analyze the internal resonance of the system without electromagnetic damping, the functions of $F(\xi)$ and $G(\xi)$ in Eq. (3.11) are plotted in Fig. 9a. Since ξ and a must be real, $F^2(\xi) \geq G^2(\xi)$. The points where $G(\xi)$ meets $F(\xi)$ correspond to $\xi' = 0$. It also means that the vibration modes $a'_1 = a'_2 = 0$. The curve G_3 which has two different crossing points with F corresponds to the steady-state solution of ξ and, hence, a_1 and a_2 . The points such as P_1 , where G_2 touches F and P_2 , where G_4 touches F represent the unique steady-state solution of ξ . On the other hand, Fig. 4 shows curves like G_1 and G_5 meeting F at no point, which means that there is no steady-state solution in the system. In addition, we should note that the steady-state motions are not always stable because any small outer disturbance would lead to the curves G_2 and G_4 similar to other curves. Figure 9b shows characteristic graphs of the vibration amplitude for different axial velocity. As shown in Fig. 9b, with an increase in the axial velocity, the characteristic curve circle gradually narrows down and moves towards the origin.

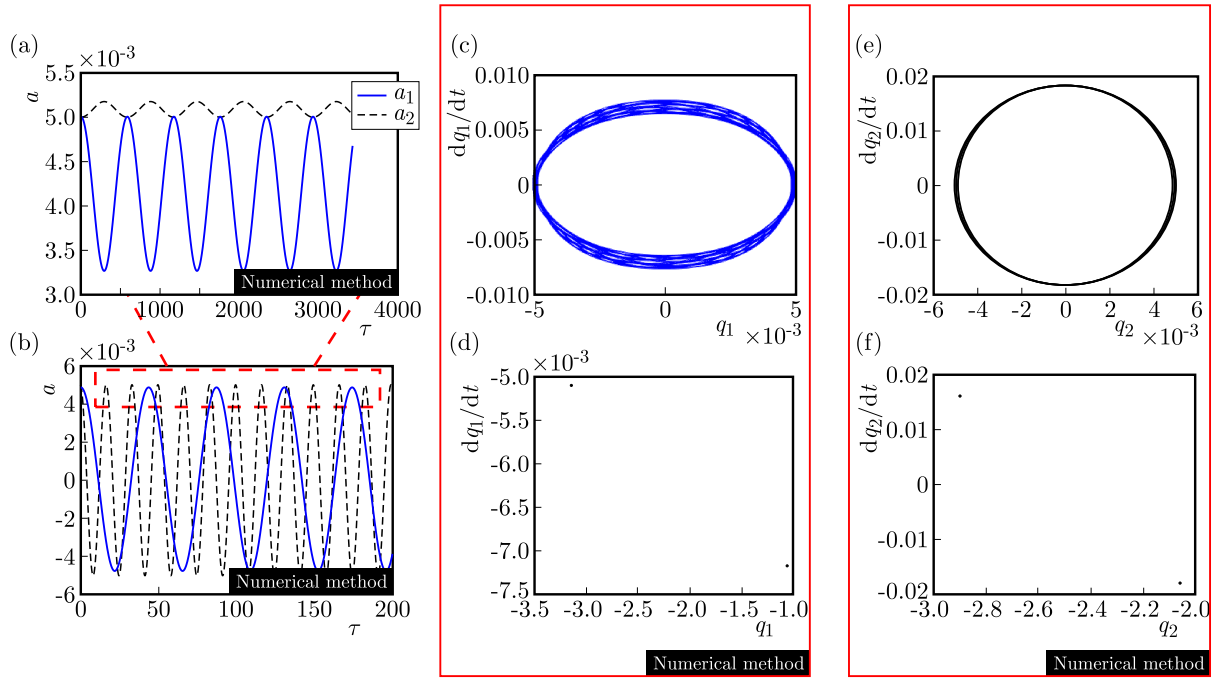


Fig. 7. Periodic motion of the system for the initial condition equal to 0.005 ($\gamma_0 = 0$, $c = 55$ m/s); (c) and (e) are phase diagrams of q_1 and q_2 , (d) and (f) are Poincaré maps of q_1 and q_2

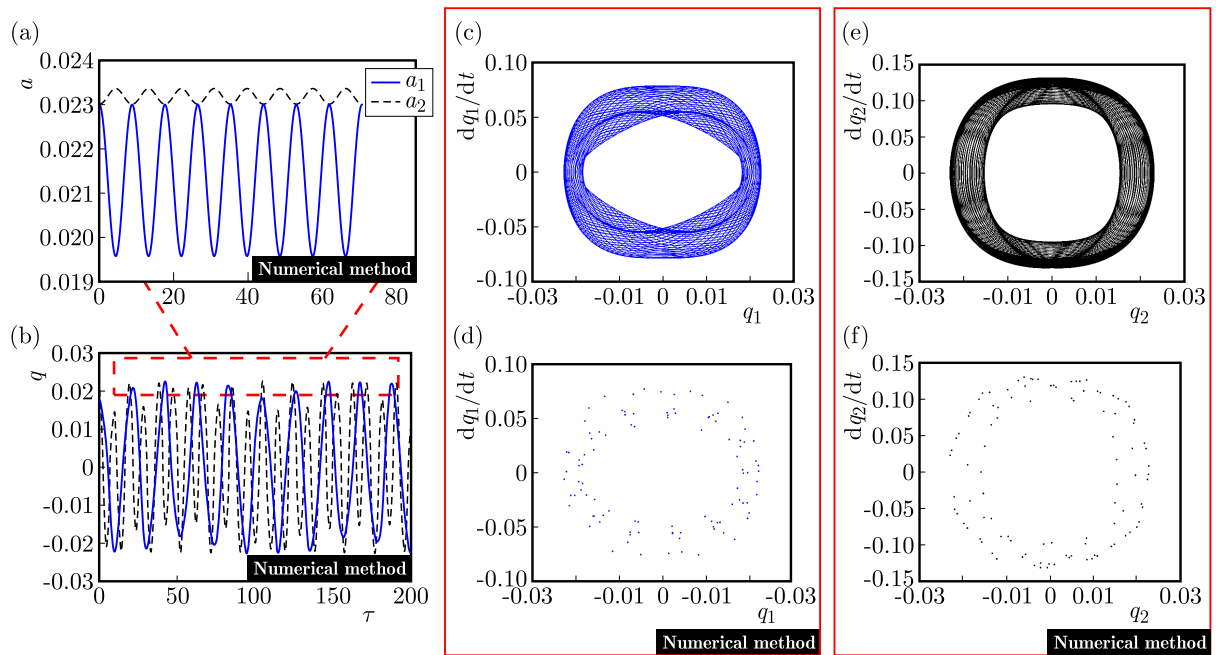


Fig. 8. Periodic motion of the system for the initial condition equal to 0.012 ($\gamma_0 = 0$, $c = 55$ m/s); (c) and (e) are phase diagrams of q_1 and q_2 , (d) and (f) are Poincaré maps of q_1 and q_2

4.1.2. Electromagnetically damped system

Similarly, basing on the numerical solution to Eqs. (3.5) in the damped free vibration system, we obtain the following decay graphs of vibration modes.

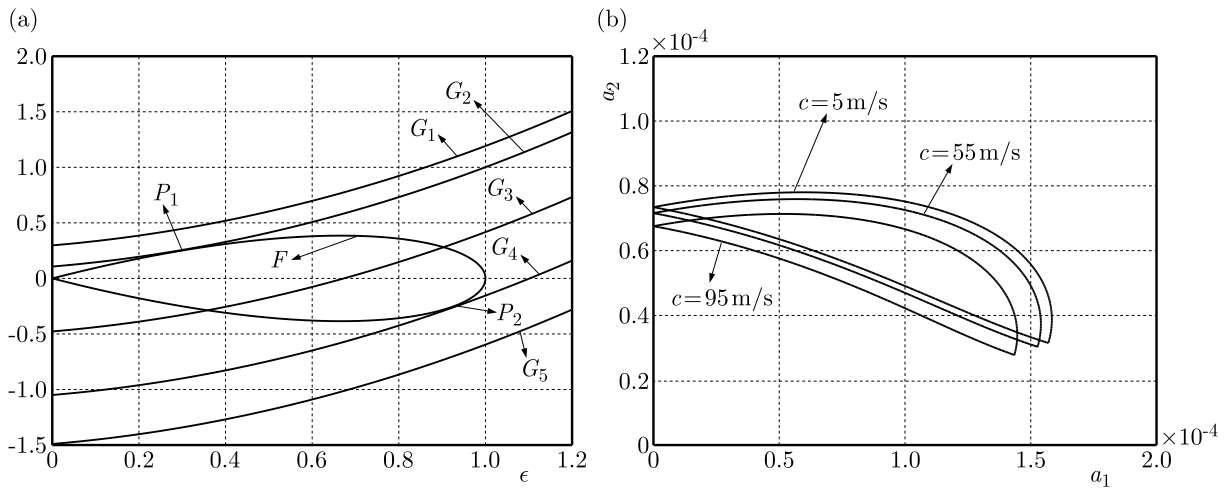


Fig. 9. (a) The curve graph of F and G . (b) The characteristic graphs of the vibration amplitude ($\sin \gamma = 0$)

4.2. Electromagnetic damped system

Figure 10a reveals the decay graphs of vibration modes for different axial velocities ($c = 5 \text{ m/s}$, $c = 55 \text{ m/s}$, $c = 95 \text{ m/s}$). It should be observed that the axial velocity may exert a more significant effect on the first-order mode than on the second one. Figure 10b exhibits the decay graphs of vibration modes for different initial conditions $a_{10} = 0.04, 0.05$ and 0.06 , as a result of which their attenuation trend is almost the same, but the difference lies in that the larger the initial value is, the more slender the waveforms of vibration mode are.

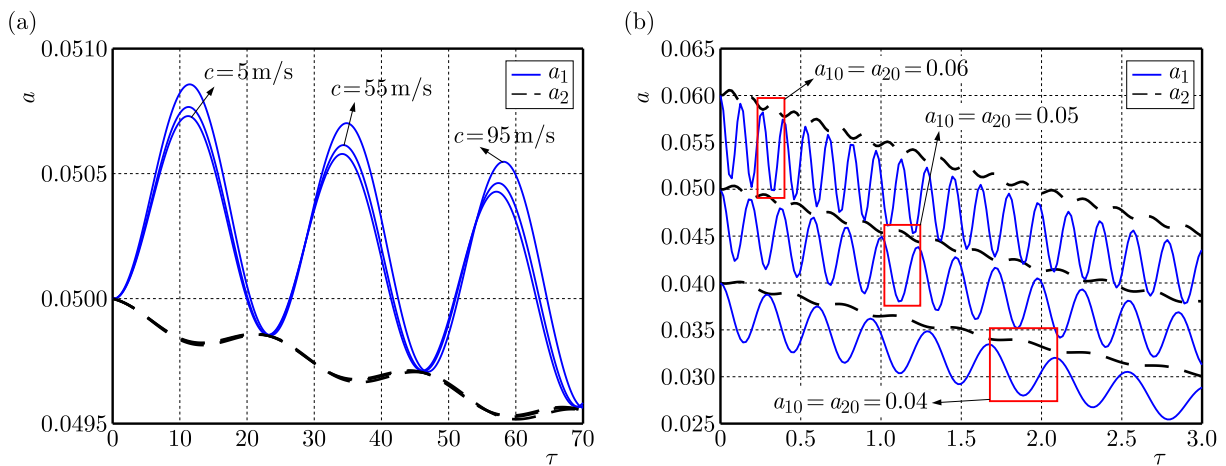


Fig. 10. The decay graphs of variation modes for different axial velocities and different initial conditions: (a) $B_{0y} = 0.3 \text{ T}$, $\gamma = 9.4$ and (b) $B_{0y} = 0.3 \text{ T}$, $\gamma = 0$

Figures 11a-h show the decay graphs of vibration modes for different magnetic field strength in the damped free vibration system. Graphs (a), (c), (e), (g) of vibration modes a_1 and a_2 , at the bottom of Fig. 11, are calculated by the perturbation approach, and curves (b), (d), (f), (h) of q_1 and q_2 , at the bottom of Fig. 11, are drawn from direct simulations of vibration equations for the magnetic field strength $B_{0y} = 0.1 \text{ T}$, $B_{0y} = 0.3 \text{ T}$, $B_{0y} = 0.6 \text{ T}$, $B_{0y} = 1.2 \text{ T}$, respectively. Thus, as reported by Nayfeh and Mook (1979) on the internal resonance phenomenon in the damped system, the curves of vibration modes in our investigation exhibit the same trend of coupled attenuation with time. Their decay rate will increase when the applied magnetic field becomes stronger.

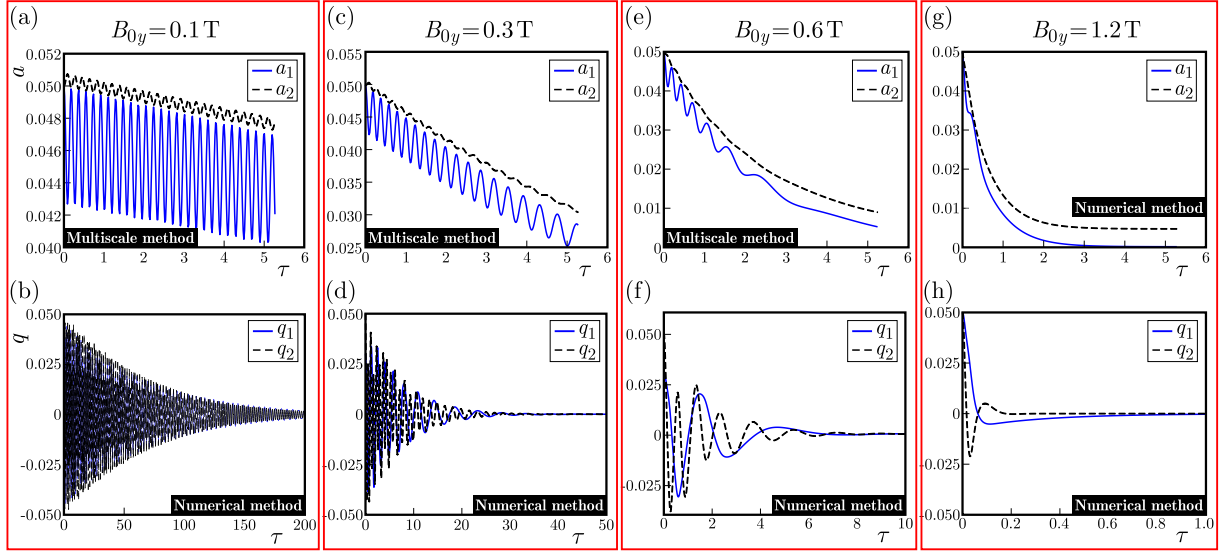


Fig. 11. The system attenuation response for different magnetic field intensity (multistate and numerical methods)

5. Conclusions

This work is mainly concerned with the 1:3 internal resonance problem of an axially moving conducting elastic beam in a magnetic field. Based on our study, the magneto-elastic vibration equation of the beam can be obtained and the vibration mode equations of free vibrating beams can be obtained through the multi-scale method. Meanwhile, we have carried out direct simulations of the vibration equations in order to evaluate the accuracy of the perturbation approach.

- In the system without electromagnetic damping, there are steady-state motions and solutions, where the system energy is constantly exchanged between the first two coupled vibration modes. The steady-state motion, however, is not always stable. As shown in Fig. 9a, any small external disturbance can cause changes. In addition, the vibration amplitudes continuously increase while the axial velocity c enhances from 5 m/s up to 95 m/s. As for the initial conditions, the amplitude changes of the first-order and second-order modes resulting from an increase in the initial amplitude of vibration modes a_{10} and a_{20} (see Appendix I). They are displayed in Figs. 4b,c and Figs. 5b,c. And unlike the whole up or down motions caused by the increase of the initial phase angle γ_0 (see Appendix I) shown in Fig. 3, they present “reversal behaviour”. The vibration modes are more sensitive to the initial amplitude of vibration modes, and the curves of vibration modes are intertwined when the initial condition satisfies $0 < \gamma_0 < 9.4$, $a_{10} = a_{20} = 0.05$ but they separate for phase angles beyond that range.
- Direct simulations of the vibration equations have been carried out in order to evaluate the accuracy of the perturbation approach. Compared to the amplitudes from the perturbation approach, see Figs. 6-8a, the amplitudes displayed in Figs. 6-8b present good consistency. Meanwhile, the corresponding phase diagram and Poincaré map of the system are obtained, which show that the responses of the system change firstly from the periodic motion to period-2 motion and, finally, develop into chaotic motion when the initial conditions increase.
- For the electromagnetically damped system, the vibration modes exhibit a trend of coupling attenuation with time. Its decay rate increases when the applied magnetic field becomes stronger. Additionally, the axial velocity may exert a more significant effect on

the first-order mode than on the second one. As for the initial amplitude of vibration modes, the larger the initial value is, the slenderer the waveforms of vibration modes seem to be.

Acknowledgement

This research was supported by the National Natural Science Foundation of China (No. 11472239), Hebei Provincial Natural Science Foundation of China (No. A2015203023) and the Key Project of Science and Technology Research of Higher Education of Hebei Province of China (No. ZD20131055).

Appendix I

Coefficients of Eq. (3.3) ($n = 1, 2; i = 1, 2$)

$$\begin{aligned}
 A_{ni} &= \int_0^l X_n X_i dx & B_{ni} &= \int_0^l \frac{dX_n}{dx} X_i dx \\
 C_{ni} &= \int_0^l \frac{d^2 X_n}{dx^2} X_i dx & D_{ni} &= \int_0^l \frac{d^4 X_n}{dx^4} X_i dx \\
 S_{1i} &= \int_0^l \frac{d^2 X_1}{dx^2} \left(\frac{dX_1}{dx} \right)^2 X_i dx & S_{3i} &= \int_0^l \left[\frac{d^2 X_1}{dx^2} \left(\frac{dX_2}{dx} \right)^2 + 2 \frac{dX_1}{dx} \frac{dX_2}{dx} \frac{d^2 X_2}{dx^2} \right] X_i dx \\
 S_{2i} &= \int_0^l \left(\frac{dX_2}{dx} \right)^2 \frac{d^2 X_2}{dx^2} X_i dx & S_{4i} &= \int_0^l \left[\left(\frac{dX_1}{dx} \right)^2 \frac{d^2 X_2}{dx^2} + 2 \frac{d^2 X_1}{dx^2} \frac{dX_1}{dx} \frac{dX_2}{dx} \right] X_i dx \\
 D_{ni} &= P_n^4 A_{n1} & B_{ii} &= 0 & A_{ij} &= C_{ij} = D_{ij} = 0
 \end{aligned}$$

Coefficients of Eqs. (3.4) ($n = 1, 2; i = 1, 2, 3, 4$)

$$\begin{aligned}
 g_1^2 &= \frac{C_{11}}{A_{11}} \eta^2 - \frac{C_{11}}{A_{11}} \zeta + 1 & g_2^2 &= \frac{C_{22}}{A_{22}} \eta^2 - \frac{C_{22}}{A_{22}} \zeta + \left(\frac{9}{5} \right)^4 & \eta &= \frac{c}{\omega_n} \\
 \zeta &= \frac{F_{0x}}{\rho A \omega_n^2} & \mu_{11} = \mu_{22} &= \frac{1}{\varepsilon} \frac{\sigma B_{0y}^2}{2 \rho \omega_n} & \mu_{12} = \mu_{21} &= \frac{1}{\varepsilon} \frac{2 B_{21} \eta}{A_{11}} \\
 k_1 &= \frac{18 l^2}{D_{11} h^2} & k_2 &= \left(\frac{9}{5} \right)^4 \frac{18 l^2}{D_{22} h^2} & s_{i1} &= k_1 \frac{S_{i1}}{\varepsilon} & s_{i2} &= k_2 \frac{S_{i2}}{ve}
 \end{aligned}$$

Definitions in multiple-scales method of Eqs. (3.5)

$$\begin{aligned}
 q_1(\tau, \varepsilon) &= q_{11}(T_0, T_1) + \varepsilon q_{12}(T_0, T_1) & q_2(\tau, \varepsilon) &= q_{21}(T_0, T_1) + \varepsilon q_{22}(T_0, T_1) \\
 q_{11} &= A_1(T_1) e^{i g_1 T_0} + \bar{A}_1(T_1) e^{i g_1 T_0} & q_{21} &= A_2(T_1) e^{i g_2 T_0} + \bar{A}_2(T_1) e^{i g_2 T_0}
 \end{aligned}$$

where \bar{A} is the conjugate of A , i is the imaginary unit.

$$A_n(T_1) = \frac{1}{2} a_n(T_1) e^{i \beta_n(T_1)} \quad n = 1, 2 \quad \gamma(T_1) = \beta_2(T_1) - 3 \beta_1(T_1) + \sigma T_1$$

where $T_0 = \tau$ and $T_1 = \varepsilon \tau$ are the time scales.

References

1. CHEN L.Q., TANG Y.Q., LIM C.W., 2010, Dynamic stability in parametric resonance of axially accelerating viscoelastic Timoshenko beams, *Journal of Sound and Vibration*, **329**, 5, 547-565
2. DING H., CHEN L.Q., 2010, Galerkin methods for natural frequencies of high-speed axially moving beams, *Journal of Sound and Vibration*, **329**, 17, 3484-3494
3. HU Y., HU P., ZHANG J., 2015, Strongly nonlinear subharmonic resonance and chaotic motion of axially moving thin plate in magnetic field, *Journal of Computational and Nonlinear Dynamics*, **10**, 2, 021010
4. HU Y., WANG J., 2017, Principal-internal resonance of an axially moving current-carrying beam in magnetic field, *Nonlinear Dynamics*, **90**, 1, 683-695
5. LI J., HU Y.D., WANG Y.N., 2017, The magneto-elastic internal resonances of rectangular conductive thin plate with different size ratios, *Journal of Mechanics*, **34**, 5, 711-723
6. MAO X.Y., DING H., CHEN L.Q., 2016, Steady-state response of a fluid-conveying pipe with 3:1 internal resonance in supercritical regime, *Nonlinear Dynamics*, **86**, 2, 795-809
7. MAO X.Y., DING H., LIM C.W., CHEN L.Q., 2016, Super-harmonic resonance and multi-frequency responses of a super-critical translating beam, *Journal of Sound and Vibration*, **385**, 267-283
8. NAYFEH A.H., MOOK D.T., 1979, *Nonlinear Oscillation*, John Wiley & Sons, New York
9. PELLICANO F., 2005, On the dynamic properties of axially moving systems, *Journal of Sound and Vibration*, **281**, 3-5, 593-609
10. PRATIHER B., 2011, Non-linear response of a magneto-elastic translating beam with prismatic joint for higher resonance conditions, *International Journal of Non-Linear Mechanics*, **46**, 5, 685-692
11. PRATIHER B., DWIVEDY S.K., 2009, Non-linear dynamics of a soft magneto-elastic Cartesian manipulator, *International Journal of Non-Linear Mechanics*, **44**, 7, 757-768
12. SAHOO B., PANDA L.N., POHIT G., 2015, Two-frequency parametric excitation and internal resonance of a moving viscoelastic beam, *Nonlinear Dynamics*, **82**, 4, 1721-1742
13. SAHOO B., PANDA L.N., POHIT G., 2016, Combination, principal parametric and internal resonances of an accelerating beam under two frequencies parametric excitation, *International Journal of Non-Linear Mechanics*, **78**, 35-44
14. TANG Y.Q., ZHANG D.B., GAO J.M., 2016, Parametric and internal resonance of axially accelerating viscoelastic beams with the recognition of longitudinally varying tensions, *Nonlinear Dynamics*, **83**, 1-2, 401-418
15. WANG L., CHEN H.H., HE X.D., 2011, Active H control of the vibration of an axially moving cantilever beam by magnetic force, *Mechanical Systems and Signal Processing*, **25**, 8, 2863-2878
16. WU G.Y., 2007, The analysis of dynamic instability on the large amplitude vibrations of a beam with transverse magnetic fields and thermal loads, *Journal of Sound and Vibration*, **302**, 1-2, 167-177
17. YAN Q., DING H., CHEN L., 2015, Nonlinear dynamics of axially moving viscoelastic Timoshenko beam under parametric and external excitations, *Applied Mathematics and Mechanics*, **36**, 8, 971-984

ON THE EIGENMODES AND EIGENFREQUENCIES OF
LOW-DIMENSIONAL DEGENERATED CARBON STRUCTURES:
OBTAINING NATURAL FREQUENCIES OF IDEAL
AND STRUCTURALLY DEFECTED SYSTEMS

SADEGH IMANI YENGEJEH

*Centre for Clean Environment and Energy, School of Environment and Science, Griffith University, Australia
e-mail: imani.sd@gmail.com*

SEYEDEH ALIEH KAZEMI

*The University of Birjand, Department of Mechanical Engineering, Birjand, Iran
e-mail: sa.kazemi83@gmail.com*

ANDREAS ÖCHSNER

*Esslingen University of Applied Sciences, Faculty of Mechanical Engineering, Esslingen, Germany
e-mail: andreas.oechsner@gmail.com*

We concentrated on evaluating the vibrational response of ideal and defected degenerated carbon nanostructures under the influence of different boundary conditions. In addition, an attempt has been made to investigate the relative deviation of the natural frequency of imperfect systems and to study the effect of defected regions on vibrational stability of the particles. It has been found that a single and pinhole vacancy defect have the least and the most impact on the natural frequency of nanostructures. Furthermore, the effect of CNT diameter on natural frequencies of low-dimensional systems has also been investigated in this research.

Keywords: carbon nanostructures, finite element method, vibrational property, vacancy defect

1. Introduction

In the recent decades significant attention has been paid to exploration of characteristics of low-dimensional carbon structures including carbon nanotubes (CNTs) and their degenerated nanostructures (Iijima, 1991; Chandra and Namilae, 2006; Yao *et al.*, 2008, Imani Yengejeh *et al.*, 2014a,b, 2015a,b). Such nano-configurations possess outstanding physical, thermal and mechanical properties and, therefore, seem to be effectively applicable in the industry domain from manufacturing to aerospace engineering (Ruoff and Lorents, 1995; Lu, 1997; Imani Yengejeh *et al.*, 2015a,b). Innumerable studies have been conducted in order to find and explore characteristics of CNTs. Prediction of tensile strength (of up to 63 GPa) and Young's modulus (of nearly 1 TPa) of CNTs was the most significant aim of those investigations (Tserpes and Papanikos, 2007; Kuang and He, 2009; Imani Yengejeh *et al.*, 2014b; Imani Yengejeh and Öchsner, 2015). Basically, there are two major categories for such studies: computational and experimental approaches. Continuum mechanics techniques such as the finite element method (FEM) and molecular dynamics (MD) simulations have been the most highlighted computational approaches to explore the characteristics of nanostructures (Mylvaganam *et al.*, 2006, Hollerer and Celigoj, 2013). Despite remarkable exploration on predicting the behavior of CNTs, far more concentration is required to evaluate the mechanical behavior of CNTs and other types of low-dimensional particles such as nanocones, junction hybrids, fullerenes, etc. In the following, the

most recent studies concerning the evaluation of vibrational property of carbon nanostructures are presented.

Bogush *et al.* (2017) developed an approach to study molecular vibrations for symmetrical systems. Their proposed method was applied to investigate vibrational characterization of the fullerene molecule C60 and to study a relative comparison of theoretical results and experimental data. Their study was mainly focusing on symmetrical models, and less attention was paid to asymmetric structures. Following this, Mohammadian *et al.* (2017) explored the vibrational response of linearly and angle-joined CNTs applying a molecular mechanics approach. They divided their investigation into two main categories. First, the influence of the junction region formation on natural frequencies of ideal hybrids was examined. Afterwards, the impact of some defects on the vibrational behavior of those models was investigated. It was noted that the frequencies and mode shapes were comparatively influenced by changing the location of the connecting region. Furthermore, it was concluded that the frequency shift of the defective configurations with lower aspect ratios was more influenced by the degree of imperfections. Although their research seemed to be effectively covering the behavior of defective low-dimensional tubes, the impact of applied impurities on the specific regions of the hybrids was not fully addressed in all details. Then, Ardehana *et al.* (2017) suggested a novel method to explore vibrational characteristics of carbon nanocones. Also, their analysis exhibited the impact of varied model lengths on natural frequencies. Based on their findings, it was noted that increasing side length of a nanocone with a constant apex angle results in a significant decline in the fundamental frequency of the models. They also suggested that smaller lengths of nanocones are more likely to be applicable as they exhibit remarkable variation in the fundamental frequencies. Despite the comparatively comprehensive investigation, the behavior of imperfect low-dimensional particles was not discussed in their study.

Undoubtedly, there are some significant gaps in this research area. The objectives of this study is to explore and to predict the vibrational response of symmetric and asymmetric carbon nano-configurations in their ideal and defective forms, namely linearly- and angle-joined CNTs, open-tip carbon nanocone, open-end and capped CNTs, and fullerenes. These low-dimensional structures possess unique properties and are applicable to the experimental area. Due to holding such outstanding characteristics, prediction of their mechanical response is effectively essential in the nanotechnology scope (Imani Yengejeh *et al.*, 2016). There are several challenges in the current paper, namely different boundary conditions, application of certain amount impurities to a particular region of the models, and evaluation and comparison of the natural frequencies of defect-free and manipulated low-dimensional configurations using FEM. The results of this research is most likely to be reliable since the majority of nanostructures found in reality are exposed to atomic and structural imperfection, and their mechanical characteristics will definitely be affected by such defects. Therefore, the proposed study will explore the possible property of imperfect degenerated nanostructures in detail.

2. Materials and approaches

The basic configuration of low-dimensional structures including homogeneous CNT, linearly- and angle-joined CNTs, nanocones, cylindrical fullerenes and bucky-balls can be imagined as pseudo two-dimensional (2D) single-layer sheets of graphene, as shown in Fig. 1.

Overall, seven different nanostructures have been modeled within this study, namely homogeneous CNT, one-side capped CNT, two-side capped CNT, open-tip nanocone, linearly- and angle-joined CNT, and bucky-ball. Furthermore, three different boundary conditions have been considered in simulations, i.e. free-free, fix-free, and fix-fix boundary conditions. The aim of considering numerous models and various boundary conditions is to evaluate the behavior of

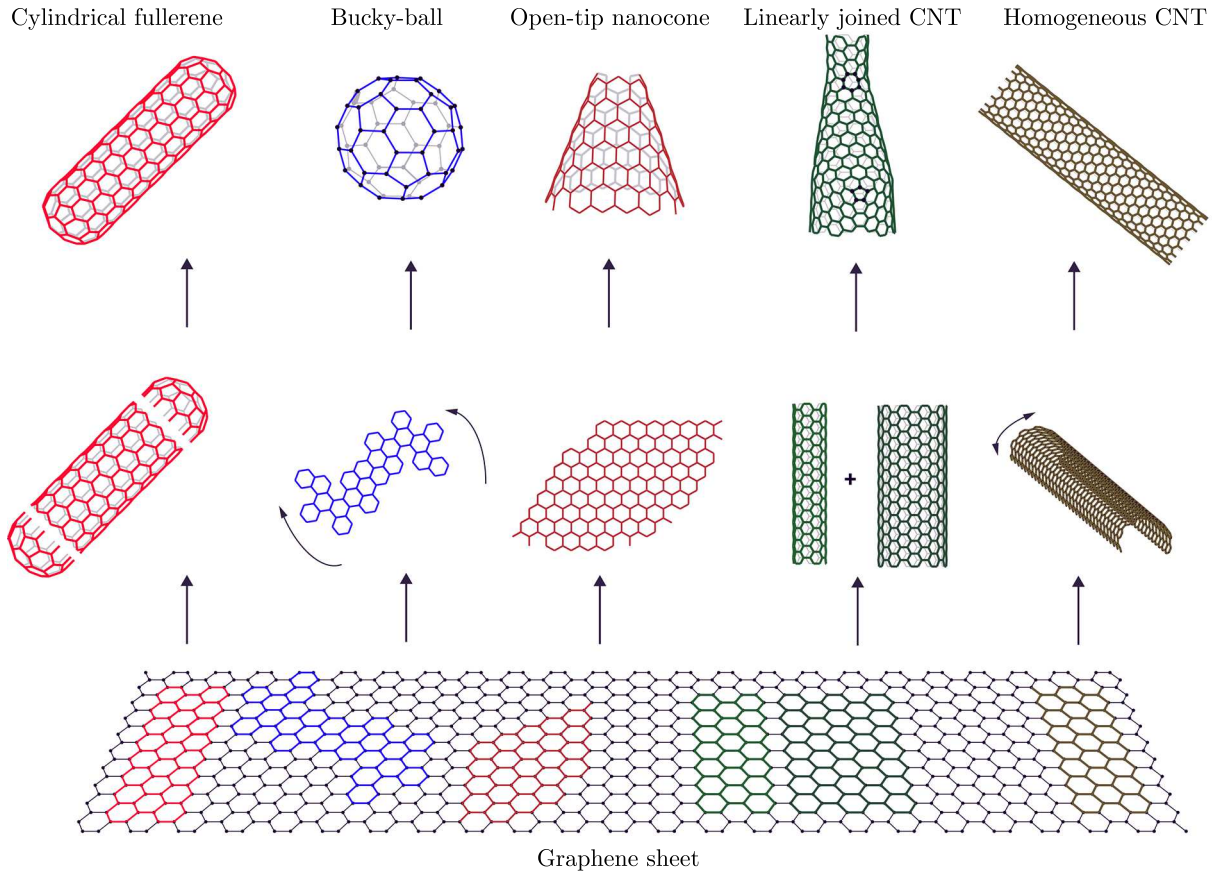


Fig. 1. Single-layer graphene sheet as carbon precursor to cylindrical fullerene, bucky-ball, open-tip nanocone, linearly-joined CNT and homogeneous CNT

different low-dimensional configurations under different boundary conditions, since they may have a significant response in different circumstances. Following the modeling and simulation of the ideal nanostructures, some common vacant sites, i.e. mono-, di-, tri-, and pinhole vacancy defects have been introduced to the perfect models to evaluate the vibrational response of low-dimensional configurations which are closer to the ones found in reality. Those mentioned atomic impurities are illustrated in Fig. 2.

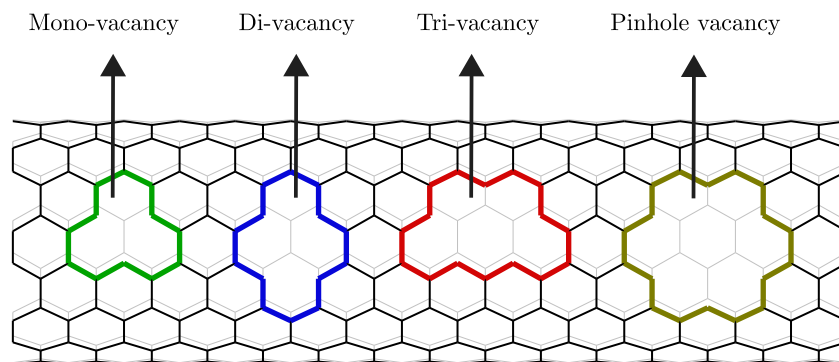


Fig. 2. Some common structural defects such as mono-, di-, tri- and pinhole vacancy introduced into configuration of the studied CNT systems

The modeling and simulation procedure is carried out in three major steps. Firstly, the spatial coordinates and connectivities of all nanostructures are imported to a commercial FE package (MSC Marc) and the first natural frequency of ideal models is obtained. Next, some of

the most common vacant sites are introduced to the defect-free configurations. These impurities are applied to the perfect models via a custom code in MATLAB to the original models and with the same impurity percentage (1%). In the final step, the fundamental frequency of defected structures is acquired and compared to those with perfect configurations.

3. Results and discussions

The simulation procedure commenced with the evaluation of natural frequencies and mode shapes of nanostructures. As an instance, Fig. 3 illustrates six mode shapes of an open-tip nanocone with original and vibrated configurations with the fix-free boundary condition.

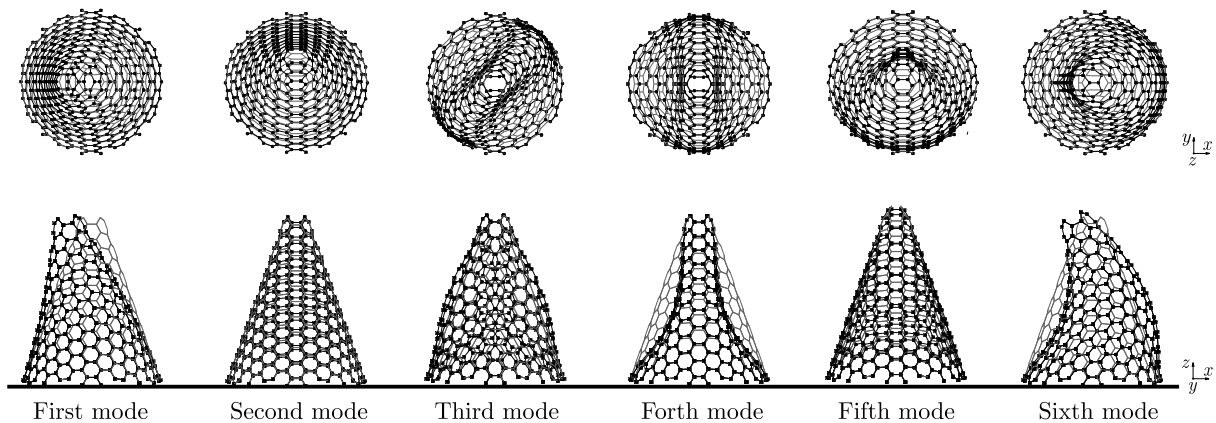


Fig. 3. Six vibrational mode shapes of an open-tip nanocone

Within this simulation, 1% of four common vacant sites are introduced to the low-dimensional structures and their first natural frequencies are obtained and also compared. Figure 4 shows the overall deviation in the natural frequencies of imperfect homogeneous CNT under the influence of various boundary conditions. Generally, the major change occurred in the fix-fix boundary condition. Nevertheless, the significant deviation happens for the fix-free boundary condition when the lower region is manipulated by impurities where the natural frequency is reduced by nearly 40% by introducing the pinhole vacancy defect in the structure of the model. The configuration with the free-free boundary condition has a comparatively moderate decline in which the maximum decrease occurs to the model with the pinhole vacancy introduced to the middle of the structure.

Comparing the change in the natural frequencies of one-side capped CNTs, as shown in Fig. 5, it is noted that a significant change occurs in the structure with the fix-free boundary condition. More specifically, the overall change for the fix-free model with single, double, triple, and pinhole vacancy defects is obtained to be approximately 13%, 14.5%, 16%, and 23%, respectively.

Figure 6 represents the comparative deviation in the natural frequency of two-side capped CNTs under the influence of three different boundary conditions. Based on the computational results, the overall trend of both the free-free and fix-fix boundary conditions are quite similar in spite of a comparatively larger decline for the free-free boundary condition. Due to the symmetric configuration of the model under these two boundary conditions, the vibrational response of the structure under the introduction of defects either in upper and lower sides of the systems is similar. In contrast to the free-free and fix-fix boundary condition, the vibrational response of the two-side capped CNT has a quite different trajectory. While the vacant sites decrease the natural frequency of the model up to maximum 18% for the impurities introduced to the upper side and middle of the structure, the change is significantly highlighted when the defect is applied

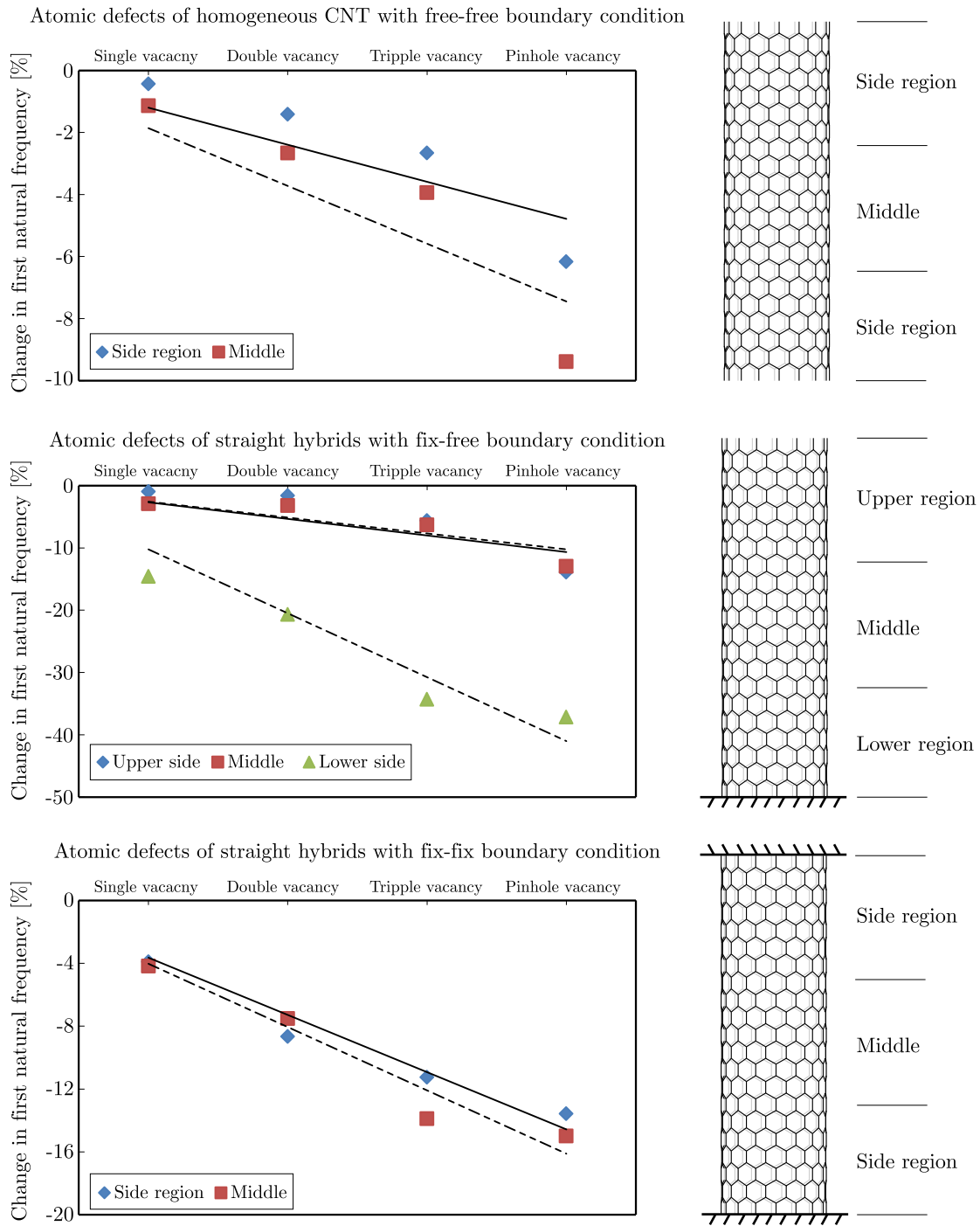


Fig. 4. Change in the natural frequency in % for a defective homogenous CNT under different boundary conditions

to the lower region of the system where the maximum deviation exceeds 35% in the case of the pinhole vacancy defect.

The vibrational response of linearly-joined CNTs has been evaluated for different boundary conditions, including free-free, fix-fix, wider tube fix, and thinner tube fix. As shown in Fig. 7, the fundamental frequency of imperfect hybrids reduces significantly, particularly in the case of the thinner tube fix boundary condition. More specifically, the overall change in the natural frequency of straight hybrids is nearly 5% for a single vacancy defect and reaches nearly 45% in the worst case which belongs to the thinner tube fix boundary condition. It is noticeable that

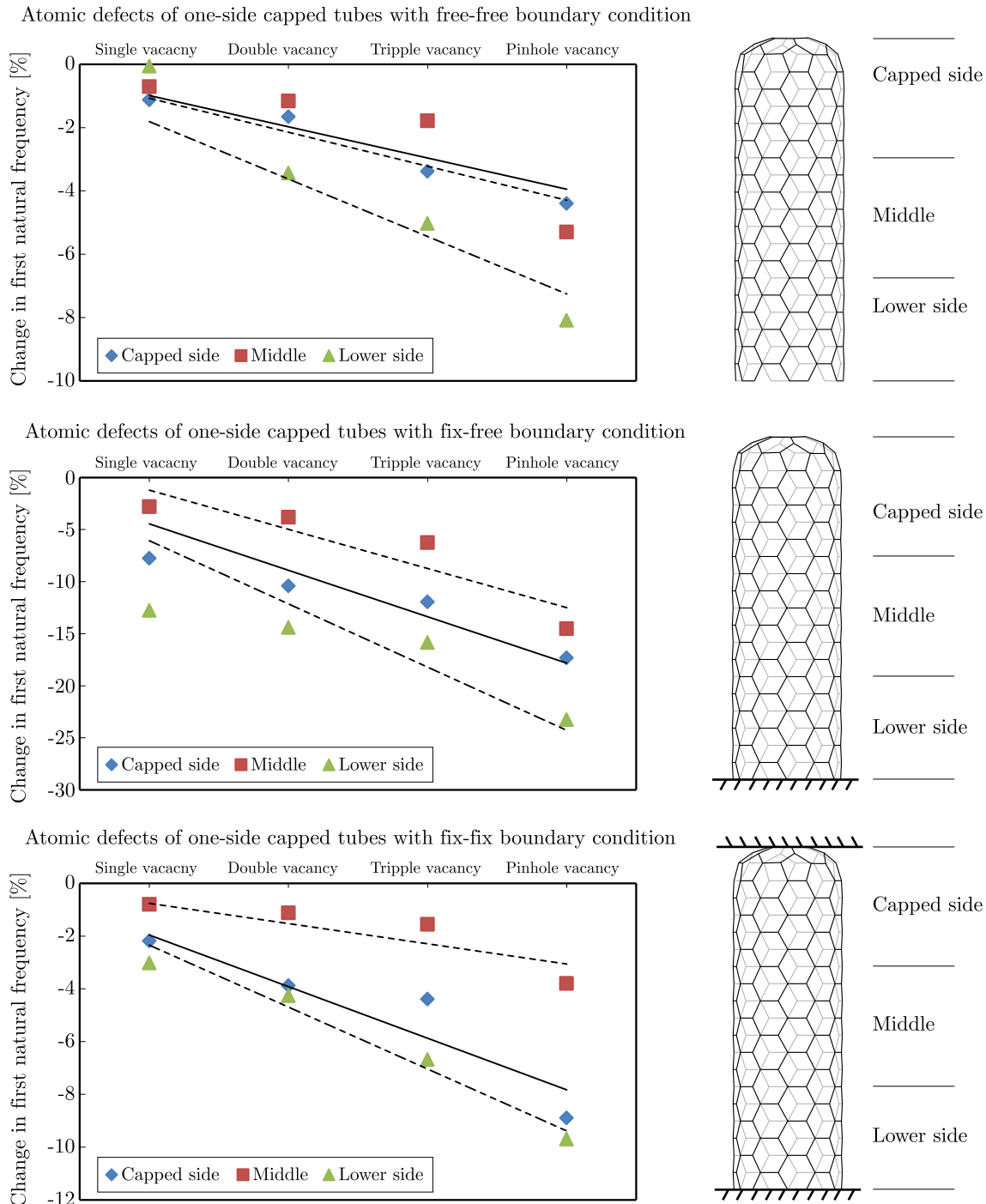


Fig. 5. Change in the natural frequency in % for a defective one-side capped CNT under different boundary conditions

the thinner fix CNTs reduces the vibrational stability of the structures in comparison with their wider counterparts.

Similarly to straight hybrids, the natural frequencies of imperfect angle-joined CNTs are evaluated under four major boundary conditions, namely free-free, fix-fix, zigzag tube fix, and armchair tube fix. Figure 8 illustrates the overall trend of deviation in the fundamental frequency of the imperfect bending junction. It is noted that the applied impurities on the zigzag tube have a greater influence on the natural frequency of the system in comparison with the armchair

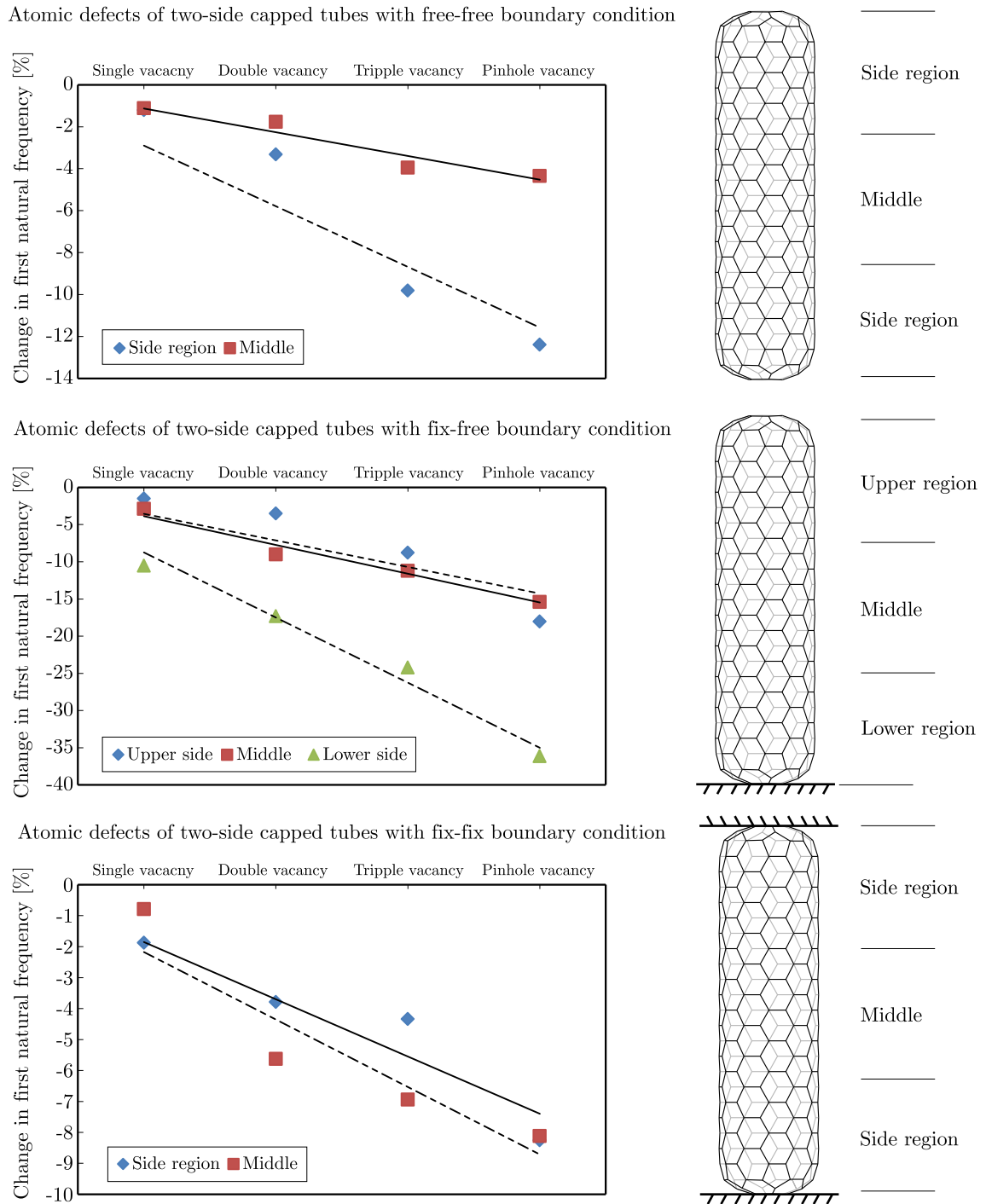


Fig. 6. Change in the natural frequency in % for a defective two-side capped CNT under different boundary conditions

CNTs. Furthermore, the vibrational stability of the angle-joined CNT under the fix-fix boundary condition is shown to be noticeable. A comparison of the straight and angle-joined hybrids indicates that the bending structures possess a relatively higher strength in vibrational stability.

Based on the results illustrated in Fig. 9, it is noted that the deviation in the natural frequencies of nanocone varies according to the defected region. More specifically, in the case of fix-free boundary conditions, the most highlighted changes in the natural frequency are reported when the atomic defects are introduced to the lower region of the structure. The maximum deviation

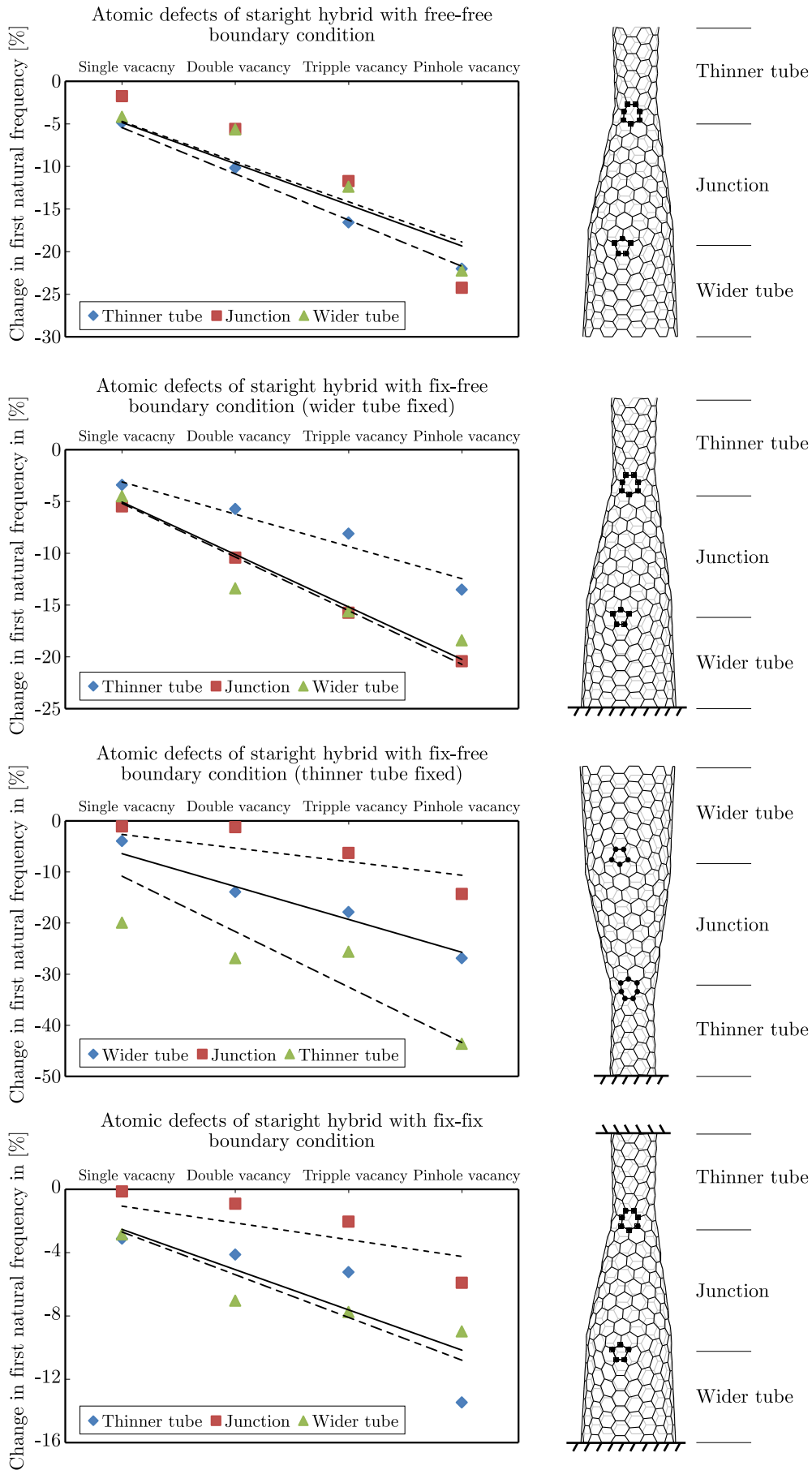


Fig. 7. Change in the natural frequency in % for a defective linearly-jointed CNT under different boundary conditions

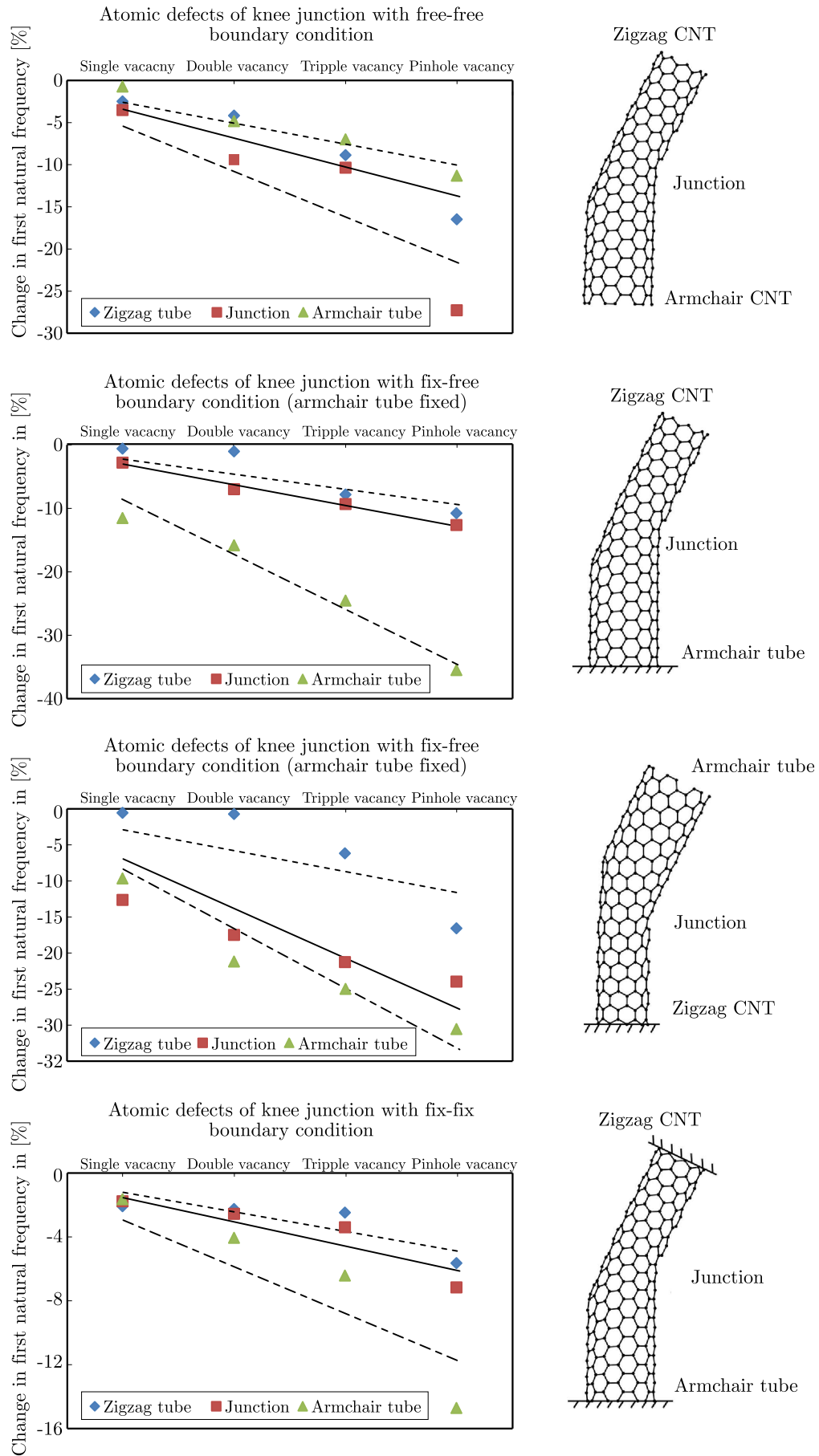


Fig. 8. Change in the natural frequency in % for a defective angle-joined CNT under different boundary conditions

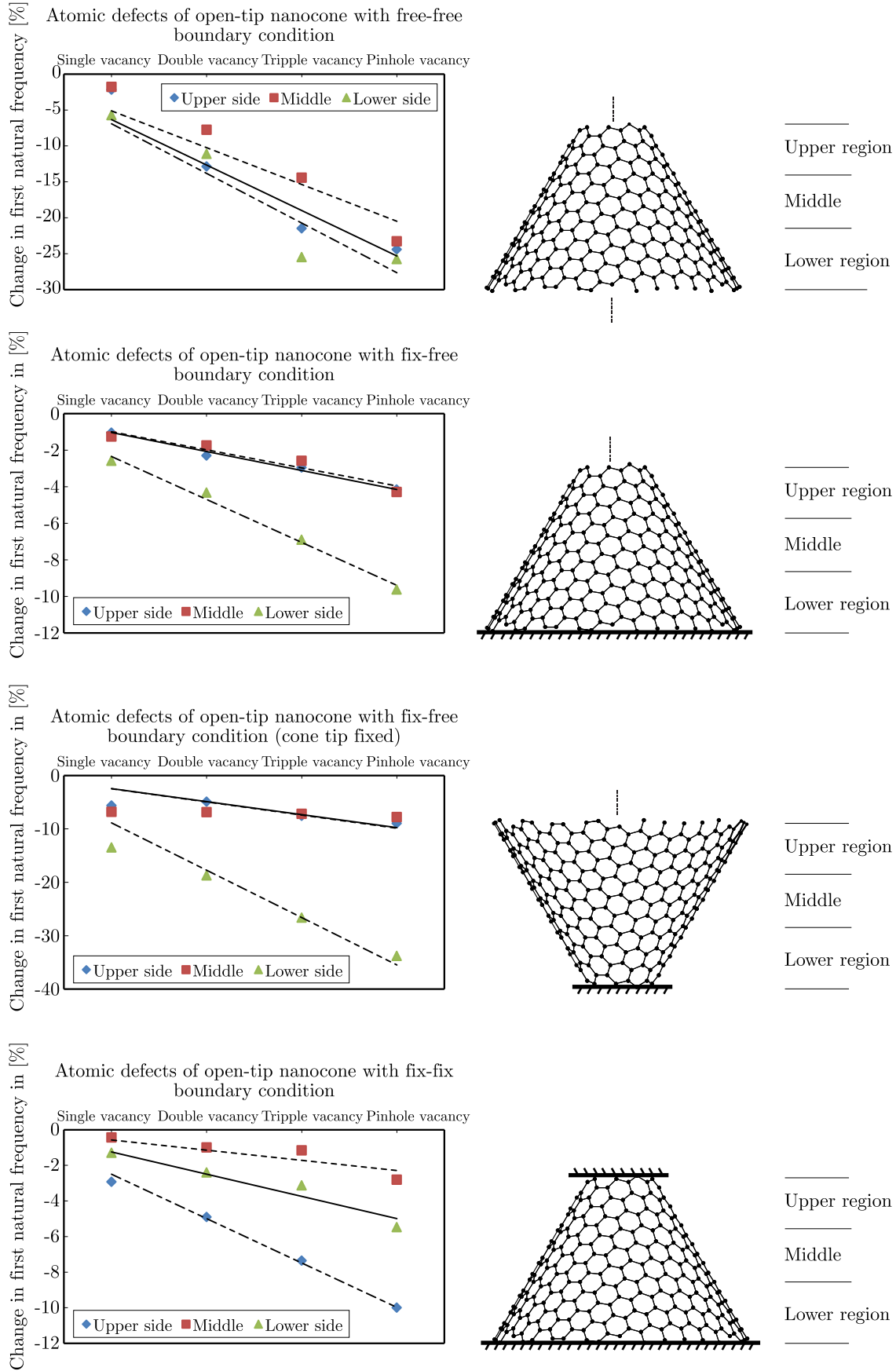


Fig. 9. Change in the natural frequency in % for a defective open-tip nanocone under different boundary conditions

observed in the cases of the cone base fix and cone tip fix is reported to be approximately 10% and 35%, respectively. Apart from some occasional high deviations, the nanocone is noted to be a typical low-dimensional structure which has a significant vibrational stability in comparison with other degenerated nanostructures.

The obtained results from Fig. 10 reveal the fact that the bucky-ball possesses the highest vibrational stability and has the lowest decline in the natural frequency in comparison with the other low-dimensional particles. The change in the natural frequency of the bucky-ball under free-free and fix-fix boundary conditions is reported to be between 1% up to nearly 9% in the case of the pinhole vacancy defect.

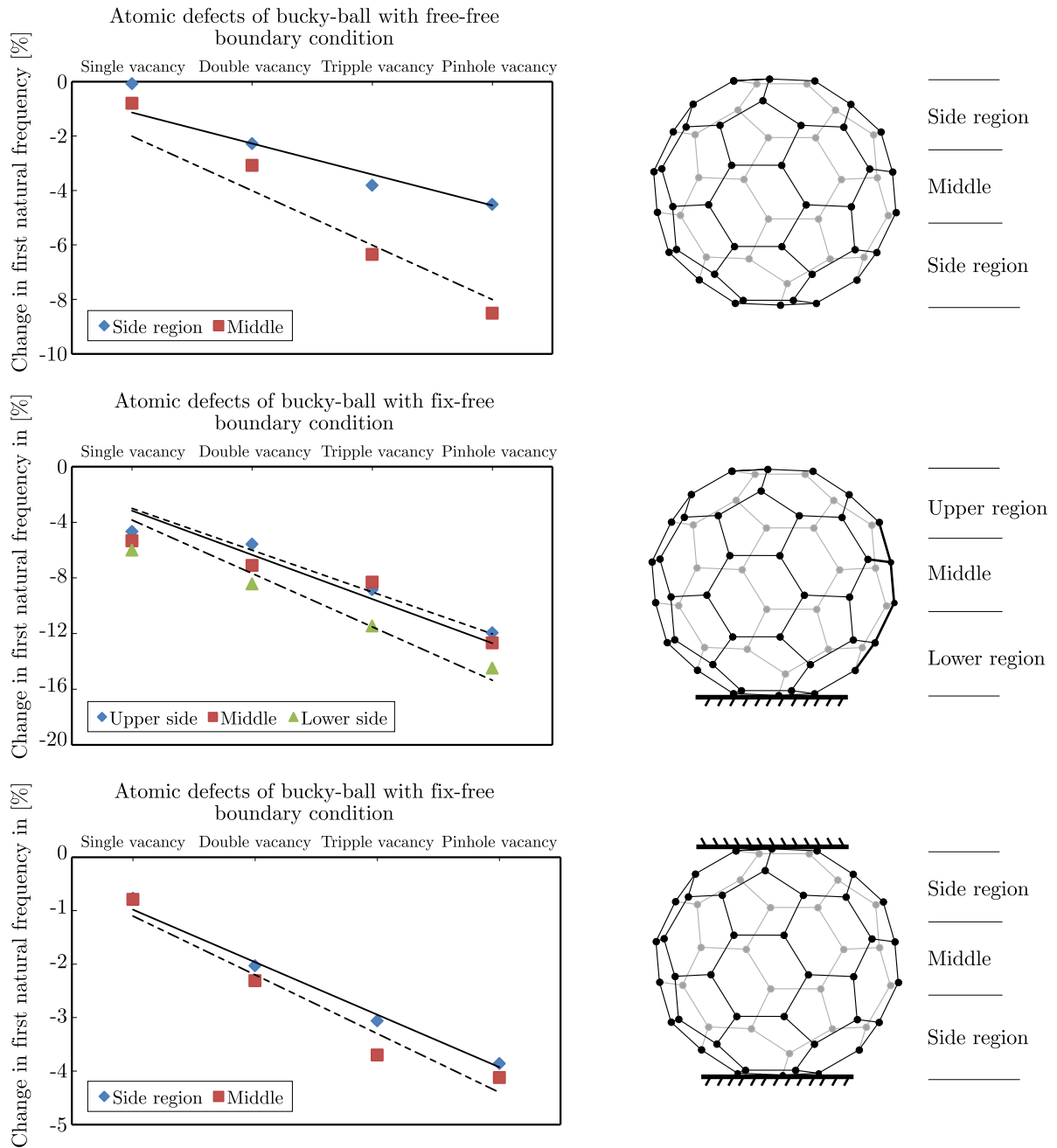


Fig. 10. Change in the natural frequency in % for a defective bucky-ball under different boundary conditions

4. Conclusion

In this study, several low-dimensional structures including nanocones, linearly- and angle-joined CNTs, bucky-balls, etc. have been simulated in their perfect and defective forms, and their vibrational stability has been evaluated by applying a FE approach. The introduced imperfections are the most common vacant sites, namely mono-, di-, tri-, and pinhole vacancy defects which are applied to the perfect configurations using a custom code in MATLAB. An attempt has been made to evaluate natural frequencies of numerous nanostructures under different boundary conditions. It has been indicated that the natural frequency of the low-dimensional systems decreases with the introduction of atomic modifications. Furthermore, the models have different responses according to their boundary conditions. It is also concluded that bucky-ball and linearly-joined CNT have the least and the most deviations in the natural frequencies, respectively. The significant point of this research is that the applied impurities introduced to the systems have various effects on the fundamental frequencies based on their position in the nanostructures. In addition, it is noted that the angle-joined CNT possesses a higher vibrational stability in comparison with the straight hybrid. Finally, it is concluded that the tube diameter holds a significant influence on the vibrational response of CNTs. The findings of this research opens an avenue for the evaluation of the mechanical property of low-dimensional degenerated systems; nevertheless, much more attention needs to be paid to other methods including density functional theory (DFT), which is the future research objective of the authors.

References

1. ARDESHANA B., JANI U., PATEL A., JOAHI A.Y., 2017, An approach to modelling and simulation of single-walled carbon nanocones for sensing applications, *AIMS Materials Science*, **4**, 1010-1028
2. BOGUSH I., CIOBU V., PALADI F., 2017, Advanced computational method for studying molecular vibrations and spectra for symmetrical systems with many degrees of freedom, and its application to fullerene, *The European Physical Journal B*, **90**, 193
3. CHANDRA N., NAMILAE S., 2006, Tensile and compressive behavior of carbon nanotubes: effect of functionalization and topological defects, *Mechanics of Advanced Materials and Structures*, **13**, 115-127
4. HOLLERER S., CELIGOJ C.C., 2013, Buckling analysis of carbon nanotubes by a mixed atomistic and continuum model, *Computational Mechanics*, **51**, 765-789
5. IJIMA S., 1991, Helical microtubules of graphitic carbon, *Nature*, **354**, 56
6. IMANI YENGEJEH S., AKBAR ZADEH M., ÖCHSNER A., 2014a, On the buckling behavior of connected carbon nanotubes with parallel longitudinal axes, *Applied Physics A*, **115**, 1335-1344
7. IMANI YENGEJEH S., AKBAR ZADEH M., ÖCHSNER A., 2015a, On the tensile behavior of hetero-junction carbon nanotubes, *Composites Part B*, **75**, 274-280
8. IMANI YENGEJEH S., KAZEMI S.A., ÖCHSNER A., 2014b, A numerical evaluation of the influence of atomic modification on the elastic and shear behavior of connected carbon nanotubes with parallel longitudinal axes, *Journal of Nano Research*, **29**, 93-104
9. IMANI YENGEJEH S., KAZEMI S.A., ÖCHSNER A., 2015b, On the buckling behavior of curved carbon nanotubes, [In:] *Mechanical and Materials Engineering of Modern Structure and Component Design*, A. Öchsner, H. Altenbach (Eds.), Switzerland, Springer International Publishing, **70**, 401-412
10. IMANI YENGEJEH S., KAZEMI S.A., ÖCHSNER A., 2016, Advances in mechanical analysis of structurally and atomically modified carbon nanotubes and degenerated nanostructures: A review, *Composites Part B: Engineering*, **86**, 95-107

11. IMANI YENGEJEH S., ÖCHSNER A., 2015, Influence of twisting and distortion on the mechanical properties of carbon nanotubes, *Journal of Computational and Theoretical Nanoscience*, **12**, 443-448
12. KUANG Y.D., HE X.Q., 2009, Young's moduli of functionalized single-wall carbon nanotubes under tensile loading, *Composites Science and Technology*, **69**, 169-175
13. LU J.P., 1997, Elastic properties of carbon nanotubes and nanoropes, *Physical Review Letters*, **79**, 1297-1300
14. MOHAMMADIAN M., HOSSEINI S.M., ABOLBASHARI M.H., 2017, Free vibration analysis of dissimilar connected CNTs with atomic imperfections and different locations of connecting region, *Physica B: Condensed Matter*, **524**, 34-46
15. MYLVAGANAM K., VODENITCHAROVA T., ZHANG L.C., 2006, The bending-kinking analysis of a single-walled carbon nanotube – a combined molecular dynamics and continuum mechanics technique, *Journal of Materials Science*, **41**, 3341-3347
16. RUOFF R.S., LORENTS D.C., 1995, Mechanical and thermal properties of carbon nanotubes, *Carbon*, **33**, 925-930
17. TSERPES K.I., PAPANIKOS P., 2007, The effect of Stone-Wales defect on the tensile behavior and fracture of single-walled carbon nanotubes, *Composite Structures*, **79**, 581-589
18. YAO X.-H., HAN Q., XIN H., 2008, Bending buckling behaviors of single- and multi-walled carbon nanotubes, *Computational Materials Science*, **43**, 579-590

Manuscript received July 12, 2018; accepted for print September 4, 2018

INVESTIGATION OF CRACK RESISTANCE IN EPOXY/BORON NITRIDE NANOTUBE NANOCOMPOSITES BASED ON MULTI-SCALE METHOD

HOSSEIN HEMMATIAN

Department of Mechanical Engineering, Semnan Branch, Islamic Azad University, Semnan, Iran
e-mail: hoseinhemmatian@gmail.com

MOHAMMAD REZA ZAMANI, JAFAR ESKANDARI JAM

Faculty of Mechanical Engineering, Malek-Ashtar University of Technology, Tehran, Iran

Boron nitride nanotubes (BNNTs) possess superior mechanical, thermal and electrical properties and are also suitable for biocomposites. These properties make them a favorable reinforcement for nanocomposites. Since experimental studies on nanocomposites are time-consuming, costly, and require accurate implementation, finite element analysis is used for nanocomposite modeling. In this work, a representative volume element (RVE) of epoxy/BNNT nanocomposites based on multi-scale modeling is considered. The bonds of BNNT are modeled by 3D beam elements. Also non-linear spring elements are employed to simulate the van der Waals bonds between the nanotube and matrix based on the Lennard-Jones potential. Young's and shear modulus of BNNTs are in ranges of 1.039-1.041 TPa and 0.44-0.52 TPa, respectively. Three fracture modes (opening, shearing, and tearing) have been simulated and stress intensity factors have been determined for a pure matrix and nanocomposite by J integral. Numerical results indicate that by incorporation of BNNT in the epoxy matrix, stress intensity factors of three modes decrease. Also, by increasing the chirality of BNNT, crack resistance of shearing and tearing modes are enhanced, and stress intensity factor of opening mode reduced. BNNTs bridge the crack surface and prevent crack propagation.

Keywords: boron nitride nanotube, epoxy, fracture modes, finite element model, multi-scale method

1. Introduction

Nanostructures as a new class of materials are prevalently used in the recent years. One of the most commonly used nanostructure is carbon nanotube (CNT), and one similar structure newer than CNTs is boron nitride nanotube (BNNT) (Chopra *et al.*, 1995). BNNTs, like CNTs, have extraordinary mechanical properties (Chopra and Zettl, 1998), high thermal conductivity (Chang *et al.*, 2005), and good resistance against oxidation at high temperature (Chen *et al.*, 2004). Despite their similar structures, BNNTs have different properties because BNNTs are composed of various atoms (Fereidoon *et al.*, 2015). Metal, semiconductor or insulator characteristics of CNTs are highly depending on chirality, diameter, and number of walls, while BNNTs behave independently as an insulator for low electric fields (Khaleghian and Azarakhshi, 2016; Molani 2017). BNNTs are also found to be nontoxic to health and environment due to their chemical inertness and structural stability. Therefore, BNNT is particularly suitable for biological applications.

The elastic properties of BNNTs have been theoretically investigated in many works. Slightly different results were presented, all of which indicated a very high Young's modulus, but slightly smaller than CNTs. So BNNTs can be widely used as a structural reinforcement of matrix materials (Zhi *et al.*, 2010).

First-principles, tight-binding, density functional and classical molecular mechanics approaches have been performed to characterize properties of BNNTs. Young's modulus of multi-walled boron nitride nanotubes (MWBNNNTs) was obtained 1.22–0.24 TPa using thermal vibration amplitude analysis (Chopra and Zettl, 1998). Many researchers employed the tight-binding method for calculating the axial Young's moduli of zigzag and armchair BNNTs (Verma *et al.*, 2007). It is also observed that zigzag nanotubes have a higher Young's modulus than armchair ones. In another study, Akdim *et al.* indicated that Young's modulus of BNNTs varied in the range of 0.71 ~ 0.83 TPa and was slightly dependent on the tube diameter (Akdim *et al.*, 2003).

Using ab-initio calculations based on the density functional theory (DFT), Young's modulus of DWBNNT was calculated and the estimated values for (2, 2) and (7, 7), (2, 2) and (9, 9) were 821 and 764 GPa, respectively (Fakhrabad and Shahtahmassebi, 2013). Also, Young's modulus of SWBNNTs with vacancy and functionalization defects was calculated by Griebel *et al.* (2009) using molecular dynamics (MD) simulation. They found that Young's modulus decreased with increasing defect concentration.

Young's modulus of BNNTs was reported to be 1.1-1.3 TPa from an experimental test (Bettinger *et al.*, 2002). In another experimental effort, Young's modulus of MWBNNT was obtained 895 GPa (Wei *et al.*, 2010). Suryavanshi *et al.* (2004) applied the electric-field-induced resonance method and specified Young's modulus as 0.8 TPa.

Polymer nanocomposite combining polymers and nano-filler components have attracted research attention from the academic and industrial communities due to their diverse functional applications, good processing and relatively low cost (Mohammadimehr and Mahmudian-Najafabadi, 2013). It is reported that nano-fillers such as particles and platelets can change the crack propagation direction and consequently stop this (Rozenberg and Tenne, 2008). Crack deflection as a result of nano-sized reinforcements in a matrix has been reported to have a significant role in toughening (Sun *et al.*, 2009). Nano-fillers can stop crack propagation along the original direction and also result in branching if agglomeration is minimized (Rozenberg and Tenne, 2008).

Lee *et al.* (2013) investigated the boron nitride nanoflake (BNNF) modification on epoxy resin. It was noted that strength of epoxy resin increased while Young's modulus did not significantly change. The highest strength increase was obtained at 0.3 wt.% BN content while the highest toughness increase was achieved with 0.5 wt.% BN content. In another work, Ulus *et al.* (2014) produced and investigated mechanical properties of boron nitride nanoplatelets (BNNP)-multiwall carbon nanotubes/epoxy hybrid nanocomposites. Young's modulus and tensile strength values were obtained via tensile tests. It is seen that tensile strength of epoxy resin increased from 60 MPa to 75 MPa (25% increases) at 0.5 wt.% BNNP content.

Applications of boron nitride nanotubes/epoxy nanocomposites to adhesive joints and composite laminates were reported by Jakubinek *et al.* (2016). Nanocomposites containing up to 7 wt.% BNNTs were fabricated by planetary mixing. The effects of BNNT loading on viscosity, tensile properties and fracture toughness were determined. The elastic modulus of nanocomposite increased progressively with the BNNT loading up to 5 wt.%. While ultimate strain only decreased with BNNT addition, the fracture toughness also reached a maximum around 5 wt.%.

Ghorbanpour Arani *et al.* (2012a) analyzed the electro-thermo-elastic stress of a piezoelectric polymeric thick-walled cylinder reinforced by BNNTs. They also investigated the electro-thermo-mechanical axial buckling behavior of a piezoelectric polymeric cylindrical shell reinforced with a double-walled boron-nitride nanotube using the principle of minimum total potential energy approach in conjunction with the Rayleigh-Ritz method (Ghorbanpour Arani *et al.*, 2012b). Bending and free vibration of a nonlocal functionally graded nanocomposite Timoshenko beam model reinforced by SWBNNT were reported based on a modified coupled stress theory (Davar and Sadri, 2016). Also, the effects of BNNTs on the elastic modulus of beta tricalcium phosphate and hydroxyapatite were analyzed using a RVE model. The predicted elastic moduli of the

β -TCP-BNNTs and HA-BNNTs composites showed 24.1% and 26.3% enhancement, respectively (Davar and Sadri, 2017). They also investigated the effect of BNNTs on the stress-intensity factor (K_I) of a semi-elliptical surface crack in a wide range of matrices using a finite element model. The results showed that a higher mismatch difference between the elastic modulus of the matrix and BNNTs resulted in further reduction in K_I value (Mortazavi *et al.*, 2013).

Experimental studies on nanocomposites are time consuming, costly, and require accurate implementation. Therefore, analytical, computational and theoretical approaches are attractive methods of predicting mechanical properties of composites. Researchers usually employ a small part of the whole composite, which is called the unit cell or RVE to avoid expensive and enormous computational calculations (Gojny *et al.*, 2005).

The experimental studies on nanocomposites are time-consuming, costly, and require accurate implementation, so the analytical, computational and theoretical approaches are attractive methods for nanocomposite simulation and predicting mechanical properties. In this work, a representative volume element (RVE) of epoxy/BNNT nanocomposites based on multi-scale modeling is considered.

Mechanical behaviors of BNNTs is studied using a three-dimensional finite element (FE) model, named as the space frame model. Ansari *et al.* (2015) used DFT calculations to obtain exact force constants of BNNT which are employed in determining the element properties. Fundamental to these approaches, BNNTs are considered as geometric space frame structures and can be analyzed by classical structural mechanics. In this paper, three-dimensional RVEs with different chirality of BNNT are simulated and analyzed in three fracture modes. In all fracture modes, the stress intensity factor of nanocomposites is determined and compared with the pure matrix one.

2. Multi-scale modeling

In fracture mechanics based on the crack surfaces displacement, three crack modes of the opening mode (tensile mode), shearing mode (sliding mode), tearing mode (out-of-plane) are considered. Stress intensity factors of RVEs are determined using the J integral technique with ANSYS Parametric Design Language (APDL) based on finite element analysis. Similar loads and boundary conditions are applied to both the neat matrix and nanocomposite in the three fracture modes, and then their stress intensity factors are determined and compared together.

In the bottom-up analysis method, one firstly obtains the effective material constants using a low-scale such as the nano, meso (Tserpes *et al.*, 2008) or micro RVE model (Gibson *et al.*, 2007), then applies it in the high-scale FE simulation in which the material is assumed to be equivalently homogeneous according to the theory of continuum mechanics. In the top-down or global-local method, one firstly finds the properties in the local region of a macro-scale sample under practical loads, then applies the resultant loads or displacements to the boundary of a smaller region as a new input.

2.1. Nanotube

BNNTs atoms are bonded together with covalent bonds forming a hexagonal lattice. The displacement of individual atoms under an external force is constrained by the bonds. Therefore, the total deformation of the nanotube is a result of the interactions between the bonds. By considering the bonds as connecting load-carrying elements, and the atoms as joints of the connecting elements, BNNTs may be simulated as space-frame structures (Ansari *et al.*, 2015).

The 3D FE model is developed using the ANSYS commercial FE code. The 3D elastic BEAM4 element is used for modeling the bonds. The properties of these elements are obtained by a linkage between the potential energy of bonds (from a chemical point of view) and the strain

energy of mechanical elements (from a mechanical point of view). To represent the covalent bond between boron and nitrogen atoms, a circular beam of length l , diameter d , Young's modulus E , and shear modulus G is considered (Ansari *et al.*, 2015). The required properties of the beam element are given in Table 1.

Table 1. The properties of beam elements for real BNNT (Ansari *et al.*, 2015)

Diameter d	1.648 Å
Cross-sectional area A	2.132 Å ²
Boron-nitrogen bond	1.45 Å
Polar inertia momentum I_{xx}	0.7250 Å ⁴
Inertia momentum $I_{zz} = I_{yy} = I$	0.3625 Å ⁴
Young's modulus E	4.2155 · 10 ⁻⁸ N/Å ²
Shear modulus G	4.9437 · 10 ⁻⁹ N/Å ²

A routine code has been created using the ANSYS macro language, for automatic generation of FE models. The thickness of BNNT is considered as 0.34 nm and also, the center of the BNNT wall is placed at the midsection of the tube thickness. The FE meshes, loading and boundary conditions of (10, 10) BNNT with length of 80 Å are shown in Fig. 1. Young's and shear modulus of BNNT are found by tension and torsion loading. They are in ranges of 1.039-1.041 TPa and 0.44-0.52 TPa, respectively. The experimental and theoretical elastic moduli of BNNT are given in Table 2. The current results are in good agreement with the simulation and experimental values.

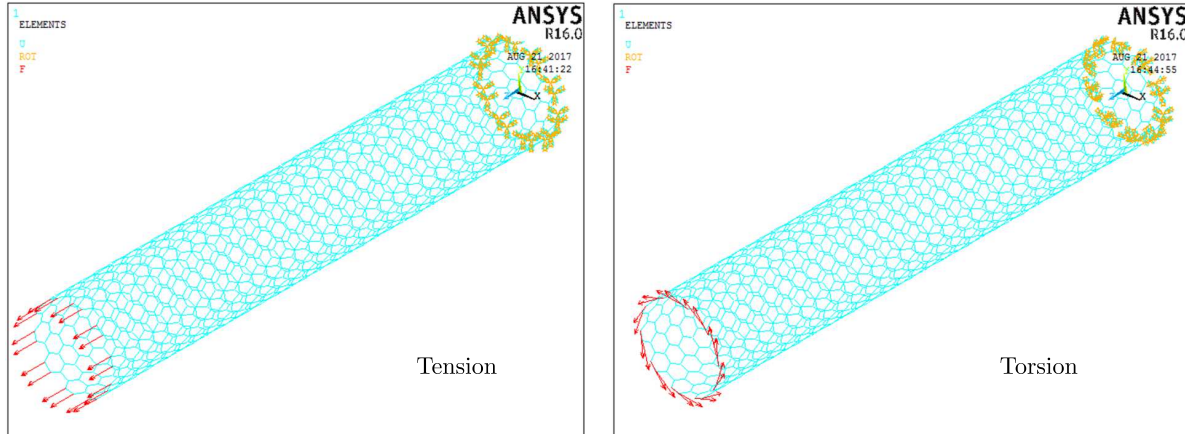


Fig. 1. FE meshes of BNNT (10, 10) with loading and boundary conditions

2.2. Inter-phase between nanotube and polymer

The bonding between the embedded BNNT and its surrounding polymer takes place through vdW and electrostatic interactions in the absence of chemical functionalization. Since vdW contributes more significantly by three higher orders of magnitude than electrostatic energy, the electrostatic interactions can be neglected in comparison with vdW interactions (Gou *et al.*, 2004). So, only vdW interactions are considered between the BNNT and the matrix. The vdW forces are most often modeled using the famous Lennard-Jones equation (Battazzatti *et al.*, 1975)

$$F_{VdW} = 4\frac{\varepsilon}{r} \left[-12\left(\frac{\sigma}{r}\right)^{12} + 6\left(\frac{\sigma}{r}\right)^6 \right] \quad (2.1)$$

Table 2. Elastic moduli from BNNT of simulation and experimental works

Elastic moduli	[TPa]	Reference
Young's modulus	1.22 ± 0.24	Chopra and Zettl (1998)
	1.022-1.112	Fereidoon <i>et al.</i> (2015)
	0.862-0.94	Verma <i>et al.</i> (2007)
	0.71-0.83	Akdim <i>et al.</i> (2003)
	0.895	Fakhrabad and Shahtahmassebi (2013)
	0.7-1.2	Gerieble <i>et al.</i> (2009)
	0.7-1.2	Bettinger <i>et al.</i> (2002)
	1.1-1.3	Wei <i>et al.</i> (2010)
	0.764-0.821	Suryavanshi <i>et al.</i> (2004)
	1	Chowdhury <i>et al.</i> (2010)
Shear modulus	1.039-1.041	Current work
	0.42	Chowdhury <i>et al.</i> , 2010
	0.44-0.52	Current work

where r is the separation distance between the pair of atoms, ε is the bond energy at the equilibrium distance, and σ is the van der Waals separation distance. The equilibrium distance between atoms is $\sqrt[6]{2}\sigma$. By introducing x as the distance from the equilibrium distance, the Lennard-Jones force is represented in Eq. (2.2)₂

$$x = r - \sqrt[6]{2}\sigma$$

$$F(X) = -24\frac{\varepsilon}{\sigma} \left[2\left(\frac{\sigma}{x + \sqrt[6]{2}\sigma}\right)^{13} - \left(\frac{\sigma}{x + \sqrt[6]{2}\sigma}\right)^7 \right] \quad (2.2)$$

$$\sigma = \frac{\sigma_n + \sigma_m}{2} \quad \varepsilon = \sqrt{\varepsilon_n \varepsilon_m}$$

where m and n sub-indexes denote the matrix and nanotube, respectively. The Lennard-Jones potential parameters (ε and σ) of the materials are given in Table 3. BNNT is a synthase from boron and nitrogen atoms, therefore the Lennard-Jones potential parameters of BNNT are approximately considered the average of boron and nitrogen parameter values. Also, these values are represented in Table 3. The Lennard-Jones potential parameters for van der Waals interaction between the BNNT and epoxy are determined as $\sigma = 3.897 \text{ \AA}$ and $\varepsilon = 0.00297 \text{ nNnm}$ by replacing L - J parameters of BNNT and epoxy. Also, the equilibrium distance between matrix and nanotube is 0.4374 nm .

Table 3. Lennard-Jones potential parameters of the materials

Materials	σ [Å]	Reference	ε	Reference
Nitrogen	3.365	Chen <i>et al.</i> (2015)	6.281 meV	Chen <i>et al.</i> (2015)
		Zhang and Wang (2016)		Zhang and Wang (2016)
Boron	3.453	Chen <i>et al.</i> (2015)	4.16 meV	Chen <i>et al.</i> (2015)
		Zhang and Wang (2016)		Zhang and Wang (2016)
BNNT	3.409	–	5.2205 meV- 0.00083642 nNnm	–
Epoxy	4.383	Yang <i>et al.</i> (2014)	1.519 kcal/mol- -0.1055 nNnm	Gou <i>et al.</i> (2004)

The vdW interactions between the BNNT and the inner surface nodes of the surrounding resin are modeled using a 3D non-linear spring element based on the corresponding data of the force-displacement curve (Hemmatian *et al.*, 2012). COMBIN39 element is used for this purpose

and the parameters are adjusted to obtain a translational spring. A macro is written to create elements between the BNNT and the inner surface of the surrounding resin nodes that their distance is lower than 0.7 nm.

2.3. Matrix

SOLID45 elements are utilized for modeling of the matrix. This element is used for the 3D modeling of solid structures. SOLID45 is defined by eight nodes having three degrees of freedom at each node: translations in the nodal x , y and z directions. Young's modulus of the epoxy matrix is considered as 2.9 GPa (Fereidoon *et al.*, 2013). Nanocomposites consisting of %5 volume fraction of BNNT with length of 80 \AA are simulated. The FE meshes of RVE used for crack analysis are shown in Fig. 2. The elements of the crack tip are refined to increase the accuracy of analysis as represented in Fig. 2.

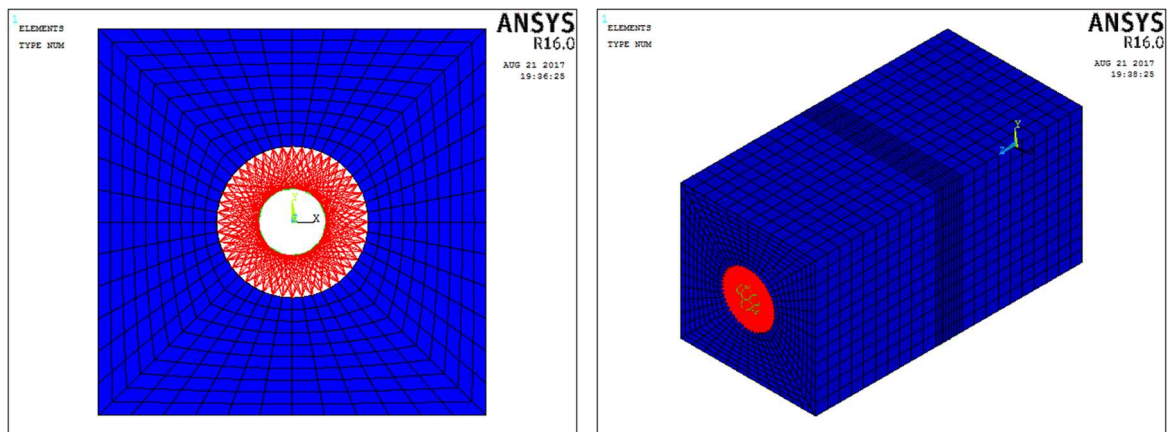


Fig. 2. The FE meshes of nanocomposite RVE

Stress intensity factors of the neat matrix and nanocomposite are compared for similar loading and boundary conditions. The loading and boundary conditions of three fracture modes including the opening, shearing and tearing of the nanocomposite with 5 Vo.% (5, 5) BNNT are shown in Fig. 3. In order to apply the conditions of the opening mode, the middle nodes of the RVE are fully built-in (zero displacement and rotation conditions), while the nodes of two ends are subjected to tensile forces. In shearing and tearing modes, the nodes of the back of the RVE are fully built-in (zero displacement and rotation conditions), while the middle nodes are constrained in the Z direction. Shearing and tearing forces are applied to the front nodes of these RVE's.

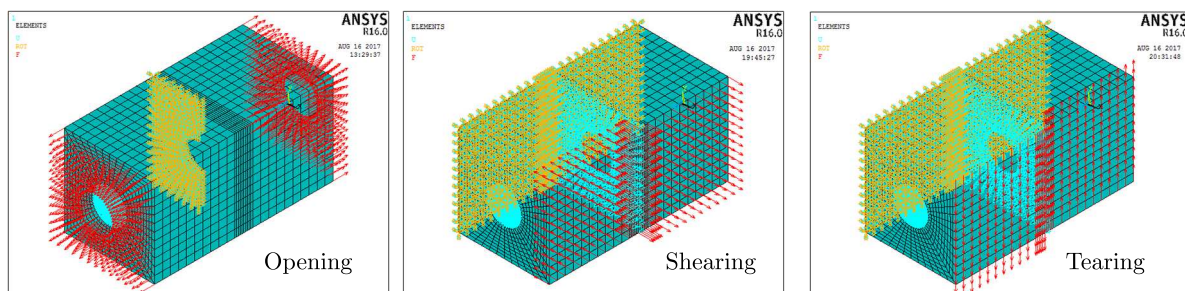


Fig. 3. Loadings and boundary conditions of RVE for three modes

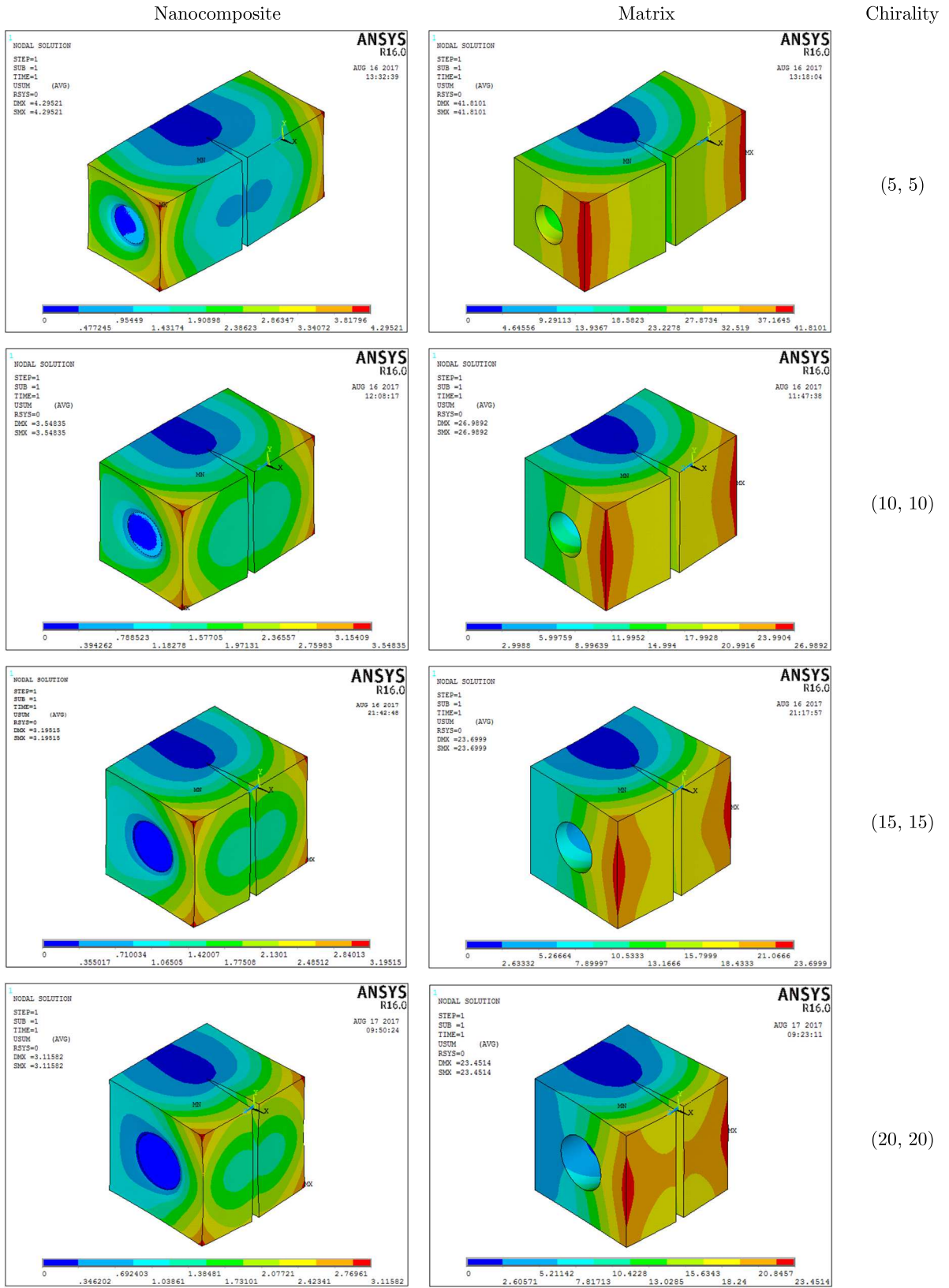


Fig. 4. Displacement [\AA] contours of the opening mode: neat matrix and nanocomposite

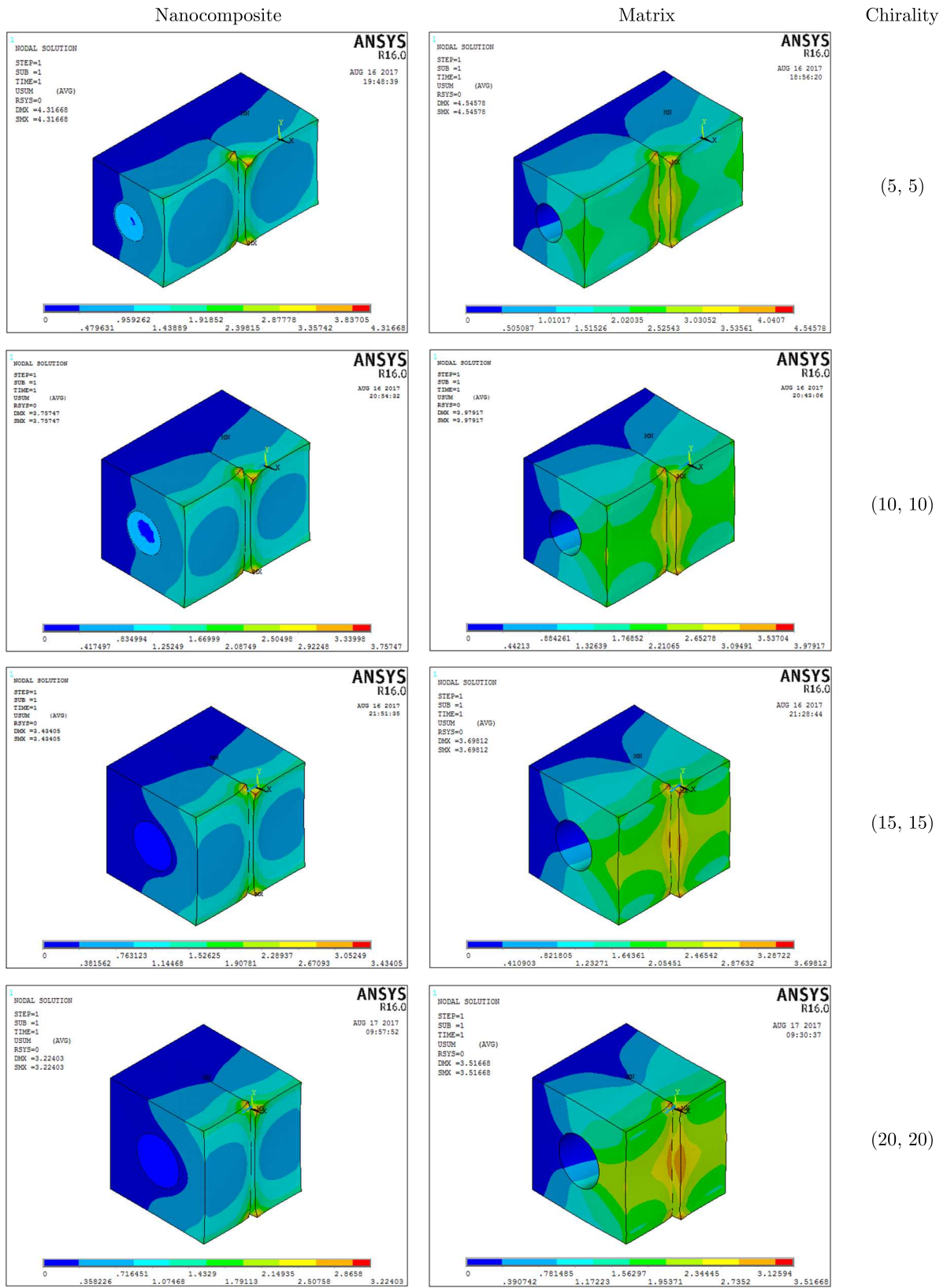


Fig. 5. Displacement [Å] contours of the shearing mode: neat matrix and nanocomposite

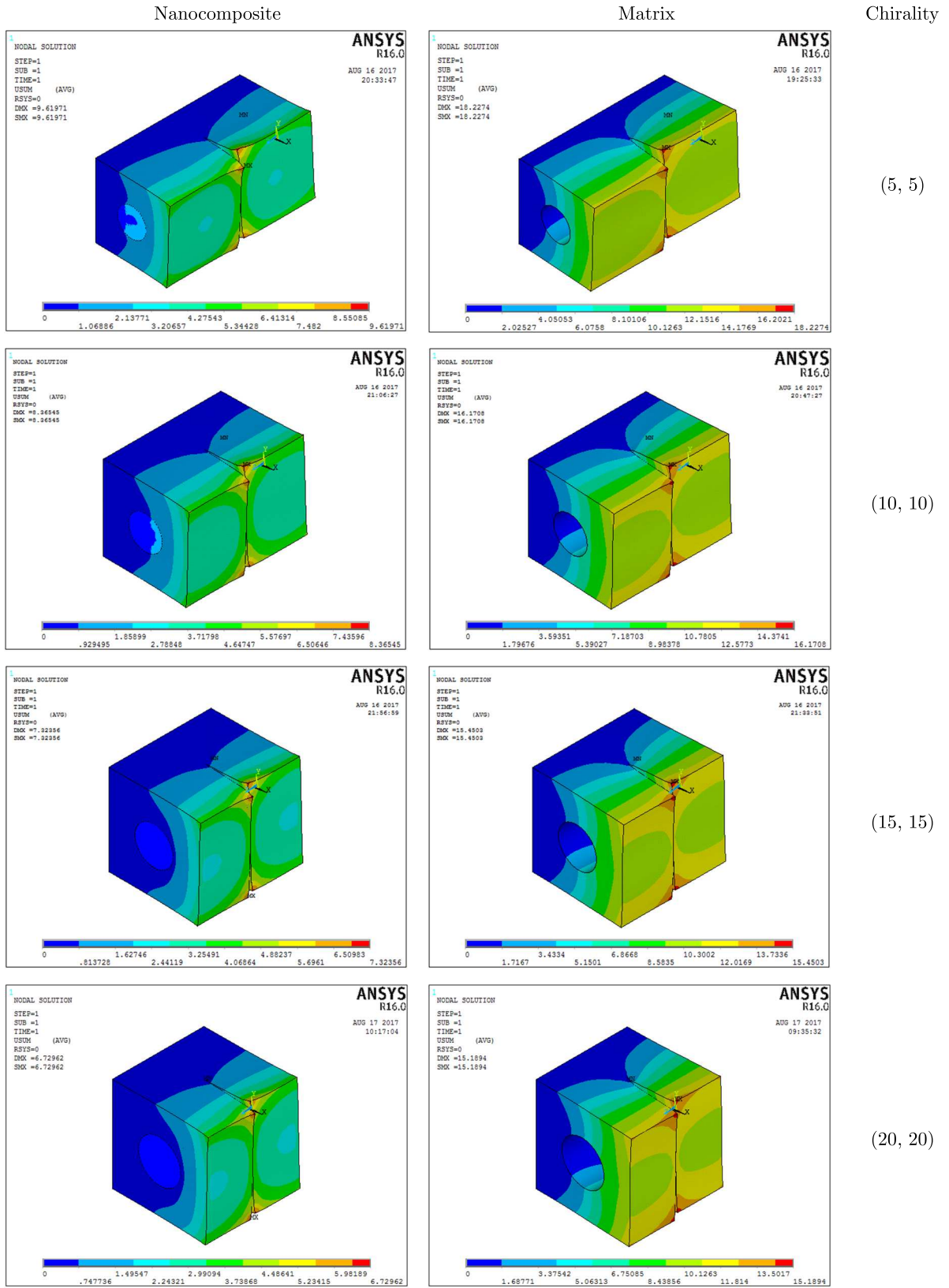


Fig. 6. Displacement [Å] contours of the tearing mode: neat matrix and nanocomposite

3. Results and discussion

In this study, fracture analysis of an epoxy/BNNT nanocomposite reinforced with four chirality (5, 5), (10, 10), (15, 15) and (20, 20) are implemented. It is observed that when nanotubes are vertical to the crack path, the minimum stress intensity factor and the maximum effect on crack resistance are achieved. In this condition, while the crack is in the middle of RVE (bridging condition), this effect is stronger. Nanotubes with constant length and different chirality have been used for the bridging condition.

Displacement contours of the neat matrix and nanocomposite in the opening, shearing and tearing modes are shown in Figs. 4, 5 and 6, respectively. The dimension of displacement is Angstrom.

The maximum displacement of RVE is decreased by adding BNNT, and this phenomenon in the opening mode is evident. Diagrams of normalized stress intensity factors (ratio of the nanocomposite stress intensity factor to that of the neat matrix) of the fracture modes are plotted against chirality in Fig. 7.

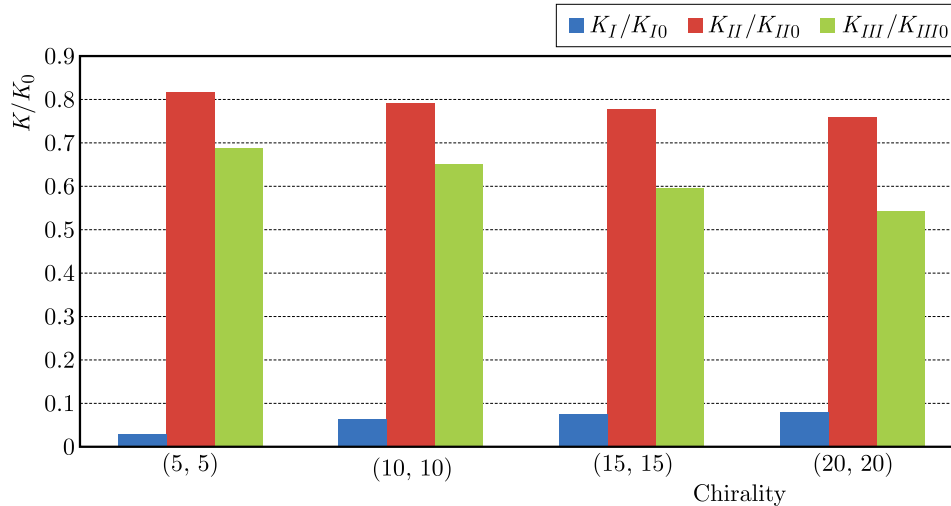


Fig. 7. Normalized stress intensity factors against chirality

The results indicate that with the addition of BNNT to epoxy, the stress intensity factors of three modes decrease. Also, by increasing the chirality and consequently, BNNT diameter, the crack resistance of shearing and tearing modes enhances, and the stress intensity factor of the opening mode reduces. Boron nitride nanotube bridges the crack path and resists against crack propagation. On the other hand, the bridging arises in all three modes, and the stress intensity factor decreases. This phenomenon is reported in experimental research about CNT too (Mirjalili and Hubert, 2010). Therefore, adding the BNNT to the matrix improves the crack resistance, which is considerable in the opening and tearing modes.

In modeling and simulation, the chirality, length, diameter, and weight percentage of the nanotube are important. But in the experimental method, the weight percentage and range of length and diameter is considered. Hence, appropriate verification between the results of experimental and simulation is difficult. Also, based on literature review, the experimental and simulation results do not deal with fracture behavior of BNNT/epoxy in the three modes. Multi-scale simulations from nano to macro, or reversely, improve the specification of toughening mechanisms.

4. Conclusions

A three-dimensional FEM of BNNTs has been proposed. Nodes are placed at locations of boron and nitrogen atoms, and bonds are modeled using three-dimensional elastic beam elements by considering a linkage between molecular and continuum mechanics. The simulation performed under minimal computational time by requiring minimal computational power. The determined elastic moduli of BNNTs are in a good agreement with the real parameters. A three-dimensional study of three fracture modes in epoxy/BNNT has been performed based on a multi-scale method. Van der Waals bonds between the resin and nanotube are simulated by non-linear spring elements based on the Lennard-Jones potential.

Stress intensity factors of three fracture modes have been computed by J integral. The effect of BNNT on the stress intensity factor of nanocomposites and crack propagation is investigated. The results indicated that BNNTs have a significant effect on preventing crack propagation. Also, by adding a nanotube, stress intensity factors decreased and, consequently, the crack resistance increased. The results indicated that the crack resistance improved by increasing the chirality (radius). Finally, by adding BNNT to the matrix, the improvement of matrix fracture properties is evident.

References

1. AKDIM B., ACHTER R.P., DUAN X.F., ADAMS W.W., 2003, Comparative theoretical study of single-wall carbon and boron-nitride nanotubes, *Physical Review B*, **67**, 245404
2. ANSARI R., ROUHI S., MIRNEZHAD M., ARYAYI M., 2015, Stability characteristics of single-walled boron nitride nanotubes, *Archives of Civil and Mechanical Engineering*, **15**, 162-170
3. BATTEZZATTI L., PISANI C., RICCA F., 1975, Equilibrium conformation and surface motion of hydrocarbon molecules physisorbed on graphite, *Journal of the Chemical Society*, **71**, 1629-1639
4. BETTINGER H.F., DUMITRIC T.T., SCUSERIA G.E., YAKOBSON B.I., 2002, Mechanically induced defects and strength of BN nanotubes, *Physical Review B*, **65**, 041406
5. CHANG C.W., HAN W.Q., ZETTL A., 2005, Thermal conductivity of B-C-N and BN nanotubes, *Applied Physics Letters*, **86**, 173102
6. CHEN X., ZHANG L., PARK C., FAY C.C., WANG X., KE C., 2015, Mechanical strength of boron nitride nanotube-polymer interfaces, *Applied Physics Letters*, **107**, 253105
7. CHEN Y., ZOU J., CAMPBELL S.J., CAER G.L., 2004, Boron nitride nanotubes: pronounced resistance to oxidation, *Applied Physics Letters*, **84**, 2430-2432
8. CHOPRA N.G., LUYKEN R.J., CHERREY K., CRESPI V.H., COHEN M.L., LOUIE S.G., ZETTL A., 1995, Boron nitride nanotubes, *Science*, **269**, 966-967
9. CHOPRA N.G., ZETTL A., 1998, Measurement of the elastic modulus of a multi-wall boron nitride nanotube, *Solid State Communications*, **105**, 297-300
10. CHOWDHURY R., WANG C.Y., ADHIKARI S., SCARPA F., 2010, Vibration and symmetry-breaking of boron nitride nanotubes, *Nanotechnology*, **21**, 365702
11. DAVAR A., SADRI S., 2016, Finite element analysis of the effect of boron nitride nanotubes in beta tricalcium phosphate and hydroxyapatite elastic modulus using the RVE model, *Composites Part B: Engineering*, **90**, 336-340
12. DAVAR A., SADRI S., 2017, Finite element analysis of boron nitride nanotubes' shielding effect on the stress intensity factor of semielliptical surface crack in a wide range of matrixes using RVE model, *Composites Part B: Engineering*, **110**, 351-360
13. FAKHRABAD D.V., SHAHTAHMASSEBI N., 2013, First-principles calculations of the Young's modulus of double wall boron-nitride nanotubes, *Materials Chemistry and Physics*, **138**, 2, 963-966

14. FEREDOON A., MOSTAFAEI M., GANJI M.D., MEMARIAN F., 2015, Atomistic simulations on the influence of diameter, number of walls, interlayer distance and temperature on the mechanical properties of BNNTs, *Superlattices and Microstructures*, **86**, 126-133
15. FEREDOON A., RAJABPOUR M., HEMMATIAN H., 2013, Fracture analysis of epoxy/SWCNT nanocomposite based on global-local finite element model, *Composites: Part B*, **54**, 400-408
16. GHORBANPOUR ARANI A., HAGHSHENAS A., AMIR S., AZAMI M., KHODDAMI MARAGHI Z., 2012a, Electro-thermo-mechanical response of thick-walled piezoelectric cylinder reinforced by BNNTs, *Journal of Nanostructures*, **2**, 113-124
17. GHORBANPOUR ARANI A., SHAMS S., AMIR S., KHODDAMI MARAGHI Z., 2012b, Effects of electro-thermal fields on buckling of a piezoelectric polymeric shell reinforced with DWBNNTs, *Journal of Nanostructures*, **2**, 345-355
18. GIBSON R., 2007, *Principles of Composite Material Mechanics*, CRC Press
19. GOJNY F.H., WICHMANN M.H.G., FIEDLER B., SCHULTE K., 2005, Influence of different carbon nanotubes on the mechanical properties of epoxy matrix composites – a comparative study, *Composites Science and Technology*, **65**, 2300-2313
20. GOU J., MINAEI B., WANG B., LIANG Z., ZHANG C., 2004, Computational and experimental study of interfacial bonding of single-walled nanotube reinforced composites, *Computational Materials Science*, **31**, 225-236
21. GRIEBEL M., HAMAEEKERS J., HEBER F., 2009, A molecular dynamics study on the impact of defects and functionalization on the Young modulus of boron-nitride nanotubes, *Computational Materials Science*, **45**, 4, 1097-1103
22. HEMMATIAN H., FEREDOON A., RAJABPOUR M., 2012, Investigation of crack resistance in single walled carbon nanotube reinforced polymer composites based on FEM, *Journal of Ultrafine Grained and Nanostructured Materials*, **45**, 13-18
23. JAKUBINEK M.B., MARTINEZ-RUBI Y., ASHRAFI B., YOURDKHANI M., RAHMAT M., DJOKIC D., GUAN J., SU KIM K., KINGSTON C.T., SIMARD B., JOHNSTON A., 2016, Nanoreinforced epoxy composites based on boron nitride nanotubes and their application to adhesive joints and composite laminates, *Proceedings of 3rd Annual Composites and Advanced Materials Expo, CAMX 2016*, Anaheim, United States
24. KHALEGHIAN M., AZARAKHSHI F., 2016, Electronic properties studies of Benzene under boron nitride nano ring field, *International Journal of Nano Dimension*, **7**, 290-294
25. LEE D., SONG S.H., HWANG J., JIN S.H., PARK K.H., KIM B.H., HONG S.H., JEON S., 2013, Enhanced mechanical properties of epoxy nanocomposites by mixing noncovalently functionalized boron nitride nanoflakes, *Small*, **9**, 2602-2610
26. MIRJALILI V., HUBERT P., 2010, Modelling of the carbon nanotube bridging effect on the toughening of polymers and experimental verification, *Composites Science and Technology*, **70**, 1537-1543
27. MOHAMMADIMEHR M., MAHMUDIAN-NAJAFABADI M., 2013, Bending and free vibration analysis of nonlocal functionally graded nanocomposite Timoshenko beam model reinforced by SWBNNT based on modified coupled stress theory, *Journal of Nanostructures*, **3**, 483-492
28. MOLANI F., 2017, The effect of C, Si, N, and P impurities on structural and electronic properties of armchair boron nanotube, *Journal of Nanostructure in Chemistry*, **7**, 243-248
29. MORTAZAVI B., BANIASSADI M., BARDON J., AHZI S., 2013, Modeling of two-phase random composite materials by finite element, Mori-Tanaka and strong contrast methods, *Composites Part B, Engineering*, **45**, 1117-1125
30. ROZENBERG B.A., TENNE R., 2008, Polymer-assisted fabrication of nanoparticles and nanocomposites, *Progress in Polymer Science*, **33**, 40-112
31. SUN L., R. GIBSON F., GORDANINEJAD F., SUHR J., 2009, Energy absorption capability of nanocomposites: a review, *Composites Science and Technology*, **69**, 2392-2409

32. SURYAVANSHI A.P., YU M., WEN J., TANG C., BANDO Y., 2004, Elastic modulus and resonance behavior of boron nitride nanotubes, *Applied Physics Letters*, **84**, 2527-2529
33. TSERPES K., PAPANIKOS P., LABEAS G., PANTELAKIS S., 2008, Multi-scale modeling of tensile behavior of carbon nanotube-reinforced composites, *Theoretical and Applied Fracture Mechanics*, **49**, 51-60
34. ULUS H., ÜSTÜN T., ESKIZEYBEK V., ŞAHİN Ö.S., AVCI A., EKREM M., 2014, Boron nitride-MWCNT/epoxy hybrid nanocomposites: Preparation and mechanical properties, *Applied Surface Science*, **318**, 37-42
35. VERMA V., JINDAL V., DHARAMVIR K., 2007, Elastic moduli of a boron nitride nanotube, *Nanotechnology*, **18**, 435711
36. WEI X., WANG M.S., BANDO Y., GOLBERG D., 2010, Tensile tests on individual multi-walled boron nitride nanotubes, *Advanced Materials*, **22**, 43, 4895-4899
37. YANG S., CUI Z. QU J., 2014, A coarse-grained model for epoxy molding compound, *The Journal of Physical Chemistry B*, **118**, 1660-1669
38. ZHANG L., WANG X., 2016, DNA sequencing by hexagonal boron nitride nanopore: a computational study, *Nanomaterials*, **6**, 111
39. ZHI C., BANDO Y., TANG C., GOLBERG D., 2010, Boron nitride nanotubes, *Materials Science and Engineering: R*, **70**, 92-111

Manuscript received April 14, 2018; accepted for print September 10, 2018

NATURAL AND MIXED CONVECTION OF A NANOFLUID IN POROUS CAVITIES: CRITICAL ANALYSIS USING BUONGIORNO'S MODEL

IMAN ZAHMATKESH, MOHAMMAD REZA HABIBI

Department of Mechanical Engineering, Mashhad Branch, Islamic Azad University, Mashhad, Iran
e-mail: zahmatkesh5310@mshdiau.ac.ir

In this paper, Buongiorno's mathematical model is adopted to simulate both natural convection and mixed convection of a nanofluid in square porous cavities. The model takes into account the Brownian diffusion and thermophoresis effects. Both constant and variable temperatures are prescribed at the side walls while the remaining walls are maintained adiabatic. Moreover, all boundaries are assumed to be impermeable to the base fluid and the nanoparticles. The governing equations are transformed to a form of dimensionless equations and then solved numerically using the finite-volume method. Thereafter, effects of the Brownian diffusion parameter, the thermophoresis number, and the buoyancy ratio on the flow strength and the average Nusselt number as well as distributions of isocontours of the stream function, temperature, and nanoparticles fraction are presented and discussed.

Keywords: natural convection, mixed convection, nanofluid, porous media, Buongiorno's model

1. Introduction

Heat transfer is a significant and widely explored engineering problem that, due to the lack of energy resources, has become truly important. One efficient way to improve heat transfer and to reduce energy consumption goes back to the use of porous media. This occurs since a porous medium provides a large surface area for heat exchange. On the other hand, the flow field in a porous medium is completely three-dimensional and irregular, which intensifies fluid mixing.

Further attempt to achieve higher heat transfer rates has led to adding nanoparticles to working liquids and producing nanofluids. The added nanoparticles are usually made up of metals or metal oxides with high thermal conductivity. So, the resulting fluid has a better thermal efficiency than the base liquid. Going into the literature, one may find that heat transfer analysis of nanofluid flows has been a hot topic among scientists over the past decade. Examples include the studies of Ali *et al.* (2014), Ghasemi *et al.* (2016), and Rostamzadeh *et al.* (2016).

Different mathematical models have been adopted to describe heat transfer in nanofluids. The simplest method with the least computational burden is the homogenous model. In this model, the concentration of nanoparticles is taken constant over the entire flow field. It is also assumed that the base liquid and the nanoparticles are in local equilibrium and move with the same velocity and temperature. In spite of previous achievements of this model, some studies have proved that more complex models provide better agreement with experimental data (e.g., Behroyan *et al.* (2016); Torshizi and Zahmatkesh, 2016).

Buongiorno (2006) introduced seven transport mechanisms which cause relative velocity between the nanoparticles and the base liquid, namely, inertia, Brownian diffusion, thermophoresis, diffusiophoresis, Magnus effect, fluid drainage, and gravitational settling. After comparing the diffusion time scales of these mechanisms he drew a conclusion that, in the absence of flow turbulence, the Brownian diffusion and thermophoresis are the most important effects. Based on this finding, he then developed a non-homogeneous but an equilibrium model for nanofluid flow

and heat transfer that incorporates the effects of the Brownian diffusion and thermophoresis. The Brownian diffusion occurs due to random variations in the bombardment of the base fluid molecules against the particles. The thermophoresis phenomenon appears as a net force acting in the opposite direction to the gradient of temperature and is a direct result of the differential bombardment of the base fluid molecules in the vicinity of the particles (Zahmatkesh, 2008b).

There are many recent papers that deal with Buongiorno's mathematical model (e.g., Sheikholeslami *et al.*, 2016; Kefayati, 2017a; Mustafa, 2017) but to the best of our knowledge, there are no previous works in literature which compare the role of parameters appearing in this model for both natural convection and mixed convection in porous media. Some simulation studies for natural convection of nanofluids in porous cavities based on Buongiorno's model are discussed below.

Sheremet *et al.* (2014) simulated natural convection of nanofluids in shallow and slender porous cavities. Their results demonstrated that an inverse relation existed between the average Nusselt number and the buoyancy ratio. Conjugate natural convection of nanofluid in a square porous cavity was discussed by Sheremet and Pop (2014a). They found that the Nusselt number was an increasing function of the buoyancy ratio and a decreasing function of the thermophoresis number and the Lewis number. A simulation study of natural convection of a nanofluid in a right-angle triangular porous cavity was reported by Sheremet and Pop (2015a). That investigation showed that the average Nusselt number increased with the enhancement of the Lewis number but any rise in the Brownian diffusion parameter, the buoyancy ratio or the thermophoresis number made it lower. Sheremet *et al.* (2015) discussed natural convection heat transfer of a nanofluid in a three-dimensional porous cavity. Their results led to the conclusion that the average Nusselt number increased with the Brownian diffusion parameter and decreased with the buoyancy ratio and the thermophoresis number. Sheremet and Pop (2015b) analyzed natural convection of a nanofluid in a porous annulus. They indicated that an increase in the thermophoresis number and the buoyancy ratio led to deterioration in the average Nusselt number while the Brownian diffusion parameter contributed neutrally. Ghalambaz *et al.* (2016) investigated the influence of viscous dissipation and radiation on natural convection of a nanofluid in a porous cavity and concluded that an increase in the Lewis number improved the heat transfer but augmentation of the buoyancy ratio and the thermophoresis number decreased it. More recently, natural convection and entropy generation of a non-Newtonian nanofluid in a porous cavity was pointed out by Kefayati (2017b). The results demonstrated that rise of the Lewis number, the thermophoresis number, and the Brownian diffusion parameter declined the average Nusselt number, but the augmentation of the buoyancy ratio enhanced it.

The role of parameters appearing in Buongiorno's mathematical model may depend on thermal boundary conditions of the cavity. In this context, Sheremet and Pop (2014b) discussed how imposition of a sinusoidal temperature distribution on the side walls may affect natural convection of the nanofluid in a square porous cavity. They found that the average Nusselt number was an increasing function of the buoyancy ratio and the thermophoresis number but a decreasing function of the Lewis number and the Brownian diffusion parameter. More recently, they extended their work to a wavy porous cavity (Sheremet *et al.*, 2017). They found that the dependence of the average Nusselt number to the pertinent parameters was similar to the square cavity, which was in contrast to the aforesaid findings in uniformly heated/cooled cavities.

The current research deals with heat transfer of a nanofluid in square porous cavities. The main purpose of this article is to analyze the effects of the buoyancy ratio, the Brownian diffusion parameter and the thermophoresis number on the flow strength and the average Nusselt number as well as developments of streamlines, isotherms and isoconcentrations. To provide a critical analysis, computations are undertaken for various cases in natural convection and mixed convection environments with both uniform and non-uniform wall temperatures.

2. Problem definition and mathematical formulation

Both natural and mixed convection heat transfer in a square cavity filled with a nanofluid-saturated porous medium are analyzed in this study. A schematic diagram of the flow problems is shown in Fig. 1, where x and y are the Cartesian coordinates and L is the size of the cavity. Here, all walls are assumed to be impermeable to mass transfer. The horizontal walls are assumed adiabatic while two different conditions are imposed on the side walls. In the first case, the sidewalls are considered to be heated/cooled uniformly while in the second case, the sidewalls are influenced by the existence of a sinusoidal temperature variation.

In this paper, Buongiorno's mathematical model is used. Thanks to this approach, the nanofluid is considered as a two-component dilute mixture. The porous medium is assumed isotropic and homogenous while the established flow is concerned to be steady, incompressible, Newtonian and laminar. The Darcy model is employed for the momentum equation. Moreover, a local thermal equilibrium is assumed between the nanoparticles, the base fluid and the porous medium. The Boussinesq approximation is adopted to determine the variations of density in the body force term within the momentum equation. Meanwhile, viscous dissipation, the work done by the pressure change and radiation heat transfer are neglected. Additionally, the thermophoresis and Brownian transport coefficients are assumed temperature-independent. On these assumptions, the conservation equations for mass, momentum, energy and flow concentration are (Nield and Bejan, 2013)

$$\begin{aligned} \nabla \cdot (\mathbf{V}) &= 0 \\ \mathbf{0} &= -\nabla P - \frac{\mu}{K} \mathbf{V} + [C\rho_p + (1 - C)\rho_f(1 - \beta(T - T_c))] \mathbf{g} \\ \mathbf{V} \cdot \nabla T &= \alpha_m \nabla^2 T + \delta \left(D_B \nabla C \cdot \nabla T + \frac{D_T}{T_c} \nabla T \cdot \nabla T \right) \\ \frac{\rho_p}{\varepsilon} \mathbf{V} \cdot \nabla C &= -\nabla \cdot \mathbf{j}_p \end{aligned} \tag{2.1}$$

Here, \mathbf{V} is the Darcy velocity vector, P is pressure, T is temperature, C is the nanoparticles fraction, \mathbf{g} is gravitational acceleration ($\mathbf{g} = -g\mathbf{j}$), ρ is density, μ is dynamic viscosity, β is the volumetric expansion coefficient, α is thermal diffusivity, ε is medium porosity, and K is permeability of the porous medium. Meanwhile, D_B is the Brownian diffusion coefficient, D_T is the thermophoretic diffusion coefficient, and δ is a parameter defined by $\delta = \varepsilon(\rho c_p)_p / (\rho c_p)_f$ with c_p being the specific heat. Moreover, the subscripts p , f , and m correspond to the nanoparticles, the base fluid and effective values, respectively.

In Eq. (2.1)₄, \mathbf{j}_p is the nanoparticles mass flux. Based on Buongiorno's model, the nanoparticles mass flux is made up of two parts, namely, Brownian diffusion $\mathbf{j}_{p,B}$, and thermophoresis $\mathbf{j}_{p,T}$. Thus

$$\mathbf{j}_p = \mathbf{j}_{p,B} + \mathbf{j}_{p,T} = -\rho_p D_B \nabla C - \rho_p D_T \frac{\nabla T}{T} \tag{2.2}$$

After using the Boussinesq approximation and taking the nanofluid as a dilute mixture, one arrives at the following form of the momentum equation (Nield and Kuznetsov, 2009)

$$\mathbf{0} = -\nabla P - \frac{\mu}{K} \mathbf{V} + [C(\rho_p - \rho_{f_0}) + \rho_{f_0}(1 - \beta(T - T_c)(1 - C_0))] \mathbf{g} \tag{2.3}$$

with subscript 0 standing for reference values.

To simplify this vector equation, cross-differentiation is adopted, which eliminates the pressure term. So, the governing equations become

$$\frac{\partial u}{\partial x} + \frac{\partial v}{\partial y} = 0 \tag{2.4}$$

and

$$\begin{aligned}
0 &= -\frac{\mu}{K} \left(\frac{\partial u}{\partial y} - \frac{\partial v}{\partial x} \right) + g(\rho_p - \rho_{f_0}) \frac{\partial C}{\partial x} - (1 - C_0) \rho_{f_0} \beta g \frac{\partial T}{\partial x} \\
u \frac{\partial T}{\partial x} + v \frac{\partial T}{\partial y} &= \alpha_m \left(\frac{\partial^2 T}{\partial x^2} + \frac{\partial^2 T}{\partial y^2} \right) \\
&+ \delta \left\{ D_B \left(\frac{\partial C}{\partial x} \frac{\partial T}{\partial x} + \frac{\partial C}{\partial y} \frac{\partial T}{\partial y} \right) + \frac{D_T}{T_c} \left[\left(\frac{\partial T}{\partial x} \right)^2 + \left(\frac{\partial T}{\partial y} \right)^2 \right] \right\} \\
\frac{1}{\varepsilon} \left(u \frac{\partial C}{\partial x} + v \frac{\partial C}{\partial y} \right) &= D_B \left(\frac{\partial^2 C}{\partial x^2} + \frac{\partial^2 C}{\partial y^2} \right) + \frac{D_T}{T_c} \left(\frac{\partial^2 T}{\partial x^2} + \frac{\partial^2 T}{\partial y^2} \right)
\end{aligned} \tag{2.5}$$

where u and v denote the velocity components in the x and y directions, respectively.

After introducing the stream function by $u = \partial\psi/\partial y$ and $v = -\partial\psi/\partial x$, the continuity equation will be satisfied. Moreover, Eqs. (2.5) lead to

$$\begin{aligned}
\frac{\partial^2 \psi}{\partial x^2} + \frac{\partial^2 \psi}{\partial y^2} &= -\frac{(1 - C_0) \rho_{f_0} g K \beta}{\mu} \frac{\partial T}{\partial x} + \frac{\rho_p - \rho_{f_0}}{\mu} g K \frac{\partial C}{\partial x} \\
\frac{\partial \psi}{\partial y} \frac{\partial T}{\partial x} - \frac{\partial \psi}{\partial x} \frac{\partial T}{\partial y} &= \alpha_m \left(\frac{\partial^2 T}{\partial x^2} + \frac{\partial^2 T}{\partial y^2} \right) \\
&+ \delta \left\{ D_B \left(\frac{\partial C}{\partial x} \frac{\partial T}{\partial x} + \frac{\partial C}{\partial y} \frac{\partial T}{\partial y} \right) + \frac{D_T}{T_c} \left[\left(\frac{\partial T}{\partial x} \right)^2 + \left(\frac{\partial T}{\partial y} \right)^2 \right] \right\} \\
\frac{1}{\varepsilon} \left(\frac{\partial \psi}{\partial y} \frac{\partial C}{\partial x} - \frac{\partial \psi}{\partial x} \frac{\partial C}{\partial y} \right) &= D_B \left(\frac{\partial^2 C}{\partial x^2} + \frac{\partial^2 C}{\partial y^2} \right) + \frac{D_T}{T_c} \left(\frac{\partial^2 T}{\partial x^2} + \frac{\partial^2 T}{\partial y^2} \right)
\end{aligned} \tag{2.6}$$

We now define the following parameters to make the above equations dimensionless

$$\begin{aligned}
X &= \frac{x}{L} & Y &= \frac{y}{L} & \Psi &= \frac{\psi}{\alpha_m} & \theta &= \frac{T - T_c}{T_h - T_c} \\
\Phi &= \frac{C}{C_0} & \text{Ra} &= \frac{(1 - C_0) g K \rho_{f_0} \beta (T_h - T_c) L}{\alpha_m \mu} \\
\text{Pe} &= \frac{V_0 L}{\alpha_m} & \text{Le} &= \frac{\alpha_m}{\varepsilon D_B} & \text{Nb} &= \frac{\delta D_B C_0}{\alpha_m} \\
\text{Nr} &= \frac{(\rho_p - \rho_{f_0}) C_0}{\rho_{f_0} \beta (T_h - T_c) (1 - C_0)} & \text{Nt} &= \frac{\delta D_T (T_h - T_c)}{\alpha_m T_c}
\end{aligned} \tag{2.7}$$

Here, Ra is the Rayleigh number, Pe is the Peclet number (with V_0 being the inlet velocity), Le is the Lewis number, Nb is the Brownian diffusion parameter, Nr is the buoyancy ratio, and Nt is the thermophoresis number.

Substituting the dimensionless parameters into the governing equations yields

$$\begin{aligned}
\frac{\partial^2 \Psi}{\partial X^2} + \frac{\partial^2 \Psi}{\partial Y^2} &= -\text{Ra} \left(\frac{\partial \theta}{\partial X} - \text{Nr} \frac{\partial \Phi}{\partial X} \right) \\
\frac{\partial \Psi}{\partial Y} \frac{\partial \theta}{\partial X} - \frac{\partial \Psi}{\partial X} \frac{\partial \theta}{\partial Y} &= \frac{\partial^2 \theta}{\partial X^2} + \frac{\partial^2 \theta}{\partial Y^2} + \text{Nb} \left(\frac{\partial \Phi}{\partial X} \frac{\partial \theta}{\partial X} + \frac{\partial \Phi}{\partial Y} \frac{\partial \theta}{\partial Y} \right) + \text{Nt} \left[\left(\frac{\partial \theta}{\partial X} \right)^2 + \left(\frac{\partial \theta}{\partial Y} \right)^2 \right] \\
\text{Le} \left(\frac{\partial \Psi}{\partial Y} \frac{\partial \Phi}{\partial X} - \frac{\partial \Psi}{\partial X} \frac{\partial \Phi}{\partial Y} \right) &= \frac{\partial^2 \Phi}{\partial X^2} + \frac{\partial^2 \Phi}{\partial Y^2} + \frac{\text{Nt}}{\text{Nb}} \left(\frac{\partial^2 \theta}{\partial X^2} + \frac{\partial^2 \theta}{\partial Y^2} \right)
\end{aligned} \tag{2.8}$$

Notice that the governing equations reduce to those of a regular fluid if one chooses $\text{Nb} = \text{Nr} = \text{Nt} = 0$.

The boundary conditions for the flow problems are:

Case I: *Natural convection with a constant temperature at the side walls*

$$\begin{aligned}
 \text{Left wall:} \quad & \Psi = 0 \quad \theta = 1 \quad j_p = 0 \left(or, Nb \frac{\partial \Phi}{\partial X} + Nt \frac{\partial \theta}{\partial X} = 0 \right) \\
 \text{Right wall:} \quad & \Psi = 0 \quad \theta = 0 \quad j_p = 0 \left(or, Nb \frac{\partial \Phi}{\partial X} + Nt \frac{\partial \theta}{\partial X} = 0 \right) \\
 \text{Horizontal walls:} \quad & \Psi = 0 \quad \frac{\partial \theta}{\partial Y} = 0 \quad \frac{\partial \Phi}{\partial Y} = 0
 \end{aligned} \tag{2.9}$$

Case II: *Natural convection with a sinusoidal temperature distribution at the side walls*

$$\begin{aligned}
 \text{Left wall:} \quad & \Psi = 0 \quad \theta = \sin(2\pi Y) \quad j_p = 0 \left(or, Nb \frac{\partial \Phi}{\partial X} + Nt \frac{\partial \theta}{\partial X} = 0 \right) \\
 \text{Right wall:} \quad & \Psi = 0 \quad \theta = \sin(2\pi Y) \quad j_p = 0 \left(or, Nb \frac{\partial \Phi}{\partial X} + Nt \frac{\partial \theta}{\partial X} = 0 \right) \\
 \text{Horizontal walls:} \quad & \Psi = 0 \quad \frac{\partial \theta}{\partial Y} = 0 \quad \frac{\partial \Phi}{\partial Y} = 0
 \end{aligned} \tag{2.10}$$

Case III: *Mixed convection with a constant temperature at the side walls*

$$\begin{aligned}
 \text{Left wall:} \quad & \Psi = 0.1Pe \quad \theta = 1 \quad j_p = 0 \left(or, Nb \frac{\partial \Phi}{\partial X} + Nt \frac{\partial \theta}{\partial X} = 0 \right) \\
 \text{Right wall:} \quad & \Psi = 0 \quad \theta = 0 \quad j_p = 0 \left(or, Nb \frac{\partial \Phi}{\partial X} + Nt \frac{\partial \theta}{\partial X} = 0 \right) \\
 \text{Inlet:} \quad & \Psi = YPe \quad \theta = 0 \quad \Phi = 1 \\
 \text{Bottom wall:} \quad & \Psi = 0 \quad \frac{\partial \theta}{\partial Y} = 0 \quad \frac{\partial \Phi}{\partial Y} = 0 \\
 \text{Upper wall:} \quad & \Psi = 0.1Pe \quad \frac{\partial \theta}{\partial Y} = 0 \quad \frac{\partial \Phi}{\partial Y} = 0 \\
 \text{Outlet:} \quad & \frac{\partial \Psi}{\partial X} = 0 \quad \frac{\partial \theta}{\partial X} = 0 \quad \frac{\partial \Phi}{\partial X} = 0
 \end{aligned} \tag{2.11}$$

Case IV: *Mixed convection with a sinusoidal temperature distribution at the side walls*

$$\begin{aligned}
 \text{Left wall:} \quad & \Psi = 0.1Pe \quad \theta = \sin(2\pi Y) \quad j_p = 0 \left(or, Nb \frac{\partial \Phi}{\partial X} + Nt \frac{\partial \theta}{\partial X} = 0 \right) \\
 \text{Right wall:} \quad & \Psi = 0 \quad \theta = \sin(2\pi Y) \quad j_p = 0 \left(or, Nb \frac{\partial \Phi}{\partial X} + Nt \frac{\partial \theta}{\partial X} = 0 \right) \\
 \text{Inlet:} \quad & \Psi = YPe \quad \theta = 0 \quad \Phi = 1 \\
 \text{Bottom wall:} \quad & \Psi = 0 \quad \frac{\partial \theta}{\partial Y} = 0 \quad \frac{\partial \Phi}{\partial Y} = 0 \\
 \text{Upper wall:} \quad & \Psi = 0.1Pe \quad \frac{\partial \theta}{\partial Y} = 0 \quad \frac{\partial \Phi}{\partial Y} = 0 \\
 \text{Outlet:} \quad & \frac{\partial \Psi}{\partial X} = 0 \quad \frac{\partial \theta}{\partial X} = 0 \quad \frac{\partial \Phi}{\partial X} = 0
 \end{aligned} \tag{2.12}$$

The physical quantities related to the problems are the local and average Nusselt numbers (Nu, \bar{Nu}) and the local and average Sherwood numbers (Sh, \bar{Sh}) (Sheremet and Pop, 2014b)

$$\begin{aligned}
 \text{Nu} &= -\left. \frac{\partial \theta}{\partial X} \right|_{X=0} & \overline{\text{Nu}} &= \frac{1}{0.9} \int_{0.1}^1 \text{Nu} \, dY \\
 \text{Sh} &= -\left. \frac{\partial \Phi}{\partial X} \right|_{X=0} & \overline{\text{Sh}} &= \frac{1}{0.9} \int_{0.1}^1 \text{Sh} \, dY
 \end{aligned} \tag{2.13}$$

In the flow problems, we limit our attention to the Nusselt number since, at the side walls, we have $\text{Sh} = -(Nt/Nb)\text{Nu}$.

3. Solution method

The governing equations constitute a system of nonlinear partial differential equations. In order to discretize them, the finite-volume approach is adopted. By integrating the governing equations over each control volume, a system of algebraic equations is produced, which is solved by the Tri-Diagonal Matrix Algorithm (TDMA). Appropriate relaxation is chosen on the basis of numerical experiments. The iteration is terminated when changes between two consecutive iterations get smaller than 10^{-5} . The solution method has been implemented in FORTRAN software.

For the purpose of acquiring an acceptable grid for each current case, four different grid independence tests have been carried out. The results indicated that the suitable grid systems are 200×200 (Case I), 400×400 (Case II and Case III), and 300×300 (Case IV).

The employed Fortran code is essentially a modified version of a code built and validated in the previous works (Zahmatkesh, 2008a, 2015; Zahmatkesh and Naghedifar, 2017). In order to evaluate the accuracy of this code for simulation of nanofluid-saturated porous cavities with Buongiorno's model, the corresponding results have been compared with those of Sheremet *et al.* (2014) in Table 1. Here, the average Nusselt numbers in a square porous cavity with isothermal vertical walls and adiabatic horizontal walls saturated with the nanofluid are presented. The compared results belong to $\text{Ra} = 100$, $\text{Le} = 1, 10, 100$, $Nr = 0.1, 0.4$, and $Nb = Nt = 0.4$. Notice that there is a trustworthy similarity with that study. This assured us that our results are reliable. So, we have applied the code to analyze the flow problems depicted in Fig. 1.

Table 1. Comparison of the present results with those of previous works at $\text{Ra} = 100$

Le	Nr	$\overline{\text{Nu}}$	
		Sheremet <i>et al.</i> (2014)	Current study
1	0.1	3.8387	3.8108
	0.4	2.7791	2.7617
10	0.1	4.6270	4.5575
	0.4	4.0088	3.9637
100	0.1	4.6252	4.4401
	0.4	4.3049	4.1542

4. Simulation results

In this Section, simulation results for both natural convection and mixed convection heat transfer of the nanofluid are presented. The results are discussed for the following values of the pertinent parameters: the Rayleigh number ($\text{Ra} = 30, 100, 300$), the Peclet number ($\text{Pe} = 25$), the Lewis number ($\text{Le} = 25$), the buoyancy ratio ($Nr = 0.05, 0.1, 0.5$), the Brownian diffusion parameter ($Nb = 0.05, 0.1, 0.5$) and the thermophoresis number ($Nt = 0.05, 0.1, 0.5$).

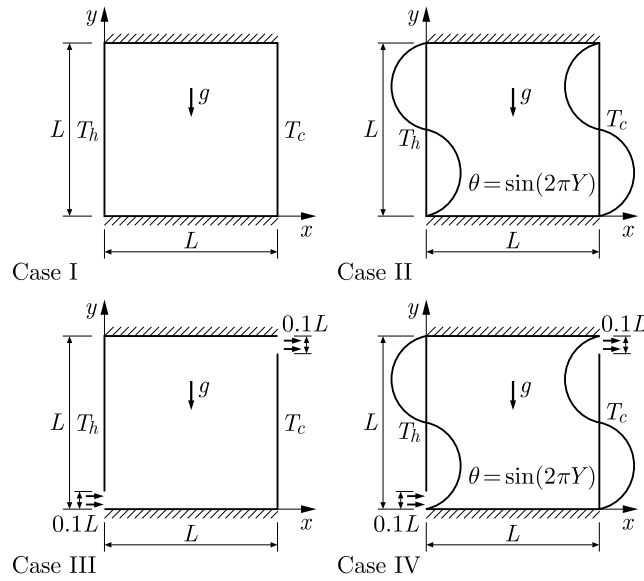


Fig. 1. Physical models of the flow problem: (a) Case I: Natural convection with a constant temperature at the side walls; (b) Case II: Natural convection with a sinusoidal temperature distribution at the side walls; (c) Case III: Mixed convection with a constant temperature at the side walls; (d) Case IV: Mixed convection with a sinusoidal temperature distribution at the side walls

Tables 2, 3, and 4 illustrate the numerical values of $|\Psi_{max}|$ and \overline{Nu} for the four configurations at $Ra = 30, 100, 300$, respectively. Here, $|\Psi_{max}|$ provides a measure of the convection vigor. In a general way, the imposition of the sinusoidal temperature distribution on the sidewalls leads to heat transfer enhancement both in the natural and mixed convection environments within the current range of the Rayleigh number. This imposition also intensifies the flow strength in the mixed convection case. In the natural convection problem, however, depending on the value of Ra , the sinusoidal wall temperature may enhance or deteriorate the flow strength.

Table 2. Numerical values of $|\Psi_{max}|$ and \overline{Nu} for the flow at $Ra = 30$

Ra = 30		Nb		Nr		Nt		Nb = Nr = Nt
		0.05	0.5	0.05	0.5	0.05	0.5	0.1
Case I	$ \Psi_{max} $	1.909	1.918	1.916	1.894	1.917	1.889	1.914
	\overline{Nu}	1.421	1.424	1.423	1.417	1.455	1.186	1.422
Case II	$ \Psi_{max} $	0.750	0.750	0.750	0.750	0.736	0.878	0.750
	\overline{Nu}	3.577	3.576	3.576	3.576	3.575	3.722	3.576
Case III	$ \Psi_{max} $	2.499	2.499	2.499	2.499	2.499	2.499	2.499
	\overline{Nu}	3.570	3.542	3.541	3.610	3.584	3.381	3.549
Case IV	$ \Psi_{max} $	3.370	3.362	3.364	3.377	3.351	3.462	3.366
	\overline{Nu}	4.613	4.610	4.611	4.616	4.590	4.914	4.611

Inspection of the numerical values of $|\Psi_{max}|$ in the conduction-dominated regime (i.e., Table 2 with $Ra = 30$) indicates that in Case I, increasing Nb leads to an insignificant growth in the flow strength (maximum 0.47%) but rising Nr or Nt causes a slight drop in it (maximum 1.15% and 1.46%, respectively). The results of Case II show that an increment in the thermophoresis number from 0.05 to 0.5 intensifies the flow strength to about 19.29%. Nb and Nr , however, contributes neutrally there. The results of Case III indicate that the value of $|\Psi_{max}|$ is not dependent in this case to Nb , Nr , and Nt . Meanwhile, notice that all current parameters are influential to the flow strength in Case IV. This is similar to Case I but the trends of the

Table 3. Numerical values of $|\Psi_{max}|$ and \overline{Nu} for the flow at $Ra = 100$

Ra = 100		Nb		Nr		Nt		Nb = Nr = Nt
		0.05	0.5	0.05	0.5	0.05	0.5	
Case I	$ \Psi_{max} $	4.707	4.725	4.722	4.676	4.722	4.668	4.717
	\overline{Nu}	2.932	2.936	2.935	2.925	2.999	2.450	2.934
Case II	$ \Psi_{max} $	2.618	2.622	2.622	2.608	2.579	2.942	2.621
	\overline{Nu}	4.265	4.252	4.254	4.254	4.247	4.536	4.258
Case III	$ \Psi_{max} $	3.264	3.240	3.245	3.288	3.237	3.342	3.251
	\overline{Nu}	4.975	4.932	4.940	5.017	5.003	4.518	4.950
Case IV	$ \Psi_{max} $	5.435	5.459	5.456	5.398	5.412	5.728	5.449
	\overline{Nu}	5.512	5.500	5.503	5.530	5.468	5.987	5.506

Table 4. Numerical values of $|\Psi_{max}|$ and \overline{Nu} for the flow at $Ra = 300$

Ra = 300		Nb		Nr		Nt		Nb = Nr = Nt
		0.05	0.5	0.05	0.5	0.05	0.5	
Case I	$ \Psi_{max} $	9.813	9.847	9.841	9.749	9.843	9.709	9.831
	\overline{Nu}	6.082	6.083	6.083	6.073	6.214	5.111	6.083
Case II	$ \Psi_{max} $	6.270	6.286	6.284	6.181	6.222	6.756	6.282
	\overline{Nu}	7.553	7.534	7.535	7.585	7.525	7.933	7.537
Case III	$ \Psi_{max} $	8.02	7.952	7.958	8.094	7.953	8.094	7.981
	\overline{Nu}	8.181	8.061	8.100	8.262	8.168	7.488	8.128
Case IV	$ \Psi_{max} $	8.898	8.951	8.918	8.903	8.898	9.470	8.916
	\overline{Nu}	8.800	8.904	8.831	8.981	8.799	9.721	8.830

variations are quite distinct. Evidently, with the increase in Nb , a slight drop in the flow strength appears (maximum 0.24%), but with an elevation in Nr or Nt , insignificant increases occur in it (maximum 0.39% and 3.31%, respectively).

Scrutiny of the \overline{Nu} values in Table 2 demonstrates that Nb and Nr possess a minor impact on the average Nusselt number in all current cases. Notice that maximum deviations of \overline{Nu} , as a result of the tenfold increase in Nb and Nr , may not exceed 0.78% and 1.95%, respectively. The pattern is completely different when we go to Nt , since this parameter affects the heat transfer rate in all configurations. Specifically, a rise in Nt from 0.05 to 0.5 increases \overline{Nu} to 4.11% and 7.06% in Case II and Case IV with sinusoidal wall temperatures, but decreases it to 18.49% and 5.66% in Case I and Case III with constant wall temperatures, respectively. This controversy in the effect of the thermophoresis number on the heat transfer of cavities with uniform wall temperatures and those with non-uniform wall temperatures is in agreement with the previous findings in the natural convection environment, as pointed out previously.

The results presented in Table 3 belonging to $Ra = 100$ indicate that, in Case I, the variations of $|\Psi_{max}|$ with Nb , Nr and Nt are similar to those of $Ra = 30$. The corresponding deviations are +0.38%, -0.97%, and -1.14%, respectively. In Case II and III, the consequences of the pertinent parameters on the flow strength are no longer negligible at this Rayleigh number. In Case II, the tenfold increase in Nb , Nt , and Nr leads to 0.15% and 14.07% growths and a 0.53% drop in $|\Psi_{max}|$, respectively. The deviations are -0.74%, +3.24%, and +1.33% in Case III and +0.44%, +5.84%, and -1.06% in Case IV, respectively. Analysis of the average Nusselt number is also interesting. Similarly to what appeared at $Ra = 30$, it is evident that Nb and Nr are not so influential on \overline{Nu} prediction at $Ra = 100$. Maximum changes of \overline{Nu} by increasing Nb and Nr are +0.14% and -0.34% in Case I, -0.30% and 0% in Case II, -0.86% and +4.93% in Case III, and -0.22% and +0.49% in Case IV, respectively. The effect of the thermophoresis number on

the heat transfer rate is more remarkable. Specifically, a rise in Nt from 0.05 to 0.5 increases \overline{Nu} to 6.80% and 9.49% in Case II and IV but decreases it to 18.31% and 9.69% Case I and III, respectively.

Table 4 indicates that when $Ra = 300$, then Nb , Nr , and Nt affect the value $|\Psi_{max}|$ in all the problems. Notice that maximum variations of $|\Psi_{max}|$ as a result of the increase in Nb are +0.35%, +0.26%, -0.85% and +0.60% in Case I, II, III, and IV, respectively. The corresponding values due to a rise in Nr are -0.93%, -1.64%, +1.71%, and -0.17%. The results also demonstrates that a rise in Nt from 0.05 to 0.5 results in 8.58%, 1.77% and 6.43% increase in the flow strength in Case II, III, and IV, respectively, but decreases the value $|\Psi_{max}|$ to 1.36% in Case I.

Numerical values of the average Nusselt number in Table 4 indicate that an increase in Nb from 0.05 to 0.5 leads to +0.02%, +0.01%, -1.47%, and +1.18% deviations in heat transfer in Case I, II, III, and IV, respectively. The corresponding changes due to a rise in Nr are -0.16%, +0.66%, +2.0%, and +1.70%. The alternation of Nt also brings -17.75%, +5.42%, -8.33%, and +10.48% variations in the average Nusselt number.

The thermophoresis parameter is found to be the most effective coefficient in the current cases. In order to provide a better picture about the consequences of this parameter on distributions of isocontours of the stream function, temperature and nanoparticles fraction, the corresponding contours for the flow problems are provided in Figs. 2-5, which belong to $Ra = 100$ with both $Nt = 0.05$ and $Nt = 0.5$.

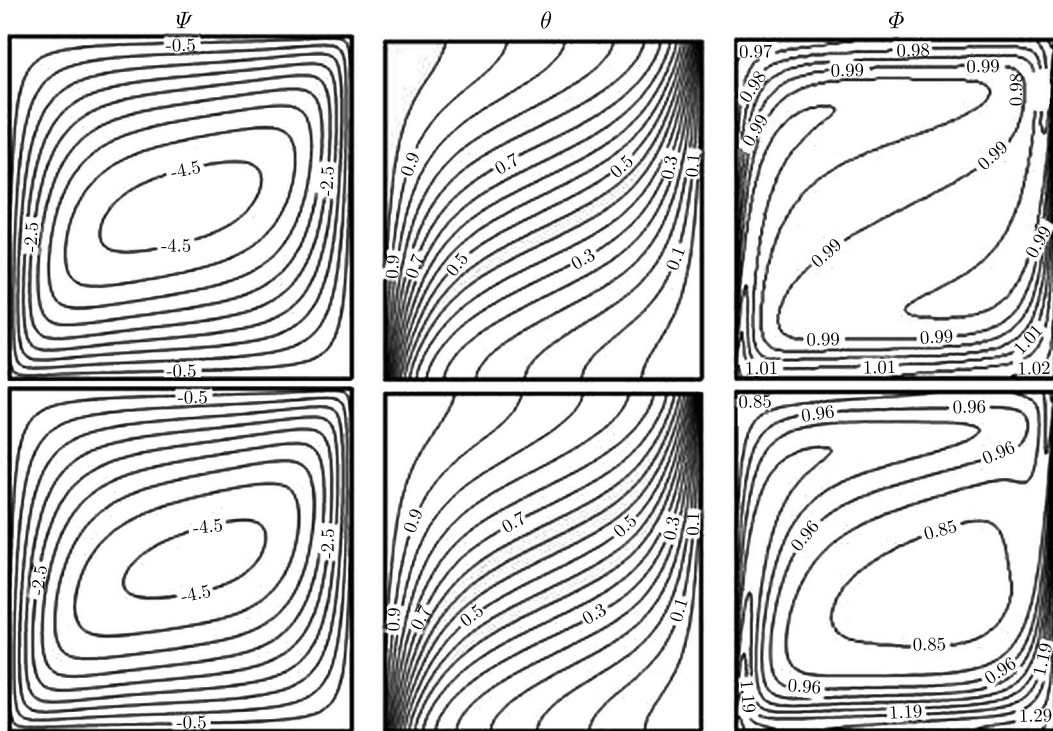


Fig. 2. Isocontours of the stream function, temperature and nanoparticles fraction for Case I at $Ra = 100$, $Le = 25$ with different values of Nt (up: $Nt = 0.05$; down: $Nt = 0.5$)

Figure 2 shows the isocontours of the stream function (left), temperature (middle) and nanoparticles fraction (right) for Case I. Regardless of the value of Nt , a single convective cell appears inside the cavity with an ascending flow near the left wall and a descending flow near the right wall. It is evident that a growth in Nt does not have a significant effect on the streamlines and isothermal lines but makes the nanoparticles distribution more non-homogeneous.

The streamlines, isotherms and isoconcentrations of Case II are provided in Fig. 3. Obviously, four convective cells appear here within the cavity. The convective cells located in the

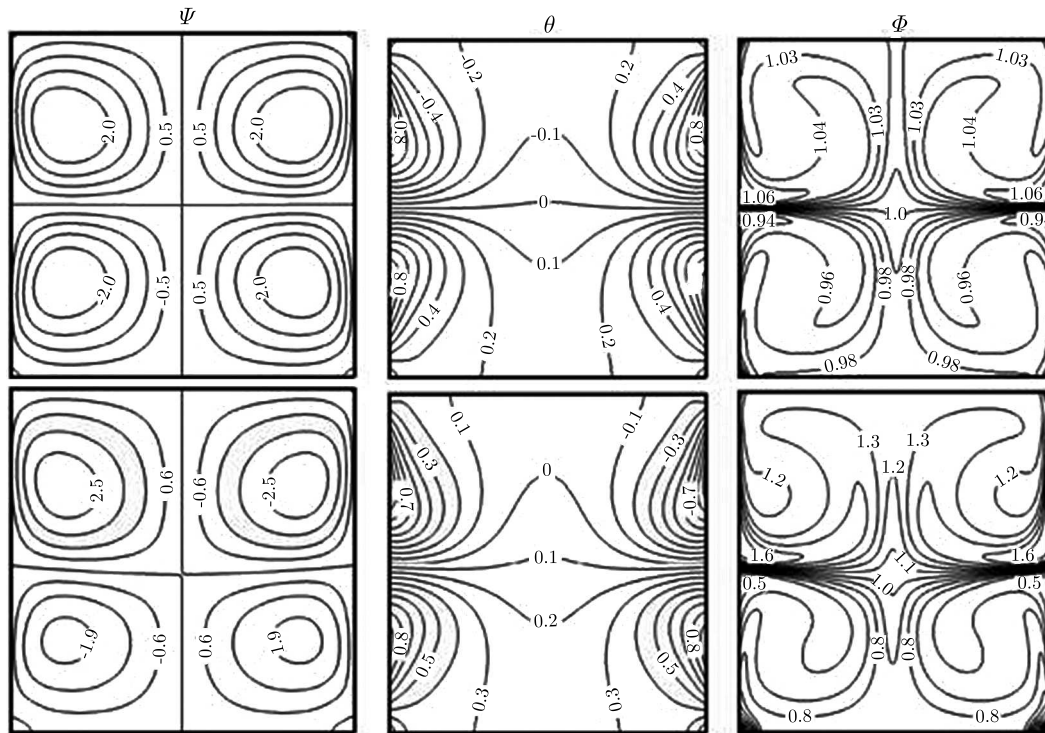


Fig. 3. Isocontours of the stream function, temperature and nanoparticles fraction for Case II at $Ra = 100$, $Le = 25$ with different values of Nt (up: $Nt = 0.05$; down: $Nt = 0.5$)

bottom-left/top-right parts of the cavity are rotating clockwise but those located in the bottom-right/top-left parts are counter-clockwise vortices. The appearance of these circulations is attributed to the imposition of the sinusoidal temperature distribution on the side walls in this case. Cores of the convective cells are located close to the side walls due to large temperature gradients there. The distributions of Ψ and θ are symmetric with respect to $X = 0.5$. It is evident that the Nt promotion leads to variations in all characteristics noticeably. Obviously, the streamlines pattern is changed in a way of growing the two top convective cells. Moreover, the bottom half of the cavity experiences more intensive heating while the opposite side transfers less heat. The main variations with Nt are related to the isoconcentrations. The Nt elevation causes a more non-homogeneous nanoparticles distribution. This is similar to Case I, but the effect is more remarkable here.

Figures 4 and 5 depict the isocontours of the stream function, temperature and nanoparticles fraction for Case III and IV, respectively. They correspond to the mixed convection environment. The effect of the Nt promotion on the distribution of the contour plots bears a strong resemblance to what is observed in the natural convection cases.

5. Concluding remarks

A critical analysis of natural and mixed convection of a nanofluid in square porous cavities has been presented here using Buongiorno's mathematical model. The findings of this study can be summarized as:

- (1) Imposition of a sinusoidal temperature distribution on the sidewalls leads to heat transfer improvement both in the natural and mixed convection environments.
- (2) The consequence of the thermophoresis number on the flow strength and the average Nusselt number is more prominent than the Brownian diffusion parameter and the thermophoresis number.

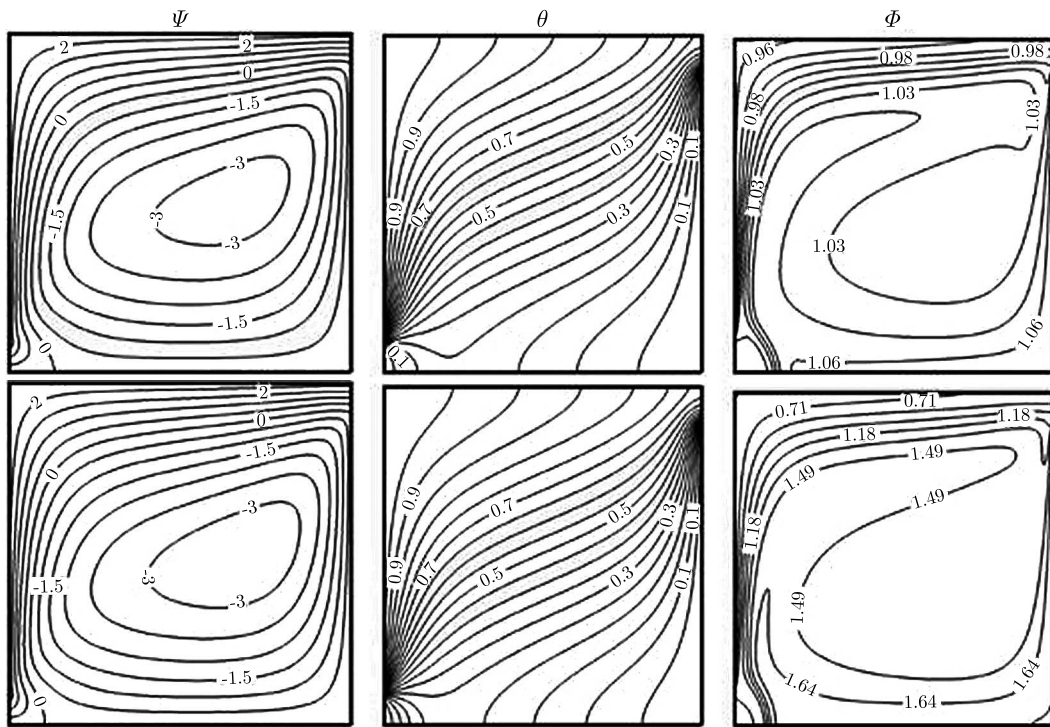


Fig. 4. Isocontours of stream the function, temperature and nanoparticles fraction for Case III at $Ra = 100$, $Pe = 25$, $Le = 25$ with different values of Nt (up: $Nt = 0.05$; down: $Nt = 0.5$)

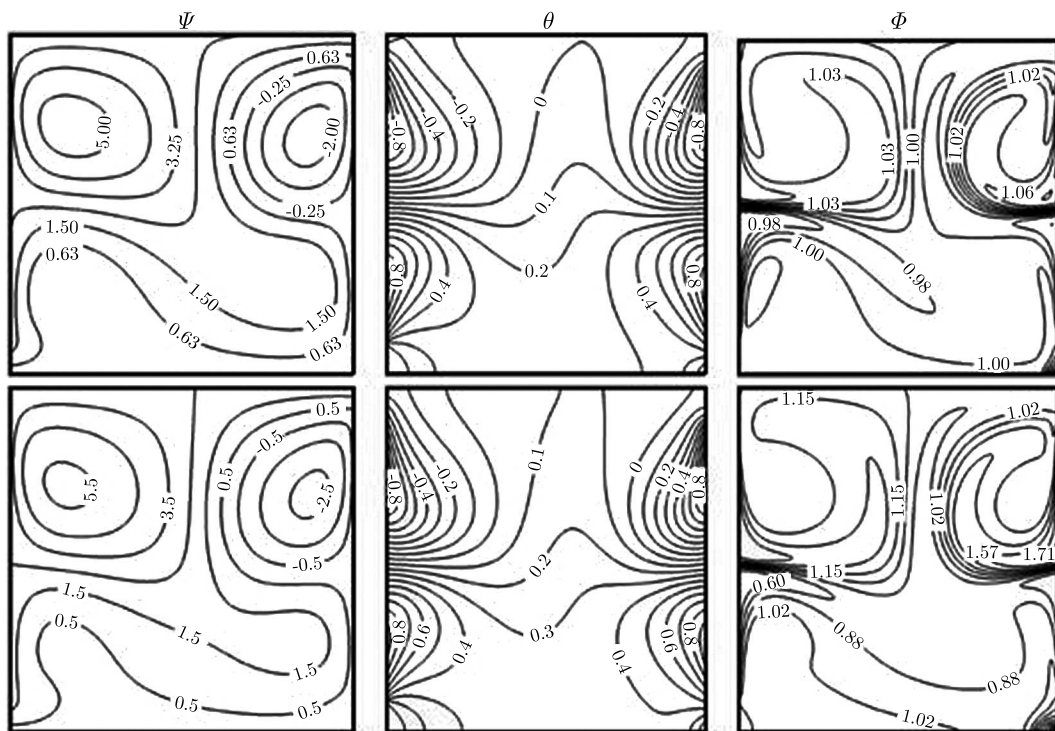


Fig. 5. Isocontours of the stream function, temperature and nanoparticles fraction for Case IV at $Ra = 100$, $Pe = 25$, $Le = 25$ with different values of Nt (up: $Nt = 0.05$; down: $Nt = 0.5$)

- (3) With an increase in the thermophoresis number, progressive changes occur in the isocontours of the stream function, temperature and nanoparticles fraction, and the nanoparticles distribution becomes more non-homogeneous.
- (4) With the sinusoidal wall temperatures, the heat transfer rate is an increasing function of the thermophoresis number, but in a cavity with uniform wall temperatures, depending on the value of the Rayleigh number, an increase in Nt may enhance or deteriorate the average Nusselt number.
- (5) The Brownian diffusion parameter and the buoyancy ratio have almost no effect on \overline{Nu} in the natural convection but with an increase in Ra , they become gradually more influential in the mixed convection.

References

1. ALI K., IQBAI M.F., AKBAR Z., ASHRAF M., 2014, Numerical simulation of unsteady water-based nanofluid flow and heat transfer between two orthogonally moving porous coaxial disks, *Journal of Theoretical and Applied Mechanics*, **52**, 1033-1046
2. BEHROYAN I., VANAKI S.M., GANESAN P., SAIDUR R., 2016, A comprehensive comparison of various CFD models for convective heat transfer of Al₂O₃ nanofluid inside a heated tube, *International Communications in Heat and Mass Transfer*, **70**, 27-37
3. BUONGIORNO J., 2006, Convective transport in nanofluids, *Journal of Heat Transfer*, **128**, 240-250
4. GHALAMBAZ M., SABOUR M., POP I., 2016, Free convection in a square cavity filled by a porous medium saturated by a nanofluid: Viscous dissipation and radiation effects, *Engineering Science and Technology*, **19**, 1244-1253
5. GHASEMI S.E., HATAMI M., SALARIAN A., DOMAIRRY G., 2016, Thermal and fluid analysis on effects of a nanofluid outside a stretching cylinder with magnetic field using the differential quadrature method, *Journal of Theoretical and Applied Mechanics*, **54**, 517-528
6. KEFAYATI G.H.R., 2017a, Mixed convection of non-Newtonian nanofluid in an enclosure using Buongiorno's mathematical model, *International Journal of Heat and Mass Transfer*, **108**, 1481-1500
7. KEFAYATI G.H.R., 2017b, Simulation of natural convection and entropy generation of non-Newtonian nanofluid in a porous cavity using Buongiorno's mathematical model, *International Journal of Heat and Mass Transfer*, **112**, 709-744
8. MUSTAFA M., 2017, MHD nanofluid flow over a rotating disk with partial slip effects: Buongiorno model, *International Journal of Heat and Mass Transfer*, **108**, 1910-1916
9. NIELD D.A., BEJAN A., 2013, *Convection in Porous Media*, Springer, New York
10. NIELD D.A., KUZNETSOV A.V., 2009, The Cheng-Minkowycz problem for natural convective boundary-layer flow in a porous medium saturated by a nanofluid, *International Journal of Heat and Mass Transfer*, **52**, 5792-5795
11. ROSTAMZADEH A., JAFARPUR K., GOSHTASBI RAD E., 2016, Numerical investigation of pool nucleate boiling in nanofluid with lattice Boltzmann method, *Journal of Theoretical and Applied Mechanics*, **54**, 3, 811-825
12. SHEIKHOLESLAMI M., GANJI D.D., RASHIDI M.M., 2016, Magnetic field effect on unsteady nanofluid flow and heat transfer using Buongiorno model, *Journal of Magnetism and Magnetic Materials*, **416**, 164-173
13. SHEREMET M.A., CIMPEAN D.S., POP I., 2017, Free convection in a partially heated wavy porous cavity filled with a nanofluid under the effects of Brownian diffusion and thermophoresis, *Applied Thermal Engineering*, **113**, 413-418

14. SHEREMET M.A., GROSAN T., POP I., 2014, Free convection in shallow and slender porous cavities filled by a nanofluid using Buongiorno's model, *Journal of Heat Transfer*, **136**, 082501-1
15. SHEREMET M.A., POP I., 2014a, Conjugate natural convection in a square porous cavity filled by a nanofluid using Buongiorno's mathematical model, *International Journal of Heat and Mass Transfer*, **79**, 137-145
16. SHEREMET M.A., POP I., 2014b, Natural convection in a square porous cavity with sinusoidal temperature distributions on both side walls filled with a nanofluid: Buongiorno's mathematical model, *Transport in Porous Media*, **105**, 411-429
17. SHEREMET M.A., POP I., 2015a, Free convection in a triangular cavity filled with a porous medium saturated by a nanofluid Buongiorno's mathematical model, *International Journal of Numerical Methods for Heat and Fluid Flow*, **25**, 1138-1161
18. SHEREMET M.A., POP I., 2015b, Free convection in a porous horizontal cylindrical annulus with a nanofluid using Buongiorno's model, *Computers and Fluids*, **118**, 182-190
19. SHEREMET M.A., POP I., RAHMAN M.M., 2015, Three-dimensional natural convection in a porous enclosure filled with a nanofluid using Buongiorno's mathematical model, *International Journal of Heat and Mass Transfer*, **82**, 396-405
20. TORSHIZI E., ZAHMATKESH I., 2016, Comparison between single-phase, two-phase mixture, and Eulerian-Eulerian models for the simulation of jet impingement of nanofluids, *Journal of Applied and Computational Sciences in Mechanics*, **27**, 55-70
21. ZAHMATKESH I., 2008a, On the importance of thermal boundary conditions in heat transfer and entropy generation for natural convection inside a porous enclosure, *International Journal of Thermal Sciences*, **47**, 339-346
22. ZAHMATKESH I., 2008b, On the importance of thermophoresis and Brownian diffusion for the deposition of micro- and nanoparticles, *International Communications in Heat and Mass Transfer*, **35**, 369-375
23. ZAHMATKESH I., 2015, Heatline visualization for buoyancy-driven flow inside a nanofluid-saturated porous enclosure, *Jordan Journal of Mechanical and Industrial Engineering*, **9**, 149-157
24. ZAHMATKESH I., NAGHEDIFAR S.A., 2017, Oscillatory mixed convection in jet impingement cooling of a horizontal surface immersed in a nanofluid-saturated porous medium, *Numerical Heat Transfer, Part A*, **72**, 401-416

Manuscript received August 19, 2017; accepted for print September 18, 2018

STRENGTH ANALYSIS OF HIP JOINT REPLACEMENT REVISION IMPLANT

PAWEŁ SKOWRONEK

*Clinic of Orthopaedics and Traumatology, Regional Hospital and Jan Kochanowski University Kielce, Poland
e-mail: pawel.skowronek@interia.pl*

KRZYSZTOF TWARDOCH, PIOTR SKAWIŃSKI

*Warsaw University of Technology, Institute of Machine Design Fundamentals, Warszawa, Poland
e-mail: krzysztof.twardoch@pw.edu.pl; psk@simr.pw.edu.pl*

MARCEL ŻOŁNIERZ

*Silesian University of Technology, Department of Mining Mechanisation and Robotisation, Gliwice, Poland
e-mail: marcel.zolnierz@polsl.pl*

The subject of the article is the evaluation of the strength of revision implants made of titanium or tantalum alloy, used during bone reconstruction of a hip joint while potentially using additional stabilizing screws, necessary due to significant bone loss. The article provides a preliminary strength analysis of implants, indispensable for further evaluation of strength limitations due to the risk of implant damage depending on the structure and number of additional screw holes. In the human locomotor system, the hip joint is the joint with the most load, hence the main problem is to establish an adequate load model which ought to be assumed for the needs of implant strength analysis. It is found necessary to perform a short, analytical review of the existing hip joint load models from the point of view of choosing the proper one, considering evaluation of implant strength by means of numerical studies using FEM. Differences in the implant load distribution depending on the used material are shown.

Keywords: implant, implant strength, prosthesis, hip joint, material loss

1. Introduction

The treatment method that WHO considers the one which completely resolved symptoms and deformations resulting from Degenerative Joint Disease (DJD) is currently the primary Total Hip Replacement (THR). With higher life expectancy of patients, the number of people suffering from advanced degenerative lesions of joints is growing (DJD). Having reduced mortality resulting from heart and cardiovascular diseases within the last two decades, the number of patients suffering from DJD and treated with THR has grown. It has become a wider problem, also in reference to biological and mechanical aspects of prostheses degenerating bone tissue, which is currently the object of a few technical studies, e.g. evaluating the strength of bone cement in configuration with titanium implants and decreased quality of bone tissue (Benouis *et al.*, 2016). Together with the number of primary joints replacements, the number of secondary-revision procedures is also growing, consisting in replacing prostheses with the new ones, e.g. due to pelvic bone or femur defects. Unfortunately, they are often implanted in acetabulum bone with bone losses that need procedures using modular reconstruction implants. These implants must possess appropriate strength and elasticity, enabling own load, must provide a reliable and multidirectional primary stabilization in bone tissue and secondary osseointegration of bone

tissue in the implant. Thus, it is more and more common to use porous revision implants during joint reconstruction, which allows one to replace bone tissue with metal elements. The most commonly used are so called “full” ones, which possess only the external porous structure (most often hydroxyapatite layer) (Dorman *et al.*, 2011) and “trabecular metal” type of implants with full spatial porous architecture enabling reconstruction of the bone tissue into the implant (Dorman *et al.*, 2011). The applied implants are made of titanium and its alloys or of tantalum. The percentage composition of the applied metals is up to the producer. In most cases, titanium implants are made of titanium alloy with addition of rare metals such as Vanadium (Ti-6Al-4V-ELI) and Niobium (Ti-6Al-7Nb). In the case of spatial tantalum implants, only a tantalum foam sintered powder is used. It is the material with better bone biocompatibility and more biologically neutral for the organism, in comparison with rare metals used in titanium alloys. The implants are manufactured in different shapes and sizes, which allows one to fully or partially adjust them to bone losses, leading to reconstruction of anatomy with proper biomechanics of the joint. The essence of proper implant functioning is, apart from osteointegration and mechanical strength, lowest risk of allergic effects or cytotoxicity of metal ions (especially in the case of implants containing vanadium and niobium, each interference or damage of the structure during implantation may result in rare metal ions secretion). Standard manufactured implants contain primary holes which enable stabilization with a patient’s bone by means of screws (Bobyne *et al.*, 1999; Dorman *et al.*, 2011; Hacking *et al.*, 2000). The elements are interconnected using polymethylmethacrylate (PMMA) (Bobyne *et al.*, 1999; Hacking *et al.*, 2000; Meneghini *et al.*, 2010). Each implant is characterized by proper elasticity, resulting from the applied metal i.e. Young’s elasticity modulus E , determining linear strength. It has to be borne in mind, however, that when mechanically interfering with an implant (related to drilling additional fixing holes) during non-standard stabilization, the fatigue strength of an implant R_z may decrease as well as further damages may occur. It results from the change in strain and may require remodeling of stiffness and strength. Performed preliminary studies are supposed to evaluate the strength of tantalum “trabecular metal” type of implants and titanium mixed with niobium (Ti-6Al-7Nb) implants, which possess standard holed enabling stabilization with a patient’s bone using screws. The research material presented in the article constitutes a starting point for research of strength evaluation of implants weakened by the holes drilled for the needs of potential additional stabilization and, at the same time, draws attention to the risk of mechanical consequences of excessive weakening of an implant and secondary biological risk of leaving drilling products behinds, especially those of rare metals.

2. State of hip joint load

In order to evaluate the risk of mechanical consequences of excessive weakening of an implant, it is decided appropriate to define the state of load by means of Finite Element Method (FEM). The main problem is to define the implant load model which must be assumed for the purpose of such an analysis. From the point of view of mechanics, precisely theory of machines and mechanisms, a hip joint is a III-class kinematic pair – spherical, enabling reciprocal spherical movement. In the human movement system, the hip joint is one of the biggest kinematic nodes, possessing three degrees of freedom ($s = 3$). The occurrence of additional degrees of freedom, connected with an incomplete close of the node is defined as hip joint instability (Harris, 1992). Transferring loads of the spine to lower extremities by means of pelvis, involving the hip joint occurs in conditions of a very complex movement (Fig. 1). It has to be borne in mind, that the hip joint together with skeletal system of the pelvic rim, connects the upper part of the human body with lower extremities by means of a complex system of muscles, tendons and ligaments. Interactions between the femur head and acetabulum as well as stresses of the muscle system

taking part in movement, determines the state of load of the entire skeletal system of the hip joint. The load of the hip joint is directly dependent on body weight and activities performed by a human during walking – it constitutes a complex system of forces and moments. In the hip joint, movement may occur around three main axes. Usually, a particular movement caused by a contraction of the appropriate muscle is prevalent and determines the essential function of the hip joint to which a system of external and internal forces is applied. The external forces are: weight related to body mass, support actions, and forces resulting from interactions of other objects with the human body. The internal forces are mainly forces resulting from muscle interactions. Evaluation of directions and values of these forces is very difficult due to a large number of muscles and place of their application (muscle attachments) (Madej, 2008). Furthermore, values and directions of loads occurring in the hip joint vary in different phases of gait (Bergman *et al.*, 1993, Bergman *et al.*, 2001; Będziński and Ścigała, 2004; Dąbrowska-Tkaczyk, 1999; Dragan, 1992; Madej and Ryniewicz, 2007; Popovic *et al.*, 2004, Włodarski, 2005).

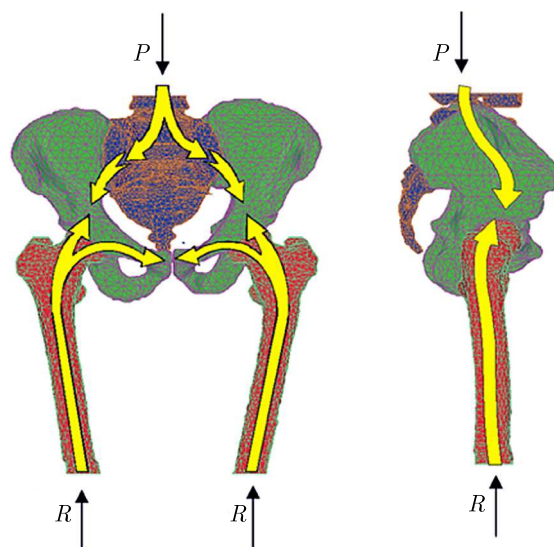


Fig. 1. Transfer of loads from the spine to lower extremities (Będziński, 1997)

During gait, the center of gravity of the body S also changes, and moves in the direction opposite to the loaded extremity (Fig. 2). Additionally, the loads in the hip joint depend on phases of foot contact with the ground. Movements in other planes occur: bow-hyperextension, ante-version and retroversion, as well as rotational movements.

The rule is to simulate static conditions in the load phase of one extremity, standing on both feet and in the phase of heel contact with the ground. Additionally, *in vivo* research is performed on the values of forces occurring in the hip joint in different phases of gait, especially in the phases, in which the highest load occurs: while standing on one foot, going up the stairs, getting up a chair. The values of forces occurring in the hip joint in patients with implanted a telemetric Moore-type implant were studied by Rydell. The research was continued by Bergman and Rohlmann, who defined vectors of forces influencing endoprosthesis head in a patient with full hip alloplasty (Dragan, 2004).

In experiments on biomechanics of hip joint, mechanical properties, especially stiffness and strength against impact stresses of constructed implants, are studied and physiological models of force and load distribution in the hip joint before and after endoprosthesis implantation are devised. Thus, the most often conducted research applies computer techniques using numerical simulation based on physical models, with holographic interferometry method or with application of resistance strain gauges (Dragan, 2004; Madej, 2008).

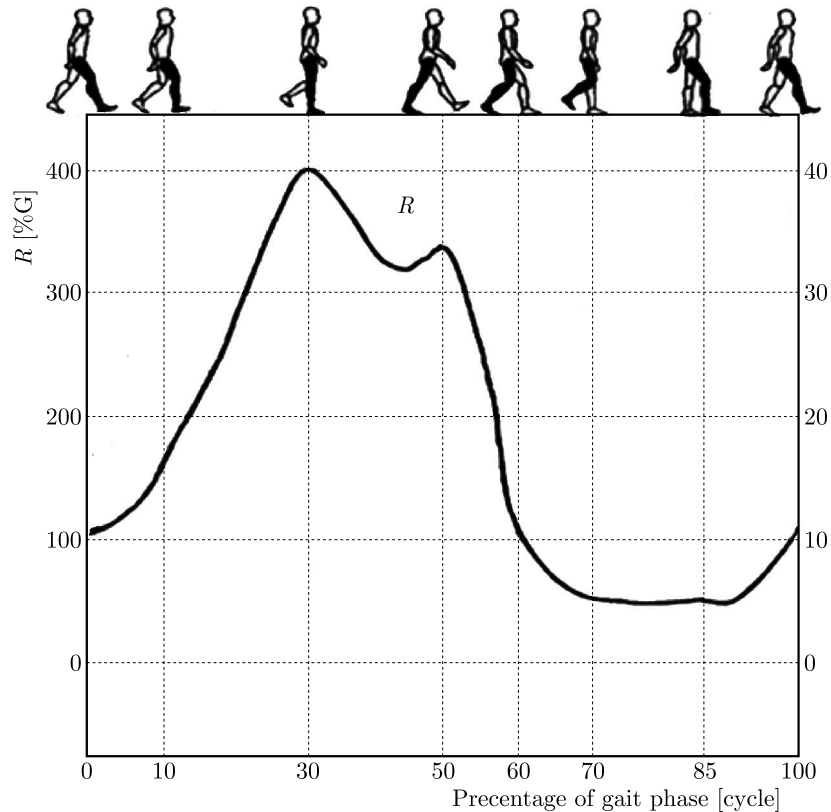


Fig. 2. The course of forces expressed as percentage of the body weight in the hip joint load in the gait cycle (according to Bergman) (Będziński, 1997)

3. Identification of the hip joint load model

The research on hip joint mechanics in numerous research centers has led to creation of multiple models of the hip joint load, e.g. Pauwels', Maquet's, Bombeli's, Huijskes', Bergman's and Będziński's models (Bergman *et al.*, 1993, 1995; Bernakiewicz and Będziński, 1999; Będziński, 1997; Bombeli, 1983; Maquet, 1985; Pauwels, 1976). Researchers, in their majority, agree that while modelling the hip joint load, the following have to be taken into consideration (Będziński, 1997):

- gluteus muscles, for lateral-medial loads,
- biceps femoris muscle, significant in front-to-back interactions,
- iliotibial band of abductors (tractus iliotibialis),
- band of abductors, more significant in femur load than band of adductors,
- a group of rotator muscles, during simulation of the extremity movement in the sagittal plane, which causes – due to their function and location – turning moment of femur.

In the light of all the above, the identification of hip joint load model is an exceptionally difficult and crucial task, considering theoretical studies aimed at strength evaluation from the perspective of e.g. deformation or risk of implant damage.

One of the most common hip joint load models is Pauwels' model, which presents two cases of the hip joint load: two-feet load and standing on one lower extremity (Fig. 3a). The resultant vector of the force R is directed at the rotation point, which is the anatomical center of the femur head. In Pauwels' model, it is assumed that during unilateral extremity load, the total value of the force loading hip joint results from the interaction between the body weight and forces of periarticular muscles (Madej, 2008).

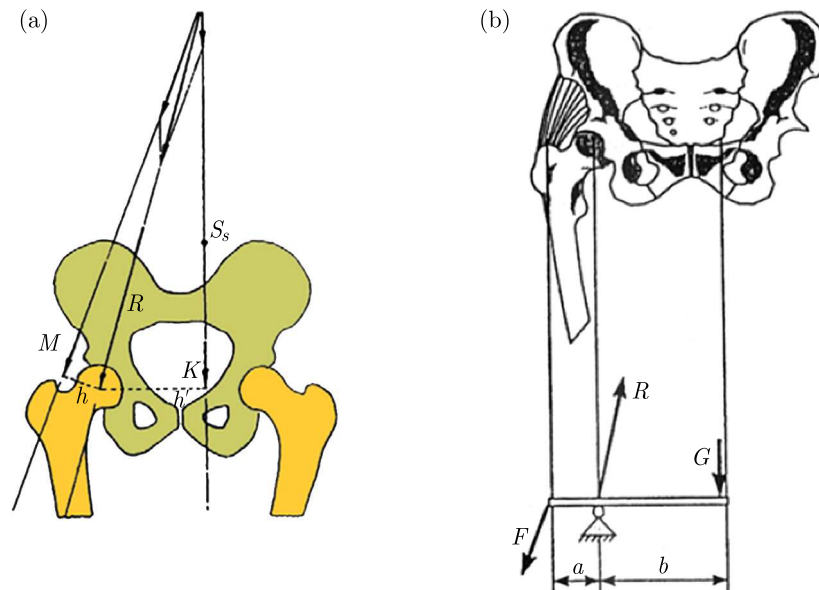


Fig. 3. (a) Hip joint load model (according to Pauwels) during movement, the phase of one leg load: S_5 – body center of gravity, impact of torso, hand-arms, head, without the other lower extremity, K – resultant force of body weight impact, M – abductor muscle impact, R – resultant reaction of impact on the femur head (Bernakiewicz, 1994). (b) Model of two-armed lever modelling loads of the femur head while standing on one leg (Będziński, 1997)

Relations of loads in the hip joint are brought to a two-armed lever, in which the point of support is in the middle of the hip joint (Fig. 3b). Such an attitude towards the issue constitutes a significant simplification of a complex state of load in the hip joint, dependent on various factors (Będziński, 1997; Pauwels, 1976). Analysis of loads based on a two-armed lever is approximately valid only in the case of the state of balance, when the body center of gravity is in the coronal plane. Performing any kind of movement will cause a change in the location of the body center of gravity, which results in the change in the state of load – directions and values of forces coming from groups of muscles which become activated in order to maintain balance of the body (Będziński, 1997).

The role of iliotibial band is presented differently by Maquet's model (Fig. 4a), which is a modification of Pauwels' model. In Maquet's model, tension of the external band of thigh fascia lata is caused by the abductor muscle. The band is simulated as a tie running along the femoral shaft from the knee joint to pelvic bone. The tie is based on the great trochanter of the femur and can slide on it. The impact of the iliotibial band modeled in this way gives an additional horizontal force, which stabilizes the hip joint. Due to a different, in comparison with other models, consideration of the impact of muscles, Maquet's model is more accurate in terms of the upper anatomy of the lower extremity (Będziński, 1997; Madej, 2008).

Both hip joint load models (Maquet's and Pauwels') present a system of forces impacting the pelvis (together with the upper part of the lower extremity) only in the coronal plane.

The model of the hip joint load, additionally considering the role of rotator muscles R_u which cause turning of the femur in relation to the pelvis (Fig. 4b), based on Maquet's model, is shown by Będziński (Będziński and Ściagała, 2004; Będziński, 1997). In this model, the iliotibial band can also move along the external surface of the great trochanter of femur. The loading system is constituted by the resultant forces of the hip joint: impact of the weight of torso on the femur head R , abductors M_a and the iliotibial band M, T (sliding on the great trochanter of femur) and rotational forces R_u . The author states (Będziński and Ściagała, 2004; Będziński, 1997; Madej and Ryniewicz, 2007; Madej, 2008; Ryniewicz and Madej, 2001, 2002) that the devised model

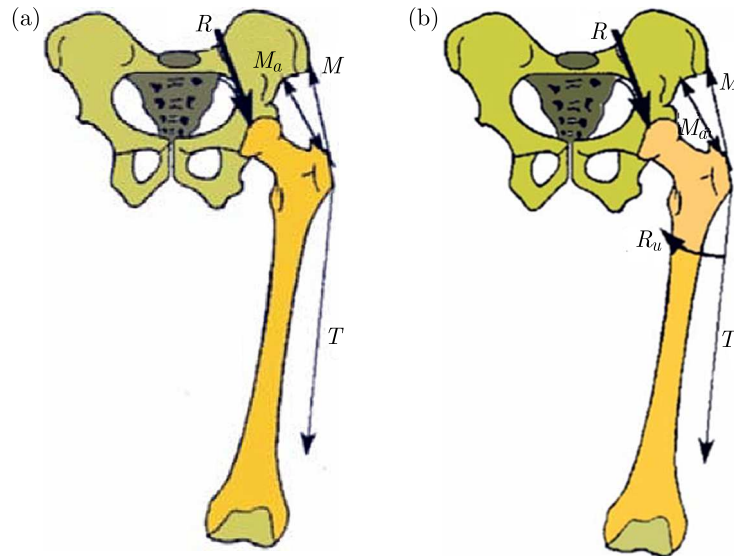


Fig. 4. (a) Maquet's hip joint load model (Będziński, 1997). (b) Będziński's model (devised at Zakład Doświadczalnej Analizy Konstrukcji Inżynierskich i Biomechanicznych) (Będziński and Ściagała, 2004; Będziński, 1997)

results from experimental studies conducted on physical models. The model groups the basic forces acting within functioning of the hip joint.

The aim of the analysis of the state of strain and deformation in an endoprosthesis of the hip joint, having an analytically revised model of the loads of this joint, is to assume the spatial hip joint load model according to Będziński.

4. Hip joint load

While defining loads for the needs of the studies, the model devised at Division of Experimental Analysis of Engineering and Biomechanical Structures of Wrocław University of Science and Technology by prof. R. Będziński has been assumed, as well as literature data taken from M. Bernakiewicz's PhD Dissertation (Bernakiewicz, 1999), and a unique software for analyzing gait HIP98, which enables to define values of forces and moments for each case of movement. The value of load for the studies is assumed based on Table 1 (Madej, 2008), in which values of the resultant force F acting upon the femur head in the case of performing movement are compiled. The values obtained from HIP98 software for different velocities of gait of particular patients and various phases – have been assumed after (Madej, 2008), based on literature (Bergman et al, 2001; Bernakiewicz, 1999; Bernakiewicz and Będziński, 1999). The aim of obtaining a comparative reference in terms of reliability of literature data, own studies have been performed at Clinic of Orthopedics and Rehabilitation of the 2nd Faculty of Medicine of Medical University of Warsaw, which include cases of patients (taking into account sex) occurring most often statistically, considering weight and load. The studies were performed for the following conditions: an 80 cm step forward without weight transfer and with total temporary transfer of weight to one foot and leap (maximum temporal result) of 100 cm from the platform for different weights (Table 2).

While performing a comparative analysis, it was concluded that in none of the cases the value of 1000 N of patient's body weight was exceeded. Arbitrarily, in strength analysis, it was decided to assume a certain surplus of load impacting the hip implant, the value of the vector of the resultant force $F = 300$ N. The load was assumed with a slight reserve of value in the light

Table 1. Values of reaction forces on the femur head for particular patients (Madej, 2008)

Phase of gait \ Patient		Phase of heel contact with the ground				Phase of standing on one foot			
		F_x	F_y	F_z	F	F_x	F_y	F_z	F
Resultant force % 100 BW		F_x	F_y	F_z	F	F_x	F_y	F_z	F
H.S. body weight 860 N	Slow gait 3.81 km/h	49	17	216	222	47	19	188	195
	Normal gait 4.41 km/h	49	22	231	237	42	16	175	181
	Fast gait 5.11 km/h	55	23	268	274	46	12	181	187
P.F. body weight 980 N	Slow gait 3.08 km/h	29	43	215	221	35	34	234	239
	Normal gait 3.71 km/h	29	35	197	202	30	23	206	209
	Fast gait 4.46 km/h	29	30	187	192	33	26	207	211
K.W. body weight 980 N	Slow gait 3.81 km/h	61	17	202	212	68	3	205	216
	Normal gait 4.05 km/h	67	20	230	240	59	-1	179	189
	Fast gait 4.64 km/h	73	19	251	262	58	4	167	177
Average for all patients	Slow gait 3.60 km/h	47	27	214	221	51	25	217	224
	Normal gait 4.09 km/h	47	23	210	216	54	8	200	207
	Fast gait 4.74 km/h	52	26	237	244	47	1	180	186

of not sufficient knowledge of the actual state of the hip joint load, according to the authors, with regard to not yet fully identified parameters of this load.

5. Geometry and conditions of the hip joint load

The assumed geometry of the cup implant system subject to strength analysis in conditions of the static load is shown in Fig. 5. The analyzed implants are a standard version, having preliminary holes which enable stabilization with a patient's bone using screws. For the assumed geometry of the model, tetra-meshing is applied, i.e. uneven division of the solid model continuum into finite elements of Tet10 type (quadrattetrahedron) is applied. Three identical cylindrical elements symbolize screws, which are screwed during a surgical procedure.

Strength analysis has been performed for the "trabecular metal" type of implants and titanium implants with the addition of niobium (Ti-6Al-7Nb), which possess primary holes enabling stabilization with a patient's bones using screws.

Mechanical properties for materials:

- "trabecular metal" – are assumed based on the article (Medlin *et al.*, 2004)

Young's modulus [MPa]	Poisson's ratio	Yield strength [MPa]	Tangent modulus [MPa]
3100	0.35	48.2 (± 5.9)	310

Table 2. Values of forces without and with transfer of weight on one foot and during leap

Sex	Weight [N]	Step forward without [N]	Step forward with [n]	Leap [N]
M	780	220	760	790
M	870	270	880	910
K	560	190	550	570
K	630	200	620	640
K	720	220	720	730
M	880	240	880	890
M	670	220	680	700
K	770	210	770	770
M	710	220	720	740
M	680	210	690	690
K	720	210	710	710
M	740	220	740	750
K	810	210	810	780
K	510	180	500	520
K	550	190	550	550
M	760	220	750	760
K	780	200	780	780
K	810	200	800	810
M	800	220	800	820
K	620	200	620	620
M	640	220	640	650
M	680	220	680	680
M	590	210	590	600
K	670	210	660	670
M	750	220	750	760
M	910	250	900	930
M	870	230	830	840
K	710	220	700	720
K	770	210	760	770

K – female, M – male

- titanium alloy with addition of niobium (Ti-6Al-7Nb) – assumed based on article (Li *et al.*, 2014)

Young's modulus [MPa]	Poisson's ratio	Yield strength [MPa]	Tangent modulus [MPa]
110000	0.36	min 800 (880-950)	5000

The analyzed case is the one of the implant load being in contact with the pelvic bone, as shown in Fig. 6. The pelvic bone is modeled conventionally, as a slice of a spherical cylinder, to which an augment cup implant is attached by means of 500 N tension screws (Fig. 6a), the pelvic bone is fixed (Fixed Support), as illustrated in Fig. 6b (blue spherical surface). The direction of impact of the acetabulum force F on the augment is illustrated by Fig. 7a. The load system of the implant by vectors of screw tension forces $F = 500$ N (axial forces resulting from fixing the cup augment to the pelvis) and the vector of the resultant force $F = 300$ N is illustrated by Fig. 7b.

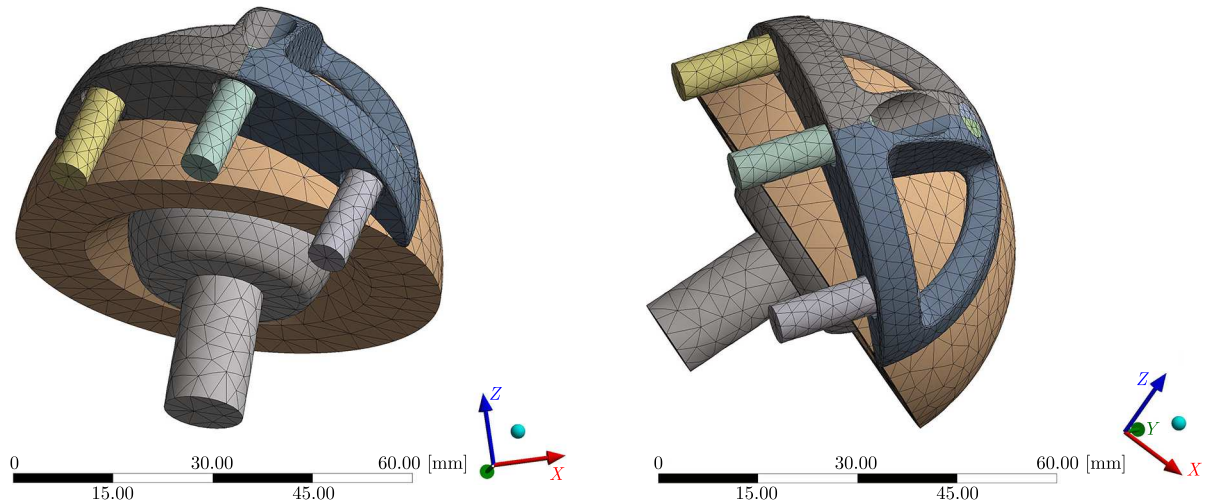


Fig. 5. Meshing process continuum of the cup implant model

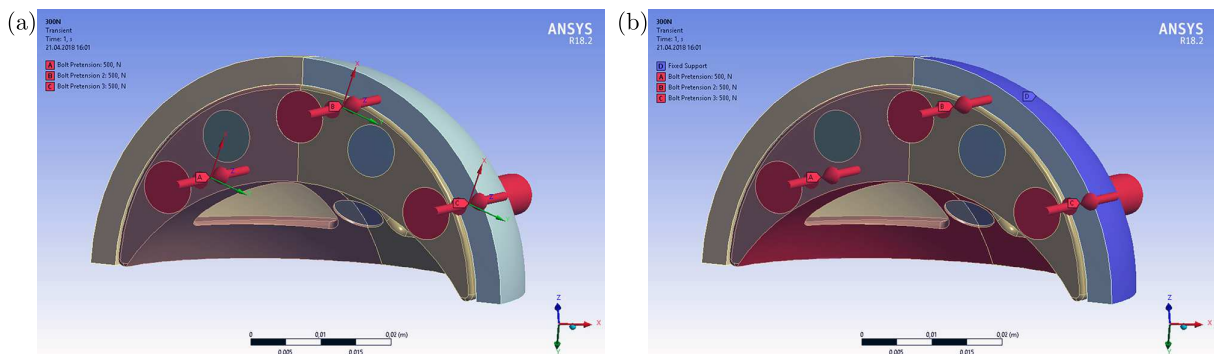


Fig. 6. Fixing the implant (cup augment) to the pelvic bone: (a) tension of screws (500 N), (b) fixed support of the pelvic bone (blue spherical surface)

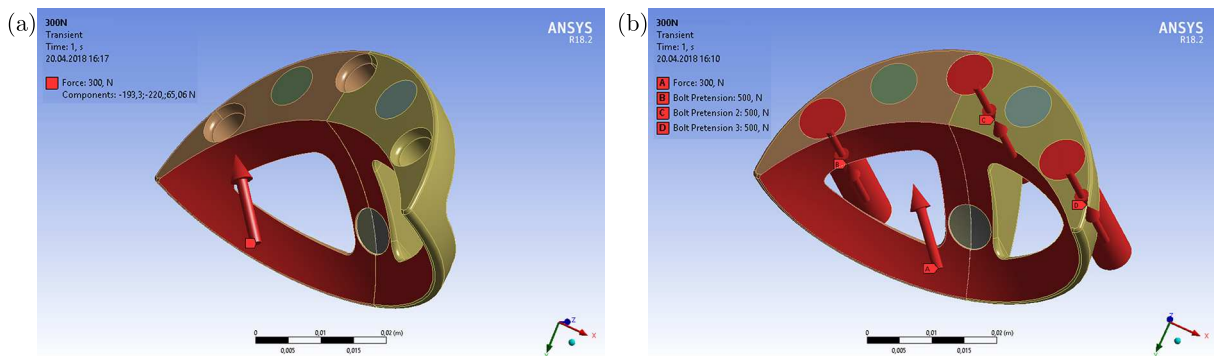


Fig. 7. System of implant (cup augment) load: (a) vector of the resultant force $F = 300$ N impacting the augment, (b) vectors of screw tension forces $F = 500$ N (axial forces resulting from fixing the augment to the pelvis) and the vector of the resultant force

Distribution (maps) of strain reduced according to HMM Hypothesis (Huber-Mises-Hencky hypothesis of specific energy of shear modulus) obtained by means of FEM analysis for the case of the “trabecular metal” type of implants and titanium implants with addition of niobium (Ti-6Al-7Nb) are shown in Figs. 8 and 9. Distributions (maps) of total deformations of the cup augment for these two cases of implant materials are shown in Figs. 10 and 11, respectively.

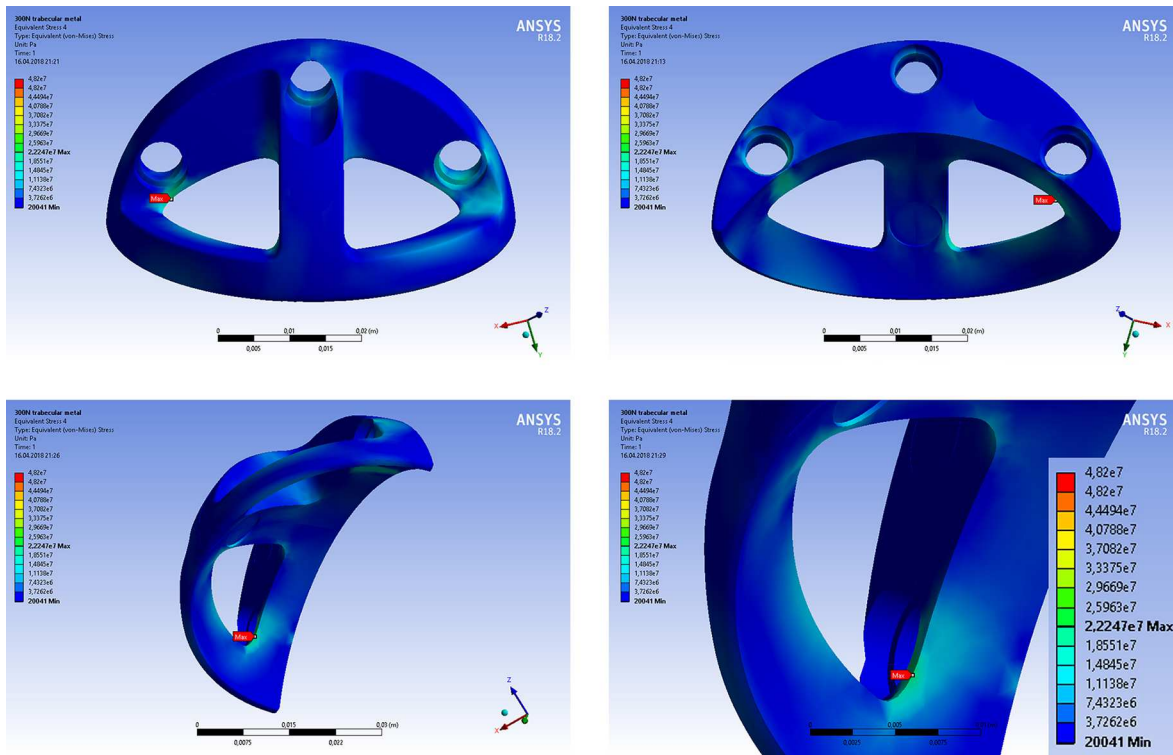


Fig. 8. Map of reduced strain according to HMH – “trabecular metal” tantalum implant loaded with a 300 N force

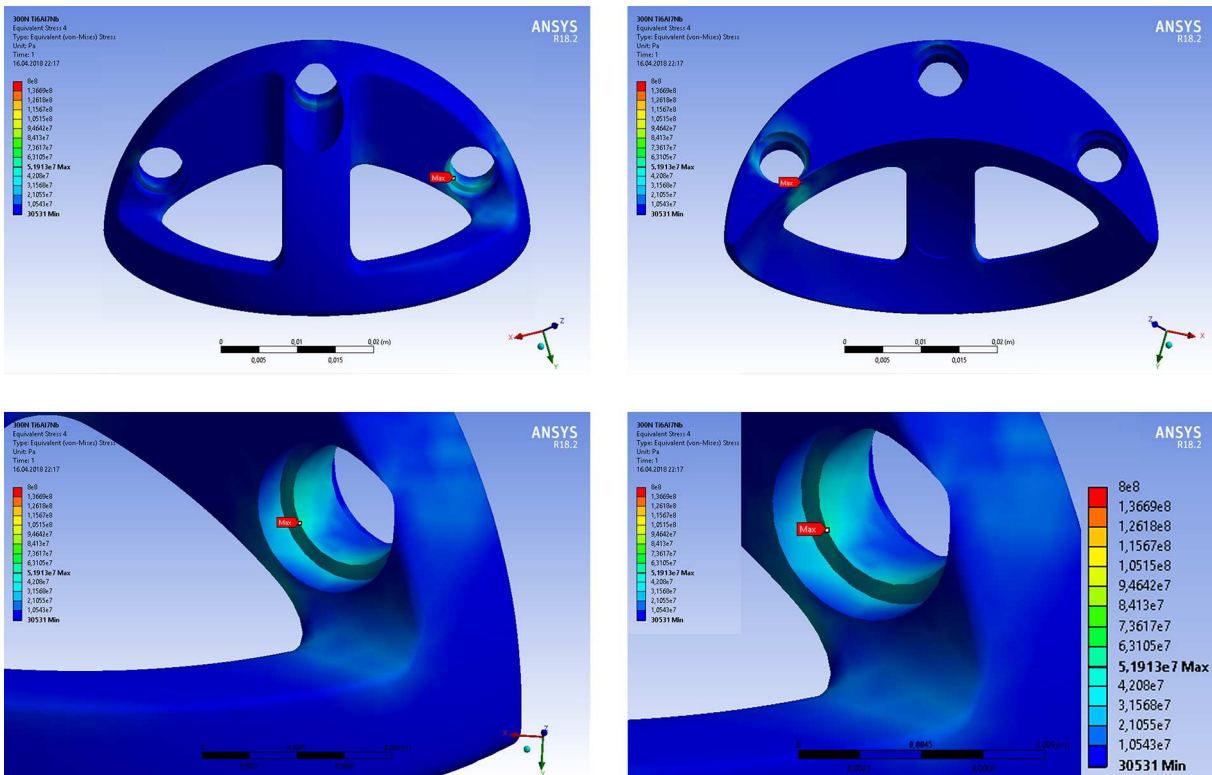


Fig. 9. Map of reduced strain according to HMH – titanium Ti-6Al-7Nb implant loaded with a 300 N force

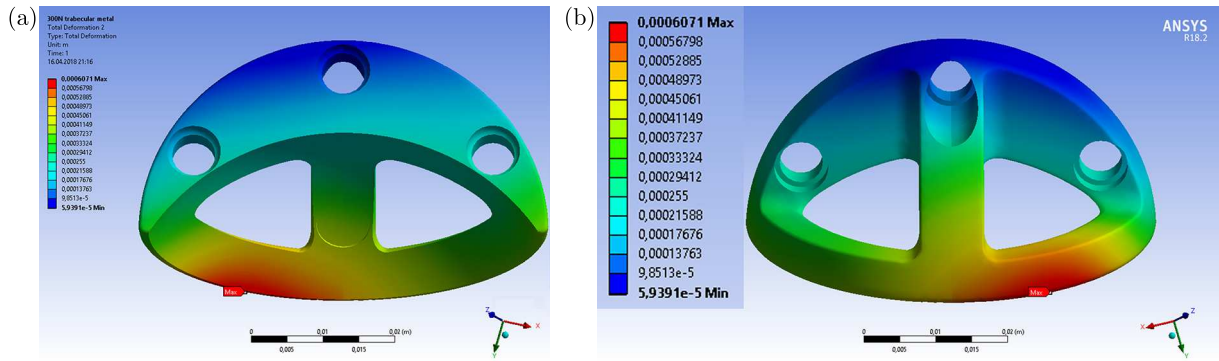


Fig. 10. Map of total deformations – “trabecular metal” tantalum implant loaded with a 300 N force

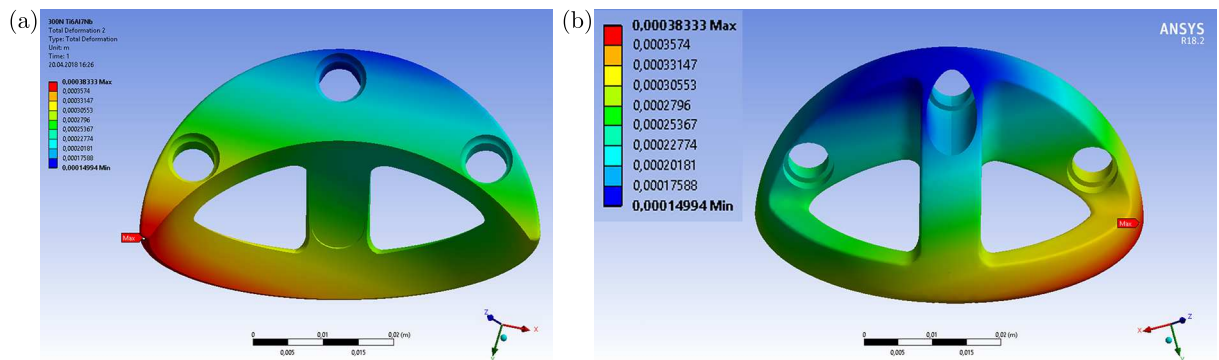


Fig. 11. Map of total deformations – titanium Ti-6Al-7Nb implant loaded with a 300 N force

In neither of the analyzed cases the values of reduced strains HMH reach the assumed ductility border $Re_{Tantalum} = 48.2$ MPa and $Re_{Titanium} = 800$ MPa. For the assumed maximum force $F = 300$ N loading of implants, the highest values of reduced strain HMH reach about 46% $Re_{tm} = 22.3$ MPa for the “trabecular metal” tantalum implant and 6.5% $Re_{Ti} = 52$ MPa for titanium Ti-6Al-7Nb implant, respectively. The maximum values of the reduced strain according to HMH occur around the fixing holes and are connected with the concentration of strains around them.

Local concentrations of strains around holes result from screw tension forces, and are connected with the assumed boundary conditions. In the actual system, where the analyzed implant will cooperate fixed to the pelvic bone (especially after it bonds with the bone), the risk of implant damage as a result of strain concentration will not occur. It has to be stressed, however, that the maximum total deformations occur in the lower rim of the cup implant and may result from the pressure of the augment on the pelvic bone due to uneven pressure during acetabulum impact. The values of maximum deformations amount to about 0.607 mm for the “trabecular metal” tantalum implant, and to 0.383 mm for the titanium implant respectively. It can be noticed, however, that the total deformations around the holes for the implant made of the “trabecular metal” material are about 50% smaller, and do not exceed approximately 0.3 mm. For the implant made of Ti-6Al-7Nb, a slight displacement of the simulated pressure of the augment to the pelvic bone occurred (along the lower rim of the cup implant towards the sharp edge), thus relatively higher values of total deformations around the hole occur, amounting to approximately 80% of the maximum, but do not exceed 0.3 mm.

The analyzed issue is considered as a static analysis. Apart from the value of the load force F , a fatigue character of the operation of the analyzed system, subject to permanent movement load, ought to be noticed.

6. Conclusions

The conducted preliminary simulation studies enable strength evaluation of “trabecular metal” tantalum implants and titanium implants with addition of niobium (Ti-6Al-7Nb). The results of performed numerical analyses indicate that implants with standard holes (i.e. without mechanical interference connected with non-standard stabilization with a patient’s bone) fulfill the strength requirements in conditions of the maximum strain in the assumed implant load system.

It has to be kept in mind, however, that during non-standard stabilization connected with drilling additional fixing holes, the implant fatigue strength R_z may decrease, which may lead to further damage. So far, it has not been studied how mechanical interference with the implant structure and their modification by drilling more holes influences the mechanical properties of such a system, i.e. change in implant ductility in terms of implant strength after drilling additional holes. The reports on the strength of the structure after drilling the holes, as well as after prolonged functioning of such implants, are scarce (Bobyn *et al.*, 1999; Levine *et al.*, 2006; Meneghini *et al.*, 2010; Meneghini *et al.*, 2010). Attention needs to be drawn to a series of significant issues connected with the risk of:

- decreasing strength and elasticity of an implant modified with holes,
- damage to prosthesis articulation caused by pieces of metal which remain after drilling and/or prior loosening of the implant,
- migration of particles in the circulatory system, nephrotoxicity while using alloys with addition of Al, Ni and V, influence of metal ions and implant corrosion around the prosthesis and weakening of implant osseointegration.

Further studies ought to identify:

- The influence of additional holes in medical implants made of Ti and Ta alloys on strength properties of such implants. During bone reconstruction of the hip joint, it is often required to perform additional holes for the needs of stabilization techniques connected with a significant bone loss.
- The influence of dependence of the remaining in the surgical field mass of metal ions on prosthesis tribology.
- The influence of the mass of tantalum and titanium particles and rare metal ions (such as Ni and V) on body toxicity.
- The risk of influence of metal ions and implant corrosion on periarticular tissues, together with the increase in the mass of tantalum and titanium, aluminum, niobium and vanadium particles.

Furthermore, studies should to be aimed at:

- Development of implant material with high mechanical properties, least possibly susceptible to weakening due to interference with the implant structure.
- Development of a technique of maximum removal of metal particles from the surgical field.

The above-mentioned issues define the authors’ goals in terms of further numerical studies of implants made of the “trabecular metal” and Ti-6Al-7Nb material.

References

1. BENOUIS A., BOULENOUAR A., SERIRER B., 2016, Finite element analysis of the behavior of a crack in the orthopedic cement, *Journal of Theoretical and Applied Mechanics*, **54**, 1, 277-284
2. BERGMAN G., GRAICHEN F., ROHLMANN A., 1993, Hip joint loading during walking and running, measured in two patients, *Journal Biomechanics*, **26**, 969-990.

3. BERGMAN G., GRAICHEN F., ROHLMANN A., 1995, Is stair case walking a risk for the fixation of hip implants? *Journal Biomechanics*, **28**, 532-533
4. BERGMAN G., DEURETZBAHER G., HELLER M., GRAICHEN F., ROHLMANN A., STRAUSS J., DUDA G.N., 2001, Hip contact forces and gait patterns from routine activities, *Journal of Biomechanics*, **34**, 859-871
5. BERNAKIEWICZ M., 1999, Elaboration the strain-stresses criteria for the selection of hip joint implants (in Polish), Ph.D. Thesis, Wrocław University of Science and Technology, Wrocław
6. BERNAKIEWICZ M., BĘDZIŃSKI R., 1999, An analysis of the stress state of femur under extreme load conditions (in Polish), *Zeszyty Naukowe Konferencji Mechaniki Stosowanej*, **9**, 15-21
7. BERNAKIEWICZ M., 1994, The concept of constructional solution of the prosthetic nail of hip joint cementless endoprosthesis (in Polish), *Biomechanika*, **94** (Prace Naukowe Instytutu Konstrukcji i Eksploatacji Politechniki Wrocławskiej, nr 75, Seria: Konferencje nr 21, Wrocław), 19-22
8. BĘDZIŃSKI R., 1997, *Engineering Biomechanics. Selected Issues* (in Polish), Oficyna wydawnicza Politechniki Wrocławskiej, Wrocław
9. BĘDZIŃSKI R., ŚCIGAŁA K., 2004, Biomechanics of the hip joint and knee joint (in Polish), [In:] *Biocybernetyka i Inżynieria Rehabilitacyjna*, **5**, Będziniński R. (Edit.), Akademicka Oficyna Wydawnicza Exit, Warszawa
10. BOBYN J.D., STACKPOOL G.J., HACKING S.A., TANZER M., KRYGIER J.J., 1999, Characteristics of bone ingrowth and interface mechanics of a new porous tantalum biomaterial, *Journal of Bone and Joint Surgery. British Volume*, **81**, 5, 907-914
11. BOMBELI R., 1983, *Structure and Function in Normal and Abnormal Hips*, Springer-Verlag, Berlin
12. DĄBROWSKA-TKACZYK A., 1999, Modeling stress and strain distribution in the pelvic bone during quasi-static backward rotation, *Proceedings Biomechanics 99, Acta of Bioengineering and Biomechanics V*, **1**, 93-96
13. DORMAN T., KMIEĆ K., POGONOWICZ E., SIBIŃSKI M., SYNDER M., KOZŁOWSKI P., 2011, Revision treatments in large acetabulum cavities using cup augment (in Polish), *Chirurgia Narządu Ruchu i Ortopedia Polska*, **76**, 1, 21-24
14. DRAGAN S., 1992, Studies on the influence of construction of the prosthetic nail of cementless endoprosthesis and the distribution of forces in femur under the influence of loads on disturbances of primary stability (in Polish), Ph.D. Thesis, Medical Academy, Wrocław
15. DRAGAN S., 2004, Clinical and biomechanical aspects of osteointegration course of hip joint endoprostheses (in Polish), [In:] *Biocybernetyka i Inżynieria Rehabilitacyjna*, **5**, Będziniński R. (Edit.), Akademicka Oficyna Wydawnicza Exit, Warszawa
16. HACKING S.A., BOBYN J.D., TOH K., TÄNZER M., KRYGIER J.J., 2000, Fibrous tissue ingrowth and attachment to porous tantalum, *Journal of Biomedical Materials Research*, **52**, 4, 631-638
17. HARRIS W.H., 1992, The problem is osteolysis, *Clinical Orthopaedics*, **247**, 6-11
18. LEVINE B.R., SPORER S., POGGIE R.A., DELIA VALLE C.J., JACOBS J.J., 2006, Experimental and clinical performance of porous tantalum in orthopedic surgery, *Biomaterials*, **27**, 4671-4681
19. LI Y., YANG C., ZHAO H., QU S., LI X., LI Y., 2014, New developments of Ti-based alloys for biomedical applications, *Materials*, **7**, 1709-1800
20. MADEJ T., RYNIOWICZ A.M., 2007, Simulation of contact mechanics with a complex load condition in the hip joint endoprosthesis (in Polish), *Materiały konferencyjne, IV Krakowskie Warsztaty Inżynierii Medycznej*, Kraków
21. MADEJ T., 2008, Modeling the movement zone of the hip joint endoprosthesis in the aspect of biomaterials (in Polish), Ph.D. Thesis, AGH University of Science and Technology, Kraków
22. MAQUET P.G.J., 1985, *Biomechanics of the Hip*, Berlin

23. MEDLIN D.J., CHARLEBOIS S., SWARTS D., SHETTY R., POGGIE R.A., 2004, Metallurgical characterization of a porous Tantalum biomaterial (Trabecular metal) for orthopaedic implant applications, *Medical Device Materials: Proceedings of the Materials and Processes for Medical Conference*, S. Shrivastava (Edit.), 394-398
24. MENEGHINI R.M., FORD K.S., MCCOLLOUGH C.H., HANSEN A.D., LEWALLEN D.G., 2010, Bone remodeling around porous metal cementless acetabular components, *Journal Arthroplasty*, **25**, 5, 741-747
25. MENEGHINI R.M., MEYER C., BUCKLEY C.A., HANSEN A.D., LEWALLEN D.G., 2010, Mechanical stability of novel highly porous metal acetabular components in revision total hip arthroplasty, *Journal of Arthroplasty*, **25**, 3, 337-341
26. PAUWELS F., 1976, *Biomechanics of the Locomotor Apparatus*, Berlin
27. POPOVIC M., HOFMANN A., HERR H., 2004, Angular momentum regulation during human walking: biomechanics and control, *Proceedings - IEEE International Conference on Robotics and Automation, ICRA 2004*, New Orleans, LA, USA, **3**, 3, 2405-2411
28. RYNIOWICZ A.M., MADEJ T., 2001, The influence technology parameters on tribology properties films have been obtained by chemical vapour deposition, *Proceedings of the 12th International DAAAM Symposium Technical University of Vienna*, 417-418
29. RYNIOWICZ A.M., MADEJ T., 2002, Analysis of stresses and displacements in the working zone of the hip joint endoprosthesis (in Polish), *Mechanika w Medycynie*, **6**, 127-134
30. WŁODARSKI J., 2005, Stability of hip joint cement endoprostheses in the light of histological, numerical and experimental studies (in Polish), *Bio-Algorithms and Med-Systems*, **1**, 2, 197-204

Manuscript received June 15, 2018; accepted for print September 24, 2018

MODELLING OF BIOLOGICAL TISSUE DAMAGE PROCESS WITH APPLICATION OF INTERVAL ARITHMETIC

ANNA KORCZAK, MAREK JASIŃSKI

Silesian University of Technology, Institute of Computational Mechanics and Engineering, Gliwice, Poland
e-mail: anna.korczak@polsl.pl; marek.jasinski@polsl.pl

In the paper, the numerical analysis of thermal processes proceeding in a 2D soft biological tissue subjected to laser irradiation is presented. The transient heat transfer is described by the bioheat transfer equation in Pennes formulation. The internal heat source resulting from the laser-tissue interaction based on the solution of the diffusion equation is taken into account. Thermophysical and optical parameters of the tissue are assumed as directed intervals numbers. At the stage of numerical realization, the interval finite difference method has been applied. In the final part of the paper, the results obtained are shown.

Keywords: directed interval arithmetic, bioheat transfer, optical diffusion equation, Arrhenius scheme

1. Introduction

One of the common problems in mathematical modelling of biological systems is the significant variation in the parameters that may result from, among others, individual characteristics. For some parameters, imprecisions in the estimation of their values may be a result of different measurement methods or specific features of tissues. The measurement is not often possible in a living organism. This may cause the values of individual parameters found in the literature to differ significantly from one another. It is also worth noting that tissue parameters may have different values depending on their degree of thermal damage. For example, the value of the scattering coefficient of tissue during the tissue damage process increases several times, what could be observed as “whitening” of the tissue (Jasiński, 2015).

One of the most widely used mathematical tools to take into account uncertainties of parameters are sensitivity analysis methods. By using them, very different problems were analysed, also in the field of heat transfer in the living organism (Jasiński, 2014; Kałuża *et al.*, 2017; Mochnacki and Ciesielski, 2016). The approach using interval or fuzzy numbers is slightly less frequently used, although one can find works in which thermal processes in the human skin or eye are under consideration (Jankowska and Sypniewska-Kaminska, 2012; Mochnacki and Piasecka-Belkhat, 2013; Piasecka-Belkhat and Jasiński, 2011). The other initial-boundary value problems for partial differential equations were also considered in many fields of science (Gajda *et al.*, 2000; Di Lizia *et al.*, 2014; Nakao, 2017).

One can distinguish between two types of interval arithmetic: directed and classical (Dawood, 2011; Hansen and Walster, 2004; Markov, 1995; Popova, 1994). Classical interval arithmetic was proposed in the 60s of the last century by Moore (1966). The two kinds of arithmetic differ mainly in the definition of an interval and the set of arithmetic operations. A classical interval $\bar{x} = [a, b]$ is defined as a set of real numbers that are between the lower bound a and upper bound b like $\bar{x} = \{x \in \mathbb{R} \mid a \leq x \leq b\}$ while a directed interval is defined by only a pair of real numbers as $\bar{x} = [a, b]$ where $a, b \in \mathbb{R}$. Because of that, during successive calculations based on the classical interval arithmetic and many computational methods, including methods based

on finite differences applied, the widths of intervals increase what leads to the so-called range overestimation problem (Hansen and Walster, 2004; Markov, 1995; Nakao, 2017). Using the directed interval arithmetic, it is possible to obtain the point (degenerated) interval $[0, 0] = 0$ by subtraction of two identical intervals $\bar{a} - \bar{a} = [0, 0]$ and the point interval $[1, 1] = 1$ as the result of the division $\bar{a}/\bar{a} = 1$, which is impossible when applying the classical interval arithmetic. From a practical point of view, it is the most important one and causes the directed interval arithmetic to be popular in numerical applications (Dawood, 2011; Piasecka-Belkhatay and Korczak, 2016, 2017).

Modelling of laser-biological tissue interactions requires appropriate mathematical description. It is known that the scattering dominates over the absorption in soft tissues for wavelengths between 650 and 1,300 nm (so-called biological window). Because of this, usually the radiative transport equation is taken into account (Dombrovsky and Baillis, 2010). There are several modifications in the discrete ordinates method or statistical Monte Carlo methods which are used to solve this equation (Banerjee and Sharma, 2010; Welch, 2011). In some cases, it is possible to approximate the light transport using the diffusion equation (Dombrovsky *et al.*, 2013; Fasano *et al.*, 2010; Jacques and Pogue, 2008).

Modelling of the laser energy deposition is the first step in the modelling of physical processes proceeding in biological tissues subjected to a laser beam. Next, the temperature distribution must be calculated by making use of the bioheat transfer equation. The Pennes equation is the earliest one known but is probably still the most popular and widely used (Abraham and Sparrow, 2007; Majchrzak and Mochnacki, 2017; Paruch, 2014). The newest achievements in this field are based on the porous media theory (GDPL equation, generalized dual-phase lag equation) which takes into account the heterogeneous structure of biological tissue (Jasiński *et al.*, 2016; Majchrzak and Mochnacki, 2017; Majchrzak *et al.*, 2015).

The last step in the analysis of the tissue heating process is to estimate the degree of its destruction (Abraham and Sparrow, 2007; Henriques, 1947; Jasiński, 2018). The Arrhenius injury integral is the most frequently applied tool for this purpose, although other models (e.g. thermal dose) are also used (Mochnacki and Piasecka-Belkhatay, 2013). The Arrhenius scheme assumes the exponential dependence between temperature and the degree of tissue destruction. Furthermore, it refers only to the irreversible tissue damage, however, there are models which allow one to take into account the withdrawal of tissue injury in the case of temporary, small local increasing of temperature (Jasiński, 2014, 2018).

The purpose of this paper is to analyse the phenomena occurring in the laser-treated soft tissue wherein thermophysical and optical parameters are defined and treated as directed interval numbers. The analysis is based on the bioheat transfer equation in the Pennes formulation, whereas, to describe the light distribution in tissue the steady-state diffuse approximation is used. The degree of tissue destruction is also estimated by the use of the Arrhenius scheme. At the stage of numerical realisation, the interval finite difference method is used (Majchrzak and Mochnacki, 2016, 2017; Mochnacki and Suchy, 1995).

2. Formulation of the problem

A transient heat transfer in biological tissue is described by the Pennes equation. The interval form of this equation can be expressed in the form (Abraham and Sparrow, 2007; Jankowska and Sypniewska-Kaminska, 2012; Jasiński, 2014; Paruch, 2014)

$$\mathbf{x} \in \Omega : \quad \bar{c} \frac{\partial \bar{T}}{\partial t} = \bar{\lambda} \nabla^2 \bar{T} + \bar{Q}_{perf} + \bar{Q}_{met} + \bar{Q}_{las} \quad (2.1)$$

where $\bar{\lambda}$ [$\text{Wm}^{-1}\text{K}^{-1}$] is the interval thermal conductivity, \bar{c} [$\text{Jm}^{-3}\text{K}^{-1}$] is the interval volumetric specific heat, \bar{Q}_{perf} , \bar{Q}_{met} and \bar{Q}_{las} [Wm^{-3}] are the interval internal heat sources containing

information connected with the perfusion, metabolism and laser irradiation, respectively, while $\bar{T} = \bar{T}(\mathbf{x}, t)$ [K] is the interval temperature.

In this paper, the 2D domain of homogeneous biological tissue of a rectangular shape Ω subjected to the laser action is considered (Fig. 1).

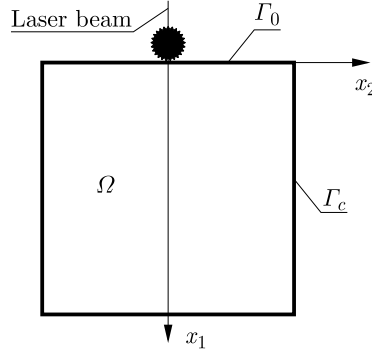


Fig. 1. The domain considered

Equation (2.1) is supplemented by the Robin condition assumed on the external boundary of tissue Γ_0 , which is subjected to laser irradiation while on the remaining parts of the boundary Γ_c the no-flux condition is accepted

$$\begin{aligned} \mathbf{x} \in \Gamma_0 : \quad & \bar{q}(\mathbf{x}, t) = \alpha(\bar{T} - T_{amb}) \\ \mathbf{x} \in \Gamma_c : \quad & \bar{q}(\mathbf{x}, t) = 0 \end{aligned} \quad (2.2)$$

where α [$\text{Wm}^{-2}\text{K}^{-1}$] is the convective heat transfer coefficient and T_{amb} is temperature of the surroundings. The initial distribution of temperature is also known

$$\mathbf{x} \in \Omega, t = 0 : \quad T(\mathbf{x}, t) = T_p \quad (2.3)$$

In the current work, the metabolic heat source \bar{Q}_{met} [Wm^{-3}] is assumed as a constant interval parameter while the perfusion heat source is described by the formula

$$\bar{Q}_{perf}(\mathbf{x}, t) = c_B \bar{w} [T_B - \bar{T}(\mathbf{x}, t)] \quad (2.4)$$

where \bar{w} [s^{-1}] is the interval perfusion coefficient, c_B [$\text{Jm}^{-3}\text{K}^{-1}$] is the volumetric specific heat of blood and T_B corresponds to the arterial temperature (Abraham and Sparrow, 2007; Mochnacki and Piasecka, 2013).

The source function \bar{Q}_{las} connected with the laser heating is defined as follows (Jasiński *et al.*, 2016)

$$\bar{Q}_{las}(\mathbf{x}, t) = \bar{\mu}_a \bar{\phi}(\mathbf{x}) p(t) \quad (2.5)$$

where $\bar{\mu}_a$ [m^{-1}] is the interval absorption coefficient, $\bar{\phi}(\mathbf{x})$ [Wm^{-2}] is the interval total light fluence rate and $p(t)$ is the function equal to 1 when the laser is on and equal to 0 when the laser is off.

The total interval light fluence rate $\bar{\phi}$ is the sum of the interval collimated part $\bar{\phi}_c$ and diffuse part $\bar{\phi}_d$ (Banerjee and Sharma, 2010; Dombrovsky *et al.*, 2013)

$$\bar{\phi}(\mathbf{x}) = \bar{\phi}_c(\mathbf{x}) + \bar{\phi}_d(\mathbf{x}) \quad (2.6)$$

The collimated fluence rate is given as (Jasiński *et al.*, 2016)

$$\bar{\phi}_c(\mathbf{x}) = \phi_0 \exp\left(-\frac{2x_2^2}{r^2}\right) \exp(-\bar{\mu}'_t x_1) \quad (2.7)$$

where ϕ_0 [Wm^{-2}] is the surface irradiance of laser, r is the radius of the laser beam and $\bar{\mu}'_t$ [m^{-1}] is the interval attenuation coefficient defined as (Banerjee and Sharma, 2010)

$$\bar{\mu}'_t = \bar{\mu}_a + \bar{\mu}'_s = \bar{\mu}_a + (1 - g)\bar{\mu}_s \quad (2.8)$$

where $\bar{\mu}_s$ and $\bar{\mu}'_s$ [m^{-1}] are the interval scattering coefficient and the effective scattering coefficient, respectively, while g is the anisotropy factor.

To determine the interval diffuse fluence rate $\bar{\phi}_d$, the steady-state optical diffusion equation should be solved (Dombrovsky *et al.*, 2013; Welch, 2011)

$$\mathbf{x} \in \Omega : \quad \bar{D}\nabla^2\bar{\phi}_d(\mathbf{x}) - \bar{\mu}_a\bar{\phi}_d(\mathbf{x}) + \bar{\mu}'_s\bar{\phi}_c(\mathbf{x}) = 0 \quad (2.9)$$

where

$$\bar{D} = \frac{1}{3[\bar{\mu}_a + (1 - g)\bar{\mu}_s]} = \frac{1}{3\bar{\mu}'_t} \quad (2.10)$$

is the interval diffusion coefficient.

Equation (2.9) is supplemented by the boundary conditions on the boundaries Γ_0 and Γ_c

$$\mathbf{x} \in \Gamma_0, \Gamma_c : \quad -\bar{D}\mathbf{n} \cdot \nabla\bar{\phi}_d(\mathbf{x}) = \frac{\bar{\phi}_d(\mathbf{x})}{2} \quad (2.11)$$

where \mathbf{n} is the outward unit normal vector.

Damage of biological tissue resulting from temperature elevation is modelled by the Arrhenius injury integral, and its interval version considered in this paper is defined as (Abraham and Sparrow, 2007; Fasano *et al.*, 2010; Henriques, 1947; Mochnacki and Piasecka-Belkhat, 2013)

$$\bar{\Psi}(\mathbf{x}, t^F) = \int_0^{t^F} P \exp\left[-\frac{E}{RT(\mathbf{x}, t)}\right] dt \quad (2.12)$$

where R [$\text{J mole}^{-1}\text{K}^{-1}$] is the universal gas constant, E [J mole^{-1}] is the activation energy and P [s^{-1}] is the pre-exponential factor while $[0, t^F]$ is the considered time interval. The criterion for tissue necrosis is $\bar{\Psi}(\mathbf{x}) \geq 1$.

3. Method of solution

In this paper, both analyzed equations: the Pennes equation and the steady-state optical diffusion equation have been solved using the interval finite difference method (Mochnacki and Piasecka-Belkhat, 2013). The information about the directed interval arithmetic are presented in (Dawood, 2011; Piasecka-Belkhat, 2011; Popova, 2011).

In order to determine the function \bar{Q}_{las} at the internal node (i, j) (cf. equation (2.5)), steady-state optical diffusion equation (2.9) is solved. The uniform differential grid of dimension $2n \times 2n$ with spacing $h/2$ is used here (Fig. 2). Using such a differential grid, it is easier to take into account boundary conditions (2.11), because a part of the nodes is located exactly on the boundary Γ_0 and Γ_c . In addition, one can distinguish common grid nodes for the temperature and diffuse fluence rate.

The following differential quotients are used

$$\left(\frac{\partial^2\bar{\phi}_d}{\partial x_1^2}\right)_{i,j} = \frac{\bar{\phi}_{di+1,j} - 2\bar{\phi}_{di,j} + \bar{\phi}_{di-1,j}}{(h/2)^2} \quad \left(\frac{\partial^2\bar{\phi}_d}{\partial x_2^2}\right)_{i,j} = \frac{\bar{\phi}_{di,j+1} - 2\bar{\phi}_{di,j} + \bar{\phi}_{di,j-1}}{(h/2)^2} \quad (3.1)$$

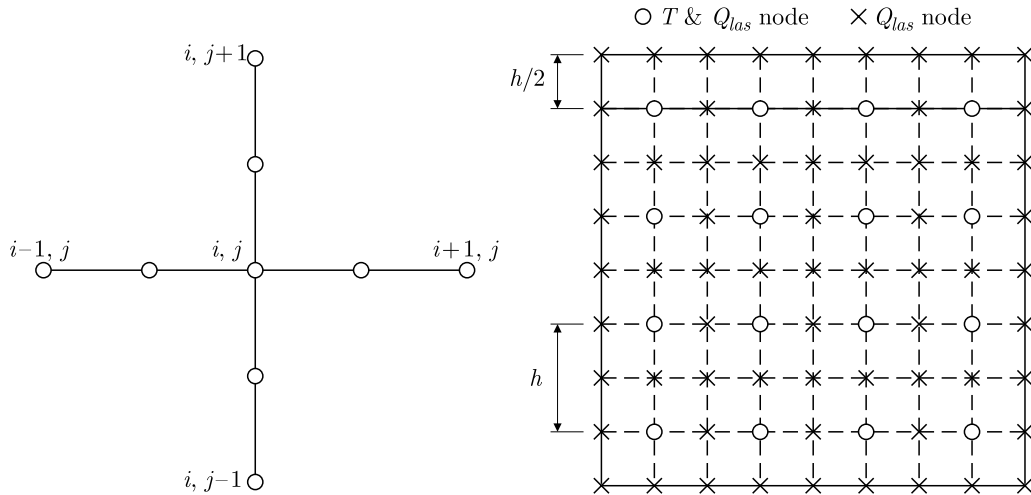


Fig. 2. Five-point stencil and differential grid

and then the approximate form of equation for the internal node (i, j) ($i = 1, 2, \dots, 2n - 1$, $j = 1, 2, \dots, 2n - 1$) is as follows

$$\bar{\phi}_{di,j} = \bar{C}_1 \bar{\Phi}_{di,j} + \bar{C}_2 \bar{\phi}_{ci,j} \tag{3.2}$$

where (superscripts “-” and “+” denote the beginning and the end of the interval, respectively)

$$\begin{aligned} \bar{\Phi}_{di,j} &= \bar{\phi}_{di-1,j} + \bar{\phi}_{di+1,j} + \bar{\phi}_{di,j+1} + \bar{\phi}_{di,j-1} \\ &= \phi_{di-1,j}^- + \phi_{di+1,j}^- + \phi_{di,j+1}^- + \phi_{di,j-1}^- + \phi_{di-1,j}^+ + \phi_{di+1,j}^+ + \phi_{di,j+1}^+ + \phi_{di,j-1}^+ \end{aligned} \tag{3.3}$$

while

$$\begin{aligned} \bar{C}_1 &= \frac{4\bar{D}}{16\bar{D} + h^2\bar{\mu}_a} = \frac{4[D^-, D^+]}{16[D^-, D^+] + h^2[\mu_a^-, \mu_a^+]} = \frac{[4D^-, 4D^+]}{[16D^- + h^2\mu_a^-, 16D^+ + h^2\mu_a^+]} \\ &= \left[\frac{4D^-}{16D^- + h^2\mu_a^-}, \frac{4D^+}{16D^+ + h^2\mu_a^+} \right] \\ \bar{C}_2 &= \frac{\bar{\mu}'_s h^2}{16\bar{D} + \bar{\mu}_a h^2} = \frac{h^2[\mu_s'^-, \mu_s'^+]}{16[D^-, D^+] + h^2[\mu_a^-, \mu_a^+]} = \frac{[h^2\mu_s'^-, h^2\mu_s'^+]}{[16D^- + h^2\mu_a^-, 16D^+ + h^2\mu_a^+]} \\ &= \left[\frac{h^2\mu_s'^-}{16D^- + h^2\mu_a^-}, \frac{h^2\mu_s'^+}{16D^+ + h^2\mu_a^+} \right] \end{aligned} \tag{3.4}$$

while for boundary nodes (cf. equation (2.11))

$$\begin{aligned} \bar{D} \frac{\bar{\phi}_{d1,j} - \bar{\phi}_{d0,j}}{h/2} &= \frac{1}{2} \bar{\phi}_{d0,j} \quad \rightarrow \quad \bar{\phi}_{d0,j} = \bar{C}_3 \bar{\phi}_{d1,j} \\ -\bar{D} \frac{\bar{\phi}_{dn,j} - \bar{\phi}_{dn-1,j}}{h/2} &= \frac{1}{2} \bar{\phi}_{dn,j} \quad \rightarrow \quad \bar{\phi}_{dn,j} = \bar{C}_3 \bar{\phi}_{dn-1,j} \\ \bar{D} \frac{\bar{\phi}_{di,j} - \bar{\phi}_{di,0}}{h/2} &= \frac{1}{2} \bar{\phi}_{di,0} \quad \rightarrow \quad \bar{\phi}_{di,0} = \bar{C}_3 \bar{\phi}_{di,1} \\ -\bar{D} \frac{\bar{\phi}_{di,n} - \bar{\phi}_{di,n-1}}{h/2} &= \frac{1}{2} \bar{\phi}_{di,n} \quad \rightarrow \quad \bar{\phi}_{di,n} = \bar{C}_3 \bar{\phi}_{di,n-1} \end{aligned} \tag{3.5}$$

where

$$\bar{C}_3 = \frac{4\bar{D}}{4\bar{D} + h} = \frac{4[D^-, D^+]}{4[D^-, D^+] + h^2} = \frac{[4D^-, 4D^+]}{[4D^- + h^2, 4D^+ + h^2]} = \left[\frac{4D^-}{4D^- + h^2}, \frac{4D^+}{4D^+ + h^2} \right] \tag{3.6}$$

It should be pointed out that the system of equations (3.2) is solved using the iterative method.

The differential quotients approximating the derivatives appearing in the Pennes equation (2.1) are defined in a similar, as previously, manner

$$\begin{aligned} \left(\frac{\partial^2 \bar{T}}{\partial x_1^2}\right)_{i,j} &= \frac{\bar{T}_{i+1,j} - 2\bar{T}_{i,j} + \bar{T}_{i-1,j}}{h^2} & \left(\frac{\partial^2 \bar{T}}{\partial x_2^2}\right)_{i,j} &= \frac{\bar{T}_{i,j+1} - 2\bar{T}_{i,j} + \bar{T}_{i,j-1}}{h^2} \\ \frac{\partial \bar{T}}{\partial t} &= \frac{\bar{T}_{i,j}^f - \bar{T}_{i,j}^{f-1}}{\Delta t} \end{aligned} \quad (3.7)$$

where Δt denotes the time step while $f-1$ and f are the subsequent time levels.

By introducing this formulas into (2.1), and after some mathematical operations for the internal nodes ($i = 1, 2, \dots, n, j = 1, 2, \dots, n$), one obtains

$$\bar{T}_{i,j}^f = \bar{A}_2 \bar{T}_{i,j}^{f-1} + \bar{A}_1 \bar{T}_{i,j}^{f-1} + \bar{A}_3 \quad (3.8)$$

where

$$\begin{aligned} \bar{T}_{i,j}^{f-1} &= \bar{T}_{i+1,j}^{f-1} + \bar{T}_{i-1,j}^{f-1} + \bar{T}_{i,j+1}^{f-1} + \bar{T}_{i,j-1}^{f-1} = \left[(T_{i+1,j}^{f-1})^- + (T_{i-1,j}^{f-1})^- + (T_{i,j+1}^{f-1})^- + (T_{i,j-1}^{f-1})^- \right. \\ &\quad \left. (T_{i+1,j}^{f-1})^+ + (T_{i-1,j}^{f-1})^+ + (T_{i,j+1}^{f-1})^+ + (T_{i,j-1}^{f-1})^+ \right] \end{aligned} \quad (3.9)$$

while

$$\begin{aligned} \bar{A}_1 &= \frac{\bar{\lambda} \Delta t}{\bar{c} h^2} = \frac{\Delta t [\lambda^-, \lambda^+]}{h^2 [c^-, c^+]} = \frac{[\Delta t \lambda^-, \Delta t \lambda^+]}{[h^2 c^-, h^2 c^+]} = \left[\frac{\Delta t \lambda^-}{h^2 c^-}, \frac{\Delta t \lambda^+}{h^2 c^+} \right] \\ \bar{A}_2 &= 1 - \bar{A}_1 - \frac{\bar{w} c_B \Delta t}{\bar{c}} = [1 - A_1^-, 1 - A_1^+] - \frac{c_B \Delta t [w^-, w^+]}{[c^-, c^+]} = [1 - A_1^-, 1 - A_1^+] \\ &\quad - \left[\frac{c_B \Delta t w^-}{c^-}, \frac{c_B \Delta t w^+}{c^+} \right] = \left[1 - A_1^- - \frac{c_B \Delta t w^-}{c^-}, 1 - A_1^+ - \frac{c_B \Delta t w^+}{c^+} \right] \\ \bar{A}_3 &= \frac{\Delta t}{\bar{c}} (\bar{w} c_B T_B + \bar{Q}_{met} + \bar{Q}_{las}) = \frac{\Delta t}{[c^-, c^+]} (c_B T_B [w^-, w^+] + [Q_{met}^-, Q_{met}^-] + [Q_{las}^-, Q_{las}^-]) \\ &= \left[\frac{\Delta t (c_B T_B w^- + Q_{met}^- + Q_{las}^-)}{c^-}, \frac{\Delta t (c_B T_B w^+ + Q_{met}^+ + Q_{las}^+)}{c^+} \right] \end{aligned} \quad (3.10)$$

The ‘‘boundary’’ nodes are located at the distance $0.5h$ from the boundary of the domain. This approach gives a better approximation of the Neumann and Robin boundary conditions, but the final form of the interval FDM equation for the boundary nodes are obtained in similar way. More details of this approach can be found in (Jasiński *et al.*, 2016; Majchrzak and Mochnacki, 2016, 2017).

On the basis of equation (3.8), the temperature at the node (i, j) for the time level can be found on the assumption that the stability condition for an explicit differential scheme is fulfilled (Mochnacki and Suchy, 1995).

4. Results of computations

At the stage of numerical computations, a 2D homogeneous tissue domain of size 4×4 cm during laser irradiation (Fig. 1) has been considered. The uniform differential grid with 40×40 nodes is introduced (Fig. 2). As has been already mentioned, the values of the effective scattering coefficient are different for the native and thermally-damaged (denaturated) tissue, so the two

simulations have been conducted (for $\mu'_s = \mu'_{s\,nat}$ and $\mu'_s = \mu'_{s\,den}$). The optical (μ_a, μ'_s) and thermophysical (λ, c, w, Q_{met}) parameters of the tissue are assumed as the directed interval numbers in form (Dombrovsky *et al.*, 2013; Popova, 2011)

$$\bar{p} = [p - 0.025p, p + 0.025p] \quad (4.1)$$

where p denotes the parameter.

The following data have been assuming in calculations: $\lambda = 0.609 \text{ Wm}^{-1}\text{K}^{-1}$, $c = 4.18 \text{ MJm}^{-3}\text{K}^{-1}$, $w = 0.00125 \text{ s}^{-1}$, $\mu_a = 40 \text{ m}^{-1}$, $\mu'_{s\,nat} = 1000 \text{ m}^{-1}$, $\mu'_{s\,den} = 4000 \text{ m}^{-1}$, $Q_{met} = 245 \text{ Wm}^{-3}$, $c_B = 3.9962 \text{ MJm}^{-3}\text{K}^{-1}$, $T_B = 37^\circ\text{C}$, $P = 3.1 \cdot 10^{98} \text{ s}^{-1}$, $E = 6.27 \cdot 10^5 \text{ J mole}^{-1}$, $R = 8.314 \text{ J mole}^{-1}\text{K}^{-1}$, $\phi_0 = 3 \cdot 10^5 \text{ Wcm}^{-2}$, $d = 2 \text{ mm}$, $t_{exp} = 25 \text{ s}$, $\alpha = 10 \text{ Wm}^{-2}\text{K}^{-1}$, $T_{amb} = 20^\circ\text{C}$, $T_p = 37^\circ\text{C}$, $\Delta t = 1 \text{ s}$.

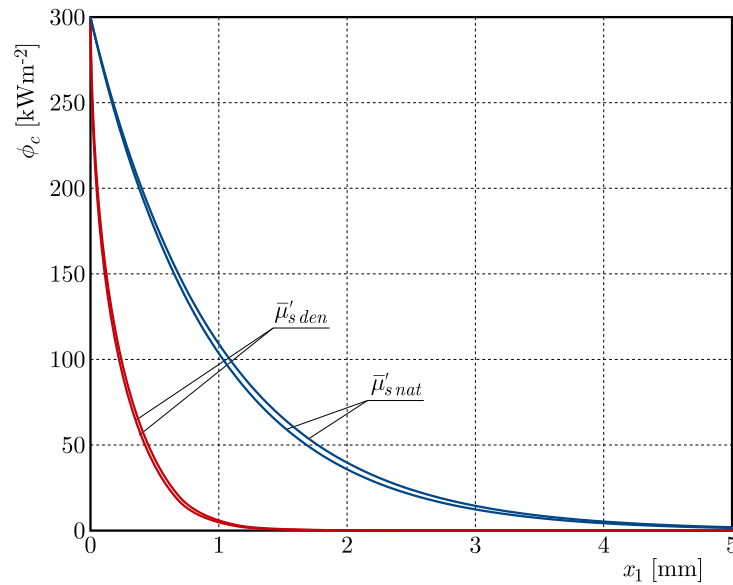


Fig. 3. Distribution of the interval collimated fluence rate $\bar{\phi}_c$ ($x_2 = 0$)

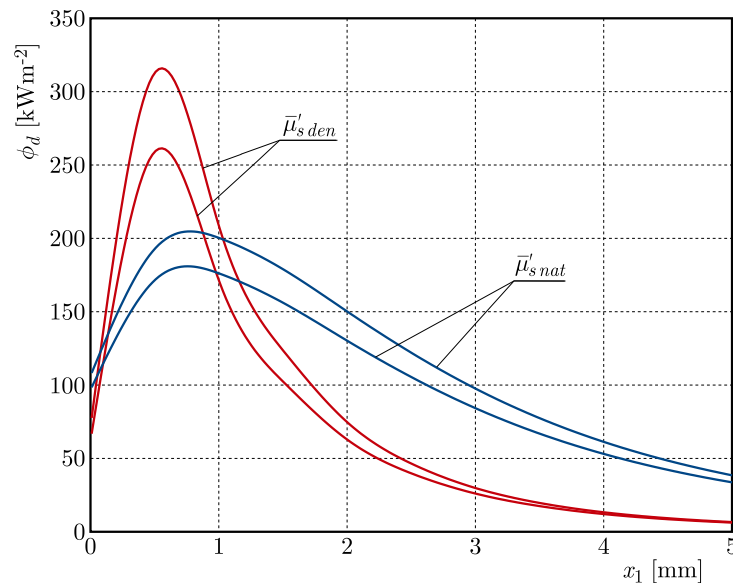


Fig. 4. Distribution of the interval diffuse fluence rate $\bar{\phi}_d$ ($x_2 = 0$)

Figures 3-5 are associated with the light fluence distribution in the domain considered. Figure 3 presents the distribution of the interval collimated fluence rate $\bar{\phi}_c$ calculated on the

basis of equation (2.7) while in Fig. 4 the distribution of the interval diffuse fluence rate $\bar{\phi}_d$ resulting from steady-state optical diffusion equation (2.9) is presented. The distribution of the interval diffuse fluence rate $\bar{\phi}_d$ is also presented in Fig. 5. It is visible that the area of scattering is larger in the case of calculation with $\bar{\mu}'_{s nat}$ although the values of $\bar{\phi}_d$ are lower than in the case of calculation with $\bar{\mu}'_{s den}$.

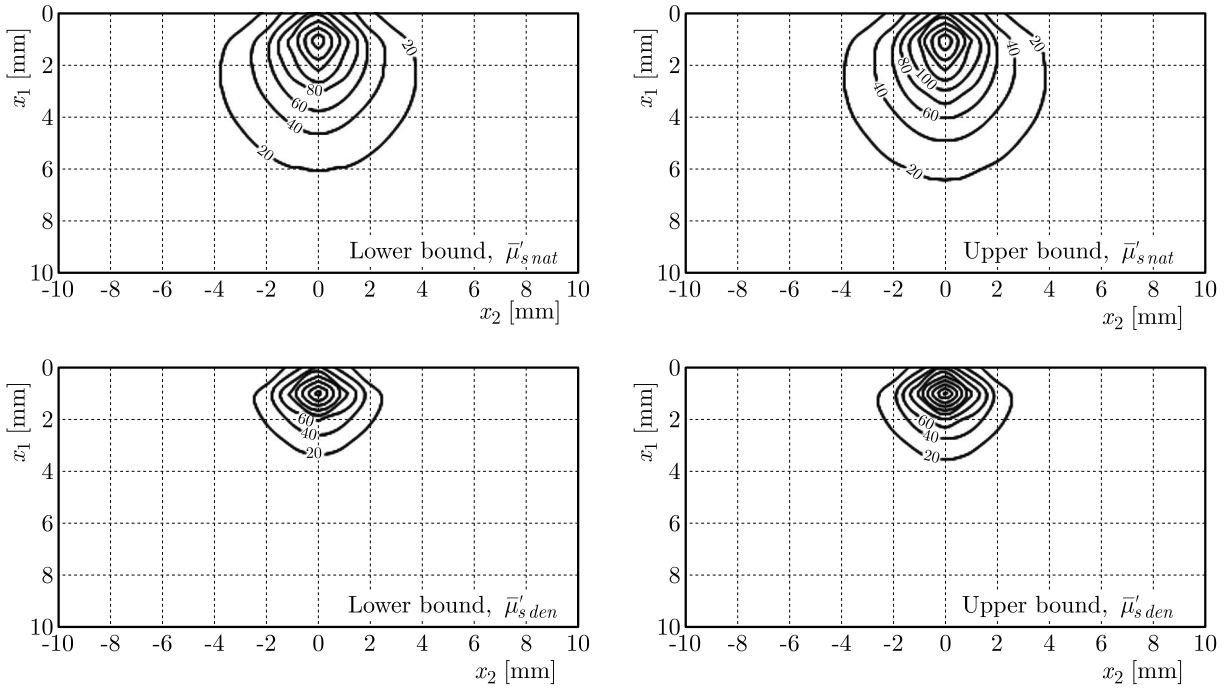


Fig. 5. Distribution of the interval diffuse fluence rate $\bar{\phi}_d$ [kWm^{-2}]

The next figure is associated with the tissue temperature. In Fig. 6, the interval tissue temperature history at the node $N_0(0,0)$ (Fig. 1) obtained for the effective scattering coefficient of native and denatured tissue is presented. As can be seen, wider temperature intervals are obtained in the case of denatured tissue.

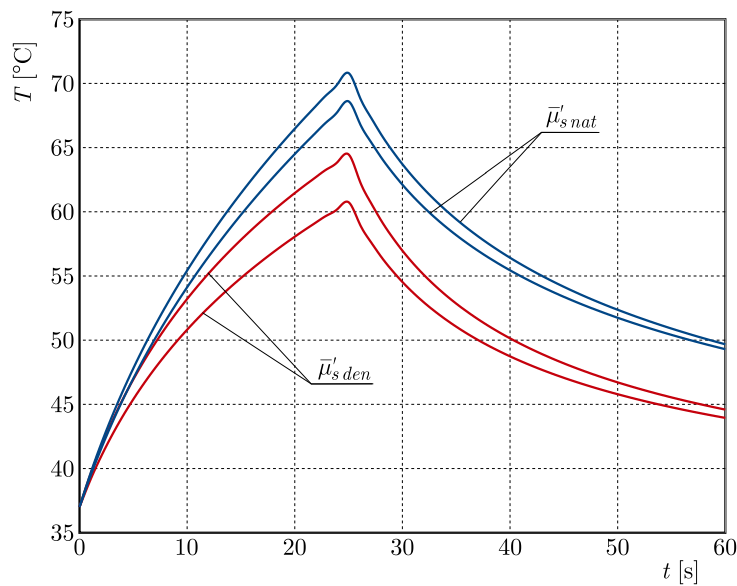


Fig. 6. History of interval tissue temperature at the node N_0

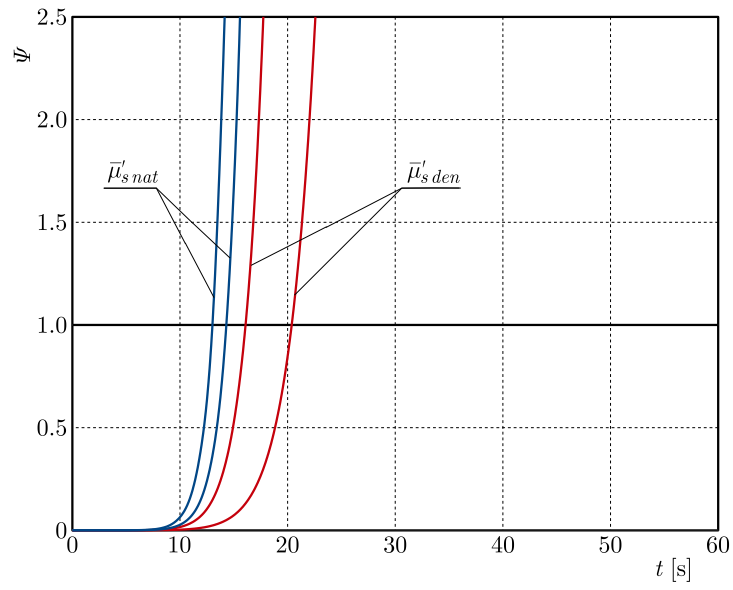


Fig. 7. History of the interval Arrhenius integral at the node N_0

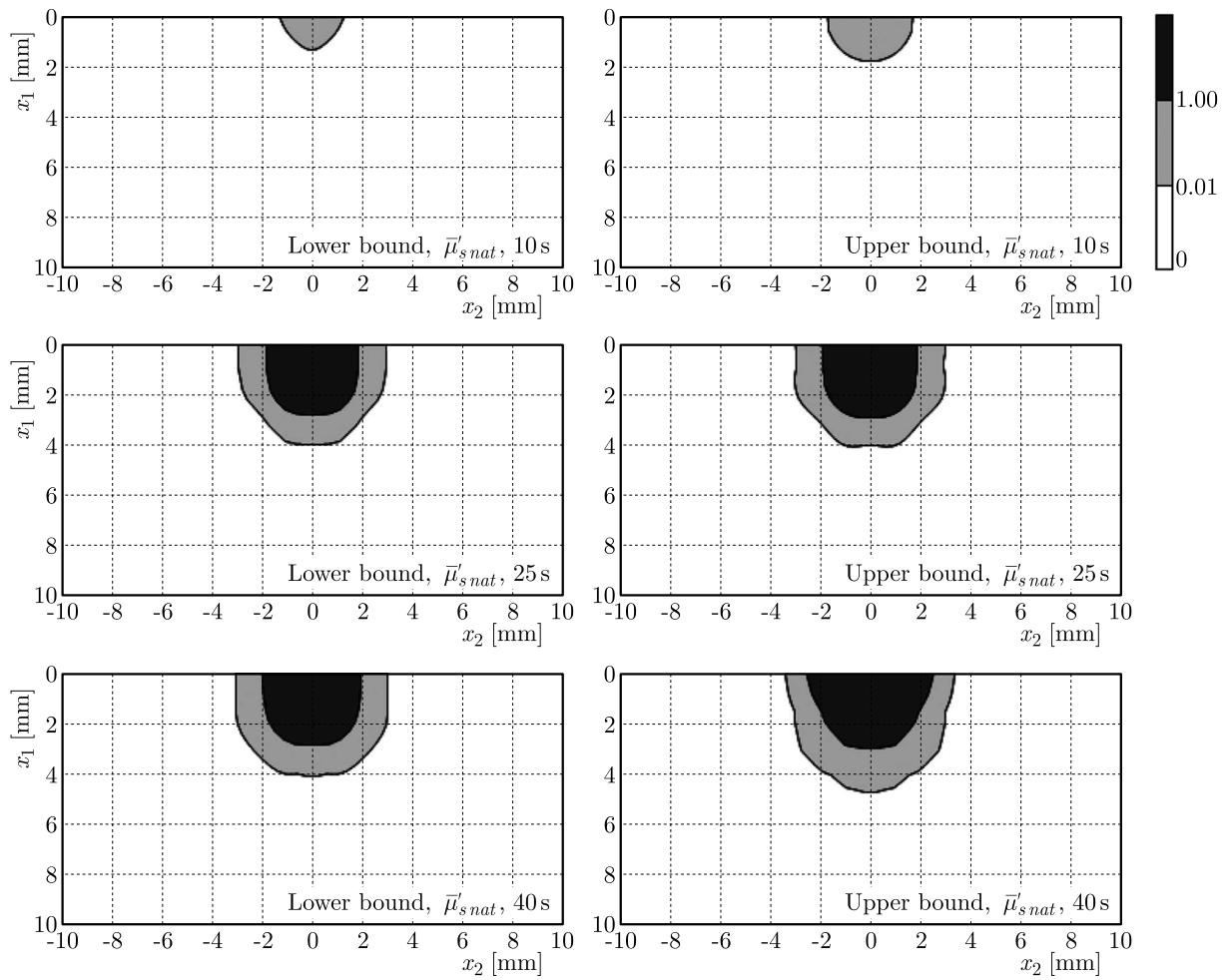


Fig. 8. Distributions of the interval Arrhenius injury integral for native tissue ($\bar{\mu}'_s = \bar{\mu}'_{s nat}$)

In Fig. 7, the history of the interval Arrhenius integral at the node N_0 is shown. As expected, due to the wider intervals obtained in the calculations with $\bar{\mu}'_{s den}$, wider intervals for the interval Arrhenius integral are also obtained for this variant of calculations. It is visible that tissue destruction occurs first in the case of native tissue – the injury integral reaches the necrosis criterion ($\Psi \geq 1$) in the time interval [14,15] s while for calculation with $\bar{\mu}'_{s den}$ this criterion is reached in the time interval [17,21] s.

The results associated with the tissue destruction are also presented in Figs. 8 and 9. In both figures, the interval injury integral distributions for selected time steps are presented. The white zone in these figures refers to the values of the injury integral below 0.01 (thermally untouched tissue), the grey zone refers to the values $0.01 < \Psi < 1$, so it is a partial damage area, and the black zone illustrates the area in which the Arrhenius integral achieved the criterion of tissue necrosis. In both cases, the coagulation zones obtained for the lower and upper bounds of intervals are slightly different, however, in the case of destroyed tissue the differences are bigger.

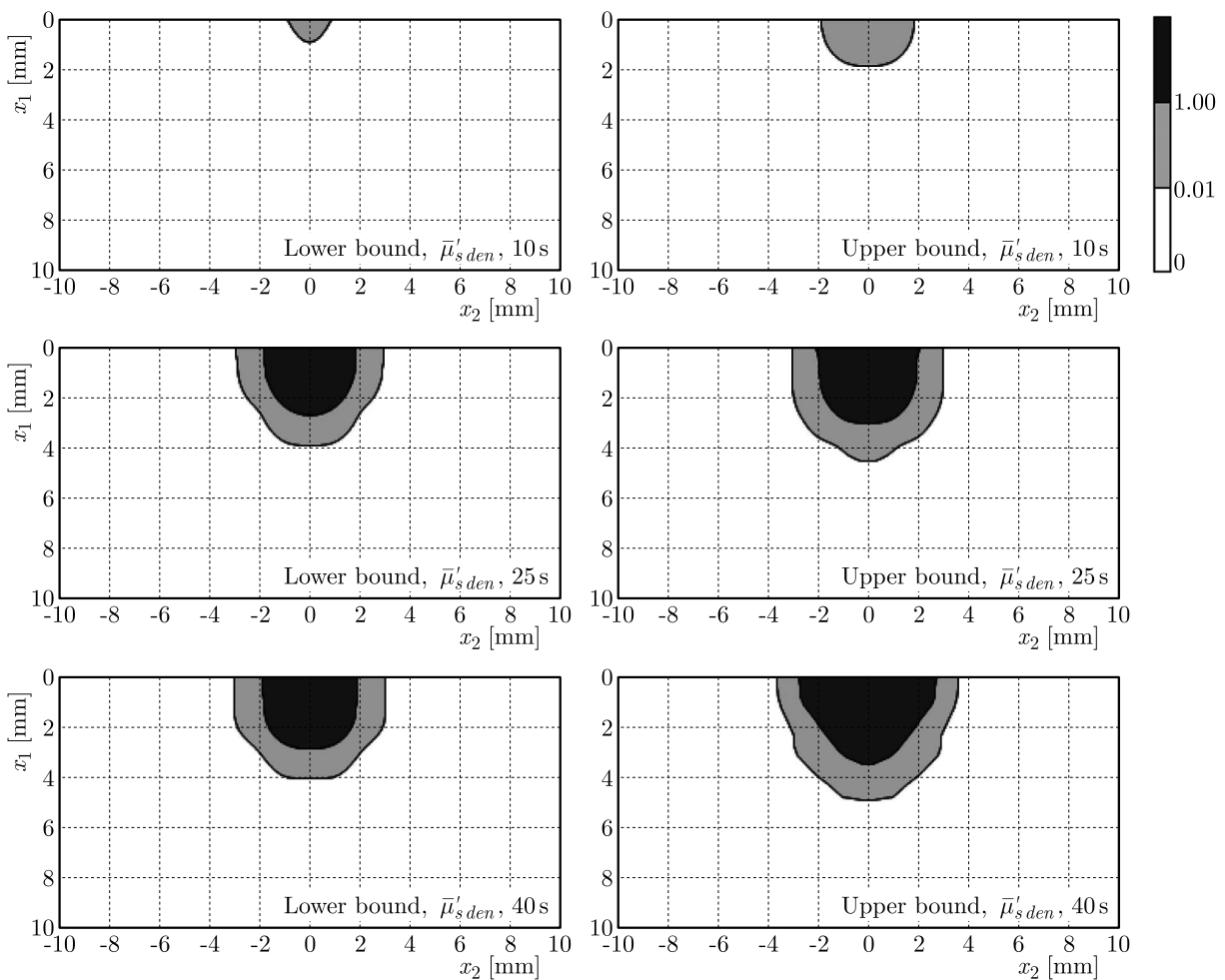


Fig. 9. Distributions of the interval Arrhenius injury integral for denaturated tissue ($\bar{\mu}'_s = \bar{\mu}'_{s den}$)

5. Discussion

As has been mentioned before, the reason for the application of the directed interval arithmetic was to take into account the inaccuracies of estimation of biological tissue parameters and their effect on thermal damage to the tissue. It can be seen that the results associated with the tissue

damage are quite reasonable for the assumed width of interval parameters. The differences between the ranges of coagulation zones (Figs. 8 and 9) obtained for both assumed values of the interval effective scattering coefficient $\overline{\mu}'_{s\,nat}$ and $\overline{\mu}'_{s\,den}$ are clearly visible. On the other hand, the differences between the lower and upper bounds of the interval Arrhenius integral for both cases of $\overline{\mu}'_s$ are not very big.

Of course, thermal damage can also expand after the impulse causing the temperature elevation ceases, what happens also in the analysed cases for $t > t_{exp}$, and the thermal injury is fully formed in less than 40 s.

Application of the Arrhenius integral also allows one to estimate the time after which the given point of the domain considered is thermally damaged, i.e. the value $\overline{\Psi}$ reaches the necrosis criterion. The results of this type are shown in Fig. 7. These results allow one to estimate the time of tissue damage in a few second intervals – at the node N_0 for the calculation with $\overline{\mu}'_{s\,nat}$ [14,15] s while for the calculation with $\overline{\mu}'_{s\,den}$ [17,21] s. Such width of intervals can be accepted as useful information from a practical point of view.

It should be pointed out that, in some cases, it is justified to assume a more restrictive necrosis criterion, i.e. $\overline{\Psi}(\mathbf{x}) \geq 4.6$ which corresponds to 99% of dead cells (e.g. laser cancer therapy). This criterion is also fulfilled at the node N_0 for the assumed width of the parameter intervals – for calculation with $\overline{\mu}'_{s\,nat}$ [15,17] s, for calculation with $\overline{\mu}'_{s\,den}$ [19,25] s. These width of intervals are a still reasonable outcome.

One should also note that an increase in the intervals for optical and thermophysical parameters leads to an increase in temperature intervals, which are the basic value in calculations of the interval Arrhenius integral. This, in turn, may lead to a situation in which the lower bound of the interval injury integral for a selected point of the domain considered would be below the threshold of necrosis, whereas the upper bound would exceed this threshold.

6. Conclusions

In the paper, the analysis of the thermal damage of biological tissue subjected to laser impulse has been presented, whereas, the optical and thermophysical parameters of tissue have been treated as the directed interval numbers. That concerned two optical parameters: absorption coefficient $\overline{\mu}_a$, effective scattering coefficient of tissue $\overline{\mu}'_s$, and four thermophysical parameters: thermal conductivity $\overline{\lambda}$, volumetric specific heat \overline{c} , perfusion coefficient \overline{w} and metabolic heat source \overline{Q}_{met} . The combined effect of those parameters has been considered, although it is known that not all of these parameters (or actual changes in parameters values) have the same influence on the temperature level and, as a result, on the estimated value of tissue damage. It has been described in numerous works related to e.g. sensitivity analysis (Majchrzak and Mochnacki, 2017; Mochnacki and Ciesielski, 2016). Of course, interval analysis for the individual parameters of tissue is also possible to perform.

The directed interval arithmetic has already been effectively applied to the modelling of bioheat transfer problems. Most of the works were based on the Pennes equation, although it is possible to use a different bioheat transfer equation (Mochnacki and Piasecka-Belkhat, 2013). Of particular interest here is the use of the GDPL equation based on the theory of porous bodies which binds the process of heat transfer with the inner tissue structure (Majchrzak and Mochnacki, 2017; Majchrzak *et al.*, 2015).

The modelling of the tissue thermal damage process also includes a number of other problems, e.g. methods of taking into account changes in parameter values caused by the degree of tissue damage (Jasiński, 2015, 2018). Further work related to the application of directed interval arithmetic in this area could concern these issues or the problems related with the use of interval numbers in other algorithms related to thermal damage (Jasiński, 2015; Mochnacki and

Piasecka, 2013). Because the interval arithmetic is a method developed by mathematicians in order to put bounds on rounding errors and measurement errors in mathematical computation, it could also be a useful approach to the modelling of various problems of bioheat transfer.

Acknowledgements

The research has been funded from the projects of Silesian University of Technology, Faculty of Mechanical Engineering.

References

1. ABRAHAM J.P., SPARROW E.M., 2007, A thermal-ablation bioheat model including liquid-to-vapor phase change, pressure- and necrosis-dependent perfusion, and moisture-dependent properties, *International Journal of Heat and Mass Transfer*, **50**, 13-14, 2537-2544
2. BANERJEE S., SHARMA S.K., 2010, Use of Monte Carlo simulations for propagation of light in biomedical tissues, *Applied Optics*, **49**, 4152-4159
3. DAWOOD H., 2011, *Theories of Interval Arithmetic: Mathematical Foundations and Applications*, LAP LAMBERT Academic Publishing GmbH & Co., Germany
4. DOMBROVSKY L.A., BAILLIS D., 2010, *Thermal Radiation in Disperse Systems: An Engineering Approach*, Begell House, New York
5. DOMBROVSKY L.A., RANDRIANALISOA J.H., LIPINSKI W., TIMCHENKO V., 2013, Simplified approaches to radiative transfer simulations in laser induced hyperthermia of superficial tumors, *Computational Thermal Sciences*, **5**, 6, 521-530
6. FASANO A., HÖMBERG D., NAUMOV D., 2010, On a mathematical model for laser-induced thermotherapy, *Applied Mathematical Modelling*, **34**, 12, 3831-3840
7. GAJDA K., MARCINIAK A., SZYSZKA B., 2000, Three- and four-stage implicit interval methods of Runge-Kutta type, *Computational Methods in Science and Technology*, **6**, 41-59
8. HANSEN E., WALSTER G.W., 2004, *Global Optimization Using Interval Analysis*, Marcell Dekker, New York
9. HENRIQUES F.C., 1947, Studies of thermal injuries, V. The predictability and the significance of thermally induced rate process leading to irreversible epidermal injury, *Journal of Pathology*, **23**, 489-502
10. JACQUES S.L., POGUE B.W., 2008, Tutorial on diffuse light transport, *Journal of Biomedical Optics*, **13**, 4, 1-19
11. JANKOWSKA M.A., SYPNIEWSKA-KAMINSKA G., 2012, Interval finite difference method for bio-heat transfer problem given by the Pennes equation with uncertain parameters, *Mechanics and Control*, **31**, 2, 77-84
12. JASIŃSKI M., 2014, Modelling of tissue thermal injury formation process with application of direct sensitivity method, *Journal of Theoretical and Applied Mechanics*, **52**, 947-957
13. JASIŃSKI M., 2015, Modelling of thermal damage in laser irradiated tissue, *Journal of Applied Mathematics and Computational Mechanics*, **14**, 67-78
14. JASIŃSKI M., 2018, Numerical analysis of soft tissue damage process caused by laser action, *AIP Conference Proceedings*, **060002**, 1922
15. JASIŃSKI M., MAJCHRZAK E., TURCHAN L., 2016, Numerical analysis of the interactions between laser and soft tissues using generalized dual-phase lag model, *Applied Mathematic Modelling*, **40**, 2, 750-762
16. KAŁUŻA G., MAJCHRZAK E., TURCHAN L., 2017, Sensitivity analysis of temperature field in the heated soft tissue with respect to the perturbations of porosity, *Applied Mathematical Modelling*, **49**, 498-513

17. DI LIZIA P., ARMELLIN R., BERNELLI-ZAZZERA F., BERZ M., 2014, High order optimal control of space trajectories with uncertain boundary conditions, *Acta Astronautica*, **93**, 217-229
18. MAJCHRZAK E., MOCHNACKI B., 2016, Dual-phase lag equation. Stability conditions of a numerical algorithm based on the explicit scheme of the finite difference method, *Journal of Applied Mathematics and Computational Mechanics*, **15**, 89-96
19. MAJCHRZAK E., MOCHNACKI B., 2017, Implicit scheme of the finite difference method for 1D dual-phase lag equation, *Journal of Applied Mathematics and Computational Mechanics*, **16**, 3, 37-46
20. MAJCHRZAK E., TURCHAN L., DZIATKIEWICZ J., 2015, Modeling of skin tissue heating using the generalized dual-phase lag equation, *Archives of Mechanics*, **67**, 6, 417-437
21. MARKOV S.M., 1995, On directed interval arithmetic and its applications, *Journal of Universal Computer Science*, **1**, 514-526
22. MOCHNACKI B., CIESIELSKI M., 2016, Sensitivity of transient temperature field in domain of forearm insulated by protective clothing with respect to perturbations of external boundary heat flux, *Bulletin of the Polish Academy of Sciences – Technical Sciences*, **64**, 3
23. MOCHNACKI B., PIASECKA-BELKHAYAT A., 2013, Numerical modeling of skin tissue heating using the interval finite difference method, *Molecular and Cellular Biomechanics*, **10**, 3, 233-244
24. MOCHNACKI B., SUCHY J.S., 1995, *Numerical Methods in Computations of Foundry Processes*, PFTA, Cracow
25. MOORE R.E., 1966, *Interval Analysis*, Prentice-Hall, Englewood Cliffs
26. NAKAO M., 2017, On the initial-boundary value problem for some quasilinear parabolic equations of divergence form, *Journal of Differential Equations*, **263**, 8565-8580
27. PARUCH M., 2014, Hyperthermia process control induced by the electric field in order to destroy cancer, *Acta of Bioengineering and Biomechanics*, **16**, 4, 123-130
28. PIASECKA-BELKHAYAT A., 2011, *Interval Boundary Element Method for Imprecisely Defined Unsteady Heat Transfer Problems* (in Polish), Silesian University of Technology, Gliwice
29. PIASECKA-BELKHAYAT A., JASIŃSKI M., 2011, Modelling of UV laser irradiation of anterior part of human eye with interval optic, [In:] *Evolutionary and Deterministic Methods for Design, Optimization and Control. Applications*, Burczyński T., Périaux J. (Eds.), CIMNE, Barcelona, 316-321
30. PIASECKA-BELKHAYAT A., KORCZAK A., 2016, Numerical modelling of the transient heat transport in a thin gold film using the fuzzy lattice Boltzmann method with alpha-cuts, *Journal of Applied Mathematics and Computational Mechanics*, **15**, 1, 123-135
31. PIASECKA-BELKHAYAT A., KORCZAK A., 2017, Modeling of thermal processes proceeding in a 1D domain of crystalline solids using the lattice Boltzmann method with an interval source function, *Journal of Theoretical and Applied Mechanics*, **55**, 1, 167-175
32. POPOVA E.D., 1994, Extended interval arithmetic in IEEE floating-point environment, *Interval Computations*, **4**, 100-129
33. POPOVA E.D., 2011, Multiplication distributivity of proper and improper intervals, *Reliable Computing*, **7**, 129-140
34. WELCH A.J., 2011, *Optical-Thermal Response of Laser Irradiated Tissue*, M.J.C. van Gemert (Eds.), 2nd edit., Springer

INFLUENCE OF THE DAMPING EFFECT ON THE DYNAMIC RESPONSE OF A PLATE

ŁUKASZ BORKOWSKI

*Lodz University of Technology, Department of Strength of Materials, Łódź, Poland
e-mail: lukasz.borkowski@p.lodz.pl*

The subject of the research is analysis of the influence of the damping effect on the dynamic response of a plate. During the tests, the areas of dynamic stability and instability for the plate with and without damping are compared. Besides, exact analysis of the nature of the solution by applying criteria such as phase portraits, Poincaré maps, FFT analysis, the largest Lyapunov exponents are carried out and found.

Key words: damping effect, dynamic stability, dynamic response, phase portraits, Poincaré maps

1. Introduction

The beginnings of studies concerning the dynamic stability of plates can be found in publications from the middle of the twentieth century. The first publication regarding dynamic stability of plates was presented by Zizicas (1952). In that paper, theoretical solutions for the joint supported plate with a time-dependent load were reported. Subsequent years of research led to creation of dynamic stability criteria which were divided into: geometric (Cooley and Tukey, 1965), energy (Raftoyiannis and Kounadis, 2000) and failure ones (Petry and Fahlbusch, 2000).

One of the major criterion was a Budiansky-Hutchinson criterion (Hutchinson and Budiansky, 1966) which concerned rods and cylindrical shells with an axial load. They analyzed the load in the form of a pulse of a finite and infinite duration. They proved that the loss of stability of dynamically loaded constructions occurs when small load increments cause a rapid increase of deflection. Budiansky was one of the authors of a similar criterion regarding cylindrical shells with a transverse load – the Budiansky-Roth criterion (Budiansky and Roth, 1962). This criterion was willingly used in research of other scientists who were involved in the similar topics (Shariyat, 2007; Kubiak, 2007; Zhang *et al.*, 2004).

Another important criterion is the Petry-Fahlbusch criterion (Petry and Fahlbusch, 2000). The researchers said that the analysis of the stress state should determine the dynamic critical load for the construction with a stable post-critical equilibrium path. Based on such an analysis, it is possible to determine the load for which destruction of the structure takes place. According to Petry-Fahlbusch's theory, if the condition – the reduced stress is smaller or equal to the boundary stress – is fulfilled at any time and at any point of the studied structure, then a dynamic response of the construction under the pulse load is dynamically stable.

The next important criterion is the Volmir criterion (Volmir, 1972). He analyzed pulses of a finite duration: a rectangular pulse and an exponentially decreasing pulse, pulses of an infinite duration and a linearly increasing load. He studied pulses that caused both compression and shear. Using the Bubnov-Galerkin (Michlin and Smolnicki, 1970) and Runge-Kutta (Collatz, 2012; Fortuna *et al.*, 2005) methods, he said that the loss of stability of pulse loaded plates occurs when the maximum deflection of the plates is equal to their thickness or half thickness.

Ari-Gur and Simonetta (1977) proposed four criteria for the loss of stability. They described the critical load depending on the following parameters: the measured deflection in the middle of length and width of the plate and the intensity of load for plates fixed at all edges and loaded with a pulse of half-wave shaped (a pulse of finite duration). The first concerns the value of deflection and the intensity of the load pulse – if a slight increase in the load pulse intensity causes a significant increase in the value of deflection then dynamic buckling takes place. According to the second criterion – if a slight increase in the amplitude of the load pulse causes a decrease in the value of deflection then dynamic buckling happens. The next two criteria are failure criteria which are based on the response analysis of the loaded edge of a plate. According to the third criterion – if a small increase in the force pulse amplitude causes a sudden increase in the shortening value of the loaded edge of the plate then dynamic buckling occurs. According to the fourth criterion – if a small increase in the pulse intensity of displacement of the loaded edge causes a change in the reaction sign on the plate edge then dynamic buckling takes place.

The behavior of rod systems was analyzed by the finite element method by Kleiber *et al.* (1987). They formulated a quasi-bifurcation criterion of dynamic stability for a construction under a jump loaded (Heaviside pulse) by using properties of a tangent stiffness matrix in the point of bifurcation. According to this criterion, the structure loses stability and the deflection begins to grow boundlessly when the determinant of the tangent stiffness matrix is equal to zero and the absolute value of the smallest eigenvalue is greater than the absolute value of the nearest maximum reached by the smallest eigenvalue.

All the above criteria are widely used in the research of many scientists who deal with the analysis of dynamic stability (Bolotin 1972; Hsu and Forman, 1975; Kołakowski, 2007; Kołakowski and Kubiak, 2007; Kowal-Michalska, 2010; Kubiak *et al.*, 2010; Mania and Kowal-Michalska, 2007; Moorthy *et al.*, 1990; Wu and Shih, 2006).

However, the analysis of plate structures with application of dynamic criteria such as phase portraits, Poincaré maps, FFT analysis, the largest Lyapunov exponents is less used (Alijani *et al.*, 2011a,b; Gilat and Aboudi, 2000; Touati and Cederbaum, 1995; Wang *et al.*, 2010; Yeh and Lai, 2002; Yuda and Zhiqiang, 2011). Therefore, this paper presents the influence of the damping effect on the dynamic response of the plate using the above tools.

2. Studied plate

A square isotropic plate with dimensions $b = l = 100$ mm, $h = 1$ mm and material constants $E = 200$ GPa, $\nu = 0.3$ is analyzed (Fig. 1). The analyzed plate is simply supported on the all edges. The plate is loaded with a dynamic compressive load. The dynamic load means the load that has been introduced suddenly and lasts for an infinitely long time.

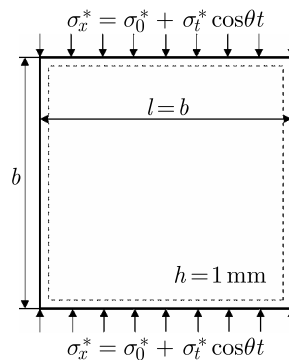


Fig. 1. Studied plate

2.1. The plate without damping

According to the research by Volmir (1972), the above plate can be described by the following equation

$$\ddot{\zeta} + \omega_0^2 \left(1 - \frac{\sigma_x^*}{\sigma_{cr}^*}\right) \zeta + \eta \zeta^3 = 0 \quad (2.1)$$

After transformations, the test plate without damping can be described using the equation

$$\ddot{\zeta} + \Omega_0^2 (1 - k \cos \theta t) \zeta + \eta \zeta^3 = 0 \quad (2.2)$$

where

$$k = \frac{\sigma_t^* / \sigma_{cr}^*}{1 - \sigma_0^* / \sigma_{cr}^*} \quad \Omega_0^2 = \omega_0^2 \left(1 - \frac{\sigma_0^*}{\sigma_{cr}^*}\right)$$

and ζ is the deflection of the plate, ω_0 – natural frequency, σ_{cr}^* – critical stress, σ_0^* – medium stress, σ_t^* – stress amplitude, η – parameter whose value is dependent on the boundary conditions.

Transform now equation (2.2) into a dimensionless form

$$\ddot{x} + a(1 - k \cos \psi \tau)x + bx^3 = 0 \quad (2.3)$$

where

$$a = 1 - \frac{\sigma_0^*}{\sigma_{cr}^*} \quad b = \frac{\eta}{\omega_0^2} \quad \ddot{x} = \frac{1}{\omega_0^2} \ddot{\zeta} \quad x = \zeta \quad x^3 = \zeta^3 \quad \psi = \frac{\theta}{\omega_0}$$

and τ is the dimensionless time. For the studied plate supported on all edges, the values of parameters are: $\omega_0 = 3014.3$ rad/s, $\eta = 0.23$ rad/s², $\sigma_{cr}^* = 72.3$ MPa. For the purpose of further numerical analysis, equation (2.3) is replaced by two first-order differential equations

$$\dot{x}_1 = x_2 \quad \dot{x}_2 = -a(1 - k \cos \psi \tau)x_1 - bx_1^3 \quad (2.4)$$

2.2. The plate with damping

Introducing damping into equation (2.2) and transforming into a dimensionless form, one obtains

$$\ddot{x} + c\dot{x} + a(1 - k \cos \psi \tau)x + bx^3 = 0 \quad (2.5)$$

where: $c = 2h/\omega_0$ – the dimensionless damping ratio, $h = 0.02$ (Kołakowski and Teter, 2013), the other parameters are the same as for the plate without damping.

Writing equation (2.5) in the form of two first-order differential equations, we get

$$\dot{x}_1 = x_2 \quad \dot{x}_2 = -cx_2 - a(1 - k \cos \psi \tau)x_1 - bx_1^3 \quad (2.6)$$

All studies are carried out for the following initial conditions: $x_1 = 0.01$, $x_2 = 0$.

3. Numerical analysis of the plate

Figure 2 shows the areas of dynamic stability and instability (circled areas) for the plate without (a) and with (b) the damping effect after earlier presentation of the full compliance of the results presented by Volmir (1972) and the results obtained with the dynamic tools for the plate without the damping effect (Borkowski, 2017).

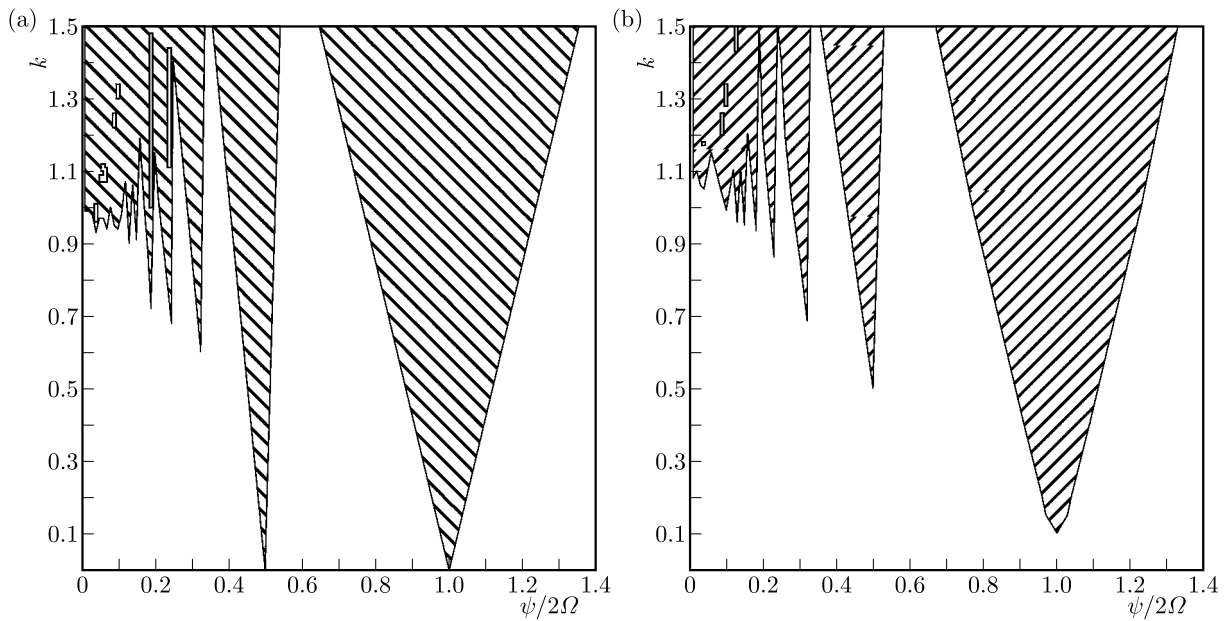


Fig. 2. Graphs of dynamic stability and instability areas for the plate without (a) and with (b) the damping effect

Both graphs in $k - \psi/2\Omega$ coordinates ($\psi = \theta/\omega_0$, $\Omega = \Omega_0/\omega_0$) by changing values of the parameters σ_0 and σ_t have been made. Calculations of the parameters k and $\psi/2\Omega$ changing every 0.01 were executed. Figure 2 has been obtained by using the criteria of phase portraits, Poincaré maps and FFT analysis.

Analyzing both charts, it can be concluded that there are larger areas of dynamic instability for the plate without damping as against the plate with damping. In addition, small dynamic stability areas within the dynamic instability range in both cases are observed (Figs. 3a and 3b).

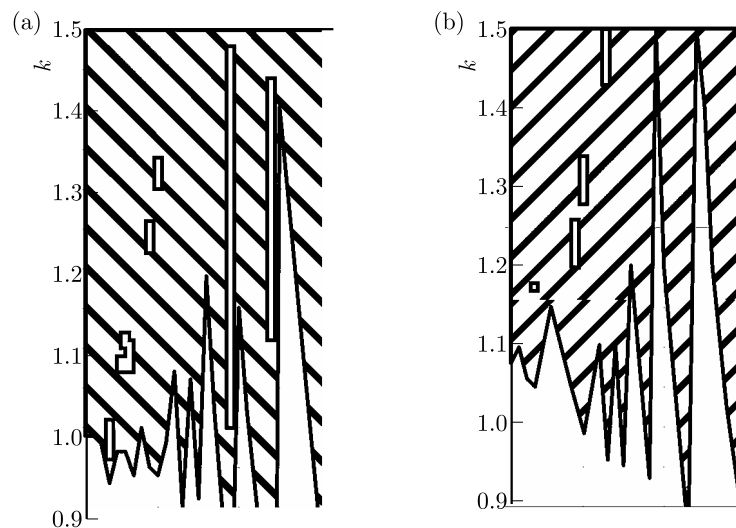


Fig. 3. Detailed graphs of dynamic stability and instability areas for the plate without (a) and with (b) the damping effect

For the plate without damping, the dynamic stability area is represented by a quasi-periodic solution. In the range of dynamic instability, both quasi-periodic as well as chaotic solutions can be specified.

For the plate with damping, in the dynamic stability area the trajectory is heading to the critical point. In the range of dynamic instability, the periodic solutions as well as the series of period-doubling bifurcations, which lead to a chaotic response, are obtained.

Therefore, for the purpose of a more detailed analysis and presentation of the above solutions, the criterion of the largest Lyapunov exponents has been used.

Figure 4 shows the areas of the chaotic solution (gray areas) for the plate without (a) and with (b) damping. The dashed lines indicates the boundary for the dynamic stability/instability areas which corresponds to the circled part in Fig. 2. Comparing the two graphs, it can be clearly stated that the introduction of damping to the analyzed plate results in obtaining much smaller areas of dynamic instability with a chaotic solution. Figure 5 presents a magnification of Figs. 4a and 4b. Gray dots correspond to specific values and gray lines to ranges for the chaotic solution.

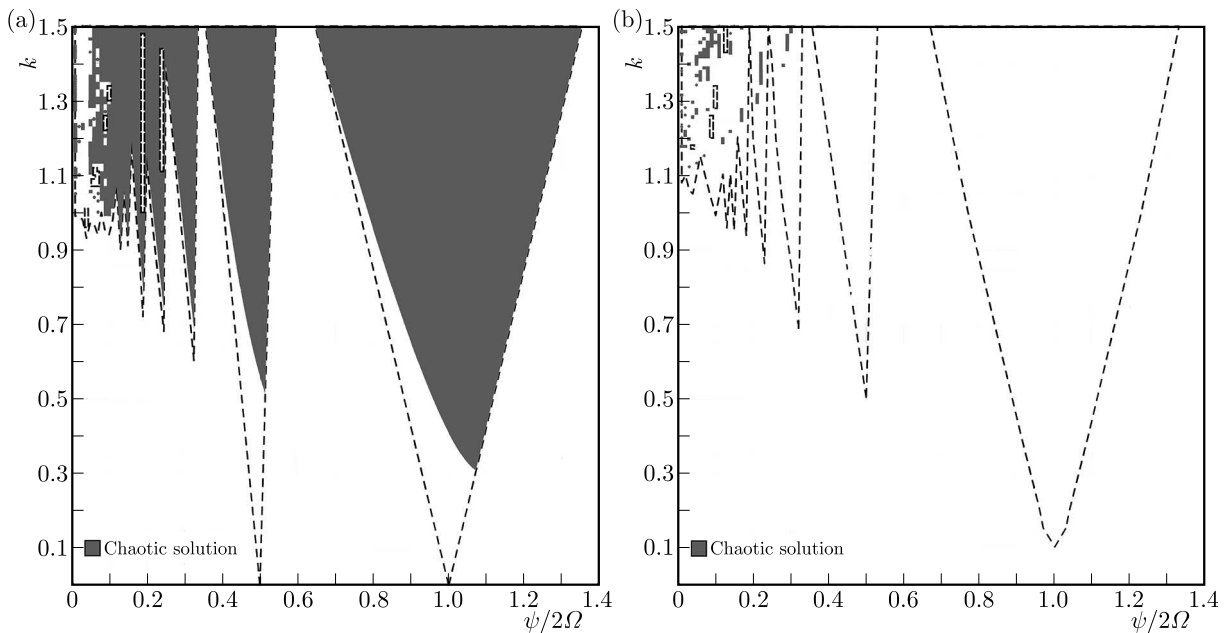


Fig. 4. Graphs of areas representing the chaotic solution for the plate without (a) and with (b) the damping effect

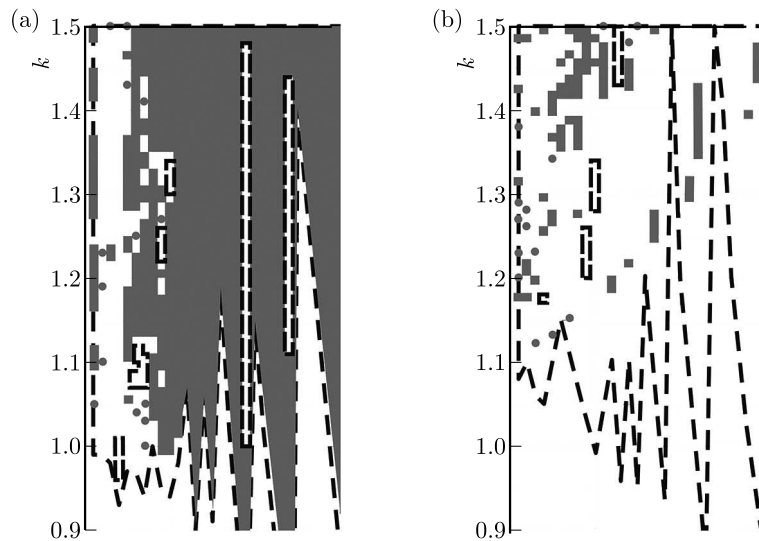


Fig. 5. The detailed graphs of areas representing the chaotic solution for the plate without (a) and with (b) the damping effect

In order to present the solutions more clearly, three points from Fig. 2 for individual ranges have been selected. These points represent solutions from the area of dynamic stability – ($k = 0.50$, $\psi/2\Omega = 0.30$), from the area of dynamic instability with a periodic/quasi-periodic solution – ($k = 0.25$, $\psi/2\Omega = 1.00$) and from the area of dynamic instability with a chaotic solution – ($k = 1.50$, $\psi/2\Omega = 0.30$).

Analyzing the obtained results and using the criteria of phase portraits as well as Poincaré maps, it can be concluded that the loss of dynamic stability is associated with a sudden increase in the displacement x_1 and velocity x_2 (Figs. 6d, 6f, 6g, 6i) when compared to the dynamic stability areas (Figs. 6a, 6c). According to the research presented in (Bazant and Cedolin, 2010), the loss of stability is related to displacement of the phase trajectory into infinity. This is the case when the analysis time corresponds to the period of natural vibration of a construction. In order to use dynamic tools such as phase portraits or Poincaré maps, the presented research concerns the analysis duration many times greater than the period of natural vibration. For a long duration, the phase trajectory does not move into infinity. It achieves some limit values of the displacement x_1 and velocity x_2 , the value of which depends on the parameter k . However, applying the criterion of phase portraits and analyzing the plate for both short and long analysis duration, the same results are obtained.

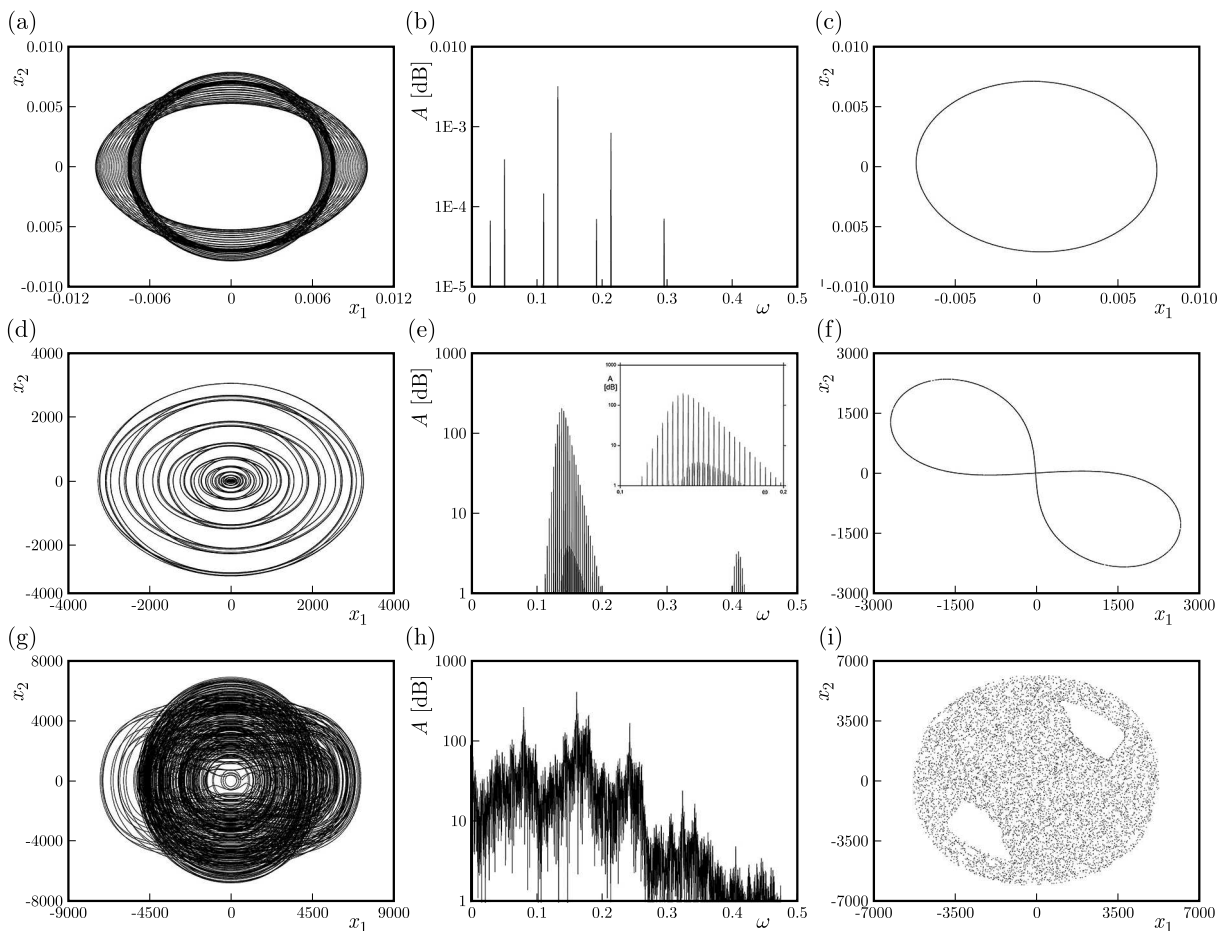


Fig. 6. The plate without damping – phase portraits (a), (d), (g), FFT analysis (b), (e), (h) and Poincaré maps (c), (f), (i) for the areas of dynamic stability (a), (b), (c), dynamic instability – quasi-periodic solution (d), (e), (f) and dynamic instability – chaotic solution (g), (h), (i)

Applying FFT analysis, it can be concluded that it is possible to precisely determine dominant frequencies in the stability range (Fig. 6b). Also in the instability range with a quasi-periodic solution, dominant frequencies can be specified (Fig. 6e). In both cases, the appearance of two

disproportionate to each other frequencies can be observed. The so-called two-dimensional torus (2D torus) is created. In both Fig. 6b and Fig. 6e, the largest Lyapunov exponents are approximately equal to zero ($\lambda_1 = 0.000002$, $\lambda_2 = -0.000002$ – for the point $k = 0.50$, $\psi/2\Omega = 0.30$; $\lambda_1 = 0.000004$, $\lambda_2 = -0.000004$ – for the point $k = 0.25$, $\psi/2\Omega = 1.00$). It should be noted that the two zero Lyapunov exponents for the stability area are the result of the absence of damping in the system (2.3). As a consequence, there is no attractor (attractors) to which the trajectory would converge.

In the instability range with a chaotic solution (Fig. 6h), the frequency spectrum is continuous. It is not possible to specify the dominant frequencies. The amplitude of the tested signal increases significantly, which is expressed in decibels. The value of the largest Lyapunov exponent is positive ($\lambda_1 = 0.043531$, $\lambda_2 = -0.043531$).

Similarly to the plate without damping, the loss of stability for the plate with damping is associated with a sudden increase in the displacement x_1 and velocity x_2 (Figs. 7d, 7f, 7g, 7i) when compared to the dynamic stability areas (Fig. 7a). In the stability area – as a result of the introduced damping – the trajectory goes to the critical point (Fig. 7a). The Lyapunov exponents are negative ($\lambda_1 = -0.019993$, $\lambda_2 = -0.020007$) and there is no solution in the FFT graphs (Fig. 7b) as well as Poincaré maps (Fig. 7c).

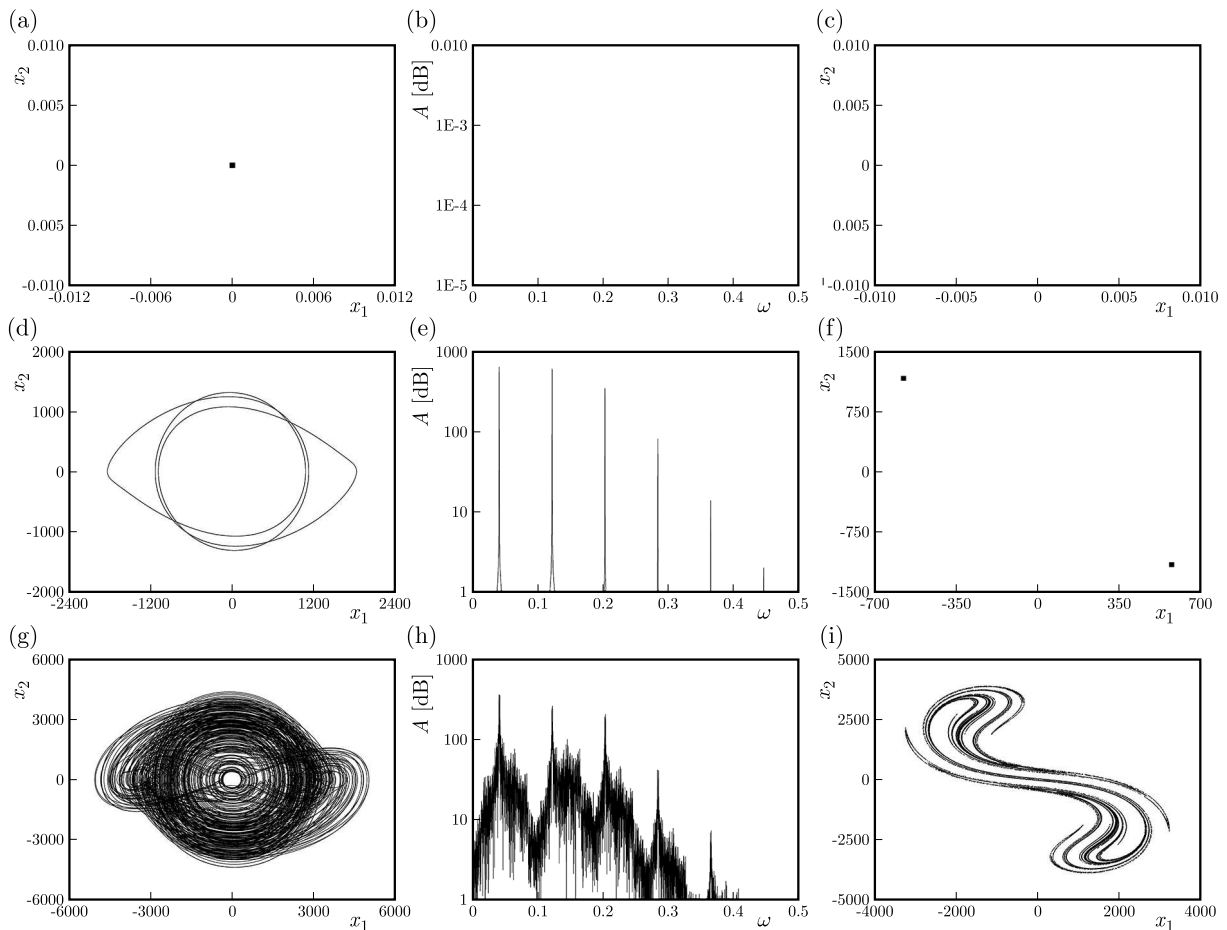


Fig. 7. The plate with damping – phase portraits (a), (d), (g), FFT analysis (b), (e), (h) and Poincaré maps (c), (f), (i) for the areas of dynamic stability (a), (b), (c), dynamic instability – periodic solution (d), (e), (f) and dynamic instability – chaotic solution (g), (h), (i)

In the areas of dynamic instability, a periodic solution has been obtained (Figs. 7d, 7e, 7f). Together with the series of period-doubling bifurcations, it leads to a chaotic solution (Figs. 7g, 7h, 7i). Figures 7d, 7e, 7f show a solution with a period equal to 2. The FFT analysis (Fig. 7e)

enables precise representation of the dominant frequencies. The Lyapunov exponents are negative ($\lambda_1 = -0.020000$, $\lambda_2 = -0.020000$).

Similarly to the plate without the damping effect, in the areas of dynamic instability with a chaotic solution, the frequency spectrum is continuous, and it is impossible to distinguish the dominant frequencies (Fig. 7h). The amplitude of the signal also increases. The value of the largest Lyapunov exponent is positive ($\lambda_1 = 0.043397$, $\lambda_2 = -0.043397$).

4. Summary

The subject of the research is to present the influence of the damping effect on the dynamic response for an isotropic plate. The areas of dynamic stability and instability for the plate with and without damping are compared. Additionally, using the criteria such as phase portraits, Poincaré maps, FFT analysis, the largest Lyapunov exponents, the nature of the solution of the analyzed plate has been presented.

After the tests, it can be concluded that the impact of damping causes changes in the instability areas of the studied structure. In addition, the introduction of damping to the system results in a significant difference in the occurrence of areas in which the solution is chaotic.

For the plate without damping, a quasi-periodic solution in the dynamic stability areas has been observed. The occurrence of two disproportionate to each other frequencies as well as formation of a 2D torus have been proved. Whereas, both the quasi-periodic as well as the chaotic solution in the instability range have been specified.

For the plate with the damping effect in the area of dynamic stability, the phase trajectory is going to the critical point. In the range of dynamic instability, the periodic solutions as well as the series of period-doubling bifurcations, which lead to the chaotic response, have been obtained.

In both analyzed cases (for the plate without and with damping), the loss of dynamic stability is associated with a significant increase in the displacement x_1 and velocity x_2 in comparison to the dynamic stability areas – the criteria of phase portraits and Poincaré maps. Using the FFT analysis, the loss of dynamic stability results in inability to precisely specify the dominant frequencies in the spectral signal (what is possible in the areas of dynamic stability), and a significant increase in their amplitude is found. Implementing the criterion of the largest Lyapunov exponents, it is possible to clearly present significant differences between the areas with a chaotic solution for plates without and with the damping effect.

Conflict of interest

The author declares that there is no conflict of interest concerning publication of this article.

References

1. ALIJANI F., AMABILI M., KARAGIOZIS K., BAKHTIARI-NEJAD F., 2011a, Nonlinear vibrations of functionally graded doubly curved shallow shells, *Journal of Sound and Vibration*, **330**, 7, 1432-1454
2. ALIJANI F., BAKHTIARI-NEJAD F., AMABILI M., 2011b, Nonlinear vibrations of FGM rectangular plates in thermal environments, *Nonlinear Dynamics*, **66**, 3, 251-270
3. ARI-GUR J., SIMONETTA S.R., 1997, Dynamic pulse buckling of rectangular composite plates, *Composites Part B: Engineering*, **28**, 3, 301-308
4. BAZANT Z.P., CEDOLIN L., 2010, *Stability of Structures: Elastic, Inelastic, Fracture and Damage Theories*, World Scientific

5. BOLOTIN V., 1962, *Dynamic Stability of Elastic Systems*, Vol. 1
6. BORKOWSKI L., 2017, Numerical analysis of dynamic stability of an isotropic plate by applying tools used in dynamics, [In:] *Dynamical Systems in Theoretical Perspective*, J. Awrejcewicz (Edit.), Springer
7. BUDIANSKY B., ROTH R.S., 1962, Axisymmetric dynamic buckling of clamped shallow spherical shells, *NASA TND1510*, 597-606
8. COLLATZ L., 2012, *The Numerical Treatment of Differential Equations*, Springer Science and Business Media
9. COOLEY J.W., TUKEY J.W., 1965, An algorithm for the machine calculation of complex Fourier series, *Mathematics of Computation*, **19**, 90, 297-301
10. FORTUNA Z., MACUKOW B., WASOWSKI J., 2005, *Metody numeryczne*, WNT, Warszawa, ISBN 83-204-3075-5
11. GILAT R., ABOUDI J., 2000, Parametric stability of non-linearly elastic composite plates by Lyapunov exponents, *Journal of Sound and Vibration*, **235**, 4, 627-637
12. HSU Y.C., FORMAN R.G., 1975, Elastic-plastic analysis of an infinite sheet having a circular hole under pressure, *Journal of Applied Mechanics*, **42**, 2, 347-352
13. HUTCHINSON J.W., BUDIANSKY B., 1966, Dynamic buckling estimates, *AIAA Journal*, **4**, 3, 525-530
14. KLEIBER M., KOTULA W., SARAN M., 1987, Numerical analysis of dynamic quasi-bifurcation, *Engineering Computations*, **4**, 1, 48-52
15. KOLAKOWSKI Z., 2007, Some aspects of dynamic interactive buckling of composite columns, *Thin-Walled Structures*, **45**, 10, 866-871
16. KOLAKOWSKI Z., KUBIAK T., 2007, Interactive dynamic buckling of orthotropic thin-walled channels subjected to in-plane pulse loading, *Composite Structures*, **81**, 2, 222-232
17. KOLAKOWSKI Z., TETER A., 2013, Influence of inherent material damping on the dynamic buckling of composite columns with open cross-sections, *Mechanics and Mechanical Engineering*, **17**, 1, 59-69
18. KOWAL-MICHALSKA K., 2010, About some important parameters in dynamic buckling analysis of plated structures subjected to pulse loading, *Mechanics and Mechanical Engineering*, **14**, 2, 269-279
19. KUBIAK T., 2007, Criteria of dynamic buckling estimation of thin-walled structures, *Thin-Walled Structures*, **45**, 10, 888-892
20. KUBIAK T., KOLAKOWSKI Z., KOWAL-MICHALSKA K., MANIA R., SWINIARSKI J., 2010, Dynamic response of conical and spherical shell structures subjected to blast pressure, *Proceedings of SSDS'Rio*
21. MANIA R., KOWAL-MICHALSKA K., 2007, Behaviour of composite columns of closed cross-section under in-plane compressive pulse loading, *Thin-Walled Structures*, **45**, 10, 902-905
22. MICHLIN S.G., SMOLNICKI C.L., 1970, *Approximate Methods for the Solution of Integral and Differential Equations*, PWN, Warsaw
23. MOORTHY J., REDDY J.N., PLAUT R.H., 1990, Parametric instability of laminated composite plates with transverse shear deformation, *International Journal of Solids and Structures*, **26**, 7, 801-811
24. PETRY D., FAHLBUSCH G., 2000, Dynamic buckling of thin isotropic plates subjected to in-plane impact, *Thin-Walled Structures*, **38**, 3, 267-283
25. RAFTOYIANNIS I.G., KOUNADIS A.N., 2000, Dynamic buckling of 2-DOF systems with mode interaction under step loading, *International Journal of Non-Linear Mechanics*, **35**, 3, 531-542
26. SHARIYAT M., 2007, Thermal buckling analysis of rectangular composite plates with temperature-dependent properties based on a layerwise theory, *Thin-Walled Structures*, **45**, 4, 439-452

27. TOUATI D., CEDERBAUM G., 1995, Influence of large deflections on the dynamic stability of nonlinear viscoelastic plates, *Acta Mechanica*, **113**, 1-4, 215-231
28. VOLMIR A.S., 1972, *Nonlinear Dynamics Plates and Shells*, Moscow, Science
29. WANG Y.G., SONG H.F., LI D., WANG J., 2010, Bifurcations and chaos in a periodic time-varying temperature-excited bimetallic shallow shell of revolution, *Archive of Applied Mechanics*, **80**, 7, 815-828
30. WU G.Y., SHIH Y.S., 2006, Analysis of dynamic instability for arbitrarily laminated skew plates, *Journal of Sound and Vibration*, **292**, 1, 315-340
31. YEH Y.L., LAI H.Y., 2002, Chaotic and bifurcation dynamics for a simply supported rectangular plate of thermo-mechanical coupling in large deflection, *Chaos, Solitons and Fractals*, **13**, 7, 1493-1506
32. YUDA H., ZHIQIANG Z., 2011, Bifurcation and chaos of thin circular functionally graded plate in thermal environment, *Chaos, Solitons and Fractals*, **44**, 9, 739-750
33. ZHANG T., LIU T.G., ZHAO Y., LUO J.Z., 2004, Nonlinear dynamic buckling of stiffened plates under in-plane impact load, *Journal of Zhejiang University – Science A*, **5**, 5, 609-617
34. ZIZICAS G.A., 1952, Dynamic buckling of thin plates, *Transactions ASME*, **74**, 7, 1257-1268

Manuscript received July 30, 2018; accepted for print October 23, 2018

ANALYSIS OF DYNAMICS AND FRICTION RESISTANCE IN THE CAM-TAPPET SYSTEM

KRZYSZTOF SICZEK

Lodz University of Technology, Department of Vehicles and Fundamentals of Machine Design, Łódź, Poland
e-mail: krzysztof.siczek@p.lodz.pl

ANDRZEJ STEFAŃSKI

Lodz University of Technology, Division of Dynamics, Łódź, Poland
e-mail: andrzej.stefanski@p.lodz.pl

In this paper, the influence of friction resistance and mutual contact interaction on dynamical properties of the cam-tappet mechanism is analyzed. A dynamical model of the cam-tappet contact has been developed. Chosen results of numerical simulations of this model are presented for cases with and without oil lubrication in contact zones. Various phenomena accompanying the cam-tappet contact dynamics have been observed, e.g., change of the global direction of tappet rotation, local oscillation of these revolutions, changes of friction in function of frequency of the camshaft longitudinal vibrations. We confirm, that the growing amplitude of camshaft longitudinal vibration causes an increase in the tappet rotational speed, whereas its reducing to small values leads to stopping the tappet rotation.

Keywords: cam-tappet mechanism, friction, lubrication

1. Introduction

Many machines like combustion engines employ mechanisms forced by a roller or plane tappet driven by cam devices. A characteristic feature observed in such mechanisms is the occurrence of concentrated line contact between the touching surfaces. There exist conditions of elasto-hydrodynamic lubrication (EHL) allowing variations of the friction type from the mixed to the boundary one. The contact zone is loaded by the force changing both, in value and its acting direction. The main component of the sliding velocity which results from the mechanism operational cycle also varies. During the time when both surfaces remain in contact, additional relative displacements, small in amplitude, may occur in peripheral, axial and normal directions of the cam motion. They may be a result of torsional vibrations of the camshaft. The axial displacements may result from bending vibrations and from forced displacement within the axial clearance. Such displacements being normal to the contacting surfaces may arise from changes of the loading force and bending vibrations of the camshaft. Obviously, they change the course of contact loading.

The amount of friction between two lubricated sliding surfaces depends primarily on the contacting materials, load, lubricant formulations and the lubrication regimes. Under boundary and mixed lubrication conditions, where some asperities of both surfaces touch each other, friction can be controlled by lubricant formulations and appropriate surface engineering.

Most studies on cam-follower contacts are addressed to friction and wear measurements for investigating the influence of lubricant additives and surface coatings, finish and texture, see Willermet *et al.* (1991), Soejima *et al.* (1999), Lindhom and Svahn (2006), Kano (2006), Lewis and Dwyer-Joyce (2002). The friction force (or torque) is often calculated by subtracting the

contributions of other components and inertia actions from the measured values, as in Kano (2006), Baş *et al.* (2003).

The action of friction forces between the cam and tappet or the valve stem can cause tappet or valve rotations. Their effects can become positive, as they decrease friction resistance between contacting surfaces. The rotations are forced when the symmetry plane of the cam is displaced relative to the tappet or valve axis. Such behavior was described in Jelenschi *et al.* (2011). For a particular application, a specific amount of valve rotation is required to maintain even the sealing level at the valve seat. Excessive amount of valve rotation will result in increased wear of the contacting surfaces, limiting the engine lifetime. In the analysis described in Refalo *et al.* (2010), a minimum engine speed of 3500 rpm was established as a target for valve rotation to begin. Over a typical driving cycle, the valves can rotate at least once. The maximum value of valve rotation can reach 15 rpm for any engine speed. Typical factors influencing valve rotation include oil temperature, assembly variation, machining variability, valve deposits, engine vibrations and engine temperature.

Hyundai in Kim *et al.* (2004) are described what influenced and contributed to valve rotation. It was explained that during opening the valve also rotated along with the valve spring. Next, during the closing phase, the valve moved back to its original position. As the speed of the motion increased, there was a greater tendency for the valve to slide at both – the maximum lift and the closing events. This sliding motion provides a rotational net movement over a given lift event. All this motion is balanced by friction between each of the contact interfaces: between the cylinder head, valve spring, valve, retainer, lock, drive mechanism, etc.

In the research described in Hiruma and Furuhashi (1978) it was observed that such a valve started to rotate after reaching the crankshaft speed of 3000 rpm. While speeding up the crankshaft, the valve rotation increased rapidly. Before reaching the level of 3000 rpm at the crankshaft, the valve did not rotate or it rotated in varying directions. Also in Beddoes (1992) similar behavior of random nature and different directions of valve rotation was reported.

The main aim of this paper is to check if the occurrence of camshaft longitudinal vibrations can decrease friction between the cam and tappet of the valve tip. Also analysis of dynamics of cam-tappet contact is discussed.

The paper is organized as follows. In Section 2, profiles of the cam mechanism are briefly described and illustrated. In Section 3, the dynamical model of the cam-tappet contact is introduced. Results of numerical simulations of the cam-tappet dynamics in the case with and without oil lubrication in the contact zones are demonstrated in Section 4. Finally, Section 5 contains discussion of the obtained results and conclusions.

2. Valve lift profiles in the cam mechanism

A very aggressive cam profile is the best when used with bucket tappets, as stated in Blair *et al.* (2005). The base circle radius R_b of the cam equals 0.02 m and the valve (and bucket tappet by definition) stroke is 8.3 mm. The bucket tappet is assumed flat. The bucket has the minimum possible diameter ($d_t = 0.03$ m) in order to keep the declared width of the cam in full contact conditions with the flat tappet surface throughout the working cycle. The design of cam profiles was presented in Rothbart (2004). They can have a polynomial form

$$h = h_{max} \left[1 + C_2 \left(\frac{\theta_c - \theta_c(h_{max})}{\beta} \right)^2 + C_p \left(\frac{\theta_c - \theta_c(h_{max})}{\beta} \right)^p + C_q \left(\frac{\theta_c - \theta_c(h_{max})}{\beta} \right)^q + C_r \left(\frac{\theta_c - \theta_c(h_{max})}{\beta} \right)^r + C_s \left(\frac{\theta_c - \theta_c(h_{max})}{\beta} \right)^s \right] \quad (2.1)$$

where $p = 22$, $q = 42$, $r = 62$, $s = 82$ is a constant power and $C_2 = -pqr s [(p-2)(q-2)(r-2)(s-2)]^{-1}$, $C_p = 2qrs [(p-2)(q-2)(r-p)(s-p)]^{-1}$, $C_q = -2prs [(q-2)(q-p)(r-q)(s-q)]^{-1}$,

$C_r = 2pqs[(r-2)(r-p)(r-q)(s-r)]^{-1}$, $C_s = -2pqr[(s-2)(s-p)(s-q)(s-r)]^{-1}$ are constant factors, $\beta = \pi/3$ – angle of rise, h_{max} – cam stroke.

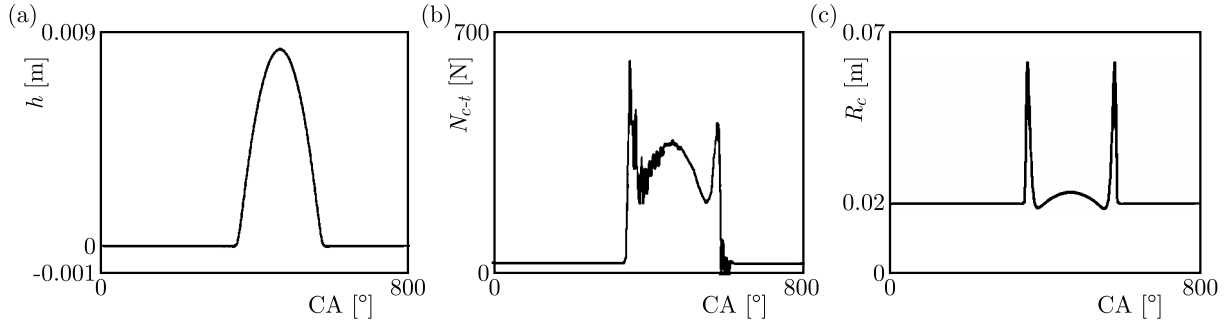


Fig. 1. (a) Diagram of the valve lift h against the crankshaft angle $\theta_c = CA$ (crankshaft angle degree). (b) Diagram of the normal force N_{c-t} between the cam and tappet against the crankshaft angle $\theta_c = CA$. (c) The instantaneous radius of curvature R_c of the cam profile against the crankshaft angle $\theta_c = CA$

The shape of the valve lift h against the crankshaft angle $\phi = CA$ is presented in Fig. 1a. The typical trace of the normal force N_{c-t} between the cam and tappet against $\phi = CA$ has been assumed to be similar as that in Taraza *et al.* (1999) for the crankshaft speed 1320 rpm, and is presented in Fig. 1b. The instantaneous radius of curvature R_c of the cam profile, shown in Fig. 1c, can be calculated from the formula

$$R_c = R_b + h + \frac{a}{\omega_c^2} \quad (2.2)$$

where R_b is the base radius of cam, ω_c – angular velocity of the crankshaft, $a = d^2l/dt^2$, $l(t)$ – varying displacement (Fig. 2b).

3. Modelling of the cam-tappet contact

Mathematical models allowing prediction of lubricant film-thickness and Hertzian pressures at the cam/tappet contact were presented in Gecim (1992). The model can predict the changes in the cam/tappet interface friction due to changing operating conditions. Also a model of tappet spin allowing for slip at the cam/tappet interface has been included. Modelling the tappet spin allows one to see the effects of the tappet crown radius and cam-taper angle on the interface frictional loss. It is found that tappet rotation is affected by design and operating conditions, and depends primarily on camshaft speed.

The use of advanced mathematical models to quantify power loss at cam/tappet contact, tappet/bore contact and camshaft bearings was presented in Calabretta *et al.* (2010). Calculated and measured friction data for the valve train of a high speed passenger car engine were compared with those obtained from tests on a motored cylinder head test rig. The system friction was measured and calculated across the operating speed range with different oil supply temperature.

The camshaft model considering both camshaft angular vibration and bending vibration was presented in Guo *et al.* (2015). Each follower element was treated as a multi-mass system. The lumped masses were connected by spring elements and damping elements. The contact force model at the cam-tappet interfaces was developed based on the elasto-hydrodynamic lubrication theory of finite line conjunction. It was that bending vibration of the camshaft was mainly in the normal direction at the cam-tappet interfaces. Bending vibration was mainly influenced by overlapping of the inlet and exhaust cam functions of each cylinder. The angular vibration of the camshaft mainly focused at the fundamental frequency and the harmonic frequency corresponding to the cylinder number.

3.1. Description of the model

The present dynamic model of the tappet-cam assembly is shown in Fig. 2a for the camshaft oscillating in the z direction and rotating about such an axis with a constant angular velocity ω_c . The tappet can rotate about its axis with the angle ε . It is assumed that friction torque M_{Tt-p} between the bucket tappet and the valve stem of diameter d or between the tappet and pushrod of cross-section diameter d_p can be estimated as follows

$$M_{Tt-p} \approx \frac{1}{3} \mu_{t-p} N_{c-t} d_p \quad (3.1)$$

where μ_{t-p} is the friction coefficient between the tappet and pushrod, which may vary depending on the amount of oil, sliding velocity of the pushrod against the tappet, and N_{c-t} represents the load of contact zone equal to the normal force between the cam and tappet (Fig. 2b). The friction between the tappet and pushrod is complex and of a mixed type, and sometimes even of the boundary type, as wear debris and pollution can cumulate in the contact zone. The friction coefficient can also vary with the loading in the contact zone and vibration amplitude. In order to ignore the effect of variation of the friction coefficient μ_{t-p} on motion of the tappet, only a constant value of that coefficient has been considered. For simplicity of calculations, it has been assumed a constant value of the friction coefficient μ_{t-p} equal to the averaged one 0.2, and diameter $d_p = 0.006$ m. The friction torque M_{Tc-t} between the cam and tappet is calculated from the equation

$$M_{Tc-t} = \mu_{c-t} N_{c-t} A_{c1} \sin(2\pi f_{c1} t) \quad (3.2)$$

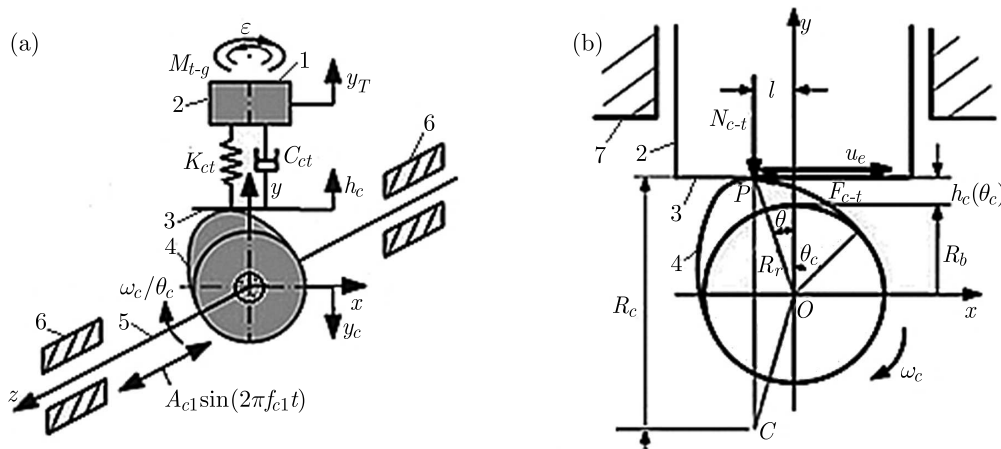


Fig. 2. (a) Dynamic model of the tappet-cam assembly for the camshaft oscillating in the z direction and rotating about such an axis. (b) The scheme of the cam-tappet contact; 1 – contact surface between the tappet and pushrod, 2 – contact surface between the tappet and its guide, 3 – plane parallel to the tappet frontal face and tangent to the cam surface, 4 – cam surface, 5 – camshaft, 6 – camshaft bearing, 7 – tappet guide

Longitudinal oscillations of the camshaft along the z axis have the amplitude A_{c1} and frequency f_{c1} . The friction coefficient μ_{c-t} between the cam and tappet is complex and varies as described further. The friction coefficient μ_{t-g} between the tappet and guide varies depending on the amount of oil, sliding velocity of the tappet against its guide and load in the contact zone. For simplicity of calculations, it has been assumed a constant value of friction coefficient μ_{t-g} equal to the averaged one, being 0.15. The friction torque M_{Tt-g} between the tappet and its guide is calculated from

$$M_{Tt-g} = \frac{1}{2} \mu_{t-g} F_{c-t} d_t = \frac{1}{2} \mu_{t-g} \mu_{c-t} N_{c-t} d_t \quad (3.3)$$

where diameter of the tappet equals $d_t = 0.03$ m. The balance of torques acting on the tappet is described by a dynamical differential

$$I_y \ddot{\varepsilon} + M_{Tt-g} + M_{Tt-p} = M_{Tc-t} \quad (3.4)$$

where I_y is the mass moment of inertia of the tappet with respect to the axis Y (see Fig. 2b). Substituting Eqs. (3.1)-(3.3) into Eq. (3.4), we have

$$I_y \ddot{\varepsilon} + \frac{1}{2} \mu_{t-g} \mu_{c-t} N_{c-t} d_t + \frac{1}{3} \mu_{t-p} N_{c-t} d_p = \mu_{c-t} N_{c-t} A_{c1} \sin(\omega_{c1} t) \quad (3.5)$$

where $\omega_{c1} = 2\pi f_{c1} t$.

The initial conditions correspond to the situation of the rest, i.e., $\varepsilon(t=0) = 0$, $\dot{\varepsilon}(t=0) = 0$.

3.2. Lubrication in the contact zone between the cam and tappet

When the camshaft rotates and undergoes axial oscillations, the oil flow in the contact zone between the cam and tappet becomes very complex. The cam motion against the tappet caused only by camshaft rotation allows the occurrence of an oil film over the contact zone between the tappet and cam. This film is characterized by varying thickness and dominant fluid motion in the periphera θ direction. The characteristic central thickness of such an oil film is equal to h_0 . Estimation of thickness h_0 is described in Section 3.3. The cam motion against the tappet caused only by camshaft longitudinal oscillations also results in varying thickness of the oil film in the mentioned contact zone. However, the dominant fluid motion in the contact zone is in the axial z direction. Averaged oil thickness of this oil film is equal to h_v . Estimation of thickness h_v is described in Section 3.4. If camshaft motions occur both due to rotation and longitudinal oscillations, the resulted oil film thickness h is higher than both h_0 and h_v . In real, the existence of such two camshaft motions influences the oil thickness h in a very complex manner but, for simplicity, it can be treated as a superposition. Therefore, it has been assumed that the oil film thickness $h \approx h_0 + h_v$, where h_0 is the central oil film thickness due to camshaft rotation, h_v – averaged oil film thickness due to camshaft longitudinal oscillation. When both rotation and axis oscillation of the camshaft occurs, the resulted normal force N_{c-t}^{res} can be estimated from the equation given in Section 3.3 and corresponding to the force N_{t-c} . Also the resulted friction force F_{c-t}^{res} in this zone can be obtained from the equations given in Section 3.3 and corresponding to the force F_{c-t} . In both these cases, the thickness h_0 is substituted by h . Then the friction coefficient μ_{c-t}^{res} between the tappet and pushrod is estimated from the equation

$$\mu_{c-t}^{res} = \frac{N_{c-t}^{res}}{T_{c-t}^{res}} \quad (3.6)$$

3.3. Elasto-hydrodynamic lubrication and the contact force model due to rotation

High pressure developed between the cam profile and the tappet requires conditions of elasto-hydrodynamic (EHD) lubrication in the contact zone. At high pressure, the viscosity of the oil increases exponentially with pressure, and an oil film can be maintained between the cam and the tappet, as described in Teodorescu *et al.* (2003). The minimum oil thickness exists at the oil exit, and the oil film can be assumed to stay nearly parallel along the lubricated zone. So the oil film thickness can be estimated at the centre point of the lubricated zone. Calculation of the central oil film thickness can be carried out from the equation

$$h_0^* = 1.67 G^{*0.421} U^{*0.541} W^{*0.059} \exp(-96.775 w_s^*) \quad (3.7)$$

developed by Rahnejat, and described in Teodorescu *et al.* (2005, 2007), Kushwaha *et al.* (2000), for finite line concentrated contact conjunction for combined entraining and squeeze film actions. The dimensionless parameters in Eq. (3.7) are described by the following formulas

$$\begin{aligned} h_0^* &= \frac{h_0}{R_C} & G^* &= \alpha_1 E_C & U^* &= u_e \eta_0 [E_C R_C]^{-1} \\ W^* &= N_{c-t} [E_C R_C L_C]^{-1} & w_s^* &= \frac{\dot{h}_0}{u_e} \end{aligned} \quad (3.8)$$

where h_0 is the central oil film thickness, α_1 – pressure viscosity coefficient, η_0 – dynamic viscosity at the inlet of contact, u_e – oil entraining velocity, E_C – effective elastic modulus, N_{c-t} – normal load responsible for local deformation of the cam/tappet contact, R_C – instantaneous radius of curvature, $L_C = 0.014$ m – cam width. The symbol w_s^* represents the squeeze-roll ratio, and its range of applicability is given, by Rahnejat, between 0 and 0.005, and in the present analysis it is assumed to be constant and equal to 0.005. The effective modulus can be calculated from the equation

$$E_C^{-1} = \frac{1}{2} [(1 - \nu_1^2) E_1^{-1} + (1 - \nu_2^2) E_2^{-1}] \quad (3.9)$$

where $E_1 = 210$ GPa is the elastic modulus of the cam material, $E_2 = 210$ GPa – elastic modulus of the tappet material, $\nu_1 = 0.3$ – Poisson's ratio of the cam material, $\nu_2 = 0.3$ – Poisson's ratio of the tappet material.

The oil entraining velocity u_e is calculated according to the formula

$$u_e = \frac{1}{2} \omega_c (R_b + h(\theta) + 2a(\theta)) \quad (3.10)$$

The value of N_{c-t} can be approximated using the following equation presented in Guo *et al.* (2011)

$$N_{c-t} = K_{c-t} (h(\theta) - y_C - y_T) + C_{c-t} (v(\theta) - \dot{y}_C - \dot{y}_T) \quad (3.11)$$

where y_C is the displacement of camshaft bending motion, y_T – displacement of the tappet, $K_{c-t} = 1.434 \cdot 10^8$ N/m, $C_{c-t} = 115.292$ Ns/m – contact stiffness and damping coefficient between the cam and tappet, respectively, as given in Guo *et al.* (2011). Values of y_C and y_T are not known, so their sum can be estimated in the following manner. Let us assume that the course of the cam force F against time t is the same as the course of N_{c-t} . Hence, we have the relationship

$$K_{c-t} (y_C + y_T) \gg C_{c-t} (\dot{y}_C + \dot{y}_T) \quad (3.12)$$

so, from Eq. (3.3), the value of $[y_C + y_T](\theta)$ can be estimated. It is represented by the approximate formula

$$[y_C + y_T](\theta) \approx [K_{c-t} h(\theta) + C_{c-t} v(\theta) - N_{c-t}(\theta)] \frac{1}{K_{c-t}} \quad (3.13)$$

Then the sum of velocities $[\dot{y}_C + \dot{y}_T](\theta)$ can be estimated from the equation

$$[\dot{y}_C + \dot{y}_T](\theta) = \omega_C \frac{\partial [y_C + y_T](\theta)}{\partial \theta} \quad (3.14)$$

and finally the corrected form of N_{c-t} can be calculated from equation (3.11). The friction force F_{c-t} between the cam and tappet is due to two different mechanisms, the asperity contact (boundary part T_b) and the shear of lubricant (hydrodynamic part T_v), as described in Teodorescu *et al.* (2003, 2005), Yang *et al.* (1996). The asperity interaction model is based on the theory

developed by Greenwood and Tripp (1971). The boundary friction T_b was determined by Guo *et al.* (2011)

$$T_b = \tau_0 A_a + m P_a \quad (3.15)$$

where $\tau_0 = 2.0$ MPa is the Eyring shear stress, described in Rothbart (2004), $m = 0.17$ – pressure coefficient of the boundary shear strength, described in Guo *et al.* (2011). Considering a Gaussian distribution of the asperities heights and fixed asperity radius of curvature, the area A_a occupied by the asperity peaks and the load P_a carried by the asperities are calculated as in Guo *et al.* (2011)

$$A_a = \pi^2 (\zeta \beta \sigma_R)^2 A F_2(\lambda) \quad P_a = \frac{8\sqrt{2}}{15} \pi (\zeta \beta \sigma_R)^2 \sqrt{\frac{\sigma_R}{\beta}} E_C A F_{5/2}(\lambda) \quad (3.16)$$

where ζ is the asperity density, β – radius of curvature, $\sigma_R = 0.4 \mu\text{m}$ – composite surface roughness parameter, A – Hertzian contact area, $\lambda = h_0/\sigma_R$ – constant. It has been assumed that $(\zeta \beta \sigma_R) = 0.055$ and $\sigma_R/\beta = 0.001$, as in Guo *et al.* (2011). The Hertzian formula for the contact of two cylinders can be used to calculate the contact area, see Patir and Cheng (1979)

$$E_C A = \sqrt{\frac{8}{\pi} E_C R_C L_C N_{c-t}} \quad (3.17)$$

Two statistical functions $F_2(\lambda)$ and $F_{5/2}(\lambda)$ are defined by the equation

$$F_n(\lambda) = \frac{1}{2\pi} \int_{h_0/\sigma}^{\infty} \left(s - \frac{h_0}{\sigma}\right)^n \exp\left(-\frac{1}{2}s^2\right) ds \quad (3.18)$$

They can be approximated by the following formulas

$$\begin{aligned} F_2(\lambda) &= -0.0018\lambda^5 + 0.0281\lambda^4 - 0.1728\lambda^3 + 0.5258\lambda^2 - 0.8043\lambda + 0.5003 \\ F_{5/2}(\lambda) &= -0.0046\lambda^5 + 0.0574\lambda^4 - 0.2958\lambda^3 + 0.7844\lambda^2 - 0.0776\lambda + 0.6167 \end{aligned} \quad (3.19)$$

The viscous friction is given by

$$T_v = \tau(A - A_a) \quad (3.20)$$

where τ is the shear stress of the lubricant. Depending on the oil film thickness, the lubricant may behave as a Newtonian or non-Newtonian oil film, as described in Teodorescu *et al.* (2003). The behavior can be estimated by the Eyring shear stress τ_0 . If the shear stress is lower than the Eyring shear stress τ_0 then Newtonian behavior occurs, otherwise non-Newtonian behavior takes place. So the shear stress can be expressed by the equation presented in Guo *et al.* (2011)

$$\tau = \begin{cases} \frac{\eta u_S}{h_0} & \text{for } \tau \leq \tau_0 \\ \tau_0 + \gamma_S p^* & \text{for } \tau > \tau_0 \end{cases} \quad (3.21)$$

where η is the oil viscosity, $\eta = \eta_0 \exp(\alpha_1 p^*)$, $\eta_0 = 0.0057$ Pa/s, $\alpha_1 = 1.8 \cdot 10^{-8}$ m²/N, u_S – sliding velocity, $\gamma_S = 0.08$ – rate of change of shear stress with pressure, and p^* – pressure on the oil film described by the (Moraru, 2005)

$$p^* = \frac{N_{c-t} - P_a}{A - A_a} \quad (3.22)$$

The sliding velocity u_S between the cam and tappet is calculated from the equation (Guo *et al.*, 2011)

$$u_S = \omega_c (R_b + h(\theta)) \quad (3.23)$$

The total friction force F_{c-t} is given by the sum (Guo *et al.*, (2011)

$$F_{c-t} = T_b + T_v \quad (3.24)$$

3.4. Elasto-hydrodynamic lubrication and the contact force model due to axis oscillations

The contact between the tappet and cam is considered as the case of two parallel plates sliding relative to each other. The loading force N_{c-t} is balanced by the load P_{a1} carried by the asperities and by the hydrodynamic force P_v as well as by the squeeze force P_S described as

$$N_{c-t} = P_{a1} + P_v + P_s \quad (3.25)$$

The load P_{a1} carried by the asperities can be estimated from the following equation

$$P_{a1} = A \left(\frac{h_{v0} - h_v}{c} \right)^{1/m} \quad (3.26)$$

similarly to Yang *et al.* (1996). It should be remembered that $A = 2bL_C$, where b is the Hertz half-width of contact between the cam and tappet. The hydrodynamic force P_v , the squeeze force P_S and the velocity w are defined by formulas presented in Siczek (2016)

$$P_v = \frac{6\eta AL_c K_p \psi v}{h_v^2} \quad P_s = \frac{\eta b^2 A w}{h_v^3} \quad (3.27)$$

and

$$w = \dot{h}_v = - \left[N_{c-t} - A \left(\frac{h_{v0} - h_v}{c} \right)^{1/m} - \frac{6\eta AL_c K_p \psi v}{h_v^2} \right] \frac{h_v^3}{\eta A b^2} \quad (3.28)$$

where $K_p = 0.0265$, $\psi = 0.06$ are coefficients characterizing hydrodynamic impacts in the contact zone and h_{v0} is the oil film thickness, as described in Siczek (2016). The initial value of velocity $v = 0$ and the film thickness h_v is equal to h_{v0} . The initial film thickness h_{v0} can be estimated assuming that, in the initial conditions, the load P_{a1} carried by the asperities is equal to P_a , see (3.16)₂. After obtaining the oil film thickness h_v , the force N_{c-t} results from equations (3.25)-(3.27) and the friction force T_{c-t} in the axial z direction from (3.15)-(3.24) by substituting force F_{c-t} by T_{c-t} , thickness h_0 by h_v and velocity u_s by v_2 given by the equation

$$v_2 = 2A_{c1} \pi f \cos(2\pi f_{c1} t) \quad (3.29)$$

Then the friction coefficient μ_{c-t} between the tappet and pushrod is estimated from the equation

$$\mu_{c-t} = \frac{F_{c-t}}{N_{c-t}} \quad (3.30)$$

4. Results

The first set of numerically simulated results have been obtained for the case of a constant (dry or mixed) friction coefficient μ_{c-t} occurring in contact between the cam and tappet, and μ_{t-p} between the tappet and the pushrod, which are equal to 0.3. In Fig. 3, an exemplary time-diagram of the F_{c-t} force obtained for the camshaft rotational speed $n_s = 1320$ rpm, the camshaft longitudinal oscillations of the amplitude $A_{cl} = 0.0001$ m and the frequency $f_{cl} = 1$ Hz, is demonstrated. It is a single segment of the force sequence for a time period of 0.1 s. The entire sequence includes a time period of 60 s. Subsequent time-diagrams of the tappet rotation angle ε for various values of the frequency f_{cl} are shown in Figs. 4a-d. The case of tappet rotation, corresponding to Fig. 3, is shown in Fig. 4a. An increase in such an angle with time in almost step-like manner can be observed.

If the frequency f_{cl} is significantly elevated, up to 10 Hz, we can observe almost a linear increase in the angle ε (see Fig. 4b). Cyclic variations of the direction of tappet rotation occur,

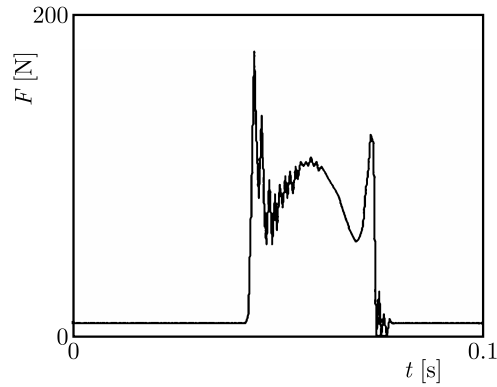


Fig. 3. Time-diagrams of the force F_{c-t} between the cam and the tappet for the frequency of camshaft longitudinal oscillations $f_{cl} = 1$ Hz. Values of remaining parameters: $\mu_{c-t} = \mu_{t-p} = 0.3$, $n_s = 1320$ rpm, $A_{cl} = 0.0001$ m

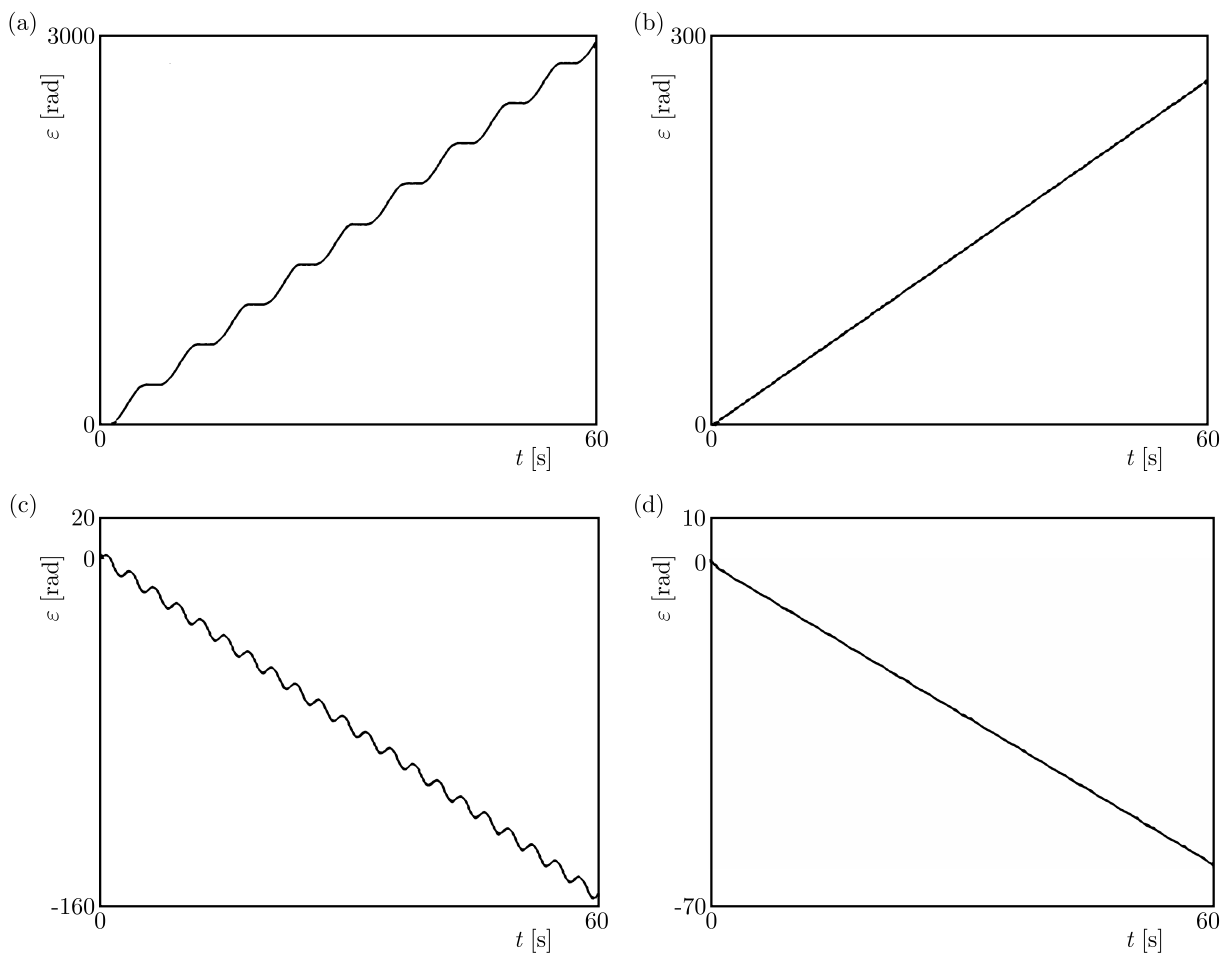


Fig. 4. Time-diagrams of the tappet rotation angle ε for various frequencies of the camshaft longitudinal oscillations f_{cl} : 1 Hz (a), 10 Hz (b), 20 Hz (c), 100 Hz (d). Values of remaining parameters:

$$\mu_{c-t} = \mu_{t-p} = 0.3, n_s = 1320 \text{ rpm}, A_{cl} = 0.0001 \text{ m}$$

but the observed oscillations have a very small amplitude. Further growth of the camshaft vibration frequency ($f_{cl} = 20$ Hz) causes reversal of the direction of tappet rotation. However, as shown in Fig. 4c, cyclic variations of this direction have a quite large amplitude. The same direction of tappet rotation and its increase with time t has been obtained for the frequency $f_{cl} = 100$ Hz, as it is depicted in Fig. 4d. However, in this case, variations of the tappet rotation direction are very small.

In the next two diagrams (Figs. 5a and 5b) the influence of the amplitude change on tappet rotation is demonstrated. In the case when the amplitude is doubled ($A_{cl} = 0.0002$ m) and the frequency $f_{cl} = 10$ Hz, the obtained time history of the tappet rotation angle ε is shown in Fig. 5a. It can be seen that an increase in the angle ε with time occurs in the same direction as in the case of A_{cl} equal to 0.0001, but 4.44 times greater than the last one. On the other hand, reducing the amplitude to a half of the initial value ($A_{cl} = 0.00005$ m and $f_{cl} = 10$ Hz) causes stopping of the tappet rotation (see Fig. 5b).

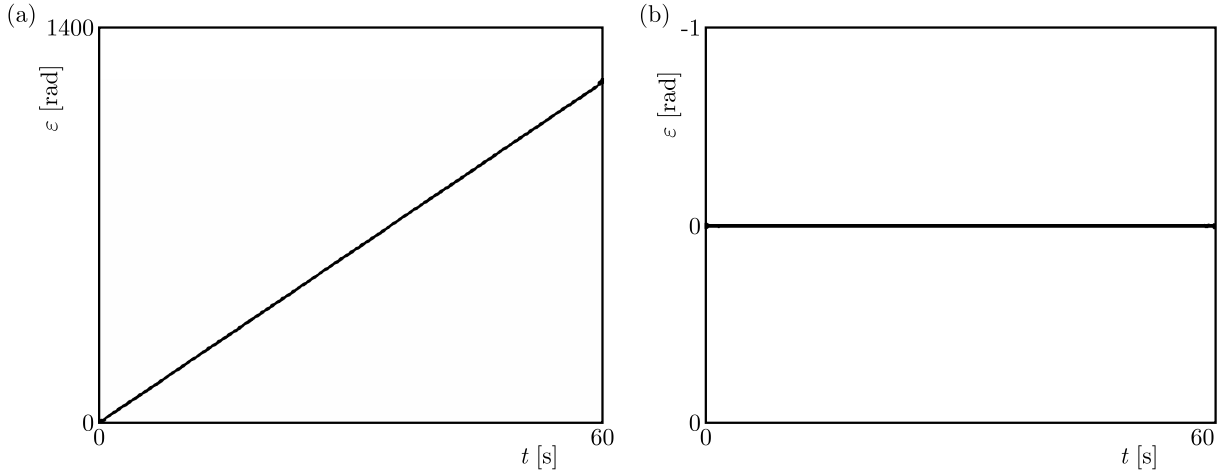


Fig. 5. Time-diagrams of the tappet rotation angle ε for two different amplitudes of the camshaft longitudinal oscillations A_{cl} : 0.0002 m (a), 0.00005 m (b). Values of remaining parameters: $\mu_{c-t} = \mu_{t-p} = 0.3$, $n_s = 1320$ rpm, $f_{cl} = 10$ Hz

The results of numerical research corresponding to the case presented in Fig. 4b ($A_{cl} = 0.0001$ m, $f_{cl} = 10$ Hz) but performed for two times larger rotational speed of the camshaft, i.e., $n_s = 2640$ rpm, are illustrated in Fig. 6. Comparison of Figs. 3b and 6 shows that such doubling of the speed n_s does not influence significantly the rotational dynamics of the tappet. The increase in the angle ε in time still has almost a linear character, and the speed of the tappet rotation is about 15% higher only.

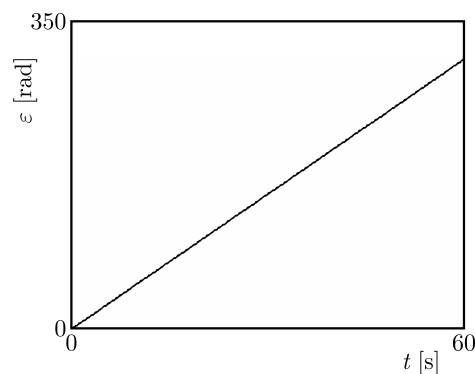


Fig. 6. Time-diagrams of the tappet rotation angle ε for the camshaft rotational speed $n_s = 2640$ rpm. Values of remaining parameters: $\mu_{c-t} = \mu_{t-p} = 0.3$, $f_{cl} = 10$ Hz, $A_{cl} = 0.0001$ m

The second group of the results have been obtained for the case (f) when the oil is present in the contact zones. Variations of mixed or hydrodynamic friction coefficients cause changes in the loading and sliding velocity of the contacting surfaces. They result in varying friction forces F_{c-t} (Eq. (3.24)) occurring in contact between the cam and tappet, and F_{t-p} (Eq. (3.1)) between the tappet and the push rod which have been calculated from the Reynolds equations.

The time-diagram of the friction force F_{c-t} between the cam and tappet corresponding to the graph shown in Fig. 4a ($n_s = 1320$ rpm, $f_{cl} = 10$ Hz) is depicted in Fig. 7a. The oil lubrication causes values of the friction forces to be a few times lower (2-4) than in the case of constant friction coefficients μ_{c-t} and μ_{t-p} . Time histories of the tappet rotation angle ε are shown in Fig. 7b. It is clearly visible that, similarly to the case presented in Fig. 4a, an increase in the angle ε has almost a step-like character.

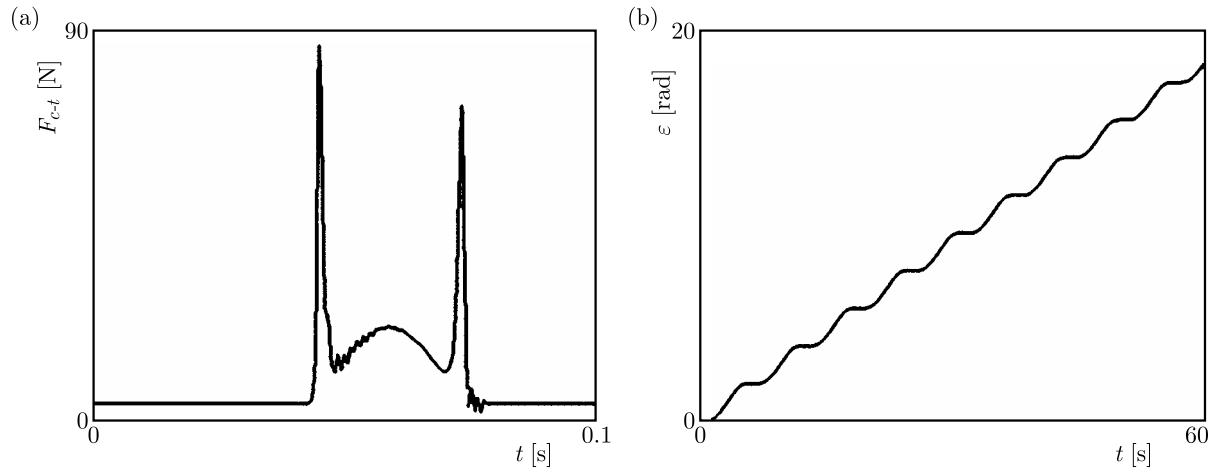


Fig. 7. Time-diagram of the force F_{c-t} between the cam and the tappet (a) and the tappet rotation angle ε (b) for the case of oil lubrication. Values of others parameters: $f_{cl} = 1$ Hz, $n_s = 1320$ rpm, $A_{cl} = 0.0001$ m

In the case when the camshaft longitudinal oscillations frequency f_{cl} is equal to 100 Hz, the time history of the friction force T_{c-t} between the cam and tappet is presented in Fig. 8a. Such values of the friction force are much lower, even two orders in magnitude lower than in the case of frequency $f_{cl} = 1$ Hz (see Fig. 7a). It is due to the dominant role of hydrodynamic lubrication in both contact zones, between the cam and tappet and between the tappet and pushrod, respectively. Such small values of friction forces also result in lack of tappet rotation, as it is shown in Fig. 8b.

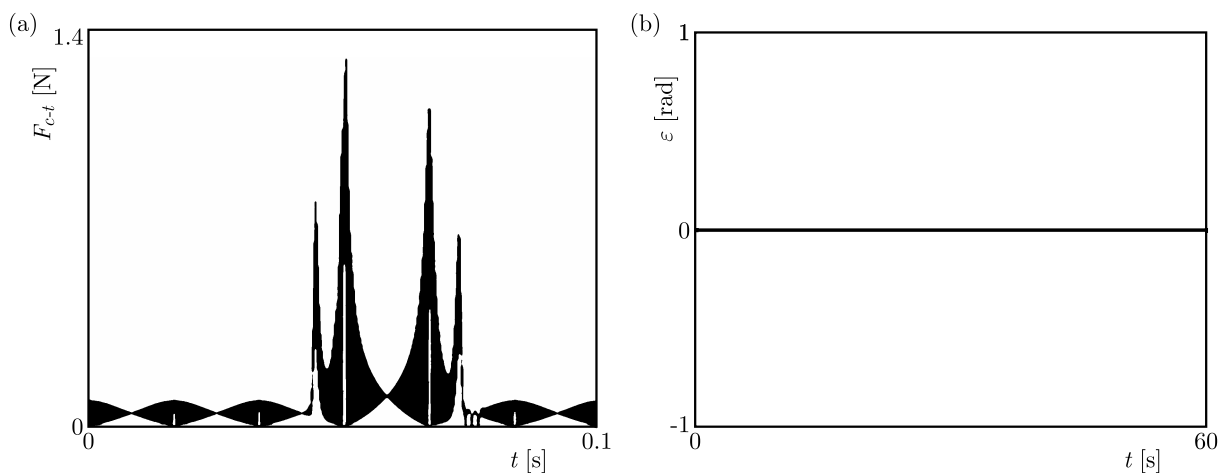


Fig. 8. Time-diagram of the force F_{c-t} between the cam and the tappet (a) and the tappet rotation angle ε (b) for the case with oil lubrication. Values of others parameters: $f_{cl} = 100$ Hz, $n_s = 1320$ rpm, $A_{cl} = 0.0001$ m

5. Summary and conclusions

We have carried out the analysis of friction resistance between the cam and its tappet for different values of the amplitude and frequency of camshaft longitudinal oscillations and camshaft rotational speeds. Depending on these parameters or presence (or not) of oil lubrication, different time diagrams of the tappet rotation angle ε are calculated and shown.

In the case of a constant value of the friction coefficient between the cam and tappet and between the tappet and pushrod, the same camshaft rotational speed and the same values of the oscillation amplitudes result with different shapes of time histories depending on the camshaft longitudinal oscillation frequency. Some results are illustrated in Figs. 4a-d. They prove that the increase in this frequency leads to a significant reduction of the average angular velocity of tappet rotation and reversal of its direction of rotation. This velocity is represented by an average slope of the time histories in Figs. 4a-d – its value is reduced from about 50 rad/s for $f_{cl} = 1$ Hz (Fig. 4a) to about -1 rad/s (opposite direction) for $f_{cl} = 100$ Hz (Fig. 4d). Other interesting phenomena detected during the analysis are:

- changes in the global direction of the tappet rotary motion (compare Figs. 4a,b with Figs. 4c,d),
- cyclic variations in the direction of rotation with a relatively large amplitude (Fig. 4c), which tend to zero with an increase in the frequency f_{cl} , then the tappet rotates slowly with an almost constant speed (Fig. 4d),
- step-like shape of the time-course of tappet rotation for small values of the frequency $f_{cl} = 1$ Hz – one can observe revolutions interrupted with stopping periods (vertical sections of the diagram in Fig. 4a) what indicates the stick-slip character of the cam-tappet dynamical contact (for an increasing frequency, the angular velocity of the tappet is stabilized – see Fig. 4b).

Analyzing the influence of camshaft rotational speed and the amplitude of longitudinal oscillations, one can draw the following conclusions:

- growing amplitude of camshaft longitudinal vibration causes a considerable increase in the tappet rotational speed (Fig. 5a), whereas its reduction to small values leads to stopping of the tappet rotation (Fig. 5b),
- even a large increase in the camshaft rotational speed does not change significantly the velocity of tappet revolutions (Fig. 6).

When the oil lubrication is applied to the contact zones between the cam and tappet and between the tappet and pushrod, rather a large reduction of the friction force and tappet rotational velocity takes place when compared to contact without any lubrication. This fact can be treated as an obvious and expected effect. The comparison with corresponding cases without lubrication (see Figs. 3 and 4a) indicates that after oil application the friction force declined several times (Fig. 7a) and tappet rotations slowed at least 150 times (Fig. 7b).

However, our results demonstrate that further large reduction of friction can be obtained for a high frequency of the camshaft longitudinal vibration. Comparison of the cases presented in Figs. 7a and 8a displays that a hundredfold increase in the frequency causes almost a hundredfold decrease in the friction force. This fact can be explained by the hydrodynamic lubrication effect (squeeze effect) described in Guran *et al.* (1996). Hence, lack of tappet revolutions, depicted in Fig. 8b, is not surprising due to the friction force which is too weak to maintain the rotations.

We can conclude that the presented phenomena, i.e., changes in the global direction of tappet rotation, its local oscillations, the friction force dependence with the frequency and the other facts mentioned above are effects of mutual interaction of camshaft rotations with its longitudinal vibrations and possible different configuration of the phase synchrony between them. However, an accurate identification and description of the mechanism governing such phenomena requires

more detailed bifurcation analysis in the system parameter space. This is our task for the nearest future and the results will be reported soon.

Acknowledgment

This work has been supported by Polish National Centre of Science (NCN) under Project No. DEC-2012/06/A/ST8/00356.

References

1. BAŞ H., BIYIKLIOĞLU A., CUVALCI H., 2003, A new test apparatus for the tribological behavior of cam mechanisms, *Experimental Techniques*, September/October, 28-32
2. BEDDOES G.N., 1992, Valve materials and design, *Ironmaking and Steelmaking*, **19**, 290-296
3. BLAIR G., MCCARTAN C.D., HERMANN H., 2005, *Making the Cam. Valvetrain Design Part Two. Special Investigation. Race Engine Technology*, Issue 9, ISSN 1740-6803
4. CALABRETTA M., CACCIATORE D., CARDEN P., 2010, Valvetrain friction – modeling, analysis and measurement of a high performance engine valvetrain system, *SAE International Journal of Engines*, **3**, 2, 72-84, DOI: 10.4271/2010-01-1492
5. GECIM B.A., 1992, Tribological study for a low-friction cam/tappet system including tappet spin, *Tribology Transactions*, **35**, 2, 225-234
6. GREENWOOD J.A., TRIPP J.H., 1971, The contact of two nominally flat rough surfaces, *Proceedings of the Institution of Mechanical Engineers*, **185**, 625-633
7. GUO J., ZHANG W., ZHANG X., 2015, Modeling and analysis of the transient vibration of camshaft in multi-cylinder diesel engine, *Advances in Mechanical Engineering*, **7**, 11, 1-14
8. GUO J., ZHANG W., ZOU D., 2011, Investigation of dynamic characteristics of a valve train system, *Mechanism and Machine Theory*, **46**, 1950-1969
9. GURAN A., PFEIFFER F., POPP K., 1996, Dynamics with friction: modeling, analysis and experiment: (Part I), *World Scientific*, 23.08.1996 – 264
10. HAN Y., CHAN C., WANG Z., SHI F., WANG J., WANG N., WANG Q.J., 2015, Effects of shaft axial motion and misalignment on the lubrication performance of journal bearings via a fast mixed EHL computing technology, *Tribology Transactions*, **58**, 2, 247-259
11. HIRUMA M., FURUHAMA S., 1978, A study on valve recession caused by non-leaded gasoline – measurement by means of R.I., *Bulletin of JSME*, **21**, 147-160
12. JELENSCHI L., COFARU C., SANDU G., ALEONTEM M., 2011, State of the art of engine valve and tappet rotation, *Bulletin of the Transilvania University of Braşov, Series I*, **4**, 53, 2
13. KANO M., 2006, Super low friction of DLC applied to engine cam follower lubricated with ester-containing oil, *Tribology International*, **39**, 1682-1685
14. KIM D., LEE J., LEE J., 2004, Effect of valve train design parameters on valve rotation performance of a diesel engine, *SAE Technical Paper*, **F2004V281**
15. KUSHWAHA M., RAHNEJAT H., JIN Z.M., 2000, Valve-train dynamics: a simplified tribo-elastomulti-body analysis, *Proceedings of the Institution of Mechanical Engineers, Part K: Journal of Multi-Body Dynamics*, **214**, 5-110
16. LEWIS R., DWYER-JOYCE R.S., 2002, Wear of diesel engine inlet valves and seat inserts, *Proceedings of the Institution of Mechanical Engineers, Part D: Journal of Automobile Engineering*, **216**, 205-216
17. LINDHOM P., SVAHN F., 2006, Study of thickness of sputtered-carbon coating for low friction valve lifters, *Wear*, **261**, 241-250

18. MENG F., WANG Q.J., HUA D. LIU S., 2010, A simple method to calculate contact factor used in average flow model, *Journal of Tribology*, **132**, 2, 024505
19. MORARU L.E., 2005, Numerical predictions and measurements in the lubrication of aeronautical, engine and transmission components, Doctoral Thesis, The University of Toledo
20. PATIR N., CHENG H.S., 1978, An average flow model for determine effects of three dimensional roughness on partial hydrodynamic lubrication, *Journal of Lubrication Technology*, **100**, 1, 12-17
21. PATIR N., CHENG H.S., 1979, Effect of surface roughness orientation on the central film thickness in EHD contacts, *Proceedings of the 5th Leeds-Lyon Symposium on Tribology*, 15-21
22. REFALO K., BOWYER S., SMITH M., HIJAWI M., 2010, Optimizing valve rotational speed using Taguchi techniques, *SAE Technical Paper*, **2010-01-1096**
23. ROTHBART H.A., 2004, *Cam Design Handbook*, McGraw Hill, New York
24. SICZEK K., 2016, *Tribological Processes in the Valve Train Systems with Lightweight Valves. New Research and Modelling*, 1st Ed., Elsevier
25. SOEJIMA M., EJIMA Y., WAKURI Y., KITAHARA T., 1999, Improvement of lubrication for cam and follower, *Tribology Transactions*, **42**, 4, 755-762
26. TARAZA D., HENAIN N.A., TEODORESCU M., CEAUSU R., BRYZIC W., 1999, Dynamics and friction of valve trains, *Arc Annual Meeting*, University of Michigan
27. TEODORESCU M., KUSHWAHA M., RAHNEJAT H., TARAZA D., 2005, Elastodynamic transient analysis of a four-cylinder valve train system with camshaft flexibility, *Proceedings of the Institution of Mechanical Engineers, Part K: Journal of Multi-body Dynamics*, **219**, 13-25
28. TEODORESCU M., TARAZA D., NAEIM A.H., 2003, Simplified elasto-hydrodynamic friction model of the cam-tappet contact, *SAE Paper*, **2003-01-0985**
29. TEODORESCU M., THEODOSSIADES S., RAHNEJAT H., 2007, Multi-physics approach to design analysis of powertrain sub-systems, *12th IFToMM World Congress*, Besançon, France
30. WILLERMET P.A., PIEPRZAK J.M., DAILEY D.P., CARTER R.O., LINDSAY N.E., HAACK L.P. AND DEVRIES J.E., 1991, The composition of surface layers formed in a lubricated cam/tappet contact, *Transaction of the ASME, Journal of Tribology*, **113**, 38-47
31. WU C.W., ZHENG L.Q., 1989, An average Reynolds equation for partial film lubrication with a contact factor, *Journal of Tribology*, **111**, 188-191
32. YANG L.S., AKEMI I., HIDEO N., 1996 A valve train friction and lubrication analysis model and its application in a cam/tappet wear study, *SAE Paper*, **962030**

Manuscript received April 7, 2017; accepted for print November 13, 2018

INFORMATION FOR AUTHORS

Journal of Theoretical and Applied Mechanics (JTAM) is devoted to all aspects of solid mechanics, fluid mechanics, thermodynamics and applied problems of structural mechanics, mechatronics, biomechanics and robotics. Both theoretical and experimental papers as well as survey papers can be proposed.

We accept articles in English only. The text of a *JTAM* paper should not exceed **12 pages of standard format A4** (11-point type size, including abstract, figures, tables and references), short communications – **4 pages**.

The material for publication should be sent to the Editorial Office via electronic journal system: <http://www.ptmts.org.pl/jtam/index.php/jtam>

Papers are accepted for publication after the review process. Blind review model is applied, which means that the reviewers' names are kept confidential to the authors. The final decision on paper acceptance belongs to the Editorial Board.

After qualifying your paper for publication we will require L^AT_EX or T_EX or Word document file and figures.

The best preferred form of figures are files obtained by making use of editorial environments employing vector graphics:

- generated in CorelDraw (*.cdr), AutoCad and ArchiCad (*.dwg) and Adobe Illustrator (*.ai). We require original files saved in the standard format of the given program.
- generated by calculation software (e.g. Mathematica) – we need files saved in *.eps or *.pdf formats.
- made in other programs based on vector graphics – we ask for *.eps, *.wmf, *.svg, *.psfiles.

Any figures created without application of vector graphics (scans, photos, bitmaps) are strongly encouraged to be supplied in *.jpg, *.tif, *.png formats with resolution of at least 300 dpi.

Requirements for paper preparation

Contents of the manuscripts should appear in the following order:

- Title of the paper
- Authors' full name, affiliation and e-mail
- Short abstract (**maximum 100 words**) and 3-5 key words (**1 line**)
- Article text (equations should be numbered separately in each section; each reference should be cited in the text by the last name(s) of the author(s) and the publication year)
- References in alphabetical order. See the following:
 1. Achen S.C., 1989, A new boundary integral equation formulation, *Journal of Applied Mechanics*, **56**, 2, 297-303
 2. Boley B.A., Weiner J.H., 1960, *Theory of Thermal Stresses*, Wiley, New York
 3. Canon W., 1955, Vibrations of heated beams, Ph.D. Thesis, Columbia University, New York
 4. Deresiewicz H., 1958, Solution of the equations of thermoelasticity, *Proceedings of Third U.S. National Congress of Applied Mechanics*, 287-305
- Titles of references originally published not in English, should be translated into English and formulated as follows:
 5. Huber M.T., 1904, Specific work of strain as a measure of material effort (in Polish), *Czasopismo Techniczne*, **XXII**, 3, 80-81

All the data should be reported in **SI units**.

Contents

Dammak K., Koubaa S., Elhami A., Walha L., Haddar M. — Numerical modeling of uncertainty in acoustic propagation via generalized Polynomial Chaos	3
Ijaz H. — Mathematical modelling and simulation of delamination crack growth in Glass Fiber Reinforced Plastic (GFRP) composite laminates	17
Ou Z.-C., Li G.-Y., Duan Z.-P., Huang F.-L. — A stereological ubiquitous softening model for concrete	27
Poński M. — Time integration of stochastic generalized equations of motion using SSFEM	37
Akbarzadeh Khorshidi M., Shariati M. — Investigation of flexibility constants for a multi-spring model: a solution for buckling of cracked micro/nanobeams	49
Kosmol J. — An extended contact model of the angular bearing	59
Sidun P., Piwnik J. — Numerical analysis of contact plastic bodies made by aluminium alloy with taking account of micro-roughness surfaces	73
Yangui M., Bouaziz S., Taktak M., Debut V., Antunes J., Haddar M. — Numerical and experimental analysis of a segmented wind turbine blade under assembling load effects	85
Lewkowicz R., Kowaleczko G. — An inverse kinematic model of the human training centrifuge motion simulator	99
Markiewicz I. — Design with SADSf method and analyses of elastic properties of torsion-loaded structures based on double-tee sections	115
Zhu T., Huang D. — Influences of the diameter and position of the inner hole on the strength and failure of disc specimens of sandstone determined using the Brazilian split test	127
Świątek M., Domagalski Ł., Jędrysiak J. — Free vibrations spectrum of periodically inhomogeneous Rayleigh beams using the tolerance averaging technique	141
Kumar R., Vohra R. — Forced vibrations of a thermoelastic double porous microbeam subjected to a moving load	155
Obara P. — Application of linear six-parameter shell theory to the analysis of orthotropic tensegrity plate-like structures	167
Wang J., Hu Y., Su Y., Gong L., Zhang Q. — Magneto-elastic internal resonance of an axially moving conductive beam in the magnetic field	179
Imani Yengejeh S., Kazemi S.A., Öchsner A. — On the eigenmodes and eigenfrequencies of low-dimensional degenerated carbon structures: obtaining natural frequencies of ideal and structurally defected systems	193
Hemmatian H., Zamani M.R., Jam J.E. — Investigation of crack resistance in epoxy/boron nitride nanotube nanocomposites based on multi-scale method	207
Zahmatkesh I., Habibi M.R. — Natural and mixed convection of a nanofluid in porous cavities: critical analysis using Buongiorno's model	221
Skowronek P., Twardoch K., Skawiński P., Żołnierz M. — Strength analysis of hip joint replacement revision implant	235
Korczak A., Jasiński M. — Modelling of biological tissue damage process with application of interval arithmetic	249
Borkowski Ł. — Influence of the damping effect on the dynamic response of a plate	263
Siczek K., Stefański A. — Analysis of dynamics and friction resistance in the cam-tappet system	273